

---

# Fundamental Analysis of Hot Subdwarf Stars in the Gaia Era

---

FUNDAMENTALE ANALYSE HEISSER UNTERZWERGE IN DER  
GAIA ÄRA

DER NATURWISSENSCHAFTLICHEN FAKULTÄT  
DER FRIEDRICH-ALEXANDER-UNIVERSITÄT  
ERLANGEN-NÜRNBERG  
ZUR  
ERLANGUNG DES DOKTORGRADES

DR. RER. NAT.

VORGELEGT VON

DAVID MIRKO SCHNEIDER

Als Dissertation genehmigt  
von der Naturwissenschaftlichen Fakultät  
der Friedrich-Alexander-Universität Erlangen-Nürnberg  
Tag der mündlichen Prüfung: 2. August 2022

Gutachter: Prof. Dr. Ulrich Heber  
Prof. Dr. Klaus Werner

*Dedicated to my lovely parents,  
Edgar Josef Schneider  
and Veronika Marie Schneider, née Bucek,  
who always back me and the decisions I make,  
believe in me and my skills,  
and, last but not least,  
give me the love and the understanding  
that I need in order to master life courageously.*

*"Treasure the experience. Dreams fade away after you wake up."  
**Hitoha Miyamizu in Kimi no Na wa***

*"I was rushing desperately, trying to reach the light. When I thought I did, I  
reached a dead end instead. Then, I decided I wanted to enter that light. And at  
the edge of it, I found you."  
**Hodaka Morishima in Tenki no Ko***

*Elizabeth: "See? Not stars. They're doors." Booker DeWitt: "Doors to...?"  
Elizabeth: "To everywhere."  
**Elizabeth and Booker DeWitt in BioShock Infinite***

The following text is extracted from **Episode Three - "Hell Is Empty"** of the video game **Life Is Strange: Before the Storm**

Rachel Dawn Amber (R. D. A.): *"I've always loved stars."*

Chloe Elizabeth Price (C. E. P.): *"Why?"*

R. D. A.: *"They remind us that there's so much beauty out there, which we almost never see."*

C. E. P.: *"Because we're blinded by what's in front of us."*

R. D. A.: *"Exactly." "But then I learned the truth. The stars we're seeing have already been dead for millions of years. They're all... lies."*

C. E. P.: *"But that doesn't make them any less beautiful, right?"*

R. D. A.: *"I don't know. If they're not even real, then what's the point?" "It's all lies. Everything. My entire life. My dad. My mom. If I can even call her that anymore. And that other woman. My real mom. She's the biggest lie of all. I can't trust any of them. I think you're the only one in the world I can trust."*

C. E. P.: *"I don't know. I bet there's, like, one other chick in Australia who's super trustworthy."*

R. D. A.: *"No chance. You're one in a hundred infinities, Chloe Price." "I wore this bracelet my entire life. I never even asked why, never even thought about it. Somehow, I think I always knew. Even when I didn't know. That my real mother was gone." "The fact that she's here right now. That she came here. For me. I think I need to see her. Is that wrong?"*

C. E. P.: *"Of course not. But it – it might be tough to track her down."*

R. D. A.: *"Yeah. That's true. Luckily, I've got my secret weapon." "But what if we can't find her? It's not like I can ask my dad. I have no idea where to start."*

C. E. P.: *"I think I know what to do. I'll call Frank and get him to connect us to her."*

R. D. A.: *"You'd do that?"*

C. E. P.: *"I'll give it a shot."*

R. D. A.: *"Of course, even if we know where she is, we'd need a way to get to her. I can't just ask my parents for a ride."*

C. E. P.: *"Don't worry. I've got that one covered too."*

R. D. A.: *"You do?"*

C. E. P.: *"Yup. In fact, anything you could come up with, I'll handle it."*

R. D. A.: *"I know you will. But even if we find her... how will I talk to her? What do I say?"*

C. E. P.: *"After my dad died, I was worried I wouldn't know how to talk to him anymore. But somehow, when we speak, I always know what to say."*

R. D. A.: *"When you speak?"*

C. E. P.: *"In my dreams. He's there, and it's so real. It's almost like it's another part of my life. It used to be the only part that mattered." "I've never told anyone about that. Weird, huh?" "Uh... Rachel?"*

R. D. A.: *"I was just thinking. Maybe I was wrong before. Who cares if the stars are dead? As long as we can still see them, that means they're real...to us. Right?"*

C. E. P.: *"Right."*

# Abstract

Hot subdwarf stars of spectral types O and B (sdOs/sdBs) are located on and beyond the very hot end of the horizontal branch in the Hertzsprung-Russell diagram. They are highly evolved (post-)extreme horizontal branch ((post-)EHB) objects that are generally believed to be in the core helium-burning phase or beyond. Since the (post-)EHB covers a wide range of objects of different subtypes showing a variety of different properties, sdOs/sdBs can be considered a stellar zoo. These rather compact objects with radii of  $\sim 0.10$ - $0.30$  solar radii have stellar masses of about half a solar mass and exhibit hydrogen envelopes that typically make up less than 1% of the total mass. Such thin envelopes cannot be reached during a canonical stellar evolution on the red giant branch involving a core helium flash. In the past, several evolutionary links between the subtypes of sdOs/sdBs and other classes of stars have been proposed. However, various investigations are lacking to fully resolve the question on how these remarkable objects form.

To this end, the present work entitled “*Fundamental Analysis of Hot Subdwarf Stars in the Gaia Era*” presents an in-depth fundamental stellar analysis of a carefully chosen set of 63 known and candidate sdOs/sdBs that represents all relevant subtypes. The sample covers the full range of atmospheric parameters (effective temperature  $T_{\text{eff}}$ , surface gravity  $\log g$ , and helium abundance  $\log n(\text{He})$ ) of single and binary stars, pulsating and non-pulsating objects, and stars with particularly peculiar abundance anomalies, including  $^3\text{He}$  enrichment.

Precise and accurate atmospheric parameters are prerequisites in order to understand the nature and the evolution of the various subtypes of hot subdwarf stars. The first part of this work therefore focuses on in-depth spectroscopic analyses, making use of observed spectra of excellent quality in terms of signal-to-noise, spectral resolution, and wavelength coverage as well as of sophisticated model atmospheres and analysis strategies. A sample of 17 stars with optimum data quality (spectra taken with the XSHOOTER spectrograph at the ESO VLT) serves as a reference. In terms of model atmospheres, three sets are used in order to study the impact of different effects in great detail, including departures from local thermodynamic equilibrium (LTE) and metal line-blanketing. Classical metal line-blanketed LTE models (Heber et al., 2000) are compared to non-LTE (NLTE) model atmospheres with limited metal line-blanketing as well as to hybrid models that allow to treat NLTE effects and extensive metal line-blanketing. In terms of analysis strategies, two different methods are compared: the classical approach of analyzing preselected suitable spectral lines versus a global approach where the whole spectrum is fitted at once and only obvious outliers are excluded.

For the very first time, precise parallax measurements of the *Gaia* satellite allow to reliably convert atmospheric parameters into fundamental ones (radius  $R$ , luminosity  $L$ , and mass  $M$ ). In order to do so, however, knowledge of the stellar angular diameter is required, which can be retrieved from spectral energy distribution (SED) fitting to appropriate photometric

data. Hence, the second part of this work deals with the construction and the analysis of SEDs as well as with the subsequent derivation of the fundamental stellar parameters. In this way, a consistent comparison to the predictions of the theoretical evolutionary models for hot subdwarf stars is ensured.

The results of the present work show that the optimum effective temperature regime for the LTE models is between  $\sim 25\,000$  K and  $\sim 32\,000$  K. For lower and in particular higher temperatures, NLTE effects prevail. On average, the hybrid models result in higher surface gravities compared to LTE (by  $\sim 0.05$  to  $\sim 0.10$  dex), but at the same time the corresponding helium abundances are lower. This is explained by the anti-correlation between  $\log(g)$  and  $\log n(\text{He})$ . Compared to LTE, the NLTE models yield significantly higher effective temperature values (up to  $\sim 1700$  K) for the hotter stars, which can mainly be explained by the backwarming effect due to the limited metal line-blanketing of the NLTE models. The same applies to the comparison between the hybrid and the NLTE models for which differences of up to  $\sim 2000$  K are measured for individual program stars. Interestingly, the hybrid models also result, on average, in higher surface gravities (by  $\sim 0.08$  to  $\sim 0.15$  dex) compared to the NLTE models. Therefore, it is highly likely that metal line-blanketing also plays an essential role here. For the effective temperature regime of  $20\,000\text{ K} \lesssim T_{\text{eff}} \lesssim 40\,000\text{ K}$ , the hybrid models can be considered the new standard because these models yield consistent results, regardless of whether the selective or the global analysis approach is used.

Additionally, regression curves are determined, allowing to update published atmospheric parameters without having to actually perform the respective spectroscopic analyses based on the new hybrid LTE/NLTE approach.

In literature, the hydrogen Paschen series has very rarely been used as a diagnostic tool for hot subdwarf stars. Instead, the Balmer series is often used. The tests performed in this work show that both series deliver consistent results. This is very promising because many of the current and future spectrographs are configured for the near-infrared wavelength regime with the Paschen series.

Building on these investigations, the hybrid models are primarily used to evaluate the spectra of the sample quantitatively. It turns out that two thirds ( $\sim 67\%$ ) of all program stars belong to the group of hydrogen-rich hot subdwarfs, whereas their (intermediate) helium-rich siblings make up  $\sim 17\%$ . The majority of the program stars ( $\sim 62\%$ ) are indeed core helium-burning objects that are located on the EHB. Another  $\sim 17\%$  are more evolved post-EHB objects for which core helium burning has already ended. The nature of two stars remains unclear. One object (GALEX J080510.9-105834) is confirmed to be a progenitor of an extremely low-mass helium-core white dwarf (pre-ELM), whereas for two other stars (Feige 36 and BD+42° 3250) a pre-ELM nature seems highly likely. Two more objects may be pre-ELMs, too, and one star could also be a post-asymptotic giant branch (post-AGB) object. Most of the observed SEDs are matched with single model atmospheres, but four targets show clear infrared excesses indicating the presence of a cool companion. Three of these spectroscopic binaries (SB 290, Feige 36, and EC 01541-1409) are new discoveries.

The isotopic abundance anomaly of helium is also investigated. For the analyzed  $^3\text{He}$  hydrogen-rich sdB program stars, it is found to be restricted to a narrow temperature strip between  $\sim 26\,000$  K and  $\sim 30\,000$  K. Strikingly, about half of the analyzed  $^3\text{He}$  program stars show

anomalous helium line profiles. The unusually broad wings and shallow cores of the spectral lines of the relevant stars indicate that the total helium abundance decreases with decreasing depth of the atmosphere by up to a factor of  $\sim 9.0$ , leading to an abundance stratification. The next analysis step comprises the determination of the metal abundances. For this, almost all lines detected in the optical and near-infrared wavelength regime of the analyzed high and medium-resolution spectra are used. The abundances of the chemical elements C, N, O, Ne, Mg, Al, Si, S, Ar, and Fe are analyzed in NLTE. In addition, P, Ca, Ti, Sr, and Zr lines are found for some program stars of the XSHOOTER reference sample and are analyzed in LTE. In consequence, the metal abundance study presented in this work represents a major improvement over published results. The analyses of the sharp metal line profiles also allow to accurately determine the projected rotational velocities. As expected, most of the program stars turn out to be slow rotators. However, eleven stars show significant rotation, including three new discoveries. The exceptionally high projected rotational velocity ( $v \sin i = 142.0^{+9.0}_{-11.0} \text{ km s}^{-1}$ ) of GALEX J203913.4+201309 is truly remarkable given the fact that faster rotation has only been reported for hot subdwarf stars that have filled their Roche lobes and started mass transfer onto a white dwarf companion.

Last but not least, the radii, the luminosities, and the masses of the sample stars are determined. The radius distribution ( $0.10\text{-}0.30 R_{\odot}$ ) determined for the hydrogen-rich hot subdwarf program stars is consistent with predictions of canonical evolutionary models, but is of bimodal shape, showing two well-defined peaks at  $R_1 = 0.138 R_{\odot}$  and  $R_2 = 0.205 R_{\odot}$ . The same applies to the corresponding luminosity distribution (with abscissa  $\log L/L_{\odot}$ ), which peaks at  $L_1 = 1.291$  and  $L_2 = 2.090$ , respectively. The mass distribution is also largely consistent with the predictions of the canonical models and can be described by a single Gaussian peaking at  $M_p = 0.465 M_{\odot}$ . Regarding suggested evolutionary scenarios, this implies that the close binaries in the sample may have resulted from envelope stripping by the companion at the end of the red giant branch. For the single hydrogen-rich hot subdwarf program stars, however, internal mixing seems to be more likely than the competing scenario of the merger of two helium-core white dwarfs, although the latter could in principle explain the observed high-mass outliers. Some outliers at the low-mass end of the mass distribution are rather difficult to reconcile with any of the formation channels of hot subdwarf stars known today.

This work represents a milestone for future studies of hot subdwarf stars by quantifying the systematic uncertainties of the three atmospheric parameters  $T_{\text{eff}}$ ,  $\log(g)$ , and  $\log n(\text{He})$ . Together with the more precise trigonometric parallaxes from future data releases of the *Gaia* mission, this will allow to reliably determine the fundamental stellar parameters of thousands of hot subdwarf stars. The corresponding radius, luminosity, and mass distribution will lead to stringent tests of the theoretical evolutionary scenarios.



# Zusammenfassung

Im Hertzsprung-Russell-Diagramm liegen die heißen Unterzweige der Spektraltypen O und B (sdOs/sdBs = *hot subdwarf stars of spectral types O and B*) auf und jenseits des sehr heißen Endes des Horizontalastes. Sie sind weit entwickelte Objekte des (post-)extremen Horizontalastes ((post-)EHB = *(post-)extreme horizontal branch*), von denen allgemein angenommen wird, dass sie sich in der Phase des Kern-Heliumbrennens oder sogar darüber hinaus befinden. Die vielfältigen Eigenschaften der verschiedenen Untertypen von sdOs/sdBs machen diese Spektralklassen zu einem stellaren Zoo. Die Masse dieser recht kompakten Objekte mit Radien von  $\sim 0,10$ - $0,30$  Sonnenradien beträgt etwa eine halbe Sonnenmasse, während die ihrer Wasserstoffhüllen sehr gering ist, typischerweise weniger als 1 % der Gesamtmasse. Solch dünne Hüllen können im Rahmen der kanonischen Entwicklung des Vorgängersterns auf dem Roten Riesenast nicht erreicht werden. In der Vergangenheit wurden mehrere evolutionäre Zusammenhänge zwischen den Unterarten von sdOs/sdBs und anderen Sternklassen vorgeschlagen. Wie diese bemerkenswerten Objekte entstehen, ist aber immer noch in vielen Details unverstanden.

Zu diesem Zweck präsentiert die vorliegende Arbeit mit dem Titel „*Fundamentale Analyse heißer Unterzweige in der Gaia Ära*“ eine eingehende fundamentale stellare Analyse eines sorgfältig ausgewählten Satzes von 63 bekannten und potenziellen sdOs/sdBs, der alle relevanten Unterarten repräsentiert. Die Stichprobe deckt den gesamten Bereich atmosphärischer Parameter (Effektivtemperatur  $T_{\text{eff}}$ , Schwerebeschleunigung  $\log g$  und Heliumhäufigkeit  $\log n(\text{He})$ ) von Einzel- und Doppelsternen, von pulsierenden und nicht-pulsierenden Objekten sowie von Sternen mit besonders auffälligen Häufigkeitsanomalien (unter anderem  $^3\text{He}$ -Anreicherung) ab.

Um die Natur und die Entwicklung der verschiedenen Unterarten heißer Unterzweige zu verstehen, sind präzise und genaue atmosphärische Parameter notwendig. Der erste Teil dieser Arbeit konzentriert sich daher auf detaillierte spektroskopische Analysen, wobei beobachtete Spektren von hervorragender Qualität (Signal-zu-Rausch-Verhältnis, spektrale Auflösung und Wellenlängenabdeckung) sowie ausgefeilte Modellatmosphären und Analysestrategien verwendet werden. Als Referenz dient eine Stichprobe von 17 Sternen mit optimaler Datenqualität (Spektren aufgenommen mit dem XSHOOTER-Spektrographen am ESO VLT). Hinsichtlich der Modellatmosphären werden drei Sets verwendet, um den Einfluss verschiedener Effekte im Detail zu untersuchen, darunter Abweichungen vom lokalen thermodynamischen Gleichgewicht (LTE = *local thermodynamic equilibrium*) und das sogenannte “Metalllinien-Blanketing”. Klassische LTE-Modelle mit Metalllinien-Blanketing (Heber et al., 2000) werden mit Nicht-LTE-Modellatmosphären (NLTE-Modellatmosphären) mit geringem Metalllinien-Blanketing verglichen. Obendrein kommen Hybridmodelle zum Einsatz, die es ermöglichen, NLTE-Effekte und umfangreiches Metalllinien-Blanketing zu behandeln. Zwei Analysestrategien werden verglichen: der klassische Ansatz der Analyse vorselektierter geeigneter Spektrallinien gegenüber einem globalen Ansatz, bei dem das gesamte Spektrum auf einmal gefittet wird und nur of-

fensichtliche Ausreißer ausgeschlossen werden.

Präzise Parallaxenmessungen des *Gaia*-Satelliten ermöglichen es erstmals, atmosphärische Parameter zuverlässig in fundamentale Parameter (Radius  $R$ , Leuchtkraft  $L$  und Masse  $M$ ) umzurechnen. Dazu ist jedoch die Kenntnis des stellaren Winkeldurchmessers erforderlich, der aus der Anpassung der spektralen Energieverteilung (SED = *spectral energy distribution*) an geeignete photometrische Daten gewonnen werden kann. Daher beschäftigt sich der zweite Teil dieser Arbeit mit der Konstruktion und der Analyse von SEDs sowie mit der anschließenden Bestimmung der fundamentalen stellaren Parameter. Auf diese Weise wird ein konsistenter Vergleich mit den Vorhersagen der theoretischen Evolutionsmodelle für heiße Unterzwerge ermöglicht.

Die Ergebnisse der vorliegenden Arbeit zeigen, dass der optimale Effektivtemperaturbereich für die LTE-Modelle zwischen  $\sim 25\,000\text{ K}$  und  $\sim 32\,000\text{ K}$  liegt. Bei niedrigeren und insbesondere bei höheren Temperaturen überwiegen NLTE-Effekte. Verglichen mit den LTE-Modellen liefern die Hybridmodelle durchschnittlich höhere Schwerebeschleunigungen (von  $\sim 0,05$  bis  $\sim 0,10$  dex), gleichzeitig sind die zugehörigen Heliumhäufigkeiten jedoch geringer. Dies wird durch die Antikorrelation zwischen  $\log(g)$  und  $\log n(\text{He})$  erklärt. Im Vergleich zu den LTE-Modellen liefern die NLTE-Modelle deutlich höhere Effektivtemperaturwerte (von bis zu  $\sim 1700\text{ K}$ ) am heißen Ende, was hauptsächlich auf den sogenannten "Backwarming-Effekt" durch das geringere Metalllinien-Blanketing der NLTE-Modelle zurückzuführen ist. Gleiches gilt für den Vergleich zwischen den Hybrid- und den NLTE-Modellen, bei dem für einzelne Programmsterne Unterschiede von bis zu  $\sim 2000\text{ K}$  gemessen werden. Interessanterweise ergeben die Hybridmodelle gegenüber den NLTE-Modellen auch durchschnittlich höhere Schwerebeschleunigungen (von  $\sim 0,08$  bis  $\sim 0,15$  dex). Daher ist es sehr wahrscheinlich, dass auch hier das Metalllinien-Blanketing eine wesentliche Rolle spielt. Für den Effektivtemperaturbereich von  $20\,000\text{ K} \lesssim T_{\text{eff}} \lesssim 40\,000\text{ K}$  setzen die Hybridmodelle den neuen Standard, da diese Modelle konsistente Ergebnisse liefern, und zwar unabhängig davon, ob der selektive oder der globale Analyseansatz verwendet wird.

Bereits veröffentlichte atmosphärische Parameter lassen sich durch hier bestimmte Regressionskurven aktualisieren, ohne die entsprechenden spektroskopischen Analysen tatsächlich mit dem neuen hybriden LTE/NLTE-Ansatz wiederholen zu müssen.

In der Literatur wurde die Paschen-Serie des Wasserstoffs bisher kaum als diagnostisches Werkzeug für heiße Unterzwerge eingesetzt. Stattdessen wird häufig die Balmer-Serie genutzt. Die in dieser Arbeit durchgeführten Tests zeigen, dass beide Serien konsistente Ergebnisse liefern. Dies ist sehr vielversprechend, da viele der aktuellen und zukünftigen Spektrographen für den nahen Infrarot-Wellenlängenbereich mit der Paschen-Serie konfiguriert sind.

Aufbauend auf diesen Untersuchungen werden vorwiegend die hybriden Modelle genutzt, um die Spektren der Stichprobe quantitativ auszuwerten. Dabei ergibt sich, dass zwei Drittel ( $\sim 67\%$ ) aller Programmsterne zur Gruppe der wasserstoffreichen heißen Unterzwerge gehören, wohingegen ihre (mittleren) heliumreichen Geschwister  $\sim 17\%$  ausmachen. Die Mehrheit der Programmsterne ( $\sim 62\%$ ) befindet sich tatsächlich in der Phase des Kern-Heliumbrennens auf dem EHB. Weitere  $\sim 17\%$  sind weiterentwickelte Post-EHB-Objekte, bei denen das Kern-Heliumbrennen bereits beendet ist. Die Natur zweier Sterne bleibt unklar. Ein Objekt (GALEX J080510.9-105834) kann als Vorläufer eines extrem massearmen Weißen Zwerges mit Heli-

umkern (pre-ELM = *progenitor of an extremely low-mass helium-core white dwarf*) bestätigt werden, während für zwei andere Sterne (Feige 36 und BD+42° 3250) eine pre-ELM-Natur sehr wahrscheinlich scheint. Zwei weitere Objekte könnten ebenfalls pre-ELMs sein und bei einem einzigen Stern könnte es sich auch um ein Objekt des post-asymptotischen Riesenastes (post-AGB = *post-asymptotic giant branch*) handeln. Die meisten der beobachteten SEDs decken sich mit Einzelmodellatmosphären, während vier Ziele deutliche Überschüsse im Infrarotbereich zeigen, verursacht durch einen kühlen Begleiter. Drei dieser spektroskopischen Doppelsterne (SB 290, Feige 36 und EC 01541-1409) sind Neuentdeckungen.

Weiterhin wird die Isotopenanomalie des Heliums untersucht. Für die analysierten wasserstoffreichen  ${}^3\text{He}$ -sdB-Programmsterne erweist sie sich auf einen engen Temperaturstreifen zwischen  $\sim 26\,000\text{ K}$  und  $\sim 30\,000\text{ K}$  beschränkt. Auffälligerweise zeigt etwa die Hälfte der analysierten  ${}^3\text{He}$ -Programmsterne anomale Heliumlinienprofile. Die ungewöhnlich breiten Flügel und flachen Kerne der Spektrallinien der betreffenden Sterne deuten darauf hin, dass die Gesamtheliumhäufigkeit mit abnehmender Tiefe der Atmosphäre um bis zu einem Faktor von  $\sim 9,0$  abnimmt, was zu einer Häufigkeitsstratifikation führt.

Im nächsten Analyseschritt werden die Häufigkeiten der Metalle bestimmt. Dazu werden nahezu alle Linien, die im optischen und nahen Infrarot-Wellenlängenbereich der analysierten hoch- und mittelaufgelösten Spektren detektiert werden, herangezogen. Die Häufigkeiten der chemischen Elemente C, N, O, Ne, Mg, Al, Si, S, Ar und Fe werden in NLTE bestimmt. Darüber hinaus werden für einige Programmsterne der XSHOOTER-Referenzprobe P-, Ca-, Ti-, Sr- und Zr-Linien gefunden, die in LTE analysiert werden. Die aus der Metallanalyse resultierenden Ergebnisse sind demzufolge wesentlich genauer als bisher veröffentlichte. Da die Profile der Metalllinien sehr schmal sind, lassen sich damit auch die projizierten Rotationsgeschwindigkeiten sehr genau bestimmen. Wie erwartet, entpuppen sich die meisten Programmsterne als langsame Rotatoren. Elf Sterne zeigen jedoch eine signifikante Rotation, darunter auch drei Neuentdeckungen. Die außergewöhnlich hohe projizierte Rotationsgeschwindigkeit ( $v \sin i = 142,0_{-11,0}^{+9,0} \text{ km s}^{-1}$ ) von GALEX J203913.4+201309 ist besonders bemerkenswert angesichts der Tatsache, dass eine schnellere Rotation nur für heiße Unterzwerge berichtet wurde, die ihre "Roche Lobes" gefüllt und mit dem Massentransfer auf einen Weißen-Zwerg-Begleiter begonnen haben.

Abschließend werden die Radien, die Leuchtkräfte und die Massen der Sterne der Stichprobe bestimmt. Die Radiusverteilung ( $0,10\text{-}0,30 R_{\odot}$ ), die für die wasserstoffreichen heißen Unterzwerg-Programmsterne bestimmt wird, stimmt mit Vorhersagen kanonischer Entwicklungsmodelle überein, ist aber von bimodaler Form mit zwei wohldefinierten Maxima bei  $R_1 = 0,138 R_{\odot}$  und  $R_2 = 0,205 R_{\odot}$ . Gleiches gilt für die zugehörige Leuchtkraftverteilung (mit Abszisse  $\log L/L_{\odot}$ ), die bei  $L_1 = 1,291$  bzw.  $L_2 = 2,090$  ihre Maxima erreicht. Die Massenverteilung stimmt auch weitgehend mit den Vorhersagen der kanonischen Modelle überein und kann durch eine einzige Gaußfunktion mit einem Maximum bei  $M_p = 0,465 M_{\odot}$  beschrieben werden. Bezüglich der Entwicklungsgeschichte der engen Doppelsterne der Stichprobe erscheint ein Szenario wahrscheinlich, bei dem die Hülle des heißen Unterzwerg-Vorgängers am Ende der Entwicklung auf dem Roten Riesenast an den Begleiter abgegeben wurde. Für die wasserstoffreichen Unterzwerg-Programmsterne ohne Begleiter scheinen derweil interne Vermischungsprozesse wahrscheinlicher zu sein als das konkurrierende Szenario der Verschmelzung zweier

Weißer Zwerge mit Heliumkernen, auch wenn Letzteres die beobachteten massereichen Ausreißer prinzipiell erklären könnte. Einige Ausreißer am massearmen Ende der Massenverteilung sind nur schwer mit einem der heute bekannten Entwicklungskanäle für heiße Unterzwerge in Einklang zu bringen.

Diese Arbeit stellt einen Meilenstein für zukünftige Studien zu heißen Unterzwerge dar, indem sie die systematischen Unsicherheiten der drei atmosphärischen Parameter  $T_{\text{eff}}$ ,  $\log(g)$  und  $\log n(\text{He})$  quantifiziert. Zusammen mit den genaueren trigonometrischen Parallaxen aus zukünftigen Datenveröffentlichungen der *Gaia*-Mission wird dies die zuverlässige Bestimmung der fundamentalen stellaren Parameter von Tausenden von heißen Unterzwerge ermöglichen. Die zugehörige Radius-, Leuchtkraft- und Massenverteilung wird zu stringenten Tests der theoretischen Evolutionsszenarien führen.

# Table of Contents

<b>List of Figures</b>	<b>xvii</b>
<b>List of Tables</b>	<b>xxv</b>
<b>List of Acronyms and Abbreviations</b>	<b>xxxii</b>
<b>1. Introduction</b>	<b>1</b>
1.1. Aim of this Work . . . . .	2
1.2. Structure of this Work . . . . .	4
<b>2. Principles of Stellar Evolution</b>	<b>5</b>
2.1. Contraction of Stars Towards the Main Sequence . . . . .	5
2.2. Main-Sequence Phase . . . . .	6
2.3. Red Giant Phase . . . . .	10
2.4. Horizontal Branch . . . . .	11
2.5. Asymptotic Giant Branch . . . . .	12
2.6. End of the Giant Phase . . . . .	12
<b>3. Hot Subdwarf Stars</b>	<b>15</b>
3.1. History of Discovery and Classification . . . . .	15
3.2. The Hot Subdwarf Population - Characteristics and Atmospheric Properties . .	19
3.3. Chemical Composition . . . . .	24
3.4. Formation and Evolution . . . . .	43
3.4.1. Hot Subdwarf Binaries . . . . .	44
3.4.2. Single Helium-Rich Hot Subdwarf Stars . . . . .	49
3.4.3. Single Hydrogen-Rich Hot Subdwarf Stars . . . . .	54
3.4.4. Theoretical Mass Distribution . . . . .	55
<b>4. Spectroscopy - Studying Stellar Spectra with Optical Instruments</b>	<b>59</b>
4.1. Grating Spectrograph . . . . .	59
4.2. Echelle Spectrograph . . . . .	63
4.3. CCD Detectors . . . . .	64
4.4. Spectrographs Used . . . . .	66
<b>5. Astrometry - Three-Dimensional Mapping of the Milky Way with Gaia</b>	<b>73</b>
5.1. History and Planning Phase . . . . .	74
5.2. Mission Science . . . . .	75
5.3. Observation Principle . . . . .	79

5.4.	The Spacecraft . . . . .	81
5.5.	Using Gaia DR2 Parallaxes . . . . .	84
5.5.1.	Systematic Effects . . . . .	84
5.5.2.	Negative Parallaxes . . . . .	87
5.5.3.	The Distance Inference Problem . . . . .	89
5.5.4.	Bayesian Methods . . . . .	92
<b>6.</b>	<b>Modelling Stellar Atmospheres</b>	<b>95</b>
6.1.	Radiative Transfer . . . . .	96
6.2.	Basic Assumptions . . . . .	98
6.3.	Structural Equations . . . . .	101
6.4.	Local vs. Non-Local Thermodynamic Equilibrium (LTE vs. NLTE) . . . . .	104
6.5.	Spectral Line Formation . . . . .	109
6.5.1.	Microscopic Line Broadening . . . . .	110
6.5.2.	Macroscopic Line Broadening . . . . .	113
6.5.3.	Level Dissolution . . . . .	117
6.6.	Metal Line-Blanketing and Treatment of Opacity . . . . .	118
6.7.	The LTE Approach . . . . .	119
6.8.	ATLAS, DETAIL, SURFACE (ADS): The Hybrid LTE/NLTE Approach . . . . .	121
6.9.	TLUSTY/SYNSPEC: The NLTE Approach . . . . .	126
<b>7.</b>	<b>Combined Spectrophotometric and Astrometric Analysis</b>	<b>129</b>
7.1.	Quantitative Spectral Analysis . . . . .	129
7.1.1.	Spectral Fitting . . . . .	129
7.1.2.	Analysis Strategies . . . . .	136
7.2.	Photometry - Studying the Stellar Spectral Energy Distribution . . . . .	144
7.2.1.	ATLAS12 . . . . .	145
7.2.2.	TLUSTY/SYNSPEC . . . . .	145
7.2.3.	Photometric Analysis Methodology . . . . .	146
7.3.	Trigonometric Parallaxes and the Fundamental Stellar Parameters . . . . .	147
<b>8.</b>	<b>Observations and Data Preparation</b>	<b>151</b>
8.1.	Spectroscopic Data . . . . .	152
8.1.1.	The XSHOOTER Reference Sample . . . . .	152
8.1.2.	Increasing the Sample Size: High-Quality Optical Spectra from Other Instruments . . . . .	159
8.2.	Data Processing and Preparation . . . . .	165
8.2.1.	Telluric Absorption Correction with Molecfit . . . . .	166
8.2.2.	Radial Velocity Correction and Co-Addition . . . . .	171
8.2.3.	Channel Merging . . . . .	172
8.2.4.	Normalization . . . . .	173
8.2.5.	Spectral Line Identification . . . . .	175
8.3.	Photometric Data . . . . .	179
8.4.	Astrometric Data . . . . .	186

<b>9. Quantitative Spectral Analysis</b>	<b>191</b>
9.1. Spectral Line Fits . . . . .	192
9.2. Detailed Comparison of Different Model Atmosphere Approaches and Analysis Strategies . . . . .	205
9.2.1. SPAS vs. FITPROF . . . . .	206
9.2.2. LTE vs. Hybrid LTE/NLTE . . . . .	206
9.2.3. Global vs. Selective . . . . .	208
9.2.4. LTE vs. NLTE . . . . .	209
9.2.5. Hybrid LTE/NLTE vs. NLTE . . . . .	209
9.2.6. Influence of Metals in Spectral Synthesis . . . . .	210
9.2.7. Total Uncertainties of the Atmospheric Parameters . . . . .	211
9.3. Influence of the Hydrogen Paschen Series . . . . .	234
9.4. Final Atmospheric Results and Projected Rotational Velocities . . . . .	235
9.4.1. Effective Temperatures, Surface Gravities and Helium Content . . . . .	236
9.4.2. Rotational Broadening . . . . .	245
<b>10. Spectroscopic Analysis of the <sup>3</sup>He Anomaly Based on the Hybrid LTE/NLTE Approach</b>	<b>249</b>
10.1. Atmospheric Parameters and Projected Rotational Velocities . . . . .	250
10.1.1. Effective Temperatures, Surface Gravities and Helium Content . . . . .	253
10.1.2. Rotational Broadening . . . . .	255
10.2. Isotopic Helium Abundances . . . . .	256
10.2.1. The <sup>3</sup> He Subdwarf B Stars EC 03263-6403, EC 14338-1445, Feige 38, PG 1710+490 and Feige 36 . . . . .	257
10.2.2. The Two New <sup>3</sup> He Subdwarf B Stars from the ESO SPY Project: HE 0929-0424 and HE 1047-0436 . . . . .	258
10.2.3. Helium Line Profile Anomalies and Vertical Abundance Stratification . . . . .	259
10.2.4. Sensitivity Study . . . . .	267
<b>11. Metal Abundance Study Based on the Hybrid LTE/NLTE Approach</b>	<b>273</b>
11.1. NLTE Metal Abundances . . . . .	288
11.2. LTE Metal Abundances Derived from the XSHOOTER Reference Sample . . . . .	299
11.3. Detection of Chlorine and Krypton . . . . .	302
11.4. Detection of Silicon Line Emission . . . . .	302
<b>12. Photometric Results</b>	<b>305</b>
12.1. Spectroscopic Binary Systems with Main-Sequence Companions . . . . .	312
12.2. The Peculiar System of Feige 36 . . . . .	313
12.3. The Objects HD 149382 and GALEX J032139.8+472718 . . . . .	317
<b>13. Fundamental Stellar Parameters</b>	<b>321</b>
13.1. Radii . . . . .	322
13.1.1. Hydrogen-Rich Hot Subdwarf Stars . . . . .	322
13.1.2. Helium-Rich Hot Subdwarf Stars . . . . .	323

13.1.3. Other Program Stars . . . . .	325
13.2. Luminosities . . . . .	326
13.2.1. Hertzsprung-Russell Diagram . . . . .	326
13.2.2. Hydrogen-Rich Hot Subdwarf Stars . . . . .	326
13.2.3. Helium-Rich Hot Subdwarf Stars . . . . .	329
13.2.4. Other Program Stars . . . . .	329
13.3. Masses . . . . .	331
13.3.1. Mass vs. Effective Temperature and Mass vs. Surface Gravity Diagrams	331
13.3.2. Hydrogen-Rich Hot Subdwarf Stars . . . . .	332
13.3.3. Helium-Rich Hot Subdwarf Stars . . . . .	338
13.4. Comparison to Bayesian Methods . . . . .	338
<b>14. Summary and Outlook</b>	<b>353</b>
<b>Appendix A. Atmospheric and Photometric Results of the Analyzed Program Stars</b>	<b>359</b>
<b>Appendix B. Comparison of the Abundance Results for PHL 25 and PHL 382 to Hämmerich (2020)</b>	<b>383</b>
<b>Bibliography</b>	<b>385</b>
<b>Acknowledgements</b>	<b>403</b>
<b>The “Real” Acknowledgements</b>	<b>407</b>

## List of Figures

2.2.1. Sketch of an HRD (I). Adopted from <a href="https://www.atnf.csiro.au/outreach/education/senior/astrophysics/stellarevolution_deathlow.html">https://www.atnf.csiro.au/outreach/education/senior/astrophysics/stellarevolution_deathlow.html</a> (last called on 21st January 2021). . . . .	9
3.1.1. Sketch of an HRD (II). Adopted from Heber (2016); original version: Heber (2009). . . . .	16
3.1.2. Comparison of typical spectra of H-sdB and He-sdO stars displaying important hydrogen and helium absorption lines. Adopted from Heber (2016); original versions: Napiwotzki (2008) and Heber (2009). . . . .	17
3.2.1. Distribution of selected hot subdwarf stars in the $T_{\text{eff}}\text{-log}(g)$ and $T_{\text{eff}}\text{-log } n(\text{He})$ planes. Adopted from Heber (2016). . . . .	21
3.3.1. Elemental abundances of H-sdB (and H-sdOB) stars as a function of effective temperature. Adopted from Heber (2016); original versions: Geier (2013). . . . .	25
3.3.2. Mean elemental abundances and ranges by number fraction relative to solar for H-sdBs/H-sdOBs and intermediate He-sdBs. Additionally, the surface abundances for another three intermediate He-sdBs are plotted separately. Adopted from Heber (2016); original versions: Naslim et al. (2013) and Jeffery et al. (2015). . . . .	26
3.3.3. Photospheric elemental abundances for the three helium-poor sdO stars AA Dor, Feige 110, and EC 11481-2303 relative to the solar abundance level. Adopted from Heber (2016); original version: Rauch et al. (2014). . . . .	33
3.3.4. Photospheric elemental abundances for the four helium-poor sdO stars Feige 34, Feige 67, AGK+81° 266, and LS II +18° 9 relative to the solar abundance level. Adopted from Latour et al. (2018). . . . .	33
3.3.5. Abundance patterns (by number fraction) of the two heavy-metal intermediate He-sdBs LS IV-14° 116 and Feige 46 relative to that of the Sun. For comparison, abundance measurements for H-sdOBs in a similar effective temperature regime are plotted. Adopted from Dorsch et al. (2020). . . . .	35
3.3.6. Helium, carbon, and nitrogen abundances of 33 He-sdO stars from the ESO SPY project. Adopted from Heber (2016); original version: Hirsch (2009). . . . .	37
3.3.7. Abundance patterns of the four prototypical extreme He-sdO stars CD-31° 4800, LSS 1274, [CW83] 0904-02, and LS IV +10° 9 with respect to the solar composition. Adopted from Schindewolf et al. (2018). . . . .	38
3.3.8. Abundance patterns of the two H-sdB stars PG 0101+039 and Feige 48 relative to the solar abundance level and compared to predicted curves calculated by turbulent diffusion models after an EHB evolution of 25 million years. Adopted from Heber (2016); original versions: Michaud et al. (2011). . . . .	41

3.4.1.	Roche-lobe-overflow and common-envelope formation channels of hot subdwarf stars. Adopted from Heber (2016); original versions: Podsiadlowski (2008). . . . .	45
3.4.2.	Schematic of the three possible double HeWD merger scenarios which are able to form single helium-rich hot subdwarf stars. Adopted from Heber (2016); original version: Zhang & Jeffery (2012). . . . .	50
3.4.3.	Theoretical HRD for hot flasher evolutions. Modified version of Figure 1 in Battich et al. (2018). . . . .	53
3.4.4.	Mass distributions of hot subdwarf stars from different evolutionary channels in simulation set 2 - the best-choice model of Han et al. (2003). Modified version of Figure 12 in Han et al. (2003). . . . .	56
3.4.5.	Mass of early and late hot flasher models at helium ignition for different initial chemical compositions computed in different works. Adopted from Battich et al. (2018). . . . .	57
4.1.1.	Schematic setup and light path of a grating spectrograph. Adopted from Irrgang (2014). . . . .	60
4.1.2.	Schematic construction of a blaze grating. Adopted from Irrgang (2014). . . . .	61
4.2.1.	Schematic setup and light path of an Echelle spectrograph. Adopted from Irrgang (2014). . . . .	63
4.4.1.	Example of a raw Echelle spectrum observed in three different channels and obtained by means of the Integrated Field Unit of the XSHOOTER spectrograph. Adopted from Mieske et al. (2019). . . . .	65
4.4.2.	Schematic overview of the XSHOOTER instrument. Adopted from Vernet et al. (2011). . . . .	66
5.2.1.	Total numbers of <i>Gaia</i> DR2. Adopted from <a href="https://www.gaia.ac.uk/data/gaia-data-release-2">https://www.gaia.ac.uk/data/gaia-data-release-2</a> (last called on 29th March 2021). . . . .	77
5.3.1.	The observation principle of the <i>Gaia</i> satellite. Adopted from <a href="https://sci.esa.int/web/gaia/-/31360-orbit-navigation">https://sci.esa.int/web/gaia/-/31360-orbit-navigation</a> (last called on 30th March 2021). . . . .	80
5.4.1.	Schematic image of the focal plane assembly installed in the payload module of the <i>Gaia</i> satellite. Adopted from Gaia Collaboration et al. (2016b). Image from de Bruijne et al. (2010), Kohley et al. (2012), courtesy Airbus DS and Boostec Industries. . . . .	81
5.4.2.	Exploded, schematic view of the <i>Gaia</i> satellite. Adopted from Gaia Collaboration et al. (2016b). Credit: ESA, ATG Medialab. . . . .	83
5.5.1.	Parallax and normalized centred parallax distributions for sources identified as quasars within <i>Gaia</i> DR2. Adopted from Lindegren et al. (2018). . . . .	85
5.5.2.	Maps of the median parallaxes for the full quasar sample of Fig. 5.5.1 and for a sample of about 2.5 million sources in the area of the Large Magellanic Cloud. Adopted from Lindegren et al. (2018). . . . .	87
5.5.3.	Example of a negative parallax arising from the processing of the astrometric <i>Gaia</i> DR2 data. Adopted from Luri et al. (2018). . . . .	88

## List of Figures

---

5.5.4.	Probability distribution function of the distance estimate $\rho = 1/\varpi$ for two extreme cases. Adopted from Luri et al. (2018). . . . .	90
5.5.5.	Example of a $p = 95\%$ highest-density interval for an arbitrary asymmetric exponential distribution. Adopted from <a href="https://mathematica.stackexchange.com/questions/173282/computing-credible-region-highest-posterior-density-from-empirical-distributio">https://mathematica.stackexchange.com/questions/173282/computing-credible-region-highest-posterior-density-from-empirical-distributio</a> (last called on 5th April 2021). . . . .	91
6.5.1.	Cartesian coordinate system for the illustration of rotational broadening caused by the varying Doppler shifts of the individual surface elements of a star. Produced by A. Irrgang and shared via private communication. . . . .	116
6.8.1.	Scheme of the hybrid LTE/NLTE model atmosphere approach based on the four generic codes ATLAS9/ATLAS12, DETAIL, and SURFACE. Modified version of Figure 4.1 in Hämmerich (2020). . . . .	122
7.1.1.	Effects of variations of selected spectroscopic fit parameters on hydrogen, helium, and carbon spectral line shapes in a model spectrum. . . . .	131
7.1.2.	Influence of the isotopic abundance ratio ${}^4\text{He}/{}^3\text{He}$ and the total helium abundance $\log n({}^4\text{He} + {}^3\text{He})$ on the shape of selected neutral helium lines. Modified version of Figure 2 in Schneider et al. (2018). . . . .	134
7.1.3.	Screenshot of SPAS' graphical user interface showing all important features. Adopted from Schneider (2017). . . . .	138
7.1.4.	Example of a color-coded $\Delta\chi^2$ confidence map as a function of the effective temperature and the surface gravity. . . . .	143
7.3.1.	Scheme of the combined spectrophotometric and astrometric analysis approach used to derive the fundamental stellar parameters of a given star. . . . .	149
8.2.1.	Quality of the telluric absorption correction for the VIS and NIR channels of the XSHOOTER spectrum of the H-sdB program star HD 4539. . . . .	167
8.2.2.	Overview of the telluric absorption correction software workflow of <code>molecfit</code> . Adopted from ESO (2019). . . . .	169
8.2.3.	Workflow of the <code>molecfit</code> routine. Adopted from ESO (2019). . . . .	170
8.2.4.	Comparison of a single and non-normalized XSHOOTER spectrum of the H-sdB program star PG 1136-003 to the corresponding co-added one for a selected wavelength region. . . . .	172
8.2.5.	Channel merging carried out for the co-added XSHOOTER spectrum of the H-sdB program star HD 4539. . . . .	173
8.2.6.	Selected wavelength region of a single and non-normalized FEROS spectrum of the ${}^3\text{He}$ H-sdB program star SB 290 in SPAS. Adopted from Schneider (2017). . . . .	174
8.2.7.	Same selected wavelength region of the single but normalized FEROS spectrum of the ${}^3\text{He}$ H-sdB program star SB 290 in SPAS as displayed in Fig. 8.2.6. Adopted from Schneider (2017). . . . .	174

8.3.1.	Normalized filter response as a function of wavelength for some of the various different photometric filter systems used for the SED fitting performed in Ch. 12. Modified version of Figure 5.1 in Hämmerich (2020). . . . .	184
8.4.1.	Distances derived from Bayesian methods (Bailer-Jones et al., 2018) vs. distances determined by the <i>Gaia</i> satellite within DR2 for all program stars. . .	187
9.1.1.	Comparison of the observation to the global best fit of the co-added XSHOOTER spectrum of the H-sdB star HD 4539 for selected spectral ranges. . . . .	195
9.1.2.	Comparison of the observation to the global best fit of the co-added XSHOOTER spectrum of the H-sdOB star PG 1505+074 for selected spectral ranges. . .	196
9.1.3.	Selected hydrogen and helium lines in the IDS spectrum of the iHe-sdB star FBS 0654+366. . . . .	197
9.1.4.	Selected hydrogen and helium lines in the IDS spectrum of the iHe-sdB star FBS 0654+366 continued. . . . .	198
9.1.5.	Selected hydrogen and helium lines in the IDS spectrum of the iHe-sdB star FBS 0654+366 continued. . . . .	199
9.1.6.	Selected helium lines as well as the $H\gamma$ /He II blend in the co-added XSHOOTER spectrum of the He-sdO star HZ 1. . . . .	200
9.1.7.	Selected helium lines as well as the $H\beta$ /He II blend in the co-added XSHOOTER spectrum of the He-sdO star HZ 1. . . . .	201
9.1.8.	Selected helium lines as well as the $H\alpha$ /He II blend in the co-added XSHOOTER spectrum of the He-sdO star HZ 1. . . . .	202
9.1.9.	Selected helium lines in the NIR of the co-added XSHOOTER spectrum of the He-sdO star HZ 1. . . . .	203
9.1.10.	Selected helium lines in the NIR of the co-added XSHOOTER spectrum of the He-sdO star HZ 1 continued. . . . .	204
9.2.1.	$T_{\text{eff}}$ vs. $T_{\text{eff}}$ comparison plots for the different model atmosphere approaches and spectroscopic analysis techniques used to analyze the hot subdwarf program stars of this work. . . . .	213
9.2.2.	$T_{\text{eff}}$ vs. $T_{\text{eff}}$ comparison plots for the different model atmosphere approaches and spectroscopic analysis techniques used to analyze the hot subdwarf program stars of this work continued. . . . .	214
9.2.3.	$T_{\text{eff}}$ vs. $T_{\text{eff}}$ comparison plots for the different model atmosphere approaches and spectroscopic analysis techniques used to analyze the hot subdwarf program stars of this work continued. . . . .	215
9.2.4.	$T_{\text{eff}}$ vs. $T_{\text{eff}}$ comparison plots for the different model atmosphere approaches and spectroscopic analysis techniques used to analyze the hot subdwarf program stars of this work continued. . . . .	216
9.2.5.	$\log(g)$ vs. $\log(g)$ comparison plots for the different model atmosphere approaches and spectroscopic analysis techniques used to analyze the hot subdwarf program stars of this work. . . . .	217
9.2.6.	$\log(g)$ vs. $\log(g)$ comparison plots for the different model atmosphere approaches and spectroscopic analysis techniques used to analyze the hot subdwarf program stars of this work continued. . . . .	218

## List of Figures

---

9.2.7. $\log(g)$ vs. $\log(g)$ comparison plots for the different model atmosphere approaches and spectroscopic analysis techniques used to analyze the hot subdwarf program stars of this work continued. . . . .	219
9.2.8. $\log(g)$ vs. $\log(g)$ comparison plots for the different model atmosphere approaches and spectroscopic analysis techniques used to analyze the hot subdwarf program stars of this work continued. . . . .	220
9.2.9. $\log n(\text{He})$ vs. $\log n(\text{He})$ comparison plots for the different model atmosphere approaches and spectroscopic analysis techniques used to analyze the hot subdwarf program stars of this work. . . . .	221
9.2.10. $\log n(\text{He})$ vs. $\log n(\text{He})$ comparison plots for the different model atmosphere approaches and spectroscopic analysis techniques used to analyze the hot subdwarf program stars of this work continued. . . . .	222
9.2.11. $\log n(\text{He})$ vs. $\log n(\text{He})$ comparison plots for the different model atmosphere approaches and spectroscopic analysis techniques used to analyze the hot subdwarf program stars of this work continued. . . . .	223
9.2.12. $\log n(\text{He})$ vs. $\log n(\text{He})$ comparison plots for the different model atmosphere approaches and spectroscopic analysis techniques used to analyze the hot subdwarf program stars of this work continued. . . . .	224
9.2.13. Comparisons of the maximum $1\sigma$ statistical uncertainties on $T_{\text{eff}}$ determined for the hot subdwarf program stars of this work. . . . .	225
9.2.14. Comparisons of the maximum $1\sigma$ statistical uncertainties on $\log(g)$ determined for the hot subdwarf program stars of this work. . . . .	226
9.2.15. Comparisons of the maximum $1\sigma$ statistical uncertainties on $\log n(\text{He})$ determined for the hot subdwarf program stars of this work. . . . .	227
9.2.16. $T_{\text{eff}}\text{-}\log(g)$ diagrams for the hot subdwarf program stars of this work comparing the results of ADS + FITPROF to LTE + FITPROF, of ADS + Global (without metals) to ADS + FITPROF as well as of ADS + Global (with metals) to ADS + Global (without metals). . . . .	228
9.2.17. $T_{\text{eff}}\text{-}\log n(\text{He})$ diagrams for the hot subdwarf program stars of this work comparing the results of ADS + FITPROF to LTE + FITPROF, of ADS + Global (without metals) to ADS + FITPROF as well as of ADS + Global (with metals) to ADS + Global (without metals). . . . .	229
9.2.18. $\log(g)\text{-}\log n(\text{He})$ diagrams for the hot subdwarf program stars of this work comparing the results of ADS + FITPROF to LTE + FITPROF, of ADS + Global (without metals) to ADS + FITPROF as well as of ADS + Global (with metals) to ADS + Global (without metals). . . . .	230
9.2.19. Histogram distributions of the deviations of $T_{\text{eff}}$ derived from the middle left-hand and middle right-hand panels of Fig. 9.2.2 as well as from the middle left-hand panel of Fig. 9.2.1. . . . .	231
9.2.20. Histogram distributions of the deviations of $\log(g)$ derived from the middle left-hand and middle right-hand panels of Fig. 9.2.6 as well as from the middle left-hand panel of Fig. 9.2.5. . . . .	232

9.2.21. Histogram distributions of the deviations of $\log n(\text{He})$ derived from the middle left-hand and middle right-hand panels of Fig. 9.2.10 as well as from the middle left-hand panel of Fig. 9.2.9. . . . .	233
9.4.1. Distribution of the program stars in the $\log(T_{\text{eff}})$ - $\log(g)$ plane (distinction according to the nature of the stars). . . . .	237
9.4.2. Distribution of the program stars in the $T_{\text{eff}}$ - $\log(g)$ plane (distinction according to the nature of the stars). . . . .	238
9.4.3. Distribution of the program stars in the $\log(T_{\text{eff}})$ - $\log(g)$ plane (XSHOOTER reference sample highlighted). . . . .	239
9.4.4. Distribution of the program stars in the $T_{\text{eff}}$ - $\log(g)$ plane (XSHOOTER reference sample highlighted). . . . .	240
9.4.5. Distribution of the program stars in the $\log(T_{\text{eff}})$ - $\log n(\text{He})$ plane (distinction according to the nature of the stars). . . . .	242
9.4.6. Distribution of the program stars in the $T_{\text{eff}}$ - $\log n(\text{He})$ plane (distinction according to the nature of the stars). . . . .	243
9.4.7. Distribution of the program stars in the $\log(T_{\text{eff}})$ - $\log n(\text{He})$ plane (XSHOOTER reference sample highlighted). . . . .	244
9.4.8. Distribution of the program stars in the $T_{\text{eff}}$ - $\log n(\text{He})$ plane (XSHOOTER reference sample highlighted). . . . .	244
10.0.1. Model spectra for He I 6678 Å calculated in LTE and NLTE for $T_{\text{eff}} = 28\,000$ K, $\log(g) = 5.60$ , and $\log n(\text{He}) = -2.00$ . Modified version of Figure 1 in Schneider et al. (2018). . . . .	250
10.1.1. Distribution of the $^3\text{He}$ program stars, for which medium or high-resolution spectra are analyzed, in the $T_{\text{eff}}$ - $\log(g)$ plane (distinction according to the nature of the stars). . . . .	254
10.2.1. $^3\text{He}$ and $^4\text{He}$ abundances of the analyzed $^3\text{He}$ program stars plotted against the effective temperature. . . . .	257
10.2.2. Selected He I lines in the FEROS spectrum of the rotating $^3\text{He}$ post-BHB star PHL 382. . . . .	260
10.2.3. Selected He I lines in the FEROS spectrum of the rotating $^3\text{He}$ post-BHB star PHL 382 continued. . . . .	261
10.2.4. Selected He I lines in the XSHOOTER spectrum of the $^3\text{He}$ H-sdB star EC 03591-3232. . . . .	262
10.2.5. Selected He I lines in the XSHOOTER spectrum of the $^3\text{He}$ H-sdB star EC 03591-3232 continued. . . . .	263
10.2.6. Distribution of the $^3\text{He}$ program stars, for which medium or high-resolution spectra are analyzed, in the $T_{\text{eff}}$ - $\log(g)$ plane (distinction between $^3\text{He}$ program stars that show no evidence for helium stratification and stratified ones). . . . .	264
10.2.7. Best fits by eye for the line cores and the line wings of He I 4026 Å and He I 4472 Å in the HRS spectrum of PHL 25. . . . .	267
11.0.1. Selected metal lines in the co-added XSHOOTER spectrum of the H-sdB star GALEX J104148.9-073031. . . . .	275

List of Figures

---

11.0.2. Selected metal (and hydrogen and helium) lines in the co-added XSHOOTER spectrum of the H-sdB star GALEX J104148.9-073031 continued. . . . .	276
11.0.3. Selected metal lines in the co-added FEROS spectrum of the rotating <sup>3</sup> He post-BHB star PHL 382. . . . .	277
11.0.4. Selected metal (and helium) lines in the co-added FEROS spectrum of the rotating <sup>3</sup> He post-BHB star PHL 382 continued. . . . .	278
11.0.5. Selected metal lines in the co-added FEROS spectrum of the <sup>3</sup> He H-sdB star EC 03591-3232. . . . .	279
11.0.6. Selected metal (and hydrogen and helium) lines in the co-added FEROS spectrum of the <sup>3</sup> He H-sdB star EC 03591-3232 continued. . . . .	280
11.0.7. Selected metal lines in the co-added FEROS spectrum of the <sup>3</sup> He H-sdB star EC 03591-3232 continued. . . . .	281
11.1.1. Chemical abundances from <sup>3</sup> He to neon plotted against the effective temperature $T_{\text{eff}}$ for the program stars, for which high and medium-resolution spectra are analyzed. . . . .	291
11.1.2. Chemical abundances from magnesium to iron plotted against the effective temperature $T_{\text{eff}}$ for the program stars, for which high and medium-resolution spectra are analyzed. . . . .	292
11.1.3. The chemical abundance patterns of selected analyzed program stars relative to the solar abundance level. . . . .	297
11.1.4. The chemical abundance patterns of selected analyzed program stars relative to the solar abundance level continued. . . . .	298
11.2.1. Measured calcium abundances plotted against the effective temperature $T_{\text{eff}}$ for the analyzed XSHOOTER program stars. . . . .	299
11.2.2. Selected metal lines in the co-added XSHOOTER spectrum of the iHe-sdB star [CW83] 0825+15. . . . .	301
11.4.1. Selected silicon emission (and other metal) lines in the co-added spectra of four analyzed program stars. . . . .	303
12.0.1. Comparison of the smoothed final synthetic spectrum of the H-sdB PG 1432+004 to photometric data. . . . .	307
12.0.2. Binary SED fit for the rapidly pulsating H-sdOB EC 01541-1409. . . . .	308
12.0.3. Binary SED fit for the rapidly rotating <sup>3</sup> He H-sdB SB 290. . . . .	309
12.0.4. Binary SED fit for the RV-variable star Feige 36. . . . .	310
12.2.1. TESS light curve observed for Feige 36. Produced by V. Schaffenroth and shared via private communication. . . . .	316
12.3.1. Single and binary SED fits for the H-sdOB HD 149382. . . . .	318
12.3.2. Single and binary SED fits for the H-sdB GALEX J032139.8+472718. . . . .	319
13.1.1. Radius distribution for the hydrogen-rich hot subdwarf program stars of this work based on the <i>Gaia</i> DR2 parallaxes. . . . .	324
13.2.1. Distribution of the program stars in the $\log(T_{\text{eff}})$ - $\log(L/L_{\odot})$ plane. . . . .	327
13.2.2. $\log(T_{\text{eff}})$ - $\log(L/L_{\odot})$ diagrams for hot subdwarf stars from parameter set 2 of Han et al. (2003). Adopted from Han et al. (2003). . . . .	328

---

13.2.3. Luminosity distribution for the hydrogen-rich hot subdwarf program stars of this work based on the <i>Gaia</i> DR2 parallaxes. . . . .	330
13.3.1. Distribution of the program stars in the $\log(T_{\text{eff}})$ - $M$ plane. . . . .	332
13.3.2. Distribution of the program stars in the $\log(T_{\text{eff}})$ - $M$ plane (enlarged). . . . .	333
13.3.3. Distribution of the program stars in the $\log(g)$ - $M$ plane. . . . .	334
13.3.4. Distribution of the program stars in the $\log(g)$ - $M$ plane (enlarged). . . . .	335
13.3.5. Mass distribution for the hydrogen-rich hot subdwarf program stars of this work based on the <i>Gaia</i> DR2 parallaxes. . . . .	337

## List of Tables

3.1.	Metallicity pattern used for the abundance analysis presented in Ch. 11. Modified version of Table 11.1 in Schneider (2017). . . . .	28
3.2.	Transitions and isotopic shifts $\Delta\lambda := \lambda_0(^3\text{He}) - \lambda_0(^4\text{He})$ of selected He I lines in the NUV, optical, and NIR spectral range up to principal quantum number $n = 8$ . Modified version of Table 1 in Schneider et al. (2018). . . . .	31
3.3.	Predicted masses and favored end products of the different evolutionary channels and scenarios forming hot subdwarf stars. . . . .	58
4.1.	References used for the descriptions of the individual instruments presented throughout Sect. 4.4. . . . .	68
5.1.	Basic performance statistics for <i>Gaia</i> DR2 astrometry and photometry. Adopted from Gaia Collaboration et al. (2018). . . . .	78
6.1.	Types of pressure broadening according to Gray (2005). . . . .	112
6.2.	LTE model grids used for the quantitative spectral analyses of the program stars. . . . .	120
6.3.	Model atoms for NLTE calculations used for the hybrid LTE/NLTE approach. . . . .	125
6.4.	Hybrid LTE/NLTE and NLTE model grids used for the quantitative spectral analyses of the program stars. . . . .	127
6.5.	Ions for which detailed model atoms are used in the model atmosphere calculations with TLUSTY/SYNSPEC. . . . .	127
8.1.	Spectroscopic data of the XSHOOTER reference sample. . . . .	153
8.2.	Spectroscopic data of the XSHOOTER reference sample continued. . . . .	154
8.3.	Spectroscopic data of the XSHOOTER reference sample continued. . . . .	155
8.4.	Spectroscopic data of the high-resolution sample. . . . .	156
8.5.	Spectroscopic data of the high-resolution sample continued. . . . .	157
8.6.	Spectroscopic data of the UVES medium-resolution sample. . . . .	158
8.7.	Spectroscopic data of the CAFOS low-resolution sample. . . . .	160
8.8.	Spectroscopic data of the CAFOS low-resolution sample continued. . . . .	161
8.9.	Spectroscopic data of the IDS low-resolution sample. . . . .	162
8.10.	Spectroscopic data of the IDS low-resolution sample continued. . . . .	163
8.11.	Spectroscopic data from literature. . . . .	164
8.12.	List of selected spectral lines observed in the (co-added) spectra of the program stars analyzed in this work. . . . .	176
8.13.	List of selected spectral lines observed in the (co-added) spectra of the program stars analyzed in this work continued. . . . .	177

8.14.	List of selected spectral lines observed in the (co-added) spectra of the program stars analyzed in this work continued. . . . .	178
8.15.	Photometric filter systems used for the SED fitting performed in Ch. 12. . .	180
8.16.	Photometric filter systems used for the SED fitting performed in Ch. 12 continued. . . . .	181
8.17.	Photometric filter systems used for the SED fitting performed in Ch. 12 continued. . . . .	182
8.18.	Comparison of <i>Gaia</i> DR2 distances and parallaxes to distances according to Bailer-Jones et al. (2018) for the program stars of this work. . . . .	189
8.19.	Comparison of <i>Gaia</i> DR2 distances and parallaxes to distances according to Bailer-Jones et al. (2018) for the program stars of this work continued. . . .	190
9.1.	Mean values and standard deviations of the Gaussian functions fitted to the histogram data shown in the lower panels of Figs. 9.2.19, 9.2.20, and 9.2.21.	208
9.2.	Mean values and standard deviations of the Gaussian functions fitted to the histogram data shown in the upper panels of Figs. 9.2.19, 9.2.20, and 9.2.21.	211
9.3.	The atmospheric parameters of the H-sdB stars HD 4539, GALEX J104148.9-073031, and Feige 38 that are derived from the respective co-added XSHOOTER spectra in three different ways. . . . .	235
9.4.	Program stars with significant projected rotational velocities. . . . .	246
10.1.	Effective temperatures, surface gravities, (isotopic) helium abundances, and isotopic abundance ratios of the $^3\text{He}$ program stars, for which medium or high-resolution spectra are analyzed. . . . .	251
10.2.	Effective temperatures, surface gravities, (isotopic) helium abundances, and isotopic abundance ratios of the $^3\text{He}$ program stars, for which medium or high-resolution spectra are analyzed, continued. . . . .	252
10.3.	Isotopic helium abundances determined for the (post-)BHB stars PHL 25 and PHL 382. . . . .	264
10.4.	Total helium abundances derived from the fits by eye performed for the line cores and the line wings of He I 4026 Å and He I 4472 Å in the spectra of the helium-stratified $^3\text{He}$ program stars of this work. . . . .	266
10.5.	Results of the sensitivity study. . . . .	269
10.6.	Influence of the He I 10 830 Å line on the sensitivity study in the case of BD+48° 2721. . . . .	271
11.1.	Carbon to phosphorus metal abundances that are determined from the hybrid LTE/NLTE model atmosphere approach and the global analysis strategy for the program stars, for which high and medium-resolution spectra are analyzed.	282
11.2.	Carbon to phosphorus metal abundances that are determined from the hybrid LTE/NLTE model atmosphere approach and the global analysis strategy for the program stars, for which high and medium-resolution spectra are analyzed, continued. . . . .	283

List of Tables

---

11.3.	Carbon to phosphorus metal abundances that are determined from the hybrid LTE/NLTE model atmosphere approach and the global analysis strategy for the program stars, for which high and medium-resolution spectra are analyzed, continued. . . . .	284
11.4.	Sulfur to zirconium metal abundances that are determined from the hybrid LTE/NLTE model atmosphere approach and the global analysis strategy for the program stars, for which high and medium-resolution spectra are analyzed.	285
11.5.	Sulfur to zirconium metal abundances that are determined from the hybrid LTE/NLTE model atmosphere approach and the global analysis strategy for the program stars, for which high and medium-resolution spectra are analyzed, continued. . . . .	286
11.6.	Sulfur to zirconium metal abundances that are determined from the hybrid LTE/NLTE model atmosphere approach and the global analysis strategy for the program stars, for which high and medium-resolution spectra are analyzed, continued. . . . .	287
12.1.	Parameters of the spectroscopic binary systems with main-sequence companions analyzed in this work. . . . .	311
13.1.	Mean values and standard deviations of the (bimodal) Gaussian functions fitted to the histogram data shown in Figs. 13.1.1, 13.2.3, and 13.3.5. . . . .	331
13.2.	Fundamental stellar parameters of the analyzed XSHOOTER program stars. . . . .	340
13.3.	Fundamental stellar parameters of the analyzed XSHOOTER program stars continued. . . . .	341
13.4.	Fundamental stellar parameters of the program stars, which are analyzed by means of high-resolution data from FEROS, FOCES, HIRES, and HRS. . . . .	342
13.5.	Fundamental stellar parameters of the program stars, which are analyzed by means of high-resolution data from FEROS, FOCES, HIRES, and HRS, continued. . . . .	343
13.6.	Fundamental stellar parameters of the program stars, which are analyzed by means of medium-resolution data from UVES. . . . .	344
13.7.	Fundamental stellar parameters of the program stars, which are analyzed by means of low-resolution data from CAFOS. . . . .	345
13.8.	Fundamental stellar parameters of the program stars, which are analyzed by means of low-resolution data from CAFOS, continued. . . . .	346
13.9.	Fundamental stellar parameters of the program stars, which are analyzed by means of low-resolution data from IDS. . . . .	347
13.10.	Fundamental stellar parameters of the program stars, which are analyzed by means of low-resolution data from IDS, continued. . . . .	348
13.11.	Fundamental stellar parameters of the program stars, which are analyzed by means of low-resolution data from IDS, continued. . . . .	349
13.12.	Fundamental stellar parameters of the program stars from literature, for which no spectra are analyzed in this work. . . . .	350

---

13.13.	Fundamental stellar parameters of the program stars, for which spectra from multiple spectrographs are analyzed. . . . .	351
A.1.	Effective temperatures, surface gravities, helium abundances, angular diameters, and monochromatic color excesses of the analyzed XSHOOTER program stars. . . . .	360
A.2.	Effective temperatures, surface gravities, helium abundances, angular diameters, and monochromatic color excesses of the analyzed XSHOOTER program stars continued. . . . .	361
A.3.	Effective temperatures, surface gravities, helium abundances, angular diameters, and monochromatic color excesses of the analyzed XSHOOTER program stars continued. . . . .	362
A.4.	Effective temperatures, surface gravities, helium abundances, angular diameters, and monochromatic color excesses of the analyzed XSHOOTER program stars continued. . . . .	363
A.5.	Effective temperatures, surface gravities, helium abundances, angular diameters, and monochromatic color excesses of the analyzed XSHOOTER program stars continued. . . . .	364
A.6.	Effective temperatures, surface gravities, helium abundances, angular diameters, and monochromatic color excesses of the program stars, which are analyzed by means of high-resolution data from FEROS, FOCES, HIRES, and HRS. . . . .	365
A.7.	Effective temperatures, surface gravities, helium abundances, angular diameters, and monochromatic color excesses of the program stars, which are analyzed by means of high-resolution data from FEROS, FOCES, HIRES, and HRS, continued. . . . .	366
A.8.	Effective temperatures, surface gravities, helium abundances, angular diameters, and monochromatic color excesses of the program stars, which are analyzed by means of high-resolution data from FEROS, FOCES, HIRES, and HRS, continued. . . . .	367
A.9.	Effective temperatures, surface gravities, helium abundances, angular diameters, and monochromatic color excesses of the program stars, which are analyzed by means of high-resolution data from FEROS, FOCES, HIRES, and HRS, continued. . . . .	368
A.10.	Effective temperatures, surface gravities, helium abundances, angular diameters, and monochromatic color excesses of the program stars, which are analyzed by means of medium-resolution data from UVES. . . . .	369
A.11.	Effective temperatures, surface gravities, helium abundances, angular diameters, and monochromatic color excesses of the program stars, which are analyzed by means of low-resolution data from CAFOS. . . . .	370
A.12.	Effective temperatures, surface gravities, helium abundances, angular diameters, and monochromatic color excesses of the program stars, which are analyzed by means of low-resolution data from CAFOS, continued. . . . .	371

## List of Tables

---

A.13.	Effective temperatures, surface gravities, helium abundances, angular diameters, and monochromatic color excesses of the program stars, which are analyzed by means of low-resolution data from CAFOS, continued. . . . .	372
A.14.	Effective temperatures, surface gravities, helium abundances, angular diameters, and monochromatic color excesses of the program stars, which are analyzed by means of low-resolution data from CAFOS, continued. . . . .	373
A.15.	Effective temperatures, surface gravities, helium abundances, angular diameters, and monochromatic color excesses of the program stars, which are analyzed by means of low-resolution data from IDS. . . . .	374
A.16.	Effective temperatures, surface gravities, helium abundances, angular diameters, and monochromatic color excesses of the program stars, which are analyzed by means of low-resolution data from IDS, continued. . . . .	375
A.17.	Effective temperatures, surface gravities, helium abundances, angular diameters, and monochromatic color excesses of the program stars, which are analyzed by means of low-resolution data from IDS, continued. . . . .	376
A.18.	Effective temperatures, surface gravities, helium abundances, angular diameters, and monochromatic color excesses of the program stars, which are analyzed by means of low-resolution data from IDS, continued. . . . .	377
A.19.	Effective temperatures, surface gravities, helium abundances, angular diameters, and monochromatic color excesses of the program stars from literature, for which no spectra are analyzed in this work. . . . .	378
A.20.	Effective temperatures, surface gravities, helium abundances, angular diameters, and monochromatic color excesses of the program stars, for which spectra from multiple spectrographs are analyzed. . . . .	379
A.21.	Effective temperatures, surface gravities, helium abundances, angular diameters, and monochromatic color excesses of the program stars, for which spectra from multiple spectrographs are analyzed, continued. . . . .	380
A.22.	Effective temperatures, surface gravities, helium abundances, angular diameters, and monochromatic color excesses of the program stars, for which spectra from multiple spectrographs are analyzed, continued. . . . .	381
A.23.	Effective temperatures, surface gravities, helium abundances, angular diameters, and monochromatic color excesses of the program stars, for which spectra from multiple spectrographs are analyzed, continued. . . . .	382



## List of Acronyms and Abbreviations

<b>2M/2MASS</b>	Two Micron All Sky Survey
<b><math>3\alpha</math></b>	Triple Alpha
<b>AAL</b>	Astronomy Australia Limited
<b>AAVSO</b>	American Association of Variable Star Observers
<b>ADC</b>	Atmospheric Dispersion Corrector
<b>ADS</b>	Astrophysics Data System
<b>ADS</b>	Hybrid Model Atmosphere Approach Based on the Four Generic Codes ATLAS9, ATLAS12, DETAIL, and SURFACE
<b>aer</b>	Atmospheric and Environmental Research Inc.
<b>AG</b>	Acquisition and Guidance
<b>AGB</b>	Asymptotic Giant Branch
<b>AGB</b>	Asymptotic Giant Branch Star/Object
<b>AGIS</b>	Astrometric Global Iterative Solution
<b>AGK</b>	Astronomische Gesellschaft Katalog
<b>ALI</b>	Accelerated Lambda Iteration
<b>ANDS</b>	Australian National Data Service
<b>ANU</b>	Australian National University
<b>APASS</b>	AAVSO (American Association of Variable Star Observers) Photometric All Sky Survey
<b>ARC</b>	Australian Research Council
<b>ASVO</b>	All-Sky Virtual Observatory
<b>ATG</b>	AOES (Advanced Operation Engineering Services) Technology Group
<b>AU</b>	Astronomical Unit
<b>BD</b>	Brown Dwarf

<b>BD</b>	Bonner Durchmusterung
<b>BHB</b>	Blue Horizontal Branch
<b>BHB</b>	Blue Horizontal Branch Star/Object
<b>BJ</b>	Bailer-Jones
<b>B MS</b>	B-Type Main-Sequence Star
<b>BOK</b>	Bok Telescope
<b>BTJD</b>	Barycentric TESS (Transiting Exoplanet Survey Satellite) Julian Date
<b>CAFOS</b>	Calar Alto Faint Object Spectrograph
<b>CAHA</b>	Centro Astronómico Hispano-Alemán
<b>CARMENES</b>	Calar Alto High-Resolution Search for M Dwarfs with Exoearths with Near-Infrared and Optical Echelle Spectrographs
<b>CASU</b>	Cambridge Astronomical Survey Unit
<b>CB</b>	Compact Binary
<b>CCD</b>	Charge-Coupled Device
<b>CD</b>	Cordoba Durchmusterung
<b>CDS</b>	Centre de Données Astronomiques de Strasbourg
<b>CE</b>	Common Envelope
<b>CL</b>	Complete Linearization
<b>CI* Melotte</b>	Star in one of the Star Clusters Listed in the Melotte Catalogue of Open Star Clusters
<b>CN</b>	Carbon-Nitrogen
<b>CNO</b>	Carbon-Nitrogen-Oxygen
<b>CNR</b>	Consiglio Nazionale delle Ricerche
<b>CNRS</b>	Centre National de la Recherche Scientifique
<b>COVID-19</b>	Coronavirus Disease 2019
<b>CRF</b>	Celestial Reference Frame
<b>CSIC</b>	Consejo Superior de Investigaciones Científicas
<b>CU</b>	Calibration Unit

## List of Acronyms and Abbreviations

---

<b>[CW83]</b>	Carnochan & Wilson (1983)
<b>DD</b>	Double Degenerate
<b>DENIS</b>	Deep Near Infrared Survey
<b>DFG</b>	Deutsche Forschungsgemeinschaft
<b>DGICT</b>	Dirección General de Investigación Científica y Técnica
<b>DM</b>	Deep Mixing
<b>dM</b>	Low-Mass Main-Sequence Star
<b>DOF</b>	Degree of Freedom
<b>DPAC</b>	Data Processing and Analysis Consortium
<b>DR</b>	Data Release
<b>DR1</b>	Data Release 1; Mainly that of the <i>Gaia</i> (Global Astrometric Interferometer for Astrophysics) Mission
<b>DR2</b>	Data Release 2; Mainly that of the <i>Gaia</i> (Global Astrometric Interferometer for Astrophysics) Mission
<b>DR3</b>	Data Release 3; Mainly that of the <i>Gaia</i> (Global Astrometric Interferometer for Astrophysics) Mission
<b>DS</b>	Defence and Space
<b>EADS</b>	European Aeronautic Defence and Space
<b>EC</b>	Edinburgh-Cape Blue Object Survey
<b>ECAP</b>	Erlangen Centre for Astroparticle Physics
<b>EDR3</b>	Early Data Release 3 of the <i>Gaia</i> (Global Astrometric Interferometer for Astrophysics) Mission
<b>EHB</b>	Extreme Horizontal Branch
<b>EHB</b>	Extreme Horizontal Branch Star/Object
<b>EHF</b>	Early Hot Flasher
<b>EIF</b>	Education Investment Fund
<b>ELM</b>	Extremely Low-Mass Helium-Core White Dwarf
<b>ELTE</b>	Eötvös Loránd University
<b>EMM</b>	ESO (European Southern Observatory) Meteo Monitor
<b>EREBOS</b>	Eclipsing Reflection Effect Binaries from Optical Surveys

<b>ESA</b>	European Space Agency
<b>ESO</b>	European Southern Observatory
<b>ESO C&amp;EE</b>	European Southern Observatory's Support Programme for Central and East European Astronomers
<b>ESO SPY</b>	European Southern Observatory Supernova Ia Progenitor Survey
<b>ESO VLT</b>	European Southern Observatory Very Large Telescope
<b>E-SVM</b>	Electrical Service Module
<b>EVR</b>	Evrscope
<b>FAPESP</b>	Fundação de Amparo à Pesquisa do Estado de São Paulo
<b>FB</b>	Faint Blue
<b>FBS</b>	First Byurakan Survey
<b>FEROS</b>	Fibre-Fed Extended Range Optical Spectrograph
<b>FFwFBWF</b>	Fonds zur Förderung der wissenschaftlichen Forschung der Behörde für Wissenschaft und Forschung
<b>FOCES</b>	Fibre Optics Cassegrain Echelle Spectrograph
<b>FUSE</b>	Far Ultraviolet Spectroscopic Explorer
<b>FUV</b>	Far Ultraviolet
<b>FWHM</b>	Full Width at Half Maximum
<b>Gaia/GAIA</b>	Global Astrometric Interferometer for Astrophysics
<b>GALEX</b>	Galaxy Evolution Explorer
<b>GALEX</b>	Catalog of GALEX (Galaxy Evolution Explorer) Ultraviolet Sources
<b>GDAS</b>	Global Data Assimilation System
<b>GSAC</b>	German-Spanish Astronomical Center
<b>GUI</b>	Graphical User Interface
<b>HB</b>	Horizontal Branch
<b>HB</b>	Horizontal Branch Star/Object
<b>HCM</b>	Human Capital and Mobility
<b>HD</b>	Henry Draper Catalogue

## List of Acronyms and Abbreviations

---

<b>HDI</b>	Highest-Density Interval
<b>HE</b>	Hamburg/ESO (European Southern Observatory) Survey
<b>He-CO WD</b>	Hybrid White Dwarf with a Carbon-Oxygen Core and a Thick Helium Envelope
<b>HeMS</b>	Helium Main Sequence
<b>He-sdB</b>	Helium-Rich Hot Subdwarf B Star
<b>He-sdO</b>	Helium-Rich Hot Subdwarf O Star
<b>HET</b>	Hobby-Eberly Telescope
<b>HeWD</b>	Helium White Dwarf
<b>HgMn</b>	Mercury-Manganese
<b>HHE</b>	Hydrogen-Helium
<b>HHeCNO</b>	Hydrogen-Helium-Carbon-Nitrogen-Oxygen
<b>HIP</b>	HIPPARCOS (High Precision Parallax Collecting Satellite) Catalogue
<b>HIPPARCOS</b>	High Precision Parallax Collecting Satellite
<b>HIRES</b>	High Resolution Echelle Spectrometer
<b>HITRAN</b>	High-Resolution Transmission Molecular Absorption Database
<b>HQS</b>	Hamburg Quasar Survey
<b>HRD</b>	Hertzsprung-Russell Diagram
<b>HRS</b>	High-Resolution Fibre-Coupled Echelle Spectrograph
<b>HRS2</b>	Second Generation of the High-Resolution Fibre-Coupled Echelle Spectrograph
<b>H-sdB</b>	Hydrogen-Rich Hot Subdwarf B Star
<b>H-sdO</b>	Hydrogen-Rich Hot Subdwarf O Star
<b>H-sdOB</b>	Hydrogen-Rich Hot Subdwarf OB Star
<b>HST</b>	Hubble Space Telescope
<b>HW Vir</b>	HW Virginis
<b>HZ</b>	Humason & Zwicky
<b>IAA</b>	Instituto de Astrofísica de Andalucía
<b>IAP</b>	Institut Astrophysique de Paris

<b>ICRF</b>	International Celestial Reference Frame
<b>ID</b>	Identification/Identity/Identifier
<b>IDS</b>	Intermediate Dispersion Spectrograph
<b>IFU</b>	Integrated Field Unit
<b>iHe-sdB</b>	Intermediate Helium-Rich Hot Subdwarf B Star
<b>INES</b>	IUE (International Ultraviolet Explorer) Newly Extracted Spectra
<b>ING</b>	Isaac Newton Group of Telescopes
<b>INSU</b>	Institut National des Sciences de l'Univers
<b>IR</b>	Infrared
<b>IRAF</b>	Image Reduction and Analysis Facility
<b>ISIS</b>	Intermediate-Dispersion Spectrograph and Imaging System
<b>ISIS</b>	Interactive Spectral Interpretation System
<b>ISM</b>	Interstellar Medium
<b>IUE</b>	International Ultraviolet Explorer
<b>JINA</b>	Joint Institute for Nuclear Astrophysics
<b>KDE</b>	K Desktop Environment
<b>Kepler</b>	Kepler Catalog
<b>KiDS</b>	Kilo-Degree Survey
<b>KPD</b>	Kitt Peak-Downes Survey of the Galactic Plane
<b>KUV</b>	Kiso Observatory Survey of UV-Excess (Ultraviolet-Excess) Objects
<b>L</b>	Level
<b>LBLRTM</b>	Line-by-Line Radiative Transfer Model
<b>LEOP</b>	Launch and Early Orbit Phase
<b>LIEF</b>	Linkage Infrastructure, Equipment and Facilities
<b>LMC</b>	Large Magellanic Cloud
<b>LS</b>	Luminous Star in the Northern Hemisphere
<b>LSS</b>	Luminous Star in the Southern Hemisphere
<b>LTE</b>	Local Thermodynamic Equilibrium

## List of Acronyms and Abbreviations

---

<b>MAST</b>	Mikulski Archive for Space Telescopes
<b>MCT</b>	Montreal-Cambridge-Tololo
<b>MEN</b>	Ministry of National Education
<b>MIDAS</b>	Munich Image Data Analysis System
<b>MIT</b>	Massachusetts Institute of Technology
<b>MK</b>	Morgan-Keenan
<b>MMT</b>	Multiple/Magnum Mirror Telescope
<b>MMTO</b>	Multiple Mirror Telescope Observatory
<b>MPG</b>	Max Planck Gesellschaft
<b>MPI</b>	Max Planck Institute/Max-Planck-Institut
<b>MPIA</b>	Max Planck Institute for Astronomy/Max-Planck-Institut für Astronomie
<b>MS</b>	Main Sequence
<b>MS</b>	Main-Sequence Star
<b>M-SVM</b>	Mechanical Service Module
<b>MUSE</b>	Multi Unit Spectroscopic Explorer
<b>NASA</b>	National Aeronautics and Space Administration
<b>NCI</b>	National Computational Infrastructure
<b>NCRIS</b>	National Collaborative Research Infrastructure Strategy
<b>NeCTAR</b>	National eResearch Collaboration Tools and Resources
<b>NIR</b>	Near Infrared
<b>NIR</b>	Near-Infrared Channel of the XSHOOTER Spectrograph
<b>NIST</b>	National Institute of Standards and Technology
<b>NLTE</b>	Non-Local Thermodynamic Equilibrium
<b>NOAO</b>	National Optical Astronomy Observatory
<b>NUV</b>	Near Ultraviolet
<b>ODF</b>	Opacity Distribution Function
<b>OGLE</b>	Optical Gravitational Lensing Experiment
<b>OS</b>	Opacity Sampling

<b>OTKA</b>	Orszagos Tudomanyos Kutatasi Alap (Hungarian: National Scientific Research Fund)
<b>PanSTARRS/Pan-STARRS</b>	Panoramic Survey Telescope and Rapid Response System
<b>PB</b>	Palomar-Berger (A Search for Faint Blue Stars in High Galactic Latitudes)
<b>PG</b>	Palomar-Green (Catalogue of Ultraviolet-Excess Stellar Objects)
<b>PHL</b>	Palomar-Haro-Luyten Catalogue
<b>PLM</b>	Payload Module
<b>Pop I</b>	Population I
<b>Pop II</b>	Population II
<b>pp</b>	Proton-Proton
<b>PS1</b>	PanSTARRS1/Pan-STARRS1 (Panoramic Survey Telescope and Rapid Response System 1) Surveys
<b>RGB</b>	Red Giant Branch
<b>RGB</b>	Red Giant Branch Star/Object
<b>RLOF</b>	Roche-Lobe Overflow
<b>RMS</b>	Root Mean Square
<b>RUWE</b>	Renormalised Unit Weight Error
<b>RV</b>	Radial Velocity
<b>SB</b>	Slettebak & Brundage
<b>SB1</b>	Single-Lined Spectroscopic Binary
<b>SB2</b>	Double-Lined Spectroscopic Binary
<b>SBS</b>	Second Byurakan Survey
<b>SD</b>	Single Degenerate
<b>sd</b>	Hot Subdwarf Star
<b>sdB</b>	Hot Subdwarf B Star
<b>sdBV</b>	Variable/Pulsating Hot Subdwarf B Star
<b>sdO</b>	Hot Subdwarf O Star
<b>sdOB</b>	Hot Subdwarf OB Star

## List of Acronyms and Abbreviations

---

<b>SDSS</b>	Sloan Digital Sky Survey
<b>SDSS-III</b>	Third Observation Period of The Sloan Digital Sky Survey
<b>SED</b>	Spectral Energy Distribution
<b>SG</b>	Subgiant
<b>SIMBAD</b>	Set of Identifications, Measurements and Bibliography for Astronomical Data
<b>SL</b>	Superlevel
<b>slurm</b>	Simple Linux Utility for Resource Management
<b>SM</b>	Shallow Mixing
<b>S/N</b>	Signal-to-Noise (Ratio)
<b>SN(e) Ia</b>	Supernova(e) of Type Ia
<b>SN(e) Iax</b>	Supernova(e) of Type Iax
<b>SO</b>	Substellar Object
<b>SPAS</b>	Spectrum Plotting and Analysis Suite
<b>STIS</b>	Space Telescope Imaging Spectrograph
<b>STScI</b>	Space Telescope Science Institute
<b>TAHB</b>	Terminal-Age Horizontal Branch
<b>TAMS</b>	Terminal-Age Main Sequence
<b>TD1</b>	Thor-Delta 1A Satellite
<b>TE</b>	Thermodynamic Equilibrium
<b>TESS</b>	Transiting Exoplanet Survey Satellite
<b>TGAS</b>	<i>Tycho-Gaia</i> (Global Astrometric Interferometer for Astrophysics) Astrometric Solution
<b>ThAr</b>	Thorium-Argon
<b>TIC</b>	TESS (Transiting Exoplanet Survey Satellite) Input Catalog
<b>TOPCAT</b>	Tool for Operations on Catalogues and Tables
<b>TSS</b>	Telluric Standard Star
<b>TYC</b>	<i>Tycho</i> Catalogue
<b>UKIDSS</b>	UKIRT (United Kingdom Infrared Telescope) Infrared Deep Sky Survey

<b>UKIRT</b>	United Kingdom Infrared Telescope
<b>US</b>	UV-Excess (Ultraviolet-Excess) Starlike
<b>UT2</b>	Unit Telescope 2 (Kueyen) of the ESO VLT (European Southern Observatory Very Large Telescope)
<b>UV</b>	Ultraviolet
<b>UVB</b>	Ultraviolet/Blue Channel of the XSHOOTER Spectrograph
<b>UVES</b>	UV-Visual (Ultraviolet-Visual) Echelle Spectrograph
<b>UWE</b>	Unit Weight Error
<b>V*</b>	Variable Star
<b>VCS</b>	Vidal, Cooper & Smith
<b>VHS</b>	VISTA (Visible and Infrared Survey Telescope for Astronomy) Hemisphere Survey
<b>VIKING</b>	VISTA (Visible and Infrared Survey Telescope for Astronomy) Kilo-Degree Infrared Galaxy Survey
<b>VIS</b>	Visual Channel of the XSHOOTER Spectrograph
<b>VISTA</b>	Visible and Infrared Survey Telescope for Astronomy
<b>VLT</b>	Very Large Telescope
<b>VMC</b>	VISTA (Visible and Infrared Survey Telescope for Astronomy) Magellanic Survey
<b>VST</b>	VLT (Very Large Telescope) Survey Telescope
<b>WD</b>	White Dwarf
<b>WEAVE</b>	WHT (William Herschel Telescope) Enhanced Area Velocity Explorer
<b>WFAU</b>	Wide Field Astronomy Unit
<b>WFCAM</b>	UKIRT (United Kingdom Infrared Telescope) Wide Field Camera
<b>WHT</b>	William Herschel Telescope
<b>WISE</b>	Wide-Field Infrared Survey Explorer
<b>Xfce</b>	Xforms Common Environment
<b>ZAHB</b>	Zero-Age Horizontal Branch
<b>ZAMS</b>	Zero-Age Main Sequence

## List of Acronyms and Abbreviations

---

**ZTF** Zwicky Transient Facility



# 1. Introduction

This work focuses on the spectral class of hot subdwarf stars (sdOs/sdBs), which covers a wide range of objects of different subtypes showing a variety of different properties and may therefore be considered a stellar zoo. In fact, sdOs/sdBs are rather compact objects that exhibit typical radii of  $R_{\text{sd}} \sim 0.10\text{-}0.30 R_{\odot}$ . Furthermore, most of these objects have stellar masses of about half a solar mass, which is close to the canonical mass of  $\sim 0.46 M_{\odot}$  at which the helium core flash occurs during stellar evolution at the tip of the red giant branch. Thus, it is general consensus that hot subdwarfs are highly evolved objects that are in the core helium-burning phase or beyond. Surprisingly, the hydrogen envelopes of sdOs/sdBs typically only make up less than 1% of the total mass (Heber, 2009, 2016). Hence, their nature cannot be explained by the canonical stellar evolution on the red giant branch/horizontal branch because an isolated red giant cannot remove more than 99% of its hydrogen envelope by itself. Interestingly, a large fraction ( $\gtrsim 50\%$ ) of sdOs/sdBs is found in single-lined spectroscopic binary (SB1) systems with white dwarf companions (see, for instance, the works of Maxted et al. 2001, Napiwotzki et al. 2004a, or Copperwheat et al. 2011), whereas composite spectrum systems (double-lined spectroscopic binaries; SB2 systems), in which the primary hot subdwarf has a cool main-sequence companion, make up  $\sim 30\%$  of the hot subdwarf population (Stark & Wade, 2003). Only about 20% of the known sdOs/sdBs are found as single stars. The large binary fraction is the reason why hot subdwarfs are mainly believed to be the stripped helium cores of red giant stars that are formed via binary interaction processes, primarily involving Roche-lobe overflow and common-envelope ejection (Han et al., 2002, 2003). But other formation channels have also been proposed for hot subdwarf stars over the years, among them the early and late hot flasher scenarios (D’Cruz et al. 1996; e.g., Battich et al. 2018) or the merger of two helium white dwarfs (Webbink, 1984; Zhang & Jeffery, 2012), which are able to produce isolated sdOs/sdBs. Despite all of the currently available (canonical) formation channels, however, various investigations are lacking to fully resolve the issue on how these remarkable objects form.

From the theoretical point of view, the deep understanding and the further development of the individual formation channels and scenarios, which are able to produce single or binary hot subdwarf stars, is certainly crucial in order to get a complete picture. For a further development of these theoretical concepts, however, input from the observational side is required. As a matter of fact, the currently existing evolutionary models predict different specific ranges for the fundamental stellar parameters (radius, luminosity, and mass) of the produced hot subdwarfs. This is particularly true for the stellar mass (Han et al., 2002, 2003). Consequently, this means that the mass determination for a subdwarf sample of meaningful size is an intuitive way to test the theoretical models. From the observational point of view, the mass determination of hot subdwarf stars can be realized in different ways.

First, the fundamental stellar parameters of a hot subdwarf star can be derived from a combined light curve and spectroscopic analysis, if the object is part of an eclipsing binary system with a low-mass or substellar companion as in HW Virginis (HW Vir) systems (for a detailed overview of HW Vir systems, see Schaffenroth et al. 2019 and references therein). Unfortunately, such systems are rather rare such that the inferred mass statistics are low. However, a large number of potential candidates for new HW Vir systems were recently discovered by the OGLE (*Optical Gravitational Lensing Experiment*; for instance, see Soszyński et al. 2015) and the EREBOS (*Eclipsing Reflection Effect Binaries from Optical Surveys*; Schaffenroth et al. 2019) projects.

Second, it is known that various classes of pulsating stars are observed among hot subdwarfs, with sdBV being the oldest, largest, and best studied one. Thanks to asteroseismology, the global (mass, surface gravity, radius, etc.) and structural (hydrogen-envelope mass, core mass, core composition, etc.) parameters of a pulsating star can be accessed. In fact, Fontaine et al. (2012) carried out the asteroseismical modelling of 15 pulsating sdB stars, resulting in a mass distribution that strongly peaks at  $\sim 0.47 M_{\odot}$ , hence almost perfectly matching the canonical mass of  $\sim 0.46 M_{\odot}$ . Unfortunately, the asteroseismical approach is also limited, namely to the number of pulsating hot subdwarfs. However, the number of asteroseismically modelled hot subdwarf stars will steadily increase in the future thanks to the observations carried out by TESS (*Transiting Exoplanet Survey Satellite*; for recent discoveries, see, for instance, the results of Charpinet et al. 2019 or Sahoo et al. 2020).

Third, the radius, the luminosity, and the mass of any star, either isolated or in a binary system, can be determined from a combination of quantitative spectral analysis and spectral energy distribution (SED) fitting to appropriate photometric data, if the distance (trigonometric parallax) to the object is known from astrometry. So far, however, this method has only been applicable to a small number of hot subdwarf stars because reliable astrometric distance, that is, parallax measurements have been limited to the results of the *High Precision PARallax Collecting Satellite* (HIPPARCOS), which provided astrometry for bright objects with a limiting visual magnitude of  $V \sim 12.4$  mag only (ESA, 1997). Moreover, many of HIPPARCOS' astrometric solutions struggled with rather imprecise parallaxes, even within the second version of the HIPPARCOS Catalogue (van Leeuwen, 2007). This complicated firm conclusions on the stellar masses derived and, thus, also on the possible evolution of the respective hot subdwarfs. In consequence, precise and accurate mass determinations of sdOs/sdBs based on the interplay of spectroscopy, photometry, and astrometry are still scarce. At the same time, however, a large-size observational testbed for a verification of the theoretical evolutionary models is highly needed.

## 1.1. Aim of this Work

In the era of the *Gaia* (*Global Astrometric Interferometer for Astrophysics*; Gaia Collaboration et al. 2016b) mission, providing access to high-precision five-parameter astrometry (position, parallax, and proper motion) and photometry in the  $G$ ,  $G_{BP}$ , and  $G_{RP}$  bands (Evans et al., 2018) for more than 1.3 billion astronomical objects already in its second data release (DR2;

## 1.1. Aim of this Work

---

see Gaia Collaboration et al. 2018), the limiting factor for the determination of reliable fundamental stellar parameters of hot subdwarf stars may not be the parallax but the atmospheric parameters (the effective temperature and the surface gravity) derived from quantitative spectral analyses. High-quality, that is, high-resolution and/or high signal-to-noise (S/N) spectra with large wavelength coverage therefore are needed.

Consequently, the first major aim of the present work is the detailed spectroscopic, photometric, and, subsequently, fundamental analysis of a carefully chosen set of 63 known and candidate hot subdwarf stars that represents all relevant subtypes of sdOs/sdBs. The sample covers the full range of atmospheric parameters (effective temperature  $T_{\text{eff}}$ , surface gravity  $\log g$ , and helium abundance  $\log n(\text{He})$ ) observed for sdOs/sdBs. Furthermore, single and binary stars, pulsating and non-pulsating objects as well as stars with particularly peculiar abundance anomalies (for instance, that of  $^3\text{He}$ ) are included. High-quality spectra and reliable trigonometric parallaxes extracted from *Gaia* DR2<sup>1</sup> should be available for the selected targets. Inter alia, the results of the sdO/sdB analyses will provide detailed insights into the mass distribution of these extraordinary stars from the observational point of view. In this way, a comparison to the theoretical predictions will be possible.

In order to derive meaningful stellar masses, radii, and luminosities for the selected program stars, however, the focus must be on the precise determination of the systematic uncertainties of the atmospheric parameters, in particular that of  $\log(g)$ , as this parameter is the most important one when it comes to stellar masses in the case of reliable parallaxes. To achieve this, the results derived from different approaches of modelling stellar atmospheres as well as from different analysis strategies have to be combined. Such an in-depth comparison of model codes and analysis methods was recently successfully carried out by Blanco-Cuaresma (2019) for main-sequence stars of spectral types A, F, G, K, and M. The main outcome of this study was that code-to-code and method-to-method differences can affect the scientific interpretation of spectroscopic analyses of these stars to a significant extent. It is not surprising that such a sophisticated analysis is still missing for O and B-type stars, in particular for sdOs/sdBs, because these stars show several peculiarities in their spectra, which are not least due to the presence of atomic diffusion or elemental stratification. However, it is out of question that code-to-code and method-to-method differences also exist for spectroscopic analyses of hot subdwarf stars. The only question is how large they are. In consequence, the second major goal of the present work is the detailed comparison of different model atmosphere approaches and analysis strategies that are nowadays used to spectroscopically investigate sdOs/sdBs. In this way, the systematic uncertainties on the derived atmospheric parameters can be constrained, which, in turn, limits the error range for the fundamental stellar parameters. Moreover, such a sophisticated comparative analysis ensures deep insights into the careful consideration of the caveats of modern spectroscopic analyses of hot subdwarf stars.

---

<sup>1</sup>During the writing phase of this thesis, the results of *Gaia* Early Data Release 3 (EDR3; Gaia Collaboration et al. 2020) were made publicly available. However, the results of this work are mainly based on DR2 data (Gaia Collaboration et al., 2018) because the parallaxes from both data releases differ only slightly for the analyzed nearby program stars. Nonetheless, EDR3 data are additionally used in some cases. It is explicitly described in the text where this is the case.

## 1.2. Structure of this Work

To begin with, Ch. 2 describes the principles of stellar evolution. In Ch. 3, a detailed review of the most important aspects of hot subdwarf stars will be provided, including the proposed theoretical evolutionary scenarios. Chapter 4 presents the study of stellar spectra with optical instruments, that is, spectroscopy. Therein, also the instruments used to gather the spectral data analyzed in the context of this work will be introduced. Chapter 5 then describes the concept of astrometry by means of the astrometric data collected within the second data release of the *Gaia* satellite. Here, the focus is on the measured trigonometric parallaxes and the intricacies, pitfalls, and problems coming along with them. After that, Ch. 6 focuses on stellar atmospheres and the different ways of modelling them, whereby the model atmosphere approaches used in this work are described at the end of this chapter. Chapter 7 presents the general concepts of the aforementioned combined spectrophotometric and astrometric analysis approach, which can be used in stellar astronomy to determine the radius, the luminosity, and the mass of a given star. This chapter also introduces the two different strategies used for the quantitative spectral analyses performed in the present work. The spectroscopic, photometric, and astrometric data of the analyzed program stars will be presented in Ch. 8. Chapters 9, 10, and 11 present the spectroscopic results for the individual program stars, whereas Ch. 12 focuses on the photometric ones. Last but not least, Ch. 13 deals with the derived fundamental stellar parameters. The thesis concludes with Ch. 14, in which a short summary and an outlook are given.

## 2. Principles of Stellar Evolution

In the following sections, the reader shall be made familiar with the fundamentals of stellar evolution, that is, with the stellar life-cycle, which covers the evolutionary path of stars from their formation to the final stages. The information provided below is extracted from the textbook “*Fundamental Astronomy*” by Karttunen et al. (2007).

### 2.1. Contraction of Stars Towards the Main Sequence

It is generally believed that stars are formed from condensations of huge gas and dust clouds in the interstellar medium. Such a molecular cloud has a typical mass of  $\sim 10\,000 M_{\odot}$  when the pressure supporting it against its own gravity no longer is strong enough. As a consequence, the cloud begins to contract (gravitational collapse), leading to a release of potential energy of the inwards falling gas. This liberated energy is transformed into thermal energy of the gas and into radiation. Initially, the radiation is able to propagate freely through the material since the density is low and the absorption coefficient is small. Thus, most of the energy is radiated away such that the temperature does not increase significantly. However, the density and the pressure slowly but steadily increase near the centre of the cloud. Therefore, a larger fraction of the released energy is turned into heat, leading to a rise of temperature and pressure, which slows down the contraction of the inner part of the cloud. A *protostar*, mainly consisting of hydrogen in molecular form ( $H_2$ ), has formed. Its outer parts, however, are still free falling. At a temperature of about 1800 K, the  $H_2$  molecules are dissociated into atoms, which consumes energy and, hence, slows down the temperature and pressure increase. Consequently, the contraction rate increases. The same happens when hydrogen (at  $\sim 10^4$  K) and helium (at  $\sim 30\,000$  K) are ionized. The gas is fully ionized in the form of stellar *plasma* at a temperature value of  $\sim 10^5$  K. However, the contraction of the protostar already completely stops, once a large fraction of plasma has been formed. For solar-mass stars, this is the case after a few hundred years only. The protostar then reaches an equilibrium state and, because of the large absorption coefficient in its inner parts, becomes fully convective, meaning that energy is carried by material motions. In this way, the surface brightness of the protostar strongly increases. The protostellar radius, however, has shrunk from initially  $\sim 100 AU$  to  $\sim 0.25 AU$  and continues to decrease, which leads to a luminosity drop. The star now is located inside a larger gas cloud from which it accretes material, hence increasing its mass, central temperature, and density. Due to the continuous rise of the central temperature, the

---

<sup>2</sup>The astronomical unit (AU) is a common unit of length used in astronomy. 1 AU roughly corresponds to the mean distance from the Earth to the Sun and equals to  $1.495978707 \cdot 10^{11}$  m.

absorption coefficient diminishes and the star becomes radiative, meaning that energy is now transported by radiation. At the same time, thermonuclear fusion reactions of lithium (Li), beryllium (Be), and boron (B) are initiated such that the luminosity and the stellar surface temperature steadily increase. This phase occurs much earlier in massive stars since their central temperatures are higher so that the nuclear reactions can set in earlier. Moreover, the process takes place much faster for these stars because of their high luminosity. For instance, a  $\sim 15 M_{\odot}$  star contracts to the long and quiet main-sequence phase<sup>3</sup> in about 60 000 years, whereas for a solar-mass star this takes up to several tens of millions of years.

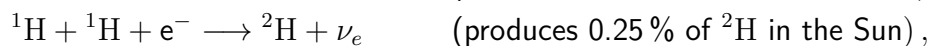
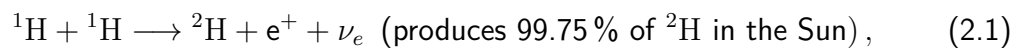
The above description details the protostellar evolution of a single star. In reality, however, a collapse of a molecular cloud leads to the production of an extensive amount of stars. In consequence, stars are never born alone.

## 2.2. Main-Sequence Phase

The *main-sequence* (MS) *phase* is the longest part of the stellar lifetime. It is characterized by two sequences, the zero-age MS (ZAMS) and the terminal-age MS (TAMS). In between both, nuclear reactions of hydrogen (*hydrogen burning*) take place in the core of the stable star. This is the only source of stellar energy during this evolutionary stage. The stellar structure only changes because of the fact that the chemical composition is gradually altered by the nuclear reactions. Hydrogen burning in MS stars (*dwarf stars*) is realized in two different ways: via the *proton-proton chain* or via the *carbon-nitrogen-oxygen cycle*, which is also referred to as the *Bethe-Weizsäcker cycle*. In the following, both processes will be presented whereby the energy released in each of the given reaction steps is omitted.

### Proton-Proton Chain

The proton-proton chain (pp chain) is the main energy production mechanism at central temperatures below  $(18 - 20) \cdot 10^6$  K (corresponding to stars with masses below  $\sim 1.5 M_{\odot}$ ). Typically, it consists of the following steps:



This is referred to as the ppl branch. For each reaction of Eq. (2.3), the reactions (2.1) and (2.2) have to occur twice. The probability of the first reaction step is very small. In fact, the time for a proton ( ${}^1\text{H}$ ) to collide with another one to form a deuteron ( ${}^2\text{H}$ ) is expected to

<sup>3</sup>Formally, the beginning of the main-sequence phase is marked by the start of hydrogen burning in the proton-proton chain at a central temperature of about  $4 \cdot 10^6$  K.

## 2.2. Main-Sequence Phase

---

be  $10^{10}$  years on average in the central part of the Sun. The slowness of this reaction is the reason why the Sun is still shining today. Furthermore, the abundance of  $^2\text{H}$  inside stars is very small because the reaction (2.2) is very fast. The net energy released by the ppl branch is about 26.20 MeV ( $\sim 4.20 \cdot 10^{-12}$  J) and it prevails at central temperatures of  $(10 - 14) \cdot 10^6$  K. Inside the Sun,  $\sim 91\%$  of  $^4\text{He}$  and, therefore, energy is produced by the ppl branch.

The last step of Eq. (2.3) can also be replaced by two different forms, which are referred to as the pplI and pplII branches. The pplI branch, producing about 9% of the energy in the Sun and prevailing at central temperatures of  $(14 - 23) \cdot 10^6$  K, is given by:



On the other hand, the pplII branch only makes up a small amount of energy that is produced in the Sun ( $\sim 0.1\%$ ). This is because it only dominates at very high central temperatures ( $\gtrsim 23 \cdot 10^6$  K), which are hardly given in the central parts of the Sun. The pplII branch is realized by the following reactions:



## Carbon-Nitrogen-Oxygen Cycle

The carbon-nitrogen-oxygen cycle (CNO cycle) becomes the dominant energy source at central temperatures higher than  $(18 - 20) \cdot 10^6$  K. This corresponds to stars with masses above  $\sim 1.5 M_\odot$ . The reaction cycle of the CNO process is given by:



Reaction step (2.14) is the slowest<sup>4</sup>. For instance, at a temperature of  $\sim 20 \cdot 10^6$  K this step needs  $\sim 10^6$  years. In massive stars, the whole CNO cycle takes up to hundreds of millions

---

<sup>4</sup>As a matter of fact, this is also the reason why the so-called CNO signature, where carbon and oxygen are underabundant but nitrogen is overabundant compared to the Sun, can be considered a remnant of the respective star's hydrogen core burning through the CNO cycle.

of years, which is faster than the pp chain (a few billion years). The net energy released by the CNO process is about 25.03 MeV ( $\sim 4.01 \cdot 10^{-12}$  J), which is a bit less than for the pp chain.

## Evolution of Upper and Lower Main-Sequence Stars

More massive stars evolve more rapidly on the MS because they radiate much more power, which is also why these objects are often referred to as luminous, hot, and young stars of Population I. For instance, the stellar lifetime on the MS of a  $\sim 15 M_{\odot}$  Pop I star is only  $\sim 10$  million years. Pop II stars, however, are less massive and, hence, tend to be older, less luminous, and cooler than stars of Pop I. Their MS phase lasts significantly longer (for instance,  $\sim 70\,000$  million years for a  $\sim 0.25 M_{\odot}$  Pop II star). Therefore, Pop II stars are observed much more frequently than Pop I objects. The Sun belongs to the group of Pop I stars and takes about 10 000 million years to evolve away from the MS.

The variety of the highly-populated MS is best seen in the so-called *Hertzsprung-Russell diagram* (HRD), in which the brightness of stars (in absolute magnitudes or in terms of the solar luminosity  $L_{\odot}$ ) is plotted against their respective surface temperature (often referred to as effective temperature) or color index<sup>5</sup>. An example HRD is displayed in Fig. 2.2.1. In this diagram, the MS is almost a straight line. It can be separated into two sequences: the richly-populated lower MS, where the less luminous Pop II stars are located, and the upper MS, which is populated by the massive Pop I objects. The boundary between the upper and the lower MS is located at a mass of  $\sim 1.5 M_{\odot}$ , for which the pp chain and the CNO cycle are equally efficient. Stars on the upper MS (Pop I stars) hence produce their energy primarily via the CNO cycle, whereas on the lower MS (Pop II stars) the pp chain dominates. As a matter of fact, the lower-mass limit of the MS lies at about  $0.08 M_{\odot}$ . Objects less massive than this never become hot enough to initiate hydrogen burning in their cores. These so-called *substellar objects* (SOs) include *brown dwarfs* (BDs), exhibiting temperatures between  $\sim 1000$  K and  $\sim 2000$  K, and also *planetary-mass objects* such as *dwarf planets*.

As the energy production in the CNO cycle is very strongly concentrated at the core, the outward energy flux cannot be maintained by radiative transport. Thus, upper MS stars with masses of  $\gtrsim 1.5 M_{\odot}$  have a convective core, in which the energy is carried by material motions. In this way, the material also gets well mixed and the amount of hydrogen in the core of these stars therefore decreases uniformly with time. Outside the convective core, however, energy transport is realized via radiative transfer. While hydrogen is being consumed, the mass of the convective core gradually decreases. At the same time, the size of the radius of the upper MS star increases and the star slowly moves towards the upper right in the HRD, meaning that its luminosity rises and the surface temperature decreases. The core contracts rapidly, once the amount of hydrogen in it is exhausted and only helium is left over. As a consequence of

<sup>5</sup>Another realization of the HRD uses the spectral classes of the Harvard classification scheme on the horizontal axis (see also Fig. 2.2.1). In this classification system, stars are arranged based on their effective temperatures alone. The order of the spectral classes in the Harvard system is O, B, A, F, G, K, and M (from hot/blue/early to cool/red/late stars).

## 2.2. Main-Sequence Phase

the quick contraction, both the surface temperature and the luminosity increase and the star quickly shifts towards the upper left in the HRD. The temperature of the hydrogen shell just around the helium core becomes hot enough to initiate hydrogen burning.

For lower MS stars, the energy production through the pp chain is spread over a significantly larger core region than for upper MS stars. In this way, the entire core remains radiative throughout the MS. Moreover, the absorption coefficient in the outer layers of these cooler stars is high enough for convection to set in. Consequently, the inner structure of lower MS

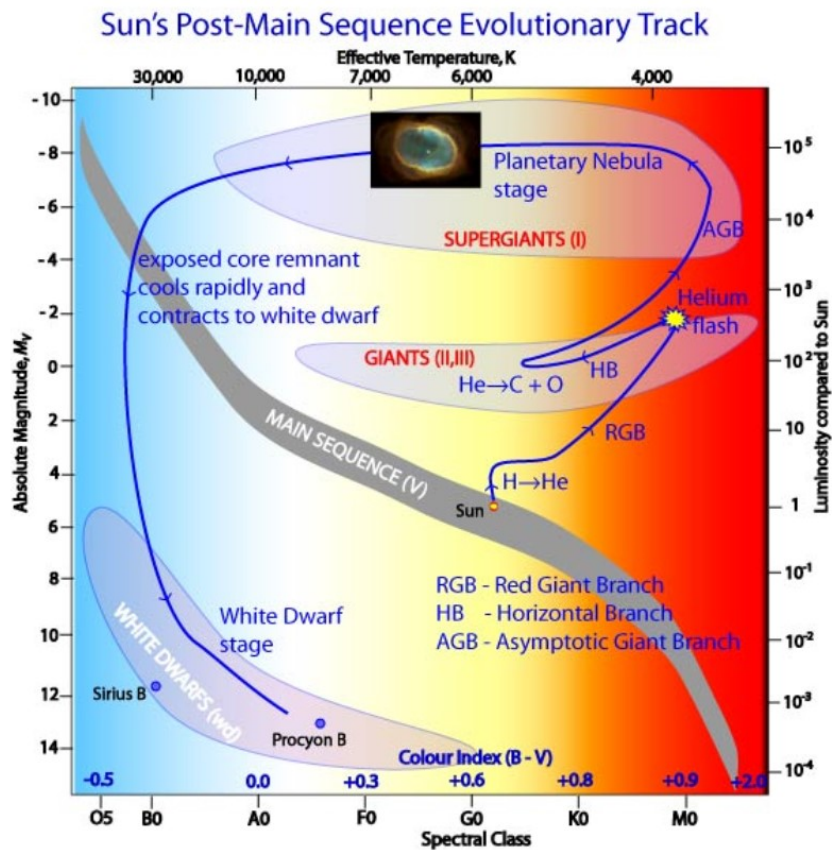


Figure 2.2.1.: Sketch of a Hertzsprung-Russell diagram (HRD) showing the position of the main-sequence (MS), giant, supergiant, and white dwarf (WD) stars. Additionally, the post-MS evolution of a solar-like star is illustrated by means of the Sun. Adopted from [https://www.atnf.csiro.au/outreach//education/senior/astrophysics/stellarevolution\\_deathlow.html](https://www.atnf.csiro.au/outreach//education/senior/astrophysics/stellarevolution_deathlow.html) (last called on 21st January 2021).

stars is opposite to that of upper MS stars. This, however, means that material cannot be mixed within the non-convective core. Hence, in lower MS stars hydrogen is most rapidly consumed at the very centre and its abundance increases outwards. While the hydrogen abundance in the core is decreasing, the star moves almost parallel to the MS in the HRD, slowly becoming brighter and hotter, but not increasing considerably in size. Near the end of hydrogen core burning, the evolution in the HRD bends to the right. At the end of the MS phase,

when the hydrogen content in the core is exhausted, hydrogen burning sets in in a thick shell around the central helium core.

It has to be noted, however, that the previous description for the evolution of lower MS stars is only valid for masses of  $0.26 M_{\odot} \lesssim M \lesssim 1.5 M_{\odot}$ . Lower MS stars with masses of  $0.08 M_{\odot} \lesssim M \lesssim 0.26 M_{\odot}$  remain fully convective throughout the whole MS phase. In these stars, the entire hydrogen content is available for burning as the material is continuously mixed. Thus, the MS evolution of these stars towards the upper left in the HRD is very slow. As a matter of fact, these objects contract and directly evolve to the *white dwarf (WD) stage*<sup>6</sup> (see also Fig. 2.2.1), once all hydrogen is burned.

### 2.3. Red Giant Phase

After hydrogen burning in the core of the MS star has ceased and hydrogen shell burning around the core has stabilized, the radius of the star increases. At the same time, the mass of the helium core increases because of the hydrogen burning around it. A former lower MS star gradually becomes more luminous and cooler, moving towards the top right in the HRD, whereas a former upper MS star makes a rapid jump towards the left, heavily increasing in surface temperature, but not in brightness. In both cases, the respective star will eventually reach the *red giant branch (RGB)*.

In stars with masses of  $0.26 M_{\odot} \lesssim M \lesssim 2.3 M_{\odot}$ , the density of the core will reach the point where the whole helium core becomes degenerate<sup>7</sup>. Although the central temperature continuously climbs, the core will have a uniform temperature because of the high conductivity of the degenerate gas. At about  $10^8$  K (corresponding to a core mass of  $\sim 0.46 M_{\odot}$ ), helium is ignited via the *triple alpha ( $3\alpha$ ) process*<sup>8</sup> in the entire central region, giving an extreme

<sup>6</sup>Degenerate dwarfs or white dwarfs (WDs) are stellar core remnants which are mostly composed of electron-degenerate matter. These stars are very dense because their masses are comparable to that of the Sun, whereas their volumes are comparable to that of the Earth. WDs resulting from usual stellar evolution are typically made of carbon and oxygen. However, if the mass of the progenitor is between  $8.0$  and  $10.5 M_{\odot}$ , also oxygen-neon-magnesium WDs may form. Furthermore, helium WDs (HeWDs) exist. These kind of stars for instance are produced by binary interaction processes (for further information, see Sect. 3.4).

<sup>7</sup>Matter is called degenerate if it is in a state that deviates from the behavior known in classical physics due to quantum mechanical effects. This generally occurs at very high densities or at very low temperatures. If fermions such as electrons are concentrated too much in the stellar core, gravity, which acts inwards and leads to higher density, is countered by a degeneracy pressure (Fermi pressure). The degeneracy pressure counteracts the gravitational pressure and has its cause in the Pauli principle, which forbids that two fermions can assume an identical quantum state.

<sup>8</sup>The triple alpha reaction ( $3\alpha$  process) is given by:



The energy released in each of the given reaction steps is omitted here. The net amount of energy released during the  $3\alpha$  process is about  $7.28$  MeV ( $\sim 1.17 \cdot 10^{-12}$  J). For this process to work, however, the three  ${}^4\text{He}$  particles involved need to collide almost simultaneously because  ${}^8\text{Be}$  is unstable and already decays in  $\sim 2.6 \cdot 10^{-16}$  s.

## 2.4. Horizontal Branch

---

rise of temperature. Despite of this temperature increase, the core cannot expand due to its degeneracy. In consequence, the rate of *helium burning* is further accelerated. Within a few seconds after the initial helium ignition, a critical temperature value will be reached such that the degeneracy of the gas is removed. This leads to a violent expansion (explosion) of the core, the so-called *helium flash*. The star suddenly drops in luminosity as its outer layers contract. However, the star is not completely disrupted because the energy released in the flash is partly turned into potential energy of the expanded core. On the other hand, it is also partly absorbed by the outer layers. After the helium flash, the star reaches a new state on the horizontal branch, in which helium burning stabilizes in the non-degenerate core.

In intermediate-mass stars ( $2.3 M_{\odot} \lesssim M \lesssim 8.0 M_{\odot}$ ), the core does not become degenerate because of the higher temperature and lower density inside. Hence, core helium burning can set in non-violently, that is, without a subsequent helium flash. These stars do not evolve to the horizontal branch. Instead, they first move towards the left in the HRD, that is, away from the RGB, but then loop back again, becoming unstable. It is assumed that such an evolution can explain the classical cepheid variables, which are used to determine distances in the Milky Way and to other nearby galaxies.

In the most massive stars ( $M \gtrsim 8.0 M_{\odot}$ ), helium ignition in the non-degenerate core even starts before the respective star reaches the RGB. The star either continues to move towards the right in the HRD, retaining its envelope and eventually ending up as a red supergiant, or it will generate a strong stellar wind, which leads to a large mass loss, for instance observed for P Cygni or Wolf-Rayet stars.

## 2.4. Horizontal Branch

As described in the previous section, former MS stars with masses of  $\lesssim 2.3 M_{\odot}$  produce a helium flash and eventually end up on the *horizontal branch* (HB), where they stably burn helium in their cores for about  $10^8$  years. Analogous to the MS, the HB is also characterized by two sequences: the zero-age HB (ZAHB) and the terminal-age HB (TAHB). The stellar luminosity is almost constant among HB stars. However, this is not the case for the effective temperature, which varies significantly. As a matter of fact, a constant core mass of slightly

---

As a matter of fact, some of the carbon nuclei produced in the  $3\alpha$  process react with helium nuclei to form oxygen. The latter, in turn, again reacts with helium nuclei to form neon. In this *alpha process* or *alpha ladder*, alpha elements (elements whose most abundant isotopes are integer multiples of four, which corresponds to the mass of the helium nucleus/alpha particle) up to nickel and iron can be produced:



⋮



Again, the energy released in each of the given reaction steps is omitted.

less than half a solar mass and a spread in hydrogen-envelope and, thus, in total mass can explain the distribution of stars along the HB. In fact, the exact envelope mass depends on the amount of mass lost during the helium flash. The hotter (bluer) the star, the smaller its hydrogen envelope. The theoretical helium main sequence (HeMS), below which pure helium stars are found, is defined for envelope masses of zero.

Several groups of stars are found on the HB, whereby the most important ones are that of the *blue horizontal branch* (BHB) and the *extreme horizontal branch* (EHB). In the HRD, BHB stars are located at the cool end of the HB, that is, close to the RGB. These stars can be explained by classical (canonical) stellar evolution. On the other hand, EHB stars are found at the very hot end of the HB (see also Fig. 3.1.1). The hydrogen envelopes of these so-called *hot subdwarf stars* typically make up less than 1% of the total stellar mass. This cannot be achieved during a canonical evolution on the RGB. Therefore, other evolutionary channels and scenarios had to be proposed to explain the nature of hot subdwarfs. This will be dealt with in the context of Ch. 3, which provides a detailed review of these truly remarkable objects.

## 2.5. Asymptotic Giant Branch

After the central helium supply has been exhausted for low and intermediate-mass stars with masses of  $0.26 M_{\odot} \lesssim M \lesssim 8.0 M_{\odot}$  (the core is now completely made of carbon and oxygen), helium fusion sets in in a shell around the core. At the same time, hydrogen burning continues in the outermost shell (double shell-burning phase). Once again, the star increases in size and moves towards the upper right in the HRD, that is, towards higher luminosities and lower surface temperatures. This evolutionary phase is called the *asymptotic giant branch* (AGB). It is rather similar to the RGB phase, although the star does not become as cool as a red giant. In the early stages of the AGB, the helium shell reaches the hydrogen shell. This is followed by a phase of *thermal pulses*, which result from the unstable alternation of hydrogen and helium shell burning. Consequently, the star loops in the HRD. At this point, stellar material may be mixed and matter may be ejected into space in a shell. The thermally pulsing phase only stops once the radiation pressure has become high enough to completely eject the outer layers, leading to the formation of a *planetary nebula*.

The most massive stars ( $M \gtrsim 8.0 M_{\odot}$ ) do not go through the AGB evolutionary phase. These objects are massive enough to initiate carbon, oxygen, and, potentially, silicon burning in their cores. This will be described in the next section.

## 2.6. End of the Giant Phase

The final part of stellar evolution again strongly depends on the stellar mass. This is because the mass determines the temperature and the degree of degeneracy in the core as *carbon*,

## 2.6. End of the Giant Phase

---

oxygen, and silicon burning set in<sup>9</sup>.

In the case of large masses ( $M \gtrsim 15 M_{\odot}$ ), the core remains non-degenerate and continues to become more contracted and hotter. Carbon, oxygen, and, finally, silicon will be burned non-violently in the core. Once each fuel runs out, the respective burning continues in a shell around the core. In this way, an onion-like structure of several nuclear burning shells with different compositions is generated. Such stars are able to burn all the way to iron in their central regions. For instance, the typical onion structure of a  $\sim 30 M_{\odot}$  star consists of the following zones (from the inside to the outside):  ${}^{56}\text{Fe}$ ,  ${}^{28}\text{Si}$ ,  ${}^{16}\text{O}$  and  ${}^{12}\text{C}$ ,  ${}^4\text{He}$ , and  ${}^1\text{H}$ . As no elements heavier than  ${}^{56}\text{Fe}$  can be produced by thermonuclear reactions, the central pressure counteracting the gravitational pressure eventually falls. Hence, the core collapses in a fraction of a second, whereby part of the released energy is used for the dissociation of the central iron nuclei into helium, protons, and neutrons (*core collapse supernova*). Slowly but steadily, the outer layers of the star also collapse. Every time the temperature in a layer of unburned nuclear fuel gets too high, an explosion is triggered, which releases massive amounts of energy in the form of neutrinos within just a few seconds. The central region of the imploded star continues to contract and the remnant can either be a neutron star or a black hole. It is not yet completely understood, which scenario produces what outcome.

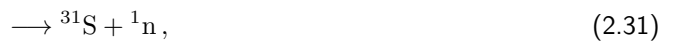
On the other hand, giant stars with masses of  $8.0 M_{\odot} \lesssim M \lesssim 15 M_{\odot}$  either produce a *carbon* or an *oxygen flash* because of the degeneracy of their cores. Compared to the helium

---

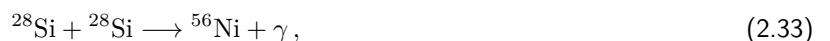
<sup>9</sup>After the helium content in the core is exhausted, carbon burning sets in at temperatures of  $(5-8) \cdot 10^{10}$  K. It is characterized by the following reactions:



At even higher temperatures, oxygen can be ignited:



Finally, after several intermediate steps, silicon burning can set in, which produces nickel and iron:



In all cases, the energy released in each of the given reaction steps is omitted. In order to produce chemical elements heavier than iron, additional energy is required. Thus, such elements cannot be produced by thermonuclear reactions. However, they can result from neutron capture processes during the final stages of stellar evolution.

flash in low-mass stars, however, these events are much more powerful. In fact, they most likely lead to the explosion of the outer layers, eventually triggering the complete destruction of the star. In the dense central region, protons and electrons are able to form neutrons by electron capture processes, which again can result in a degenerate core. The degeneracy pressure of the neutrons may actually be strong enough to stop the collapse of a small mass core, resulting in a neutron star. If the core mass is large enough, however, a black hole may be formed.

Giant stars with masses of  $M \lesssim 8.0 M_{\odot}$  never become hot enough to initiate carbon (and oxygen) fusion in the core. These stars contract, cool down and end up as WDs with a carbon-oxygen core. In the HRD, they first move from the tip of the AGB towards the top left (contraction phase once energy production in the core has ceased). This is followed by a downwards movement to the WD cooling sequence below the MS. Using the example of the Sun, this kind of stellar evolution is shown in Fig. 2.2.1.

## 3. Hot Subdwarf Stars

Subdwarf stars can be subdivided into two different groups: *cool* and *hot* subdwarfs. Both have the same color and, therefore, surface/effective temperature ( $T_{\text{eff}}$ ) as usual MS dwarf stars, but are much less luminous (1.5 to 2.0 mag). The term 'subdwarf' or 'subdwarf star' refers to the position below the MS in the HRD (see also Fig. 3.1.1).

Cool subdwarfs are low-mass stars and have surface temperatures ranging from  $\sim 7000$  K down to  $\sim 3000$  K, which corresponds to spectral types between F and M. Like MS dwarf stars, cool subdwarfs are in the core hydrogen-burning evolutionary phase. However, their metallicity<sup>10</sup> is significantly lower. Thus, they are classified as Pop II stars (Kaler, 1994). The low metallicity also leads to very few absorption lines in the ultraviolet (UV) region of their spectra such that a higher percentage of UV light is emitted compared to dwarf stars with the same effective temperatures (Jao et al., 2008). Hence, cool subdwarfs appear bluer than metal-rich (Pop I) MS dwarfs, which locates them - correctly said - to the left of the low-temperature MS in the HRD (see also Fig. 3.1.1). It is generally believed that cool subdwarfs have been formed before metals could be enriched by supernova explosions. Most of these stars have high radial velocities and are observed in the Galactic halo or in globular clusters.

However, cool subdwarfs will not be dealt with in this work. Instead, the focus is on their hotter counterparts. To this end, this chapter shall provide detailed insights into hot subdwarf stars. First, the history of discovery and the classification scheme of these remarkable stars will be outlined in Sect. 3.1. Section 3.2 then provides a closer look at the hot subdwarf population, detailing the characteristics and atmospheric properties of the individual subtypes. A detailed overview of their chemical compositions will be given afterwards in Sect. 3.3, whereas Sect. 3.4 focuses on the different evolutionary channels and formation scenarios that may produce single and binary hot subdwarf stars.

### 3.1. History of Discovery and Classification

In the 1950s, the first hot subdwarf star was discovered by means of data of the Humason & Zwicky photometric survey (Humason & Zwicky, 1947) of the North Galactic Pole and

<sup>10</sup>Metallicity  $Z$  describes the collective effect of all metals (chemical elements heavier than hydrogen and helium) on the temperature-density stratification of a stellar atmosphere (see also Sect. 7.1.1). Luminous, hot, and young Pop I stars like the Sun, which are concentrated in the disks of spiral galaxies (particularly in the spiral arms), exhibit metallicities ranging from approximately 1/10th to three times that of the Sun ( $Z_{\odot} \sim 0.02$ ). Pop II stars, which are mostly found in globular clusters and in the nuclei of galaxies, tend to be older, less luminous, and cooler than Pop I stars, as presented in Sect. 2.2. Therefore, their metallicities are much lower ranging from approximately 1/1000th to 1/10th that of the Sun. A value of  $Z \sim 0.001$  is often used to represent Pop II stars in model calculations.

the Hyades regions (see, for instance, the works of Luyten 1953, Greenstein 1956, or Münch 1958). Over the next  $\sim 30$  years, however, the number of known objects remained relatively small. It was only the Palomar-Green (PG; Green et al. 1986) survey of the northern Galactic hemisphere that heavily increased the number of known hot subdwarfs. Other successful

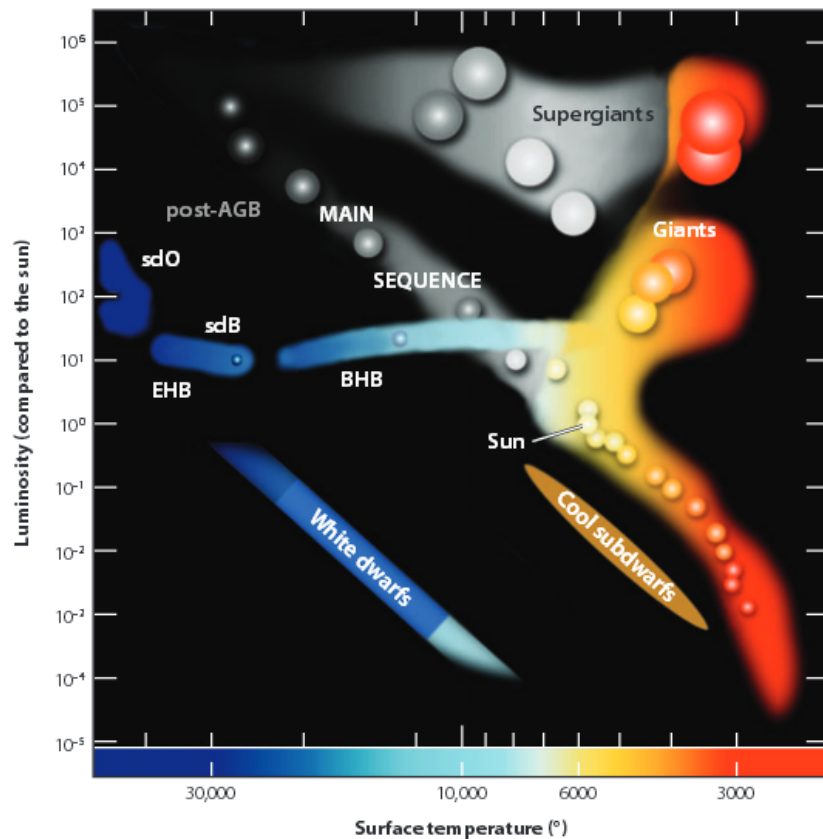


Figure 3.1.1.: Sketch of a Hertzsprung-Russell diagram (HRD) separating the blue horizontal branch (BHB) from the extreme horizontal branch (EHB). The latter is populated by the hot subdwarf B stars (sdBs), which skip the (post-)asymptotic giant branch ((post-)AGB) phase due to their very thin hydrogen envelopes. The EHB is located to the left and below the hot end of the main sequence but above the white dwarf cooling sequence. The position of the hotter and more luminous hot subdwarf O stars (sdOs) as well as the position of the Sun on the main sequence are also marked. The traditional cool subdwarfs, however, are located below (to the left of) the lower main sequence. Giants and supergiants illustrate the red giant branch. Adopted from Heber (2016); original version: Heber (2009).

surveys followed, including the Kitt Peak-Downes (KPD; Downes 1986) survey of the Galactic plane, the Edinburgh-Cape (EC; Stobie et al. 1997) survey for the southern sky, the First and Second Byurakan Surveys (FBS, SBS; Markarian et al. 1989, Stepanian 2005, Mickaelian et al. 2007), the Hamburg Quasar Survey (HQS; Hagen et al. 1995) for the northern and

### 3.1. History of Discovery and Classification

the Hamburg/ESO<sup>11</sup> (HE; Wisotzki et al. 1996) survey for the southern sky as well as the ESO Supernova Ia Progenitor Survey (ESO SPY; Napiwotzki et al. 2001a). The Sloan Digital Sky Survey (SDSS) and the Galaxy Evolution Explorer (GALEX) all-sky survey extended the

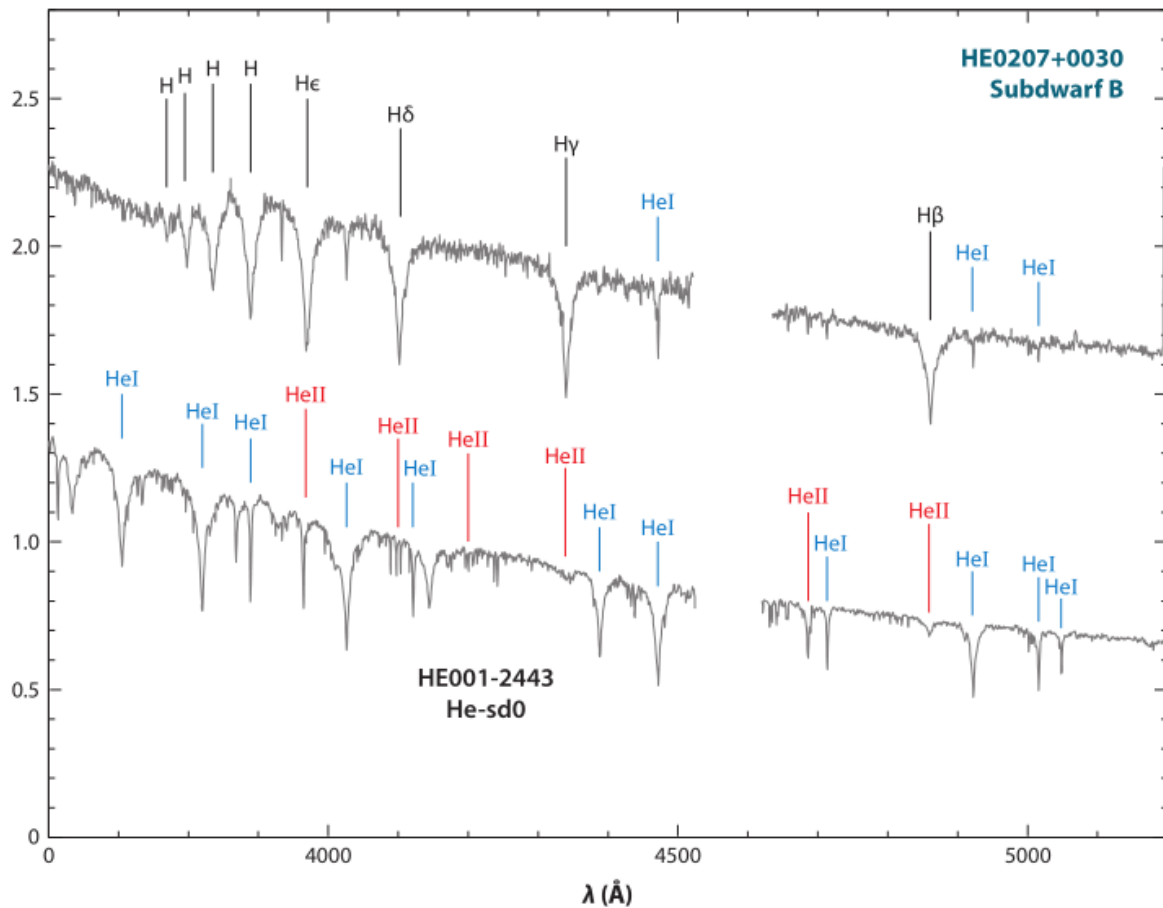


Figure 3.1.2.: Comparison of a typical spectrum of a H-sdB (HE 0207+0030, top) and a He-sdO (HE 0001-2443, bottom) star displaying important hydrogen and helium absorption lines. The hydrogen Balmer series dominates in H-sdBs and helium lines are weak. In contrast, the Balmer series is absent and additionally blended with the He II Pickering series in He-sdOs (see also Table 8.12). Note that both spectra are not absolutely flux calibrated and shifted to each other for illustrative purposes. Adopted from Heber (2016); original versions: Napiwotzki (2008) and Heber (2009).

list even further<sup>12</sup> (Heber, 2016). Ongoing spectroscopic surveys and the availability of new all-sky data from ground-based photometric surveys as well as the second data release of the *Gaia* mission (see also Ch. 5) increased the number of entries in the catalog of known

<sup>11</sup>ESO stands for European Southern Observatory.

<sup>12</sup>Many of the analyzed program stars in this work also resulted from the listed surveys (see Sect. 8.1).

hot subdwarfs to a total of 5874 unique objects (status as of March 2020; Geier 2020). Many formerly misclassified objects have been removed throughout the years thanks to the more accurate photometry and astrometry. The listed objects have a broad range of visual apparent magnitudes ( $8.5 \text{ mag} \lesssim B \lesssim 20 \text{ mag}$ ) and are observed both in globular clusters and in the field<sup>13</sup>. Today, it is known that hot subdwarf stars come in several flavors whose individual characteristics, atmospheric properties and chemical compositions will be detailed in the following sections. At this point, a brief overview of the spectral classification scheme, which has been developed over the past  $\sim 50$  years, shall be given.

The spectra of hot subdwarf stars can be quite different, whereby the effective temperature and the predominant helium to hydrogen ratio in the stellar atmosphere, also called helium abundance<sup>14</sup>, play important roles. This is illustrated in Fig. 3.1.2, which compares the spectrum of a typical hydrogen-rich hot subdwarf B star (HE 0207+0030; top) to that of a typical helium-rich hot subdwarf O star (HE 0001-2443, bottom).

The original definition of hydrogen-rich hot subdwarf B stars (**H-sdBs**) stems from Sargent & Searle (1968). According to them, H-sdBs have colors of normal B-type MS stars but also abnormally broad optical hydrogen Balmer lines, which is very unusual for typical Pop I B-type MS dwarf stars. In addition, H-sdBs are He I weak-lined (Moehler et al., 1990). In contrast, hydrogen-rich hot subdwarf O stars (**H-sdOs**) barely show neutral helium but strong He II lines in their spectra, in particular He II 4686 Å. Relative to O-type MS dwarfs, these stars also have strong Balmer lines for the color (Sargent & Searle, 1968). Vauclair & Liebert (1987) and Moehler et al. (1990) confirmed that H-sdOs and a third group of hydrogen-rich hot subdwarf OB stars (**H-sdOBs**), which exhibit H-sdB-like spectra but with weak He II 4686 Å, are related to H-sdBs with correspondingly earlier spectral type. The classification scheme of hot subdwarf stars nowadays is extended by the two classes of **He-sdBs** and **He-sdOs**, which both exhibit helium-dominated spectra. He-sdBs are rare and for most of them the effective temperatures are close to the ones of H-sdOBs. Spectra of He-sdBs therefore still show strong Balmer lines, but are dominated by He I. Sometimes, He II 4686 Å is weakly present. In contrast, He-sdOs are completely dominated by He II (and He I), whereas the hydrogen Balmer lines are only weak or may even be occasionally absent. Naslim et al. (2012, 2013) suggested to subdivide the helium-rich hot subdwarfs (He-sdBs and He-sdOs) into extreme and intermediate helium-rich objects, drawing a line at a helium abundance of  $\log n(\text{He}) \sim 0.6$ . Accordingly, about 95 % of all He-sdBs and He-sdOs have extreme helium abundances and only  $\sim 5$  % are intermediate helium-rich. Intermediate He-sdBs (**iHe-sdBs**) are of special interest since they could possibly link the evolution of H-sdBs/H-sdOBs to that of He-sdOs or vice versa (Jeffery et al., 2012). For instance, it has been suggested that iHe-sdBs may be the immediate progenitors of H-sdBs, before helium has had time to be depleted from the stellar atmosphere due to gravitational settling<sup>15</sup>.

<sup>13</sup>This section mainly focuses on the field population of hot subdwarf stars. For a detailed review of the globular cluster population, see, for instance, Heber (2016).

<sup>14</sup>This quantity is most often defined as the logarithm of the ratio of helium to hydrogen number density:  $\log n(\text{He}) := \log \left[ \frac{N(\text{He})}{N(\text{H})} \right]$  (see Sect. 7.1.1 for further information).

<sup>15</sup>Gravitational settling is one of the main atomic transport processes caused by diffusion, with radiative levitation being the second one. Their combined effects on the atmospheric composition of hot subdwarf stars will be outlined in Sect. 3.3.

### 3.2. The Hot Subdwarf Population - Characteristics and Atmospheric Properties

---

The presented classification scheme for hot subdwarf stars is commonly used and, hence, will also be employed throughout this work. However, it has to be pointed out that it is less detailed than the Morgan-Keenan-like (MK-like) system of spectral classification for hot subdwarf stars, which was introduced by Drilling et al. (2013)<sup>16</sup>.

## 3.2. The Hot Subdwarf Population - Characteristics and Atmospheric Properties

As presented in Ch. 2, canonical HB stars are assumed to be in the stable core helium-burning phase of evolution that follows the helium core flash at the tip of the RGB. For the latter to take place, the ignition of helium needs to occur under electron-degenerate conditions, which is only possible for stars with ZAMS masses of  $\lesssim 2.3 M_{\odot}$ . Sweigart (1987) showed that the core mass is fixed at the onset of the core helium flash, that is, between  $0.46$  and  $0.50 M_{\odot}$  (canonical mass regime), depending only slightly on the metallicity and the helium abundance. Hot subdwarf stars (in particular H-sdBs) are located on the EHB (see also Fig. 3.1.1). Therefore, it is believed that the progenitors of these stars are also low-mass objects with ZAMS masses of  $\lesssim 2.3 M_{\odot}$  that must have undergone a helium core flash during the RGB evolution. As a matter of fact, however, EHB stars exhibit almost no hydrogen envelopes at all (typically  $M_{\text{env}} < 0.01 M_{\odot}$ )<sup>17</sup>. Why this is the case, cannot be explained by the canonical HB evolution because an isolated red giant cannot simply remove all of its envelope on the RGB (Heber, 2009, 2016).

Due to their thin hydrogen envelopes, EHB stars are unable to sustain hydrogen-shell burning and, thus, avoid the double shell-burning phase on the AGB. Instead, the post-EHB evolution proceeds towards higher temperatures until the WD cooling track is reached and gravity increases (Heber, 2009, 2016). In fact, most of the known H-sdOs (and H-sdOBs) have been identified as the direct progeny of H-sdB stars. H-sdOBs represent a transition stage. For H-sdOs, core helium burning has ceased, but helium continues to be burned in a shell around the carbon-oxygen core. Hence, these stars already have evolved away from the EHB to higher effective temperatures and are directly on their way to the WD graveyard. Post-EHB evolutionary tracks that are able to successfully link the H-sdBs and H-sdOBs to the further evolved H-sdOs have, for instance, been developed by Dorman et al. (1993), Han et al. (2002), and Hu et al. (2008).

Surprisingly, extensive surveys of H-sdBs, H-sdOBs, and H-sdOs in the past revealed a large

---

<sup>16</sup>Due to their highly chemically peculiar spectra, hot subdwarf stars cannot be classified in the usual Morgan-Keenan (MK) spectral classification scheme, which, compared to the Harvard system presented in Sect. 2.2, also makes use of the stellar luminosity as a classifier. Nonetheless, Drilling et al. (2013) introduced an MK-like system of spectral classification for hot subdwarfs, consisting of three luminosity classes as well as numerous helium classes (0-40). However, this MK-like system is rarely used.

<sup>17</sup>The small amount of hydrogen is still sufficient to produce more intense absorption lines than observed for O and B-type MS stars. It is general consensus that the atmospheres of H-sdBs are dominated by hydrogen because of the influence of atomic transport, that is, diffusion processes occurring in the stellar atmosphere. Diffusion will be topic in Sect. 3.3.

binary fraction. Most of these objects ( $\gtrsim 50\%$ ) are observed as close binaries with orbital separations of a few solar radii at most and with WD companions (see, for instance, the results of Maxted et al. 2001, Napiwotzki et al. 2004a, or Copperwheat et al. 2011). Therefore, these systems belong to the group of single-lined binaries (SB1 systems). On the other hand, double-lined binaries (SB2 systems), in which the primary hot subdwarf has a cool MS companion, make up  $\sim 30\%$  of the hot subdwarf population (Stark & Wade, 2003). From the original theoretical point of view, H-sdB, H-sdOB, and H-sdO binaries come in two flavors: close ones with orbital periods of  $0.10 \text{ d} \lesssim P \lesssim 10 \text{ d}$  and with WD/MS companions and wide ones with MS companions and  $10 \text{ d} \lesssim P \lesssim 500 \text{ d}$  (Han et al., 2002, 2003; Podsiadlowski, 2008). For the latter, however, observations also revealed systems with  $700 \text{ d} \lesssim P \lesssim 1400 \text{ d}$  (Vos et al., 2012, 2013, 2014, 2017), which lead to a refinement of the theoretical models (more on this throughout Sect. 3.4.1). The large binary fraction of hot subdwarf stars strongly implies a formation via binary interaction processes. This will be discussed in detail in Sect. 3.4.

Most hot subdwarf stars, notably H-sdBs, are slow rotators (the projected rotational velocities  $v \sin i$  are typically smaller than  $\sim 10 \text{ km s}^{-1}$ ; Geier & Heber 2012<sup>18</sup>) that form a homogenous class. They are rather compact objects ( $R_{\text{sd}} \sim 0.10\text{-}0.30 R_{\odot}$ ) with stellar masses of  $M_{\text{sd}} \sim 0.50 M_{\odot}$  (Heber, 1986; Saffer et al., 1994) and have about the same luminosity as the Sun in the visual range, but are 10-100 times more luminous in total (see Fig. 3.1.1). At visual apparent magnitudes of  $B \gtrsim 18 \text{ mag}$ , H-sdB stars were found to outnumber all types of faint blue objects, including WDs. Nowadays, the all in all sdB to sdO frequency is about 3 to 1 (Heber, 2009, 2016). In fact, the flux maximum of hot subdwarf stars is located in the UV regime because of their general high effective temperatures of  $T_{\text{eff}} \gtrsim 20\,000 \text{ K}$ . Furthermore, the number density of these stars in old stellar populations like elliptical galaxies or globular clusters is quite high. Therefore, these stars can be perfectly used in order to understand the spectra of these populations. Code & Welch (1979) discovered a UV excess (below  $2500 \text{ \AA}$ ) in the spectrum of old early-type galaxies (UV upturn phenomenon) which, back then, was a big surprise and led to numerous speculations about its origin because UV light is usually associated with young stellar populations. According to Yi & Yoon (2004), however, hot subdwarfs may indeed explain this phenomenon.

The classes of hot subdwarf stars outlined in Sect. 3.1 exhibit different effective temperature regimes. While H-sdBs are located at the cool end of the EHB with  $20\,000 \text{ K} \lesssim T_{\text{eff}} \lesssim 35\,000 \text{ K}$ , the H-sdOs and He-sdOs are much hotter ( $T_{\text{eff}} \gtrsim 38\,000 \text{ K}$ ; Drilling et al. 2013). Even temperatures above  $60\,000 \text{ K}$  are not rare for evolved H-sdOs (see, for instance, the works of Latour et al. 2013, 2015, 2018). The temperatures of H-sdOBs partly overlap

<sup>18</sup>The projected rotational velocity  $v \sin i$  will be explained in Sect. 6.5.2. Geier & Heber (2012) measured projected rotational velocities for single H-sdB stars from high-resolution spectra. Binary stars were also considered single if the orbital periods exceeded 1.2 days such that the separations of the components are so wide that tidal interaction can safely be neglected. The distribution of  $v \sin i$  values from Geier & Heber (2012) is consistent with an average projected rotational velocity of  $8 \text{ km s}^{-1}$ . So far, only two apparently single stars (the H-sdBs EC 22081-1916 and SB 290) have been found to be rapidly rotating (Geier et al., 2011a, 2013b). Hence, these stars must have been spun-up by tidal forces from a close companion, favoring the double helium WD merger scenario of Sect. 3.4.2, although this channel is believed to produce mainly helium-rich objects. In fact, SB 290 is one of the program stars analyzed in this work (see Sect. 8.1) and, surprisingly, is found to be a binary (see Sect. 12).

### 3.2. The Hot Subdwarf Population - Characteristics and Atmospheric Properties

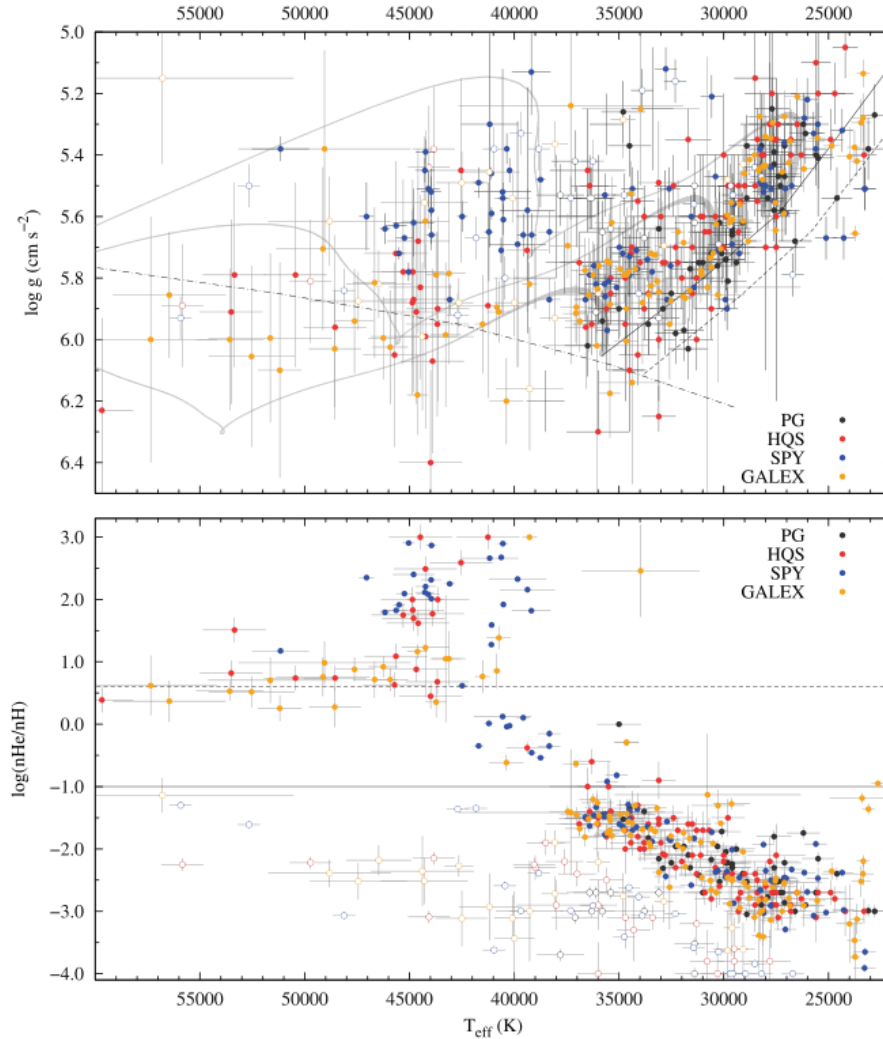


Figure 3.2.1.: Distribution of selected hot subdwarf stars in the  $T_{\text{eff}}\text{-}\log(g)$  plane (Kiel diagram; upper panel) and in the  $T_{\text{eff}}\text{-}\log n(\text{He})$  plane (helium abundance vs. effective temperature; lower panel). Different colors mark the major hot subdwarf surveys presented in Sect. 3.1: PG and EC (combined; black), HQS (red), ESO SPY (blue), and GALEX (yellow). The minority groups of H-sdOs and lower helium-sequence H-sd(O)Bs are marked with open dots. In the  $T_{\text{eff}}\text{-}\log(g)$  plane, the location of the zero-age extreme horizontal branch is highlighted for two different hot subdwarf core masses of  $0.45 M_{\odot}$  (dashed dark gray line) and  $0.50 M_{\odot}$  (solid dark gray line) according to Han et al. (2002). In addition, evolutionary tracks from Han et al. (2002) for the same hot subdwarf core mass of  $0.50 M_{\odot}$  but three different hydrogen-envelope masses ( $\sim 0.000 M_{\odot}$ ,  $\sim 0.001 M_{\odot}$ , and  $\sim 0.005 M_{\odot}$  in light gray lines, from bottom to top) with line widths proportional to evolutionary timescales are also displayed. The helium main sequence according to Dorman et al. (1993) is plotted as a dashed-dotted dark gray line. In the  $\log n(\text{He})\text{-}T_{\text{eff}}$  plane, the solar helium abundance of  $\log n(\text{He}) \sim -1.0$  from Asplund et al. (2009) is marked by a solid horizontal line. Additionally, the dashed horizontal line marks a helium abundance of  $\log n(\text{He}) \sim 0.6$ . According to Naslim et al. (2012, 2013), this abundance value can be used in order to separate the intermediate from the extreme He-sdBs/He-sdOs. Adopted from Heber (2016).

with that of the H-sdBs and H-sdOs/He-sdOs:  $33\,000\text{ K} \lesssim T_{\text{eff}} \lesssim 45\,000\text{ K}$ . The same is true for most of the He-sdBs, both the extreme and the intermediate helium-rich ones:  $33\,000\text{ K} \lesssim T_{\text{eff}} \lesssim 40\,000\text{ K}$ . However, a minor group of iHe-sdBs has also been found in the cooler temperature regime of normal H-sdBs between  $\sim 22\,000\text{ K}$  and  $\sim 32\,000\text{ K}$  (see, for instance, Naslim et al. 2012).

Apart from the effective temperature and the helium abundance, which have already been introduced, the surface gravity  $\log(g[\text{cm s}^{-2}])$  is the third important characteristic of hot subdwarf stars. sdBs, sdOBs, and sdOs are more or less homogeneously distributed within a range of  $5.0 \lesssim \log(g) \lesssim 6.0$ . However, He-sdBs (both extreme and intermediate helium-rich) have been found to exhibit somewhat lower surface gravities than most of their hydrogen-rich counterparts, the H-sdBs (Heber, 2009). The upper panel of Fig. 3.2.1 shows the distribution of hot subdwarf stars in the  $T_{\text{eff}}\text{-}\log(g)$  plane (Kiel diagram) based on the results from the major surveys of ESO SPY, GALEX, HQS, PG, and EC. The vast majority of hot subdwarfs (H-sdBs and H-sdOBs) are located in the effective temperature regime between  $\sim 25\,000\text{ K}$  and  $\sim 37\,000\text{ K}$  and have  $5.2 \lesssim \log(g) \lesssim 6.0$ . There is a trend visible for most of these stars: The higher the effective temperature, the higher the respective surface gravity. This can be explained by the link of luminosity  $L$  and stellar mass  $M$ :

$$L := 4\pi R^2 \sigma T_{\text{eff}}^4 \quad (3.1)$$

$$M := \frac{gR^2}{G}, \quad (3.2)$$

where  $R$  denotes the stellar radius,  $\sigma$  is the Stefan-Boltzmann constant, and  $G$  is the gravitational constant. This yields  $R^2 = \frac{GM}{g} = \frac{L}{4\pi\sigma T_{\text{eff}}^4}$  and, therefore, the following relation:

$$g = \frac{4\pi\sigma GM T_{\text{eff}}^4}{L}. \quad (3.3)$$

Qualitatively, the surface gravity hence increases with increasing temperature. However, the quotient of the other quantities involved ( $\frac{M}{L}$ ) certainly also has an influence when it comes to details.

The most intriguing distribution in the  $T_{\text{eff}}\text{-}\log(g)$  plane is the one of the He-sdOs. A bunch of them shows surface gravities of  $\log(g) \lesssim 6.0$ , meaning that these stars are located on or above the theoretical HeMS which is still consistent with their EHB nature<sup>19</sup>. However, a large population of high-gravity He-sdOs with  $6.0 \lesssim \log(g) \lesssim 6.4$  is located below the HeMS (see the upper panel of Fig. 3.2.1), meaning that these objects should have no hydrogen envelopes at all. This observation is at odds with a position on the EHB in the HRD. There is evidence, however, that the very high surface gravities of some of the He-sdOs may be due to insufficient metal line-blanketed<sup>20</sup> model spectra used for quantitative spectral analyses

<sup>19</sup>Many He-sdOs are believed to result from the double helium WD merger scenario, which will be presented in Sect. 3.4.2. Thus, they can have stellar masses that are higher than the canonical one of  $\sim 0.46 M_{\odot}$  (see also Sect. 3.4.4). This places them above the canonical EHB regime shown in the upper panel of Fig. 3.2.1.

<sup>20</sup>Metal line-blanketing will be topic in Ch. 6.

### 3.2. The Hot Subdwarf Population - Characteristics and Atmospheric Properties

---

(for instance, compare the results of Stroeer et al. 2007 to the reanalysis of Hirsch 2009). Furthermore, it is known that  $\log(g)$  and  $T_{\text{eff}}$  are steeply correlated in the case of He-sdOs, which leads to large systematic uncertainties<sup>21</sup> (Heber, 2016).

The lower panel of Fig. 3.2.1 shows the distribution of hot subdwarf stars in the  $T_{\text{eff}}\text{-}\log n(\text{He})$  plane. The helium abundance strongly depends on the spectral class, as has already been discussed qualitatively in Sect. 3.1. Most of the hydrogen-rich hot subdwarfs (H-sdBs, H-sdOBs, and H-sdOs) have  $-3.5 \lesssim \log n(\text{He}) \lesssim -1.5$ . However, He-sdOs exhibit significantly higher values of  $\log n(\text{He})$ . For some of them, the measured helium abundance may even exceed  $\log n(\text{He}) = +3.0$ . The rare class of He-sdBs has helium abundances ranging from slightly below solar (solar helium abundance:  $\log n(\text{He}) = -1.07$ ; Asplund et al. 2009) to almost pure helium. He-sdBs and He-sdOs are subdivided into extreme ( $\log n(\text{He}) \gtrsim 0.6$ ) and intermediate ( $-1.3 \lesssim \log n(\text{He}) \lesssim 0.6$ ) helium-rich objects according to Naslim et al. (2012, 2013). Most of the known iHe-sdBs are located in the centre of the  $T_{\text{eff}}\text{-}\log n(\text{He})$  plane displayed in Fig. 3.2.1.

Edelmann et al. (2003) found a linear correlation between the effective temperature and the helium abundance for the class of H-sdBs (and H-sdOBs), that is, the higher  $T_{\text{eff}}$ , the higher  $\log n(\text{He})$ . This can also be seen in the lower panel of Fig. 3.2.1. Additionally, Edelmann et al. (2003) subdivided their analyzed H-sdBs and H-sdOBs into two different groups. The first one (the upper helium sequence) contained about 5/6 of their sample stars and showed a much higher helium content than the smaller second group (the lower helium sequence) at the same effective temperatures. The authors fitted the following two linear regressions:

$$\log n(\text{He}) = -3.53 + 1.35 \cdot \left( \frac{T_{\text{eff}}}{10^4\text{K}} - 2.00 \right) \text{ for the bulk of H-sdBs/H-sdOBs and} \quad (3.4)$$

$$\log n(\text{He}) = -4.79 + 1.26 \cdot \left( \frac{T_{\text{eff}}}{10^4\text{K}} - 2.00 \right) \text{ for the smaller group.} \quad (3.5)$$

The two helium sequences are also visible in the  $T_{\text{eff}}\text{-}\log n(\text{He})$  plane of Fig. 3.2.1. This behavior of the H-sdBs and H-sdOBs more or less remains a mystery although several different suggestions have been made in order to explain it. In principle, the same applies to the general linear correlation between  $T_{\text{eff}}$  and  $\log n(\text{He})$  observed for H-sdBs/H-sdOBs. For instance, Aznar Cuadrado & Jeffery (2002) and Edelmann et al. (2003) argued that H-sdBs in short-period binaries might exhibit higher helium abundances than the ones in long-period systems or the isolated ones because of the strongly acting tidal forces leading to mixing in the stellar atmosphere. Later, however, this was disproved by Geier et al. (2012) and Geier et al. (2013a), respectively. Moreover, diffusion models from Michaud et al. (2011) predicted neither the two sequences nor the observed correlation with temperature.

---

<sup>21</sup>One of the most significant sources of systematic uncertainty results from the helium-line-broadening theory, which unfortunately is still incomplete. In particular, for many of the neutral helium-line transitions observed in the spectra of He-sdOs (especially in the near infrared) no sophisticated broadening tables are available yet.

### 3.3. Chemical Composition

Hot subdwarf stars are known to show various different abundance anomalies. Therefore, this section is dedicated to the surface composition of these chemically peculiar stars<sup>22</sup>. In terms of metal content, the spectra of hydrogen-rich hot subdwarfs (H-sdBs, H-sdOBs, H-sdOs) strongly differ from those of intermediate and extreme helium-rich ones (He-sdBs, He-sdOs). This is why both groups will be discussed separately in the following. The spotlight will also be on the <sup>3</sup>He anomaly, which is only observed for H-sdBs on the EHB.

#### H-sdBs and H-sdOBs

The chemical composition of H-sdBs (and H-sdOBs) is best studied among hot subdwarf stars as these classes are by far the most frequent ones. Besides hydrogen and helium, a typical optical H-sdB/H-sdOB spectrum shows prominent metal lines that can be associated with carbon (C), nitrogen (N), oxygen (O), neon (Ne), magnesium (Mg), aluminum (Al), silicon (Si), sulfur (S), argon (Ar), and iron (Fe). In addition, phosphorus (P), potassium (K), calcium (Ca), scandium (Sc), vanadium (V), titanium (Ti), chromium (Cr) and sometimes also cobalt (Co) and zinc (Zn) may be found. Due to the effective temperature regime of H-sdBs/H-sdOBs and, hence, the predominant local temperatures in the stellar atmosphere, the typical ionization stages of the observed metals are II, III, and IV, depending on the specific chemical element. The most sophisticated metal abundance analysis for H-sdBs/H-sdOBs in the optical wavelength regime has been performed by Geier (2013), including more than 100 individual objects and elemental abundances of up to 24 different ions per star (see Fig. 3.3.1). However, since quantitative spectral analyses of this size are very time-consuming, the author concentrated on a semi-automatic analysis pipeline to fit the synthetic spectra computed from standard local thermodynamic equilibrium models<sup>23</sup> to a small set of selected and representative spectral lines per ion only. Although only upper limits on the abundances of several of the chemical elements investigated could be derived, some similarities have been found among the H-sdBs (and H-sdOBs). However, also relatively large star-to-star variations are present and several abundance anomalies, in particular among the heavier elements, have been observed. All of this shall be detailed in the following, whereby the discussed abundances from Geier (2013) are given according to the nomenclature of Asplund et al. (2009), that is:  $\log \epsilon_X := \log N(X)/N(H) + 12$ , where  $N(X)$  and  $N(H)$  are the number densities of the elements  $X$  and  $H$  (hydrogen), respectively<sup>24</sup>.

The observed C abundance derived from C II/III lines varies by orders of magnitude from star

<sup>22</sup>Depending on the specific chemical composition of a stellar atmosphere, various different hydrogen, helium, and metal absorption (emission) lines can be observed in a stellar spectrum. The line profiles can be fitted by means of model spectra in order to derive individual abundances which together form the surface composition of a star. The theoretical concepts of spectral line formation will be detailed in Sect. 6.5, whereas quantitative spectral analysis and spectral fitting will be dealt with in Sect. 7.1.

<sup>23</sup>The concept of local thermodynamic equilibrium will be presented in Sect. 6.4.

<sup>24</sup>This means that a value of 12 has to be subtracted from  $\log \epsilon_X$  in order to derive the “standard” base-10 logarithmic number densities relative to the density of hydrogen.

### 3.3. Chemical Composition

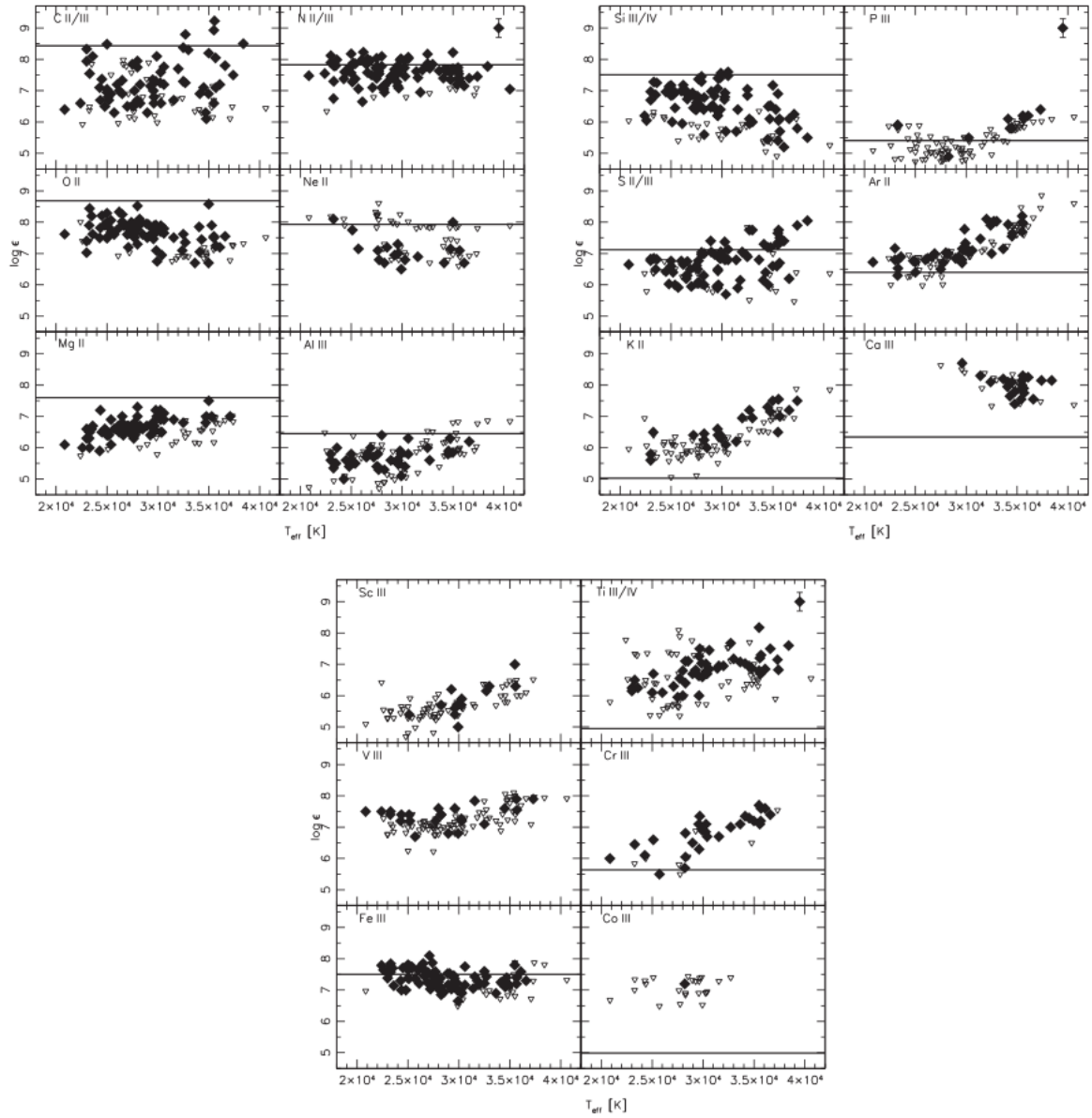


Figure 3.3.1.: Elemental abundances of H-sdB (and H-sdOB) stars as a function of effective temperature: carbon to aluminum (upper left-hand panel), silicon to calcium (upper right-hand panel), and scandium to cobalt (lower panel). In cases where more than a single ionization stage has been observed, the average abundance is given. While filled diamonds mark measured abundances, open triangles represent upper limits. The solid horizontal lines mark the respective solar abundances from Asplund et al. (2009). The size of typical error bars is given in the upper right-hand corners of the individual panels. Abundances are given according to the nomenclature of Asplund et al. (2009), that is:  $\log \epsilon_X := \log N(X)/N(H) + 12$ , where  $N(X)$  and  $N(H)$  are the number densities of the elements  $X$  and  $H$  (hydrogen), respectively. This means that a value of 12 has to be subtracted from the plotted  $\log \epsilon_X$  values in order to derive the “standard” base-10 logarithmic number densities relative to the density of hydrogen. Adopted from Heber (2016); original versions: Geier (2013).

to star and ranges from  $\sim -2.5$  dex subsolar to slightly supersolar (solar abundance: 8.43) in most cases. However, some H-sdBs/H-sdOBs with  $T_{\text{eff}} > 32\,000$  K have supersolar abundances of up to more than  $+1.0$  dex (see Fig. 3.3.1).

The N II/III abundances do not vary with effective temperature. They range from  $\sim -1.0$  dex subsolar to  $\sim +0.5$  dex supersolar (solar abundance: 7.83). The measured O II abundances,

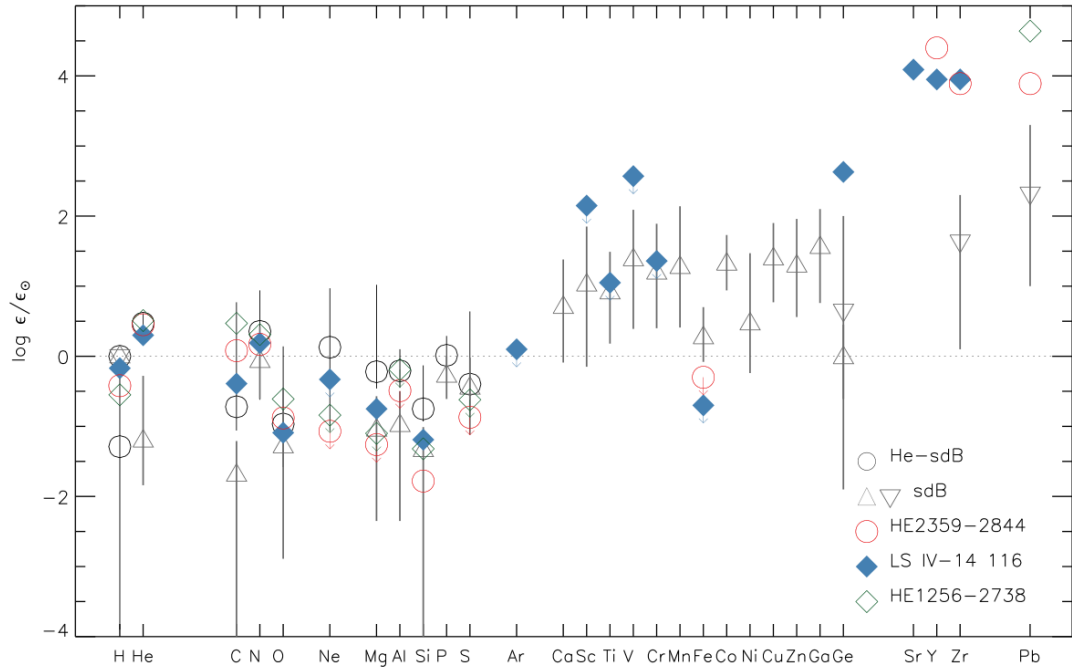


Figure 3.3.2.: Mean elemental abundances (symbols) and ranges (lines) by number fraction relative to solar for H-sdBs/H-sdOBs (open gray triangles; Pereira 2011) and intermediate He-sdBs (open black circles; Naslim et al. 2010). Additionally, the surface abundances for another three intermediate He-sdBs are plotted separately: the zirconium star LS IV-14<sup>o</sup> 116 (full blue diamonds; Naslim et al. 2011) and the lead-rich stars HE 2359-2844 (open red circles; Naslim et al. 2013) and HE 1256-2738 (open green diamonds; Naslim et al. 2013). Abundances are given according to the nomenclature of Asplund et al. (2009), that is:  $\log \epsilon_X := \log N(X)/N(H) + 12$ , where  $N(X)$  and  $N(H)$  are the number densities of the elements  $X$  and  $H$  (hydrogen), respectively. The dashed horizontal line marks the solar abundance level according to Asplund et al. (2009). Upper limits are indicated by downward arrows. Adopted from Heber (2016); original versions: Naslim et al. (2013) and Jeffery et al. (2015).

however, show a larger scatter and are on average one to two orders of magnitude lower than the solar one, which is 8.69. Interestingly, the average O abundance is shifted by  $\sim -0.5$  dex at  $T_{\text{eff}} \sim 30\,000$  K with respect to the cooler H-sdBs.

Although neon could only be measured for a small number of sample stars (most frequently, only upper limits were derived), its abundance derived from Ne II lines can still be specified.

### 3.3. Chemical Composition

---

It scatters from  $\sim -1.5$  dex subsolar to  $\sim +0.1$  dex supersolar (solar abundance: 7.93). The average magnesium abundance derived from Mg II lines is subsolar by about one order of magnitude (solar abundance: 7.60). However, a slight subsolar trend with temperature ranging from  $\sim -1.5$  dex to  $\sim -0.2$  dex is visible.

The aluminum abundance derived from Al III lines ranges from  $\sim -1.5$  dex subsolar to about solar (solar abundance: 6.45). For this element, also a slight trend with temperature can be detected. The silicon abundance derived from Si III/IV lines largely scatters between  $\sim -2.0$  dex subsolar and solar (solar abundance: 7.51). Interestingly, the mean Si abundance drops by  $\sim -1.0$  dex at  $T_{\text{eff}} \gtrsim 35\,000$  K.

Regarding phosphorus (P III), the determined abundances are mostly upper limits. Nonetheless, a trend with temperature is visible since from  $T_{\text{eff}} \sim 28\,000$  K onwards the elemental abundance increases from  $\sim -0.5$  dex subsolar to  $\sim +1.0$  dex supersolar (solar abundance: 5.41). S II and S III, however, show a large scatter between  $\sim -1.5$  dex subsolar and  $\sim +1.0$  dex supersolar (solar abundance: 7.12).

The Ar abundance derived from Ar II lines also shows a trend with temperature. It ranges from solar at the cool end to  $\sim +1.8$  dex supersolar at the hot end (solar abundance: 6.40). An even stronger trend is observed for potassium (K II, solar abundance: 5.03) whose abundance increases with temperature from  $\sim +0.7$  dex to  $\sim +3.0$  dex supersolar. Ca III is only present at  $T_{\text{eff}} \gtrsim 29\,000$  K. Its abundance scatters from  $\sim +1.0$  dex to  $\sim +2.5$  dex supersolar (solar abundance: 6.34). It has to be pointed out that Geier (2013) were not able to derive abundances for Ca II because the most prominent lines (the H and K lines at 3968 Å and 3934 Å) were blended with interstellar lines<sup>25</sup>.

Scandium (Sc III) could also be measured for a few stars only, but is strongly enriched compared to the solar abundance of 3.15. The elemental abundance increases with temperature from  $\sim +2.0$  dex to  $\sim +4.0$  dex. Titanium (Ti III/IV; solar abundance: 4.95) is also strongly enhanced and scatters from  $\sim +1.0$  dex to  $\sim +3.0$  dex supersolar. The same is true for vanadium (V III, solar abundance: 3.93) whose abundance ranges from  $\sim +2.0$  dex to  $\sim +4.0$  dex supersolar, mostly independent of temperature. Chromium (Cr III, solar abundance: 5.64) has also been detected in a few stars only, but is most often strongly enriched, if observed. Its abundance increases with temperature from about solar to  $\sim +2.0$  dex supersolar.

The iron abundance (Fe III, solar abundance: 7.50), however, is constant throughout the effective temperature regime. It ranges from  $\sim -0.7$  dex subsolar to  $\sim +0.5$  dex supersolar. For cobalt (Co III, solar abundance: 4.99) and zinc (Zn III, solar abundance: 4.56), Geier (2013) mostly derived upper limits. Nonetheless, these elements are also highly enhanced (up to  $\sim +2.0$  dex supersolar). Zn III is not shown in Fig. 3.3.1 because Geier (2013) were able to derive upper limits from a single line only.

Geier (2013) found no significant difference between the metal abundance patterns of close binary and apparently single isolated stars. The author therefore concluded that moderate tidal influence of close companions does not change the abundances in the atmospheres of hydrogen-rich hot subdwarfs. However, Geier (2013) was not able to determine the metal abundances for H-sdBs/H-sdOBs that have been spun up to very high rotational velocities of the order of  $v \sin i \sim 100 \text{ km s}^{-1}$  as the broadening of the spectral lines in these cases was too

---

<sup>25</sup>The origin of interstellar lines will be described in Sect. 8.2.5.

Table 3.1.: Metallicity pattern used for the abundance analysis presented in Ch. 11. Values are given as base-10 logarithmic particle densities relative to the density of all particles. Red entries are adjusted to roughly match the mean metal abundances for H-sdBs/H-sdOBs according to Naslim et al. (2013). These values roughly correspond to the abundances shown in Fig. 3.3.2. Note, however, that the abundance information provided in this table differs from the one used in Fig. 3.3.2. Solar abundances taken as a basis in this table stem from Asplund et al. (2009). Modified version of Table 11.1 in Schneider (2017).

Sp.	Ab.	Tim. sol.												
Li	-10.99	1	V	-7.11	10	Tc	-20.30	-	Eu	-11.52	1	Bi	-11.39	-
Be	-10.66	1	Cr	-5.40	10	Ru	-10.28	1.02	Gd	-10.99	0.95	Po	-20.30	-
B	-9.34	1	Mn	-5.61	10	Rh	-10.98	1.41	Tb	-11.72	1.05	At	-20.30	-
C	-4.84	0.06	Fe	-4.54	1	Pd	-10.39	1.20	Dy	-10.91	1.07	Rn	-20.30	-
N	-4.44	0.59	Co	-6.05	10	Ag	-10.84	1.82	Ho	-11.57	0.97	Fr	-20.30	-
O	-4.34	0.10	Ni	-4.82	10	Cd	-10.33	-	Er	-11.12	1	Ra	-20.30	-
F	-7.62	0.72	Cu	-6.85	10	In	-11.28	0.91	Tm	-11.92	1.05	Ac	-20.30	-
Ne	-5.04	0.12	Zn	-6.48	10	Sn	-8.00	100	Yb	-11.12	1.20	Th	-11.95	1.17
Na	-5.80	1	Ga	-8.00	10	Sb	-11.03	-	Lu	-11.95	0.98	Pa	-20.30	-
Mg	-5.24	0.16	Ge	-7.39	10	Te	-9.86	-	Hf	-11.33	0.72	U	-12.02	1
Al	-6.34	0.18	As	-9.74	-	I	-10.49	-	Ta	-12.16	-	Np	-20.30	-
Si	-5.54	0.10	Se	-8.70	-	Xe	-9.80	1	W	-11.19	1	Pu	-20.30	-
P	-6.63	1	Br	-9.50	-	Cs	-10.96	-	Re	-11.78	-	Am	-20.30	-
S	-5.54	0.24	Kr	-8.79	1	Ba	-9.86	1	Os	-10.64	1	Cm	-20.30	-
Cl	-6.81	0.54	Rb	-9.52	1	La	-10.94	1	Ir	-10.72	0.87	Bk	-20.30	-
Ar	-5.64	1	Sr	-7.17	100	Ce	-10.46	1	Pt	-10.42	-	Cf	-20.30	-
K	-7.01	1	Y	-7.83	100	Pr	-11.28	1.10	Au	-11.24	0.76	Es	-20.30	-
Ca	-4.70	10	Zr	-7.46	100	Nd	-10.62	1	Hg	-10.87	-			
Sc	-7.89	10	Nb	-10.63	0.89	Pm	-20.30	-	Tl	-11.27	0.74			
Ti	-6.09	10	Mo	-10.10	1.15	Sm	-11.08	1	Pb	-8.29	100			

### 3.3. Chemical Composition

---

strong (see also Sect. 7.1.1 for details on the effects of  $v \sin i$  on spectral fitting). Hence, such objects may still show abundances that are (completely) different from the ones presented.

Furthermore, Geier (2013) compared the metal abundances of the sample stars belonging to the upper helium sequence of Edlmann et al. (2003) to that associated with the lower one, but found that most species are not significantly affected by the difference in helium content. Only carbon, sulfur (and to a less extent also silicon) show significant differences. While the C abundance for stars on the upper helium sequence largely scatters up to supersolar values, the H-sdBs and H-sdOBs on the lower helium sequence exhibit abundances that are on average  $\lesssim -1.0$  dex below the solar one. Regarding the S abundance, a trend with temperature up to supersolar abundance values in the helium-rich sample can be observed, whereas the helium-poor sample only shows subsolar abundances.

Spectral analyses of near-UV (NUV) and far-UV (FUV) spectra overall confirm the findings from optical analyses (see, for instance, the works of Chayer et al. 2006, O’Toole & Heber 2006, or Blanchette et al. 2008), but also added heavier elements such as krypton (Kr) and manganese (Mn) as well as trans-iron elements such as nickel (Ni), copper (Cu), gallium (Ga), germanium (Ge), strontium (Sr), yttrium (Y), zirconium (Zr), tin (Sn), and lead (Pb) to the list of observed chemical species in the spectra of many H-sdBs and H-sdOBs. Moreover, these studies extended the information on elements for which only upper limits could be derived from the optical wavelength regime.

Naslim et al. (2013) proposed a mean abundance pattern for H-sdB/H-sdOB stars. It is displayed in Fig. 3.3.2. While the mean abundances for the lighter metals C, N, O, Ne, Mg, Al, Si, and S are clearly subsolar, the heavier elements beyond Ar show strong anomalies because of supersolar abundances. On average, the latter are 10 times enhanced compared to the solar abundance level, but the overabundance can also be as high as 1000 times solar depending on the effective temperature of the specific star. The sole exception is Fe, which has a solar mean abundance. The most promising explanation for the observed abundance anomalies is atomic transport (diffusion) in the stellar atmosphere. This will be discussed in the further course of this section.

Table 3.1 lists the metallicity pattern used for the abundance analysis presented in Ch. 11. Red entries are adjusted to roughly match the mean metal abundances for H-sdBs/H-sdOBs according to Naslim et al. (2013). In consequence, the respective values roughly correspond to the abundances shown in Fig. 3.3.2. Note, however, that the abundance information provided in Table 3.1 differs from the one used in Fig. 3.3.2.

### The $^3\text{He}$ Anomaly

Usually, the measured helium abundance of stars refers to the one of the “standard”  $^4\text{He}$  isotope. However, a small amount of B-type MS, BHB, and EHB stars have been found to show surface compositions that are (strongly) enriched by the lighter  $^3\text{He}$  isotope. This phenomenon is generally referred to as the  $^3\text{He}$  abundance anomaly, leading to significantly lower  $^4\text{He}/^3\text{He}$  isotopic abundance ratios than the solar one, which is of the order of  $\sim 10^4$  (Michaud et al., 2015). It is widely accepted that the  $^3\text{He}$  anomaly must also be related to

special diffusion processes occurring in the stellar atmosphere.

Typically,  $^3\text{He}$  enrichment is identified by precisely measuring the small isotopic line shifts of the He I absorption lines in the optical part of a stellar spectrum. The isotopic shifts with respect to the “normal”  $^4\text{He}$  isotope vary from line to line. As first elaborated by Hughes & Eckart (1930), two effects are physically important: I) a shift of term energies affecting all terms at the same time,  $\Delta E = (\Delta\mu/m)E$ , where  $\Delta\mu$  is the difference between the reduced masses of the two helium isotopes,  $m$  is the electron mass, and  $E$  is the  $^4\text{He}$  term energy; II) a specific shift which depends on the wave functions and is non-zero for a two-electron system such as He I only for the  $P$  terms. The reduced mass effect leads to an overall reduction of the term energies for  $^3\text{He}$  compared to  $^4\text{He}$ , whereas the specific shift reduces the singlet  $P$  term energies and increases the triplet ones (Schneider et al., 2018). All neutral helium line transitions in the NUV, optical, and near-infrared (NIR) spectral range up to principal quantum number  $n = 8$  are listed in Table 3.2. Both effects cancel out to some extent for the  $^3P$  series (all corresponding transitions have isotopic shifts of  $|\Delta\lambda| \lesssim 0.1 \text{ \AA}$ ). However, larger shifts occur for the  $^1S$ ,  $^3S$ , and  $^1P$  series ( $|\Delta\lambda| \gtrsim 0.13 \text{ \AA}$ ). For instance,  $^3\text{He I } 5875 \text{ \AA}$  is shifted only slightly ( $\sim 0.04 \text{ \AA}$ ) towards redder wavelengths and can therefore be used as a reference line to check against other effects that may shift the He I positions relative to lines of other elements. Such effects may be pressure shifts<sup>26</sup> or shifts resulting from the presence of magnetic fields. Amongst others, the strongest isotopic line shifts in the optical are observed for  $^3\text{He I } 7281 \text{ \AA}$ ,  $^3\text{He I } 6678 \text{ \AA}$ , and  $^3\text{He I } 4922 \text{ \AA}$ ; they are  $\sim 0.55 \text{ \AA}$ ,  $\sim 0.50 \text{ \AA}$ , and  $\sim 0.33 \text{ \AA}$ , respectively (see Table 3.2 and Fred et al. 1951)<sup>27</sup>. Apart from the large expected isotopic shift,  $^3\text{He I } 6678 \text{ \AA}$  has two other advantages. First, it is a singlet, which leads to an expected symmetric line profile. Second, it is usually not blended by other lines as it is located in a relatively uncrowded region of the stellar spectrum. High S/N spectra are desirable in order to precisely measure the position of the optical helium lines, in particular that of  $^3\text{He I } 6678 \text{ \AA}$ . To this end, however, the radial velocity (RV; see also Sect. 7.1.1) of the respective  $^3\text{He}$  star has to be well determined before the wavelengths of the observed lines can be interpreted. This is because the RV strongly influences the measured isotopic line shifts and, hence, the abundance ratio  $^4\text{He}/^3\text{He}$ . It is obvious that helium lines should be avoided for the determination of the RV when aiming at  $^3\text{He}$ . Instead, RVs should be measured from sharp metal lines. Thus, slowly rotating stars are preferred for detailed  $^3\text{He}$  abundance studies (Schneider et al., 2018). The  $^3\text{He}$  abundance anomaly was first observed among helium-weak B-type MS stars in the temperature strip of  $14\,000 \text{ K} \lesssim T_{\text{eff}} \lesssim 21\,000 \text{ K}$  (Hartoog & Cowley, 1979), with 3 Centauri A (3 Cen A) being the prototype star (Sargent & Jugaku, 1961). These stars are located in between the helium-rich B dwarf stars (with  $T_{\text{eff}}$  up to  $\sim 32\,000 \text{ K}$ ) and a group of helium-weak ones (with  $T_{\text{eff}}$  down to  $\sim 13\,000 \text{ K}$ ) that do not show any traces of  $^3\text{He}$  (Michaud et al., 2015). Later, the search for  $^3\text{He}$  was extended to the BHB since these stars observed in globular clusters and in the Galactic halo were also found to be helium-weak. The first BHB star to show the  $^3\text{He}$  anomaly was Feige 86 and it was discovered by Hartoog (1979). A few

<sup>26</sup>Pressure broadening will be topic in Sect. 6.5.1.

<sup>27</sup>Section 7.1.1 will provide a closer look at the  $^4\text{He}/^3\text{He}$  line formation by means of He I 4922 Å, 5875 Å, and 6678 Å. In this context, the effects of the  $^4\text{He}/^3\text{He}$  isotopic abundance ratio and the total helium abundance  $\log n(^4\text{He} + ^3\text{He})$  on the respective line shapes will be discussed (see also Fig. 7.1.2).

### 3.3. Chemical Composition

Table 3.2.: Transitions and isotopic shifts  $\Delta\lambda := \lambda_0(^3\text{He}) - \lambda_0(^4\text{He})$  of selected He I lines in the NUV, optical, and NIR spectral range up to principal quantum number  $n = 8$ . Modified version of Table 1 in Schneider et al. (2018).

Transition	$\lambda_0$ ( $^4\text{He}$ ) [Å]	$\lambda_0$ ( $^3\text{He}$ ) [Å]	$\Delta\lambda$ [Å]	Transition	$\lambda_0$ ( $^4\text{He}$ ) [Å]	$\lambda_0$ ( $^3\text{He}$ ) [Å]	$\Delta\lambda$ [Å]
1s 2s $^3\text{S}_1$ -1s 2p $^3\text{P}_2^0$	10 830.340	10 831.658	1.318	1s 2p $^1\text{P}_1^0$ -1s 3s $^1\text{S}_0$	7281.351	7281.904	0.553
1s 2s $^3\text{S}_1$ -1s 3p $^3\text{P}_2^0$	3888.649	3888.862	0.213	1s 2p $^1\text{P}_1^0$ -1s 3d $^1\text{D}_2$	6678.152	6678.654	0.502
1s 2s $^3\text{S}_1$ -1s 4p $^3\text{P}_2^0$	3187.745	3187.903	0.158	1s 2p $^1\text{P}_1^0$ -1s 4s $^1\text{S}_0$	5047.739	5048.078	0.339
1s 2s $^3\text{S}_1$ -1s 5p $^3\text{P}_2^0$	2945.104	2945.246	0.142	1s 2p $^1\text{P}_1^0$ -1s 4d $^1\text{D}_2$	4921.931	4922.262	0.331
1s 2s $^3\text{S}_1$ -1s 6p $^3\text{P}_2^0$	2829.081	2829.216	0.135	1s 2p $^1\text{P}_1^0$ -1s 5s $^1\text{S}_0$	4437.553	4437.841	0.288
1s 2s $^3\text{S}_1$ -1s 7p $^3\text{P}_2^0$	2763.803	2763.934	0.131	1s 2p $^1\text{P}_1^0$ -1s 5d $^1\text{D}_2$	4387.929	4388.213	0.284
1s 2s $^3\text{S}_1$ -1s 8p $^3\text{P}_2^0$	2723.192	2723.320	0.128	1s 2p $^1\text{P}_1^0$ -1s 6s $^1\text{S}_0$	4168.971	4169.237	0.266
				1s 2p $^1\text{P}_1^0$ -1s 6d $^1\text{D}_2$	4143.759	4144.023	0.264
				1s 2p $^1\text{P}_1^0$ -1s 7s $^1\text{S}_0$	4023.980	4024.233	0.253
				1s 2p $^1\text{P}_1^0$ -1s 7d $^1\text{D}_2$	4009.257	4009.509	0.252
				1s 2p $^1\text{P}_1^0$ -1s 8s $^1\text{S}_0$	3935.945	3936.192	0.247
				1s 2p $^1\text{P}_1^0$ -1s 8d $^1\text{D}_2$	3926.544	3926.790	0.246
1s 2s $^1\text{S}_0$ -1s 3p $^1\text{P}_1^0$	5015.678	5015.890	0.212	1s 2p $^3\text{P}_1^0$ -1s 3s $^3\text{S}_1$	7065.215	7065.205	-0.010
1s 2s $^1\text{S}_0$ -1s 4p $^1\text{P}_1^0$	3964.729	3964.912	0.183	1s 2p $^3\text{P}_1^0$ -1s 3d $^3\text{D}_1$	5875.625	5875.669	0.044
1s 2s $^1\text{S}_0$ -1s 5p $^1\text{P}_1^0$	3613.642	3613.812	0.170	1s 2p $^3\text{P}_2^0$ -1s 4s $^3\text{S}_1$	4713.139	4713.208	0.069
1s 2s $^1\text{S}_0$ -1s 6p $^1\text{P}_1^0$	3447.589	3447.753	0.164	1s 2p $^3\text{P}_2^0$ -1s 4d $^3\text{D}_1$	4471.470	4471.544	0.074
1s 2s $^1\text{S}_0$ -1s 7p $^1\text{P}_1^0$	3354.555	3354.715	0.160	1s 2p $^3\text{P}_2^0$ -1s 5s $^3\text{S}_1$	4120.811	4120.887	0.076
1s 2s $^1\text{S}_0$ -1s 8p $^1\text{P}_1^0$	3296.773	3296.930	0.157	1s 2p $^3\text{P}_2^0$ -1s 5d $^3\text{D}_1$	4026.184	4026.262	0.078
				1s 2p $^3\text{P}_2^0$ -1s 6s $^3\text{S}_1$	3867.472	3867.550	0.078
				1s 2p $^3\text{P}_2^0$ -1s 6d $^3\text{D}_1$	3819.602	3819.680	0.078
				1s 2p $^3\text{P}_2^0$ -1s 7s $^3\text{S}_1$	3732.863	3732.942	0.079
				1s 2p $^3\text{P}_2^0$ -1s 7d $^3\text{D}_1$	3704.995	3705.074	0.079
				1s 2p $^3\text{P}_2^0$ -1s 8s $^3\text{S}_1$	3651.982	3652.060	0.078
				1s 2p $^3\text{P}_2^0$ -1s 8d $^3\text{D}_1$	3634.231	3634.310	0.079

**Notes:** The listed transitions are implemented in non-local thermodynamic equilibrium in the  $^3\text{He}$  and  $^4\text{He}$  model atoms used in this work (see Sects. 6.4 and 6.8 for details). All rest-frame wavelengths  $\lambda_0$  for the  $^3\text{He}$  and  $^4\text{He}$  components of the listed He I lines are extracted from the *Atomic Spectra Database* of the National Institute of Standards and Technology (NIST; [https://physics.nist.gov/PhysRefData/ASD/lines\\_form.html](https://physics.nist.gov/PhysRefData/ASD/lines_form.html), last called on 13th February 2021). For each individual line, only one of the transitions with the highest relative intensity according to NIST is listed.

years later, Heber (1987) classified two additional BHBs (PHL 25 and PHL 382) as  $^3\text{He}$  stars. For over 30 years, the number of  $^3\text{He}$  BHB stars has remained the same until very recently Hämmerich (2020) detected the  $^3\text{He}$  isotope in another two BHBs (HD 110942 and Feige 6). However, the  $^3\text{He}$  anomaly has also been found at the very blue end of the HB, that is, among EHB stars, with the rotating H-sdB SB 290 being the first discovery (Heber, 1987). Later, another three H-sdBs (Feige 36, BD+48° 2721, PG 0133+114) in which  $^3\text{He}$  is enriched in the atmosphere were found (Edelmann et al., 1997, 1999, 2001). Geier et al. (2013a) added another seven  $^3\text{He}$  H-sdBs (EC 14338-1445, EC 03591-3232, EC 12234-2607, EC 03263-6403, PG 1519+640, PG 1710+490, and Feige 38). So far, the  $^3\text{He}$  anomaly on the EHB has only been observed in H-sdB stars. Despite of all the discoveries, however,  $^3\text{He}$  stars are still a rare subclass of H-sdBs. Heber & Edelmann (2004) estimated that less than 5% of the H-sdB stars show the  $^3\text{He}$  anomaly. Geier et al. (2013a) estimated a somewhat higher fraction of 18%.

Most of the  $^3\text{He}$  BHBs and  $^3\text{He}$  H-sdBs known up to date do not show periodic RV variations. In consequence, there is no evidence that binary evolution facilitates the photospheric  $^3\text{He}$  enrichment in these stars. However, three close binaries are known among  $^3\text{He}$  H-sdBs: Feige 36, PG 1519+640, and PG 0133+114. Feige 36 has a RV semi-amplitude of  $K = 134.6 \text{ km s}^{-1}$  (Saffer et al., 1998) and a period of  $P = 0.35386 \pm 0.00014 \text{ d}$  (Moran et al., 1999). PG 1519+640 has  $K = 36.7 \pm 1.2 \text{ km s}^{-1}$  and  $P = 0.539 \pm 0.003 \text{ d}$  (Morales-Rueda et al., 2003a; Edelmann et al., 2004; Copperwheat et al., 2011), whereas PG 0133+114 exhibits  $K = 82.0 \pm 0.3 \text{ km s}^{-1}$  and  $P = 1.23787 \pm 0.00003 \text{ d}$  (Morales-Rueda et al., 2003b; Edelmann et al., 2005). Remarkably, the  $^3\text{He}$  H-sdBs were found to cluster in a narrow effective temperature strip between  $\sim 27\,000 \text{ K}$  and  $\sim 31\,000 \text{ K}$  (Geier et al., 2013a), with BD+48° 2721 being the sole exception. This narrow temperature strip resembles the one found for the helium-weak B-type MS stars, although the latter are observed at lower temperatures. Interestingly, all of the  $^3\text{He}$  H-sdBs belong to the upper helium sequence of Edelmann et al. (2003). Therefore, it was suggested by Geier et al. (2013a) to divide this sequence into “normal” helium H-sdBs,  $^3\text{He}$  H-sdBs, and helium-rich ones, similar to what has been observed for the  $^3\text{He}$  anomaly on the MS.

Some  $^3\text{He}$  H-sdBs/BHBs show clear displacements of the He I 6678 Å line, indicating that  $^4\text{He}/^3\text{He} < 1$ , whereas others exhibit strong lines of  $^3\text{He}$  that are blended with  $^4\text{He}$  components of similar strength. However, there is no correlation between the  $^4\text{He}/^3\text{He}$  abundance ratio and  $T_{\text{eff}}$  (Geier et al., 2013a).

Detailed information on isotopic helium abundances and  $^4\text{He}/^3\text{He}$  abundance ratios for selected  $^3\text{He}$  H-sdBs/BHBs shall not be provided at this point, but will be presented within the detailed  $^3\text{He}$  analysis of Ch. 10.

## H-sdOs

Many of the measured elemental abundances for H-sdO stars resulted from FUV spectra. Hence, the number of H-sdOs, whose surface compositions have been studied in great detail, is by far lower than that of the H-sdBs and H-sdOBs. Consequently, the results for only eight H-sdOs shall be presented here. These are Feige 110, AA Dor, and EC 11481-2303 (Rauch et al., 2010, 2014; Klepp & Rauch, 2011), Feige 34, Feige 67, AGK+81° 266, and LS II +18° 9 (Latour et al., 2018) as well as BD+28° 4211 (Latour et al., 2013, 2015), which has a higher helium content (solar) than the other considered objects.

As can be seen from the abundance patterns of Feige 110, AA Dor, and EC 11481-2303 (see Fig. 3.3.3), the star-to-star scatter is large, as in the case of the H-sdBs and H-sdOBs. In addition, the pattern strongly resembles the mean abundance one for H-sdBs/H-sdOBs (compare Fig. 3.3.3 to Fig. 3.3.2). The lighter metals (C to S) are mainly subsolar (by  $\sim -2.0$  dex) to solar, with the exception of Feige 110 for which C, O, and Si are clearly depleted. The general strong enrichment of iron-group and trans-iron elements is clearly visible and increases with increasing temperature. This indicates that diffusion processes, which are responsible for these overabundances, must act in a similar way over a wide temperature range covering the H-sdBs, H-sdOBs, and H-sdOs. This is quite surprising since over such a large range both the

### 3.3. Chemical Composition

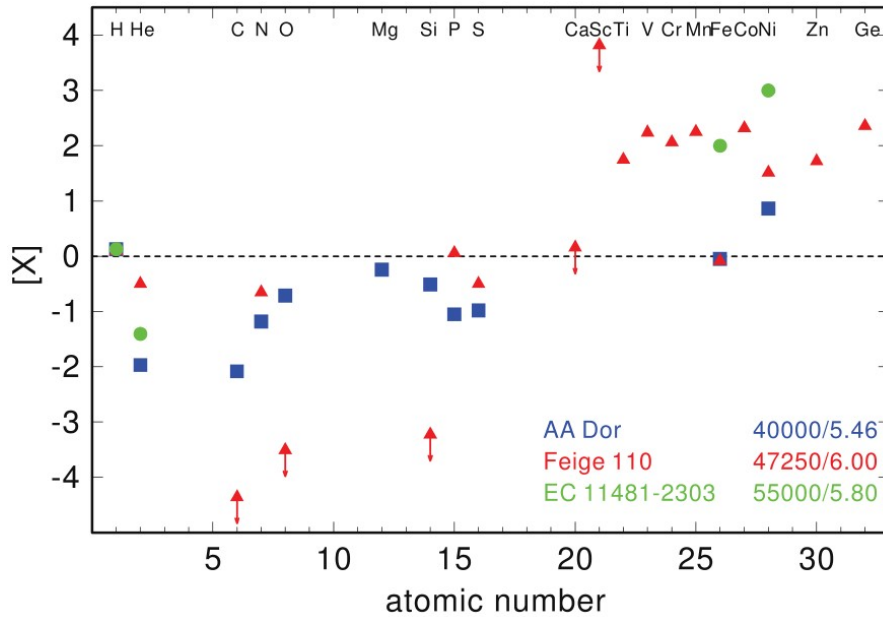


Figure 3.3.3.: Photospheric elemental abundances for the three helium-poor sdO stars AA Dor (blue squares), Feige 110 (red triangles), and EC 11481-2303 (green circles) relative to the solar abundance level (dashed horizontal line) from Asplund et al. (2009). Downward arrows indicate upper limits. The atmospheric parameters ( $T_{\text{eff}}$  and  $\log g$ ) of the three stars are shown in the legend.  $[X] := \log N(X)/N(\text{all elements}) - \log N(X)/N(\text{all elements})_{\odot}$ . Adopted from Heber (2016); original version: Rauch et al. (2014).

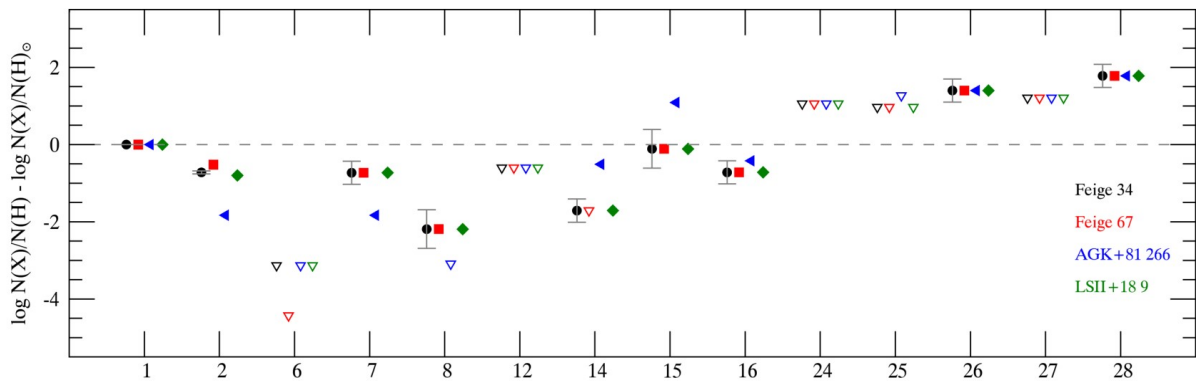


Figure 3.3.4.: Photospheric elemental abundances for the four helium-poor sdO stars Feige 34 (full black circles), Feige 67 (full red squares), AGK+81° 266 (full blue left triangles), and LS II +18° 9 (full green diamonds) relative to the solar abundance level (dashed horizontal line) from Asplund et al. (2009). Open downward triangles with the same color code indicate upper limits. Typical error bars are shown in the case of Feige 34. The numbers on the abscissa refer to the atomic numbers of the individual chemical elements. Adopted from Latour et al. (2018).

degree of ionization and the luminosity change, which, in theory, should strongly affect the atomic transport. Interestingly, Fe is solar for Feige 110 and AA Dor, but heavily enriched (by  $\sim +2.0$  dex) in EC 11481-2303 (Heber, 2016).

Overall, the results for Feige 34, Feige 67, AGK+81° 266, and LS II +18° 9 determined by Latour et al. (2018) fit the picture. Nonetheless, it is really remarkable how similar these four stars are in terms of metal abundances (see also Fig. 3.3.4).

BD+28° 4211 is the only sdO star whose abundance pattern does not fit into the general scheme. As for the other H-sdOs, the lighter elements (C to S) are subsolar to solar, but the abundances of the heavy metals are on average subsolar (see Figure 8 in Latour et al. 2013). However, it has to be pointed out that BD+28° 4211 may also be a post-AGB star, not least because of its higher temperature of  $T_{\text{eff}} \sim 81000\text{-}82000$  K and higher surface gravity of  $\log(g) \sim 6.2\text{-}6.5$  (Latour et al., 2013, 2015). This together with its solar helium abundance, which also clearly differs from that of the other presented objects, makes the star not comparable to the other considered H-sdOs (Heber, 2016).

Feige 34, Feige 67, AGK+81° 266, LS II +18° 9, and BD+28° 4211 are also part of this work's analysis, even though no spectra of these stars will be analyzed (see Sect. 8.1.2). Instead, the spectroscopic results for  $T_{\text{eff}}$ ,  $\log(g)$ , and  $\log n(\text{He})$  from literature (Latour et al., 2013, 2015, 2018) will be used.

## He-sdBs

Figure 3.3.2 also shows the mean elemental abundances of intermediate He-sdBs analyzed by Naslim et al. (2010). The intermediate and, thus, also the extreme He-sdBs have much more helium than their standard hydrogen-rich siblings, the H-sdBs. In He-sdBs, the lighter metals (carbon to sulfur) seem to be slightly more abundant than in H-sdBs. The studies of Naslim et al. (2011, 2013) on intermediate He-sdBs revealed a significant enrichment of several transition elements for some of the analyzed program stars, much larger than observed for H-sdB stars of similar effective temperature. The first He-sdB star, where this chemical peculiarity has been observed, was LS IV-14° 116 (Naslim et al., 2011), followed by HE 2359-2844 and HE 1256-2738 (Naslim et al., 2013). The surface abundances for these three intermediate He-sdBs are also plotted in Fig. 3.3.2. More such chemically peculiar objects were found in recent studies: [CW83] 0825+15<sup>28</sup> (Jeffery et al., 2017), EC 22536-4304 (Jeffery & Miszalski, 2019), Feige 46 (Latour et al., 2019a; Dorsch et al., 2020), PG 1559+048 and FBS 1749+373 (Naslim et al., 2020) as well as PHL 417 (Østensen et al., 2020). In particular, the elements Ge, Kr, Sr, Y, Zr, Sn, and Pb have not only been observed in the FUV and NUV spectral ranges of these stars, as is the case for many H-sdBs as well, but also in the optical as Ge III/IV, Kr III, Sr II/III, Y III, Zr III/IV, Sn IV, and Pb IV (see, for instance, Dorsch et al. 2020). In fact, the overabundances for these heavy metals in the respective stars can be up to four orders of magnitude compared to the solar composition (see Figs. 3.3.2 and 3.3.5). Therefore, their abundances are 10-100 times higher than in standard H-sdBs (Heber, 2016).

<sup>28</sup>[CW83] 0825+15 is also part of this work's target sample (see Sect. 8.1).

### 3.3. Chemical Composition

LS IV-14° 116, Feige 46, and PHL 417 might be the most remarkable *heavy-metal* stars because all three belong to the class of V366 Aqr variables, showing long- and multi-periodic luminosity variations which cannot be explained by the usual opacity<sup>29</sup> ( $\kappa$ -) pulsation mechanism predominantly acting in the respective  $T_{\text{eff}}\text{-log}(g)$  regime<sup>30</sup>. Furthermore, LS IV-14° 116

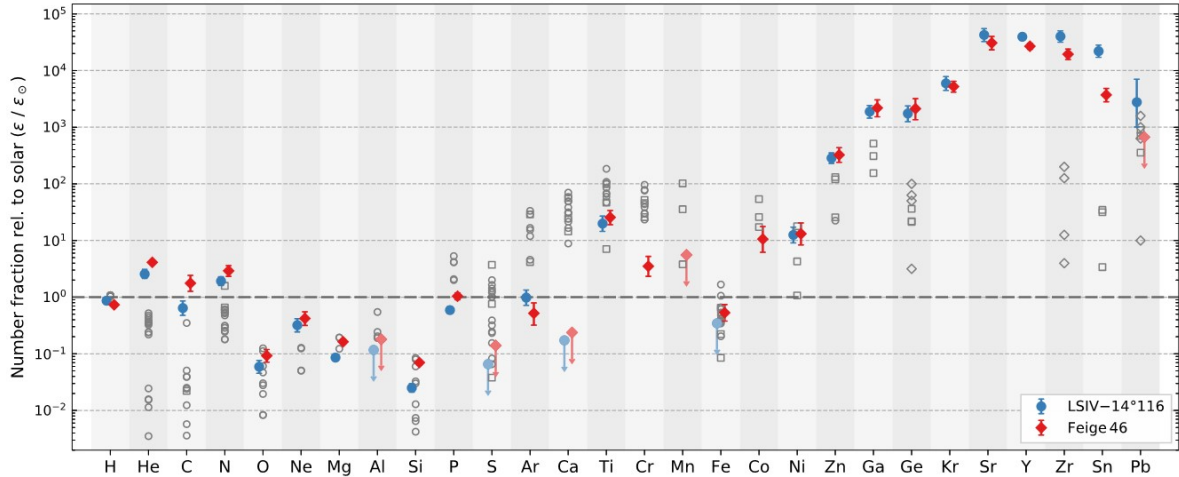


Figure 3.3.5.: Abundance patterns (by number fraction) of the two heavy-metal intermediate He-sdBs LS IV-14° 116 (blue circles) and Feige 46 (red diamonds) relative to that of the Sun (dashed horizontal line; Asplund et al. 2009).  $\epsilon_X := N(X) / \sum_i N(i)$ . Downward arrows and less saturated colors mark upper limits. For comparison, abundance measurements for H-sdOBs in a similar effective temperature regime ( $33\,000\text{ K} \lesssim T_{\text{eff}} \lesssim 36\,500\text{ K}$ ) are plotted as gray open symbols: circles (based on optical data; Geier 2013), diamonds (based on FUV data; Chayer et al. 2006), and squares (based on UV data; O’Toole & Heber 2006). Adopted from Dorsch et al. (2020).

<sup>29</sup>The term ‘opacity’ will be explained in Sect. 6.1.

<sup>30</sup>The vast majority of pulsating hot subdwarfs are found among H-sdBs. Only a small group of sdOs shows pulsational characteristics (Woudt et al., 2006; Randall et al., 2011; Østensen, 2012; Van Grootel et al., 2014), whereby most of these objects are found in globular clusters ( $\omega$  Cen variables) rather than in the field. The pulsational light variations in H-sdB stars are well established. Both pressure (p-mode) and gravity (g-mode) oscillations have been observed. While the former have periods of a few minutes (short periods), the latter exhibit periods ranging from  $\sim 30$  minutes to a few hours (long periods; see, for instance, the recent works of Holdsworth et al. 2017 and Reed et al. 2018). It is assumed that the pulsations observed in H-sdB stars are driven by the opacity ( $\kappa$ -) mechanism which is related to an iron and nickel opacity bump in the thin stellar envelope. This mechanism is able to produce both short-periodic oscillations (Charpinet et al., 1996, 1997) at effective temperatures of LS IV-14° 116, Feige 46, and PHL 417 ( $T_{\text{eff}} \sim 35\,000\text{ K}$ ), which are, however, not observed in these stars, and long-periodic ones (Green et al., 2003; Jeffery & Saio, 2006), but at lower temperatures. For LS IV-14° 116, excited oscillations with periods of  $P \sim 2\,000 - 5\,000\text{ s}$  were measured (Ahmad & Jeffery, 2005; Jeffery, 2011; Green et al., 2011), whereas Feige 46 exhibits periods of  $P \sim 2\,300 - 3\,400\text{ s}$  (Latour et al., 2019b). PHL 417 has  $P \sim 2\,280 - 6\,300\text{ s}$  (Østensen et al., 2020). Therefore, in all three cases the observed period ranges are remarkably long for the corresponding effective temperature regime and it still remains a mystery how the respective excited oscillations could be produced in these stars.

and Feige 46 were found to have retrograde orbits (Randall et al., 2015; Latour et al., 2019b), meaning that these stars orbit the Galactic centre in the opposite direction to the disk, which implies that both objects belong to the halo population unlike most of the known helium-rich hot subdwarfs (see, for instance, Martin et al. 2017).

The heavy-element anomalies in intermediate He-sdBs are unlikely to be caused by thermonuclear burning (nucleosynthesis) reaching the stellar surface. Instead, special diffusion processes must be at work (Heber, 2016). At first, it was believed that radiative levitation<sup>31</sup> in a particularly quiet atmosphere invoked by a strong magnetic field ( $\gtrsim$  kG) may be responsible for the overabundances in the first heavy-metal star LS IV-14° 116. However, Randall et al. (2015) could rule out a mean longitudinal magnetic field of more than 300 G.

## He-sdOs

Most of what is known about the surface composition of intermediate and extreme He-sdO stars refers to the elemental abundances of helium, carbon, and nitrogen. Figure 3.3.6 shows these abundances for the 33 He-sdOs from the ESO SPY project, as determined by Hirsch (2009). Note that the abundances are given as logarithmic mass fractions and that they are sorted by descending carbon content.

Helium only varies slightly. However, Fig. 3.3.6 clearly reveals a bimodal distribution in terms of carbon, that is, either the element is strongly depleted or enhanced with respect to the solar value. Regarding nitrogen, the vast majority of stars (about two thirds) have abundances which are 3-10 times higher compared to the Sun. However, three stars are strongly depleted by more than a factor of 15 and another three are only mildly depleted. Two stars have a solar nitrogen content. He-sdOs can therefore be classified in terms of their carbon and nitrogen abundances. C-rich (C-type) He-sdOs are enhanced in carbon compared to the Sun, whereas N-rich (N-type) He-sdOs show supersolar nitrogen abundances. There is a group in between, which are enhanced in carbon but also show significant amounts of nitrogen. These stars are referred to as CN-enriched (CN-type) He-sdOs (Heber, 2016).

Interestingly, all C-type He-sdOs from ESO SPY are located at the hot end ( $T_{\text{eff}} \gtrsim 43\,900$  K) of the Kiel diagram, with the exception of only two, whereas the N-type He-sdOs are found at much cooler temperatures (Hirsch, 2009). However, no correlation between the carbon/nitrogen content and the effective temperature has been found. The same holds for a possible correlation between the carbon/nitrogen abundance and the surface gravity (Heber, 2016).

Schindewolf et al. (2018) analyzed the abundances of four prototypical extreme He-sdOs in greater detail, including the heavier elements Ne, Mg, Al, Si, P, S, Fe and Ni: an N-type one (CD-31° 4800) and three C(N)-type ones (LSS 1274, [CW83] 0904-02, and LS IV +10° 9<sup>32</sup>). Figure 3.3.7 shows their abundance patterns with respect to the solar composition. As expected, all stars are clearly depleted in hydrogen but strongly enriched in helium compared

<sup>31</sup>The term ‘radiative levitation’ will be explained in the context of diffusion in the further course of this section.

<sup>32</sup>LS IV +10° 9 is also part of this work’s target sample (see Sect. 8.1). However, no metal abundances will be derived for the star (see Ch. 11).

### 3.3. Chemical Composition

to the Sun. Overall, correlations among the C, N, O, and Ne abundances are observed: The oxygen-to-nitrogen and neon-to-nitrogen ratios correlate positively with the nitrogen-to-carbon ratio. However, the heavier elements show pronounced star-to-star variations. For CD-31° 4800 (see the left-hand panel of Fig. 3.3.7), nitrogen is enriched and carbon and

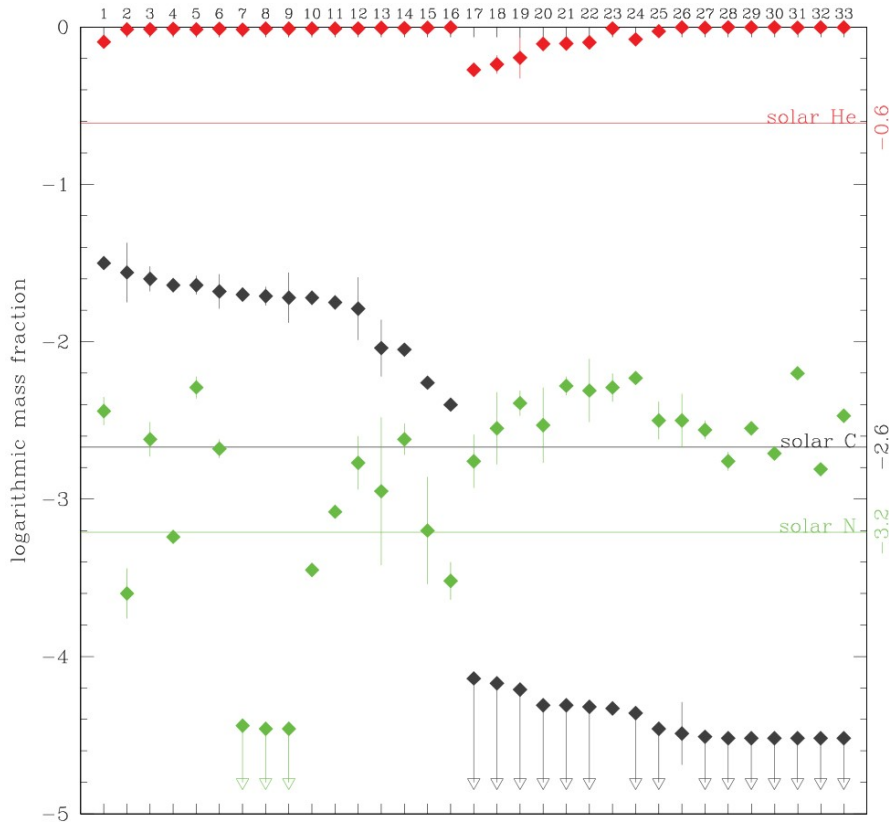


Figure 3.3.6.: Helium (red), carbon (dark gray), and nitrogen (green) abundances of 33 He-sdO stars from the ESO SPY project. The abundances are given as logarithmic mass fractions and are sorted by descending carbon abundance. Solar abundances according to Asplund et al. (2009) are marked by the respective solid horizontal lines and downward arrows represent upper limits. Adopted from Heber (2016); original version: Hirsch (2009).

oxygen are depleted, which indicates a clear CNO bi-cycle abundance pattern. Moreover, neon is only slightly above solar and the other intermediate mass elements (Mg to S) are below solar by a factor of up to  $\sim 2$ . Fe is clearly depleted compared to the Sun, whereas Ni is slightly enriched (Schindewolf et al., 2018).

No CNO bi-cycle is observed for LSS 1274, [CW83] 0904-02, and LS IV +10° 9 since carbon is strongly enriched in all three stars (see the right-hand panel of Fig. 3.3.7). Oxygen is depleted, but less pronounced than in CD-31° 4800. The nitrogen abundance of LS IV +10° 9 is comparable to that of CD-31° 4800, whereas LSS 1274 and [CW83] 0904-02 are less enriched in N (the latter even has a nitrogen content that is about solar). Compared to the solar abundance

value, neon is enhanced by factors between  $\sim 3$ -10 in LSS 1274, [CW83] 0904-02, and LS IV +10° 9. Interestingly, the other intermediate mass elements (Mg to S) show a strong scatter around their solar abundance levels for all three stars, whereby LS IV +10° 9 seems to have the highest abundances. The nickel-to-iron ratio is significantly supersolar in all three stars as Fe is clearly subsolar and the Ni abundances are (slightly) supersolar. In fact, the latter show a small trend to higher abundances from [CW83] 0904-02 over LS IV +10° 9 to LSS 1274 (Schindewolf et al., 2018).

Interestingly, Dorsch et al. (2019) found heavy-metal enrichment in the intermediate He-sdO

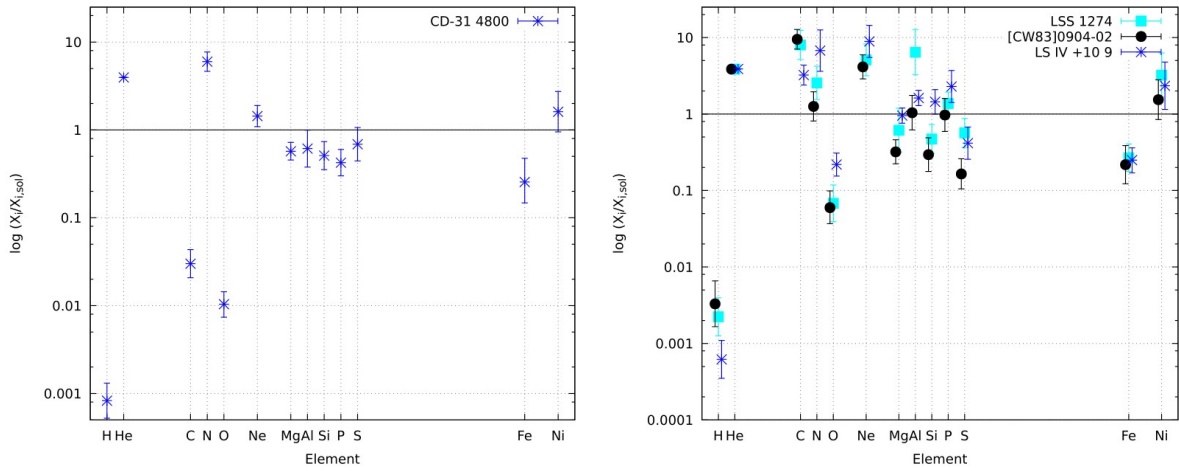


Figure 3.3.7.: Abundance patterns of the four prototypical extreme He-sdO stars CD-31° 4800, LSS 1274, [CW83] 0904-02, and LS IV +10° 9 with respect to the solar composition (solid horizontal lines) according to Asplund et al. (2009). The abundances  $X_i$  and  $X_{i,solar}$  represent mass fractions. *Left-hand panel*: the N-type He-sdO CD-31° 4800 (blue crosses). *Right-hand panel*: the C(N)-type He-sdOs LSS 1274 (turquoise squares), [CW83] 0904-02 (black circles), and LS IV +10° 9 (blue crosses). Adopted from Schindewolf et al. (2018).

stars HZ 44 and HD 127493, very similar to the one observed for the heavy-metal intermediate He-sdBs. In the case of HZ 44 and HD 127493, the heavy metals turned out to be overabundant by one to four orders of magnitude with respect to the solar composition (see Figure 13 in Dorsch et al. 2019). Again, Zr and Pb are among the most enriched elements. In fact, with measured abundances for 29 metals, including that for the trans-iron elements Ga, Ge, As, Se, Zr, Sn, and Pb, and additional upper limits for ten other metals, HZ 44 is the best-described hot subdwarf in terms of chemical composition so far (Dorsch et al., 2019).

The heavy-element anomalies in the intermediate He-sdOs HZ 44 and HD 127493 are also not caused by nucleosynthesis. As for the heavy-metal intermediate He-sdBs, special diffusion processes are needed in order to explain them. The surface compositions of extreme He-sdOs, however, are most likely not affected by atomic transport processes. This is mainly due to convection caused by the ionization of He II (Groth et al., 1985). In any case, the C, N, O, and Ne abundances in both intermediate and extreme He-sdOs strongly depend on the individual formation scenario from which these stars have resulted. This will be further discussed in Sect.

### 3.3. Chemical Composition

---

3.4. Vice versa, chemical abundance determinations for He-sdOs in terms of C, N, O, and Ne can therefore also be used to constrain the evolutionary scenarios (see, for instance, Zhang & Jeffery 2012 or Schindewolf et al. 2018).

## Diffusion Theory

As described in the previous sections, most hot subdwarf stars show abundance anomalies and, thus, are highly chemically peculiar. It is commonly agreed that these anomalies do not result from thermonuclear burning, but from atomic transport, that is, diffusion processes occurring in the stellar atmosphere (Greenstein 1967; see Michaud et al. 2015 for a detailed review). Simplistic atmospheric diffusion models predict the equilibrium abundance of a particular element in the photosphere<sup>33</sup> to be set by a balance between *gravitational settling* caused by the gravitational force and *radiative levitation* caused by the radiation pressure.

Gravitational settling is closely linked to the mass  $m$  of atoms/ions associated with the corresponding chemical element in question as well as to the surface gravity  $g$  of a star. Hence, the heavier elements sink out of the photosphere right after a star has been born, whereas the lightest ones remain.

On the other hand, the radiative pressure and the radiative levitation are linked to the radiative acceleration  $g_{\text{rad}}$ <sup>34</sup>. In the case of bound-bound atomic transitions only, the radiative acceleration  $g_{ikm}$  due to a single transition from the lower energy level  $k$  to the upper level  $m$  of an atom/ion associated with species  $A$  and in ionization stage  $i$  is given by (Michaud et al., 2015):

$$g_{ikm} = \frac{1}{m_{A_i} c} \int_0^{\infty} \frac{N_{ik}}{N_i} \sigma_{ikm} F_{\nu} d\nu. \quad (3.6)$$

Here,  $m_{A_i}$  denotes the mass of the atom/ion,  $c$  is the vacuum speed of light,  $F_{\nu} d\nu$  is the net outward radiative energy flux in the frequency interval  $d\nu$ , and  $\sigma_{ikm}$  is the absorption cross section for the considered bound-bound transition. The fraction  $N_{ik}/N_i$  describes the ratio of atoms/ions  $A_i$  in energy level  $k$  per unit volume to the total number of atoms/ions  $A_i$  per unit volume. It is referred to as the *population* or *occupation number* of state  $k$ .

The higher the elemental abundance of an ion, the larger the number of absorbers and, therefore, the higher the absorption coefficient  $\kappa_{ikm} := N_{ik} \sigma_{ikm}$ . According to Eq. (3.6), a higher abundance hence directly affects the radiative acceleration and, consequently, the radiation pressure. However, this only applies as long as the respective absorption line does not saturate<sup>35</sup> because in this case  $F_{\nu} \sim \kappa_{ikm}^{-1}$ , resulting in  $N_{ik} \sigma_{ikm} F_{\nu} = \text{const.}$ . Thus, the integrand in

<sup>33</sup>The photosphere is defined as the innermost layer of a stellar atmosphere where the optical part of the stellar spectrum originates from (see also Ch. 6).

<sup>34</sup>The radiative acceleration  $g_{\text{rad}}$  will also be topic in Sect. 6.2.

<sup>35</sup>Line saturation occurs when more absorbers are available than photons can actually be absorbed. In fact, this effect first occurs in the line core as the absorber material initially starts to be optically thick for the central line frequency. At this time, the line wings are still desaturated since the absorber material is still optically thin for the respective frequencies.

Eq. (3.6) is  $\sim \frac{1}{N_i}$ , which limits the radiation pressure since the integrand rapidly vanishes outside a narrow frequency range determined by the saturated line profile (Schneider, 2017). Due to this limitation, an equilibrium state between gravitational settling and radiative levitation is set up on timescales that are much shorter than the typical evolutionary one of  $\sim 10^8$  years for EHB stars (Michaud et al., 2015).

The interplay of gravitational settling expressed through  $g$  and radiative levitation expressed through  $g_{\text{rad}}$  in the case of a standard H-sdB star shall be demonstrated in the following. However, a simple scenario with non-saturated lines is used.

Assuming a chemical element for which the initial abundance is high enough such that  $g_{\text{rad}} > g$  throughout the whole stellar atmosphere (in the case of a H-sdB this could be, for instance, nitrogen with solar abundance), the element streams upwards, that is, out of the photosphere. Therefore, the photospheric nitrogen abundance slowly decreases over time, also reducing  $g_{\text{rad}}$ . In consequence, an equilibrium state with  $g_{\text{rad}} = g$  will be reached after some time. As a result of the upstream, the photospheric nitrogen abundance will have fallen below the initial solar value.

If the initial abundance of a particular chemical element is low enough such that  $g_{\text{rad}} < g$  in the entire stellar atmosphere (in the case of a H-sdB this could be, for instance, nickel with solar abundance), the element settles into the photosphere. Thus, the photospheric nickel abundance slowly increases over time, also increasing  $g_{\text{rad}}$ . Again, a balance between gravitational settling and radiative levitation will be set up after some time, whereby the final photospheric nickel abundance will be higher than the initial solar value.

Due to saturation, the upper limit of  $g_{\text{rad}}$  for a particular chemical element can also be lower than  $g$ . As a result, the element keeps on settling as no balance  $g_{\text{rad}} = g$  is reached. In the atmospheres of WDs, this is in fact the case for all elements heavier than hydrogen, that is, for helium and the metals. This explains their hydrogen-dominated spectra in a very simple and natural way (Michaud et al., 2015). However, this simplified model cannot be applied to hot subdwarf stars (Schneider, 2017).

The most prominent abundance anomaly in hot subdwarf stars is related to helium. While it is usually the trace element in the atmospheres of hydrogen-rich hot subdwarf O and B stars (H-sdBs, H-sdOBs, H-sdOs), it dominates the spectra of helium-rich ones (He-sdBs/He-sdOs). Current atomic diffusion theories cannot successfully link both classes. Furthermore, the average observed helium abundance in H-sdB stars is still two orders of magnitude higher than predicted by the simple diffusion model, which only involves an interplay of gravitational settling and radiative levitation. In fact, the diffusion timescale needed for the depletion of helium in H-sdBs is much shorter than the evolutionary one because helium atoms and ions lack radiative support from the UV region, where the radiation flux is highest<sup>36</sup>. Accordingly, the models predict no helium spectral lines at all to be detectable in the optical spectra of H-sdB stars, which is at odds with observations (see, for instance, Fontaine & Chayer 1997 for a review). On the other hand, the radiative acceleration  $g_{\text{rad}}$  for metals that show plenty of spectral lines in the UV region may be large enough such that their equilibrium abundances

<sup>36</sup>For details on the dependence of the radiative acceleration  $g_{\text{rad}}$  on the net outward radiative energy flux and the absorption coefficient, see again Eq. (3.6). Almost all lines in the UV *line forest* region are associated with metals and not with helium (and hydrogen).

### 3.3. Chemical Composition

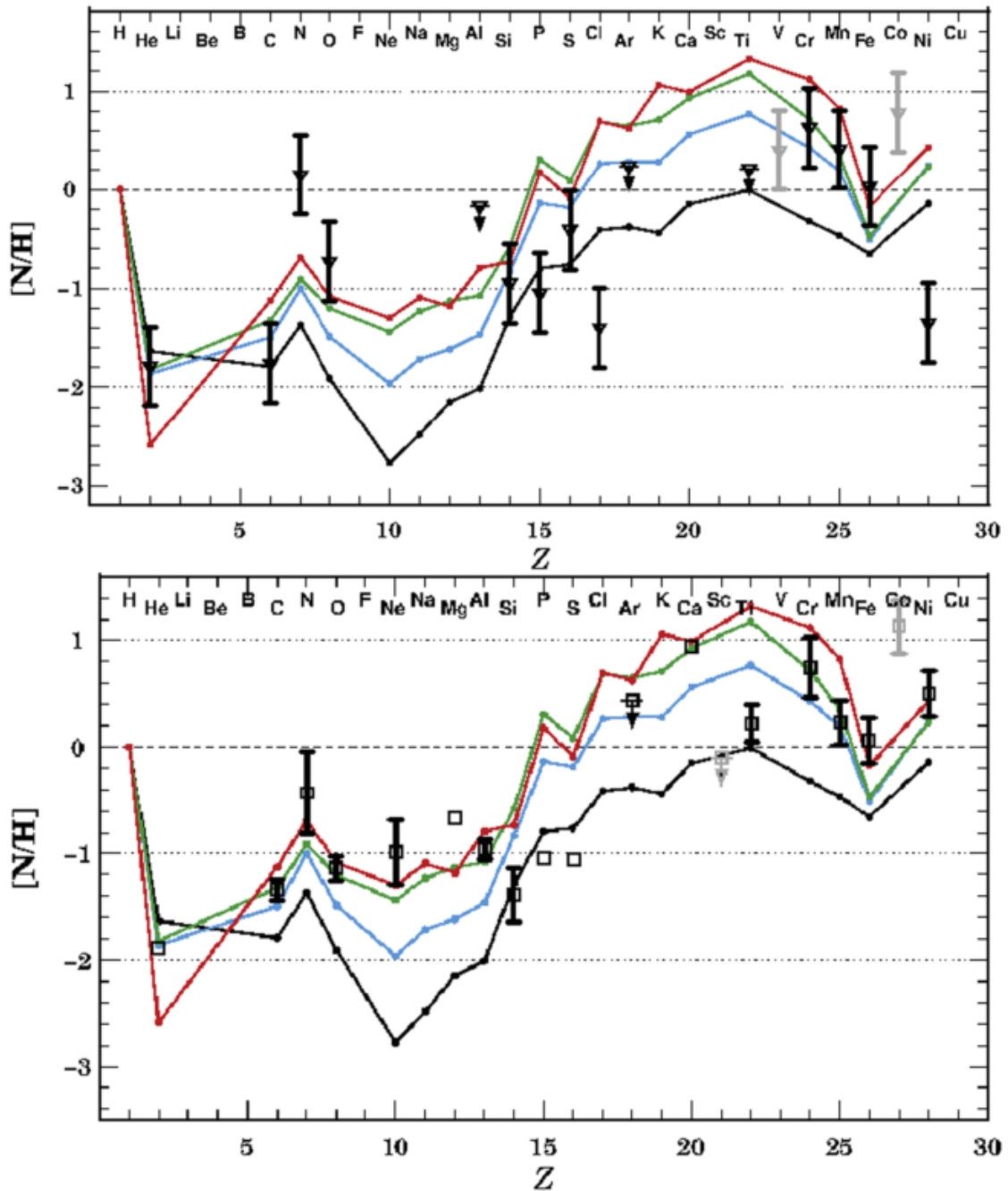


Figure 3.3.8.: Abundance patterns of the two H-sdB stars PG 0101+039 (top panel; Blanchette et al. 2008) and Feige 48 (bottom panel; O’Toole & Heber 2006) relative to the solar abundance level (dashed horizontal lines) according to Asplund et al. (2009) and compared to predicted curves calculated by turbulent diffusion models of Michaud et al. (2011) after an EHB evolution of 25 million years. Colors represent different initial metallicities  $Z_0$  applied to the diffusion models:  $Z_0 = 0.0001$  (solid black lines),  $Z_0 = 0.001$  (solid blue lines),  $Z_0 = 0.004$  (solid green lines), and  $Z_0 = 0.02$  (solid red lines). Cobalt (Co; gray symbol) was not included in the models due to a lack of atomic data. Adopted from Heber (2016); original versions: Michaud et al. (2011).

end up to be (extremely) supersolar. This may serve as a possible explanation for the extreme overabundances observed for some (trans-)iron-group elements in H-sdBs and particularly in heavy-metal stars. However, these abundance anomalies are not seen for all metals at the same time (see, for instance, Figs. 3.3.2 and 3.3.5). The strong chemical peculiarities, in particular for the heavy metals, as seen in the atmospheres of some intermediate He-sdBs, further suggest that some atomic transport process may have led to clouds of high concentration in the line-forming region (Heber, 2016).

For instance, to support helium against gravitational settling, a radiatively driven stellar wind with a mass-loss rate of  $\dot{M} \sim 10^{-13} - 10^{-14} M_{\odot} \text{ yr}^{-1}$  was suggested by Fontaine & Chayer (1997) and Unglaub & Bues (2001). Later, however, Unglaub (2008) showed that the stellar winds in H-sdBs just fractionate and become metallic because of the predominant atmospheric densities which are too low to support momentum share of metals with hydrogen and helium atoms/ions through collisions. A second possibility to slow down atomic helium diffusion in H-sdB stars is weak turbulent mixing of the outer  $10^{-6} M_{\odot}$  (Hu et al., 2011), which in fact can reproduce the surface abundances of helium and metals lighter than iron in H-sdBs moderately well (Michaud et al., 2011). This is illustrated in Fig. 3.3.8, where the abundance patterns of two H-sdB stars (PG 0101+039 and Feige 48) are compared to the results of detailed turbulent diffusion calculations in hot subdwarf stars by Michaud et al. (2011). However, it has to be highlighted that such detailed diffusion calculations have not been possible yet for all chemical elements due to a lack of atomic data. In particular, results for the trans-iron elements are still missing. Unfortunately, the idea of a turbulent stellar atmosphere in H-sdBs is not supported by any physical model. According to Hu et al. (2011), thermohaline mixing<sup>37</sup> might play a role (Heber, 2016).

In addition to the aforementioned suggestions, different pulsation models have been proposed to explain the observed helium abundances in hot subdwarf stars. However, this explanation may only be valid for the subclass of pulsating H-sdBs/H-sdOs and the V366 Aqr variables (LS IV-14° 116, Feige 46, and PHL 417) since these stars are the only ones among hot subdwarfs that show light variations. As presented earlier in this section, the majority of pulsations observed for H-sdBs can be explained by the  $\kappa$ -mechanism which is related to an opacity bump created by iron-group elements. Mass loss, however, slowly weakens the opacity bump and eventually ceases the pulsations, if it exceeds a certain critical limit. Hence, a sufficiently high radiative levitation in subphotospheric layers is needed to sustain the pulsations. As a matter of fact, calculations by Hu et al. (2011) have shown that the measured helium abundances in H-sdBs require mass-loss rates that are inconsistent with the ones derived from the observed pulsations. In consequence, pulsations are highly unlikely to produce the helium abundances of H-sdBs. Appropriate model calculations for H-sdOs and the V366 Aqr variables are still

<sup>37</sup>Thermohaline convection or thermohaline mixing describes a special type of convection in which an outwards-increasing (inverted) composition gradient  $\mu$  leads to the modification of the usual Schwarzschild stability criterion, which precisely determines the boundaries of convection in case of chemically homogeneous atmospheres. The standard Schwarzschild criterion reads  $-\frac{dT}{dz} < \frac{g}{C_p}$ , where  $g$  is the surface gravity,  $C_p$  is the heat capacity at constant pressure,  $T$  is the temperature, and  $z$  is the altitude. In the thermohaline mixing scenario,  $\mu$  tends to destabilize the entire convective region. The opposite of thermohaline convection is semi-convection. Here,  $\mu$  increases inwards, therefore leading to a stabilized convective region (see, for instance, Michaud et al. 2015 for further information).

### 3.4. Formation and Evolution

---

missing (Heber, 2016).

The existence of  $^3\text{He}$  isotope enhancement in H-sdB stars is also difficult to reconcile with the simplified diffusion model, in which only gravitational settling and radiative levitation are involved. Again, this is because of the general weakness of the radiative acceleration of helium. In principle, the  $^4\text{He}/^3\text{He}$  abundance ratio decreases with time since the more massive  $^4\text{He}$  settles more quickly than  $^3\text{He}$  (Michaud et al., 2011, 2015), but the time needed to obtain the observed  $^3\text{He}$  overabundances is too long compared to the evolutionary timescale of the EHB (Vauclair et al., 1974; Michaud et al., 1979, 2011). This is why other suggestions such as the diffusion mass-loss model (Vauclair, 1975) in combination with stellar fractionated winds<sup>38</sup> (Babel, 1996; Hunger et al., 1996; Hunger & Groote, 1999), the light-induced drift<sup>39</sup> (Atutov, 1986; LeBlanc & Michaud, 1993), meridional circulations<sup>40</sup> (Quievy et al., 2009; Michaud et al., 2008, 2011), or thermohaline mixing (Michaud et al., 2015) have been made. Identifying the possible diffusion processes occurring in the atmospheres of  $^3\text{He}$  H-sdBs (and  $^3\text{He}$  B-type stars in general) is an important task since it is indispensable for the detailed understanding of the stellar evolution of these chemically peculiar stars. Furthermore, empirical information on the photospheric  $^4\text{He}/^3\text{He}$  abundance ratios can be used in order to constrain the diffusion models.

To summarize this section, it can be said that atomic transport in hot subdwarf stars is a highly complex issue which is anything but easy to understand. Therefore, it is of no surprise that none of the known diffusion models up to date is able to explain all of the observed abundance anomalies in these stars at the same time.

## 3.4. Formation and Evolution

As outlined in Sect. 3.2, the mystery of the very thin hydrogen envelopes of hot subdwarf stars cannot be explained by canonical HB evolutionary models. This is why different other theoretical formation scenarios and evolutionary channels had to be proposed for these stars. This section shall shed light on each of them. A distinction is made between scenarios and channels that form hot subdwarfs in binary systems (Sect. 3.4.1) and those that form isolated

---

<sup>38</sup>The diffusion mass-loss model was initially developed in order to explain the  $^3\text{He}$  anomaly in helium-weak B-type MS stars. For a brief and comprehensible explanation of this model and stellar fractionated winds, see, for instance, Michaud et al. (2015) or Schneider (2017).

<sup>39</sup>For a brief and comprehensible explanation of the light-induced drift, see, for instance, Michaud et al. (2015) or Schneider (2017).

<sup>40</sup>A necessary prerequisite for meridional circulations is a rotating star. Due to the centrifugal acceleration, the distances from the centre to the surfaces of constant gravity potential are larger at the equator than at the poles. Hence, the polar regions are expected to be hotter since energy (heat) diffusing from the centre needs to travel a shorter distance to a given equipotential (level) surface along the polar (rotational) axis than in the equatorial plane. This leads to an unstable and, thus, significant temperature imbalance on an equipotential surface. While matter rises and, subsequently, cools by expansion in regions of extensive heat, it contracts and warms up in cooler regions. In consequence, a global circulation is triggered, which can be described by a meridional velocity field (see, for instance, Michaud et al. 2015 for further information).

ones (Sects. 3.4.2 and 3.4.3). The individual evolutionary models also predict different specific mass regimes for the formed hot subdwarf stars. These will be presented in Sect. 3.4.4.

### 3.4.1. Hot Subdwarf Binaries

As presented in Sect. 3.2, most hot subdwarf stars are observed as close binaries (at least 50 %), whereas the percentage of hot subdwarfs in wide binary systems is significantly smaller. Nevertheless, both observation types strongly imply a formation via binary interaction processes. Binary population synthesis predicts that hydrogen-rich hot subdwarf binaries (H-sdB+X, H-sdOB+X, or H-sdO+X, where X stands for the individual companion type) are generally formed by a red giant progenitor star, which loses most of its hydrogen envelope due to strong mass transfer onto the companion star just before reaching the tip of the RGB, that is, where the helium core flash kicks in (Han et al., 2002, 2003; Podsiadlowski, 2008). To this end, however, the system has to be half-separated, that is, one of the two stars has to fill its Roche lobe, leading to *Roche-lobe overflow* (RLOF). As the initial size of the red giant is much larger than the observed orbits in close hot subdwarf binaries, these systems also must have undergone a subsequent *common-envelope* (CE) phase, during which the orbital period shrank (see also Hilditch 2001 for further information on close binary interaction).

As a matter of fact, the formation of a hot subdwarf binary during RLOF strongly depends on the initial mass ratio  $q := \frac{m_d}{m_a}$  of both stars involved, where  $m_d$  and  $m_a$  denote the masses of the donor (primary) and the accretor (secondary), respectively. This shall be detailed in the following.

#### Second CE Ejection Channel

For  $q < 1.2 - 1.5$  (see the left-hand panel of Fig. 3.4.1), that is, in cases where the mass of the primary hardly differs from that of the secondary, two mass transfer phases can occur. For this purpose, consider a binary system composed of two MS stars with an initial orbital period of  $P \lesssim 1$  yr such that interaction between both stars is possible. Due to the correlation of mass and luminosity<sup>41</sup>, the slightly more massive star evolves faster, hence reaching the RGB earlier. If the red giant fills its Roche lobe at a certain time before reaching the tip of the RGB and before the helium flash sets in, its expansion rate is not excessively high such that the hydrogen mass transfer from its atmosphere onto the companion is dynamically stable. This results in stable RLOF and, therefore, slow accretion rates, not least because of the fact that the secondary has not reached the RGB yet. The accreted gas molecules have a certain angular momentum with respect to the secondary star and undergo the effects of the Coriolis force within the new gravitational potential. Depending on the size of the accretor, either an accretion disk is formed or the gas is directly accreted onto the companion's surface. The result of this first mass transfer is a wide binary system consisting of a more massive MS star

<sup>41</sup>According to Harwit (1988):  $\frac{L}{L_\odot} = \left(\frac{M}{M_\odot}\right)^4$  for  $0.43 M_\odot \lesssim M \lesssim 2 M_\odot$  and  $\frac{L}{L_\odot} \approx 1.4 \left(\frac{M}{M_\odot}\right)^{3.5}$  for  $2 M_\odot \lesssim M \lesssim 55 M_\odot$ .

### 3.4. Formation and Evolution

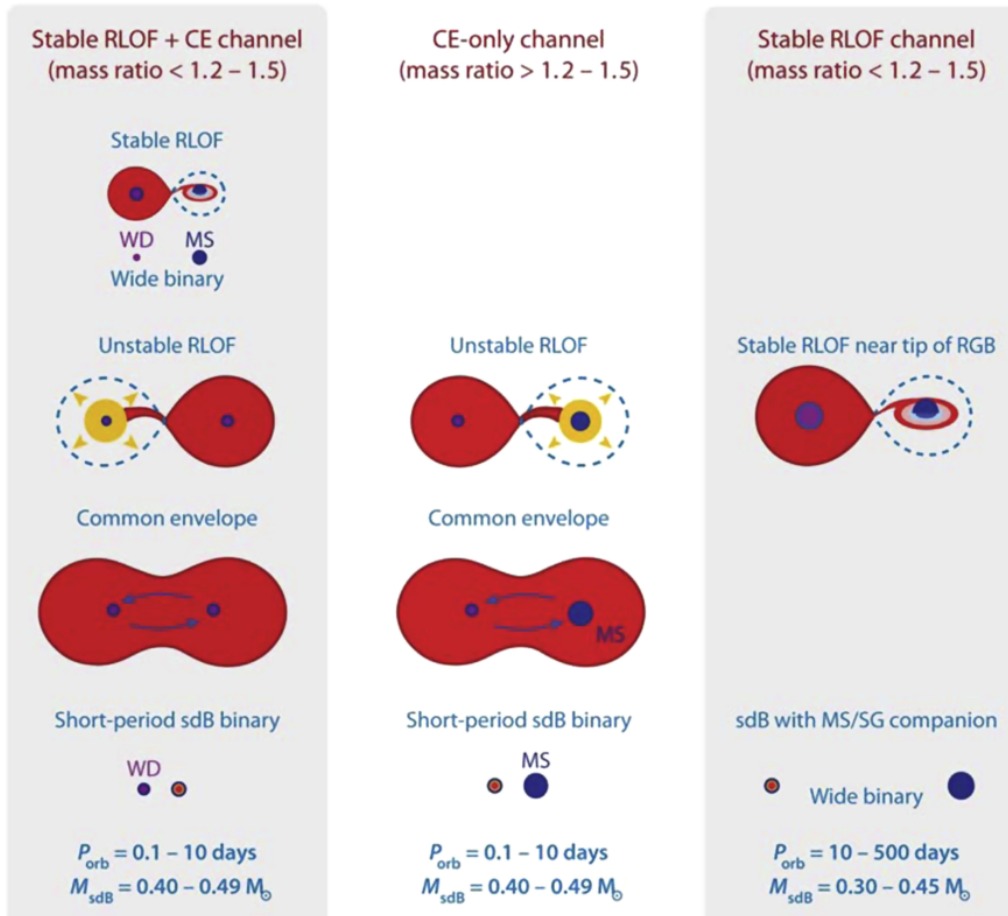


Figure 3.4.1.: Roche-lobe-overflow (RLOF) and common-envelope (CE) formation channels of hot subdwarf stars showing the evolution of the binary system proceeding from top to bottom. *Left-hand panel:* Small initial mass ratios ( $q < 1.2 - 1.5$ ) lead to two phases of mass transfer. First, mass is transferred via stable RLOF between a red giant and a main-sequence (MS) star, leading to a wide binary consisting of an MS star and a helium white dwarf (HeWD). This is followed by an unstable RLOF, leading to the formation of a surrounding CE, which is ultimately ejected after a spiral-in phase. The resulting binary composed of a hot subdwarf and a HeWD has a short-period orbit of around 0.10-10 days. The whole process is referred to as the second CE ejection channel. *Middle panel:* Larger initial mass ratios ( $q > 1.2 - 1.5$ ) directly lead to an unstable RLOF between the original red giant and the MS star and, hence, to a surrounding CE, which is ejected once the spiral-in phase has stopped. Here, also a short-period ( $0.10 \text{ d} \lesssim P \lesssim 10 \text{ d}$ ) binary composed of a hot subdwarf and most often an MS companion is formed. This channel is referred to as the first CE ejection channel. *Right-hand panel:* In the case of low initial mass ratios ( $q < 1.2 - 1.5$ ), the hot subdwarf star may also form in a single stable RLOF between the original red giant and the MS star, resulting in a wide, long-period ( $10 \text{ d} \lesssim P \lesssim 500 \text{ d}$ ) hot subdwarf binary with a non-degenerate companion (either an MS star or a subgiant; SG). This is referred to as the first stable RLOF channel. Adopted from Heber (2016); original versions: Podsiadlowski (2008).

and a helium white dwarf (HeWD) companion, whereby now  $q > 1.2 - 1.5$ .

Once the remaining MS star runs out of hydrogen in its core, it starts hydrogen shell burning and also expands on the RGB. Before reaching the tip of the RGB, however, the red giant also fills its Roche lobe, leading to a second mass transfer phase. As both components strongly differ in masses, the HeWD companion cannot accrete all of the transferred matter at once, leading to unstable RLOF and, ultimately, to Roche-lobe overfilling. This, in turn, results in the formation of a CE, which surrounds both orbiting objects (*immersed binary system*). While both gravitationally and centrifugally acting forces heavily deform the CE, both stars lose orbital energy and angular momentum due to friction with the envelope such that they spiral towards each other (spiral-in phase). The spiral-in stops as soon as enough orbital energy has been released to eject the CE (Paczynski, 1976). During the post-CE phase, a much closer binary with orbital periods between 0.10 and 10 days is formed, whereby the constituents are two compact hydrogen-deficient objects. Since the CE phase is generally short on evolutionary timescales, the companion remains almost unchanged (HeWD) and the remaining primary red giant core most often becomes a hot subdwarf (see the left-hand panel of Fig. 3.4.1). However, a close binary consisting of two HeWDs is also possible. The further evolution of the resulting system depends on its type. While a double HeWD merger is possible (this scenario will be presented in Sect. 3.4.2) if the orbital period of the respective system is shorter than  $\sim 8$  hours, an additional stable RLOF phase may occur for a hot subdwarf binary with a HeWD companion (Han et al., 2002, 2003; Podsiadlowski, 2008). However, both components may also merge in the latter case, which would only take place after the helium-burning phase of the hot subdwarf has ended and the star has evolved into a hybrid WD with a carbon-oxygen core and a thick helium envelope (post-sdB He-CO WD). If the orbital period of the former binary system is short enough, gravitational radiation can drive the binary components towards each other until mass transfer (mainly helium) is initiated from the lighter HeWD onto the post-sdB He-CO WD. As soon as a sufficiently thick helium shell has been built up around the carbon-oxygen core of the post-sdB He-CO WD, helium will (re)ignite in this shell. It has been shown that such objects show all the main observational characteristics of helium-rich hot subdwarf O stars (Justham et al., 2011).

However, close hot subdwarf binaries with WD companions resulting from the second CE ejection channel have also been shown to be viable as possible progenitor systems for supernovae of type Ia<sup>42</sup> (SNe Ia; see, for instance, Maxted et al. 2000, Geier et al. 2007, and Wang & Han 2010). Such a binary evolves into a double-degenerate system composed of two WDs within the EHB lifetime of  $\sim 10^8$  years. This is shorter than the merger time for most known sdO/sdB+WD systems, which qualifies them as possible SN Ia progenitors, if sufficiently massive. The merger of two WDs is driven by gravitational wave radiation and only leads to a SN Ia, if the combined (total) mass is larger than a certain critical one (Chandrasekhar mass) such that the degeneracy pressure of the high-density electron gas can no longer compensate for

<sup>42</sup>A supernova of type Ia (SN Ia) is caused by the thermonuclear explosion of a WD in a close binary. The second component can either be another WD or a non-degenerate companion (a normal MS or a helium star, for instance, a hot subdwarf). The former is referred to as the *double-degenerate* (DD) scenario, whereas the latter is called the *single-degenerate* (SD) scenario. Further information on SNe Ia can, for instance, be found in Hillebrandt et al. (2013), Maoz et al. (2014), Postnov & Yungelson (2014), or Ruiz-Lapuente (2014).

### 3.4. Formation and Evolution

---

the gravitational pressure. If the double-degenerate system is not massive enough to trigger a SN Ia, it simply merges. If the corresponding orbital period is shorter than about half a day, the merger takes place within a Hubble time ( $\sim 14.4$  billion years; Heber 2016).

A close hot subdwarf binary with a WD companion resulting from the second CE ejection channel may also become a single-degenerate SN Ia progenitor system, if the hot subdwarf transfers parts of its helium envelope to the WD, which then alone exceeds the critical Chandrasekhar mass limit. This mass transfer, however, must happen before the hot subdwarf reaches the WD cooling sequence (Heber, 2016).

There is another scenario that can result in a SN Ia in which close hot subdwarf binaries with WD companions are involved. This is referred to as the *double-detonation scenario* or as a supernova of *type Iax* (SN Iax). This scenario predicts that an (underluminous) supernova may result from accretion of helium by the WD. The accreted helium shell detonates once a sufficient amount of helium ( $\sim 0.1 M_{\odot}$ ) is accumulated (Livne & Glasner, 1990). The explosion of the helium shell then triggers a subsequent detonation in the core, which may produce (underluminous) SNe Ia explosions if the minimum core mass of  $0.8 M_{\odot}$  is exceeded (see Fink et al. 2007, 2010, or Sim et al. 2010 for further information). SNe Iax do not completely destroy the WD progenitor, but instead leave behind a zombie star as a remnant, which still has about half of the initial WD mass (see, for instance, Raddi et al. 2019). The best candidate for a binary evolving into a double-detonation supernova is CD-30° 11223 (Vennes et al., 2012; Geier et al., 2013c), for which the detonation in the accreted helium layer of the WD will be so strong that the hot subdwarf star will be ejected at such a high velocity that it can escape the Milky Way (Geier et al., 2013d). In fact, such *hyper-velocity stars* have been observed (for instance, the He-sdO US 708; Hirsch et al. 2005, Geier et al. 2015, Brown et al. 2015).

#### First CE Ejection Channel

Larger initial mass ratios ( $q > 1.2 - 1.5$ ) of the original  $P \lesssim 1$  yr binary system composed of two MS stars also lead to unstable RLOF as soon as the more massive MS star has evolved to the RGB, that is, before the helium core flash kicks in (see the middle panel of Fig. 3.4.1). As in the second mass transfer phase of the second CE ejection channel, the mass transfer rate is sufficiently high such that the secondary is not able to accrete all the matter at once. In consequence, this results in an immersed binary system with a surrounding CE. After the CE ejection at the end of the spiral-in phase, that is, during the post-CE phase, a short-period binary ( $0.10 \text{ d} \lesssim P \lesssim 10 \text{ d}$ ) as in the case of the second CE ejection channel is formed. The successors of this evolution are a hot subdwarf and a non-degenerate object, most often an MS star. However, the evolution of the system progresses as the MS star evolves to a red giant. Once it has filled its Roche lobe before reaching the tip of the RGB, a second CE ejection phase takes place, which results in a close hot subdwarf binary with a HeWD companion. This system can then further evolve as described in the previous section. In this case, thermonuclear supernovae therefore are also possible (Han et al., 2002, 2003; Podsiadlowski, 2008).

### First Stable RLOF Channel

If the hot subdwarf progenitor star in the original binary system composed of two MS stars ( $P \lesssim 1$  yr) starts to fill its Roche lobe near the tip of the RGB and the initial mass ratio of the system is sufficiently low ( $q < 1.2 - 1.5$ ), a slow and stable RLOF may also set in (see the right-hand panel of Fig. 3.4.1). In these cases, the amount of hydrogen in the envelope of the red giant has already decreased sufficiently enough during the RGB phase such that the material can slowly be accreted onto the companion. Hence, no surrounding CE is formed and the red giant loses its entire envelope. As no spiral-in phase sets in, the outcome is a wide hot subdwarf binary ( $10 \text{ d} \lesssim P \lesssim 500 \text{ d}$ ) with an MS or a subgiant (SG) companion. The orbital separation of the system is large enough such that no RLOF takes place, once the MS companion has evolved into a red giant. One of the postulated final stages is a long-period hot subdwarf binary with a WD companion. However, no such systems have been observed so far (Han et al., 2002, 2003; Podsiadlowski, 2008).

In principle, a second stable RLOF channel, for which the initial components (MS+HeWD) have resulted from the first mass transfer phase of the second CE ejection channel, is possible. However, Han et al. (2002, 2003) showed that stable RLOF in this case would require very massive HeWDs. Since such massive WDs are very rare, the authors concluded that this channel can only marginally contribute to the whole hot subdwarf population.

### Double-Core CE Evolution

This is a special case of CE evolution, in which both MS components have comparable intermediate masses and, therefore, may both have expanded to red giants by the onset of CE formation. Both red giants overfill their Roche lobes before helium ignition occurs, leading to the CE and the subsequent spiral-in phase. Once the CE is ejected, both cores emerge and a binary system with two helium-rich hot subdwarf stars may be formed (see Justham et al. 2011 for further information). Indeed, such systems with helium-rich constituents (He-sdBs) have been found (PG 1544+488; Ahmad et al. 2004, Şener & Jeffery 2014 and HE 0301-3039; Lisker et al. 2004). However, it cannot be excluded that the constituents of these systems have been formed individually by a late helium flash. This scenario will be presented in Sect. 3.4.2. However, the double HeWD merger scenario (see also Sect. 3.4.2) is highly unlikely for PG 1544+488 and HE 0301-3039 since it would require (a) two mergers of two HeWDs within a few thousands of years of one another, and (b) to be preceded by the formation of two compact double HeWD binaries in a quadruple HeWD system (Şener & Jeffery, 2014).

### Summary

CE evolution is able to reproduce the observed close hot subdwarf binaries with  $0.10 \text{ d} \lesssim P \lesssim 10 \text{ d}$  and HeWDs or MS stars as companions. To explain the long-period hot subdwarf binaries with MS companions, the CE ejection scenario, however, is not suitable. Here, the presented first stable RLOF channel only provides remedy to some extent as it also struggles to explain

### 3.4. Formation and Evolution

---

the extremely long-period systems with  $700 \text{ d} \lesssim P \lesssim 1400 \text{ d}$ , which, for instance, have been observed by Vos et al. (2012, 2013, 2014, 2017). However, newer binary population synthesis calculations based on the results of Han et al. (2002, 2003) showed that wide subdwarf binaries with  $0.50 \text{ d} \lesssim P \lesssim 1600 \text{ d}$  can in fact result from the first stable RLOF channel, if atmospheric RLOF<sup>43</sup> is included and if a sophisticated treatment of angular momentum losses during the formation of these systems is used. Also, it could be shown that the initial ZAMS mass of the donor star and its metallicity affect the orbital period of the resulting system (see Chen et al. 2013 for further information).

#### 3.4.2. Single Helium-Rich Hot Subdwarf Stars

Although a large fraction of hot subdwarf stars are observed in binaries and may be explained by the RLOF and CE ejection phases, still a high percentage is found as single stars, in particular the helium-rich ones (He-sdBs and He-sdOs; Napiwotzki 2008). In fact, two rivaling scenarios are used to explain the hydrogen deficiency of single hot subdwarf stars: the coalescence of two HeWDs (see, for instance, Webbink 1984, Iben & Tutukov 1984, Zhang & Jeffery 2012, Schwab 2018) and a late helium flash (see, for instance, Castellani & Castellani 1993, Lanz et al. 2004, Miller Bertolami et al. 2008). Both scenarios shall be explained in the following.

##### Double Helium White Dwarf Merger

The lack of extremely helium-rich subdwarfs in binary systems can be explained naturally by the complete coalescence of two low-mass HeWDs, as first suggested by Webbink (1984). This scenario assumes that the two components orbit each other with periods of about 8 hours. This is when they start to lose energy and angular momentum through gravitational wave emission. While this leads to a further decrease in orbital separation, the centrifugally and gravitationally acting forces increase. At some point, the latter become so strong that one of the two HeWDs fills its Roche lobe such that mass transfer of helium-rich material through RLOF sets in. As the mass-radius relation for WDs is  $R \sim M^{-\frac{1}{3}}$ , the less massive component (secondary) first fills its Roche lobe and transfers mass onto the more massive one (primary). The more mass has been transferred, the larger the radius of the secondary. Therefore, the merging process is self-reinforcing. The actual resulting atmospheric chemical composition of the merger product (hot subdwarf) depends on the mass transfer rate. According to Zhang & Jeffery (2012), three different merging scenarios are possible: slow, fast, and composite

---

<sup>43</sup>In a simplified model, it is assumed that the RLOF is switched on (off) sharply once the photospheric stellar radius (defined at an optical depth of  $\tau_\nu \sim 2/3$ ; see Sect. 6.1 for details) of the donor is larger (smaller) than its Roche-lobe radius. This assumption, however, does not take the atmospheric material outside the photospheric stellar radius into account. In fact, when the photospheric stellar radius approaches the Roche-lobe radius, some atmospheric material will already overflow the Roche lobe and will be transferred to the companion. This is referred to as atmospheric RLOF. Due to the fact that the Roche lobe is larger than the photospheric stellar radius during mass transfer, if atmospheric RLOF is included, a larger separation and, hence, a longer orbital period of the resulting binary system is accomplished (see Chen et al. 2013 and references therein for details).

(fast+slow) mergers. These are illustrated in Fig. 3.4.2.

In the *slow* merger model (see the left-hand panel of Fig. 3.4.2), the mass transfer through stable RLOF is sufficiently slow such that the entire transferred mass of the secondary forms a cold accretion disk around the more massive HeWD within a few minutes. The material remains cold and is slowly accreted onto the primary's surface during the next several million years. During this accretion phase, helium is ignited at the surface of the primary (helium-shell burning) via the  $3\alpha$  process once a critical total primary mass has been reached. Furthermore, other  $\alpha$ -capture reactions (on to carbon, nitrogen, and oxygen) are ignited. Subsequently, the

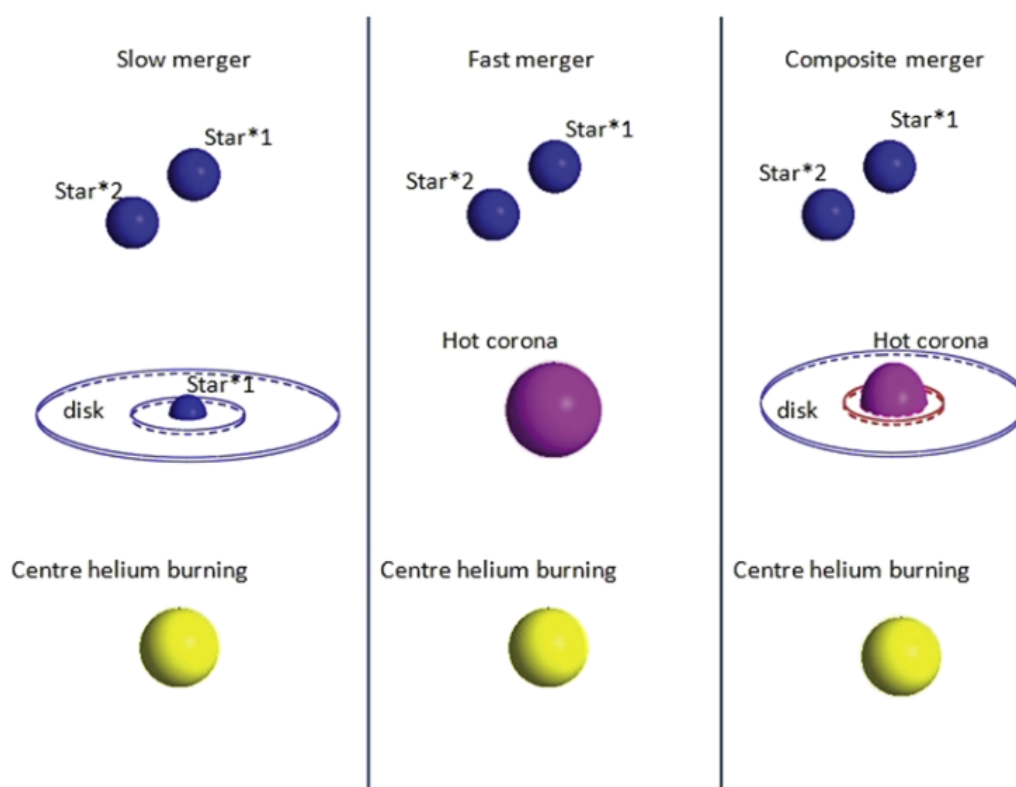


Figure 3.4.2.: Schematic of the three possible double HeWD merger scenarios which are able to form single helium-rich hot subdwarf stars. Adopted from Heber (2016); original version: Zhang & Jeffery (2012).

helium-burning flame moves inwards in a series of shell flashes, leading to convection zones in the stellar interior, which are located on top of the burning flame. The energy released during these flashes causes the primary's radius to increase until the accretion stops. Zhang & Jeffery (2012) showed that significant amounts of carbon are produced by helium-shell burning in the primary's surface during a slow merger, whereas primarily nitrogen is destroyed by  $\alpha$ -capturing. After the accretion phase, the helium-burning shell further moves inwards, whereby the power of each occurring shell flash decreases. However, the flashes lead to an increase of the effective temperature and to a decrease of the stellar radius. About  $10^5$  -  $10^6$  years after the accretion phase has ended, the helium-burning flame reaches the centre of the star and

### 3.4. Formation and Evolution

---

stable core helium burning on the EHB begins.

During a slow merger, no nuclear fusion is possible inside of the original accretion disc due to the predominant low temperatures. Moreover, the flash and opacity-driven convection zones in the remnant's interior, which occur during helium flashes and move inwards along with the helium-burning flame, are not extensive enough to reach the carbon-rich and nitrogen-poor regions produced by the  $3\alpha$  process and the  $\alpha$ -capturing. Hence, convection cannot dredge fresh carbon up to the surface such that the resulting surface composition of the hot subdwarf star resembles that of the donor HeWD. Therefore, a nitrogen-rich and carbon-poor (N-type) helium-rich hot subdwarf is formed by a slow merger.

In the *fast* merger model (see the middle panel of Fig. 3.4.2), the mass transfer through RLOF is dynamically unstable, leading to the total tidal disruption of the secondary. No accretion disk is formed, but the entire mass of the less massive HeWD is transferred instantly forming a shock-heated hot envelope (corona) around the primary within a few minutes. During accretion, the  $3\alpha$  and other  $\alpha$ -capture processes on to carbon, nitrogen, and oxygen are almost immediately ignited at the primary's surface. Helium-burning is stable (no flashes) due to the high accretion rate. The energy released is mostly deposited into the corona, whose material is strongly heated up to temperatures of about  $10^8$  K which leads to expansion. Zhang & Jeffery (2012) showed that lots of carbon is produced by helium burning, whereas primarily nitrogen again is destroyed by the  $\alpha$ -capturing. The latter leads to a fast increase of the oxygen abundance and, eventually, to that of neon as the temperatures are still high enough to support  $\alpha$ -capturing on to oxygen. At the end of the coalescence, the entire envelope is fully convective such that it is completely mixed. The remnant hence shows high abundances of carbon, oxygen, and neon.

Schwab (2018) showed that about 100 years after the end of the fast accretion, the remnant starts to expand as it thermally adjusts to the increasing nuclear luminosity. After this expanding phase, which lasts for  $\sim 10^3 - 10^4$  years, the merger product contracts as it radiates away much of the thermal energy deposited in the original corona within  $\sim 10^4$  years. At the same time, helium-burning is ignited off-centre and the burning-shell moves inwards in a series of flashes. Within about  $10^5 - 10^6$  years, it eventually reaches the centre of the star such that the long-lived ( $\sim 10^8$  years) core helium-burning phase on the EHB begins. A carbon, oxygen, and neon-rich, but nitrogen-poor (C-type) helium-rich hot subdwarf is born.

The *composite* merger model (see the right-hand panel of Fig. 3.4.2) combines the concepts of slow and fast merging. More than half of the secondary's mass is rapidly accreted by the primary, forming a hot corona as in the fast merging scenario. The remaining material from the secondary forms a cold debris disk, from which the material is slowly accreted onto the hot corona. During the fast accretion phase, the star expands and the  $3\alpha$  and other  $\alpha$ -capture processes are immediately ignited at the primary's surface. Helium-burning is stable, that is, no flashes occur and almost complete corona convection dredges carbon, oxygen, and neon-rich material up to the surface. Slow accretion, however, leads to unstable helium ignition at the surface of the primary, further heating the corona and forcing additional expansion. As the hot corona is still fully convective at the beginning of this accretion phase, the surface abundances of C, O, and Ne further increase via the  $3\alpha$  process and  $\alpha$ -capturing until a dynamic balance is achieved during the commencing helium-flash cycles. At the same time,

nitrogen-rich material from the accretion disc is continuously accreted onto the corona. Zhang & Jeffery (2012) showed that the actual surface composition of the remnant depends on the final merger mass. While composite models with final masses of  $\lesssim 0.65 M_{\odot}$  result in N-rich (N-type) stars, models with  $\gtrsim 0.65 M_{\odot}$  tend to produce C-rich ones with, however, significant amounts of nitrogen (CN-type stars).

After slow accretion has ended during a composite merger, the nuclear burning temperature is reduced such that the temperature profile slowly resembles that of the slow merger model. As in the slow and fast merger models, the helium-burning flame slowly propagates inwards until it reaches the centre after about  $10^5 - 10^6$  years. Then, core helium burning on the EHB begins.

### The Hot Flasher Scenario

The coalescence of two HeWDs is not the only scenario that is able to form single hot subdwarf stars. A star may depart from its usual (canonical) post-RGB evolution, if sufficiently mass of its hydrogen envelope has been removed near the tip of the RGB just before the helium core flash would occur. For instance, this could be achieved by strong rotational effects, stellar winds (Sweigart, 1997a), or by CE ejection scenarios in which substellar companions are involved (see, for instance, the results of Charpinet et al. 2011 or Schaffenroth et al. 2014). Once enough mass of the envelope has been removed, the post-RGB star evolves to high temperatures, before following the WD cooling sequence. During this evolution, the helium flash can occur off-centre at different stages depending on the remaining envelope mass. This is referred to as “hot flashers” (D’Cruz et al., 1996).

In fact, Lanz et al. (2004) proposed three types of hot flasher evolution: *early hot flashers* (EHFs), *shallow mixing* (SM), and *deep mixing* (DM). The individual scenarios mainly differ in the extend to which the remaining hydrogen shell is mixed with the helium core (helium flash mixing; see also Castellani & Castellani 1993 and Sweigart 1997a, 1997b). Figure 3.4.3 shows a theoretical HRD with up-to-date evolutionary sequences for the different types of hot flashers (Battich et al., 2018). All tracks have different helium ignition times (marked by the red circles), which lead to different temperatures and surface compositions on the ZAHB (D’Cruz et al., 1996; Brown et al., 2001; Cassisi et al., 2003). However, after these initial off-centre helium flashes, all cases follow a similar pattern. The stellar structure changes and the post-RGB star evolves towards lower luminosities and temperatures. This is always followed by a phase in which the surface luminosity rises again since the helium-burning luminosity increases. At the end, several subsequent helium flashes (represented by the loops in Fig. 3.4.3) occur as the helium-burning shell slowly propagates inwards. The flashes stop once the helium-burning flame has reached the centre such that the stable core helium-burning phase on the EHB begins.

Due to the high temperature of the initial off-centre helium flash, a convection zone is driven towards the core. Usually, this convection does not affect the hydrogen envelope because both are separated by the hydrogen-burning shell. Thus, the remnant simply shares the surface composition of the RGB progenitor. This is true for EHFs, which occur during the phase of constant luminosity (post-RGB phase; see the corresponding red circles in Fig. 3.4.3) and

result in hot subdwarf B stars with standard photospheric hydrogen and helium abundances (H-sdBs). In the case of SM, however, the initial off-centre helium flash only occurs at the beginning of the WD cooling track (see the corresponding red circle in Fig. 3.4.3). Hence, the RGB progenitor has already lost sufficient mass of its hydrogen envelope such that the thin hydrogen-burning shell cannot prevent mixing of the stellar envelope with the helium core. In

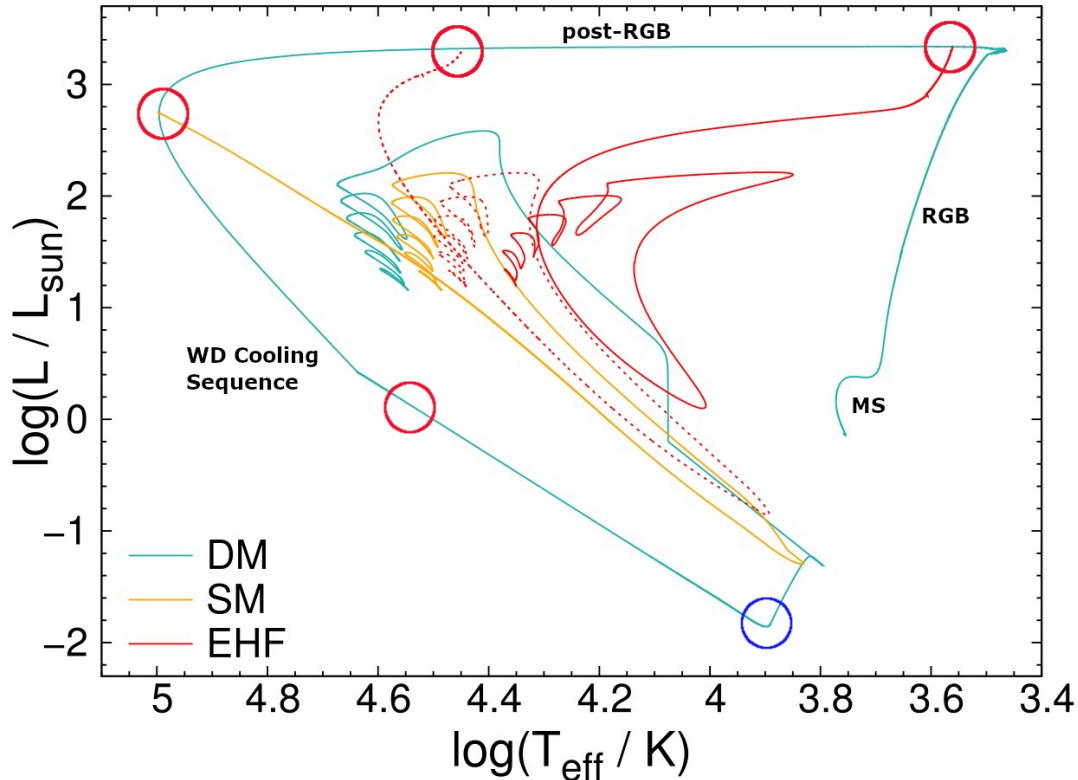


Figure 3.4.3.: Theoretical HRD for hot flasher evolutions based on a solar metallicity of  $Z = 0.02$ . Shown evolutionary sequences correspond to two cases of early hot flashers (EHFs, dotted and solid red lines) and two cases of late hot flashers: one with shallow mixing (SM, solid yellow line) and the other one with deep mixing (DM, solid turquoise line). The peak of the initial off-centre helium flash for each of the evolutionary tracks is indicated by a red circle, whereas the blue circle on the DM track marks the occurrence of a secondary flash during which the amount of hydrogen mixed into the hot and helium-rich core is completely burned. The main sequence (MS), the red giant branch (RGB), the post-red giant branch (post-RGB), and the white dwarf (WD) cooling sequence are also marked. Modified version of Figure 1 in Battich et al. (2018).

consequence, the SM scenario can produce intermediate He-sdBs/He-sdOs. In addition, the SM remnants have been shown to be also enriched in carbon and nitrogen (CN-type stars). Initial off-centre helium flashes that take place even later on the WD cooling sequence (see the corresponding red circle in Fig. 3.4.3) result in DM, whereby almost the complete hydrogen-burning shell is engulfed by the convective zone. Detailed evolutionary computations for the

DM scenario, for instance performed by Miller Bertolami et al. (2008) and Battich et al. (2018), revealed that hydrogen, once mixed into the hot and helium-rich core, is completely burned in a secondary flash (see the blue circle in Fig. 3.4.3). This consumes most of the remaining envelope. The computations always resulted in extremely helium-rich EHB stars, most often with carbon (and nitrogen-)enriched surfaces (C and CN-type stars). Although hot subdwarf stars are generally affected by diffusion, the atomic processes coming along with it cannot convert a carbon-rich atmosphere into a carbon-poor, but nitrogen-rich one. Therefore, DM scenarios produce extreme He-sdBs/He-sdOs of the C and CN-types, but not of the N-type.

### Summary

Both the coalescence of two HeWDs and the late hot flasher scenarios (SM, DM) can produce single isolated helium-rich hot subdwarf stars. In fact, Zhang & Jeffery (2012) showed that the post-evolutionary tracks of slow, fast, and composite double HeWD mergers all cross the regions in the  $T_{\text{eff}}\text{-}\log(g)$  diagram, where known intermediate and extreme helium-rich hot subdwarfs (He-sdBs, He-sdOs) are located. The same applies to the late hot flasher scenarios (Battich et al., 2018). However, the surface composition of the respective remnant depends on the individual scenario type. While slow HeWD mergers produce N-type stars, fast mergers generally result in C-type ones. Composite mergers, however, produce two types of stars depending on the final merger mass: N-type ones for  $\lesssim 0.65 M_{\odot}$  and CN-type ones for  $\gtrsim 0.65 M_{\odot}$ . As the late hot flashers only produce C and CN-type stars (the former only in the case of DM, the latter in the case of SM and DM), merger scenarios are preferred over hot flasher models in order to produce N-type He-sdBs/He-sdOs. As a matter of fact, CN-type stars are best explained by the hot flasher scenario, although they may also result from composite mergers (Zhang & Jeffery, 2012).

Unfortunately, the coalescence of two HeWDs has one major problem. It predicts rotational velocities of  $v \sin i \sim 30\text{-}100 \text{ km s}^{-1}$  for the remnant (Schwab, 2018), which barely have been observed for helium-rich hot subdwarf stars so far. The majority of the observed isolated hot subdwarfs exhibit  $v \sin i \lesssim 10 \text{ km s}^{-1}$  (see, for instance, the results of Hirsch 2009 and Geier & Heber 2012), suggesting that these objects may have been formed via other channels or that the double HeWD merger models are still incomplete (Schwab, 2018).

Last but not least, it has to be mentioned that the rather large spread in surface gravities observed for He-sdO stars (see also Sect. 3.2 and the upper panel of Fig. 3.2.1) can hardly be explained by the hot flasher and the merger scenarios.

### 3.4.3. Single Hydrogen-Rich Hot Subdwarf Stars

Besides the merger of two HeWDs and the late hot flasher scenario, additional other scenarios have been proposed in order to explain the formation of single isolated hot subdwarf stars. Most of them refer to the formation of hydrogen-rich ones. For instance, Politano et al. (2008) suggested the coalescence of low-mass MS stars (dMs) or BDs with red giant cores, which could result in rapidly rotating single H-sdBs, if the fast rotation removes sufficient hydrogen

### 3.4. Formation and Evolution

---

from the outer envelope of the merger product. A different approach was proposed by Clausen & Wade (2011), that is, the coalescence of a HeWD with a dM, which may form a single non-rotating star with a thick hydrogen envelope. This progenitor may evolve to a standard H-sdB within a time period of  $\sim 0.5\text{--}6.0$  Gyr.

#### 3.4.4. Theoretical Mass Distribution

The theoretical evolutionary scenarios and formation channels presented in the previous sections predict different specific mass regimes for the resulting hot subdwarf stars. Table 3.3 summarizes them together with the favored type of end product. Figure 3.4.4 is based on the best-choice model (parameter set 2<sup>44</sup>) of Han et al. (2003) and shows the mass distributions of hot subdwarf stars from different evolutionary channels, including that of the first and the second CE ejection, that of the first stable RLOF, and that of the double HeWD merger.

According to Han et al. (2003), the mass distribution for the CE ejection channel, in which the secondary is an MS star (first CE ejection channel), has a sharp major peak at  $\sim 0.46 M_{\odot}$  and a secondary one at  $\sim 0.40 M_{\odot}$ . Furthermore, three peaks are predicted for the CE channel mass distribution, if the secondary is a HeWD (second CE ejection channel): a minor one at  $\sim 0.33 M_{\odot}$ , and two pronounced ones at  $\sim 0.40 M_{\odot}$  and  $\sim 0.46 M_{\odot}$ , respectively. The theoretical mass distribution for the first stable RLOF channel, however, has a broad peak (plateau) at low masses (with a minimum mass of  $\sim 0.30 M_{\odot}$  under non-degenerate core conditions), which drops sharply at  $\sim 0.47 M_{\odot}$ , hence limited by the canonical mass for hot subdwarf stars (the core mass at the tip of the RGB at which the helium flash occurs). Moreover, Han et al. (2003) predict the double HeWD merger channel to produce single hot subdwarf stars with masses between  $\sim 0.42$  and  $0.72 M_{\odot}$ . Thus, this is the only channel that is able to produce massive hot subdwarfs.

The mass distribution for the hot flasher scenario is more or less constrained by the canonical hot subdwarf mass. Therefore, it ranges from  $\sim 0.43$  to  $\sim 0.50 M_{\odot}$ , depending on whether an EHF or SM/DM occurs and what initial abundances (defined by the metallicity and the helium abundance) are adopted for the hot flasher progenitor (D’Cruz et al. 1996; Brown et al. 2001; Cassisi et al. 2003; Castellani et al. 2006; Miller Bertolami et al. 2008; Xiong et al. 2017; Battich et al. 2018; see also Fig. 3.4.5).

According to Politano et al. (2008), the coalescence of dMs or BDs with red giant cores results in hot subdwarf stars with masses between  $0.47$  and  $0.54 M_{\odot}$ , whereas the mass regime for hot subdwarfs formed from the coalescence of a HeWD and a dM is  $0.44 M_{\odot} \lesssim M_{\text{sd}} \lesssim 0.50 M_{\odot}$  (Clausen & Wade, 2011).

---

<sup>44</sup>In total, Han et al. (2003) produced twelve simulation sets for different values of the following quantities: CE ejection efficiency  $\alpha_{\text{CE}}$ , fraction  $\alpha_{\text{th}}$  of thermal energy used for the CE ejection, critical mass ratio  $q_{\text{crit}}$  above which mass transfer is stable on the red giant branch, initial mass-ratio distribution of the progenitor binary systems, and metallicity. This was done in order to examine the effects of the individual parameters on the formation channels. Later, Lisker et al. (2005) favored parameter set 10 of Han et al. (2003) based on a maximum likelihood analysis of their own observational sample. However, an entire group of sets, including the best-choice model (parameter set 2) of Han et al. (2003), still matched the observations of Lisker et al. (2005) well.

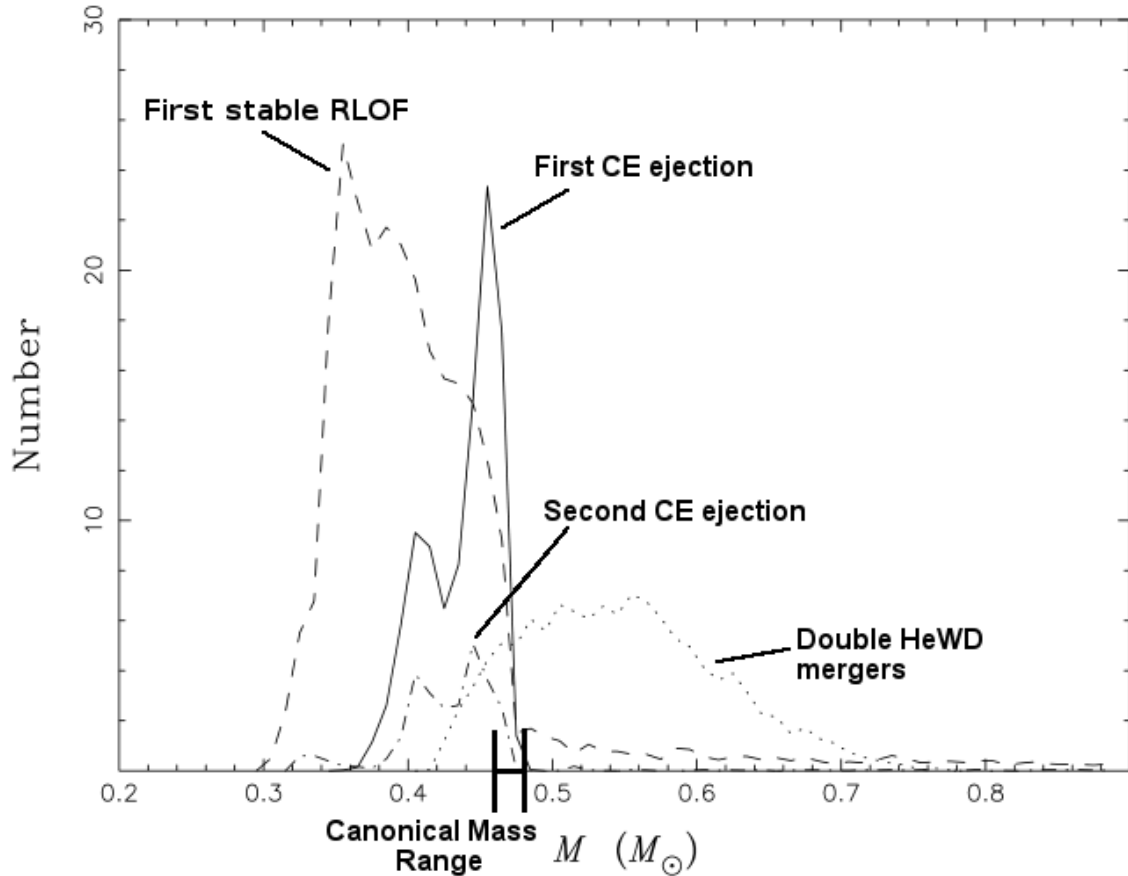


Figure 3.4.4.: Mass distributions of hot subdwarf stars from different evolutionary channels in simulation set 2 - the best-choice model of Han et al. (2003). Solid line: the first common-envelope (CE) ejection channel; dashed line: the first stable Roche-lobe-overflow (RLOF) channel; dashed-dotted line: the second CE ejection channel; dotted line: the double helium white dwarf (HeWD) merger channel. The canonical mass range ( $\sim 0.46\text{-}0.48 M_{\odot}$ ) is indicated. Modified version of Figure 12 in Han et al. (2003).

### 3.4. Formation and Evolution

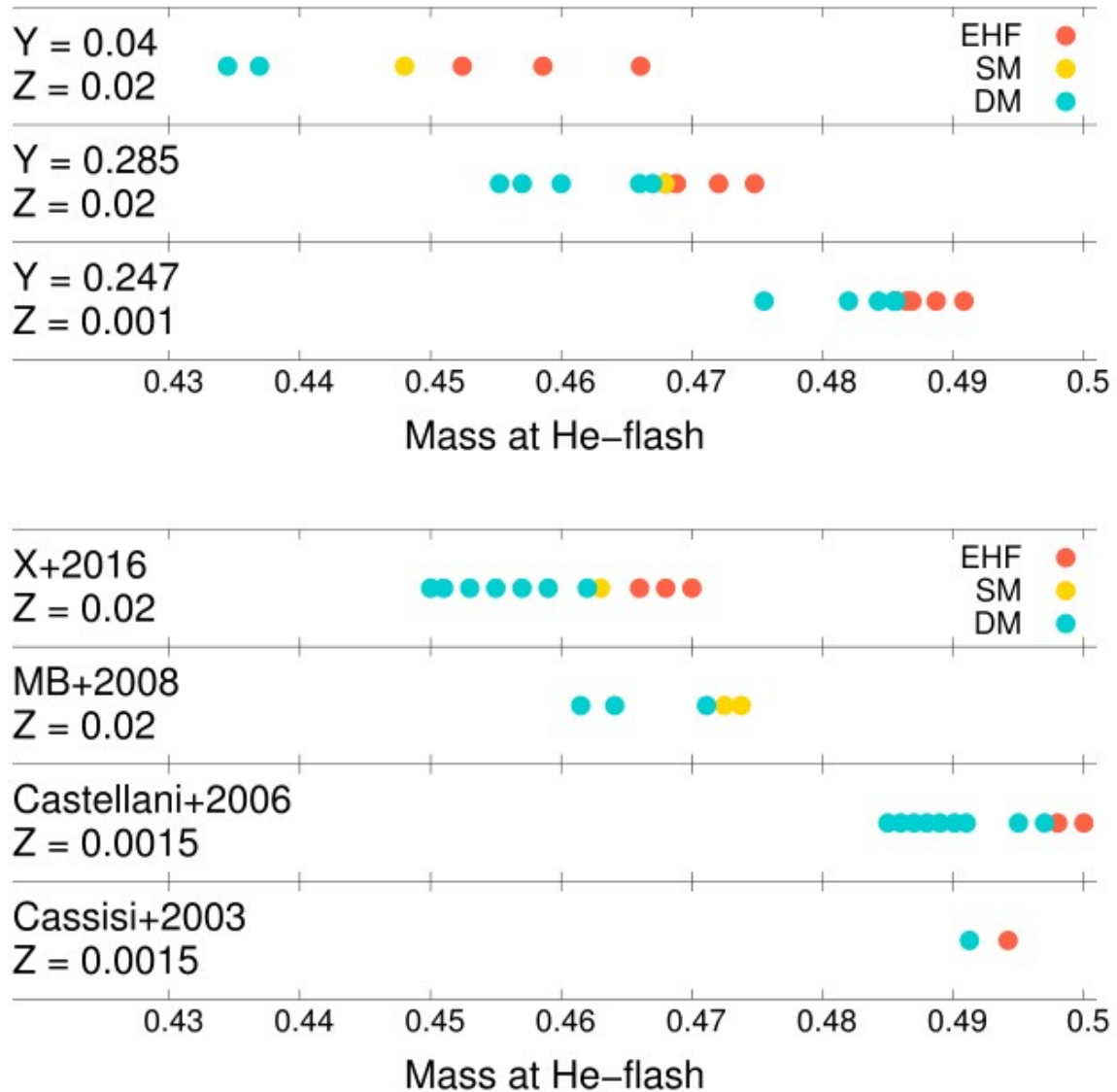


Figure 3.4.5.: *Upper panel:* Mass of early and late hot flasher models at helium ignition for different initial chemical compositions computed in Battich et al. (2018). The initial metallicity  $Z$  and the initial helium abundance  $Y$  are given by mass fraction. *Lower panel:* Same as the upper panel, but for the works of Xiong et al. (2017) (X+2016) and Miller Bertolami et al. (2008) (MB+2008) for  $Z = 0.02$  as well as for the works of Castellani et al. (2006) (Castellani+2006) and Cassisi et al. (2003) (Cassisi+2003) for  $Z = 0.0015$ . Adopted from Battich et al. (2018).

Table 3.3.: Predicted masses and favored end products of the different evolutionary channels and scenarios forming hot subdwarf stars (sds).

Channel/Scenario <sup>a</sup>	Mass Range	End Product
First CE ejection	Two peaks: $\sim 0.40 M_{\odot}$ , $\sim 0.46 M_{\odot}$ <sup>b</sup>	short-period H-rich sd+MS
Second CE ejection	Three peaks: $\sim 0.33 M_{\odot}$ , $\sim 0.40 M_{\odot}$ , $\sim 0.46 M_{\odot}$ <sup>b</sup>	short-period H-rich sd+HeWD
First stable RLOF	Plateau: $0.30 M_{\odot} \lesssim M_{sd} \lesssim 0.47 M_{\odot}$ <sup>b</sup>	long-period H-rich sd+MS
Double HeWD merger (slow, fast, comp.)	$0.42 M_{\odot} \lesssim M_{sd} \lesssim 0.72 M_{\odot}$ <sup>b</sup>	single He-rich sd <sup>f</sup>
Hot flasher scenario (EHF, SM, DM)	$0.43 M_{\odot} \lesssim M_{sd} \lesssim 0.50 M_{\odot}$ <sup>c</sup>	single H/He-rich sd <sup>g</sup>
dM/BD + red giant core	$0.47 M_{\odot} \lesssim M_{sd} \lesssim 0.54 M_{\odot}$ <sup>d</sup>	single H-rich sd
HeWD + dM	$0.44 M_{\odot} \lesssim M_{sd} \lesssim 0.50 M_{\odot}$ <sup>e</sup>	single H-rich sd

**Notes:**

- (a) First and second common-envelope (CE) ejection channels, first stable Roche-lobe-overflow (RLOF) channel, double helium white dwarf (HeWD) merger channel (slow, fast, and composite merger), hot flasher scenario (early hot flasher, EHF; shallow mixing, SM; and deep mixing, DM), coalescence of a low-mass main-sequence star (dM) or brown dwarf (BD) with a red giant core, and coalescence of a HeWD with a dM.
- (b) According to the best-choice model (parameter set 2) from Han et al. (2003). In total, Han et al. (2003) produced twelve simulation sets for different values of the following quantities: CE ejection efficiency  $\alpha_{CE}$ , fraction  $\alpha_{th}$  of thermal energy used for the CE ejection, critical mass ratio  $q_{crit}$  above which mass transfer is stable on the red giant branch, initial mass-ratio distribution of the progenitor binary systems, and metallicity. This was done in order to examine the effects of the individual parameters on the formation channels. Later, Lisker et al. (2005) favored parameter set 10 of Han et al. (2003) based on a maximum likelihood analysis of their own observational sample. However, an entire group of sets, including the best-choice model (parameter set 2) of Han et al. (2003), still matched the observations of Lisker et al. (2005) well.
- (c) According to the results of D’Cruz et al. (1996), Brown et al. (2001), Cassisi et al. (2003), Castellani et al. (2006), Miller Bertolami et al. (2008), Xiong et al. (2017), and Battich et al. (2018).
- (d) According to Politano et al. (2008).
- (e) According to Clausen & Wade (2011).
- (f) Both intermediate and extreme He-sdB/He-sdO stars are possible as an outcome. Slow mergers produce N-type stars, whereas fast mergers generally result in C-type ones. Composite mergers can produce two types of He-sdBs/He-sdOs depending on the final merger mass: N-type ones for  $\lesssim 0.65 M_{\odot}$  and CN-type ones for  $\gtrsim 0.65 M_{\odot}$ .
- (g) Early hot flashers (EHFs) produce hot subdwarf B stars with standard photospheric hydrogen and helium abundances (H-sdBs), whereas late hot flashers (shallow and deep mixing; SM/DM) result in intermediate and extreme He-sdB/He-sdO stars, respectively. C-type He-sdBs/He-sdOs are only produced from DM, whereas CN-type ones can result from SM and DM.

## 4. Spectroscopy - Studying Stellar Spectra with Optical Instruments

Spectroscopy is an important tool in astronomy. Studying the distribution of electromagnetic radiation as a function of wavelength (frequency) is the only means to gain access to many important parameters describing the physical state and the behavior of stars or other astronomical objects. To be able to analyze high-quality spectra, that is, high-resolution spectra with high S/N, not only the development of larger telescopes is required, but also high-resolution spectrographs of high precision and stability have to be built.

The following Sects. 4.1 and 4.2 deal with the basic structure and functionality of spectrographs. A distinction is made between (long-slit) grating and Echelle spectrographs. Both sections are based on Sects. 2.1 and 2.2 of the thesis “*Spectroscopic Analysis of the  $^3\text{He}$  Anomaly in B-Type Stars*” (Schneider, 2017) and Sects. 4.1.1 and 4.1.2 of the thesis “*Origin of runaway OB stars*” (Irrgang, 2014). Section 4.3 is based on Sect. 4.1.3 of Irrgang (2014) and describes the optical resolving power of a charge-coupled device (CCD) detector which is responsible for image acquisition. The last section of this chapter (Sect. 4.4) gives a brief overview of the properties and capabilities of the spectrographs used in this work.

### 4.1. Grating Spectrograph

In general, a spectrograph is designed to disperse starlight into its components. The simplest way to achieve this is the use of a *long-slit grating spectrograph*. It consists of the following components which are also displayed in Fig. 4.1.1: telescope, slit, collimator, dispersion element (for instance, either a prism, a grism<sup>45</sup> or a tilted reflection grating, also known as a *blaze grating*), camera lens, and CCD detector. A detailed description of each of the individual components can, for instance, be found in Drechsel et al. (2020). Here, only the functionality and the properties of the dispersion element, which is the core of the long-slit spectrograph, will be described in detail by means of a blaze grating. Furthermore, detailed insights into the spectral resolution of a grating spectrograph will be given.

Figure 4.1.2 shows a schematic construction of a blaze grating consisting of periodic reflecting grooves with spacing  $d$  tilted by the so-called blaze angle  $\Theta$  relative to the grating's surface

---

<sup>45</sup>A *grism*, also called a *grating grism*, is a combination of a prism and a grating arranged such that light at a chosen central wavelength passes straight through. In this way, the same camera can be used for spectroscopy (with grism) and imaging (without grism) without having to be moved. Various types of grisms differ in dispersion, resolution, blaze angle, grating, and, hence, in the optical range that can be observed.

normal. As for a double slit or a normal grating, constructive interference occurs if the path difference  $\Delta s$  between two light beams equals  $n\lambda$ , where  $\lambda$  is the respective wavelength used and  $n \in \mathbb{Z}$  is the diffraction order number (Huygens-Fresnel principle). Using  $\alpha$  as the signed angle of incidence and  $\beta$  as the signed angle of reflection relative to the grating's surface normal, this results in:

$$\Delta s = d \sin \alpha + d \sin \beta = d(\sin \alpha + \sin \beta) \stackrel{!}{=} n\lambda . \quad (4.1)$$

Since the quantities  $d$  and  $\alpha$  are device-specific and  $n \in \mathbb{Z}$ , the reflection angle  $\beta$  as a function of  $\lambda$  can be determined from Eq. (4.1). Calculating  $\beta$  for higher diffraction orders ( $n > 1$ )

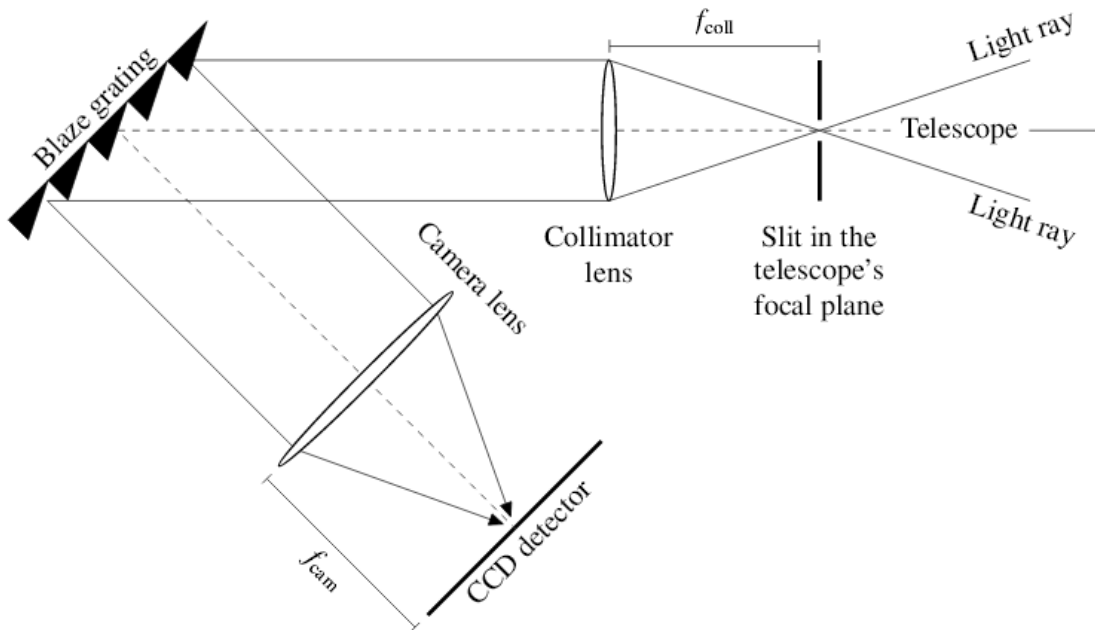


Figure 4.1.1.: Schematic setup and light path of a grating spectrograph. The telescope focuses the light beam at the slit with slit width  $b$  and the collimator lens with focal length  $f_{\text{coll}}$  is responsible for the parallelization of the light rays. The light is dispersed by the blaze grating and the resulting spectrum is imaged onto a CCD detector afterwards. The latter is achieved by a camera lens with focal length  $f_{\text{cam}}$ . Adopted from Irrgang (2014).

in the optical wavelength regime between 380 nm and 750 nm results in the same reflection angle  $\beta$  for different diffraction orders, meaning that the individual orders overlap.

The intensity for a given diffraction order  $n$  is maximal at the so-called *blaze wavelength*  $\lambda_n^0$ .  $\lambda_n^0$  can be deduced from Eq. (4.1) by means of the trajectory of a classical photon, which fulfills  $\alpha + \beta = 2\Theta$  (see also Fig. 4.1.2):

$$d(\sin \alpha + \sin \beta) \stackrel{\alpha+\beta=2\Theta}{=} d[\sin \alpha + \sin (2\Theta - \alpha)] \stackrel{!}{=} n\lambda_n^0 . \quad (4.2)$$

#### 4.1. Grating Spectrograph

---

The ratio of the wavelength  $\lambda$  to its corresponding minimal resolvable wavelength difference  $\Delta\lambda$  is called the spectrograph's *optical resolving power* or the *spectral resolution*. Two major processes are responsible for a smearing of wavelengths, hence limiting the spectral resolution. First, diffraction at a blaze grating exhibits an intrinsic resolving power of

$$R_{\text{grating}} = \left( \frac{\lambda}{\Delta\lambda} \right)_{\text{grating}} = nN, \quad (4.3)$$

where  $n$  again is the diffraction order and  $N$  is the number of illuminated grooves (Rayleigh criterion). This is often called the theoretical resolving power since it is significantly larger than the actual resolution of a spectrograph, which is defined by the slit width  $b$ . The slit

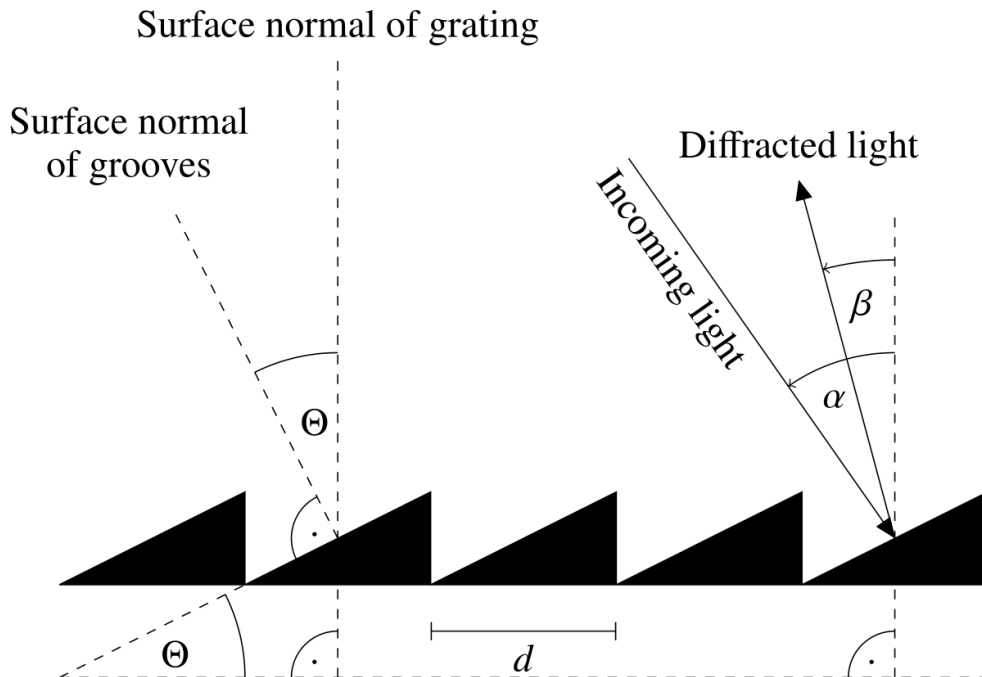


Figure 4.1.2.: Schematic construction of a blaze grating displaying all parameters involved when a light beam falls onto the grating.  $d$  is the distance between two grating grooves,  $\Theta$  is the blaze angle,  $\alpha$  is the signed angle of incident, and  $\beta$  is the signed angle of reflected radiation relative to the grating's surface normal. Adopted from Irrgang (2014).

width determines the spatial extent of the star's projection in the telescope's focal plane (see also Fig. 4.1.1). Light that passed the slit and the collimator falls not entirely parallelized onto the blaze grating because of the slit's finite size, resulting in a small but measurable variation

#### 4. Spectroscopy - Studying Stellar Spectra with Optical Instruments

$\Delta\alpha = b/f_{\text{coll}}$  of the incident angle  $\alpha$ . This introduces a smearing of wavelengths  $\Delta\lambda$  that can be calculated by:

$$\begin{aligned} d\lambda &= \frac{\partial\lambda}{\partial n} \cdot \underbrace{dn}_{=0} + \frac{\partial\lambda}{\partial d} \cdot \underbrace{dd}_{=0} + \frac{\partial\lambda}{\partial\beta} \cdot \underbrace{d\beta}_{=0} + \frac{\partial\lambda}{\partial\alpha} \cdot d\alpha = \frac{\partial\lambda}{\partial\alpha} \cdot d\alpha \stackrel{\text{Eq.(4.1)}}{=} \frac{d \cos \alpha}{n} \cdot d\alpha \\ \Rightarrow \frac{d\lambda}{d\alpha} &\stackrel{b \ll 1}{\approx} \frac{\Delta\lambda}{\Delta\alpha} = \frac{d \cos \alpha}{n} \\ \Rightarrow \Delta\lambda &= \frac{d \cos \alpha}{n} \cdot \Delta\alpha = \frac{d \cdot b \cos \alpha}{n \cdot f_{\text{coll}}} = \text{const.} , \end{aligned} \quad (4.4)$$

where it was used that  $n$  and  $d$  are fixed device-specific quantities and  $\beta$  has a fixed value for a given  $\alpha$ . The linear approximation  $\frac{d\lambda}{d\alpha} \approx \frac{\Delta\lambda}{\Delta\alpha}$  is valid since the slit width  $b$  causing the smearing is small. The actual resolving power of a long-slit spectrograph therefore reads:

$$R_{\text{slit}} = \left( \frac{\lambda}{\Delta\lambda} \right)_{\text{slit}} = \frac{n f_{\text{coll}}}{d b \cos \alpha} \cdot \lambda \sim \lambda \quad \text{with } R_{\text{slit}} \ll R_{\text{grating}}. \quad (4.5)$$

Thus,  $R_{\text{slit}}$  is linearly dependent on  $\lambda$  and significantly lower than the theoretical resolving power  $R_{\text{grating}}$ .

Obviously, high-quality spectra with a high S/N as well as a high resolution are desirable in order to analyze the features of an astronomical object. If the weather plays along, high S/N is ensured by several exposures of the same target that can be co-added afterwards (see also Sect. 8.2.2 for details on the co-addition of stellar spectra). Depending on the brightness of the individual astronomical object under investigation, however, it is important to choose an appropriate exposure time for the single exposures because of possible saturation effects. To this end, exposure time calculators have been developed by the major observatories.

Two simple possibilities for increasing the resolving power and, hence, the quality of a spectrum can be derived from Eq. (4.5). On the one hand, the slit width  $b$  should be chosen preferably small. However, due to the local *seeing*, that is, atmospheric disturbances (for instance, turbulences within different layers of the Earth's atmosphere), point sources like stars appear to be larger in the focal plane of the telescope. If the star's seeing disk in the focal plane is larger than the slit width, this results in light and information loss. Consequently, seeing sets a lower limit on the proper choice of  $b$  and a good location with preferably good seeing is necessary in order to achieve very high resolutions. In the case of perfectly small seeing, the projection of the star may even be smaller than the slit width  $b$ . In this case, the spectrograph's correct resolving power is calculated by substituting  $b$  in Eq. (4.5) by the star's projection size. Modern telescopes use so-called fibre-fed spectrographs, where the astronomical object's light is transported via optical fibres to the spectrograph. In this case, the size of the projected star is given by the fibre's diameter  $D$ , replacing  $b$  in Eq. (4.5) if  $D < b$ .

On the other hand, it is recommended to observe in high diffraction order numbers  $n$ , which has the aforementioned disadvantage of overlapping orders for  $n > 1$ . But this issue can be solved to some extent by making use of an *Echelle spectrograph*, which will be presented in the next section.

## 4.2. Echelle Spectrograph

Compared to the constituents of a usual grating spectrograph, an Echelle<sup>46</sup> spectrograph consists of an additional grating or prism which is placed between the camera lens and the dispersion element (blaze grating), perpendicular to the initial dispersion. This so-called *cross-dispersion element* or *cross disperser* separates the individual overlapping diffraction orders. In this way, a striped Echelle spectrum of up to  $n \approx 100$  orders is created, whereby the individual orders do not image the whole spectrum as usual for a transmission grating. Instead, by choosing a convenient geometry via the parameters  $n$ ,  $\alpha$ ,  $\beta$ , and  $d$ , large overlaps of

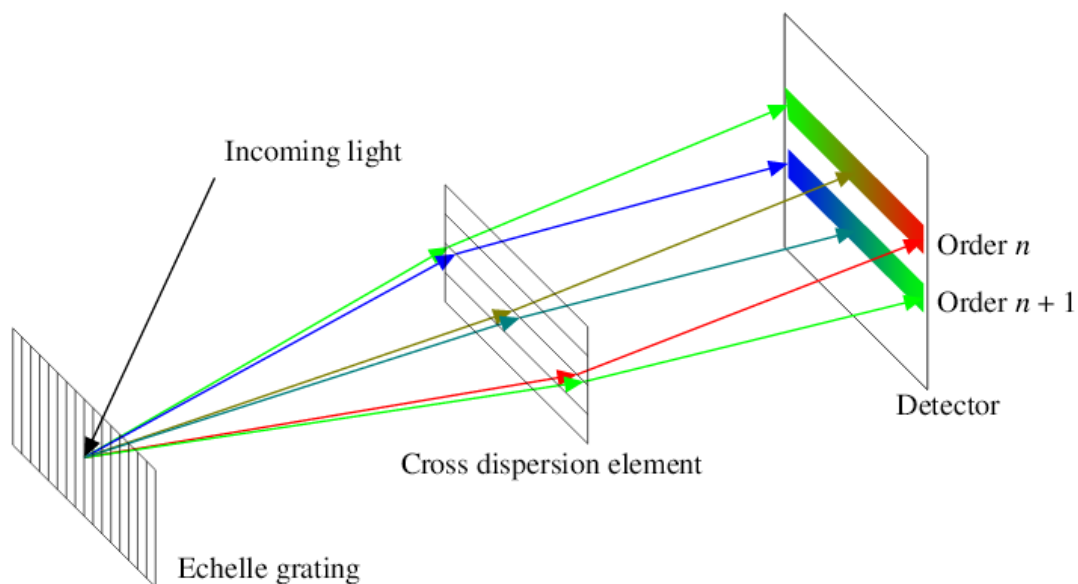


Figure 4.2.1.: Schematic setup and light path of an Echelle spectrograph. The additional cross-dispersion element compared to a usual grating spectrograph separates the overlapping higher diffraction orders before the light is imaged onto the CCD detector. Each of the individual orders only covers a section of the whole spectrum. For the sake of simplicity, the telescope, the slit as well as the collimator and camera lenses are not displayed here. Adopted from Irrgang (2014).

neighboring orders are suppressed and each individual order almost covers a unique spectral range (see Fig. 4.2.1). By merging the individual orders during data processing, the whole continuous high-resolution spectrum (with  $R$  up to  $\approx 100\,000$ ) can be created. In consequence, a CCD detector must be sufficiently large in dispersion direction to cover an entire order to avoid gaps in the spectrum and to cover as many orders as possible. If this cannot be achieved in the individual setup, the light beam can be split by dichroics into different channels (arms) beforehand, whereby each channel is optimized for the individual wavelength regime to be

<sup>46</sup>*Echelle* = French word for 'stair' or 'ladder'

covered (for instance, via the grating angle, the camera lens, and the CCD detector used). Thus, the whole continuous spectrum can be reconstructed from the images of more than one CCD with optimized sensitivities for the individual wavelength regimes (see also Fig. 4.4.1). Moreover, the blaze wavelengths  $\lambda_n^0$  are located at the central positions of the respective CCD detectors in order to minimize the light loss within each order. This leads to the effect that only the spectral range around  $\lambda_n^0$  is covered in each of the orders ( $|\lambda_n^0 - \lambda|/\lambda_n^0 \ll 1$ ) and that each order's intensity profile is given by the blaze function which has a maximum at  $\lambda_n^0$  and drops sharply to the sides. Therefore, the resolving power of an Echelle spectrograph can simply be approximated by substituting  $\lambda$  by  $\lambda_n^0$  in Eq. (4.5), whereby the definition of  $\lambda_n^0$  in Eq. (4.2) is used:

$$\begin{aligned} R_{\text{echelle}} &= \left( \frac{\lambda}{\Delta\lambda} \right)_{\text{echelle}} \approx \frac{n f_{\text{coll}}}{d b \cos \alpha} \cdot \frac{d[\sin \alpha + \sin (2\Theta - \alpha)]}{n} \\ &= \frac{f_{\text{coll}}[\sin \alpha + \sin (2\Theta - \alpha)]}{b \cos \alpha} = \text{const.} \end{aligned} \quad (4.6)$$

In contrast to  $R_{\text{slit}}$ ,  $R_{\text{echelle}}$  hence is independent of  $\lambda$ . However,  $\Delta\lambda \sim \lambda$ .

### 4.3. CCD Detectors

The digital image of the spectrum obtained is created in a CCD chip. The spatial distribution of pixels on the CCD has to be fine enough such that all spectral features can be resolved. This means that the spectral resolution of the CCD detector should match the one of the spectrograph. In fact, it can also be higher than that of the spectrograph, which results in an oversampled spectrum. According to the Nyquist criterion, the spatial resolving power of a CCD chip with spatial pixel width (size)  $b_{\text{pixel}}$  is  $2b_{\text{pixel}}$ . In order to derive the detector's spectral resolution for a long-slit and an Echelle spectrograph, the following substitutions in Eqs. (4.5) and (4.6) have to be made:  $\alpha \rightarrow \beta$ ,  $b \rightarrow 2b_{\text{pixel}}$ , and  $f_{\text{coll}} \rightarrow f_{\text{cam}}$ . Thus, the respective optical resolving powers for the CCDs are:

$$R_{\text{CCD, slit}} = \left( \frac{\lambda}{\Delta\lambda} \right)_{\text{CCD, slit}} = \frac{n f_{\text{cam}}}{2d b_{\text{pixel}} \cos \beta} \cdot \lambda \sim \lambda \quad (4.7)$$

$$R_{\text{CCD, echelle}} = \left( \frac{\lambda}{\Delta\lambda} \right)_{\text{CCD, echelle}} = \frac{f_{\text{cam}}[\sin \beta + \sin (2\Theta - \beta)]}{2b_{\text{pixel}} \cos \beta} = \text{const.} \quad (4.8)$$

Equations (4.7) and (4.8) lead to an equidistant spacing in wavelength data points (pixels read from the CCD) in the case of long-slit spectrographs and to a steadily increasing spacing for Echelle spectrographs (see, for instance, Irrgang 2014 for details).

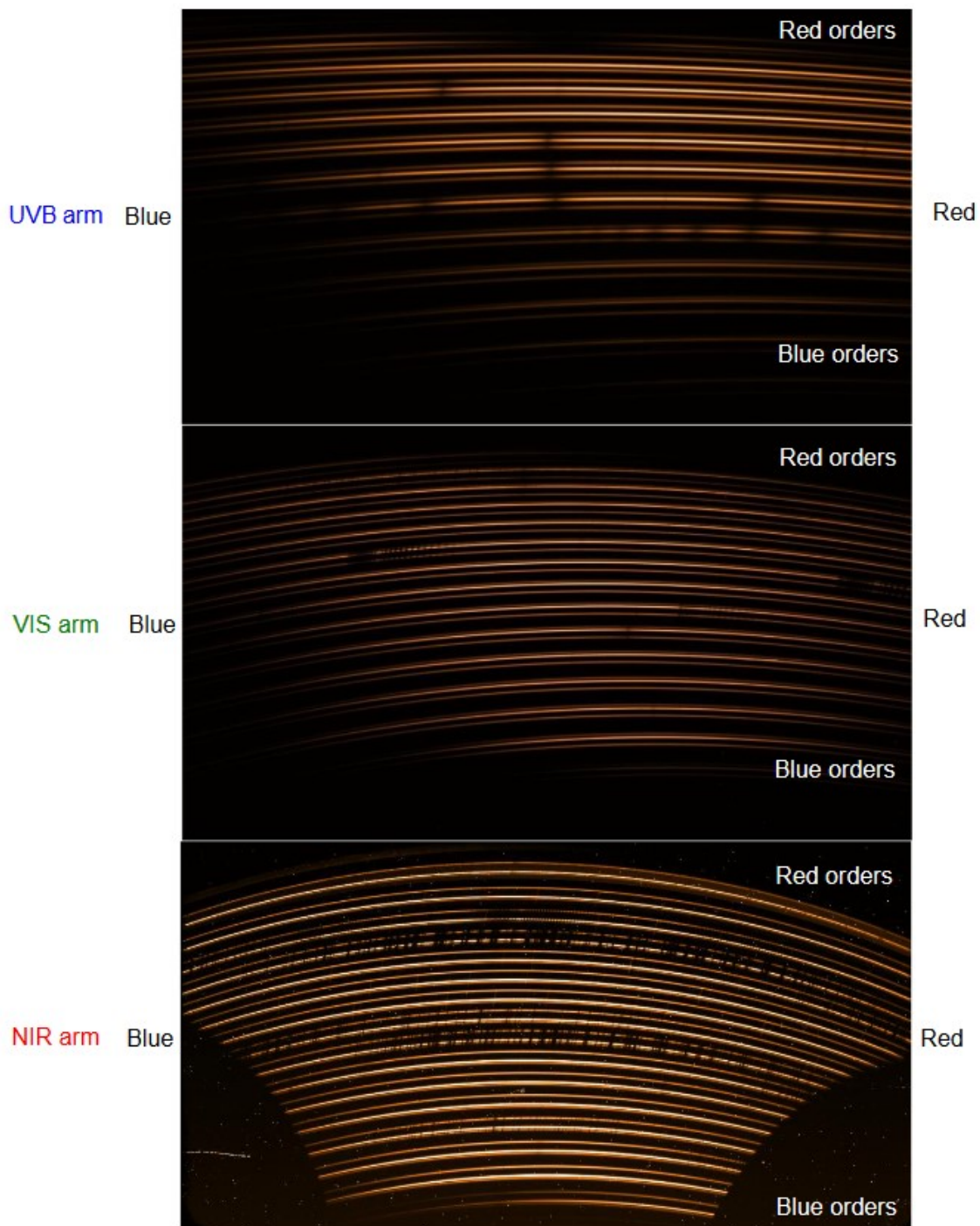


Figure 4.4.1.: Example of a raw Echelle spectrum observed in three different channels (UVB, VIS, NIR) and obtained by means of the Integrated Field Unit (IFU) of the XSHOOTER spectrograph. Each Echelle order consists of three slices. Telluric absorption lines (see also Sect. 8.2.1) are clearly visible in the VIS and NIR channels. Furthermore, the effect of atmospheric dispersion is observed by means of distance changes between the slices of blue and red orders in the UVB and VIS channels. Adopted from Mieske et al. (2019).

## 4.4. Spectrographs Used

Following and extending the elaborations of Schneider (2017), this section describes the majority of instruments used in order to obtain the stellar spectra presented in Sect. 8.1. Table 4.1 lists the sources from which the descriptions of the individual spectrographs are extracted. Additional sources and references used are marked within the text.

### XSHOOTER

XSHOOTER was installed at the Cassegrain focus of Unit Telescope 2 (UT2, Kueyen) as the first second generation instrument of the ESO Very Large Telescope (ESO VLT) at Cerro Paranal, Chile, in 2009, operating as a wide band intermediate-resolution spectrograph. By means of dichroic splitting in three channels with optimized optics, coatings, dispersive and

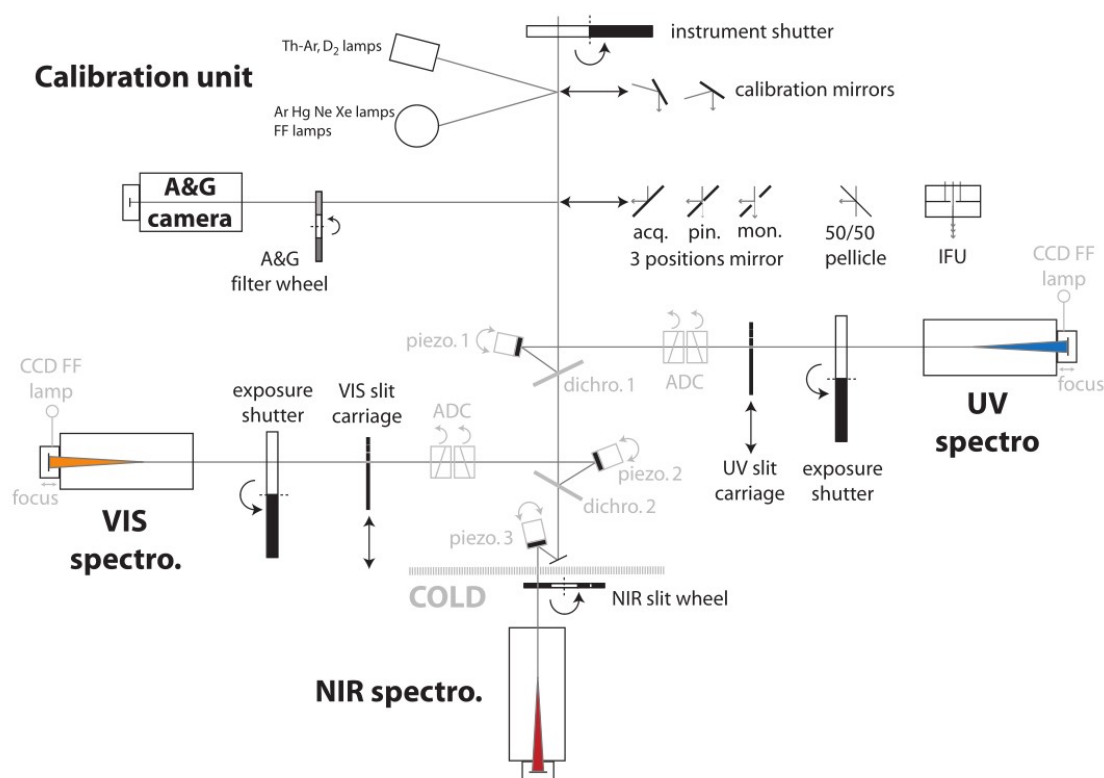


Figure 4.4.2.: Schematic overview of the XSHOOTER instrument. The light path runs from top to bottom. Adopted from Vernet et al. (2011).

cross-dispersion elements as well as detectors, it is efficiently designed to maximize the sensitivity over the vast wavelength regime of  $\sim 3000\text{-}24\,800\text{ \AA}$ . The three independent wavelength ranges that can be covered in a single target exposure are: ultraviolet/blue (UVB,  $\sim 3000\text{-}5595\text{ \AA}$ ), visual (VIS,  $\sim 5595\text{-}10\,240\text{ \AA}$ ), and near infrared (NIR,  $\sim 10\,240\text{-}24\,800\text{ \AA}$ ). The

#### 4.4. Spectrographs Used

---

spectral resolution of XSHOOTER ( $R \sim 4000\text{-}17\,000$ ) depends on both the individual channel and the slit width used. Figure 4.4.1 shows an example of a raw Echelle spectrum obtained with XSHOOTER.

Figure 4.4.2 shows a schematic overview of the XSHOOTER instrument. At first, the incoming light travels through the instrumental shutter and an Integrated Field Unit (IFU), whereby the latter redirects the light such that it can be easily passed to the three subsequent Echelle spectrographs, which are found at the end of the respective channels. Each channel has its own shutter and slit mask. Slits with different widths are positioned on a wheel such that they can be changed easily. Furthermore, field lenses, placed in front of the slits, are used in order to focus the light beam on the dispersive element of the individual spectrograph, enhancing the sensitivity. In total, two dichroics are used for splitting the light beam, whereby the first one sends light into the UVB channel and the second one splits the beam for the VIS and the NIR spectrograph. Three small piezo controlled mirrors, placed right after the dichroics, compensate for flexures. In order to correct for atmospheric dispersion in the UVB and VIS channels and to enhance the amount of light reaching the corresponding spectrographs, Atmospheric Dispersion Corrector (ADC) prisms are placed right after the piezo controlled mirrors. The NIR spectrograph is cooled within a cryostat filled with liquid nitrogen such that the emission of infrared (IR) light resulting from thermal emission is avoided. In addition, an acquisition and guidance (AG) system for target acquisition and an internal calibration unit (CU), containing different lamps for flat field and calibration frames, are integrated. Fully calibrated two-dimensional spectra covering the full wavelength range can be extracted by means of a dedicated data reduction package (see Goldoni et al. 2006 and Modigliani et al. 2010 for details).

## FEROS

The Fibre-fed Extended Range Optical Spectrograph (FEROS) was first attached to the now decommissioned ESO 1.52 m-telescope in November 1998. Since October 2002, the instrument has been mounted permanently on the MPG<sup>47</sup>/ESO-2.20 m telescope in La Silla, Chile. FEROS operates as a state-of-the-art bench-mounted high-resolution and thermally controlled prism-crossdispersed Echelle spectrograph. It is commonly used for a large variety of stellar and extragalactic spectroscopic observation programs that require high spectral stability and efficiency. Over a total amount of 39 Echelle orders, covering almost the complete optical spectral region between  $\sim 3500\text{ \AA}$  and  $\sim 9200\text{ \AA}$  in a single exposure, the FEROS instrument offers high efficiency ( $\sim 20\%$ ) and high resolution ( $R \sim 48\,000$ ). Due to its long-term mechanical and thermal stability as well as the daily performed calibrations, an accurate wavelength calibration and, hence, a large amount of useful scientific output data is guaranteed. Moreover, RV measurements with accuracies of  $\sim 25\text{ m s}^{-1}$  or better are ensured by an integrated Object-Calibration mode.

The FEROS instrument consists of three main parts: the spectrograph itself, a CU and an adapter allowing for an instant change between spectroscopy and imaging with the Wide Field

---

<sup>47</sup>MPG stands for Max Planck Gesellschaft.

## 4. Spectroscopy - Studying Stellar Spectra with Optical Instruments

Instrument	References
XSHOOTER	<a href="https://www.eso.org/sci/facilities/paranal/instruments/xshooter.html">https://www.eso.org/sci/facilities/paranal/instruments/xshooter.html</a> Last called on 5th March 2021 Vernet et al. (2011) Mieske et al. (2019)
FEROS	<a href="https://www.eso.org/sci/facilities/lasilla/instruments/feros.html">https://www.eso.org/sci/facilities/lasilla/instruments/feros.html</a> Last called on 5th March 2021 Kaufer et al. (1999) Sterzik et al. (2006)
FOCES	Pfeiffer et al. (1998)
HIRES	<a href="https://www2.keck.hawaii.edu/inst/hires/">https://www2.keck.hawaii.edu/inst/hires/</a> Last called on 8th March 2021 Vogt et al. (1994)
HRS	<a href="https://mcdonald.utexas.edu/">https://mcdonald.utexas.edu/</a> Last called on 8th March 2021 <a href="http://hydra.as.utexas.edu/?a=help&amp;h=11">http://hydra.as.utexas.edu/?a=help&amp;h=11</a> Last called on 8th March 2021 Tull (1998)
UVES	<a href="https://www.eso.org/sci/facilities/paranal/instruments/uves.html">https://www.eso.org/sci/facilities/paranal/instruments/uves.html</a> Last called on 10th March 2021 Dekker et al. (2000) Mieske et al. (2020)
CAFOS	<a href="http://www.caha.es/telescope-2-2m/cafos">http://www.caha.es/telescope-2-2m/cafos</a> Last called on 11th March 2021 Meisenheimer (1998)
IDS	<a href="https://www.ing.iac.es/astronomy/instruments/ids/">https://www.ing.iac.es/astronomy/instruments/ids/</a> Last called on 12th March 2021

Table 4.1.: References used for the descriptions of the individual instruments presented throughout Sect. 4.4.

Imager. The spectrograph is fed from the Cassegrain focus of the 2.20 m telescope by two science fibres, which are illuminated by 2.0 arcsec apertures on the sky separated by 2.9 arcmins. In this way, a science frame of the individual object under investigation and an exposure of a sky background region can be produced at the same time. The CU offers special fibres for flat-field and wavelength-calibration lamps. The light of the latter two is guided to the science fibres via the Sliding Calibration Selection Mirror. The instrument's high detection efficiency mostly results from the thinned and back-illuminated 2k x 4k CCD detector with an excellent quantum efficiency of  $\sim 98\%$  measured at 4500 Å. Data calibration and reduction is very user-friendly because both can be performed within the FEROS reduction pipeline, which is also included in the standard ESO MIDAS (**M**unich **I**mage **D**ata **A**nalysis **S**ystem) distribution.

### FOCES

Designed and built in 1996, the Fibre Optics Cassegrain Echelle Spectrograph (FOCES) was mounted until 2009 on the Cassegrain focus of either the 2.2 m or the 3.5 m telescope at the Calar Alto Observatory (German-Spanish Astronomical Center, GSAC; Centro Astronómico Hispano-Alemán, CAHA) located in the Sierra de Los Filabres to the north of Almería, Spain. After extensive lab tests at the Munich University Observatory, the instrument has now been reinstalled at the 2 m Wendelstein Observatory in the German Alps (see Kellermann et al. 2015 for details). The following descriptions refer to the spectrograph's initial installation since the FOCES spectra analyzed in this work were all taken at Calar Alto.

At Calar Alto, FOCES used to be fed by 100  $\mu\text{m}$  optical fibres and the incident light was collimated by means of two off-axis parabolic mirrors. Scattered light was efficiently removed by a small folding mirror which was placed between the two parabolic mirrors. The optical spectral region ranged from 3800 to 7500  $\text{\AA}$  and was covered by 70 Echelle orders in total. The instrument reached a maximum spectral resolution of  $R \sim 40\,000$  with a two-pixel resolution element. A tandem prism mounting was used for cross-dispersion separating the individual diffraction orders. Eventually, the light beam was imaged onto a field centred on a 1024  $\times$  1024 thinned CCD with 24  $\mu\text{m}$  pixels making use of an  $f/3$  transmission camera. In order to correct spectra of extremely faint objects, FOCES also offered a second fibre system which carried the sky background signal. However, an additional prism for higher cross-dispersion had to be used for this alternative mode. This also resulted in a reduced spectral range.

### HIRES

The High Resolution Echelle Spectrometer (HIRES) is mounted on the right Nasmyth focus of the Keck 1 telescope near the summit of Mauna Kea, Hawaii. Constructed as a grating cross-dispersed Echelle spectrograph, which is capable of operating between 3000 and 10 000  $\text{\AA}$  at spectral resolutions that range from  $R \sim 25\,000$  to  $\sim 85\,000$  depending on the slit and the different gratings used, HIRES' design tries to meet the specifications, limits and environment conditions of its outstanding workplace.

The incoming light first enters the slit and then passes a filter wheel, where it is modulated. After that, the light beam passes a shutter and hits one of two tilted spherical mirrors which are used for collimation and subsequent redirection towards the Echelle grating. Both collimators have different coatings either optimized for the blue (3000 to 5500  $\text{\AA}$ , HIRESb) or the red (3400 to 10 000  $\text{\AA}$ , HIRESr) part of the wavelength range. In order to minimize the light loss and due to the optimization of the system throughput, three single gratings form a large Echelle grating, which exhibits a blaze angle of over 70°. Depending on the chosen setup (HIRESb or HIRESr), two different cross dispersers then split the light beam again before it is sent through a setup of correction lenses onto a large mirror and a field flattener. Behind the latter, a standard CCD detector is placed, whereby a tailored setup of lenses is used in order to maximize the efficiency. For extremely accurate calibration, HIRES uses several calibration lamps and an iodine cell, which are all placed in front of the viewing slit.

### HRS

Commissioned in March 2001 and constructed for one of the largest optical telescopes in the world, that is, the Hobby-Eberly Telescope (HET) located at the McDonald Observatory in Davis Mountains, Texas, the first version of the high-resolution fibre-coupled Echelle spectrograph (HRS) covered an overall spectral range between 4200 and 11 000 Å. HRS was a single channel spectrograph which was linked to the corrected primary focus of the HET through its Fibre Instrument Feed. Depending on the four available effective slit widths used, the instrument's spectral resolution ranged from  $R \sim 15\,000$  over  $\sim 30\,000$  and  $\sim 60\,000$  up to  $\sim 120\,000$ .

HRS used a two-mirror collimator system. The first mirror served as the main collimator and was located off-axis, whereas the second one was placed even farther off-axis in order to re-collimate the beam and to compensate for the off-axis aberrations of the main mirror. In this way, all dispersed rays were directed to the "white pupil" of the spectrograph, which coincided with the surface of the cross-dispersing grating. A mosaic of two R-4 Echelle gratings, exhibiting a nominal blaze angle of  $76^\circ$ , and a selection of two cross-dispersing gratings were used for the separation of the individual spectral orders. Furthermore, imaging was possible by means of an all-refracting camera and a  $4096 \times 4096$  mosaic of two thinned and anti-reflection coated  $2k \times 4k$  CCDs with a pixel size of  $15\ \mu\text{m}$ .

HRS was replaced by the second generation high-resolution fibre-coupled Echelle spectrograph (HRS2) within the HET wide field upgrade (Hill et al., 2018).

### UVES

The UV-Visual Echelle Spectrograph (UVES) for the ESO VLT at the Paranal Observatory was mounted on the Nasmyth B focus of Kueyen (UT2) in the late 1990s and started operation in April 2000. Covering a wavelength range of 3000 to 5000 Å (UV/blue channel) and 4200 to 11 000 Å (visual/red channel) with two-pixel resolutions of up to  $R \sim 80\,000$  and  $\sim 110\,000$ , respectively, UVES is designed as a versatile and highly efficient cross-dispersed Echelle spectrograph. A narrow slit mode offers a resolution of  $R \sim 40\,000$ .

Entering UVES through the telescope shutter, the collected light first reaches the CU, consisting of a mirror system, different image slicers, calibration lamps, and an iodine cell for RV calibration. The CU ensures that both the calibration and the source light enter UVES in the exact same way. A derotator parallelizes the light beam and compensates for losses due to telescope rotation. The beam then passes an optional filter wheel and an ADC. A depolarizer is used to get rid of undesired polarization introduced by the telescope and stray light is prevented from entering the setup by a pupil-stop. Depending on the mode selected for the individual observation, the light either enters the red or the blue channel only (single-channel mode) or both channels at the same time (two-channel mode), whereby in the latter case dichroic beam splitters are used. Two versions of the two-channel mode are available, differing in wavelength coverage (DICH#1 and DICH#2). Light entering one of the two channels first goes through a slit unit consisting of a filter wheel and interference filters in

#### 4.4. Spectrographs Used

---

order to reject stray light and to isolate certain Echelle orders. Behind the slit unit, a mirror is placed which reflects the light beam to the main collimator. The collimated beam enters the Echelle grating and then again is redirected towards the main collimator. However, a small fraction of the light (about 1%) goes through an exposure-meter that measures the amount of light within the system resulting from both the background sky and the scientific object under investigation. The major light part hits the cross-disperser elements through a mirror and transfer collimator system. In the end, the light beam is focused onto the camera and then is recorded by the detector, which is composed of thin and cooled 15  $\mu\text{m}$  CCD chips. Their sizes are 2048 x 3000 (blue channel) and 4096 x 4096 (red channel), respectively.

### CAFOS

The Calar Alto Faint Object Spectrograph (CAFOS) is permanently mounted on the Cassegrain station of the Zeiss 2.2 m reflector telescope of the Calar Alto Observatory. Designed to work in visible light and capable of spectroscopy with grisms and a long-slit or multi-object masks, polarimetry (direct and with grisms), and imaging (direct and through a Fabry-Pérot-Etalon), it is a focal-reducer which changes the 2.2 m telescope's f/ratio from f/8.0 to f/4.4. CAFOS is primarily designed for spectroscopy of faint objects with magnitudes larger than 18 mag. The whole instrument, including the CCD camera system, can be controlled via a user-friendly graphical user interface (GUI).

The imaging optics of CAFOS consists of a collimator with a focal length of 310 mm which re-images the entrance pupil of the telescope in a secondary pupil of 40 mm diameter. The light beam is focused onto the SITe#1d CCD chip (2048 x 2048 pixels, 24  $\mu\text{m}$  pixel size, 0.53 arcsec per pixel) by a camera optics from the Max Planck Institute for Astronomy, which has a focal length of 163 mm (MPIA CCD camera). The shutter is placed in front of the last lens of the camera (flattening lens), that is, inside the instrument, but not between the flattening lens and the entrance window of the CCD. Moreover, a filter wheel with twelve positions and 50 mm filter diameter is located in front of the shutter. The main body of the camera system is moved automatically towards the secondary pupil such that the focus shift introduced by the individual filters can be compensated. A grism wheel equipped with eight different grisms is placed in the collimated beam near the secondary pupil. The grism wheel also includes a Lyot stop for flare reduction and a narrow pupil stop. If combined, the different grisms available cover the total spectral range between  $\sim 3200$  and  $\sim 11\,000$  Å, resulting in dispersions ranging from 2.00 to 9.76 Å per pixel, that is, spectral resolutions of 1125 and 231, respectively, at 4500 Å. Additionally, three different aperture masks (a long-slit with tunable width and two focal plane masks for multi-object spectroscopy) can be inserted at the position of the telescope focus, enabling a narrow spectral resolution of extended objects and a reduction of the sky background. Thanks to very accurate encoders, the movement of the aperture masks and the rotation of the grism wheel are very stable. Furthermore, the overall flexure of the different components usually does not exceed 10  $\mu\text{m}$ . Due to the fact that the slit view is not displayed during the observation, the individual object under investigation has to be positioned on the slit. This is done by means of an acquisition exposure followed by

an offsetting of the telescope. CAFOS is also equipped with an internal CU containing three spectral lamps for wavelength calibration and a continuum lamp for flat fielding.

### IDS

The Intermediate Dispersion Spectrograph (IDS) is a standard long-slit spectrograph mounted on the Cassegrain focus of the 2.5 m Isaac Newton Telescope, which is part of the Roque de los Muchachos Observatory on La Palma. After having measured its first light in March 1984, IDS was decommissioned in July 2003, but recommissioned in August 2006. The instrument uses a 235 mm focal length camera and offers two 4096 × 2048 pixels CCD detectors: RED+2 (with 15.0 μm pixel size and a spatial scale of 0.44 arcsec per pixel) and EEV10 (with 13.5 μm pixel size and a spatial scale of 0.40 arcsec per pixel), being sensitive in the red and blue wavelength regimes, respectively. While RED+2 only suffers from low fringing below the 2% level, the usage of EEV10 is heavily limited in the red spectral range due to strong fringing. Approximately only 2200 and 2275 of the CCD pixels are clear and unvignetted in the case of RED+2 and EEV10, respectively, since the camera optics severely vignette the outer regions of the dispersed light beam. The maximum unvignetted slit length usable with IDS is 3.3 arcmin. IDS provides a total set of 16 different gratings, which combined cover the total spectral range between ~4000 and ~10 000 Å. This allows for various different grating and CCD combinations, resulting in dispersions ranging from 0.24 to 4.03 Å per pixel, that is, spectral resolutions of 9375 and 558, respectively, at 4500 Å. An AG unit is attached to the spectrograph, also offering calibration and comparison lamps as well as neutral-density and color filters. Both the spectrograph and the AG unit are computer-controlled, but changes of the grating and the collimator used can be handled manually.

## 5. Astrometry - Three-Dimensional Mapping of the Milky Way with Gaia

Astrometry describes the astronomical discipline of the accurate measurement and study of the (changing) positions of celestial objects. Since the spectroscopic analysis only provides an accurate measurement of the RV component (movement in the line of sight) of an individual object through the Doppler formula (see also Sect. 7.1.1), additional information is needed in order to be able to reconstruct the specific spatial movement. This additional information includes the distance  $d$ , measured via the trigonometric stellar parallax  $\varpi$  (usual relation:  $d = 1/\varpi$ ), the position on the celestial sphere (defined by the two angles right ascension  $\alpha$  and declination  $\delta$  in the equatorial coordinate system), and the proper motion, that is, the movement on the celestial sphere in direction of  $\alpha$  and  $\delta$ . Due to the difficulty of controlling the systematic errors as well as of overcoming the disturbing effects of the Earth's atmosphere and because of the need to convert the measured relative parallaxes into absolute ones, however, obtaining accurate parallaxes from ground-based astrometry is challenging. For instance, this is why the number of stars with ground-based parallaxes was limited to  $\sim 8000$  until the mid-1990s (van Altena et al., 1995; Finch & Zacharias, 2016). Hence, space-based observations are crucial in this regard.

Accepted into the scientific program of the European Space Agency (ESA) in 1980 and operating from August 1989 to March 1993, the HIPPARCOS satellite measured absolute parallaxes with 0.001 arcsec accuracy of  $\sim 118\,000$  objects in total (ESA, 1997). A by-product of the main HIPPARCOS Catalogue was the *Tycho-1* Catalogue, which resulted from an auxiliary star mapper on board of HIPPARCOS and pinpointed many more stars with a lesser but still unprecedented accuracy of 0.02 arcsec. *Tycho-1* included more than one million objects and was revised within *Tycho-2*, which was completed in 2000, adding around 1.5 million stars to *Tycho-1* and increasing the accuracy through improved data reduction. Allowing astronomers to probe stellar distances that extended out to more than 300 light years, the HIPPARCOS and *Tycho* data have influenced different areas of astronomy: from the internal structure and the evolution of stars in general over the kinematics of stars and stellar groups in the solar neighborhood to the knowledge of the structure and the dynamics of our Galaxy, the Milky Way. Beyond the Milky Way, stellar distances derived from HIPPARCOS' parallax measurements also lead to more precise estimates for the age of the Universe and its expansion rate. Last but not least, data from the HIPPARCOS satellite additionally contributed to the popular field that searches for extrasolar planets. While upper limits for the masses of several exoplanets could be derived, which confirmed their nature, the masses of others could be accurately determined and the properties of their individual parent stars could be characterized (see Perryman 2009 for a detailed review of the astronomical breakthroughs based on HIPPARCOS data). Due to

its great success, it was not surprising that an astrometric next-generation space-based successor mission (*Gaia*) with precision of one millionth of an arcsecond was proposed in order to increase the sample size and the observed volume of HIPPARCOS.

The following Sects. 5.1-5.5 describe the *Gaia* space mission in detail. While Sect. 5.1 gives a historical review and Sect. 5.2 describes the scientific goals of the mission, the observation principle and the design of the spacecraft are outlined in Sects. 5.3 and 5.4, respectively. The chapter concludes with a detailed description of the trigonometric parallaxes measured by *Gaia*, whereby special focus is on their proper use (Sect. 5.5).

### 5.1. History and Planning Phase

The *Gaia* mission was already proposed by the Swedish astronomer Lennart Lindegren and the British astronomer Michael Perryman in 1993. After an extensive concept and technology study, the resulting science case as well as the mission and spacecraft concept were described by Perryman et al. (2001). Spelled as *GAIA* in the early phases, *Gaia* was selected as an ESA-only mission in 2000, providing a final payload design which was non-interferometric and based on monolithic mirrors as well as direct imaging. Following further preparation studies during the first half of the 2000s, the implementation phase started in 2006, whereby the EADS<sup>48</sup> Astrium (later renamed Airbus Defence and Space; Airbus DS) in Toulouse (France) was selected as the prime contractor of the project, being responsible for the development and the implementation of the spacecraft and its payload. Just one year later, a pan-European and nationally funded collaboration of several hundreds of expert scientists and software developers from over 20 countries, known as DPAC (Data Processing and Analysis Consortium), was founded in order to provide the algorithms, the software, and the information technology infrastructure which is necessary to manage the complex processing and analysis of the mission data. DPAC's main objective is the provision of the final *Gaia* Catalogue. The spacecraft was launched from Kourou (French Guiana) by a Soyuz-Fregat launcher on 19th December 2013. A single Fregat boost at the end of the two-day Launch and Early Orbit Phase (LEOP) injected the spacecraft on its transfer trajectory towards its operating point, that is, the second Lagrange point ( $L_2$ ) of the Sun-Earth-Moon system, where it arrived a few weeks later after the transfer and in-orbit commissioning phase had been successfully completed. After a final commissioning, calibration and performance verification phase which lasted around half a year, the five-year nominal science operations phase officially started on 19th July 2014. The first four weeks were used for special, south ecliptic-pole scanning which eventually transferred into all-sky scanning mode (Gaia Collaboration et al., 2016b).

The *Gaia* collaboration does not have rights on the mission data. Instead, all data obtained can be retrieved from the *Gaia* Archive<sup>49</sup> without limitations by several query, visualization, exploration, and collaboration tools (Salgado et al., 2017a,b) after having been processed, calibrated, and validated inside DPAC. To this end, several intermediate data releases (DRs)

---

<sup>48</sup>EADS stands for European Aeronautic Defence and Space.

<sup>49</sup><https://gea.esac.esa.int/archive/>, last called on 28th March 2021

## 5.2. Mission Science

---

were defined. DR1 was made public on 14th September 2016 and included data collected over a time span of 14 months in total (Gaia Collaboration et al., 2016a). DR2, which is based on 22 months of continuous observations, was published on 25th April 2018 (Gaia Collaboration et al., 2018). The third release is composed of *Gaia* Early Data Release 3 (EDR3), which was released on 3rd December 2020, and the full *Gaia* Data Release 3 (DR3), which is expected in the first half of 2022<sup>50</sup>. At the time of this work's submission, the release date for the complete *Gaia* Catalogue still has to be determined. Currently, the *Gaia* mission has been extended to 31st December 2022.

## 5.2. Mission Science

Following in the footsteps of HIPPARCOS, *Gaia* was built to sample a large and representative part of the Milky Way down to a limit of  $\sim 20.7$  mag in the *Gaia*  $G$  band (reminder: HIPPARCOS' limiting magnitude was  $V = 12.4$  mag). The mission aimed to measure the present-day, three-dimensional spatial (right ascension, declination, distance/parallax) and three-dimensional velocity distribution (RV, proper motion) of at least seven million stars brighter than  $G \sim 17$  mag in the thin and thick disks, in the bulge, and in the halo in order to be able to determine their orbits and the underlying Galactic gravitational potential as well as the mass distribution. In this context, *Gaia* also allows astronomers to determine the astrophysical properties of the observed stars (for instance, the surface gravity and the effective temperature) in order to understand the formation and the structure as well as the past and the future evolution of the Milky Way. *Gaia* astrometry delivers absolute parallaxes and transverse kinematics of outstanding quality. In addition, photometric data from three passband filters, that is, broad-band (3300-10 500 Å) in the unfiltered  $G$  band as well as integrated broad-band photometry from the blue ( $G_{BP}$ , 3300-6800 Å) and the red ( $G_{RP}$ , 6400-10 500 Å) photometers are obtained for a large subset of the target objects. RVs, interstellar extinctions<sup>51</sup>, and chemical abundances for a large number of objects can also be derived from *Gaia* data. In this way, it is possible to set up a coherent picture of all of the individual aspects in the Milky Way (Gaia Collaboration et al., 2016b).

Although *Gaia*'s science case has already been outlined almost two decades ago (Perryman et al., 2001) and various large ground-based surveys have been completed within the time span of *Gaia*'s construction phase, the astrometric part of the *Gaia* science case is still unique since global, micro-arcsecond astrometry is only available from space. Last but not least, both the space environment and the design of *Gaia* guarantee an outstanding accuracy, sensitivity, dynamic range, and sky coverage that cannot be obtained from ground-based observations with

---

<sup>50</sup><https://www.cosmos.esa.int/web/gaia/release>, last called on 28th March 2021

<sup>51</sup>In astronomy, extinction is referred to as the absorption and the scattering of electromagnetic radiation by dust and gas between an emitting astronomical object and the observer. For Earth-bound observers, extinction arises both from the interstellar medium (see also Sect. 8.2.5) and the Earth's atmosphere. It may also arise from circumstellar dust around an observed object. Due to the fact that blue light is much more strongly attenuated than red light, extinction causes objects to appear redder than expected. This phenomenon is also referred to as interstellar reddening.

a similar scientific scope. After its five-year nominal science operations, *Gaia* was expected to ultimately deliver stellar parallaxes with standard errors less than  $10 \mu\text{as}$  for stars brighter than  $G \approx 13$  mag, errors around  $30 \mu\text{as}$  for stars with  $G \approx 15$  mag, and errors around  $600 \mu\text{as}$  for stars with  $G \approx 20$  mag. The end-of-life photometric standard errors were estimated to be in the milli-magnitude regime (Gaia Collaboration et al., 2016b). Thanks to the approved extension phase, however, these initial estimates for the uncertainties in the final *Gaia* Catalogue will become even smaller.

### Data Release 1

The first data release of *Gaia* (Gaia Collaboration et al., 2016a) consisted of the following three main components:

- The **astrometric data set** consisted of a primary data set containing the positions, parallaxes, and mean proper motions for about two million of the brightest stars in common with the *Gaia* DR1, HIPPARCOS and *Tycho*-2 Catalogues. This was realized within the *Tycho-Gaia* Astrometric Solution (TGAS, Michalik et al. 2015), for which measurements from all three catalogs were combined in a single global astrometric solution such that the ambiguity between parallax and proper motion in a short stretch of *Gaia* observations could be disentangled and a full five-parameter astrometric solution could be provided. The typical uncertainty for the positions and parallaxes was  $\sim 0.3$  mas, whereas for the proper motions it was about 1 mas per year. It was suggested to add a systematic component of  $\sim 0.3$  mas to the parallax uncertainties due to parallax zero-point variations (Arenou et al., 2017). For the subset of the HIPPARCOS stars, the proper motions were much more precise (0.06 mas per year). An additional secondary astrometric data set based on *Gaia* data only and, therefore, only providing the two-component solution, contained the positions for a total number of 1.1 billion sources, whereby the typical uncertainty was  $\sim 10$  mas.
- The **photometric data set** consisted of mean  $G$ -band magnitudes for all sources observed. The median uncertainties ranged from the milli-mag level to around 0.03 mag over the magnitude range from 5 to 20.7.
- **Light curves** in the  $G$ -band and characteristics of  $\sim 3000$  variable stars (Cepheids and RR Lyrae stars) that were observed at high cadence around the south ecliptic pole during the first four weeks of the operations phase.

Additionally, positions and  $G$  magnitudes for more than 2000 extragalactic sources (quasars) were measured in order to define the first version of the celestial reference frame (CRF) *Gaia*-CRF, which is a new materialization of the International Celestial Reference Frame (ICRF) in the optical.

Via workshops<sup>52</sup> and several accompanying publications, the *Gaia* collaboration informed as-

---

<sup>52</sup><https://gaia.ari.uni-heidelberg.de/gaia-workshop-2016/index.html>, last called on 29th March 2021

tronomers from all over the world about DR1 data and the possible pitfalls coming along with them (see, for instance, Lindegren et al. 2016; Carrasco et al. 2016; van Leeuwen et al. 2017; Evans et al. 2017; Arenou et al. 2017).

## Data Release 2

With respect to DR1, the second data release of *Gaia* (Gaia Collaboration et al., 2018) represented a major advance in terms of completeness, performance, and richness of the data products for sources brighter than magnitude 21. Most importantly, however, it was the first data release exclusively based on *Gaia* data, therefore avoiding alignments to other catalogs as was required in DR1. DR2 provided the five-parameter astrometric solution (positions, parallaxes and proper motions) for over 1 billion stars, as outlined in the initial science case (Perryman et al., 2001). Thus, DR2 covered a substantial fraction of the volume of the Milky Way. The specific contents of DR2 were (see also Fig. 5.2.1):

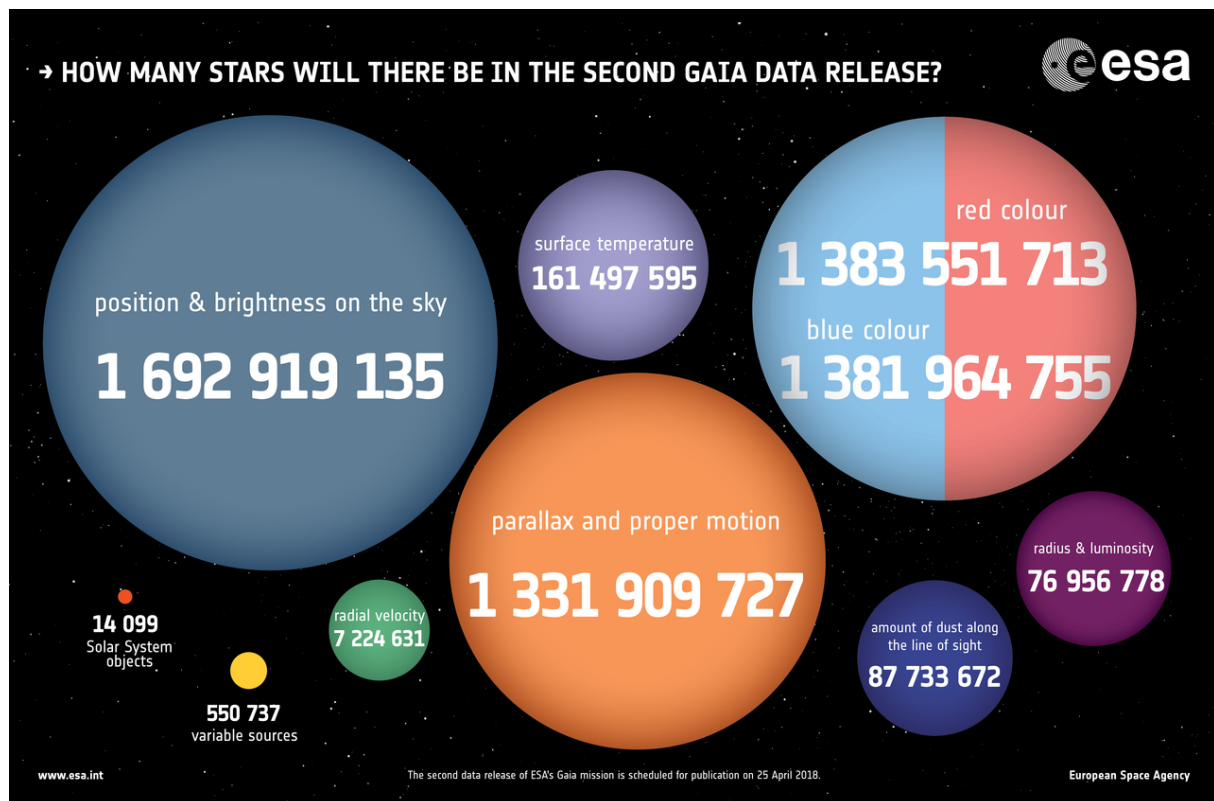


Figure 5.2.1.: Total numbers of *Gaia* DR2. Adopted from <https://www.gaia.ac.uk/data/gaia-data-release-2> (last called on 29th March 2021).

- Celestial positions and  $G$  magnitudes for approximately 1.7 billion sources
- Parallaxes and proper motions for more than 1.3 billion sources

## 5. Astrometry - Three-Dimensional Mapping of the Milky Way with Gaia

Data Product	Typical Uncertainty
Five-parameter astrometry (position & parallax)	0.02-0.04 mas at $G < 15$ mag 0.1 mas at $G = 17$ mag 0.7 mas at $G = 20$ mag 2 mas at $G = 21$ mag
Five-parameter astrometry (proper motion)	0.07 mas per year at $G < 15$ mag 0.2 mas per year at $G = 17$ mag 1.2 mas per year at $G = 20$ mag 3 mas per year at $G = 21$ mag
Two-parameter astrometry (position only)	1-4 mas
Systematic astrometric errors (averaged over the sky)	$< 0.1$ mas
Mean $G$ -band photometry	0.3 mmag at $G < 13$ mag 2 mmag at $G = 17$ mag 10 mmag at $G = 20$ mag
Mean $G_{BP}$ and $G_{RP}$ -band photometry	2 mmag at $G < 13$ mag 10 mmag at $G = 17$ mag 200 mmag at $G = 20$ mag

Table 5.1.: Basic performance statistics for *Gaia* DR2 astrometry and photometry. The astrometric uncertainties refer to epoch J2015.5 (barycentric coordinate time), whereas the photometric ones refer to the mean magnitudes listed in the main *Gaia* DR2 Catalogue. Adopted from Gaia Collaboration et al. (2018).

- $G$ -band light curves and classification of about 0.5 million variable stars
- Broad-band color information based on  $G_{BP}$  and  $G_{RP}$  magnitudes for about 1.4 billion sources
- Median radial velocities for more than seven million sources
- Astrophysical parameters, that is, effective temperatures of more than 161 million stars, extinction and reddening of more than 87 million stars as well as radii and luminosities of about 77 million stars
- Positions and epochs of about 14 100 known solar system objects (mainly asteroids) based on more than 1.5 million observations
- *Gaia*-CRF2 based on the positions and  $G$  magnitudes of more than 0.5 million extragalactic sources (quasars)

Table 5.1 lists the typical uncertainties for the astrometric and photometric results of *Gaia* DR2 (Gaia Collaboration et al., 2018). Compared to DR1, they have improved tremendously. The basic performance statistics for the other determined quantities, that is, the RV, the effective temperature, the extinction, the reddening, the radius, the luminosity, the solar system object epoch astrometry as well as the *Gaia*-CRF2 alignment with the ICRF and the *Gaia*-CRF2 rotation with respect to the ICRF are not listed here since they are not used within the framework of this thesis. However, they can be found in Gaia Collaboration et al. (2018). In order to derive model-dependent parameters such as the effective temperature, the extinction,

### 5.3. Observation Principle

---

or the reddening, *Gaia* makes use of a RV spectrometer which obtains medium-resolution spectra in a narrow band. This will be further described in Sect. 5.4.

As in the case of *Gaia* DR1, the *Gaia* collaboration informed scientists from around the globe about DR2 data. To this end, workshops<sup>53</sup> were held and numerous papers (see, for instance, Lindegren et al. 2018; Arenou et al. 2018; Luri et al. 2018; Evans et al. 2018; Riello et al. 2018; Bailer-Jones et al. 2018) were published at the time of DR2. In particular, the proper use of the measured trigonometric parallaxes was emphasized. This specific topic will be discussed in detail in Sect. 5.5 as parallax data from *Gaia* DR2 are primarily used for the present work (see also Sect. 8.4).

## 5.3. Observation Principle

The *Gaia* satellite operates in a Lissajous-type orbit around the  $L_2$  point of the Sun-Earth-Moon system, which co-rotates with the Earth in its one-year orbit around the Sun and is located  $\sim 1.5$  million km away from Earth in the anti-Sun direction.  $L_2$  not only offers a very stable thermal environment, but also a low radiation environment with a very high observing efficiency due to the fact that the Sun, the Earth, and the Moon are all behind the instrument's field of view. In addition, the orbit (size: 120 000 km  $\times$  340 000 km and 120 000 km  $\times$  180 000 km in and perpendicular to the ecliptic plane, respectively), typically lasting  $\sim 180$  days, is not affected by solar eclipses by the Earth. In this way, sky mapping without interruption is ensured (Gaia Collaboration et al., 2016b).

*Gaia*'s astrometric measurement principle was derived from the global-astrometry concept of its predecessor mission HIPPARCOS (Perryman et al., 1989). Therefore, the crossing times of targets, representing the one-dimensional, along-scan stellar positions relative to the instrument axes, are systematically and repeatedly measured in a common focal plane by means of a slowly spinning satellite with two fields of view, separated by a constant, large angle (basic angle  $\Gamma$ ) on the sky along the scanning circle (see Lindegren & Bastian 2010 for details). The observation times are converted into both large-scale angular separations between objects in the two fields of view and small-scale separations between stars inside each field of view. An Astrometric Global Iterative Solution (AGIS) process, taking the simultaneous reconstruction of the instrument's pointing (attitude) as a function of time as well as the geometrical calibration into account, generates the astrometric output catalogue (see Lindegren et al. 2012, 2016 for details). In this context, *Gaia* is self-calibrating since the parameters for the astrometric source, the attitude and the geometrical calibration are derived at the same time from the observation data alone. No additional calibration data are needed (Gaia Collaboration et al., 2016b).

Figure 5.3.1 shows the uniform revolving scanning of *Gaia*. The satellite slowly rotates at a constant angular rate of about  $60''$  per second (in-flight value:  $59.9605''$  per second), which corresponds to about  $1^\circ$  per minute such that a full circle in the sky is covered within  $\sim 6$  hours. This is a good compromise taking various different arguments such as the total mission

---

<sup>53</sup><https://gaia.ari.uni-heidelberg.de/gaia-workshop-2018/>, last called on 29th March 2021

## 5. Astrometry - Three-Dimensional Mapping of the Milky Way with Gaia

duration, the revisit frequency, the S/N ratio, or the detector characteristics into account. The spin axis is oriented perpendicular to the two fields of view, which are separated by a basic angle of  $\Gamma = 106.5 \pm 0.1^\circ$ , meaning that the same object transits the second field of view 106.5 minutes after having crossed the first one. An extremely stable basic angle and, thus, a thermally stable payload during the rotation is necessary for the global-astrometry concept to work. Therefore, *Gaia* is also equipped with a basic angle monitor, which continuously measures the basic angle with high precision during the satellite's operating phase such that periodic variations can be measured at the  $\mu\text{as}$  level. Furthermore, a constant solar-aspect

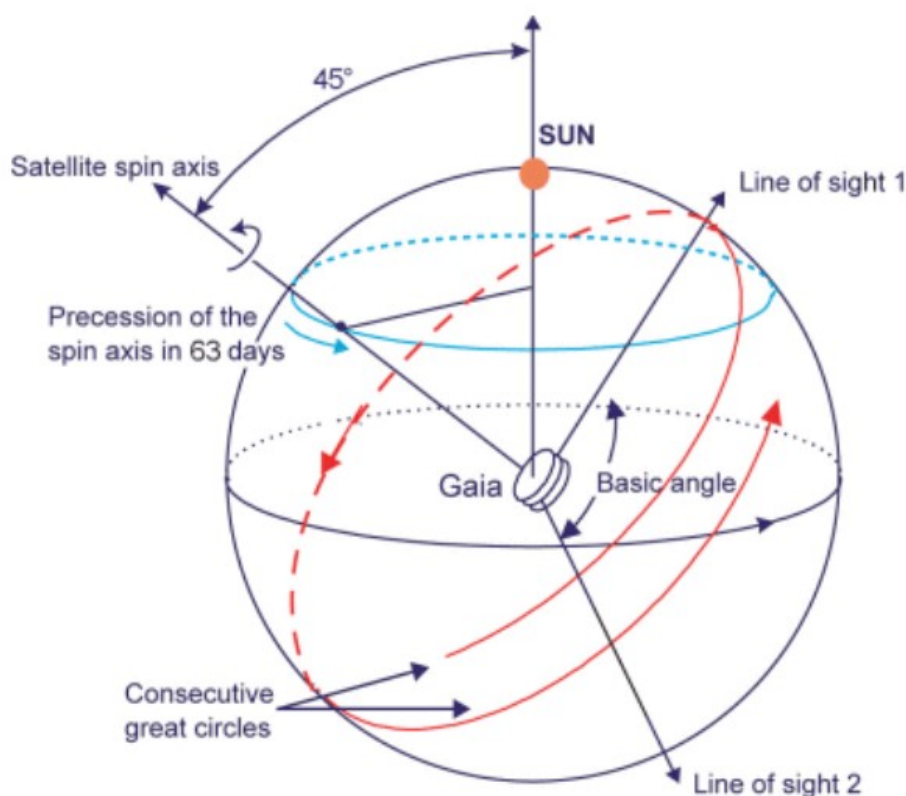


Figure 5.3.1.: The observation principle of the *Gaia* satellite. Adopted from <https://sci.esa.int/web/gaia/-/31360-orbit-navigation> (last called on 30th March 2021).

angle of  $\xi = 45^\circ$ , representing the angle between the Sun and the spin axis, is chosen for *Gaia*. This is a good compromise between implementation constraints (for instance, the solar-array efficiency or the required size of the sunshield used in order to keep the payload in permanent shadow) and astrometric-performance requirements. Moreover, the spin axis exhibits a slow precession motion with a period of  $\sim 63.12$  days, resulting in a series of overlapping loops around the Sun-to-Earth direction. In this way, at least six distinct epochs of observations per year are obtained for any celestial object on the sky.

The choice of this scanning law makes it independent of the satellite's orbital motion around  $L_2$

## 5.4. The Spacecraft

and maximizes the uniformity of the sky coverage at the same time such that the astrometric accuracy is optimized (Lindgren & Bastian, 2010). However, there is also a modified scanning law available (see Gaia Collaboration et al. 2016b for details), which is explicitly used for crowded regions (for instance, globular clusters), where the star density exceeds the storage capabilities of *Gaia* (about 750 000 objects per square degree). For instance, this modified scanning law has been used in order to increase the number of successive transits in the case of the south ecliptic-pole scanning performed during the first weeks of the nominal science operations (Gaia Collaboration et al., 2016b).

## 5.4. The Spacecraft

The *Gaia* satellite consists of three major functional modules, which are briefly described below. The description is based on Gaia Collaboration et al. (2016b), where a more detailed review is given.



Figure 5.4.1.: Schematic image of the focal plane assembly installed in the payload module of the *Gaia* satellite: broadband CCDs used for sky mapping, astrometry, and wave-front sensing (green), CCDs used for blue photometry (blue), and CCDs used for basic angle monitoring, red photometry, and RV spectrometry (red). The across and along-scan directions, the size of the installed CCDs as well as a human hand for scale indication are displayed in the bottom panel. The CCD support structure is shown in gray. Adopted from Gaia Collaboration et al. (2016b). Image from de Bruijne et al. (2010), Kohley et al. (2012), courtesy Airbus DS and Boostec Industries.

- The **payload module (PLM)** is built around an optical bench, providing structural support for the two identical on-board telescopes (preceding and following with apertures of 1.45 m x 0.50 m each) as well as the single integrated focal plane assembly (see Fig. 5.4.1). The latter is responsible for (i) metrology, that is, basic angle monitoring and wave-front sensing (monitoring of the optical performance of the telescopes, including realignment and refocusing); (ii) object detection in the sky mapper; (iii) astrometry in the astrometric field; (iv) low-resolution spectro-photometry making use of the blue and the red photometers; and (v) spectroscopy by means of the RV spectrometer, which is an integral-field spectrograph. While the astrometric instrument takes care of the five-parameter astrometric solution, measuring stellar positions, proper motions, and parallaxes, the photometric instrument primarily measures the SED of all detected objects in the full band available (3300-10 500 Å), which is composed of the blue and the red photometers, optimized for the 3300-6800 Å and 6400-10 500 Å wavelength regimes, respectively. In this way, information on the astrophysical properties of the observed objects such as the object type, the interstellar reddening, the effective temperature, or the surface gravity is ensured (see also Sect. 7.2 for further details). The RV spectrometer provides medium-resolution spectra ( $R \sim 11\,700$ ) in a narrow band (8450-8720 Å), covering the Ca II triplet at 8498 Å, 8542 Å, and 8662 Å, part of the hydrogen Paschen series, and a diffuse interstellar band, which is located at 8620 Å. Hence, accurate radial velocities for a wide range of stars, in particular for abundant red (cool) MS stars of spectral types F, G, K, and M, having effective temperatures of  $\lesssim 7500$  K and, therefore, showing Ca II in their spectra, can be measured making use of appropriate model spectra. But also information on the atmospheric parameters, the rotational velocity, or the interstellar reddening can be derived from the medium-resolution spectra. Furthermore, a coarse stellar parametrization may be possible (see, for instance, Recio-Blanco et al. 2016). Last but not least, the clock distribution unit (the spacecraft master clock) and the necessary electronics for the management of the instrument operation and the processing and storage of the science data (for instance, the video processing units and the payload data-handling unit) functionally belong to the PLM. However, all of them are physically located in the service module in order to maintain the thermal stability of the payload.
- Optimized for the stability of the basic angle, the **mechanical service module (M-SVM)** comprises all of the mechanical, structural, and thermal components, which are used to support the instrument and the electronics. The M-SVM further consists of the flat and uniform deployable sunshield assembly that prevents Sun illumination of the spacecraft, in particular of the PLM, and also includes the solar-array panels. Moreover, the propellant tanks (chemical and micro-propulsion), the electrical harness, and the payload thermal tent technically belong to the M-SVM, whereby the latter provides thermal insulation of the PLM from the external environment and protects it from micro-meteoroid impacts. For this purpose, the thermal tent only exhibits openings for the two telescope apertures and for the focal plane, warm-electronics radiator.

## 5.4. The Spacecraft

---

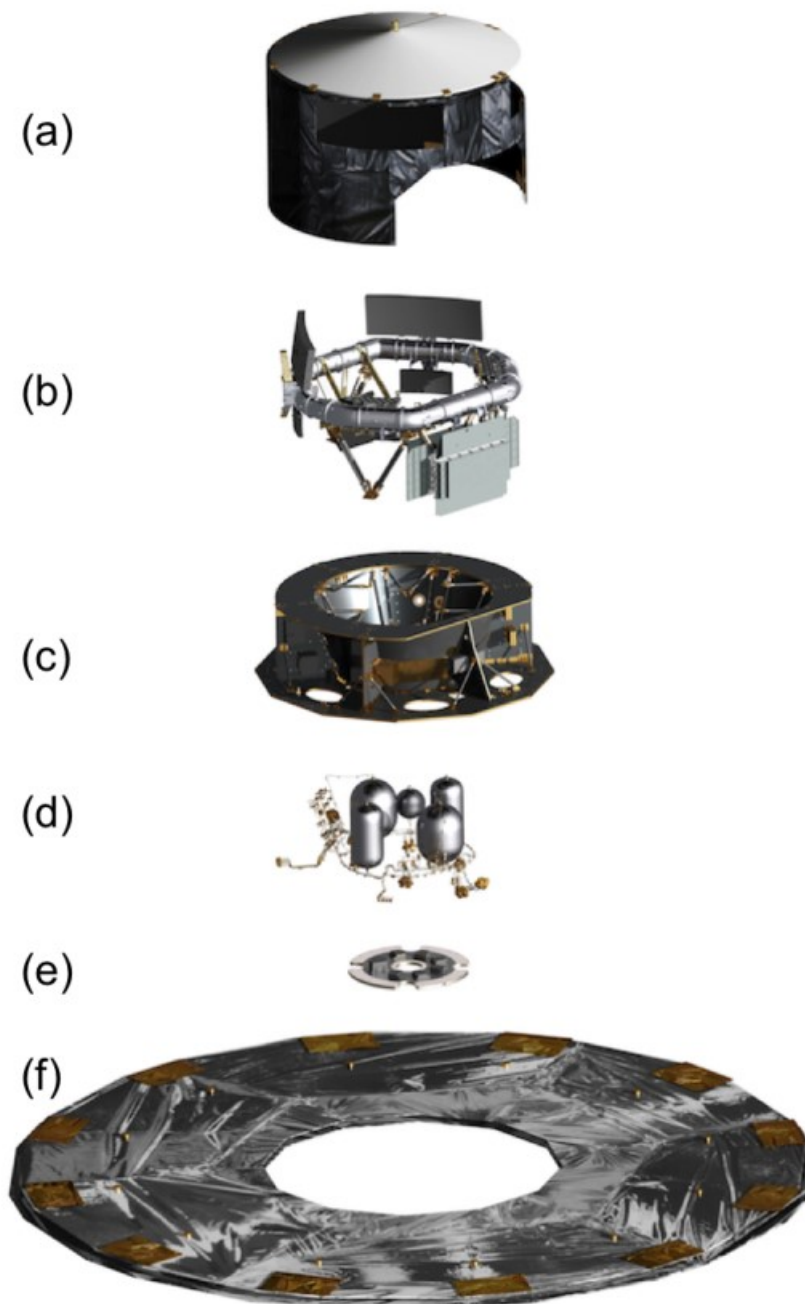


Figure 5.4.2.: Exploded, schematic view of the *Gaia* satellite. (a) Payload thermal tent; (b) payload module with optical bench, telescopes, instruments (astrometric, photometric, and spectroscopic), and focal plane assembly; (c) structure of the service module, also housing parts of the payload module (clock distribution unit, video processing units, and payload data-handling unit); (d) propellant systems; (e) phased-array antenna; and (f) deployable sunshield assembly with solar arrays. Adopted from Gaia Collaboration et al. (2016b). Credit: ESA, ATG Medialab.

- The **electrical service module (E-SVM)** supports *Gaia* in terms of the central computer, the data management, the electrical power control and distribution, the attitude (pointing) and orbit control, and the communication with Earth. The latter mainly is achieved by a special high-gain phased-array antenna, which is able to transmit the science data to Earth while the spacecraft is rotating and orbiting.

Figure 5.4.2 shows an exploded, schematic view of the *Gaia* satellite, displaying the aforementioned modules together with their main individual constituents. The whole setup is arranged in a sandwich panel such that the main structure of the spacecraft is of hexagonal conical shape.

### 5.5. Using Gaia DR2 Parallaxes

This work primarily makes use of absolute trigonometric parallaxes measured within *Gaia* DR2. Therefore, it is important to know the intricacies, pitfalls, and problems coming along with them. This section provides a summary of the most important properties of *Gaia* DR2 parallaxes and is based on the recommendations of Luri et al. (2018), Arenou et al. (2018) and Lindegren et al. (2018).

It has to be pointed out that *Gaia* DR2 data cover only 22 months of continuous measurements, which corresponds to not even two orbits of the Earth around the Sun. Hence, there is little redundancy and binary discrimination is difficult or impossible since a proper separation of the annual trigonometric parallax and proper motion cannot be achieved in these cases. A brief introduction to *Gaia*'s five-parameter astrometric solution will be given in Sect. 5.5.2. First, the systematic effects of parallax measurements in DR2 shall be recapped.

#### 5.5.1. Systematic Effects

Although the aforementioned design of the spacecraft and the implementation of the data processing software and algorithms are chosen to prevent biases and systematic effects in the astrometric data, systematic errors at low levels nevertheless exist in *Gaia* DR2. Most of these systematics are almost impossible to deal with because they are complicated and largely unknown functions of positions on the sky, magnitude, and color.

- **Zero point offset:** As *Gaia* is able to measure absolute parallaxes without zero-point error, small variations of the basic angle show up as small offsets in the parallaxes (Butkevich et al. 2017; Lindegren et al. 2018). Thus, an investigation of the parallax zero point is important. For instance, such an investigation can make use of astrophysical sources with known parallaxes such as quasi-stellar objects/quasars. Quasars are almost ideal for this purpose since they are most often point-like sources with extremely small parallaxes ( $< 0.0025 \mu\text{as}$  for redshifts of  $z > 0.1$ ), which are available in large numbers over most of the celestial sphere. Therefore, their parallax distribution should peak at zero. Lindegren et al. (2018) cross-matched the final *Gaia* DR2 data with the ALLWISE

## 5.5. Using Gaia DR2 Parallaxes

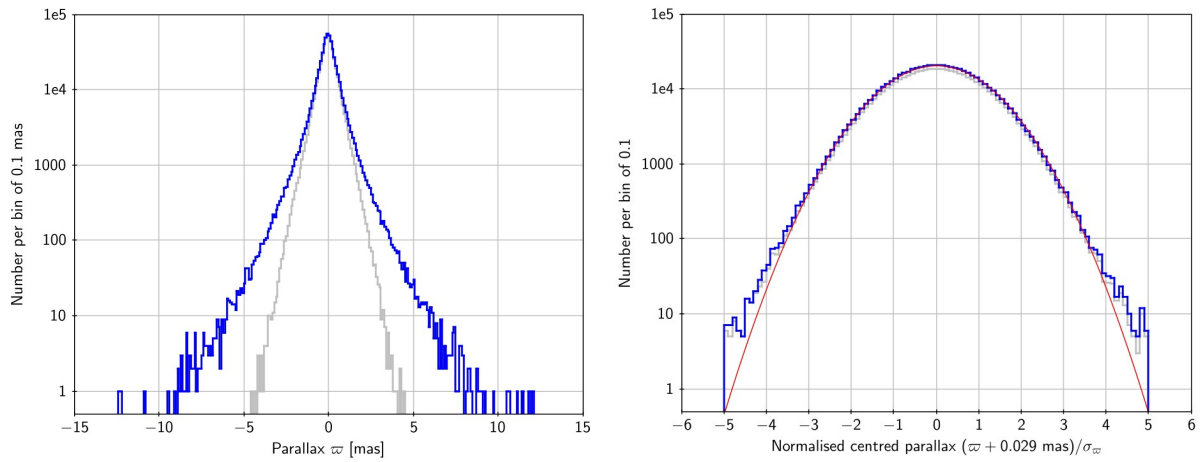


Figure 5.5.1.: *Left-hand panel*: Parallax distribution for 556 869 sources identified as quasars within *Gaia* DR2. While the full sample is represented by the blue curve, the gray curve shows the high-precision subset of 492 928 sources with statistical uncertainties of  $\Delta\varpi < 1$  mas. *Right-hand panel*: Distributions of the normalized centred parallaxes  $(\varpi + 0.029 \text{ mas})/\Delta\varpi$  for the same samples as in the left-hand panel. In addition, a normal distribution with the same standard deviation of  $\sigma = 1.081$  as determined for the normalized centred parallaxes of the full sample (blue curve) is shown in red. For details on the source selection criteria used, see Equation 14 in Lindegren et al. (2018). Adopted from Lindegren et al. (2018).

catalog of active galactic nuclei from Secret et al. (2015) in order to create the largest possible quasar sample for validation purposes of the zero point offset. The left-hand panel of Fig. 5.5.1 shows the parallax distributions for the full quasar sample of 556 869 sources and the high-precision subset of 492 928 sources with statistical uncertainties of  $\Delta\varpi < 1$  mas. While the full sample has mean and median parallaxes of  $-0.0308$  mas and  $-0.0287$  mas, respectively, the corresponding values for the high-precision subset are  $-0.0288$  mas and  $-0.0283$  mas. Hence, Lindegren et al. (2018) estimated the global mean parallax zero point offset to be  $-0.029$  mas. This means that *Gaia* DR2 parallaxes are too small and that this offset has to be added to the measured parallaxes. Furthermore, Lindegren et al. (2018) derived systematic trends with a change of  $\sim 0.02$  mas over the  $G$  magnitude and the color ranges covered by the quasar data, whereas the offset dependency on the ecliptic latitude showed a roughly quadratic variation resulting in around  $-0.010$  mas smaller *Gaia* parallaxes at the ecliptic poles. In consequence, the actual offset, which is applicable for a given combination of magnitude, color, and position, may differ by several  $\mu\text{as}$  with respect to the statistically well-determined global mean offset of  $-0.029$  mas. The right-hand panel of Fig. 5.5.1 shows the distributions of the quasar parallax samples corrected for the global mean offset. In addition, the values on the abscissa are normalized by the individual statistical uncertainties  $\Delta\varpi$  ( $\sigma_{\varpi}$ ). Ideally, this should follow a Gaussian distribution with a mean value of zero and a standard deviation of unity. However, the actual standard deviation for the full quasar

sample is  $\sigma = 1.081$ .

In order to correct for the zero point offset and to infer distances from the measured parallaxes, it is tempting to apply  $d = 1/(\varpi + 0.029 \text{ mas})$  to the DR2 Archive data. However, the actual value of the zero point offset is controversial and still under debate, which will hopefully be solved within the complete *Gaia* DR3. For instance, Graczyk et al. (2019) reported an offset value of  $-0.031 \pm 0.011 \text{ mas}$ , which is fully consistent with the one derived by Lindegren et al. (2018). Yet, numerous investigations by other authors showed larger zero point offsets:  $-0.046 \pm 0.013 \text{ mas}$  (Riess et al., 2018),  $-0.052 \pm 0.002 \text{ mas}$  (Leung & Bovy, 2019),  $-0.053 \pm 0.003 \text{ mas}$  (Zinn et al., 2019),  $-0.054 \pm 0.006 \text{ mas}$  (Schönrich et al., 2019),  $-0.075 \pm 0.029 \text{ mas}$  (Xu et al., 2019), and  $-0.082 \pm 0.033 \text{ mas}$  (Stassun & Torres, 2018). Arenou et al. (2018) derived  $-0.067 \pm 0.012 \text{ mas}$  and  $-0.064 \pm 0.017 \text{ mas}$ , respectively, depending on the reference star cluster catalog used. This wide range of possible offsets mainly results from different types of astrophysical objects investigated, exhibiting different colors and magnitudes that are used to compute the zero point estimates. Second, the parallax zero point offset is also a function of the coordinates because it depends on *Gaia's* scanning pattern (Arenou et al., 2018). For these reasons, DPAC forewent to correct for the zero point offset in DR2 data. Since there is no simple recipe which accounts for the systematic errors due to the zero point, the general recommendation of the *Gaia* collaboration is to keep the systematics in mind when interpreting *Gaia* DR2 data and to use the statistical uncertainties reported in DR2. Nevertheless, the systematic effects should be somehow modelled during the analysis. However, this is not possible for all science cases, especially not in the case of single target analyses as performed in the present work. Consequently, this work completely avoids the correction of the zero point (see Sect. 8.4 for further information).

- **Spatial variations:** Lindegren et al. (2018) also searched for spatial variations of the parallax zero point, which could also be derived from the quasar samples. The left-hand panel of Fig. 5.5.2 shows a map of the median parallaxes for the full quasar sample, calculated in cells of about  $3.7 \times 3.7 \text{ deg}^2$  and adjusted for a global zero point offset of  $-0.029 \text{ mas}$ . As can be seen from the yellow and turquoise areas, the parallaxes are on average systematically offset from the global mean in most regions (by  $\sim \pm 0.05 \text{ mas}$ ). These large-scale variations are due to the presence of correlated errors on spatial scales of about 10-20 deg and root-mean-square (RMS) values of a few tens of  $\mu\text{as}$ . In fact, Lindegren et al. (2018) were able to estimate a characteristic spatial scale of about 14 deg and an RMS amplitude of  $\sim 17 \mu\text{as}$  by calculating the covariance of the parallax errors in the high-precision quasar sample as a function of the angular separation and a subsequent exponential fit to the received values.

Moreover, variations on much smaller scales were found by means of distant stars in dense regions such as the Large Magellanic Cloud (LMC). This is displayed in the right-hand panel of Fig. 5.5.2, where a map of median parallaxes for about 2.5 million sources in the area of the LMC, calculated in cells of about  $0.057 \times 0.057 \text{ deg}^2$ , is shown. The mean and median values are  $-0.014 \text{ mas}$ , but the left part of the circular area, exhibiting a straight and rather sharp boundary, is offset by  $\sim 0.02 \text{ mas}$  from the rest. The observed

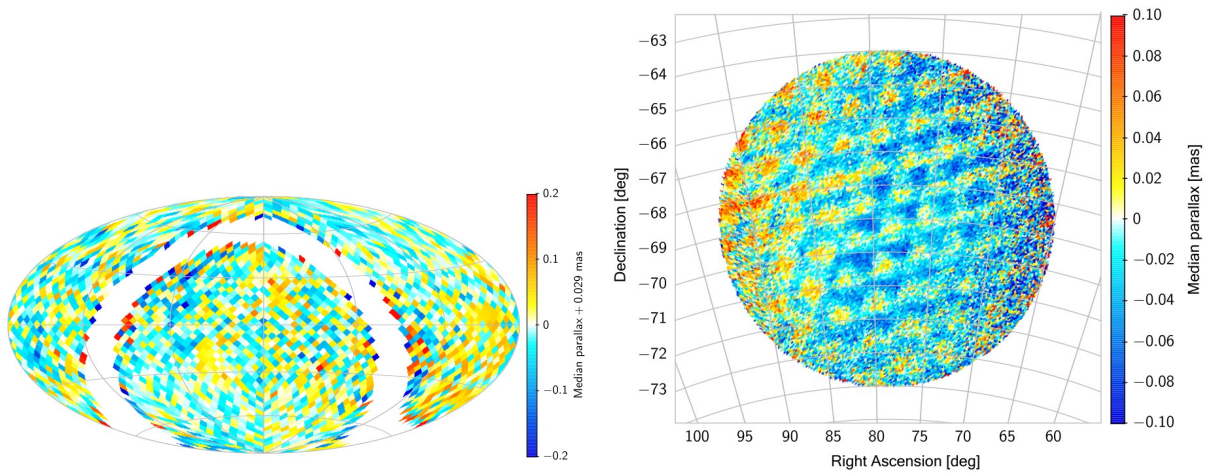


Figure 5.5.2.: *Left-hand panel*: Map of the median parallaxes for the full quasar sample of Fig. 5.5.1 ( $\alpha$  and  $\delta$  are zero at the centre, north is up, and  $\alpha$  increases from right to left). Median values are calculated in cells of about  $3.7 \times 3.7 \text{ deg}^2$  and only cells with  $|\sin b| > 0.2$  are plotted ( $b$  represents the Galactic latitude). Large-scale variations of the parallax zero point are clearly visible (see the text for details). *Right-hand panel*: Map of the median parallaxes for a sample of about 2.5 million sources in the area of the Large Magellanic Cloud. Median values are calculated in cells of about  $0.057 \times 0.057 \text{ deg}^2$ . Small-scale variations are clearly visible (see the text for details). Adopted from Lindegren et al. (2018).

quasi-regular triangular pattern has a typical amplitude of  $\sim 0.03 \text{ mas}$  and a period of  $\sim 1 \text{ deg}$ . Both patterns are related to *Gaia*'s scanning law and its slow precession motion. This is a clear evidence for strong correlated errors or systematic effects on small spatial scales, that is, also below  $1 \text{ deg}$ . Within the high-precision quasar sample, Lindegren et al. (2018) even proved small-scale variations with an RMS amplitude of  $43 \mu\text{as}$  for angular separations below  $0.125 \text{ deg}$ .

As in the case of the global zero point offset, it is almost impossible to handle these large- and small-scale variations when it comes to the analysis of single targets in the field. In consequence, this work does not take any spatial variations into account. This is not least because of the fact that most of the program stars are close enough such that the zero point offset and the spatial variations make up only a few percent of the individual total parallax uncertainties (see Sect. 8.4 for further information).

### 5.5.2. Negative Parallaxes

As already seen in Fig. 5.5.1 and 5.5.2, *Gaia* observes parallaxes of zero or even negative ones for a non-negligible amount of sources on the sky. In order to understand these occurrences, the model of the source motion on the sky describing the time-dependent coordinate direction from the observer (*Gaia*) towards an object outside the solar system needs to be explained.

This model predicts a helix or wave-like pattern for the apparent motion of a given source. According to Luri et al. (2018) and based on Lindegren et al. (2012, 2016), the pattern is described by the unit vector:

$$\mathbf{u}(t) = \langle \mathbf{r} + (t_B - t_{\text{ep}})(\mathbf{p}\mu_{\alpha^*} + \mathbf{q}\mu_{\delta} + \mathbf{r}\mu_r) - \varpi \mathbf{b}_O(t)/A_u \rangle, \quad (5.1)$$

where  $t$  is the time of observation,  $t_{\text{ep}}$  is a reference time referring to epoch J2015.5, and  $t_B$  is the time of observation corrected for the Rømer delay<sup>54</sup> (all three times are given in units of

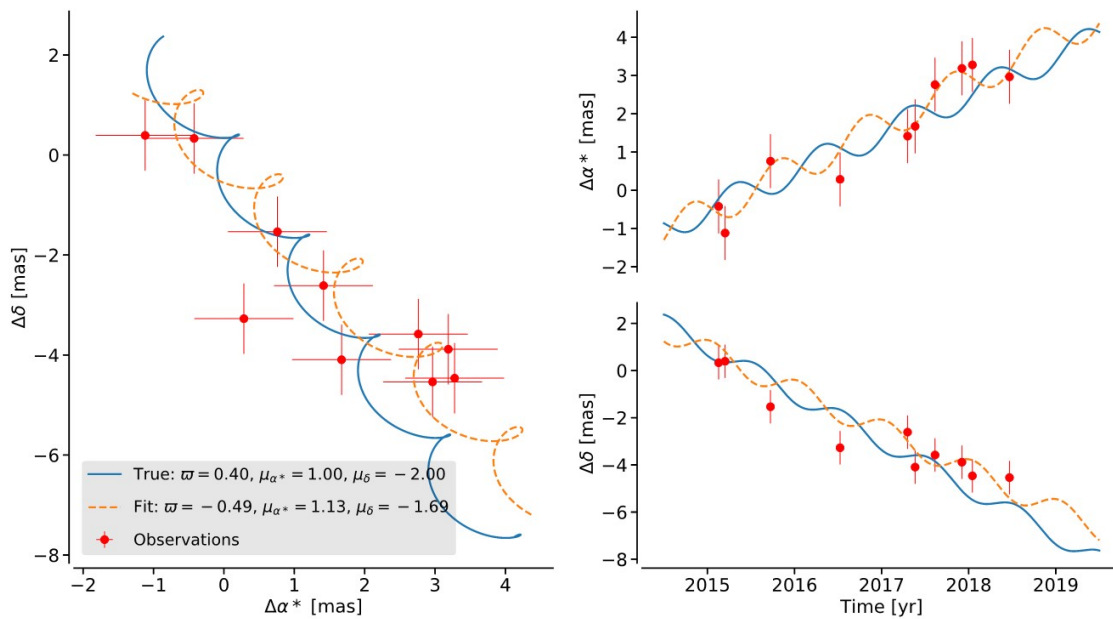


Figure 5.5.3.: Example of a negative parallax arising from the processing of the astrometric *Gaia* DR2 data. While solid blue lines represent the true paths of the object, the individual measurements of the source position on the sky are shown as red dots (error bars indicate uncertainties of 0.7 mas). The source paths resulting from the least-squares astrometric solution of Eq. (5.1) are shown as dashed orange lines. *Left-hand panel*: Path on the sky (declination  $\Delta\delta$  vs. right ascension  $\Delta\alpha^*$ ) showing the effects of the proper motion (linear trend) and the parallax (loops). *Right-hand panel*: Right ascension (top) and declination (bottom) of the source as a function of time. In this case, the negative parallax effect can be understood as a yearly motion of the object in the opposite direction of the true parallactic motion, resulting in a phase shift of  $180^\circ$  ( $\pi$ ) in the respective sinusoidal curves. The uncertainties on  $\Delta\alpha^*$  and  $\Delta\delta$  are assumed to be uncorrelated for this example case. Adopted from Luri et al. (2018).

<sup>54</sup>As the second Lagrange point  $L_2$  co-rotates with the Earth around the Sun, the distance between the *Gaia* satellite and any celestial object varies over the year. The classical Rømer delay is defined as the light travel time across the Earth's orbit around the Sun. However, the term can also be used to describe the light travel time across the orbit of a spacecraft around the Sun.

## 5.5. Using Gaia DR2 Parallaxes

---

the barycentric coordinate time<sup>55</sup>);  $\mathbf{p}$ ,  $\mathbf{q}$ , and  $\mathbf{r}$  are unit vectors which point in the direction of increasing right ascension, increasing declination, and towards the position  $(\alpha, \delta)$  of the source, respectively;  $\mathbf{b}_O(t)$  is the barycentric position of the observer (*Gaia*) at the time of the observation;  $A_u$  is the astronomical unit; and  $\langle \mathbf{a} \rangle$  denotes vector normalization, which is defined for a given vector  $\mathbf{a}$  as  $\langle \mathbf{a} \rangle := \mathbf{a}|\mathbf{a}|^{-1}$ .  $\mu_{\alpha*} := \mu_\alpha \cos \delta$  and  $\mu_\delta$  are the components of the proper motion along the directions of  $\mathbf{p}$  and  $\mathbf{q}$ ,  $\varpi$  is the parallax, and  $\mu_r := v_r \varpi / A_u$  describes the ‘radial proper motion’ that accounts for distance changes to the object resulting from its radial motion, which, in turn, also affects the parallax and the proper motion. In most cases, however,  $\mu_r$  is usually negligibly small such that it is ignored in the following.

Figure 5.5.3 shows a fit of Eq. (5.1) to observations with large measurement noise, which is comparable to the size of the estimated parallax. In this case, the derived parallax is negative. This is due to the fact that the parallax appears as the factor of  $-\varpi$  in front of the barycentric position of the observer in Eq. (5.1). In this way, the parallactic motion of the individual source on the sky “will have a sense which reflects the sense of the motion of the observer around the Sun” (Luri et al., 2018) such that parallaxes of zero or even negative ones are measured for noisy observations. In fact, a negative parallax therefore may be a consistent measurement, but the source is going “the wrong way around on the sky” (Luri et al., 2018) because of the movement of the observer along the baseline (see the right-hand panels of Fig. 5.5.3). On the other hand, however, a negative parallax may also be an indicator that the object is located at a large but highly uncertain distance.

### 5.5.3. The Distance Inference Problem

As will be described in Ch. 7, the *Gaia* DR2 parallaxes measured for the program stars presented in Ch. 8 will be used to infer distances and, from that, further astrophysical quantities like the stellar radius, the luminosity, and the stellar mass. However, inferring these astrophysical parameters from parallaxes is a task which is less trivial than it seems because the usual and naive inversion of the parallax  $\varpi$  to derive a reliable distance  $\rho$  ( $\rho = 1/\varpi$ ) is limited to precise parallaxes only. For instance, the simple inversion is impossible in cases where the observed parallax is negative. Moreover, when working with large samples of objects for which the relative statistical uncertainties on the observed parallaxes (apparent or observed fractional parallax uncertainties)  $\Delta\varpi/\varpi$  are large, a proper statistical treatment of the parallaxes is necessary in order to derive correct distances. As will be shown in the following, large statistical parallax errors can lead to strong biases.

Given an object with true distance  $d$ , its true but unknown parallax is defined as  $\varpi_{\text{True}} = 1/d$ . The measured parallax  $\varpi$ , however, is a noisy (statistical) measurement of  $1/d$ . In the following,  $\varpi$  is assumed to be free of any systematic measurement errors. Further assuming

---

<sup>55</sup>The barycentric coordinate time is a coordinate time standard that is used as the independent variable of time for all calculations pertaining to orbits of planets, asteroids, comets, and interplanetary spacecraft in the Solar system. As a matter of fact, it is equivalent to the proper time measured by a clock at rest in a coordinate frame which co-moves with the barycentre (centre of mass) of the Solar system. Such a clock performs exactly the same movements as the Solar system but is located outside the system’s gravity well. Hence, it is not influenced by the gravitational time dilation caused by the Sun and the rest of the system.

that  $\varpi$  follows a Gaussian distribution with unknown mean  $1/d$  but known standard deviation  $\sigma_\varpi := \Delta\varpi$  and full width at half maximum (FWHM) of  $2\sigma_\varpi\sqrt{2\ln 2} \approx 2.35\sigma_\varpi$ , the measurement model or likelihood that provides the probability density function of  $\varpi$  for a given  $d$  and  $\sigma_\varpi$  thus is described by (Bailer-Jones, 2015):

$$P(\varpi|d, \sigma_\varpi) = \frac{1}{\sqrt{2\pi}\sigma_\varpi} \exp\left[-\frac{1}{2\sigma_\varpi^2} \left(\varpi - \frac{1}{d}\right)^2\right], \quad (5.2)$$

where  $\sigma_\varpi \geq 0$ . In the case of *Gaia*, providing  $\varpi$  and  $\sigma_\varpi$  as measured quantities,  $d$  needs to be inferred. For positive values of  $\varpi$ , it is tempting to do that via simple inversion, defining the distance estimate  $\rho$  as  $\rho = 1/\varpi$ . However, the statistical properties of  $\rho$  need to be understood beforehand.

It has to be highlighted that the inversion to distance  $\rho$  typically leads to a skewed unimodal

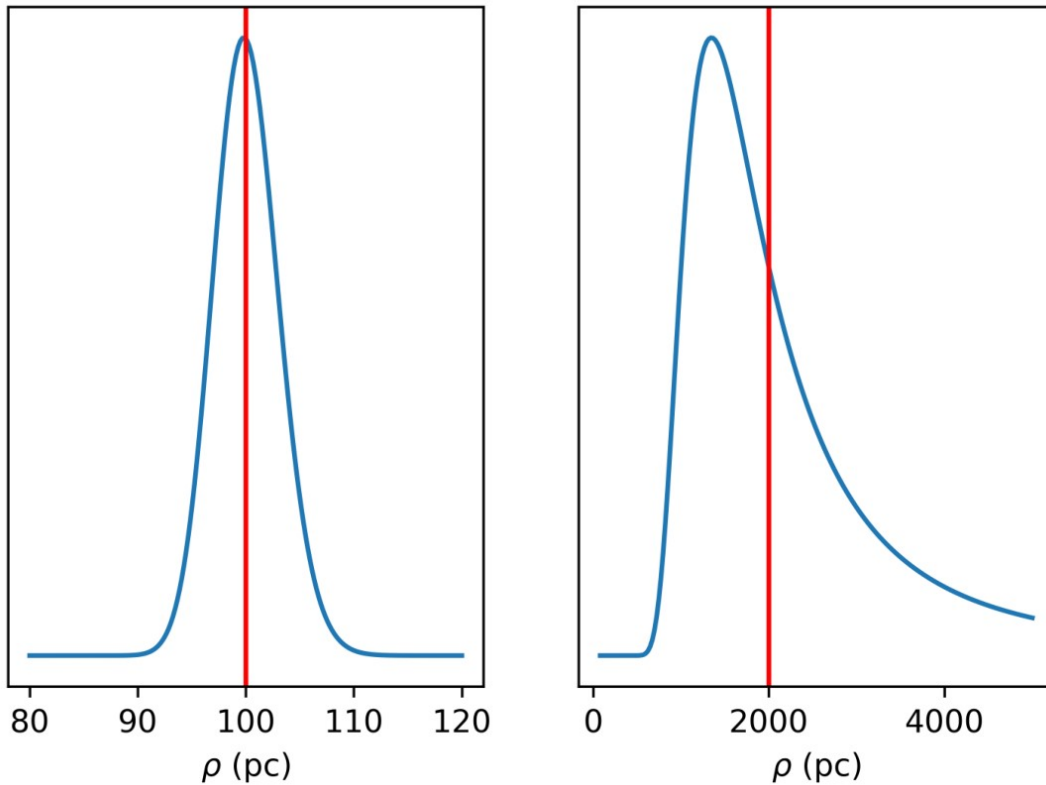


Figure 5.5.4.: Probability distribution function of the distance estimate  $\rho = 1/\varpi$  for two extreme cases (solid blue lines). The respective positions of the true distance  $d$  are marked by the red vertical lines. *Left-hand panel*: Object at  $d = 100$  pc with an uncertainty on the observed parallax of  $\sigma_\varpi = 0.3$  mas. The true fractional parallax uncertainty therefore is very small:  $\sigma_\varpi/\varpi_{\text{True}} = 0.03$ . *Right-hand panel*: Object at  $d = 2000$  pc with an uncertainty on the observed parallax of  $\sigma_\varpi = 0.3$  mas. The true fractional parallax uncertainty therefore is very large:  $\sigma_\varpi/\varpi_{\text{True}} = 0.6$ . Adopted from Luri et al. (2018).

## 5.5. Using Gaia DR2 Parallaxes

distribution. The larger the relative FWHM of the individual parallax distribution described by Eq. (5.2), the larger the skewness of the respective distance distribution (see Fig. 5.5.4). The probability density function of  $\rho$  for a given true distance  $d$  and a measured uncertainty  $\sigma_\varpi$  on  $\varpi$  can be obtained from Eq. (5.2) as (Luri et al., 2018):

$$P(\rho|d, \sigma_\varpi) = P(\varpi = 1/\rho | d, \sigma_\varpi) \cdot \left| \frac{d\varpi}{d\rho} \right| = \frac{1}{\sqrt{2\pi}\sigma_\varpi\rho^2} \exp \left[ -\frac{1}{2\sigma_\varpi^2} \left( \frac{1}{\rho} - \frac{1}{d} \right)^2 \right]. \quad (5.3)$$

Equation (5.3) describes what can be expected when  $\rho$  is used as an estimate of the true distance  $d$ . Figure 5.5.4 shows the distribution of  $P(\rho|d, \sigma_\varpi)$  for two extreme cases of very low (left-hand panel) and very high (right-hand panel) true fractional parallax uncertainty, which is defined as  $\sigma_\varpi/\varpi_{\text{True}} = d\sigma_\varpi$ . The left-hand distribution is Gaussian, hence looking

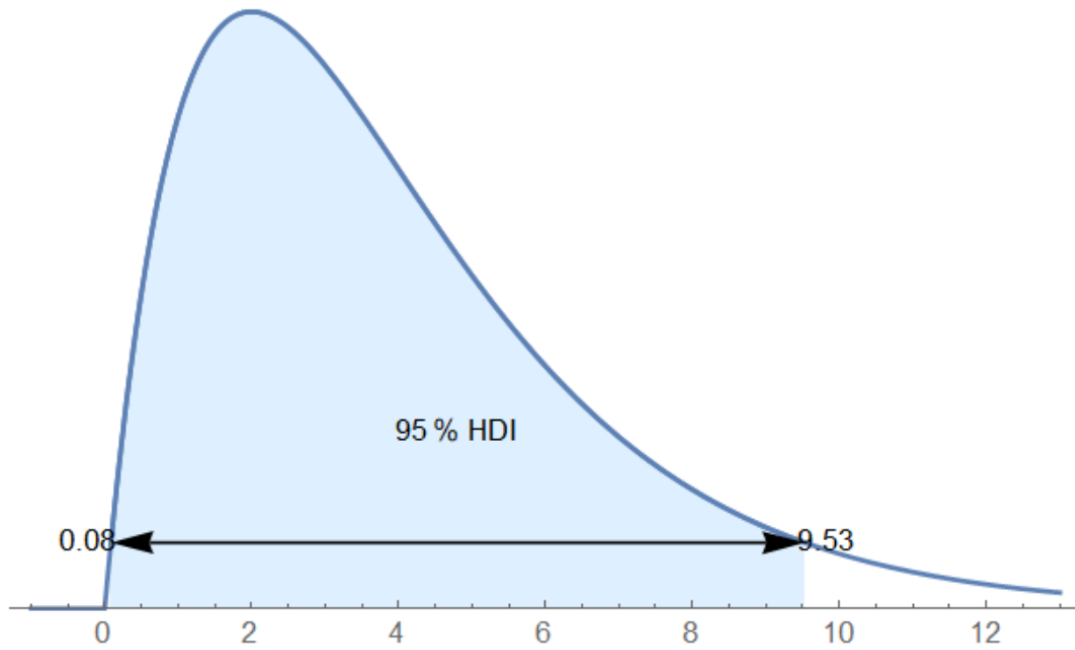


Figure 5.5.5.: Example of a  $p = 95\%$  highest-density interval (HDI) for an arbitrary asymmetric exponential distribution. The horizontal arrow marks the corresponding quantiles. Adopted from <https://mathematica.stackexchange.com/questions/173282/computing-credible-region-highest-posterior-density-from-empirical-distributio> (last called on 5th April 2021).

unbiased and symmetrical such that the mode (the most probable value) coincides with the true distance value  $d$ . This is a good example, in which  $\rho = 1/\varpi$  as a distance estimate is relatively safe and leads to reliable results. However, for a high true fractional parallax uncertainty the distribution shows a non-Gaussianity, leading to strong asymmetry/skewness

and a long tail towards large values of  $\rho$ <sup>56</sup>. Furthermore, in this case the mode is not at the position of  $d$  (see the right-hand panel of Fig. 5.5.4) such that the expected value of  $\rho$  also differs from  $d$ , indicating a strong bias. Therefore, the distance estimate  $\rho$  becomes unusable in cases of high true fractional parallax uncertainties  $\sigma_{\varpi}/\varpi_{\text{True}}$  and, likewise, for high apparent fractional parallax uncertainties  $\sigma_{\varpi}/\varpi$ .

Due to the skewness of the distribution displayed in the right-hand panel of Fig. 5.5.4, neither the mean, nor the median, nor the FWHM are meaningful quantities in the case of large relative uncertainties, although all of them are well defined for  $P(\rho|d, \sigma_{\varpi})$ . As shown by Bailer-Jones et al. (2018), the proper quantities characterizing the unimodal distribution  $P(\rho|d, \sigma_{\varpi})$  and, hence, providing a reasonable point estimate  $\rho_{\text{est}}$  along with some measure of the uncertainty are the mode and the highest-density interval (HDI) with certain probability  $p$  (typically  $p = 0.6827$  is used, which is equal to the probability contained within  $\pm 1\sigma$  of the mode for a usual Gaussian distribution). The HDI is defined as the span of the distance between the lower and the upper bounds,  $\rho_{\text{lo}}$  and  $\rho_{\text{hi}}$ , which enclose the region of highest probability density such that the value of the corresponding definite integral over  $P(\rho|d, \sigma_{\varpi})$  equals  $p$ . Therefore, the HDI is always unique in the case of a unimodal distribution and always contains the mode  $\rho_{\text{est}}$ . This is also extremely convenient for an asymmetric distribution, for which  $\rho_{\text{hi}} - \rho_{\text{est}}$  and  $\rho_{\text{est}} - \rho_{\text{lo}}$  are unequal. Conceptually, the HDI can be found “by lowering a horizontal line over the distribution until the area contained under the curve between [the line’s] intercepts with the curve ( $\rho_{\text{lo}}$  and  $\rho_{\text{hi}}$ ) is equal to  $p$ ” (Bailer-Jones et al. 2018; see Bailer-Jones 2017 for further information). Figure 5.5.5 shows an example of a  $p = 95\%$  HDI for an arbitrary asymmetric exponential distribution.

The main message of this section thus is that observed parallaxes should generally not be treated as direct distance measurements to given sources. It is important to take the uncertainty of the individual parallax measurement into account before the distance (and other astrophysical quantities relying on it) can be estimated from the observation. For this reason, Luri et al. (2018) mainly recommended to always handle the derivation of astrophysical quantities from parallaxes with proper statistical, that is, Bayesian methods, for which prior assumptions have to be made. This shall be briefly discussed in the following section.

### 5.5.4. Bayesian Methods

As discussed in the previous section, it should not be tried to directly infer the true distance  $d$  as  $1/\varpi \pm \sigma_{\varpi}/\varpi^2$  from the observed parallax  $\varpi$  because of the noise  $\sigma_{\varpi}$  involved. A possible solution to this distance inference problem is the definition of a posterior probability distribution

---

<sup>56</sup>In principle, a noticeable negative tail to the distribution displayed in the right-hand panel of Fig. 5.5.4 could also be added for more extreme values of the true fractional parallax uncertainty. This would then correspond to the negative tail of the parallax distribution observed in these cases, which results from Eq. (5.2).

## 5.5. Using Gaia DR2 Parallaxes

---

$P(d|\varpi, \sigma_\varpi)$  over the possible values of  $d$ . Making use of the Bayes theorem,  $P(d|\varpi, \sigma_\varpi)$  is related to the likelihood of Eq. (5.2) by:

$$P(d|\varpi, \sigma_\varpi) = \frac{1}{Z} P(\varpi|d, \sigma_\varpi) P(d). \quad (5.4)$$

Here,  $Z$  is the normalization constant, which is defined as:

$$Z = \int_{d'=0}^{d'=\infty} P(\varpi|d', \sigma_\varpi) P(d') dd'. \quad (5.5)$$

$P(d)$  is the prior, expressing the knowledge of (or assumptions about) the distance independently of the measured parallax  $\varpi$ . By making use of a prior, an expression (the likelihood  $P(\varpi|d, \sigma_\varpi)$ ) for the probability of the known data (parallax  $\varpi$ ) given the unknown parameter (distance  $d$ ) can hence be transformed into an expression (the posterior  $P(d|\varpi, \sigma_\varpi)$ ) for the probability of the parameter given the data (Bailer-Jones, 2015).  $P(d|\varpi, \sigma_\varpi)$  typically follows a unimodal and asymmetric distribution, for which the mode and the HDI are suitable parameters, as discussed in the previous section. In the rare case of a bimodal posterior probability distribution (see, for instance, the examples shown in Bailer-Jones 2015), a different treatment may be necessary, meaning that the median of the distribution is used as the distance estimator  $d_{\text{est}}$  and the 16th and 84th percentiles (that is,  $(1 \pm p)/2$ ) are reported as  $d_{\text{lo}}$  and  $d_{\text{hi}}$ , respectively. Thus, the latter form an equal-tailed interval that has as much probability below the span (given by  $d_{\text{lo}}$  and  $d_{\text{hi}}$ ) as above, with the probability  $p$  in between (see Bailer-Jones et al. 2018 for details).

Bailer-Jones (2015) investigated the consequences of using different types of priors and found that an isotropic prior converging asymptotically to zero as the distance goes to infinity is best suited. According to the author, the best choice is the minimalist, isotropic exponentially decreasing space density prior:

$$P(d) = \begin{cases} \frac{1}{2L^3} d^2 e^{-d/L} & \text{if } d > 0 \\ 0 & \text{otherwise} \end{cases} \quad (5.6)$$

with a fixed length scale  $L$ , which has to be chosen appropriately. For distances  $d \ll L$ , this prior corresponds to a constant space density of stars and the probability drops exponentially at distances much larger than the single mode, which lies at  $2L$ .

The isotropic exponentially decreasing space density prior of Eq. (5.6) was successfully used on simulated *Gaia*-like catalog data (Astraatmadja & Bailer-Jones, 2016a) and real DR1 data (Astraatmadja & Bailer-Jones, 2016b) with a fixed length scale of  $L = 1.35$  kpc. However, a prior given by the distribution of stars along each line of sight as determined from a Milky Way model and also accounting for interstellar extinction and *Gaia*'s selection function was additionally considered. In fact, the differences between both priors were found to be significant for objects beyond 2 kpc, where the ‘‘Milky Way prior’’ performed much worse because it assumed that stars are more likely to be closer in the disk than further away. For distances

closer than 2 kpc, the “Milky Way prior” only lead to slightly better results, making it not worth the effort.

Bailer-Jones et al. (2018) applied a slightly modified version of the exponentially decreasing space density prior to DR2 data. The modifications included a smooth variation of  $L$  as a function of longitude and latitude according to an appropriate model in order to reflect the expected variation in the distribution of stellar distances in the *Gaia*-observed Milky Way. This is a good compromise between the complexity of the line-of-sight-dependent distribution shapes obtained from the sophisticated Milky Way model and the simplicity of the isotropic prior with fixed length scale  $L$ . Furthermore, Bailer-Jones et al. (2018) implemented the global parallax zero point offset of 0.029 mas determined by Lindegren et al. (2018). In this way, the authors were able to successfully infer distances to 1.33 billion stellar objects based on Bayesian statistical methods.

The non-linearity of the usual relation  $d = 1/\varpi$  and the asymmetry of the resulting probability distribution in the case of high apparent fractional parallax uncertainties can therefore be bypassed, if Bayesian methods with an adequate prior are used. However, as different types of stellar objects usually need individually defined distance priors with suitable length scales  $L$  and not a general one that is used for the whole Milky Way, Bayesian methods also have disadvantages. In the case of nearby and/or bright objects with positive parallaxes and apparent fractional parallax uncertainties below  $\sim 20\%$ , working with astrophysical variables rather than sticking to the data space typically is allowed because the uncertainties of the derived quantities such as the distance are relatively small (Luri et al., 2018). Within the framework of this thesis, it is therefore possible to use the classical approach  $d = 1/\varpi$  and to ignore the Bayesian method in order to infer distances because of the excellent astrometric data available for most of the program stars (see Sect. 8.4). Nevertheless, a comparison of the classical *Gaia* distances to the distances inferred from Bayesian statistics according to Bailer-Jones et al. (2018) shall also be given in Sect. 8.4. A further comparison to Bayesian results derived from other priors such as the aforementioned Milky Way one is not necessary for all program stars since most of them are close-by ( $\lesssim 2$  kpc; see also Fig. 8.4.1) so that differences related to the prior choice are rather small. Nonetheless, such a comparison would be rather interesting for the program stars that are located beyond 2 kpc. In these cases, the results of Bailer-Jones et al. (2018) and the distances derived from the “Milky Way prior” should differ significantly. However, an elaborated investigation of this is beyond the scope of this work.

## 6. Modelling Stellar Atmospheres

The structure of a star is governed by the *stellar structure equations*, describing a system of four differential equations that link the radial distributions of the mass  $M(r)$ , pressure  $P(r)$ , luminosity  $L(r)$ , temperature  $T(r)$ , and density  $\rho(r)$  to each other. To this end, mass continuity, hydrostatic equilibrium, energy conservation, and energy transport (either by convection or by radiation) are assumed. The stellar structure equations hold in every layer of the star, including the outer ones that form the *stellar atmosphere*<sup>57</sup>. The latter is mainly responsible for the formation of the stellar spectrum, whereby the optical part originates from the *photosphere* (the innermost layer of the atmosphere). The different parameters which describe the condition, the composition, the structure and, hence, the physical state of an individual stellar atmosphere can be derived from quantitative spectral analysis, that is, the analysis of observed spectral lines in a stellar spectrum. This will be dealt with in detail in Ch. 7. However, quantitative spectral analyses rely on grids of precalculated synthetic spectra which are able to model the stellar atmosphere and the radiative transfer. Available methods of calculating synthetic spectra differ in the treatment of the interaction of radiation and matter in the stellar plasma. This is detailed in the theory of stellar atmospheres, whose basic theoretical concepts shall be presented in the following.

This chapter is based on the textbooks “*The Fundamentals of Stellar Astrophysics*” by Collins (1989), “*The Observation and Analysis of Stellar Photospheres*” by Gray (2005), and “*Theory of Stellar Atmospheres*” by Hubeny & Mihalas (2014) as well as on the respective chapters of the theses “*Origin of runaway OB stars*” by Irrgang (2014), “*Spectroscopic Analysis of the <sup>3</sup>He Anomaly in B-Type Stars*” by Schneider (2017), and “*Quantitative spectral analyses of blue horizontal branch stars*” by Hämmerich (2020). Sections 6.1-6.6 summarize the theoretical concepts of modelling stellar atmospheres, including the *radiative transfer* (Sect. 6.1), the derivation, description, and solution of the *structural equations* which inter alia determine the density and temperature stratification (Sects. 6.2 and 6.3), the comparison between *local* and *non-local thermodynamic equilibrium* (Sect. 6.4), the *spectral line formation* (Sect. 6.5) and, last but not least, the importance of *metal line-blanketing* and the possible treatments of opacity (Sect. 6.6). The chapter concludes with a description of the different model atmosphere approaches used and compared within the framework of this thesis (Sects. 6.7-6.9; see Ch. 9 for their application to the quantitative spectral analyses performed in this work).

---

<sup>57</sup>The general system of the four stellar structure equations mainly is used to describe the inner structure of a star. In the context of stellar atmospheres, however, several simplifications can be made such that an atmosphere can be described by a set of three so-called *structural equations* only. This will be presented throughout this chapter.

## 6.1. Radiative Transfer

Radiative transfer is the generic term for all changes of the macroscopic radiation field due to absorption (including scattering) and emission processes in the traversed matter of a stellar atmosphere. It is described by the radiative transfer equation:

$$dI_\nu = -\kappa_\nu I_\nu ds + \eta_\nu ds, \quad (6.1)$$

where:

$$I_\nu := \frac{dE}{d\nu dt d\Omega dA \cos \theta} \quad (6.2)$$

describes the specific intensity, which is defined as the energy  $dE$  per frequency interval  $d\nu$  and time interval  $dt$  passing in the direction of the solid angle element  $d\Omega = \sin \theta d\theta d\varphi$  through an area element  $dA$  with surface normal  $\vec{n}$  inclined by an angle  $\theta$  towards  $d\Omega$ .  $ds$  is the distance interval in the direction of  $d\Omega$ .  $\kappa_\nu$  and  $\eta_\nu$  are the (macroscopic) absorption and emission coefficients, often referred to as opacity and emissivity, respectively<sup>58</sup>. Both quantities are used to subsume all absorption processes, that is, true absorption (bound-bound, bound-free, and free-free atomic transitions) and electron scattering as well as all emission processes occurring in a stellar atmosphere<sup>59</sup>.  $\kappa_\nu$  and  $\eta_\nu$  therefore are non-trivial functions of variables such as the temperature, the occupation numbers, or the elemental abundances that describe the state of the matter. In fact,  $\lambda := \kappa_\nu^{-1}$  describes the mean free path, that is, the mean distance a photon can travel before it is absorbed.

The contribution of  $I_\nu$  to the specific intensity in direction of  $\vec{n}$  is given by  $I_\nu \cos \theta$ , which is often abbreviated as  $I_\nu(\cos \theta)$ . By integrating the specific intensity  $I_\nu$  over all frequencies, the total intensity  $I$  of the radiation field in direction of  $d\Omega$  can be derived:

$$I := \int_0^\infty I_\nu d\nu. \quad (6.3)$$

Hence, in direction of  $\vec{n}$ :  $I(\cos \theta) := I \cos \theta$ .

Furthermore, the contribution  $dF_\nu$  to the net (spectral) flux  $F_\nu$  in direction of  $\vec{n}$  is given by:

$$dF_\nu := I_\nu \cos \theta d\Omega. \quad (6.4)$$

Thus,  $F_\nu$  can be calculated via:

$$F_\nu := \int_0^{2\pi} \int_0^\pi I_\nu \cos \theta \sin \theta d\theta d\varphi. \quad (6.5)$$

<sup>58</sup> $\kappa_\nu$  = number of absorbers  $\times$  atomic cross section( $\nu$ ) and  $\eta_\nu \sim$  number of emitters  $\times$  transition probability( $\nu$ ).

<sup>59</sup>While spectral absorption (emission) lines only result from bound-bound transitions, bound-free and free-free transitions as well as electron scattering processes are responsible for the continuum formation in a stellar spectrum.

## 6.1. Radiative Transfer

---

In consequence, the total net flux  $F$  in direction of  $\vec{n}$ , which can also be derived from the Stefan-Boltzmann law ( $F := \sigma T_{\text{eff}}^4$ , where  $\sigma$  is the Stefan-Boltzmann constant), is linked to the specific intensity  $I_\nu$ :

$$F := \int_0^\infty F_\nu d\nu = \int_0^{2\pi} \int_0^\pi \int_0^\infty I_\nu \cos \theta \sin \theta d\nu d\theta d\varphi := \sigma T_{\text{eff}}^4 . \quad (6.6)$$

The stellar luminosity  $L$  can be obtained from an integration of  $F$  over the complete stellar surface:

$$L := \int_0^{2\pi} \int_0^\pi F R^2 \sin \theta d\theta d\varphi = 4\pi R^2 F = 4\pi R^2 \sigma T_{\text{eff}}^4 , \quad (6.7)$$

where  $R$  denotes the stellar radius.

The radiative transfer equation (Eq. 6.1) can be rewritten making use of the *plane-parallel geometry* and the (*chemical*) *homogeneity* of a stellar atmosphere. As the thickness of the stellar atmosphere is small compared to the radius of the individual star, the curvature of the star is negligible on length scales of interactions occurring in the atmosphere (**plane-parallel geometry**). In this way, the stellar atmosphere can be divided into separate layers. In each of them, no variations perpendicular to the normal direction are considered. This includes variations caused by magnetic fields, spots, granules, etc. (**homogeneity**). Moreover, the atomic abundances are specified and assumed to be constant throughout the entire stellar atmosphere (**chemical homogeneity/constant elemental abundances**).

Due to these assumptions, it is sufficient to use only one single coordinate (perpendicular to the atmospheric plane, that is, parallel to  $\vec{n}$ ) in order to describe the location within a stellar atmosphere. This coordinate is called the geometrical depth  $z$ , whereby the stellar surface is located at  $z_0$  and the distance element can be expressed as  $dz = ds \cos \theta$ . By introducing the unitless frequency-dependent optical depth<sup>60</sup> as  $d\tau_\nu := -\kappa_\nu dz$  and  $\tau_\nu := -\int_{z_0}^z \kappa_\nu dz'$ , respectively,  $ds$  in Eq. (6.1) can be transformed into  $ds = dz / \cos \theta = -d\tau_\nu (\kappa_\nu \cos \theta)^{-1}$ , resulting in the following rewritten radiative transfer equation:

$$\cos \theta dI_\nu = I_\nu d\tau_\nu - \frac{\eta_\nu}{\kappa_\nu} d\tau_\nu . \quad (6.8)$$

The ratio  $\frac{\eta_\nu}{\kappa_\nu}$  is defined as the source function  $S_\nu$ , yielding the more simple form:

$$\cos \theta \frac{dI_\nu}{d\tau_\nu} = I_\nu - S_\nu . \quad (6.9)$$

---

<sup>60</sup>The geometrical depth  $z$  increases from inwards to outwards. For the optical depth  $\tau_\nu$ , however, the reverse is true. The thickness of an absorber from which a fraction of  $1/e$  photons can escape is described by a distance of one optical depth. The lower boundary of the photosphere is defined by an optical depth of  $\tau_\nu \sim 2/3$ , meaning that about half of the photons at this optical depth are able to escape the photosphere. However, it has to be pointed out that the exact value for the lower boundary of the photosphere depends on the individual wavelength (frequency) of the absorbed photons. It is also useful to mention that a medium is optically thin at a given frequency if  $\tau_\nu < 1$ , but optically thick if  $\tau_\nu > 1$ . Therefore,  $\tau_\nu = 1$  defines the visible edge of a star.

The formal solution to this first-order differential equation is:

$$\begin{aligned}
 I_\nu(\tau_{\nu,1}, \cos \theta) &= I_\nu(\tau_{\nu,2}, \cos \theta) \exp\left(-\frac{\tau_{\nu,2} - \tau_{\nu,1}}{\cos \theta}\right) \\
 &+ \int_{\tau_{\nu,1}}^{\tau_{\nu,2}} S_\nu(t_\nu) \exp\left(-\frac{t_\nu - \tau_{\nu,1}}{\cos \theta}\right) \frac{dt_\nu}{\cos \theta}.
 \end{aligned} \tag{6.10}$$

In direction of positive  $\cos \theta$ , that is, from the inner parts of the stellar atmosphere to its outer parts, the specific intensity emitted at an optical depth  $\tau_{\nu,2}$  further inside of the stellar atmosphere therefore drops exponentially on its way towards the outer regions, represented by the optical depth  $\tau_{\nu,1}$  (first term in Eq. 6.10). The intensity at  $\tau_{\nu,1}$  increases by the sum of intensities  $S_\nu$  that originate at each point  $t_\nu$  along the line, but also suffer from exponential decay based on the optical-depth separation  $t_\nu - \tau_{\nu,1}$  (second term in Eq. 6.10).

Eq. (6.10) can only be evaluated numerically, if the exact form of the source function  $S_\nu$  is known, that is, if  $S_\nu$  itself is not a function of the specific intensity  $I_\nu$ . However, this is not the case because of the interaction between the radiation field and the matter, which simultaneously influences the opacity  $\kappa_\nu$  and the emissivity  $\eta_\nu$ . Thus, Eq. (6.10) only represents a formal solution and cannot be used to determine the radiative transfer in reality. In practice,  $S_\nu$  may be approximated locally. For instance, this can be done by means of a polynomial in the optical depth (see Schmid-Burgk 1975 for further details).

## 6.2. Basic Assumptions

Several assumptions have to be made in order to derive the set of equations that governs the structure (for instance, the temperature and electron density structure) of a stellar atmosphere. Three of them - the **plane-parallel geometry**, the **homogeneity**, and the **constant elemental abundances** - have already been discussed in the last section. This resulted in the radiative transfer equation in the form of Eq. (6.9). Further assumptions are described below:

- **Stationarity:** The stellar atmosphere is considered stationary, that is, no relative motion of the individual atmospheric layers in direction of  $\vec{n}$  is considered. Consequently, pulsations, convection, and other time-dependent effects are neglected.
- **Hydrostatic equilibrium:** Following the concept of stationarity, hydrostatic equilibrium holds in each of the atmospheric layers. Therefore, the pressure gradient  $\frac{dP(z)}{dz}$  is time-independent and fulfills the following relation:

$$\frac{dP(z)}{dz} = -\frac{GM(z)\rho(z)}{z^2} \approx -\frac{GM\rho(z)}{R^2} =: -g\rho(z), \tag{6.11}$$

whereby  $G$  is the Gravitational constant,  $R$  is the stellar radius,  $g := GM/R^2$  is the surface gravity, and  $z$  is the geometrical depth (the radial distance to the star centre).

## 6.2. Basic Assumptions

$\rho(z)$  denotes the mass density at the distance  $z$  and  $M(z)$  describes the total mass within a sphere with radius  $z$ . Since the thickness of the stellar atmosphere is small compared to  $R$  and the mass of the stellar atmosphere is negligible compared to the total stellar mass  $M$ , the approximation in Eq. (6.11) is valid. Eq. (6.11) hence demonstrates that the atmospheric pressure is described by the depth-dependent density  $\rho(z)$  and the stellar parameters  $R$  and  $M$ , that is,  $g$ . Or, in other words, the surface gravity  $g$  is the first important parameter for the characterization of a stellar atmosphere as it is closely linked to the atmospheric pressure and the density stratification.

The pressure  $P$  consists of two components:  $P_{\text{Gas}}$  and  $P_{\text{Radiation}}$ <sup>61</sup>. While the former describes the pressure caused by the matter in the stellar plasma (electrons, atoms, and ions), the latter results from the interactions of photons with the material particles and is called the radiation pressure. Making use of Eqs. (6.1) and (6.5) as well as of  $dz = ds \cos \theta$ , the radiation pressure gradient can be linked to the net flux  $F_\nu$  in the case of an isotropic opacity  $\kappa_\nu$  and an isotropic emissivity  $\eta_\nu$ :

$$\begin{aligned}
 \frac{dP_{\text{Radiation}}(z)}{dz} &:= \frac{1}{c} \int_0^{2\pi} \int_0^\pi \int_0^\infty \frac{dI_\nu}{dz} \cos^2 \theta \sin \theta d\nu d\theta d\varphi \\
 &= \frac{1}{c} \int_0^{2\pi} \int_0^\pi \int_0^\infty \frac{dI_\nu}{ds} \cos \theta \sin \theta d\nu d\theta d\varphi \\
 &\stackrel{\text{Eq.(6.1)}}{=} \frac{1}{c} \int_0^{2\pi} \int_0^\pi \int_0^\infty (-\kappa_\nu I_\nu + \eta_\nu) \cos \theta \sin \theta d\nu d\theta d\varphi \\
 &= -\frac{1}{c} \int_0^{2\pi} \int_0^\pi \int_0^\infty \kappa_\nu I_\nu \cos \theta \sin \theta d\nu d\theta d\varphi \\
 &\quad + \underbrace{\frac{1}{c} \int_0^{2\pi} \int_0^\pi \int_0^\infty \eta_\nu \cos \theta \sin \theta d\nu d\theta d\varphi}_{=0, \text{ since integration over } d\theta \text{ yields zero}} \\
 &\stackrel{\text{Eq.(6.5)}}{=} -\frac{1}{c} \int_0^\infty \kappa_\nu F_\nu d\nu, \tag{6.12}
 \end{aligned}$$

where  $c$  denotes the vacuum speed of light. Introducing the radiative acceleration  $g_{\text{rad}} := \frac{1}{\rho(z)c} \int_0^\infty \kappa_\nu F_\nu d\nu$ , Eq. (6.12) can be rewritten as:

$$\frac{dP_{\text{Radiation}}(z)}{dz} = -g_{\text{rad}}\rho(z). \tag{6.13}$$

<sup>61</sup>The ‘‘turbulence pressure’’  $P_{\text{Turb}}$  is ignored here.  $P_{\text{Turb}} \sim \rho(z)\xi^2$  can be introduced to mimic a pressure associated with the random motion of ‘‘turbulent eddies’’.  $\xi$  is the microturbulent velocity or microturbulence. It will be further described in Sect. 6.5.1.

Thus, the pressure gradient of the stellar plasma can be derived from the action of the true gravitational acceleration  $g$  (acting downwards) minus the radiative acceleration  $g_{\text{rad}}$  (acting outwards):

$$\frac{dP_{\text{Gas}}(z)}{dz} = \frac{dP(z)}{dz} - \frac{dP_{\text{Radiation}}(z)}{dz} = -\rho(z)(g - g_{\text{rad}}) . \quad (6.14)$$

- **Radiative equilibrium:** A static atmosphere also implies energy (flux) conservation at each depth point because the energy source of the star lies far below the atmosphere and no additional energy enters the atmosphere from the outside. Eq. (6.6) represents the differential form of the radiative equilibrium equation. The integral form is given by the equality of the total absorbed and emitted energy:

$$\int_0^{2\pi} \int_0^{\pi} \int_0^{\infty} (\kappa_{\nu} I_{\nu} - \eta_{\nu}) \sin \theta d\nu d\theta d\varphi = 0 . \quad (6.15)$$

Making use of Eqs. (6.1) and (6.6) as well as of  $ds = dz/\cos \theta$ , Eq. (6.15) can be rewritten as:

$$\begin{aligned} 0 &= \int_0^{2\pi} \int_0^{\pi} \int_0^{\infty} (-\kappa_{\nu} I_{\nu} + \eta_{\nu}) \sin \theta d\nu d\theta d\varphi \stackrel{\text{Eq. (6.1)}}{=} \int_0^{2\pi} \int_0^{\pi} \int_0^{\infty} \frac{dI_{\nu}}{dz} \cos \theta \sin \theta d\nu d\theta d\varphi \\ &= \frac{d}{dz} \int_0^{2\pi} \int_0^{\pi} \int_0^{\infty} I_{\nu} \cos \theta \sin \theta d\nu d\theta d\varphi \stackrel{\text{Eq. (6.6)}}{=} \frac{dF}{dz} . \end{aligned} \quad (6.16)$$

Eq. (6.16) shows that the total net flux  $F := \sigma T_{\text{eff}}^4$  (see Eq. 6.6) is constant throughout the atmosphere. Hence, the second important parameter that describes the state of a stellar atmosphere is the effective temperature  $T_{\text{eff}}$ .

- **Charge conservation:** In a stellar atmosphere, the total charge is considered conserved. This is described by:

$$\sum_k \sum_i N_{ik} Z_{ik} - n_e = 0 . \quad (6.17)$$

The sum runs through all ionization levels  $i$  of all the individual chemical elements  $k$  that are present in the stellar atmosphere.  $Z_{ik}$  denotes the charge associated with ionization state  $i$  of the individual element  $k$ , whereby  $i = 0$  represents the neutral state,  $i = 1$  represents singly-ionized atoms, and so on.  $N_{ik}$  is the corresponding ion density and  $n_e$  denotes the electron density of the stellar plasma.

## 6.3. Structural Equations

Important factors for the structure of a stellar atmosphere are the ionization degrees of atoms and ions in the stellar plasma and the material properties defined by the opacity  $\kappa_\nu$  and the emissivity  $\eta_\nu$ . The latter two generally depend on the chemical composition, the temperature, and the density and define the source function  $S_\nu$ . The “turbulence pressure”  $P_{\text{Turb}}$ , which is related to the microturbulence  $\xi$  (see Sect. 6.5.1), may also play an important role for the atmospheric structure<sup>62</sup>. However, it will be ignored in the following. In this case, the atmospheric structure for a given chemical composition only depends on the effective temperature  $T_{\text{eff}}$  and the surface gravity  $g$  as input. This results in the following structural equations that hold in each atmospheric layer and need to be solved in order to obtain the model atmosphere:

$$\frac{dP_{\text{Gas}}(z)}{dz} = -\rho(z) \left( g - \frac{1}{\rho(z)c} \int_0^{2\pi} \int_0^\pi \int_0^\infty \kappa_\nu I_\nu \cos \theta \sin \theta d\nu d\theta d\varphi \right) \quad (6.18)$$

$$\int_0^{2\pi} \int_0^\pi \int_0^\infty I_\nu \cos \theta \sin \theta d\nu d\theta d\varphi = \sigma T_{\text{eff}}^4 \quad (6.19)$$

$$\cos \theta \frac{dI_\nu}{d\tau_\nu} = I_\nu - S_\nu . \quad (6.20)$$

Equation (6.18) results from hydrostatic equilibrium, Eq. (6.19) is based on radiative equilibrium, and Eq. (6.20) describes the radiative transfer. Together, all three govern the structure of a stellar atmosphere, including the temperature and electron density structure (temperature-density stratification). In this regard, charge conservation according to Eq. (6.17) and the equation of state of an ideal gas certainly also need to be fulfilled. The latter is given by:

$$P_{\text{Gas}} = Nk_B T , \quad (6.21)$$

linking the gas pressure to the total particle number density  $N$  and the electron temperature  $T$ .  $k_B$  is the Boltzmann constant.

In practice, an iteration process is used for the convergence of a model atmosphere with input parameters  $T_{\text{eff}}$  and  $g$ . In the early days, the structural equations were typically solved one at a time, iterating between them. However, these iterations were slow and the scheme sometimes failed to converge at all. The decisive breakthrough was the development of the *complete linearization* (CL) method by Auer & Mihalas (1969). CL was the first scheme which was able

<sup>62</sup>Turbulence in a stellar atmosphere is described by the effects of microturbulence  $\xi$  and macroturbulence  $\zeta$ . However, only the microturbulence affects the radiative transfer (see Sect. 6.5 for further information). At the same time, only it is responsible for the “turbulence pressure”  $P_{\text{Turb}}$ .

to solve the highly complex, coupled, non-linear system of structural equations at once. The CL scheme describes the physical state of the stellar atmosphere by a set of state vectors:

$$\boldsymbol{\psi}_d := \left( J_{d1}, \dots, J_{d,NF}, N_d, T_d, n_e^d, n_{d1}, \dots, n_{d,NL} \right), \quad (6.22)$$

one for each discretized<sup>63</sup> depth point  $d$  ( $d = 1, \dots, ND$ ;  $ND$  denotes the total number of depth points). Each state vector includes all structural parameters, that is, the mean intensities of radiation  $J_i$  in discretized frequency points  $i$  ( $i = 1, \dots, NF$ ), the local total particle density of all atoms/ions  $N$ , the local temperature  $T$ , the local electron density  $n_e$ , and the occupation numbers of the atomic energy levels  $j$  ( $j = 1, \dots, NL$ ). The dimension of a state vector is  $NN$ ,  $NN = NF + NL + NC$ , where  $NF$  is the total number of frequency points,  $NL$  is the total number of atomic energy levels for which the rate equations<sup>64</sup> are solved, and  $NC$  is the total number of constraint equations (usually  $NC = 3$  for  $N$ ,  $T$ , and  $n_e$ ). A trial atmosphere (usually a *gray atmosphere*<sup>65</sup>) with state vectors  $\boldsymbol{\psi}_d^0$  that do not fulfill Eqs. (6.18-6.20) is chosen, whereby the individual vectors provide hints of what has to be changed. The required solution  $\boldsymbol{\psi}_d$  can therefore be written in terms of the current, but imperfect solution  $\boldsymbol{\psi}_d^0$  as  $\boldsymbol{\psi}_d = \boldsymbol{\psi}_d^0 + \delta\boldsymbol{\psi}_d$ . In order to determine the correction  $\delta\boldsymbol{\psi}_d$ , the entire set of structural equations is formally written as an operator  $\boldsymbol{P}$  that acts on  $\boldsymbol{\psi}_d$  as:

$$\boldsymbol{P}_d(\boldsymbol{\psi}_d) = \boldsymbol{P}_d(\boldsymbol{\psi}_d^0 + \delta\boldsymbol{\psi}_d) = 0. \quad (6.23)$$

Assuming that  $\delta\boldsymbol{\psi}_d$  is small compared to  $\boldsymbol{\psi}_d^0$ , a Taylor expansion of  $\boldsymbol{P}$  can be used to solve for  $\delta\boldsymbol{\psi}_d$ , whereby only the first-order term is taken into account. Therefore, the set of structural equations is *linearized*. Mathematically, this represents the Newton-Raphson method for solving a set of non-linear algebraic equations. Hence, a block tridiagonal matrix system needs to be solved. In order to do so, the matrix of partial derivatives of all the structural equations with respect to all the unknowns at all depths (Jacobi matrix or Jacobian) needs to be inverted, which is a real problem since it becomes so huge for realistic cases that it can no longer be inverted numerically. More precisely, iterative numerical solution methods cannot be used because physically they lead again to the iterative procedure that converges poorly or not at all. Yet, a special elimination procedure (the Gauss-Jordan procedure), also known as the Feautrier elimination method (Feautrier, 1964, 1967, 1968), can be used to solve for  $\delta\boldsymbol{\psi}_d$ . This method represents an efficient recursive forward-elimination and backward-substitution procedure, in which only combined sub-matrices of the Jacobian need to be inverted. Once the correction  $\delta\boldsymbol{\psi}_d$  has been determined, it is applied and the whole procedure starts all over.

<sup>63</sup>Discretization is the re-expression of analytical operators in terms of algebraic operations, for instance, by means of geometric grids, interpolation, finite differences, quadratures, indexing, or depth grids.

<sup>64</sup>The term ‘rate equations’ will be explained in the context of non-local thermodynamic equilibrium (see Sect. 6.4).

<sup>65</sup>In a gray atmosphere, it is assumed that the opacity  $\kappa_\nu$  and the emissivity  $\eta_\nu$  are frequency-independent. Therefore, any frequency can be treated as any other frequency, when it comes to radiative transfer. In this way, the mathematical solution of the radiative transfer equation for any frequency is the solution for all frequencies and, thus, also for the sum of all frequencies. This makes the condition of radiative equilibrium relatively simple to apply because the aspect of the solution specifying the radiative flux then also refers to the total flux (see, for instance, Collins 1989 for further information).

### 6.3. Structural Equations

---

In this way, the deviations from linearity are also corrected for step by step. The iterations are performed until the chosen convergence criterion for all state vectors at all depths is fulfilled. A typical necessary (but not sufficient) condition for convergence may be that the maximum relative change of all components of the state vectors in all depths is smaller than  $\sim 10^{-3}$ . The final structural parameters are then used to set up the model atmosphere and to compute the corresponding synthetic spectrum. For a compact summary of the detailed formalism of the CL method and for further information, see, for instance, the respective chapters in the textbook of Hubeny & Mihalas (2014).

The CL scheme is a stringent method because it applies corrections to all structural parameters simultaneously. Therefore, it has inherent power. At the same time, it is also very robust. It is, however, very time-consuming. This is mainly because of the fact that a very large number of frequency points  $NF$  (typically  $\sim 10^5$  to  $10^6$ ) is used in realistic calculations in order to describe the radiation field with sufficient accuracy. Hence, CL is not practicable, unless a high-speed massively parallel computer, where each node has a large memory, can be used in order to invert matrices of this dimension.

A much faster scheme is the *accelerated lambda iteration* (ALI) method, which is based on the original idea of CL (Hubeny & Lanz, 2003). The essence is the expression of the mean intensity of radiation as:

$$J_\nu^{(n)} = \Lambda_\nu^* S_\nu^{(n)} + (\Lambda_\nu - \Lambda_\nu^*) S_\nu^{(n-1)} \equiv \Lambda_\nu^* S_\nu^{(n)} + \Delta J_\nu, \quad (6.24)$$

where  $\Lambda_\nu$  and  $\Lambda_\nu^*$ , respectively, are the exact and the approximate lambda operators and  $S_\nu$  is the source function, all at frequency  $\nu$ . The iteration number is indicated by the superscript  $n$ . Thus, the mean intensity of radiation is represented by two terms, whereby the second one (the correction term  $\Delta J_\nu$ ) is derived from the previous iteration. The first term is determined from the action of the approximate (simple)  $\Lambda_\nu^*$ -operator on the thermal (without the scattering terms) source function  $S_\nu$ , which is a function of temperature, density, and atomic level populations. By applying Eq. (6.24), the radiative transfer equations are eliminated from the coupled system of structural equations. Therefore, in the case of ALI the state vectors  $\psi_d$  of Eq. (6.22) are replaced by the reduced state vectors:

$$\tilde{\psi}_d := (N_d, T_d, n_e^d, n_{d1}, \dots, n_{d,NL}) . \quad (6.25)$$

As in the case of CL, the correction  $\delta\tilde{\psi}_d$  for the current, but imperfect solution  $\tilde{\psi}_d^0$  is determined via linearization, whereby this time only the rate equations, the radiative equilibrium equation, and the charge conservation equation need to be linearized. To this end, the radiation field given by Eq. (6.24) is used. In the simplest case, a diagonal  $\Lambda_\nu^*$ -operator is used such that its action is a simple multiplication by a scalar quantity. Consequently, the resulting set of equations for the corrections  $\delta\tilde{\psi}_d$  is diagonal (Werner, 1986). In principle, an extension to the nearest neighbor depth points  $d-1$  and  $d+1$  is also possible. This can be achieved by a tridiagonal  $\Lambda_\nu^*$ -operator, which leads to a block tridiagonal matrix system, as in the case of the original CL method (Werner, 1989). Thanks to the Feautrier scheme, however, which is able to break down the (tri)diagonal Jacobian into sub-matrices that subsequently need to be inverted in order to determine  $\delta\tilde{\psi}_d$ , the dimensionality is greatly reduced in both cases. In

the end, the determined corrections  $\delta\tilde{\psi}_d$  are applied and the whole iterative process starts all over until a chosen convergence criterion for all state vectors is fulfilled. The final structural parameters are then used to set up the model atmosphere and to compute the corresponding synthetic spectrum. For a compact summary of the detailed formalism of the ALI method and for further information, see, for instance, Werner (1986, 1989) and the respective chapters in the textbook of Hubeny & Mihalas (2014). Therein, the reader also finds more information on the exact lambda operator  $\Lambda_\nu$ , as well as on possible shapes of the approximate lambda operator  $\Lambda_\nu^*$ .

As described, ALI is able to solve the structural equations simultaneously, whereby an approximate solution for the radiative transfer (expressed by Eq. 6.24) is used. In consequence, the computation times for ALI are much shorter than that for CL. This is the main reason why modern codes for atmospheric modelling rely on ALI rather than on CL.

## 6.4. Local vs. Non-Local Thermodynamic Equilibrium (LTE vs. NLTE)

The radiation field is described by the source function  $S_\nu$  and, thus, by the statistical properties of the stellar plasma, that is, the opacity  $\kappa_\nu$  and the emissivity  $\eta_\nu$ . Both variables depend on the occupation numbers of all energy levels of all atomic species present in the stellar atmosphere. In a simple way, level populations are calculated in *local thermodynamic equilibrium* (LTE) according to Saha-Boltzmann statistics. However, departures from LTE - so-called non-LTE (NLTE) effects - may be necessary in order to reproduce the absorption and the emission lines in observed stellar spectra. As shown by Auer & Mihalas (1973), this is particularly true for the red neutral helium lines He I 5875 Å and He I 6678 Å, which are very pronounced in the spectra of the program stars analyzed in this work (see Ch. 9 for details). NLTE effects are described by statistical equilibrium, which can be derived from the requirement of stationarity. In the following, a brief explanation of the terms *thermodynamic equilibrium* (TE), LTE, and NLTE shall be given.

### Thermodynamic Equilibrium (TE)

Strict TE is characterized by the following physical properties:

- The velocities of all particles (other than photons<sup>66</sup>) along the line of sight follow a **Maxwellian (Maxwell-Boltzmann) velocity distribution**:

$$p(v)dv = \left(\frac{m}{2\pi k_B T}\right)^{3/2} \exp\left(-\frac{mv^2}{2k_B T}\right) 4\pi v^2 dv, \quad (6.26)$$

<sup>66</sup>Photons are described by the Bose-Einstein quantum statistics.

#### 6.4. Local vs. Non-Local Thermodynamic Equilibrium (LTE vs. NLTE)

---

where  $m$  and  $v$  denote the individual particle mass and velocity, respectively, and  $T$  is the absolute system temperature.  $k_B$  is the Boltzmann constant.

- Considering all particles that are associated with a specific atom/ion (for instance, H I, He I/II, etc.), the corresponding ratio of the total occupation numbers (total occupation number densities<sup>67</sup>) of two energy levels is given by the **Boltzmann excitation formula**:

$$\frac{n_{\text{up}}}{n_{\text{low}}} = \frac{N_{\text{up}}}{N_{\text{low}}} = \frac{g_{\text{up}}}{g_{\text{low}}} \exp\left(-\frac{E_{\text{up}} - E_{\text{low}}}{k_B T}\right). \quad (6.27)$$

Here,  $n_{\text{up}}$ ,  $N_{\text{up}}$ ,  $g_{\text{up}}$ , and  $E_{\text{up}}$  denote the total occupation number, the total occupation number density, the statistical weight, and the energy of the upper level of the atom/ion in question.  $n_{\text{low}}$ ,  $N_{\text{low}}$ ,  $g_{\text{low}}$ , and  $E_{\text{low}}$  refer to the lower energy level.  $E_{\text{up}}$  and  $E_{\text{low}}$  are measured with respect to the ground state. The statistical weight of the  $i$ th energy level of the considered atom/ion describes the maximum number of electrons that can be contained in that level or, equivalently, the maximum number of different states with the same energy  $E_i$ . The statistical weight is defined as  $g_i := 2J_i + 1$ , where  $J_i$  is the total angular momentum quantum number associated with level  $i$ .

Moreover, the ratio of the total occupation number associated with energy level  $i$  to the total number density of the corresponding atoms/ions in ionization stage  $I$  ( $I = 0$  represents the neutral state) can be derived from:

$$\frac{n_i}{N_I} = \frac{g_i \exp(-E_i/k_B T)}{\sum_{j=0}^{j_{\text{max}}} g_j \exp(-E_j/k_B T)} = \frac{g_i \exp(-E_i/k_B T)}{U_I}. \quad (6.28)$$

$U_I := \sum_{j=0}^{j_{\text{max}}} g_j \exp(-E_j/k_B T)$  is the partition function of the considered atoms/ions in ionization stage  $I$ .

- The ratio of the total number densities of different ionization stages associated with a single chemical element is given by the **Saha ionization equation**:

$$\frac{N_I}{N_{I+1}} = \frac{n_e}{2} \frac{U_I}{U_{I+1}} \left(\frac{h^2}{2\pi m_e k_B T}\right)^{3/2} \exp\left(\frac{\chi_I}{k_B T}\right). \quad (6.29)$$

Here,  $h$  denotes the Planck constant and  $m_e$  is the electron mass.  $N_I$  is the total number density associated with ionization stage  $I$ ,  $\chi_I$  is the corresponding ionization potential (ionization energy), and  $U_I$  again is the partition function.  $N_{I+1}$  and  $U_{I+1}$  refer to the ionization stage  $I+1$ .

---

<sup>67</sup>The *occupation number density*  $N_i$  of an energy level  $i$  is defined as the number of atoms/ions in that state per unit volume. Hence, the total number density (measured per unit volume) of the atoms/ions in question is given by  $N = \sum_i N_i$ . The *population* or *occupation number*  $n_i$  of the energy level  $i$ , however, is defined as  $n_i := N_i/N$ .

- Furthermore, the source function  $S_\nu$  can be described by the specific intensity  $I_\nu$  according to **Kirchhoff's law of thermal radiation**.  $I_\nu$  itself is given by the distribution function for thermal radiation, that is, the **Planck function**  $B_\nu$ . This yields:

$$S_\nu = I_\nu = B_\nu = \frac{2h\nu^3}{c^2} \frac{1}{e^{h\nu/k_B T} - 1}. \quad (6.30)$$

$c$  is the vacuum speed of light. Consequently, the opacity  $\kappa_\nu$  and the emissivity  $\eta_\nu$  do not need to be known in order to derive the source function  $S_\nu$  as it is given by the system temperature  $T$  and the frequency  $\nu$  only.

- Last but not least, the **photon number density**  $N_\nu$  is given by:

$$N_\nu = \frac{B_\nu}{ch\nu}. \quad (6.31)$$

Due to the stellar radiation and the fact that quantities such as the gravitational force, the pressure, and the temperature depend on the local position within the stellar atmosphere, the assumption of TE only is valid within each atmospheric layer, but not throughout the entire atmosphere. This is described by the concept of local thermodynamic equilibrium, which will be dealt with next.

## Local Thermodynamic Equilibrium (LTE)

TE cannot be applied globally within a stellar atmosphere, but each atmospheric layer may be described by its own local temperature  $T$  and electron density  $n_e$ . This is referred to as LTE. The occupation numbers for each individual layer can then be derived from Eqs. (6.27-6.29), if charge conservation according to Eq. (6.17) is additionally considered. In combination with the information on the atomic structure provided by model atoms, the source function  $S_\nu$  and, hence, the atmospheric structure can be derived. The individual velocity distributions for particles other than photons are considered Maxwellian as in the case of strict TE (see Eq. 6.26).

Throughout a stellar atmosphere, strict LTE is valid for electrons but not necessarily for photons. First, the mean free path between collisions of photons with other particles is significantly larger than that between collisions of material particles. Second, the particle density of a stellar atmosphere decreases from its inner parts to the outer ones. The notion of LTE only holds, if interactions between photons and other particles remain local, that is, occur in atmospheric layers of almost the same local temperature. However, this may not be the case within the entire atmosphere, in particular towards its outer parts because the particle densities there may be low enough such that the mean free path of photons is larger than the typical distance between two atmospheric layers of different local temperatures. Moreover, the photon flux within a stellar atmosphere can be high enough such that part of the photons may leave one atmospheric layer and may interact with the matter of a second one. Both scenarios

## 6.4. Local vs. Non-Local Thermodynamic Equilibrium (LTE vs. NLTE)

---

introduce departures from LTE (loosely summarized by the term NLTE effects), meaning that the resulting occupation numbers and, hence, the final atmospheric structure differ from the ones derived from strict LTE. In fact, the higher the effective temperature of a star and, thus, the higher the total net flux according to Eq. (6.6), the larger the departures from LTE. The same applies to low surface gravities, which imply low particle densities.

It is general consensus that the atmospheres of cool/lukewarm dwarf stars of spectral types A and later are well described by LTE model atmospheres. However, the spectral lines of early O-type MS stars are strongly influenced by NLTE effects. This is because of the high photon fluxes predominant in the atmospheres of these stars which lead to deviations from the LTE occupation numbers and affect the atmospheric structure. For B and late O-type MS as well as for giant stars in the effective temperature regime of  $15\,000\text{ K} \lesssim T_{\text{eff}} \lesssim 35\,000\text{ K}$ , the surface gravities and, therefore, the atmospheric particle densities are high enough such that the typical mean free path of photons is small enough so that, from this perspective, LTE should be conserved. But, on the other hand, the energy density of the radiation field of these stars may also be strong enough to cause deviations from the LTE occupation numbers. As a matter of fact, however, the atmospheric LTE and NLTE temperature-density stratifications of dwarf and giant stars over the range  $15\,000\text{ K} \lesssim T_{\text{eff}} \lesssim 35\,000\text{ K}$  are essentially equivalent, at least for the optical depths that are relevant for the formation of the observable line spectra and continua (see, for instance, Figure 2 in Przybilla et al. 2011). In other words, the influence of NLTE effects on the atmospheric temperature-density stratification of these stars can safely be neglected when it comes to the modelling of the respective line spectra and continua. In fact, the same applies to hot subdwarfs and blue horizontal branch stars of the same effective temperatures. Nevertheless, their spectral lines may also be influenced by NLTE effects caused by high photon fluxes which lead to deviations from the LTE occupation numbers. Particularly, this is true for the hotter hydrogen and helium-rich sdO/sdB program stars analyzed in this work (see Sect. 8.1). It has to be mentioned, however, that the influence of NLTE effects on individual spectral lines always depends on the population and depopulation rates of the atomic energy levels associated with the underlying transition processes. This will be described in more detail in the next section.

### Non-Local Thermodynamic Equilibrium (NLTE)

In NLTE, the velocities of all material particles remain Maxwellian distributed according to Eq. (6.26) and the same local temperatures  $T$  and electron densities  $n_e$  as for LTE can be applied to the individual atmospheric layers. However, the occupation numbers cannot be derived from the Saha-Boltzmann equations (Eqs. 6.27-6.29). Instead, both are replaced by a more general approach of stationarity, which assumes that the population of any atomic energy level is stationary with time. This means that the corresponding population and depopulation rates are balanced. This is described by the concept of *statistical/kinetic equilibrium*, which can

be expressed by the *rate equations*. For a single atomic energy level  $i$  of a single chemical element in a certain ionization stage, the latter are given by:

$$n_i \sum_{j \neq i} (R_{ij} + C_{ij}) = \sum_{j \neq i} n_j (R_{ji} + C_{ji}), \quad (6.32)$$

where  $n_i$  and  $n_j$  denote the occupation numbers of the levels  $i$  and  $j$ , respectively, and  $R_{ij}$  and  $C_{ij}$  are the radiative and collisional rates for atomic transitions from level  $i$  to  $j$ .  $R_{ij}$  and  $C_{ij}$  are functions of the radiation field, the particle velocity distribution, and the individual atomic cross sections.  $R_{ji}$  and  $C_{ji}$  are defined in a similar way. While  $R_{ij}$  and  $R_{ji}$  include transitions  $i \leftrightarrow j$  caused by an interaction with photons or by a spontaneous emission of a photon,  $C_{ij}$  and  $C_{ji}$  only refer to a transition caused by an interaction with material particles. Whether a spectral absorption line is strongly influenced by NLTE effects or not depends on the ratios of the corresponding collisional and radiative rates for the atomic energy levels of the underlying bound-bound transition. While some lines like He I 5875 Å or He I 6678 Å are strongly influenced, others such as He I 4472 Å or He I 4922 Å are less affected.

It is possible to express the statistical equilibrium or the rate equations in terms of departure coefficients  $b$  from LTE, which are defined as the ratio of the actual occupation number of the  $i$ th atomic energy level to the theoretically expected occupation number derived from LTE. By definition, these coefficients restore LTE occupation numbers for the deeper layers of a stellar atmosphere ( $b \rightarrow 1$ ) because of the strong increase of the particle density. This is true even though the temperature and, hence, the photon flux increases with increasing depth of the atmosphere.

Each atom/ion in a given ionization stage (for instance, H I, He I/II, etc.) has its own linearly-dependent system of rate equations, which is set up by all energy levels of the individual model atom/ion. The total number density of the corresponding chemical species is conserved and is given by:

$$N_{\text{total}} := \sum_j \sum_i N_{ji}. \quad (6.33)$$

The sum includes all energy levels  $i$  of all ionization stages  $j$  that need to be considered for the respective chemical species.  $N_{ji}$  denotes the corresponding occupation number density. Together with the individual total number densities of the chemical elements that are present in the stellar atmosphere, the rate equations allow for the calculation of all necessary occupation numbers in order to determine the source function  $S_\nu$  and, in turn, the atmospheric structure via Eqs. (6.18), (6.19), and (6.20). Due to the high complexity involved, all of this can only be done numerically, whereby extensive computing resources are needed in order to manage the gigantic number of atomic energy levels that need to be taken into account. In practice, the following strategy therefore is adopted: the lowest  $i_{\text{low}}$  levels of any atom/ion in any ionization stage  $j$  are considered in detail. The remaining higher levels are not treated in detail, but their contribution to the total number density of the respective chemical species is taken into account. The occupation numbers of the higher levels are considered in LTE with respect to the ground state of the next ion (see, for instance, Hubeny & Mihalas 2014 for further information).

## 6.5. Spectral Line Formation

Observed spectral lines are associated with different ionization stages of numerous chemical elements present in the stellar atmosphere, whereby each line can be described by a discrete atomic transition from one state to another one (bound-bound process). Photons with appropriate energies either are absorbed by the atom/ion in question, resulting in spectral absorption lines, or emitted, manifesting as emission lines in the stellar spectrum. The specific photon energy and, thus, the frequency (wavelength) associated with the individual atomic transition can be calculated from the difference between the upper and the lower energy level. However, the atomic structure and the possible atomic transitions differ per chemical element and ionization stage. Hence, the analysis of spectral lines provides lots of information about the atmospheric composition of a star. Such a quantitative spectral analysis (see also Sect. 7.1), however, requires detailed knowledge of the occupation numbers of atoms/ions absorbing (emitting) radiation at different frequencies as well as of the individual absorption (emission) profiles, that is, the frequency distributions of the individual line opacities (emissivities). These frequency distributions depend on the temperature and the density of the stellar plasma and are derived from a combination of various different line-broadening mechanisms. The latter will be detailed in the further course of this section. First, the formation of spectral absorption lines shall be explained qualitatively by the simplified “black body” model, which serves as a good starting point.

The radiation emitted from gas in the stellar plasma is strongly temperature-dependent. The lower (higher) the atmospheric temperature, the less (more) atoms and ions are in higher excitation and ionization states. According to Eq. (6.30),  $I_\nu = B_\nu$  in TE such that the specific intensity in each atmospheric layer is described by its own Planck function and black body in the case of LTE. On average, however, the continuum photons (the continuum flux) originate(s) from the optical depth, where the effective temperature  $T_{\text{eff}}$  is reached. Thus, the continuum radiation is mainly described by a black body with  $I_\nu = B_\nu(T_{\text{eff}})$ . In each atmospheric layer, the temperature dependence of the respective black-body radiant power (the luminosity  $L$ ) is given by  $L \sim T^4$  (see also Eq. 6.7). In consequence, hot matter “shines brighter”, meaning that it has a higher intensity than cool matter. The atmospheric temperature decreases from inwards to outwards and, therefore, so do the specific intensity and the flux of the radiation emitted from the gas. Hence, frequency regimes in the stellar spectrum, for which opacities are high and fluxes are low (the line cores of spectral absorption lines), are formed in the cooler outer layers of the stellar atmosphere. On the other hand, regions with lower opacities and higher fluxes (the line wings and the neighboring continuum) result from hotter matter at larger optical depths.

In order to characterize the strength of an individual spectral line, the equivalent width  $W_\nu$  (the first moment of a line profile<sup>68</sup>) is often used. It is defined as:

$$W_\nu := \int_0^\infty \frac{F_c - F_\nu}{F_c} d\nu. \quad (6.34)$$

<sup>68</sup>For instance, the bisector is another moment of a line profile. It describes the asymmetry of a line.

Here,  $F_c$  denotes the continuum flux and  $F_\nu$  is the flux in the line. The integral covers those frequencies for which the integrand significantly differs from zero. Thus, the equivalent width can be interpreted as the width of a rectangle with a height of  $F_c$  and an area that is equal to the area in the spectral line. The determination of  $W_\nu$  strongly depends on the individual line profile and it has to be highlighted that different line shapes may result in the same equivalent widths.

The following subsections briefly introduce the effects and parameters that generally influence the total line profile, that is, the strength (equivalent width) and the shape of spectral lines. A distinction is made between microscopic and macroscopic line-broadening mechanisms. In addition, the importance of level dissolution will be outlined.

### 6.5.1. Microscopic Line Broadening

Microscopic line-broadening mechanisms directly affect the interaction of light with matter as they generally influence the number of absorbed and re-emitted photons by affecting the frequency dependence of the corresponding bound-bound processes in an atom/ion. Hence, microscopic line-broadening mechanisms are part of the radiative transfer equation and have a large impact on the respective spectral line profiles, both in terms of strength and shape. There are four types of microscopic line-broadening mechanisms known: natural (radiation) broadening, pressure (collisional) broadening, thermal Doppler broadening, and non-thermal Doppler broadening. The latter is also referred to as microturbulence.

#### Natural or Radiation Broadening

Only atomic ground states are stable. Excited states have a certain intrinsic lifetime (typically of the order of  $10^{-8}$  s) before they spontaneously decay to a lower energy state. The exact time period that an atom/ion can remain in a certain excited state, however, is uncertain. Via the Heisenberg uncertainty principle of  $\Delta E \Delta t \geq \hbar$ , where  $\hbar$  is the Planck constant  $h$  divided by  $2\pi$ , the uncertainty  $\Delta t$  of the lifetime is related to an energy uncertainty  $\Delta E$ . This means that more energies than the one linked to the central frequency are involved in the transition into or out of the respective state. Obviously, this leads to a natural broadening of the corresponding spectral line. The broadening profile of the absorbed or emitted energy can be derived from a classical damped harmonic oscillator. It is of Lorentzian shape:

$$I_{\text{natural}}(\nu) = \frac{\gamma_{\text{rad}}/4\pi^2}{(\nu - \nu_0)^2 + (\gamma_{\text{rad}}/4\pi)^2} . \quad (6.35)$$

Here,  $\nu_0$  denotes the central frequency defined by the usual energy difference  $\Delta E_0 = h\nu_0$  between the upper and the lower level of the atomic transition in question.  $\gamma_{\text{rad}}$  describes the full width at half maximum of the profile and can be obtained from quantum mechanical calculations of transition probabilities. For a transition between two energy levels, whereby

## 6.5. Spectral Line Formation

---

the upper level is labelled by  $u$  and the lower one by  $l$ ,  $\gamma_{\text{rad}}$  is determined by the sum of all possible radiative decays via spontaneous emission of both levels:

$$\gamma_{\text{rad}} = \sum_{i < u} A_{ui} + \sum_{i < l} A_{li} = \frac{1}{\tau_{\text{up}}} + \frac{1}{\tau_{\text{low}}} . \quad (6.36)$$

$A_{ui}$  and  $A_{li}$  denote the Einstein probability coefficients for spontaneous emission for the upper and the lower level, respectively. The individual sums of all possible radiative decays for both energy levels are given by the respective reciprocal mean lifetimes  $1/\tau_{\text{up}}$  and  $1/\tau_{\text{low}}$ .

### Pressure or Collisional Broadening

Pressure broadening arises from the collisional Coulomb interaction between the absorbing and emitting atoms/ions (radiators) and other material particles in the stellar plasma (perturbers). The latter can be electrons, protons, or atoms/ions of the same or of a different type as that of the radiators. Since the Coulomb force is stronger if the particles involved are closer to each other, the effect of pressure broadening increases with increasing atmospheric pressure<sup>69</sup>. Due to the Coulomb interaction, all atomic levels of the radiators are disturbed and their energies are altered. Most frequently, the energies of the upper transition levels are more strongly altered than that of the lower ones. The distortion depends on the separation  $R$  between the radiator and the perturber, whereby the change of energy  $\Delta W$  for a certain level as a function of  $R$  can be approximated by a power law:

$$\Delta W = \text{constant}/R^n . \quad (6.37)$$

The actual exponent  $n$  depends on the type of interaction (see Table 6.1). The energy change described by Eq. (6.37) can directly be converted into a change of frequency  $\Delta\nu$  in the observed stellar spectrum. To this end, Eq. (6.37), evaluated for the lower energy level, needs to be subtracted from Eq. (6.37) evaluated for the upper level.  $\Delta\nu$  hence can be derived from:

$$\Delta\nu = C_n/R^n . \quad (6.38)$$

$C_n$  denotes the interaction constant. It depends on the type of interaction related to pressure broadening and can be calculated for any atomic transition. The different types of pressure broadening are summarized in Table 6.1. Van der Waals forces mainly result from collisions with neutral hydrogen. In consequence, this kind of pressure broadening has an impact on most of the spectral lines observed in cool stars. Hot (blue) stars such as the O and B-type stars investigated in this work, however, have a large number of charged particles (mainly ions, protons, and electrons) in their atmospheres so that the dominant types of Coulomb interactions are related to the linear and the quadratic Stark effect. While the former mostly affects the hydrogen line profiles, the latter is important for almost all the spectral lines that can be observed in hot stars.

---

<sup>69</sup>In the case of moderate stellar plasma densities short-term perturbations dominate.

$n$	Type	Lines affected	Perturber
2	Linear Stark	Hydrogen	Protons, electrons
4	Quadratic Stark	Most lines, in particular for hot stars	Ions, electrons
6	Van der Waals	Most lines, in particular for cool stars	Neutral hydrogen

Table 6.1.: Types of pressure broadening according to Gray (2005).

The profile for the different types of pressure broadening is also of Lorentzian shape. It is given by:

$$I_{\text{pressure},n}(\nu) = \frac{\gamma_n/4\pi^2}{(\nu - \nu_0)^2 + (\gamma_n/4\pi)^2}. \quad (6.39)$$

The damping constant  $\gamma_n$  (the full width at half maximum of the individual profile) is different for each type. It strongly depends on the perturber density. For hot stars,  $\gamma_n$  therefore is mainly determined by the electron density  $n_e$  (see Gray 2005 for further information).

### Thermal Doppler Broadening

All particles in a stellar atmosphere, including atoms and ions, thermally move. The velocity component  $v$  for each atom/ion along the line of sight to the star is Maxwellian distributed according to Eq. (6.26). Due to the Doppler effect, the rest-frame frequency  $\nu_0$  of an absorbed or emitted photon thus is shifted to a frequency  $\nu$  (see also Sect. 7.1.1 for further information on the Doppler effect). The thermal Doppler line profile can be approximated by a Gaussian distribution:

$$I_{\text{thermal}}(\nu) \approx \frac{1}{\sqrt{\pi}\Delta\nu_{\text{thermal}}} \exp\left(-\frac{(\nu_0 - \nu)^2}{\Delta\nu_{\text{thermal}}^2}\right). \quad (6.40)$$

Here,  $\Delta\nu_{\text{thermal}} := v_0\nu_0/c$  is the thermal Doppler width, whereby the variance  $v_0$  is related to the local temperature  $T$  by  $v_0^2 = 2k_B T/m$  ( $m$  denotes the mass of the atom/ion in question and  $k_B$  is the Boltzmann constant). Consequently, lines associated with heavier chemical elements are intrinsically less strongly broadened by thermal motions than hydrogen or helium lines because  $\Delta\nu_{\text{thermal}} \sim 1/\sqrt{m}$ .

### Non-Thermal Doppler Broadening or Microturbulence

The idea behind non-thermal Doppler broadening or microturbulence in a stellar atmosphere is additional small-scale material mass motions in direction of the surface normal (along the line of sight), whereby their characteristic dimensions (cells) are well below the typical photon mean free path. Microturbulence was postulated for cases where the stationary model spectra in hydrostatic equilibrium that are based on no relative motion of the atmospheric layers in the normal direction were not enough to match the observed line profiles. This indicated an additional line-broadening mechanism. The effect of microturbulence results in small Doppler shifts

## 6.5. Spectral Line Formation

---

analogous to the one arising from thermal motions such that the microturbulent broadening profile is identical to that given in Eq. (6.40). Therefore, it is also of Gaussian shape:

$$I_{\text{non-thermal}}(\nu) = \frac{1}{\sqrt{\pi}\Delta\nu_{\text{non-thermal}}} \exp\left(-\frac{(\nu_0 - \nu)^2}{\Delta\nu_{\text{non-thermal}}^2}\right). \quad (6.41)$$

The variance  $\nu_0$  in Eq. (6.40) is replaced by the microturbulent dispersion parameter (microturbulent velocity or microturbulence)  $\xi$  such that  $\Delta\nu_{\text{non-thermal}} := \xi\nu_0/c$ .

The exact physical origin of microturbulence is still under debate. For hot stars, the microturbulent non-thermal motion could be explained by an additional sub-surface iron convection zone (see, for instance, Cantiello et al. 2009 for further information). As a matter of fact, however, microturbulence turned out to be negligible for hot subdwarf stars (Geier & Heber, 2012). Hence, it will not be considered throughout this work (see also Ch. 7).

### Combination of Microscopic Broadening Effects

All of the aforementioned microscopic broadening mechanisms are uncorrelated but take place at the same time. In consequence, the total microscopic broadening profile is given by the multiple convolution of the individual line profiles:

$$\begin{aligned} I_{\text{total}}(\nu) &= I_{\text{natural}}(\nu) * I_{\text{pressure}}(\nu) * I_{\text{thermal}}(\nu) * I_{\text{non-thermal}}(\nu) \\ &= I_{\text{Lorentz}}(\nu) * I_{\text{Gauss}}(\nu) \equiv I_{\text{Voigt}}(\nu). \end{aligned} \quad (6.42)$$

Here, it was used that convolutions are associative and commutative and that the convolution of two Lorentzian or Gaussian profiles remains Lorentzian or Gaussian. Furthermore, the convolution of a Lorentzian and a Gaussian distribution results in a Voigt profile. Near the line centre, the Voigt profile is Gaussian, whereas it approaches a Lorentzian shape far off from the line centre. In Eq. (6.42),  $I_{\text{pressure}}(\nu)$  represents the convolved Lorentzian profile that results from all types of pressure broadening involved (see Eq. 6.39).

### 6.5.2. Macroscopic Line Broadening

In contrast to microscopic line broadening, macroscopic broadening mechanisms are not part of the radiative transfer and can therefore be incorporated after the computation of a synthetic spectrum. Mathematically, the combined effects of macroscopic broadening can be described by a convolution of the calculated synthetic spectrum with an appropriate broadening profile. Hence, macroscopic broadening simply redistributes photons and only affects the shape of spectral lines, but not their strength (equivalent width). Macroscopic broadening mechanisms include instrumental broadening, rotational broadening, macroturbulence, and pulsational broadening.

### Instrumental Broadening

Spectral lines are blurred because of the finite spectral resolving power of the spectrograph and the CCD detector used<sup>70</sup>. The exact shape of the instrumental profile is very hard to determine. However, a Gaussian profile of the form:

$$\Phi(\delta\lambda) = \frac{2\sqrt{\ln(2)}}{\sqrt{\pi}\Delta\lambda} \exp\left(-4\ln(2)\left(\frac{\delta\lambda}{\Delta\lambda}\right)^2\right) \quad (6.43)$$

usually works well enough.  $\Delta\lambda$  is the full width at half maximum and  $\delta\lambda := \lambda - \lambda_0$ , whereby  $\lambda_0$  denotes the central wavelength position of the spectral line in question.  $\Delta\lambda$  is related to the spectral resolving power of the spectrograph ( $R = \lambda/\Delta\lambda$ ; see Ch. 4 for details). It is determined empirically by fitting Gaussian profiles to spectral features, which are intrinsically very narrow and, thus, are only instrumentally smeared. For instance, this can be emission lines of the reference lamp used for wavelength calibration (these lines are very narrow due to the lamp's low temperature) or telluric lines<sup>71</sup>.

### Rotational Broadening and Macroturbulence

Rotational broadening results from stellar rotation. It is caused by the varying Doppler shifts of the individual surface elements of a rigid body (star) with radius  $R$ , rotational axis  $\vec{\Omega}$ , and inclination angle  $i$  (see Fig. 6.5.1). For a Cartesian coordinate system that has its origin in the centre of the star and has axes  $x$ ,  $y$ , and  $z$ , whereby the  $z$ -axis coincides with the direction to the observer, the rotational velocity  $\vec{v}$  of a given surface element (described by the vector  $\vec{x}$ ) can be derived from the cross product  $\vec{v} = \vec{\Omega} \times \vec{x}$ . The projected line-of-sight rotational velocity therefore is given by:

$$v_z = y \cdot \underbrace{\Omega_x}_{=0} - x \cdot \underbrace{\Omega_y}_{=\Omega \sin i} = -x\Omega \sin i. \quad (6.44)$$

Thus:

$$|x| \leq R \Rightarrow |v_z| \leq R \Omega \sin i = v_{\text{eq}} \sin i \equiv v_{\text{rot}} \sin i \equiv v \sin i \equiv v_L, \quad (6.45)$$

where  $v_{\text{eq}} \equiv v_{\text{rot}} \equiv v := R \Omega$  denotes the equatorial rotational velocity such that  $v_L = v \sin i$  is the projected equatorial rotational velocity. In astronomy, however, it is common practice to simply refer to  $v \sin i$  as the projected rotational velocity. Typical values of measured projected rotational velocities  $v \sin i$  for stars range from a few  $\text{km s}^{-1}$  up to several hundred  $\text{km s}^{-1}$  for the most massive O-type stars on the main sequence. The detection limit of  $v \sin i$  is given by the typical spectral resolution element of the instrumental profile. For a high-resolution

<sup>70</sup>Typically, the spectral resolving power of the CCD detector is larger than that of the spectrograph used (see Sect. 4.3). Consequently, instrumental smearing mainly is caused by the spectrograph's finite slit width, which defines the resolving power (see Eqs. 4.5 and 4.6).

<sup>71</sup>Telluric lines will be explained in Sect. 8.2.1.

## 6.5. Spectral Line Formation

---

spectrograph such as FEROS (see Sect. 4.4), this is of the order of  $\sim 5\text{-}8 \text{ km s}^{-1}$ .

The rotational broadening profile is obtained by an integration over the whole projected stellar disk. According to Gray (2005), the integration can be performed analytically for a spherical star rotating as a rigid body. The resulting broadening profile in the velocity space is a function of two parameters only ( $v_z/v_L$  and  $\epsilon$ ):

$$\Phi(v_z/v_L, \epsilon) = \frac{2(1 - \epsilon)\sqrt{1 - \left(\frac{v_z}{v_L}\right)^2} + \frac{1}{2}\pi\epsilon\left(1 - \left(\frac{v_z}{v_L}\right)^2\right)}{\pi v_L(1 - \epsilon/3)}. \quad (6.46)$$

Converted into the wavelength space, this yields:

$$\Phi(\delta\lambda/\delta\lambda_L, \epsilon) = \frac{2(1 - \epsilon)\sqrt{1 - \left(\frac{\delta\lambda}{\delta\lambda_L}\right)^2} + \frac{1}{2}\pi\epsilon\left(1 - \left(\frac{\delta\lambda}{\delta\lambda_L}\right)^2\right)}{\pi\delta\lambda_L(1 - \epsilon/3)} \quad (6.47)$$

with the parameter  $\delta\lambda/\delta\lambda_L$  instead of  $v_z/v_L$ . Again,  $v_z$  denotes the projected line-of-sight rotational velocity and  $v_L$  is the projected equatorial rotational velocity.  $\delta\lambda_L := \lambda_0 v \sin(i)/c$  is the maximum wavelength shift, which corresponds to the disk points on the limb at the equator, and  $\delta\lambda := \lambda - \lambda_0$ .  $\lambda_0$  denotes the central wavelength and  $\epsilon = \epsilon(\lambda, T_{\text{eff}}, \log g)$  is the linear limb-darkening<sup>72</sup> coefficient.

Turbulent large-scale mass motions in direction of the surface normal (along the line of sight) can lead to additional Doppler shifts. In contrast to microturbulence, their characteristic dimensions (cells) are well above the usual photon mean free path, which is why these large-scale mass motions are referred to as macroturbulence  $\zeta$ . It is assumed that the macroturbulent velocity vectors with directions along the stellar radius or tangential to the stellar surface are of Gaussian shape. Each of the individual “macrocells” emits an individual spectrum that is Doppler shifted according to the cell’s specific velocity. Physically, macroturbulence in hot massive stars can be interpreted as the collective effect of stellar pulsations, whereas in cool low-mass stars it is mostly driven by granulation on top of the convection zone.

The macroturbulent broadening profile is obtained by an integration over the projected stellar disk and the Gaussian velocity distributions. It has a characteristic “cuspy” shape (see Gray 2005 for details). As in the case of microturbulence, no evidence for macroturbulence has been found in hot subdwarf stars (Geier & Heber, 2012). Therefore, it will not be considered

---

<sup>72</sup>*Limb darkening* describes the observation that the limb of a stellar disk is less bright than its centre. The visible edge of a star is defined by an optical depth of unity ( $\tau_\nu = 1$ , see Sect. 6.1). When an observer looks near the edge of a star, he cannot see to the same optical depth as if he looked at the centre because the line of sight must travel at an oblique angle  $\theta$  through the stellar gas when looking near the limb. In other words, the geometrical distance at which the observer sees the optical depth of unity (the visible edge of the star) increases towards the limb. Due to the temperature decrease from inwards to outwards, observed light from the limb hence results from the cooler outer layers of the stellar atmosphere. This leads to a lower limb intensity compared to the central one. Limb darkening is often approximated by a linear function of  $I(\theta) = I(\theta = 0^\circ) \cdot (1 - \epsilon + \epsilon \cos \theta)$ , which describes the intensity decrease from the centre of the stellar disk ( $\theta = 0^\circ$ ) to the limb ( $\theta = 90^\circ$ ).  $\epsilon$  is called the linear limb-darkening coefficient. Physically, values of  $0 \leq \epsilon \leq 1$  are possible for this coefficient. For most stars, however,  $\epsilon$  is in the range of  $0.3 \lesssim \epsilon \lesssim 0.6$ .

throughout this work (see also Ch. 7).

The Doppler shifts caused by stellar rotation and macroturbulence need to be combined numerically across the stellar disk (point by point) in order to derive the joint macroscopic broadening profile as a function of the three parameters  $v \sin i$ ,  $\epsilon$ , and  $\zeta$ . The combined profile can then be used in order to convolve the calculated synthetic spectrum.

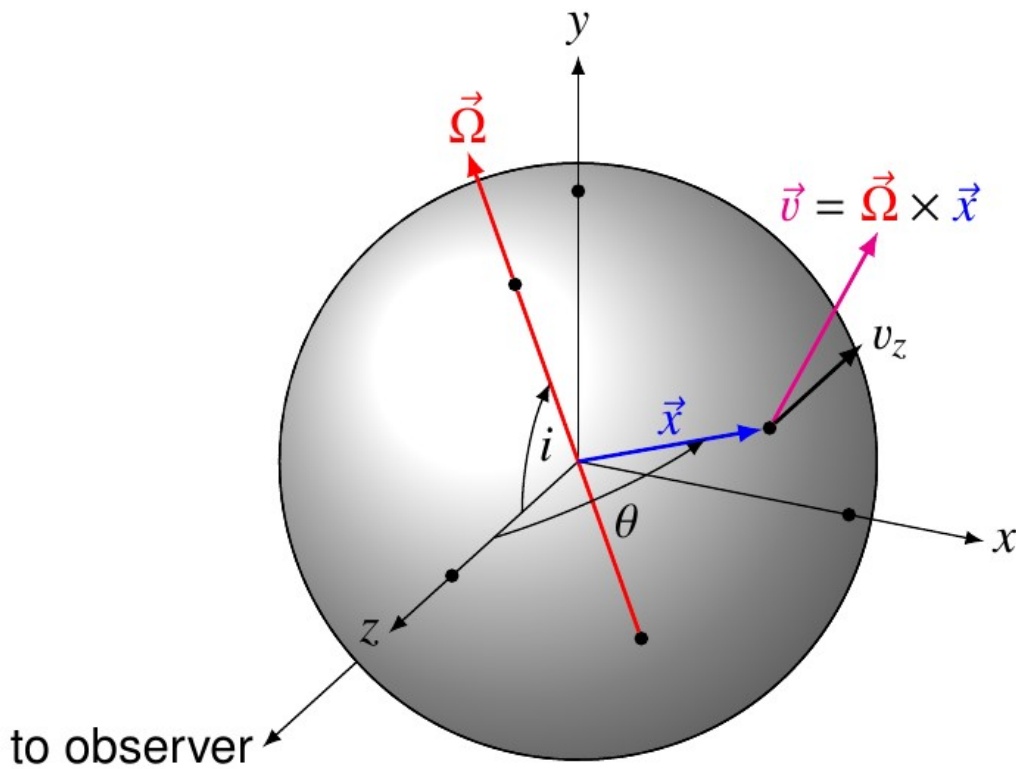


Figure 6.5.1.: Cartesian coordinate system that has its origin in the centre of a star and has axes  $x$ ,  $y$ , and  $z$  (the  $z$ -axis coincides with the direction to the observer) for the illustration of rotational broadening caused by the varying Doppler shifts of the individual surface elements. The vector  $\vec{\Omega}$  describes the direction of the rotational axis,  $i$  is the inclination angle between  $\vec{\Omega}$  and  $z$ ,  $\vec{x}$  describes the vector to a given surface element,  $\theta$  denotes the angle between  $\vec{x}$  and  $z$ , and  $\vec{v} = \vec{\Omega} \times \vec{x}$  is the vector of the rotational velocity of the respective surface element.  $v_z$  denotes the line-of-sight component ( $z$ -component) of  $\vec{v}$ . Produced by A. Irrgang and shared via private communication.

### Pulsational Broadening

Stellar pulsations also may contribute to macroscopic broadening of spectral lines. Such light variations are present throughout the Hertzsprung-Russell diagram and can, for instance, be classified according to the oscillation properties or the driving mechanisms. Different types of pulsations are observed for stars of different evolutionary statuses (main-sequence, red/blue evolved, and compact variable stars) and masses (low, intermediate, and high-mass pulsators). Examples for different classes of oscillators are RR Lyrae Stars, Classical Cepheids,  $\beta$  Cepheids, or slowly pulsating B stars. However, pulsations have also been observed among hot subdwarf stars, in particular for H-sdBs (see also Ch. 3).

The individual pulsational broadening profiles depend on the pulsational velocity field on the surface of the star. Pulsation modes are described by the three quantized numbers  $n$ ,  $l$ , and  $m$  ( $n$  is the number of radial nodes between the centre and the surface of the star,  $l$  denotes the number of surface nodes perpendicular to the pulsational axis, and  $m$  represents the number of surface nodes passing through the pulsational axis). The radial fundamental mode is assigned 0,0,0 ( $n = 0$ ,  $l = 0$ , and  $m = 0$ ). Negative  $n$  denote gravity (g) modes, whereas positive  $n$  describe pressure (p) modes. As different combinations of spherical harmonics  $Y_l^m$  are involved, the pulsational profiles are very complex. For instance, Schrijvers et al. (1997) provided a formulation of a rotating, adiabatically pulsating star, for which atmospheric changes are neglected and the pulsational and rotational axes are assumed to be aligned. However, this model is only valid for slowly rotating stars because it only accounts for the effects of the Coriolis force, but not for those resulting from the centrifugal one. Furthermore, it only considers mono-periodic modes although multiple modes are excited at the same time in most pulsating stars. Despite of all the simplifications, however, the model still has ten free parameters.

In the case of non-radial pulsators, phase-dependent line asymmetries arise, which are characteristic but require a very high spectral resolution to be detected. This is because the corresponding amplitudes are rather small. On the other hand, radial pulsators show a phase-dependent line shift, which can look like the RV line shift observed in SB1 systems. Thus, the phase-dependent line shift may be mistakenly viewed as an indication of an invisible companion. Additionally, the lines are smeared, if the respective exposure time is longer than the pulsation period. In this case, the smearing may be falsely misinterpreted as rotation.

Due to its complexity, the application of pulsational broadening to spectral fitting is beyond the scope of this work. Hence, no pulsations are modelled throughout this work, although some of the program stars are known pulsators (see Sect. 8.1 for details).

### 6.5.3. Level Dissolution

Interactions of atoms/ions (radiators) with neighboring particles (perturbers) affect the electrostatic potential of the atomic nucleus, leading to a consequent distortion of all atomic energy levels. This has already been discussed for pressure broadening in Sect. 6.5.1. However, there is another aspect of distortion called *Debye shielding*, which has not been mentioned yet. This

effect lowers the ionization potential  $\chi_I$  for the radiator in question by a specific amount  $\Delta\chi_I$  which, in addition to the charge of the radiator, depends on the local temperature, on the electron density as well as on the densities and the charges of the other perturbing particles (atoms, ions, protons). Consequently, there is some probability that an energy level of the respective radiator is dissolved, meaning that it lies in the continuum such that the corresponding electron is free and the atom/ion with a given charge  $Z$  in the dissolved state needs to be counted among ions with charge  $Z + 1$ . For hydrogen and singly-ionized helium, which both show several series of spectral lines that are very important for spectral modelling (for instance, the Balmer and the Paschen series for H I as well as the Pickering series for He II; see also Sect. 7.1.1 and Table 8.12), all of this is treated within the concept of the *occupation probability formalism* introduced by Hummer & Mihalas (1988). Later, this formalism was updated by Hubeny et al. (1994). According to the formalism, the LTE occupation number of an atomic energy level  $i$  relative to the total number density of its ionization stage  $I$  (see also Eq. 6.28) can directly be generalized by:

$$\frac{n_i}{N_I} = w_i \frac{g_i \exp(-E_i/k_B T)}{U_I}. \quad (6.48)$$

Here,  $w_i$  denotes the occupation probability that the atom/ion in question is in state  $i$  relative to that in a similar ensemble of non-interacting atoms/ions. Correspondingly,  $1 - w_i$  describes the probability that the state  $i$  is dissolved. The partition function  $U_I$  in this formalism is defined as  $U_I := \sum_{j=0}^{j_{\max}} w_j g_j \exp(-E_j/k_B T)$ .

The rate equations in their original form (see Eq. 6.32) need to be rewritten to account for level dissolution. This is done by multiplying any transition rate by the occupation probability of the final state, that is,  $R_{ij} \rightarrow w_j R_{ij}$ ,  $C_{ij} \rightarrow w_j C_{ij}$ ,  $R_{ji} \rightarrow w_i R_{ji}$ , and  $C_{ji} \rightarrow w_i C_{ji}$ . Additionally, effective total ionization and recombination rates need to be defined. Despite of all the modifications, however, the resulting rate equations resemble the original ones (see Hubeny & Mihalas 2014 for further information).

## 6.6. Metal Line-Blanketing and Treatment of Opacity

As described at the beginning of Sect. 6.5, the absorption of photons of specific energies by hydrogen, helium, and the different metals in the atmosphere causes absorption lines in the respective stellar spectrum. For the O and B-type stars that are investigated in this work, iron-group elements are the main opacity sources. In particular, Fe and Ni have a huge number of atomic transitions in the UV (*line forest*), therefore significantly blocking the outgoing flux. According to radiative equilibrium (see Sect. 6.2), however, the total net flux (integrated over all frequencies) is conserved. Hence, the absorbed energy (flux) in the UV is redistributed to other (optical) frequencies, thereby also increasing the respective continuum flux. According to Haas (1997), a steeper temperature gradient in the region where the continuum originates is required in order to drive the flux because the absorption lines restrict the bandwidth of the spectrum in which the energy transport is efficient. This leads to higher temperatures

## 6.7. The LTE Approach

---

of  $\sim 1000$  K to  $\sim 2000$  K (Dorsch, 2017) in the line-forming region of optical absorption lines such as the ones associated with hydrogen and helium (*backwarming effect*). At the same time, the outer parts of the stellar atmosphere, where many metal lines in the UV are formed, are cooled significantly (*surface cooling*). The collective effect of backwarming and surface cooling is referred to as (*metal*) *line-blanketing*.

There are basically two different ways to treat opacity when modelling a stellar atmosphere. One has to distinguish between *opacity distribution functions* (ODFs) and *opacity sampling* (OS). Calculated only once for a certain (standard) chemical composition and tabulated as a function of frequency, temperature, and pressure, ODFs simplify the detailed line opacity distribution to a smooth monotonic function, whereby an adequate number of discrete frequency intervals is used for resampling. Hence, an interpolation of the precalculated ODF values allows to quickly access the source function. OS, however, samples the line opacity for each chemical element in each layer of the atmosphere on a suitable grid of frequency points. The total opacity for each frequency point in a specific atmospheric layer then is calculated by summing up the corresponding opacities associated with the individual elements. In this way, the direct influence of all surrounding spectral lines on a given frequency point is taken into account. Thus, OS treats opacity at a higher accuracy level than ODFs. However, it also needs much more computation time as the radiative transfer is evaluated for the chosen number of frequency points. In contrast to ODFs, OS is very flexible and can also be applied to stars with non-standard chemical compositions because the opacities are directly calculated for the current atmosphere to be set up.

Sections 6.1-6.6 summarized the general concepts of modelling stellar atmospheres. In the following Sects. 6.7-6.9, the different model atmosphere approaches used in this work will be described.

## 6.7. The LTE Approach

The LTE approach has been used successfully for a large set of several hundred hot subdwarf stars (see, for instance, Maxted et al. 2001; Edlmann et al. 2003; Morales-Rueda et al. 2003b; Lisker et al. 2005; Stroeer et al. 2007; Copperwheat et al. 2011; Geier et al. 2013a). It is based on synthetic spectra obtained from the metal line-blanketed LTE model atmospheres of Heber et al. (2000), who used an updated version of the LTE code of Heber et al. (1984), whereby Kurucz' ATLAS6 ODFs were included. Plane-parallel and chemically homogeneous model atmospheres in hydrostatic and radiative equilibrium were computed. For the spectral synthesis of the hydrogen Balmer lines (from  $H_\alpha$  up to  $H_{22}$ ) as well as of He I and He II lines in the optical, Michael Lemke's version of the LINFOR<sup>73</sup> program was used (see Heber et al. 2000 for details). No metals were synthesized. For hydrogen, extended Stark broadening tables according to Lemke (1997) were used. These were computed based on the unified

---

<sup>73</sup>The LINLTE.FOR (LINFOR) program was originally developed by Holweger, Steffen, and Steenbock at Kiel University.

Table 6.2.: LTE model grids used for the quantitative spectral analyses (see Ch. 9) of the program stars presented in Sect. 8.1.

LTE (solar metallicity)			LTE (supersolar metallicity)		
Parameter	Grid size	Step size	Parameter	Grid size	Step size
$T_{\text{eff}}$	10 000 K to 40 000 K	2500 K	$T_{\text{eff}}$	27 500 K to 45 000 K	2500 K
$\log(g)$	4.5 to 6.5 <sup>b</sup>	0.25	$\log(g)$	5.0 to 6.5	0.25
$\log n(^4\text{He})^a$	-4.0 to -0.3	0.5 to 1.0	$\log n(^4\text{He})^a$	-3.0 to -1.0	0.5 to 1.0

**Notes:**

(a)  $\log n(^4\text{He}) := \log \left[ \frac{N(^4\text{He})}{N(\text{H})} \right]$

(b) For the coolest program stars analyzed in this work, that is, blue horizontal branch and main-sequence stars, a range between 3.5 and 5.0 with the same step size is used. However, the model grid has gaps in this regime because models for some combinations of  $T_{\text{eff}}$  and  $\log(g)$  values were not calculated by Heber et al. (2000). Hence, some of the program stars of this work cannot be fitted making use of the LTE approach.

theory of Stark broadening from Vidal, Cooper & Smith (VCS; Vidal et al. 1970, 1971, 1973). For He I 4026 Å, 4388 Å, and 4922 Å, Stark broadening tables according to Shamey (1969) were used. For He I 4471 Å, those of Barnard et al. (1974) were applied, whereas for various other neutral helium lines the results of Dimitrijevic & Sahal-Brechot (1990) were implemented. Furthermore, Stark broadening according to Schoening & Butler (1989) was applied to various singly-ionized helium lines, including He II 4101 Å, 4200 Å, 4339 Å, 4542 Å, 4686 Å, 4860 Å, 5412 Å, and 6561 Å. However, no level dissolution was implemented. The calculated synthetic spectra cover the spectral range of 3300-7000 Å. Consequently, neither the hydrogen Paschen and Brackett series nor available helium lines in the NIR can be fitted with the LTE models. The LTE model grids used in this work are based on solar and supersolar (10 times solar) metallicity. While the solar metallicity grid will be chosen for program stars with moderate effective temperatures of  $T_{\text{eff}} \lesssim 30\,000$  K, the hotter H-sdOB program stars will be fitted with supersolar metallicity (see Sect. 8.1 for a detailed overview of the analyzed stars). This is due to a substantial improvement of the fit quality as first shown by O'Toole & Heber (2006). Later, this procedure was taken over by Copperwheat et al. (2011) and Geier et al. (2013a). Table 6.2 lists the two LTE model grids and their individual multi-dimensional meshes spanned by the effective temperature  $T_{\text{eff}}$ , the surface gravity  $\log(g)$ , and the helium abundance  $\log n(^4\text{He}) := \log \left[ \frac{N(^4\text{He})}{N(\text{H})} \right]$ . For the coolest program stars analyzed in this work, that is, blue horizontal branch and main-sequence stars (see also Sect. 8.1), the covered  $\log(g)$  values range from 3.5 to 5.0.

## 6.8. ATLAS, DETAIL, SURFACE (ADS): The Hybrid LTE/NLTE Approach

As outlined at the end of Sect. 6.4, NLTE model atmosphere calculations are very time consuming. For the O and B-type program stars analyzed in this work, however, atmospheric NLTE effects are not negligible because of the high effective temperatures of these stars and the resulting high atmospheric photon fluxes. On the other hand, the effective temperatures and the surface gravities of many of these stars ensure that the departures from LTE affect the occupation numbers (occupation number densities) associated with the atmospheric chemical elements, but only have a marginal effect on the atmospheric temperature-density stratification for the optical depths that are relevant for the formation of the observable line spectra and continua (see also Sect. 6.4). This calls for a hybrid LTE/NLTE approach, in which the structural equations are solved in LTE and the level populations are subsequently derived from statistical equilibrium, allowing for departures from LTE. In addition, this approach is a good compromise in terms of metal line-blanketing, which may be of great importance for hot subdwarf stars, because it also allows to include very detailed line-blanketing for the atmospheric stratification at moderate computing costs.

The hybrid approach has been proven to be fully consistent with NLTE modelling of A and B-type stars (see, for instance, the results of Przybilla et al. 2006a, 2006b, 2011; Nieva & Przybilla 2007, 2008). It has also been successfully applied to hot subdwarf B stars and blue horizontal branch stars (see, for instance, Przybilla 2005; Geier et al. 2007; Latour et al. 2016; Schneider 2017; Schneider et al. 2017, 2018; Hämmerich 2020). Moreover, its sophistication has been improved constantly throughout the last decade (Irrgang et al., 2014, 2018). The hybrid approach is based on the four generic codes ATLAS9 (Kurucz, 1993), ATLAS12 (Kurucz 1996, extended and updated by Irrgang et al. 2018), DETAIL, and SURFACE (Giddings 1980; Butler & Giddings 1985, extended and updated by Irrgang et al. 2018), hereafter ADS. Following the approach of Irrgang et al. (2018), its basic concepts shall be described in the following (see also Fig. 6.8.1):

1. **ATLAS9:** In a first step, the model atmosphere is divided into 72 layers. Based on the chosen atmospheric parameter set (see Sect. 7.1.2 for further details), an initial guess of the atmospheric structure is obtained by solving the structural equations in LTE, whereby the line opacity is treated with ODFs. The resulting ATLAS9 model atmosphere serves as a starting point to speed up the following calculations.
2. **ATLAS12:** Next, the calculated ATLAS9 model atmosphere is passed to ATLAS12. Now, a more detailed plane-parallel and chemically homogeneous model atmosphere in hydrostatic and radiative equilibrium is computed in LTE. To cope with metal line-blanketing, the opacity is treated in a more detailed way making use of the OS approach. Furthermore, the mean abundance pattern for H-sdB/H-sdOB stars according to Naslim et al. (2013) is underlain (see also Table 3.1).
3. **DETAIL:** Based on the calculated ATLAS12 model atmosphere, the statistical equilibrium and the radiative transfer for hydrogen, helium, and the metals included (only one at a

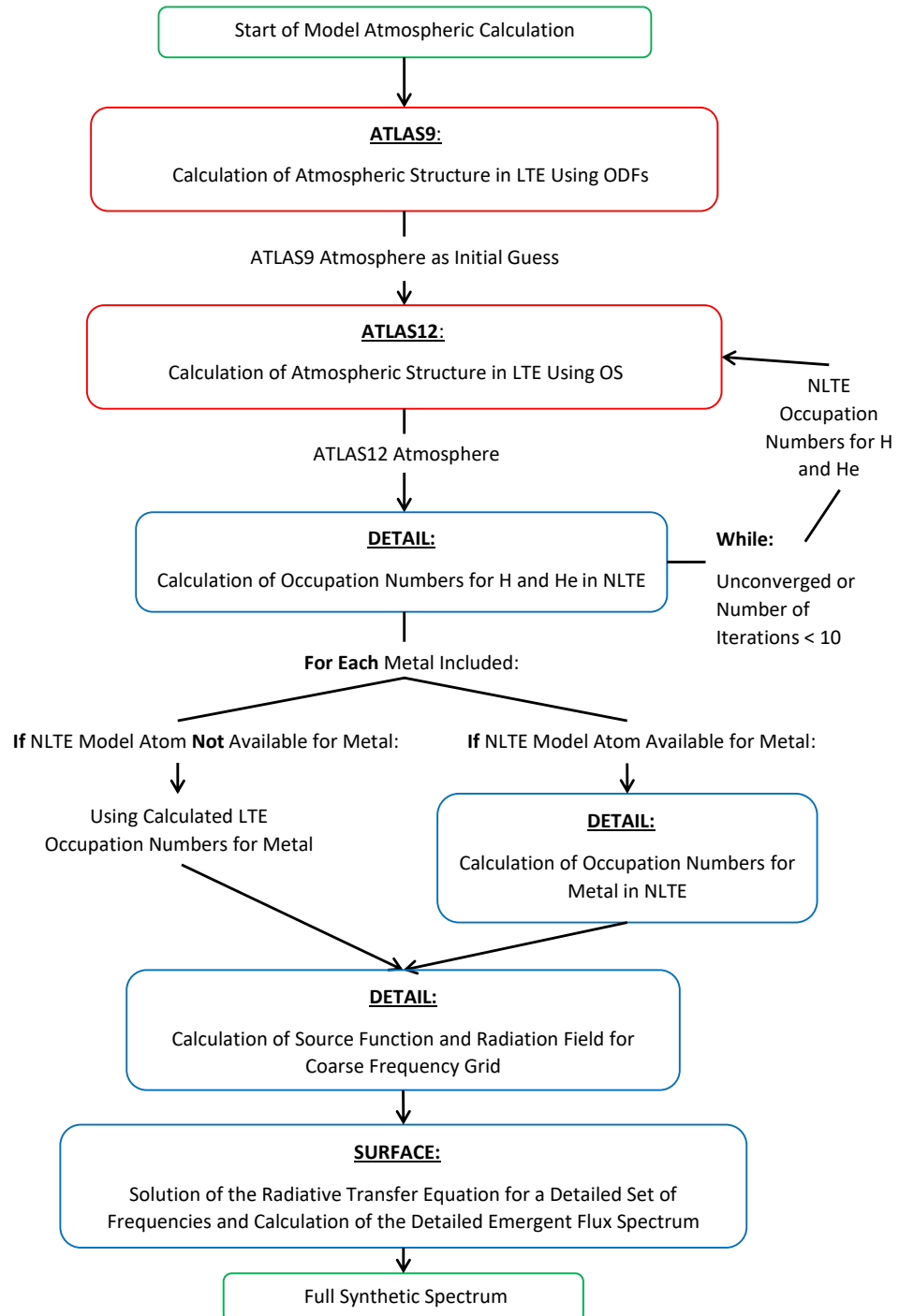


Figure 6.8.1.: Scheme of the hybrid LTE/NLTE model atmosphere approach based on the four generic codes ATLAS9/ATLAS12 (red), DETAIL, and SURFACE (blue). Modified version of Figure 4.1 in Hämmereich (2020).

time) are simultaneously solved within DETAIL, whereby detailed NLTE model atoms are used if available (see Table 6.3). The rate equations for the individual metals are solved making use of LTE occupation numbers for the other “background” metals. All of this is done via an ALI scheme with an appropriate approximate lambda operator (Rybicki & Hummer, 1991). In this way, DETAIL delivers the accessible NLTE occupation numbers, the source function and, hence, the radiation field. However, DETAIL only uses a relatively coarse grid in order to calculate the frequency-dependent source function. Additionally, only approximated line-broadening profiles are used for the spectral synthesis, which is not sufficient to reproduce the actual shape of observed spectral lines.

In the original ADS approach, the radiative transfer is considered in NLTE, but not the temperature-density stratification. However, DETAIL has been updated by Irrgang et al. (2018) in order to deal with NLTE feedback on the atmospheric structure, at least to some extent. For this purpose, DETAIL passes the NLTE occupation numbers for hydrogen and helium back to ATLAS12 before metals are included. Then, ATLAS12 calculates a refined atmospheric structure based on the given NLTE input. Once finished, the refined structure is again passed to DETAIL, which derives updated NLTE occupation numbers for hydrogen and helium, and the whole process starts all over. This iterative process either stops when changes of the temperature structure become small enough (less than one per thousand) or when ten iterations are reached.

As mentioned at the beginning of this section, departures from LTE are not that important for the atmospheric temperature-density stratification of many of the O and B-type stars analyzed in this work, at least for the optical depths that are relevant for the formation of the observable line spectra and continua. However, a refined atmospheric structure generally ensures a more realistic representation of the SED<sup>74</sup>.

Irrgang et al. (2018) also modified the ADS code in order to account for level dissolution of the H I and He II levels as described by Hubeny et al. (1994). Amongst others, this allows to exploit the region around the Balmer ( $\sim 3600\text{--}3800 \text{ \AA}$ ) and the Paschen ( $\sim 8150\text{--}8850 \text{ \AA}$ ) jump, which can be resolved in medium and high-resolution spectra of appropriate wavelength coverage. Both jumps are important indicators for the effective temperature and the surface gravity (see Sect. 7.1.1 for details). However, the proper implementation of level dissolution is also useful in terms of SED fitting at lower resolutions.

4. **SURFACE:** DETAIL’s occupation numbers are passed to SURFACE, which is responsible for the detailed spectral synthesis of the emergent flux spectrum. To this end, SURFACE evaluates the formal solution of the radiative transfer equation (Eq. 6.10) on a sufficiently fine frequency grid. The emergent flux is calculated by inserting this solution into Eq. (6.5), whereby the integration in Eq. (6.5) only covers one hemisphere of the star ( $0 \leq \theta \leq \pi/2$ ). In order to obtain a normalized synthetic spectrum, the emergent flux at a certain frequency point is divided by the respective continuum flux. SURFACE also makes use of realistic state-of-the-art line-broadening functions, that is, Stark broadening for hydrogen according to Tremblay & Bergeron (2009) and Stark broadening for

---

<sup>74</sup>The SED fitting procedure based on ADS models will be described in Sect. 7.2.

He I according to Beauchamp et al. (1997). The latter is used in the parameter space of  $T_{\text{eff}}$ ,  $\log(g)$ , and  $\log n(\text{He})$ , for which the respective atmospheric electron densities of the helium line formation depths are available. Otherwise, Stark broadening tables for He I according to Dimitrijevic & Sahal-Brechot (1990) are implemented. For He II, Stark broadening according to Schoening & Butler (1989) is applied.

The NLTE part of ADS, that is, the solution of the rate equations and the subsequent calculation of the source function and the radiative transfer, requires detailed knowledge of the underlying atomic data. Consequently, sophisticated NLTE model atoms are used. For instance, these model atoms contain information on the energy levels, the transition probabilities, and the cross sections for the interactions of photons with other material particles. The model atoms can be adjusted to the specific science case in terms of atomic transitions and ionization stages considered for a particular chemical element. A list of ionization stages for elements (treated in NLTE), which are observed in the stellar spectra of the O and B-type program stars of this work, can be found in Table 6.3. Therein, also the references for the underlying NLTE model atoms are listed. For the  $^3\text{He}$ -enriched program stars analyzed in this work, a detailed  $^3\text{He}$  model atom is used. This model atom has already been successfully applied by Maza et al. (2014a) and Schneider et al. (2018). It is identical to that of  $^4\text{He}$  developed by Przybilla (2005), except that isotopic line shifts according to the *Atomic Spectra Database* of the National Institute of Standards and Technology (NIST<sup>75</sup>) are taken into account (see also Sect. 3.3 and Schneider et al. 2018 for more details). Due to the overlap of their spectral lines, both isotopes ( $^3\text{He}$  and  $^4\text{He}$ ) are treated simultaneously during the solution of the statistical equilibrium and radiative transfer equations within DETAIL/SURFACE.

Additional metals observed in the stellar spectra of the analyzed program stars, for which NLTE model atoms are not available (these elements are: P, Ca, Ti, Sr, and Zr; see also Ch. 11), are treated in LTE and the corresponding DETAIL part is left out. As described in Sect. 6.4, the partition functions are used to calculate the ionization fractions in these cases. Furthermore, as in the case of the NLTE metals, the energies of the lower levels of transition, the corresponding statistical weights, and the respective central transition wavelengths are needed. In order to calculate individual spectral line shapes, up-to-date oscillator strengths are used.

Model spectra are calculated considering only hydrogen, helium and one metal at a time (HHE + X). A model spectrum, which contains the spectral lines of a single metal only, results from the division of the (HHE + X)-model by a HHE-only model with the same spectroscopic parameters. A full model spectrum that includes spectral lines for all metals as well as for hydrogen and helium is generated by multiplying all of the single-metal spectra with each other and with the corresponding HHE-only model (this will be detailed in Sect. 7.1.2). Although being very effective, this method also has a big disadvantage, namely that no line blends of any kind can be analyzed. This is not so much of a problem for the O and B-type program stars investigated in this work, but for cool stars that show crowded spectra with lots of line blends<sup>76</sup>.

<sup>75</sup>[https://physics.nist.gov/PhysRefData/ASD/lines\\_form.html](https://physics.nist.gov/PhysRefData/ASD/lines_form.html), last called on 13th February 2021

<sup>76</sup>The NLTE model approach based on TLUSTY/SYNPEC, which is presented in Sect. 6.9, does not use a multiplicative method for the calculation of full model spectra. However, this approach comes along with

Table 6.3.: Model atoms for NLTE calculations used for the hybrid LTE/NLTE approach.

Ion	Model atom reference
H I	Przybilla & Butler (2004)
He I/II	Przybilla (2005)
C II/III	Nieva & Przybilla (2006, 2008)
N II/III	Przybilla & Butler (2001) <sup>a</sup>
O I/II	Przybilla et al. (2000), Becker & Butler (1988) <sup>a</sup>
Ne I/II	Morel & Butler (2008) <sup>a</sup>
Mg II	Przybilla et al. (2001)
Al II/III	Przybilla (in prep.), Irrgang et al. (2014)
Si II/III/IV	Przybilla & Butler (in prep.), Irrgang et al. (2014)
S II/III	Vrancken et al. (1996) <sup>a</sup> , Irrgang et al. (2014)
Ar II	Butler (in prep.), Irrgang et al. (2014)
Fe II/III	Becker (1998), Morel et al. (2006) <sup>a</sup>

**Notes:**<sup>(a)</sup> Updated and corrected as described in Nieva & Przybilla (2012).

A complete synthetic spectrum calculated with ADS includes spectral lines of hydrogen (H I), helium (He I/II), and various metals. The latter are considered either in NLTE (C II/III, N II/III, O I/II, Ne I/II, Mg II, Al II/III, Si II/III/IV, S II/III, Ar II, and Fe II/III; see Table 6.3) or in LTE (P II, Ca II, Ti II, Sr II, and Zr II) and their calculated sharp line profiles are ideal for precise projected rotational velocity measurements. The wavelength coverage of ADS spectra can be adjusted to the spectral range of the observations. In contrast to the LTE approach, ADS models therefore allow to fit the NIR spectral range covering the hydrogen Paschen and Brackett series as well as several useful helium lines (see also Table 8.12). In Table 6.4, the covered  $T_{\text{eff}}$  and  $\log(g)$  ranges of the full hybrid LTE/NLTE model grid calculated for the purpose of this work are listed on the left-hand side. (Isotopic) helium as well as metal abundances are adjusted individually to the program stars, allowing for detailed  $^3\text{He}$ ,  $^4\text{He}$ , and metal abundance analyses. For the blue horizontal branch and main-sequence stars analyzed in this work, which are not covered by the main grid, small appropriate grids are calculated, whereby the same step sizes as given in Table 6.4 are used.

---

significantly longer computation times, mostly due to the sophisticated NLTE treatment. This is the main reason why the metal abundance analysis presented in Ch. 11 is based on the hybrid LTE/NLTE model atmosphere approach rather than on model spectra calculated with TLUSTY/SYNSPEC.

## 6.9. TLUSTY/SYNSPEC: The NLTE Approach

Complex model atmospheres in NLTE and the corresponding synthetic spectra are calculated with the latest versions of the public codes TLUSTY 205 and SYNSPEC 51 (Hubeny, 1988; Hubeny & Lanz, 1995, 2003, 2017a,b,c). TLUSTY also makes use of an ALI scheme, in which an appropriate approximate lambda operator is implemented (see Hubeny & Mihalas 2014 for details). By simultaneously treating a large number of metal line transitions in NLTE, its great strength is the accurate atmospheric modelling of compact hot stars. However, the atmospheres of the hottest stars or of low-surface gravity objects (for instance, Wolf-Rayet stars) cannot be modelled properly with TLUSTY because the code is not able to consider the stellar winds that become important for these objects. In this work, TLUSTY NLTE models hence will be primarily used in order to determine the atmospheric parameters of the hot program stars with  $T_{\text{eff}} \gtrsim 30\,000\text{ K}$ . In particular, this includes the hot subdwarf O/OB stars (either hydrogen or helium-rich), for which departures from LTE are large. As is the case for the LTE and the hybrid LTE/NLTE approach, the NLTE models are calculated in radiative and hydrostatic equilibrium and plane-parallel geometry as well as chemical homogeneity are assumed. Possible stratification due to diffusion effects therefore is neglected. However, level dissolution of the H I and He II levels according to Hubeny et al. (1994) is implemented. To save computation time and because of the fact that the temperature-density stratification in the hydrogen and helium line-forming regions is already quite well constrained once the most abundant metals are included as absorber material (see Schindewolf et al. 2018 for details), no fully opacity-sampled metal line-blanketed models, which would include C, N, O, Ne, Mg, Al, Si, P, S, Fe, and Ni, are calculated. Instead, the approach of Németh et al. (2012) is realized, focusing on carbon, nitrogen, and oxygen that are most prominent for helium-rich subdwarf O stars. Starting with model atmospheres that include only hydrogen and helium in NLTE, more detailed models are constructed within TLUSTY by adding C, N, and O in small steps in order to make sure that the models converge properly. This is the case if the relative changes of temperatures, occupation number densities, electron densities, and mean intensities of radiation in discretized frequency points, which are all described by a set of state vectors for given discretized depth points, fall below a value of  $10^{-3}$ . The goal is to construct complex HHeCNO model atmospheres based on the mean metallicities for H-sdB/H-sdOB stars (Naslim et al. 2013; see also Table 3.1). Based on these model atmospheres, H I and He I/II as well as C II/III/IV, N II/III/IV/V, and O II/III/IV are subsequently synthesized within SYNSPEC. For this, a separate line list is used. This list specifies the energies of the lower levels of transition, the central transition wavelengths, the oscillator strengths as well as the necessary total angular momentum quantum numbers (statistical weights). The same model atoms as used by TLUSTY are applied to SYNSPEC (see Table 6.5 for details). Each of the different model atoms contains the necessary information on energy levels, transition probabilities, and photoionization cross sections. For each atom/ion, the ground state of the next higher ionization stage is also included. In order to obtain detailed line-broadened synthetic spectra, Stark broadening tables for H I according to Tremblay & Bergeron (2009), for He I 4026 Å, 4388 Å, and 4922 Å according to Shamey (1969) and for He I 4471 Å according to Barnard et al. (1974) are used. To He II 4101 Å, 4200 Å, 4339 Å, 4542 Å, 4686 Å, 4860 Å, 5412 Å,

## 6.9. TLUSTY/SYNSPEC: The NLTE Approach

Table 6.4.: Hybrid LTE/NLTE and NLTE model grids used for the quantitative spectral analyses (see Ch. 9) of the program stars presented in Sect. 8.1.

Hybrid LTE/NLTE			NLTE		
Parameter	Grid size	Step size	Parameter	Grid size	Step size
$T_{\text{eff}}$	20 000 K to 45 000 K <sup>d</sup>	1000 K	$T_{\text{eff}}$	30 000 K to 50 000 K	1000 K
$\log(g)$	5.0 to 6.2 <sup>d</sup>	0.2	$\log(g)$	5.0 to 6.2	0.2
$\log n(^4\text{He})^a$	$e$	0.2	$\log n(^4\text{He})^a$	-4.0 to +4.0	0.5
$\log n(^3\text{He})^b$	$e$	0.2	-	-	-
$\log n(X)^c$	$e$	0.2	-	-	-

**Notes:**

(a)  $\log n(^4\text{He}) := \log \left[ \frac{N(^4\text{He})}{N(\text{H})} \right]$

(b)  $\log n(^3\text{He}) := \log \left[ \frac{N(^3\text{He})}{N(\text{H})} \right]$

(c)  $\log n(X) := \log \left[ \frac{N(X)}{N(\text{all elements})} \right]$ , where  $X \in \{\text{C, N, O, Ne, Mg, Al, Si, P, S, Ar, Ca, Ti, Fe, Sr, Zr}\}$ .

(d) For the coolest program stars analyzed in this work (blue horizontal branch and main-sequence stars), which are not covered by the main grid, small appropriate grids with the same step sizes are used.

(e) Depending on the individual star.

Table 6.5.: Ions for which detailed model atoms are used in the model atmosphere calculations with TLUSTY/SYNSPEC.

Ion	L	SL	Ion	L	SL	Ion	L	SL	Ion	L	SL	Ion	L	SL
H I	16	1	He I	24	0	C II	17	5	N II	32	10	O II	36	12
			He II	20	0	C III	34	12	N III	25	7	O III	28	13
						C IV	21	4	N IV	34	14	O IV	31	8
									N V	10	6			

**Notes:** For each atom/ion, the ground state of the next higher ionization stage is also included, but is not listed here. The number of levels (L) and superlevels (SL) is listed. The idea of *superlevels* consists of grouping several (possibly many) individual energy levels together, whereby it is assumed that all genuine levels within a superlevel are in Boltzmann equilibrium with respect to each other (see Eq. 6.27). For this to work, levels forming a superlevel have to exhibit close energies and similar properties. For instance, they can belong to the same multiplet or to the same spin system. Alternatively, they can have the same parity.

6561 Å, and 10 125 Å, Stark broadening according to Schoening & Butler (1989) is applied. The treatment of Dimitrijevic & Sahal-Brechot (1984), which is available for numerous He I lines, is not realized. Instead, all neutral helium line profiles that are not included in the Shamey (1969) or Barnard et al. (1974) tables are treated by a Voigt profile with appropriate natural, Stark, and van der Waals damping parameters according to Kurucz (1979). For more information, see also Hubeny & Lanz (2017a).

The right-hand side of Table 6.4 summarizes the atmospheric parameter coverage of the full NLTE model grid calculated for the purpose of this work. Helium abundances range from

-4.0 to +4.0 such that the helium-rich subdwarf O program stars are covered. Moreover, the calculated synthetic spectra have a wavelength coverage of  $3400 \leq \lambda \leq 13\,500 \text{ \AA}$ . Therefore, they also cover the hydrogen Paschen series. It is important to note, however, that no metal abundances can be derived from the calculated NLTE model grid. C, N, and O are only synthesized according to their mean abundances in H-sdB/H-sdOB stars (Naslim et al. 2013; see also Table 3.1), but not for varying abundances.

## 7. Combined Spectrophotometric and Astrometric Analysis

This chapter presents the general concepts of the combined spectrophotometric and astrometric analysis approach, a tool which is used in stellar astronomy in order to determine the fundamental stellar parameters, that is, the radius  $R$ , the luminosity  $L$ , and the mass  $M$  of a certain star. This approach combines astrometric data (parallaxes  $\varpi$ ) with results derived both from spectroscopy (effective temperature  $T_{\text{eff}}$ , surface gravity  $\log g$ ) and photometry (stellar angular diameter  $\theta$ ).

Section 7.1 presents the general concept of the *quantitative spectral analysis*. While Sect. 7.1.1 describes the fit parameters and discusses their individual influence on spectral fitting, Sect. 7.1.2 details two different strategies on how to perform quantitative spectral analyses (a selective and a global approach), which are used and compared within the framework of this thesis (see Ch. 9 for details). In Sect. 7.2, a detailed overview of SED fitting to appropriate photometric data is given. The chapter concludes with a summary on how to determine  $R$ ,  $L$ , and  $M$  from the individual spectrophotometric and astrometric parameters involved (Sect. 7.3).

### 7.1. Quantitative Spectral Analysis

The quantitative spectral analysis allows to determine the atmospheric parameters of stars ( $T_{\text{eff}}$ ,  $\log g$  as well as the hydrogen and the helium abundance) by fitting precalculated grids of synthetic spectra to real observations (see Ch. 6 for details on how to set up a model atmosphere and for detailed information on the different model grids used in the context of this work). In this way, also the RV  $v_{\text{rad}}$ , the projected rotational velocity  $v \sin i$ , the micro-turbulence  $\xi$ , the macroturbulence  $\zeta$ , and the individual metal abundances can be derived.

#### 7.1.1. Spectral Fitting

Due to the fact that the effective temperature, the surface gravity, and the helium and hydrogen abundances are correlated, these parameters cannot be determined separately from spectral fitting, but rather need to be derived simultaneously during the fitting process. In fact, a similar correlation also holds for  $\xi$  and  $\zeta$ . The spectroscopic fit parameters mentioned are primarily constrained from characteristic spectral line features. It is necessary to explain these line features in order to understand the influence of the individual parameters on synthetic model

spectra that are used to match the observations. In Fig. 7.1.1, the effects of variations of the individual spectroscopic fit parameters on selected spectral lines are shown. In the following, these individual parameters and their respective effects on characteristic spectral line features will be discussed. The text sections below are based on the elaborations of Irrgang (2014) and Schneider (2017).

## Radial Velocity

The line-of-sight component of the motion of the target causes a Doppler shift of the observed spectrum, which can be described by a velocity defined as  $v := v_{\text{rad}} + v_{\text{bary}}$ .  $v_{\text{rad}}$  is the RV with respect to the barycentre (the mass centre of the solar system).  $v_{\text{bary}}$  describes the season-dependent component caused by Earth's rotation and its motion around the barycentre. The well-known Doppler formula:

$$\frac{\lambda - \lambda_0}{\lambda_0} = \frac{v}{c} = \frac{v_{\text{rad}} + v_{\text{bary}}}{c} \quad (7.1)$$

can be used to derive  $v_{\text{rad}}$ . Here,  $c$  is the vacuum speed of light,  $\lambda$  denotes the observed wavelength, and  $\lambda_0$  is the rest-frame wavelength.  $v_{\text{bary}}$  ranges from  $\sim -30$  to  $\sim +30 \text{ km s}^{-1}$ , depending on the coordinates of the target, the telescope site, and the time of observation. Since all of these parameters are known, it is possible to precisely determine  $v_{\text{bary}}$  and to correct for it. According to Eq. (7.1), however, this can only be done in combination with  $v_{\text{rad}}$ :

$$\lambda_0 = \frac{\lambda}{1 + v/c} = \frac{\lambda}{1 + (v_{\text{rad}} + v_{\text{bary}})/c} . \quad (7.2)$$

However, the error that is introduced if the barycentric correction is applied in a first step and  $v_{\text{rad}}$  is only measured in a second step is negligible (Irrgang, 2014). In practice, the barycentric corrected wavelength  $\lambda_{\text{corr}}$  hence can be calculated via:

$$\lambda_{\text{corr}} = \frac{\lambda}{1 + v_{\text{bary}}/c} . \quad (7.3)$$

The RV  $v_{\text{rad}}$  can then simply be determined via:

$$v_{\text{rad}} = \frac{\lambda_{\text{corr}} - \lambda_0}{\lambda_0} c . \quad (7.4)$$

The effect of  $v_{\text{rad}}$  variations on spectral lines is shown in the upper left-hand panel of Fig. 7.1.1. While positive values of  $v_{\text{rad}}$  lead to a spectrum that is red-shifted towards higher wavelengths (lower frequencies), negative values of  $v_{\text{rad}}$  shift the spectrum towards lower (bluer) wavelengths, that is, higher frequencies.

## 7.1. Quantitative Spectral Analysis

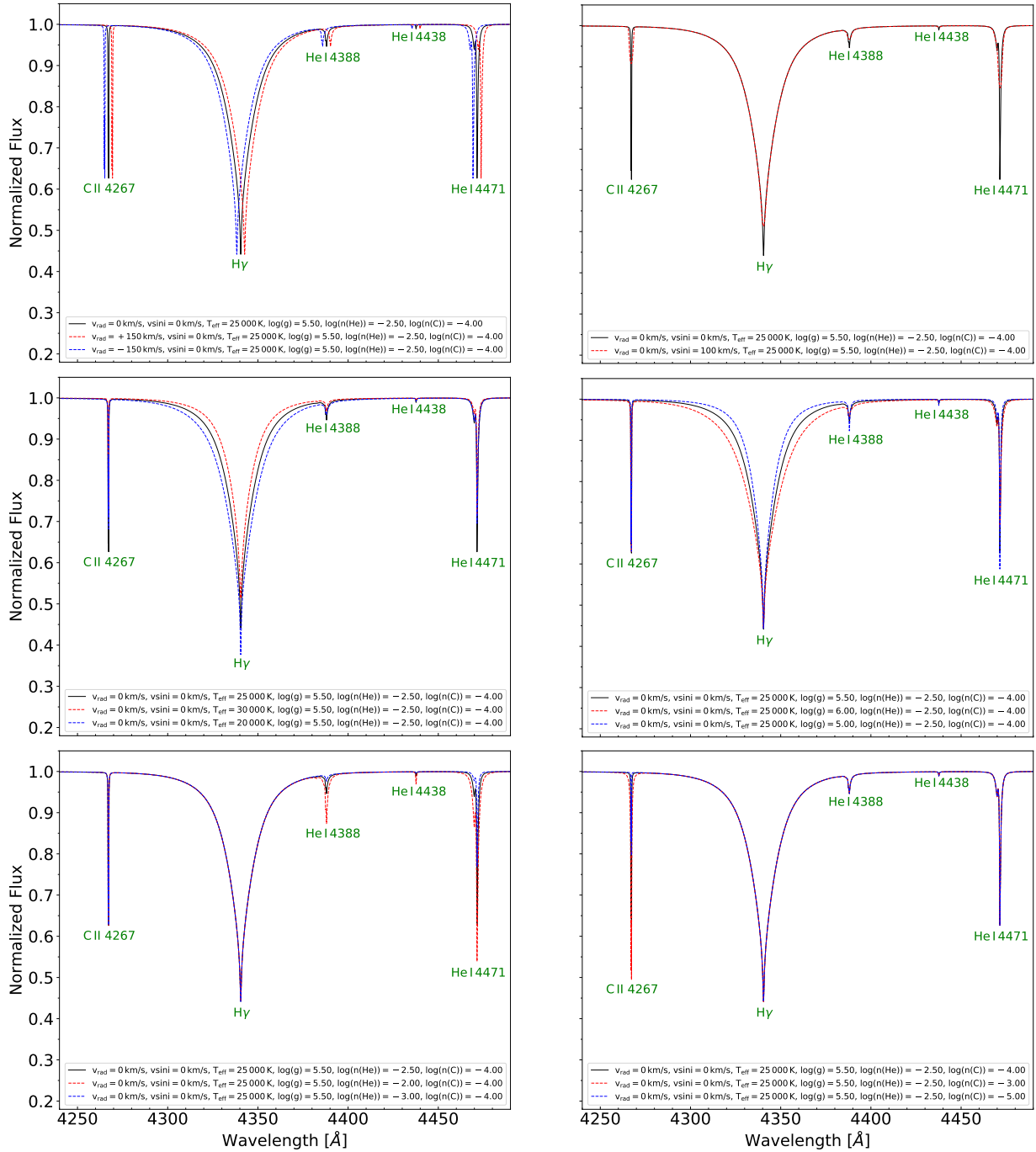


Figure 7.1.1.: Effects of variations of selected spectroscopic fit parameters on hydrogen, helium, and carbon spectral line shapes in a model spectrum. The original reference model ( $v_{\text{rad}} = 0 \text{ km s}^{-1}$ ,  $v \sin i = 0 \text{ km s}^{-1}$ ,  $T_{\text{eff}} = 25\,000 \text{ K}$ ,  $\log g = 5.50$ ,  $\log(n(\text{He})) = -2.50$ , and  $\log(n(\text{C})) = -4.00$ ) is shown as a solid black line in all six panels. The dashed red and blue lines represent new models after increasing or decreasing one of the respective parameters (see the legends of the individual panels for details). For all models, the microturbulence  $\xi$  and the macroturbulence  $\zeta$  are set to zero. Moreover, the mean metallicity for H-sdB/H-sdOB stars (Naslim et al. 2013; see also Table 3.1) is used in all cases.

### Projected Rotational Velocity

The projected rotational velocity  $v \sin i$  as a macroscopic broadening parameter has already been discussed in Sect. 6.5.2. It leads to a blurring of spectral lines that can be best investigated by means of intrinsically sharp and narrow metal lines. This is due to the fact that lines associated with heavier chemical elements are intrinsically less strongly broadened by thermal motions than hydrogen or helium lines because the thermal Doppler width is inversely proportional to the square root of the atomic mass ( $\Delta\nu_{\text{thermal}} \sim 1/\sqrt{m}$ ; see also Sect. 6.5.1). The effect of  $v \sin i$  variations on spectral lines is shown in the upper right-hand panel of Fig. 7.1.1. For extremely large projected rotational velocities ( $v \sin i \gtrsim 300 \text{ km s}^{-1}$ ), the spectral fitting is very difficult because the major part of the observed absorption/emission lines may become completely blurred.

### Effective Temperature

As described in Ch. 6, the effective temperature  $T_{\text{eff}}$  is a measure of the conserved net energy flux in a stellar atmosphere. As the temperature stratification is linked to flux conservation and, therefore, to  $T_{\text{eff}}$ , the latter is one of the key parameters in order to describe the atmospheric structure of a star. In particular, changes of  $T_{\text{eff}}$  directly affect the local temperature in any of the numerous photospheric layers where most of the optical spectral lines form. An increase (decrease) of  $T_{\text{eff}}$  leads to higher (lower) local temperatures and, hence, to higher (lower) excitation and ionization stages of the chemical elements in a certain layer. This, however, directly affects the number of observed absorption/emission lines and their respective profiles. It has to be pointed out that the strength of an individual spectral line increases quantitatively with  $T_{\text{eff}}$  until the level population of the lower state of the underlying atomic transition has reached its maximum. At this critical temperature, which increases with the level of excitation and ionization of the individual chemical elements, the level population of the lower state starts to decrease again because hotter temperatures lead to more and more atoms associated with energetically higher excitation and ionization stages. For neutral hydrogen (H I), which is responsible for prominent absorption lines like the Balmer, Paschen and Brackett series, the critical temperature lies near 10 000 K. This is equivalent to stars of spectral type A0. Neutral helium (He I) lines, however, are most pronounced for temperatures of  $\sim 25\,000$  K, that is, for stars of spectral class B0. On the other hand, spectral lines associated with singly-ionized helium (He II) become strongest only above 50 000 K. As the strength of spectral lines associated with lower (higher) ionization stages decreases (increases) with higher  $T_{\text{eff}}$ , the actual effective temperature of a certain star can be derived from the simultaneous fit of spectral lines belonging to two or more ionization stages (*ionization equilibrium*). Furthermore,  $T_{\text{eff}}$  can be constrained by the widths of spectral lines that show prominent thermal Doppler broadening since the latter depends on the local temperature of the line-forming region in the stellar photosphere (see Sect. 6.5.1 for details). Due to the indirect proportionality of the thermal Doppler width to the square root of the atomic mass, hydrogen line cores are best suited to determine  $T_{\text{eff}}$  in this way. However, thermal Doppler broadening is the dominant microscopic broadening effect for lighter metals as well such that the associated lines can also

## 7.1. Quantitative Spectral Analysis

---

be used to determine  $T_{\text{eff}}$ .

The effective temperatures of the hot subdwarf O and B stars analyzed in this work are thus well constrained from the strongly thermally Doppler-broadened hydrogen line cores and from the ionization equilibria of the various different ionization stages of the detected chemical elements (see also Sect. 8.2.5). For the hotter program stars with  $T_{\text{eff}} \gtrsim 35\,000$  K, inter alia the ionization equilibrium of He I/He II can be used to constrain  $T_{\text{eff}}$ . Moreover, stellar spectra obtained with the XSHOOTER Echelle spectrograph (see Sect. 4.4) include the Balmer and the Paschen jump, enabling a more accurate determination of  $T_{\text{eff}}$  because the ratio of Balmer to Paschen line strengths depends on the ratio of the occupation numbers associated with energy levels two and three of the neutral hydrogen atom. The latter ratio is given by the Boltzmann excitation formula and, therefore, depends on the system temperature (see Eq. 6.27).

The middle left-hand panel of Fig. 7.1.1 shows the effects of  $T_{\text{eff}}$  variations on spectral lines. Note that not only the hydrogen line cores are affected by changes of  $T_{\text{eff}}$ , but also the line wings.

### Surface Gravity

As described in Ch. 6, the surface gravity  $\log(g[\text{cm s}^{-2}])$  is closely linked to the atmospheric pressure and the density stratification of a stellar atmosphere through hydrostatic equilibrium. Therefore, it also strongly affects the shape of all spectral lines. An increase (decrease) of  $\log(g)$  leads to a denser (looser) hot stellar plasma and, thus, to an increasing (decreasing) likelihood of electron captures by free ions. Hence, the total ionization level of the plasma is decreased (increased), if  $\log(g)$  is increased (decreased). This can also be deduced from the ratio of the total number densities of two different ionization stages associated with a certain chemical element, which is direct proportional to the electron density  $n_e$  ( $N_I/N_{I+1} \sim n_e$ ; see Saha's ionization equation of Eq. 6.29). This implies, however, that spectral lines of elements which show two or more different ionization stages in a stellar spectrum are best suited in order to constrain  $\log(g)$ . Moreover, an increase (decrease) of  $\log(g)$  results in broader (narrower/steeper) line wings, in particular in the case of hydrogen lines. This can be explained by the fact that these lines are strongly pressure-broadened due to the linear and quadratic Stark effect (see Sect. 6.5.1 for details). But the hydrogen line wings are also affected by effective temperature changes, as described in the previous section. Hence, there is a correlation between  $T_{\text{eff}}$  and  $\log(g)$  such that the hydrogen lines alone are not enough to determine both quantities at the same time. However, the regions around the Balmer and the Paschen jump may provide remedy because both jumps are also important indicators for  $\log(g)$ , if they are modelled properly (see Irrgang et al. 2018 for further information).

In the case of the hot subdwarf O and B stars investigated in this work, a higher (lower) effective temperature  $T_{\text{eff}}$  decreases (increases) the hydrogen line strength and narrows (broadens) the corresponding wings. On the other hand, this may be compensated by a higher (lower) surface gravity  $\log(g)$ , leading to strongly (less strongly) pressure-broadened lines. Fortunately, the various different ionization stages of the chemical elements that can be detected in the spectra of these stars (see also Sect. 8.2.5) again provide remedy. The use of XSHOOTER spectra,

which cover both the Balmer and the Paschen jump, also guarantees an accurate determination of  $\log(g)$ .

The middle right-hand panel of Fig. 7.1.1 shows the effects of  $\log(g)$  variations on spectral lines. Note that not only the hydrogen line wings are affected, but also the ones of helium and metal lines, albeit to a lower extent. In fact, individual helium lines are affected very differently by pressure broadening because for some of them (for instance, He I 4471 Å) Stark broadening is the dominant microscopic broadening effect, whereas for others (for instance, He I 4713 Å) it is not.

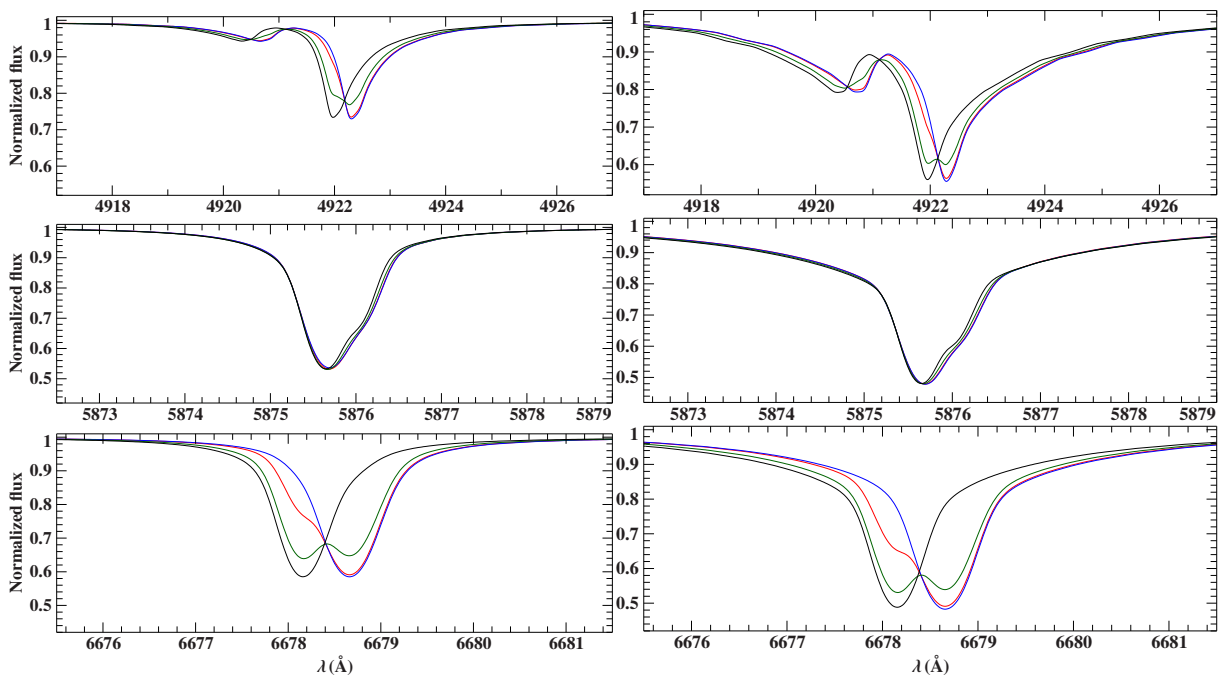


Figure 7.1.2.: Influence of the isotopic abundance ratio  ${}^4\text{He}/{}^3\text{He}$  and the total helium abundance  $\log n({}^4\text{He} + {}^3\text{He})$  on the shape of selected neutral helium lines. *Left-hand panels:* Folded ( $R = 50\,000$ ) model spectra showing He I 4922 Å, He I 5875 Å, and He I 6678 Å for fixed effective temperature  $T_{\text{eff}} = 28\,000$  K, fixed surface gravity  $\log(g) = 5.60$ , fixed total helium abundance  $\log n({}^4\text{He} + {}^3\text{He}) \sim -2.00$ , but for four different combinations of  ${}^3\text{He}$  and  ${}^4\text{He}$  isotopic abundances. The respective isotopic helium abundances are  $\log n({}^3\text{He}) = -4.00$  and  $\log n({}^4\text{He}) = -2.00$  (black line),  $\log n({}^3\text{He}) = -2.30$  and  $\log n({}^4\text{He}) = -2.30$  (green line), and  $\log n({}^3\text{He}) = -2.00$  and  $\log n({}^4\text{He}) = -4.00$  (blue line), respectively. In addition, a model spectrum for  $\log n({}^3\text{He}) = -2.05$  and  $\log n({}^4\text{He}) = -3.05$  is shown in red. *Right-hand panels:* Same as the left-hand panels, but for a fixed total helium abundance of  $\log n({}^4\text{He} + {}^3\text{He}) \sim -1.00$ . For all models, the microturbulence  $\xi$  and the macro-turbulence  $\zeta$  are set to zero. Moreover, the mean metallicity for H-sdB/H-sdOB stars (Naslim et al. 2013; see also Table 3.1) is used in all cases. Modified version of Figure 2 in Schneider et al. (2018).

## Helium Abundance

Denoted as  $\log n(\text{He}) := \log \left[ \frac{N(\text{He})}{N(\text{H})} \right]$  throughout this work, where  $N(\text{He})$  and  $N(\text{H})$  are the number densities of helium and hydrogen, respectively, the helium abundance strongly affects the temperature-density stratification of a stellar atmosphere because helium usually is the second most abundant element right after hydrogen. Particularly, this is true for the hot subdwarf O and B stars investigated in this work.

The lower left-hand panel of Fig. 7.1.1 shows the effect of variations of  $\log n(\text{He})$  on spectral lines. The higher/lower the helium abundance, the stronger/weaker the respective helium lines.

In the context of  $^3\text{He}$ -enriched stars (see Sect. 3.3), the  $^4\text{He}/^3\text{He}$  isotopic abundance ratio and the total helium abundance  $\log n(^4\text{He} + ^3\text{He})$  play a crucial role. This is because the different isotopic line shifts (see Table 3.2) that strongly influence the helium line shapes depend on both quantities. The dependence on the  $^4\text{He}/^3\text{He}$  ratio is demonstrated in the left-hand panels of Fig. 7.1.2, where different synthetic profiles for the three neutral helium lines He I 4922 Å (top panel), He I 5875 Å (middle panel), and He I 6678 Å (bottom panel) are displayed. The profiles are calculated for  $T_{\text{eff}} = 28\,000\text{ K}$ ,  $\log(g) = 5.60$ , and  $\log n(^4\text{He} + ^3\text{He}) \sim -2.00$ , which is typical for a normal hydrogen-rich hot subdwarf B star. Variations of the abundance ratio between  $^4\text{He}/^3\text{He} = 1/100$  and 100 do not significantly influence the shape of He I 5875 Å since this reference line only exhibits a small isotopic shift of  $\Delta\lambda \sim 0.044\text{ Å}$ . However, the line shapes of He I 4922 Å and He I 6678 Å change significantly based on the abundance ratio. For a ratio of unity, the effect of the isotopic anomaly is most pronounced as the He I 6678 Å line develops a hump absorption profile. The distortion of the line profiles by the minority isotope becomes invisible to the eye for  $^4\text{He}/^3\text{He}$  as high as 100, or as low as 1/100. Thus, it is possible to determine the isotopic ratio from He I 4922 Å and He I 6678 Å if it lies within this range. The line asymmetry still remains detectable for He I 6678 Å but not for He I 4922 Å in the case of  $^4\text{He}/^3\text{He} = 1/10$  (see the red line in Fig. 7.1.2). This is because of the smaller isotopic line shift of He I 4922 Å ( $\Delta\lambda \sim 0.331\text{ Å}$ ) compared to He I 6678 Å ( $\Delta\lambda \sim 0.502\text{ Å}$ ). Hence, He I 6678 Å is the more sensitive diagnostic tool. An increase/decrease of the total helium abundance generally results in stronger/weaker absorption lines with much broader/narrower line wings. This is shown in the right-hand panels of Fig. 7.1.2, where the same profiles are shown as in the left-hand panels, but this time for a total helium abundance of  $\log n(^4\text{He} + ^3\text{He}) \sim -1.00$ . In fact, the hump absorption profile in the case of an abundance ratio of unity is now also detectable for He I 4922 Å (Schneider et al., 2018).

## Metal Abundances

The abundances of different metals<sup>77</sup> are described by  $\log n(X) := \log \left[ \frac{N(X)}{N(\text{all elements})} \right]$  throughout this work, where  $X \in \{\text{C, N, O, Ne, Mg, etc.}\}$  and  $N(X)$  and  $N(\text{all elements})$  are the number densities of element  $X$  and all elements, respectively. The higher (lower) the individual metal

---

<sup>77</sup>In astronomy, all chemical elements with larger atomic masses than hydrogen and helium are generally referred to as metals.

abundance, the larger (lower) the number density of the respective absorbers in the stellar atmosphere. The effect of all metals on the temperature-density stratification of a stellar atmosphere is considered collectively as *metallicity*  $Z$ . Metallicity takes both the mean atomic weight and the number of free electrons that originate from all metals present in the hot stellar plasma into account. The metal abundances enter the continuum opacity and, therefore, affect the atmospheric structure and the individual spectral line profiles. As a matter of fact, however, metals can be treated as trace elements for atmospheric modelling because their individual abundances are typically several orders of magnitude lower than those of the most abundant elements (hydrogen and helium). This means that the continuum flux is mostly unaffected by changes of the individual metal abundances. A higher (lower) individual metal abundance results in stronger (weaker) absorption/emission lines of the chemical element in question since the number of absorbing/emitting atoms/ions increases (decreases). In order to derive the atmospheric abundances of different metals, the respective spectral line profiles in the stellar spectrum thus need to be investigated. Section 8.2.5 will provide a detailed overview of the chemical elements, the ionization stages, and the spectral lines that are observed for the hot subdwarf O and B stars investigated in this work.

The lower right-hand panel of Fig. 7.1.1 shows how changes of the carbon abundance  $\log n(\text{C})$  affect spectral lines. While the profiles of hydrogen and helium lines are barely affected, the line core and the wings of all carbon lines strongly depend on  $\log n(\text{C})$ . This is exemplarily shown by means of the C II 4267 Å line.

### Micro- and Macroturbulence

Apart from the aforementioned primary spectroscopic parameters, microturbulence  $\xi$  and macroturbulence  $\zeta$  (if non-zero) may also affect the spectral line profiles. Both quantities describe additional broadening mechanisms as outlined in Sects. 6.5.1 and 6.5.2. As a matter of fact, both quantities have been found to be consistent with zero for hot subdwarf O and B stars studied by Geier & Heber (2012). Therefore,  $\xi$  and  $\zeta$  are both set to zero for the quantitative spectral analyses performed in this work. All of the synthetic spectra shown in Figs. 7.1.1 and 7.1.2 are also calculated without taking  $\xi$  and  $\zeta$  into account.

### 7.1.2. Analysis Strategies

The quantitative spectral analysis strategies used within the framework of this thesis can be subdivided into two traditional selective approaches and a more objective global one. Both categories mainly differ in the treatment of the stellar continuum normalization and the selection of lines to be fitted. This shall be presented in the following.

### SPAS and FITPROF: The Selective Approaches

In the case of the selective fitting routines used (SPAS and FITPROF) not the whole stellar spectrum is fitted. Instead, the user manually defines preselected ranges that cover the individual spectral lines to be fitted. In this way, the stellar continuum is set at the edges of the preselected ranges. In this work, SPAS and FITPROF will be used in combination with all model atmosphere approaches available, that is, LTE (see Sect. 6.7), hybrid LTE/NLTE (see Sect. 6.8), and NLTE (see Sect. 6.9).

- **SPAS:** The analysis program SPAS (**S**pectrum **P**lotting and **A**nalysis **S**uite) is a downsized and more user-friendly version of FITSB2, a spectral analysis code that was designed by Napiwotzki et al. (2004b) in order to analyze both components of SB2 systems found within the framework of ESO SPY (Napiwotzki et al., 2001a). SPAS was developed by Hirsch (2009) and provides a GUI (see Fig. 7.1.3). In this way, an easy and fast access to important parameters such as the spectral resolution, the above mentioned fit ranges, or the starting fit parameters is ensured. However, no SB2 systems can be analyzed with SPAS.

Before performing the actual fit, SPAS normalizes the preselected spectral ranges, whereby the stellar continuum is set to unity at the edges. Making use of  $\chi^2$ -minimization, calculated synthetic spectra from model grids can be fitted to observed hydrogen (H I), helium (He I/II), and metal lines.  $\chi^2$  is defined as:

$$\chi^2 := \sum_{i=1}^n \chi_i^2 = \sum_{i=1}^n \frac{(f_{\text{obs},i} - f_{\text{model},i})^2}{(\delta f_{\text{obs},i})^2}. \quad (7.5)$$

Here,  $f_{\text{obs},i}$  is the observed flux and  $f_{\text{model},i}$  is the model flux at data point (pixel)  $i$ .  $\delta f_{\text{obs},i}$  denotes the corresponding uncertainty of the observed flux.

SPAS uses the downhill simplex algorithm from Nelder & Mead (1965) in order to simultaneously determine the best fit parameters for  $T_{\text{eff}}$ ,  $\log(g)$ , and  $\log n(X)$ , where  $X$  denotes the varied chemical element (for this work, only helium is considered here). simplex is a rather slow but robust non-gradient method, which evaluates each vertex of the current simplex. A vertex consists of a combination of the four coordinates  $T_{\text{eff}}$ ,  $\log(g)$ ,  $\log n(\text{He})$ , and  $\chi^2$ . The goodness of each vertex is determined on the basis of its corresponding  $\chi^2$ . In each iteration step, the vertex with the poorest (the largest)  $\chi^2$  is replaced by a new one within or outside of the current simplex. This is done until a maximum number of iterations has been performed or until the maximum difference between the  $\chi^2$  values at the individual vertices of the simplex falls below a certain value. The best fit is given by the vertex of the final simplex that has the lowest  $\chi^2$ . This, however, has not to be the global minimum. The vertices of the simplex are determined by cubic spline interpolation in the three-dimensional grid of synthetic spectra provided, whereby the interpolation order is: 1.)  $\log n(\text{He})$ , 2.)  $\log(g)$ , 3.)  $T_{\text{eff}}$ . In order to determine the  $\chi^2$  for each vertex, the interpolated synthetic spectra are rebinned to the observation. This is done by linearly interpolating between the two nearest neighboring wavelength points, whereby their individual fluxes are also scaled to the one of the ob-

## 7. Combined Spectrophotometric and Astrometric Analysis

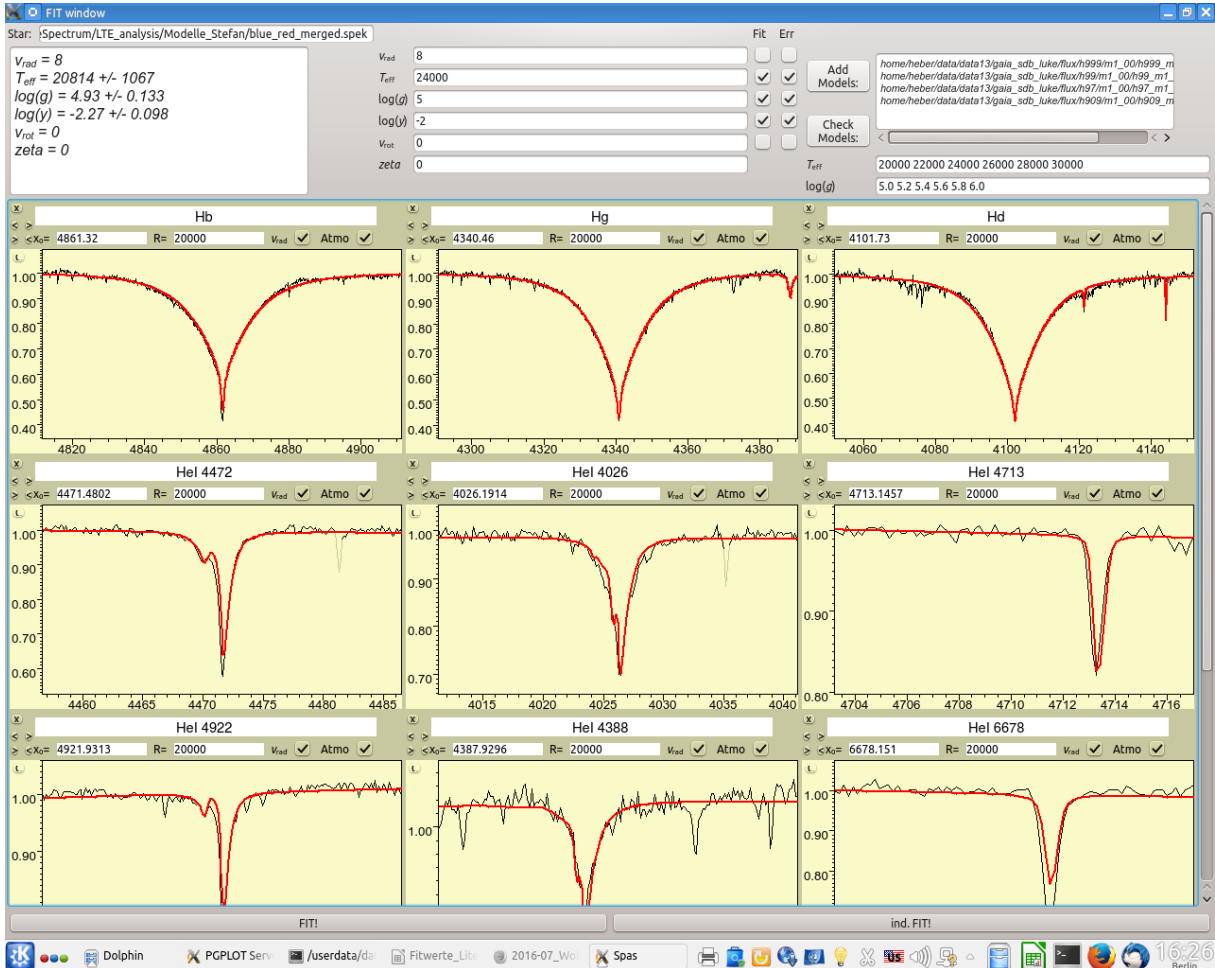


Figure 7.1.3.: Screenshot of SPAS' graphical user interface (GUI) showing all important features. *Upper Part:* For each helium abundance  $\log(y) = \log n(\text{He}) := \log \left[ \frac{N(\text{He})}{N(\text{H})} \right]$ , a separate binary synthetic model file is used. The paths to all of them are entered in order of increasing abundance in the right-hand text field. Below the paths to the individual binary model files, the grid points for the effective temperature and the surface gravity that are used for the cubic spline interpolation are listed. The fit parameters and their individual start values are selected in the centre, whereas the current best fit values are displayed in the left-hand text field. *Lower Part:* Selected spectral lines can be added or deleted manually. Their respective fit ranges and, therefore, the stellar continuum can also be quickly adjusted by the user. Furthermore, the spectral resolution  $R$  can be adjusted individually for each line. The current best fit (red line) is plotted over the observed spectrum (black line). Adopted from Schneider (2017).

## 7.1. Quantitative Spectral Analysis

---

served spectrum. The scaling is realized by dividing the model by the observation and performing a linear fit to the resulting values, which is then used to scale the synthetic fluxes (Hirsch, 2009).

For the RV determination, no models are needed because a convolved profile of a Lorentzian and a Gaussian (Voigt function) can be fitted to selected absorption and emission lines (in particular to sharp and narrow ones produced by metals). The Voigt profile gives the individual line core position  $\lambda$  for each spectral line (with rest-frame wavelength  $\lambda_0$ ) investigated. By means of the Doppler formula (see Sect. 7.1.1), this can then be transformed into a corresponding RV value  $v_{\text{rad}}$ . Moreover, the projected rotational velocity  $v \sin i$  and the macroturbulence  $\zeta$  can be determined from a convolution of the model spectrum with an appropriate profile function, whereby the respective Gaussian instrumental profile is also taken into account (see Sect. 6.5.2). However, as the macroturbulence  $\zeta$  is not of importance for the stars analyzed in this work (see Geier & Heber 2012), it is always set to zero.

SPAS does not use  $\chi^2$ -statistics for error estimation. Instead, it relies on bootstrapping. This method removes data points randomly with replacement a large number of times, whereby for each of the iterations a new parameter fit is performed. The  $1\sigma$  ( $\approx 68.3\%$ ) standard error for an individual fit parameter is given by the standard deviation of the Gaussian-shape bootstrap distribution determined for the parameter in question. Since this method is quite slow and requires long computation time (in particular in the case of high-resolution spectra), 100 bootstrapping iterations are considered sufficient for this work in order to produce meaningful results for  $T_{\text{eff}}$ ,  $\log(g)$ , and  $\log n(\text{He})$ . 200 iterations will be used for the  $v_{\text{rad}}$  determination of all single spectra available. The results for  $v_{\text{rad}}$  are needed for the co-addition of the single spectra (see Sect. 8.2.2).

In general, SPAS is limited to the determination of the parameters  $v_{\text{rad}}$ ,  $v \sin i$ ,  $\zeta$ ,  $T_{\text{eff}}$ ,  $\log(g)$ , and  $\log n(\text{He})$ . Therefore, a distinction between  $^3\text{He}$  and  $^4\text{He}$  in the case of  $^3\text{He}$ -enriched stars cannot be realized. Furthermore, the RV is treated separately within SPAS such that it cannot be fitted along with the other parameters. Hence, SPAS is not suited for the analysis of  $^3\text{He}$  stars (see Sect. 3.3 and Schneider et al. 2018). In consequence, none of the  $^3\text{He}$  program stars of this work will be fitted with SPAS. Moreover, no metal abundances will be determined with SPAS.

As will be detailed in Ch. 9, the  $1\sigma$  bootstrapped statistical errors on the atmospheric parameters  $T_{\text{eff}}$ ,  $\log(g)$ , and  $\log n(\text{He})$  are in some cases inexplicably large compared to the ones derived from the global analysis strategy, which uses  $\chi^2$ -statistics for error estimation and is described later in this section. Thus, it is not clear to the user whether the given bootstrapped SPAS errors are indeed  $1\sigma$  or something else, making them somehow unreliable. Consequently, an older selective analysis strategy approach called FITPROF (Napiwotzki, 1999) will be used additionally for comparison because it also makes use of  $\chi^2$ -statistics to estimate the statistical uncertainties. FITPROF will be presented next.

- **FITPROF:** Just like SPAS, this approach relies on the simultaneous fit of selected hydrogen and helium line profiles, whereby the line flux, in both the observed and the model spectrum, also is normalized to a continuum set to unity at the edges of the chosen fit ranges (Bergeron et al., 1992). In contrast to SPAS, however, no GUI can be used in order

to quickly adjust the most important parameters and to visualize the fit. Instead, the user needs to specify the spectral resolution, the starting fit parameters, the model grids to be used, the spectral lines to be fitted (including the individual fit ranges), etc. within two input files. The model spectra are convolved with a Gaussian instrumental profile that corresponds to the spectral resolution of the respective observation. In addition, they are linearly interpolated to the observed wavelength scale. A bicubic spline is used in order to interpolate between the individual model spectra. Wavelength shifts ( $v_{\text{rad}}$ ) are dealt with an appropriate cross-correlation method and they are separately applied to the full spectrum (Napiwotzki, 1999). Neither the projected rotational velocity nor the macroturbulence can be fitted, but both quantities can be fixed to certain values within the input files. The fit algorithm used differs from the one implemented in SPAS. While SPAS makes use of the non-gradient `simplex` method, FITPROF relies on the non-linear least-squares and steepest-descent method of Levenberg-Marquardt (Press et al., 1986) in order to minimize the  $\chi^2$ . Hence, the program needs to be provided with good initial estimates for the fit parameters  $T_{\text{eff}}$ ,  $\log(g)$ , and  $\log n(\text{He})$ . The noise of the spectra ( $\delta f_{\text{obs},i}$  in Eq. 7.5) used for the  $\chi^2$ -fit is estimated from the neighboring continuum of each fitted line and the S/N is considered constant throughout the individual fit ranges. In the end,  $1\sigma$  statistical uncertainties for the fitted atmospheric parameters are obtained from the covariance matrix (Napiwotzki, 1999). FITPROF is limited to the determination of the four parameters  $v_{\text{rad}}$ ,  $T_{\text{eff}}$ ,  $\log(g)$ , and  $\log n(\text{He})$ . Thus, no  $^3\text{He}$  stars and no metal abundances will be analyzed with FITPROF in this work.

Although the noise estimation for the fit is handled differently within FITPROF and the global analysis approach (the latter will be presented next), both analysis strategies make use of  $\chi^2$ -statistics in order to estimate the statistical uncertainties. Hence, the  $1\sigma$  single parameter errors derived from both approaches are much more comparable to each other than in the case of SPAS and the global approach (see Ch. 9).

### ISIS: The Global Approach

In this work, the global analysis approach will only be used in combination with the hybrid LTE/NLTE ADS models described in Sect. 6.8. It is an updated version of the fitting routine developed by Irgang et al. (2014) and uses the whole observed spectrum at once, including the continuum and metal lines. The global analysis strategy is carried out completely within ISIS (**I**nteractive **S**pectral **I**nterpretation **S**ystem), which was designed at the Massachusetts Institute of Technology (MIT) by Houck & Denicola (2000) and allows to perform many-parameter fits. This is also why the global approach is very suitable for the analysis of  $^3\text{He}$  stars (see Sect. 10), for which both isotopic helium abundances need to be fitted at the same time. If needed, ISIS is able to simultaneously fit multiple normalized spectra of the same star, handling them as individual data sets. In this case, the best global fit is obtained by tying the spectroscopic fit parameters of all data sets to those of the first one.

Remaining emission peaks after data reduction (see Sect. 8.2) that are produced by high-energetic cosmic particles (cosmics) hitting the CCD detector are removed from the observed spectrum by comparing the flux of each data point (pixel) to the continuum flux of the region

## 7.1. Quantitative Spectral Analysis

---

around it. If flux values deviate by at least three standard deviations from the continuum flux, they are defined as cosmics and are replaced by the median value of the adjacent continuum. Dead pixels which lead to flux values of zero and hot pixels that show emission bumps in the observed spectrum are excluded from the spectral fitting. The same holds to possible non-overlapping diffraction orders at the red end of an individual spectrum as well as to extraction errors and other reduction artefacts. Remaining telluric (see Sect. 8.2.1) or interstellar lines (see Sect. 8.2.5) are also excluded. Furthermore, photospheric lines with inappropriate, inaccurate, or missing atomic data are avoided because they cannot be modelled correctly. Moreover, the observed spectrum is rebinned to an optimal wavelength grid, taking the respective spectral resolution of the long-slit or Echelle spectrograph used into account. The noise level is estimated by comparing the flux at one pixel  $i$  to the (weighted) flux average of data points  $i - 2$  and  $i + 2$  (see Irrgang et al. 2014 for details). A spline function with predefined anchor points spread over the entire spectral range to be analyzed can be used in order to perform a global normalization, if a non-normalized spectrum is investigated. However, as most of the science spectra analyzed in this work have already been normalized beforehand (see also Sect. 8.2.4), this feature is more of secondary importance here. Much more important is the local continuum correction that can be applied manually by eye during the spectral fitting. This feature can be used to renormalize spectral ranges for which the global normalization procedure is not successful or where it is not enough to reproduce the actual shape of the continuum. The local continuum correction makes use of a local filter which is able to smooth the problematic regions.

As described in Irrgang et al. (2014), a single ADS model spectrum is calculated for a set of parameter combinations of  $T_{\text{eff}}$ ,  $\log(g)$ ,  $\log n(\text{He})$  ( $\log n(^4\text{He})$  and  $\log n(^3\text{He})$ , if an isotopic distinction is needed),  $\xi$ ,  $\zeta$ ,  $Z$ , and  $\log n(\text{X})$  and only contains synthesized hydrogen and helium lines as well as the ones of a single metal trace element X (HHE + X). Note that throughout this work  $\xi = \zeta = 0$  is used according to the results of Geier & Heber (2012). Moreover,  $Z = 0$  is used which corresponds to the mean metallicity pattern for H-sdB/H-sdOB stars (Naslim et al. 2013; see also Table 3.1). A model spectrum that only contains spectral lines of the respective metal X is produced by dividing the (HHE + X)-model by a HHE-only model with the same spectroscopic parameters. Multiplying all of the single-metal spectra, which can be generated individually for each of the metals to be investigated, with each other and with the corresponding HHE-only model results in a full model spectrum that is based on the chosen set of spectroscopic fit parameters<sup>78</sup>. In order to account for the spectral resolution of the respective instrument used, the full model spectrum is additionally convolved with the corresponding instrumental profile. In this way, the observation can be fitted by a precalculated ADS model grid to obtain  $T_{\text{eff}}$ ,  $\log(g)$ ,  $\log n(\text{He})$ , and  $\log n(\text{X})$ . This is done by linearly interpolating the different spectroscopic parameter combinations within the calculated model grid. If needed,  $\log n(^4\text{He})$  and  $\log n(^3\text{He})$  can be determined individually as described

---

<sup>78</sup>Due to the multiplicative approach of combining the individual spectra in order to determine the full model spectrum, the presented method does not allow to treat line blends in general. Therefore, it is not suited for spectroscopic analyses of crowded spectra with lots of line blends as is the case for cool stars. However, the method is perfectly suited for the O and B-type program stars investigated in this work because these stars barely show any line blends. Another important aspect of the multiplicative approach is the fact that it is very efficient.

in Schneider et al. (2018). Furthermore, the RV  $v_{\text{rad}}$  can be determined very accurately by adjusting the entire wavelength range of the model spectrum to the observed spectrum according to the Doppler formula (see Sect. 7.1.1). The projected rotational velocity  $v \sin i$ , however, is derived from a convolution of the model spectrum with a simplified version of the profile function described by Eq. (6.47). The best fit for all free spectroscopic fit parameters is determined via  $\chi^2$ -minimization.

A combination of two different fit algorithms can be used in order to find the global  $\chi^2$ -minimum: `mpfit` and `powell`. `mpfit` (Bevington & Robinson, 1992) is used by default. It is a gradient method based on the Levenberg-Marquardt algorithm (Press et al., 1986). On the other hand, `powell` (Powell, 1964; Zangwill, 1967) is a non-gradient method to find the minimum of a function. Ideally, the global minimum of the investigated  $\chi^2$ -landscape is well behaved such that the best fit with a reduced  $\chi^2$  of approximately unity can be found after a small number of steps ( $\chi_{\text{red}}^2 := \chi^2/\text{DOFs}$ , where  $\text{DOFs} := n - m$  denotes the degrees of freedom which can be calculated via the total number of data points/pixels  $n$  and the total number of fit parameters  $m$ ). Depending on the quality of the fit, however,  $\chi_{\text{red}}^2$  can be two to three times greater than unity at the best fit found because there are always some spectral features that the model cannot reproduce. These features have a large impact on the  $\chi^2$ , in particular in the case of high S/N spectra. This is why it is assumed that the deviations between the model and the observation are due to systematic errors only such that appropriate values can be added in quadrature to the  $\delta f_{\text{obs},i}$  of the corresponding spectral features. In this way, their  $\chi_i$  values approach  $\pm 1$  (see Eq. 7.5) and an overall  $\chi_{\text{red}}^2$  of about unity is ensured (see Irrgang et al. 2014 for further information).

Statistical uncertainties result from the estimated noise in the observed spectrum.  $1\sigma$  single parameter confidence intervals in ISIS are calculated for all spectroscopic fit parameters in a serial or parallel way following  $\chi^2$ -statistics: Starting from the best fit with  $\chi_{\text{red}}^2 \approx 1$ , the parameter under consideration is increased/decreased, whereas all other parameters are fitted until an increment of  $\Delta\chi^2 = 1$  from the minimum  $\chi^2$  is reached. The  $1\sigma$  single confidence interval is constrained by the two values of the parameter in question, for which  $\Delta\chi^2 = 1$ . The  $2\sigma$  ( $\approx 95.5\%$ ) single confidence interval would be defined by an increment of  $\Delta\chi^2 = 4$  and the  $99\%$  ( $2.58\sigma$ ) interval by  $\Delta\chi^2 = 6.635$  (see Bevington & Robinson 1992 for details). It may happen that an improved fit with a better  $\chi^2$  is found during the determination of the confidence intervals. If so, the whole error estimation for all parameters starts from scratch.

The aforementioned local continuum correction by eye, the fit algorithms, deficient line broadening, or the incomplete atomic data and model atoms used for the analysis (for instance, in terms of oscillator strengths, energy levels, and photoionization cross sections) are several sources that produce systematic uncertainties. As these systematics need to be considered as well, this calls for a full systematic error estimation for which all possible sources that cause systematics as well as their possible correlations are taken into account. However, such a systematic error estimation is not feasible at all because it is impossible to quantify all of the systematic error sources. As the spectroscopic parameters are derived from multiple features in the entire spectral range, however, the systematics on the parameters resulting from these individual features are typically independent from each other. Therefore, they average out to some extent such that the overall systematics can be considered low (Irrgang et al., 2014).

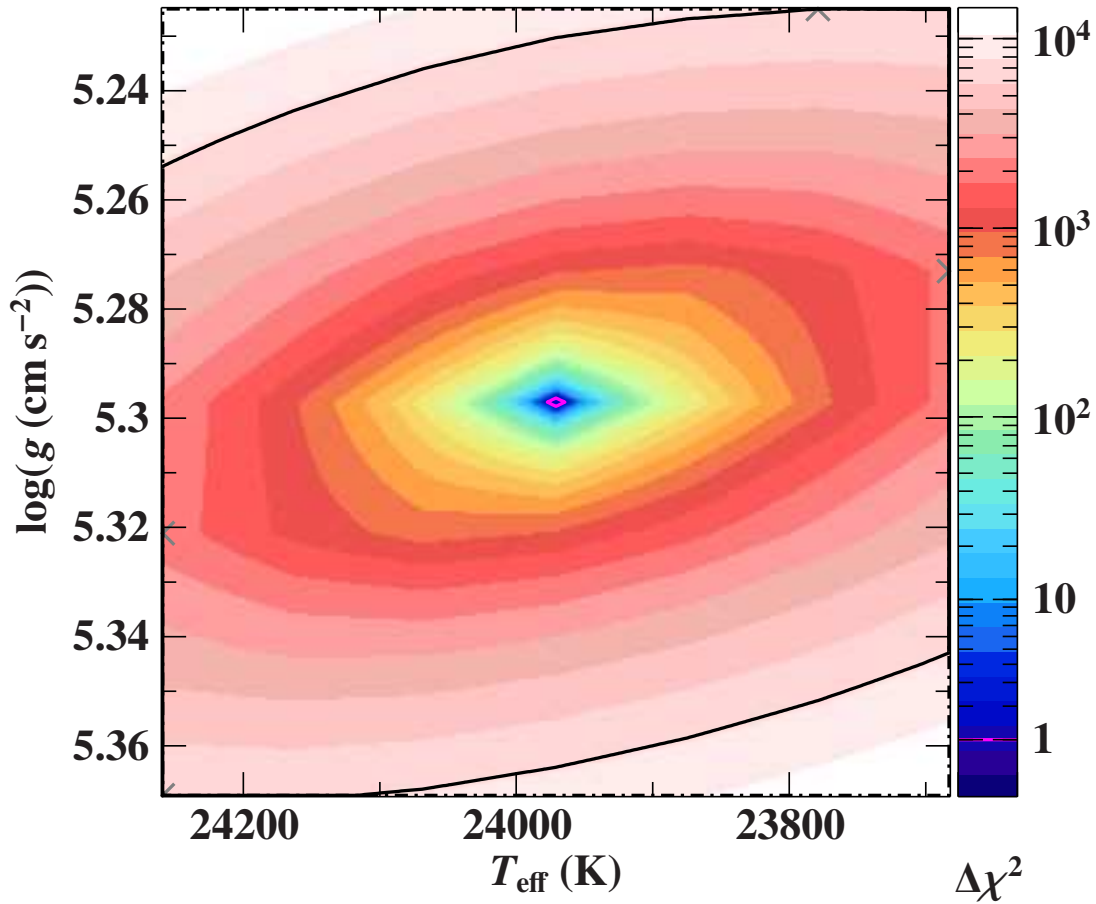


Figure 7.1.4.: Example of a color-coded  $\Delta\chi^2$  confidence map as a function of the effective temperature and the surface gravity. The confidence map has been calculated for the quantitative spectral analysis of the XSHOOTER spectrum of the HsdB program star HD 4539 making use of the global analysis approach in ISIS (note, however, that this is an example map which does not correspond to the best fit determined in this thesis). The magenta line represents a contour line that corresponds to an increment of  $\Delta\chi^2 = 1$ , indicating the  $1\sigma$  ( $\approx 68.3\%$ ) statistical single parameter confidence interval for the abscissa and the ordinate. The four corners of the confidence map are defined by the four pairs of values for  $T_{\text{eff}}$  and  $\log(g)$  that result from the addition or the subtraction of the respective total uncertainty (given by the added quadrature of the  $1\sigma$  systematic and  $1\sigma$  statistical uncertainties) from the best fit located in the centre. The gray crosses mark the points of minimum  $\Delta\chi^2$  on each of the edges of the confidence map. The region within the confidence map, for which  $\Delta\chi^2$  is lower than or equal to the maximum of the four  $\Delta\chi^2$  values extracted from the gray crosses, is marked by the solid black line. In this way, regions of the confidence map, for which the observation is fitted worst, are excluded. At the same time, it is ensured that at least one point of the four edges contributes to the black line. From the region surrounded by the solid black line, the  $1\sigma$  systematic uncertainties for the fitted helium and metal abundances can be derived (see the text and Irrgang et al. 2014 for further information).

As also described in Irrgang et al. (2014), it can be assumed that the systematic uncertainties on  $T_{\text{eff}}$  and  $\log(g)$  are the dominant contributors to the overall systematics on the elemental abundances of helium ( $\log n(\text{He})$ ,  $\log n(^4\text{He})$ , and  $\log n(^3\text{He})$ ) and the different metals investigated ( $\log n(\text{X})$ ). As will be shown in Ch. 9, the systematics on  $T_{\text{eff}}$  and  $\log(g)$  can be estimated to be of the order of 1% and 0.06 dex, respectively. In ISIS, the ranges given by these errors are formally treated as  $1\sigma$  confidence intervals. The effective temperature and the surface gravity are varied through  $7 \times 7$  different parameter combinations according to their respective total uncertainties (given by the added quadrature of the  $1\sigma$  systematic and the  $1\sigma$  statistical uncertainties). The best fit is located in the centre of the  $7 \times 7$  mesh. A fit of the abundances of helium and the different metals under investigation is performed for each of the fixed combinations of  $T_{\text{eff}}$  and  $\log(g)$ . In this way, a confidence map is created (see Fig. 7.1.4). For the estimation of the systematic uncertainties on the individual abundances, only  $T_{\text{eff}}$  and  $\log(g)$  parameter combinations within the solid black line displayed in Fig. 7.1.4 are taken into account. In this way, regions of the confidence map, for which the model fits the observation worst, are excluded. The  $1\sigma$  systematic uncertainties for an individual abundance are retrieved from the minimum and the maximum value determined for the respective fit parameter within the region surrounded by the solid black line. The total  $1\sigma$  error on the respective abundance then is calculated by taking the square root of the sum of the quadratic statistical and systematic uncertainties.

It has to be pointed out that the systematic uncertainties on  $T_{\text{eff}}$  and  $\log(g)$  are not the dominant sources of systematic errors for  $v_{\text{rad}}$  and  $v \sin i$ . In order to derive the systematics on these parameters, the aforementioned method therefore cannot be applied. For  $v_{\text{rad}}$ , systematic uncertainties resulting from the accuracy of the wavelength calibration (see Sect. 8.2) are taken into account. These systematics range from 0.1 to 2.0  $\text{km s}^{-1}$ , depending on the specific instrument used. Due to simplifications in the profile function of Eq. (6.47) (for instance, in the treatment of limb darkening), most of the systematics on the projected rotational velocity  $v \sin i$  are introduced. They are accounted for by adding in quadrature a few  $\text{km s}^{-1}$  to the statistical uncertainties derived.

For high-quality spectra such as the ones analyzed in this work (see Sect. 8.1), the statistical errors for each of the spectroscopic fit parameters are generally small. Hence, the total uncertainties are clearly dominated by the systematics.

## 7.2. Photometry - Studying the Stellar Spectral Energy Distribution

The atmospheric parameters ( $T_{\text{eff}}$ ,  $\log g$ , and  $\log n(\text{He})$ ) and their respective uncertainties, which can be derived from quantitative spectral analyses, may be used as input for SED fitting to appropriate photometric data. In this way, it is possible to derive the stellar angular diameter  $\theta$  and the monochromatic color excess  $E(44 - 55)$  described in Fitzpatrick et al. (2019). Performing an SED fit also allows to distinguish between single stars/systems with a WD companion (SB1 systems) and composite spectrum systems (SB2 systems), in which

## 7.2. Photometry - Studying the Stellar Spectral Energy Distribution

---

the primary star has a cool main-sequence or giant star companion that contributes to the IR part of the SED. The photometric data used for the SED fits performed in this work will be described in detail in Sect. 8.3. In the following, the two different types of models used (ATLAS12 and TLUSTY/SYNSPEC) and the applied SED analysis methodology shall be presented.

### 7.2.1. ATLAS12

In principle, the same model grid as presented in Heber et al. (2018) will be used for the synthesis of hot subdwarf SEDs with ATLAS12. This grid has a spectral coverage of  $300 \text{ \AA} \leq \lambda \leq 100\,000 \text{ \AA}$  and covers the following atmospheric parameter ranges:  $15\,000 \text{ K} \leq T_{\text{eff}} \leq 55\,000 \text{ K}$  (step size: 1000 K),  $4.60 \leq \log(g) \leq 6.20$  (step size: 0.40 dex), and  $-3.00 \lesssim \log n(\text{He}) \lesssim -0.25$  (step size: 2.00 dex and 0.75 dex). Scaled logarithmic metallicities  $Z$  cover a range of  $-1 \leq Z \leq +1$ , whereby  $Z = 0$  corresponds to the mean abundance pattern for H-sdB/H-sdOB stars (Naslim et al. 2013; see also Table 3.1). For the SED fits,  $Z$  will generally be fixed to a value of zero. For program stars that are not covered by the described model grid, specific SEDs with ATLAS12 will be calculated, whereby the atmospheric parameters derived from the corresponding quantitative spectral analyses as well as the mean H-sdB/H-sdOB metallicity will be used. A grid of PHOENIX models<sup>79</sup> ( $500 \text{ \AA} \leq \lambda \leq 55\,000 \text{ \AA}$ ) from Husser et al. (2013) will be used for the SED synthesis of cool companions with  $2300 \text{ K} \leq T_{\text{eff,sec}} \leq 15\,000 \text{ K}$  (step size: 100 K),  $2.00 \leq \log(g_{\text{sec}}) \leq 5.50$  (step size: 0.50 dex), and  $\log n(\text{He})_{\text{sec}} = -1.01$  (fixed). Scaled-solar logarithmic metallicities  $Z_{\text{sec}}$  cover a range of  $-2 \leq Z_{\text{sec}} \leq 0$ , whereby  $Z_{\text{sec}} = 0$  corresponds to the solar abundance pattern according to Asplund et al. (2009).

### 7.2.2. TLUSTY/SYNSPEC

TLUSTY and SYNSPEC will be used to calculate SEDs for the hotter program stars, in particular for the He-sdOs and the post-EHB H-sdOs. This is because these stars show pronounced NLTE effects (see, for instance, Schindewolf et al. 2018) and, therefore, cannot be modelled properly making use of ADS models derived from the hybrid LTE/NLTE approach presented in Sect. 6.8. In order to calculate the individual SEDs within TLUSTY/SYNSPEC, the atmospheric parameters derived from the corresponding quantitative spectral analyses will be used. Regarding the metallicity, not all of the metals described by the mean abundance pattern of H-sdB/H-sdOB stars (Naslim et al. 2013; see also Table 3.1) will be included. Only carbon, nitrogen, and oxygen will be treated and will be synthesized according to their respective mean abundances in H-sdB/H-sdOB stars. The calculated TLUSTY/SYNSPEC SEDs cover a spectral range of 900-60 000 Å.

---

<sup>79</sup><http://phoenix.astro.physik.uni-goettingen.de/>, last called on 2nd May 2021

### 7.2.3. Photometric Analysis Methodology

As described in Irrgang (2014) and Heber et al. (2018), respectively, synthetic magnitudes for photometric passbands  $x$  can be calculated via the individual filter response functions  $r_x(\lambda)$ , the model flux  $F(\lambda)$  at the stellar surface, the observed flux  $f(\lambda) = [\theta^2 F(\lambda)]/4$  at the detector position, and the flux  $f_{\text{ref}}(\lambda)$  of a reference star (typically Vega) according to:

$$\text{mag}_x = -2.5 \log_{10} \left( \frac{\theta^2 \int_0^{\infty} r_x(\lambda) 10^{-0.4A(\lambda)} F(\lambda) \lambda d\lambda}{4 \int_0^{\infty} r_x(\lambda) f_{\text{ref}}(\lambda) \lambda d\lambda} \right) + \text{mag}_{x,\text{ref}}. \quad (7.6)$$

Here,  $\text{mag}_{x,\text{ref}}$  is the predefined zero point magnitude of filter  $x$  and  $10^{-0.4A(\lambda)}$  is a reddening factor that accounts for interstellar extinction.  $A(\lambda)$  describes the interstellar extinction in magnitude at wavelength  $\lambda$  and is given by Equation 1 in Fitzpatrick et al. (2019)<sup>80</sup>.

The  $\chi^2$ -based SED fitting will be completely carried out within ISIS, whereby the same minimization algorithms as described in Sect. 7.1.2 will be used. The microturbulence  $\xi$  and the macroturbulence  $\zeta$  will be set to zero because the SED is not at all sensitive to these two parameters. As the atmospheric parameters ( $T_{\text{eff}}$ ,  $\log g$ , and  $\log n(\text{He})$ ) and their uncertainties will be fixed to the values derived from the corresponding quantitative spectral analyses and due to the fact that the metallicity  $Z$  will also be fixed as described in Sects. 7.2.1 and 7.2.2, the only two free fit parameters to model the SEDs of single stars are the stellar angular diameter  $\theta$  and the monochromatic color excess  $E(44 - 55)$ . The former shifts the model spectrum up and down according to  $f(\lambda) = [\theta^2 F(\lambda)]/4$ , whereas the latter reddens the spectrum. If a binary SED fit needs to be performed, the atmospheric parameters of the secondary star ( $T_{\text{eff,sec}}$  and  $\log g_{\text{sec}}$ ) as well as the surface ratio between both stars ( $S := A_{\text{sec}}/A_{\text{pri}}$ ) can additionally be fitted. However,  $\log(g_{\text{sec}})$  is typically unconstrained. Hence, only  $T_{\text{eff,sec}}$  and  $S$  will be fitted, whereas for  $\log(g_{\text{sec}})$  a value of 4.50, typical for main-sequence stars, will be assumed. Since the metallicity of the companion ( $Z_{\text{sec}}$ ) is also usually unconstrained, it will be fixed to the solar value.

If no uncertainties are measured for the observed magnitudes or colors used (see Sect. 8.3) or in cases where their uncertainties are zero, a generic error of 0.025 mag will be assumed. In order to guarantee a best fit of  $\chi_{\text{red}}^2 \approx 1$ , a generic excess noise will be added in quadrature to all observed magnitudes and colors, if needed.  $1\sigma$  statistical single confidence intervals for all fit parameters except for  $\theta$  will be determined in ISIS, whereby the same error analysis as described in Sect. 7.1.2 will be used.  $\Delta\theta$  needs to be treated specifically because of two

<sup>80</sup> $A(\lambda)$  is expressed as a function of the monochromatic color excess  $E(44 - 55) := m(4400) - m(5500) - (m(4400) - m(5500))_{\text{intrinsic}}$  and the extinction coefficient  $R(55) := A(5500)/[E(44 - 55)]$  via Equations 2, 3, and 8 and Table 3 in Fitzpatrick et al. (2019). Here,  $m(4400)$  and  $m(5500)$  denote the monochromatic magnitudes at wavelengths  $\lambda = 4400 \text{ \AA}$  and  $\lambda = 5500 \text{ \AA}$  such that  $E(44 - 55)$  is the monochromatic equivalent of the usual color excess  $E(B - V)$  in the Johnson system. As a matter of fact,  $E(44 - 55)$  is identical to  $E(B - V)$  for high effective temperatures ( $T_{\text{eff}} \gtrsim 20\,000 \text{ K}$ ) and low interstellar extinction values ( $E(44 - 55) \lesssim 0.50 \text{ mag}$ ), which can be seen from Table 4 in Fitzpatrick et al. (2019). Within the framework of this thesis,  $R(55)$  is fixed to a value of 3.02, which corresponds to the extinction coefficient of the diffuse interstellar medium in the Milky Way.

reasons. First, the precision of the photometric observations leads to an uncertainty on the observed flux  $f(\lambda)$ . Second, the uncertainties of the effective temperature propagate into the predicted synthetic flux  $F(\lambda)$ . In consequence,  $\Delta\theta$  will be discussed in detail in the context of the determination of the fundamental stellar parameters (see the next section). Examples for performed single and binary SED fits can be found in Ch. 12. This chapter presents the results of the photometric analyses.

### 7.3. Trigonometric Parallaxes and the Fundamental Stellar Parameters

As described in the previous Sects. 7.1 and 7.2, the spectrophotometric analysis of a star gives its effective temperature  $T_{\text{eff}}$ , surface gravity  $\log(g)$ , and helium abundance  $\log n(\text{He})$  from spectroscopy as well as its angular diameter  $\theta$  from photometry. By combining  $T_{\text{eff}}$ ,  $\log(g)$ , and  $\theta$  with the distance  $d$  to/the parallax  $\varpi$  of the stellar object under investigation, which can be taken from *Gaia* data release 2 (Gaia Collaboration et al., 2018), the stellar radius  $R$ , the luminosity  $L$ , and the stellar mass  $M$  can be calculated (see, for instance, Heber et al. 2018; Schindewolf et al. 2018). This is realized by the following astrophysical relations (see also Fig. 7.3.1):

$$R \stackrel{\theta \ll 1}{\approx} d \cdot \frac{\theta}{2} = \frac{\theta}{2\varpi} \quad (7.7)$$

$$\log\left(\frac{L}{L_{\odot}}\right) \stackrel{\text{Eq.(6.7)}}{=} \log\left(\frac{4\pi R^2 \sigma T_{\text{eff}}^4}{L_{\odot}}\right) \stackrel{\text{Eq.(7.7)}}{=} \log\left(\frac{\pi \sigma \theta^2 T_{\text{eff}}^4}{\varpi^2 L_{\odot}}\right) \quad (7.8)$$

$$M = \frac{10^{\log(g)} R^2}{G} \stackrel{\text{Eq.(7.7)}}{=} \frac{10^{\log(g)} \theta^2}{4G\varpi^2}, \quad (7.9)$$

where  $\sigma$  is the Stefan-Boltzmann constant and  $G$  is the Gravitational constant. The corresponding uncertainties can be derived from Gaussian error propagation by the following formulas:

$$\Delta R = \frac{1}{2\varpi} \sqrt{(\Delta\theta)^2 + \theta^2 \cdot \left(\frac{\Delta\varpi}{\varpi}\right)^2} \quad (7.10)$$

$$\Delta \log(L/L_{\odot}) = \frac{2}{\ln 10} \sqrt{\left(\frac{\Delta R}{R}\right)^2 + 4 \cdot \left(\frac{\Delta T_{\text{eff}}}{T_{\text{eff}}}\right)^2} \quad (7.11)$$

$$\Delta M = M \sqrt{(\ln 10 \cdot \Delta \log g)^2 + 4 \cdot \left(\frac{\Delta\theta}{\theta}\right)^2 + 4 \cdot \left(\frac{\Delta\varpi}{\varpi}\right)^2}. \quad (7.12)$$

The relative uncertainty on the stellar angular diameter ( $\Delta\theta/\theta$ ) can be derived from the assumption of a spherically symmetric object and from photon conservation, whereby the

energy penetrating a sphere of radius  $d$  (centred at the object's position) per unit time is identical to that emitted by the object:

$$4\pi d^2 f(\lambda) = 4\pi R^2 F(\lambda) \rightarrow \frac{f(\lambda)}{F(\lambda)} = \frac{R^2}{d^2}. \quad (7.13)$$

Here,  $\lambda$  is the wavelength,  $f(\lambda)$  is the object's flux observed at the detector position,  $F(\lambda)$  is the model flux at the stellar surface, and  $R$  is the object's radius. Furthermore:

$$\theta \stackrel{\text{Eq.(7.7)}}{\approx} \frac{2R}{d} \stackrel{\text{Eq.(7.13)}}{=} 2 \left[ \frac{f(\lambda)}{F(\lambda)} \right]^{1/2}. \quad (7.14)$$

Since the program stars of this work are blue (hot) stars, it can be assumed that the Rayleigh-Jeans part dominates the SED. Thus,  $F(\lambda) = \frac{2c\pi k_B}{\lambda^4} T_{\text{eff}} d\lambda$ , where  $c$  is the vacuum speed of light and  $k_B$  is the Boltzmann constant. In combination with Eq. (7.14), this results in:

$$\begin{aligned} d\theta &= \frac{\partial \theta}{\partial T_{\text{eff}}} dT_{\text{eff}} = \frac{\partial \theta}{\partial F(\lambda)} \cdot \frac{\partial F(\lambda)}{\partial T_{\text{eff}}} dT_{\text{eff}} + \frac{\partial \theta}{\partial f(\lambda)} \cdot \frac{\partial f(\lambda)}{\partial T_{\text{eff}}} dT_{\text{eff}} \\ &= -\frac{2c\pi k_B}{\lambda^4} [f(\lambda)]^{1/2} [F(\lambda)]^{-3/2} dT_{\text{eff}} d\lambda, \end{aligned} \quad (7.15)$$

whereby it was used that  $f(\lambda)$  is independent of  $T_{\text{eff}}$  such that  $\frac{\partial f(\lambda)}{\partial T_{\text{eff}}} = 0$ . Consequently:

$$\frac{d\theta}{\theta} = -\frac{1}{2} \frac{dT_{\text{eff}}}{T_{\text{eff}}}, \quad (7.16)$$

whereby Eqs. (7.14) and (7.15) and  $F(\lambda) = \frac{2c\pi k_B}{\lambda^4} T_{\text{eff}} d\lambda$  were used. Eventually:

$$\frac{\Delta \theta}{\theta} = \left| \frac{d\theta}{\theta} \right| = \frac{\sqrt{(\Delta T_{\text{eff,photo}})^2 + (\Delta T_{\text{eff,model}})^2}}{2T_{\text{eff}}}. \quad (7.17)$$

There are two types of errors for SED fitting that contribute to  $dT_{\text{eff}}$ .  $\Delta T_{\text{eff,photo}}$  describes the error that results from the statistical uncertainties on the individual photometric observations used. These statistical uncertainties lead to an uncertainty on the observed flux  $f(\lambda)$ . Due to the very precise photometric data available for the program stars of this work (see Sect. 8.3),  $\Delta T_{\text{eff,photo}}$  is very small and, therefore, can be neglected. On the other hand,  $\Delta T_{\text{eff,model}}$  represents the intrinsic uncertainty of the models used, which leads to an uncertainty on the predicted synthetic flux  $F(\lambda)$ . In principle, the same model grids of synthetic spectra as used for spectroscopy will also be used for SED fitting. Hence,  $\Delta T_{\text{eff,model}}$  can be replaced by the total uncertainty on  $T_{\text{eff}}$  derived from the spectroscopic analyses, combining statistical and systematic errors:  $\Delta T_{\text{eff,model}} = \Delta T_{\text{eff,spectr.}} = \sqrt{(\Delta T_{\text{eff,spectr.,stat.}})^2 + (\Delta T_{\text{eff,spectr.,syst.}})^2}$ . How the systematic uncertainty  $\Delta T_{\text{eff,spectr.,syst.}}$  can be estimated will be dealt with in Ch. 9. Given the total uncertainties on  $T_{\text{eff}}$  derived from spectroscopy (see the results of Ch. 9),  $\Delta \theta / \theta$  will typically be of the order of 1-3 % only. Since the *Gaia* parallaxes for most of the program

### 7.3. Trigonometric Parallaxes and the Fundamental Stellar Parameters

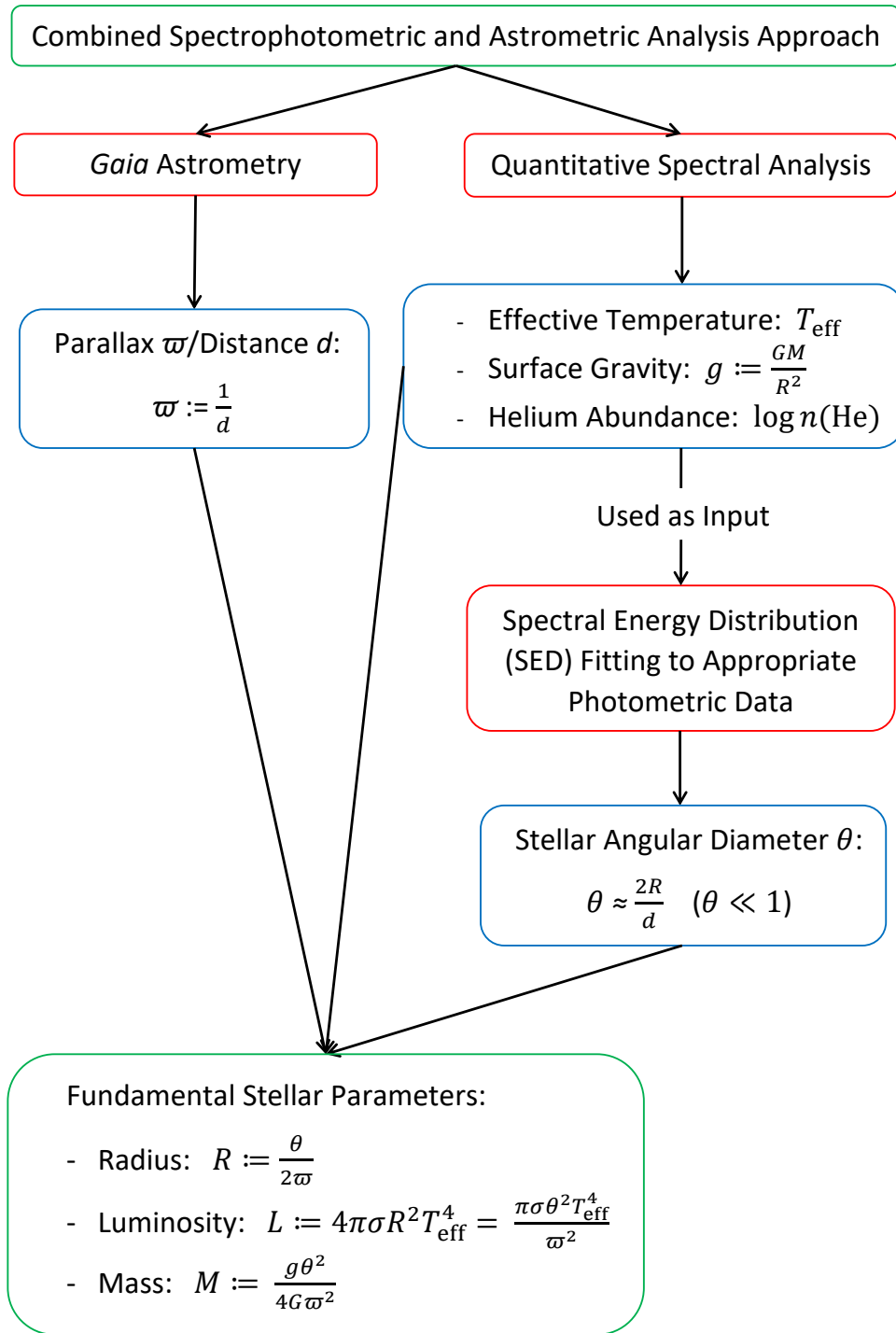


Figure 7.3.1.: Scheme of the combined spectrophotometric and astrometric analysis approach used to derive the fundamental stellar parameters (radius  $R$ , luminosity  $L$ , and mass  $M$ ) of a given star.  $G$  is the Gravitational constant and  $\sigma$  denotes the Stefan-Boltzmann constant.

## 7. Combined Spectrophotometric and Astrometric Analysis

---

stars investigated in this work are very precise with typical relative statistical uncertainties of  $\Delta\varpi/\varpi \lesssim 0.05$  (see Tables 8.18 and 8.19 of Sect. 8.4), the stellar radii derived from Eqs. (7.7) and (7.10) will also be very precise. The same applies to the luminosities derived from Eqs. (7.8) and (7.11) because  $T_{\text{eff}}$  can be determined quite well from spectroscopy. However, as  $T_{\text{eff}}$  enters to the power of four, the relative luminosity uncertainties  $\Delta L/L$  will usually be not as small as  $\Delta R/R$ . The surface gravity remains the most problematic quantity when it comes to the mass determination (see Eqs. 7.9 and 7.12). Assuming a very conservative uncertainty of  $\Delta \log(g) = 0.10$  already results in a relative mass uncertainty of  $\Delta M/M \sim 26\%$  for most of the program stars with  $\Delta\varpi/\varpi \lesssim 0.05$  and  $\Delta\theta/\theta \sim 1\text{-}3\%$ . Therefore, it is very important to constrain  $\log(g)$  as precisely as possible. This will be dealt with in Ch. 9.

## 8. Observations and Data Preparation

In total, the initial target sample of this work consists of a zoo of 66 bright stars, most of them being known hydrogen-rich or (intermediate) helium-rich hot subdwarf stars. A number of hot subdwarf candidates and three  $^3\text{He}$ -enriched (post-)BHB stars (PHL 25, PHL 382, and BD+48° 2721) are included. Spectra of single and binary as well as of pulsating and non-pulsating program stars, which have been obtained with 13 different spectrographs, will be analyzed (most of these spectrographs are described in detail in Sect. 4.4). For several program stars (HD 4539, Feige 38, EC 03591-3232, [CW83] 0512-08, PG 0314+146, and HD 149382), spectra from multiple instruments will be investigated. The complete target sample can be divided into low, medium, and high-resolution spectra.

During the analysis, the variety of stars increased, particularly because part of the initial hot subdwarf candidates turned out to be either B-type MS stars or progenitors of extremely low-mass helium-core white dwarfs (pre-ELMs<sup>81</sup>). These new discoveries will be discussed in the later stages of this work. Because of them, the total analyzed sample consists of 33 H-sdBs (one of them is confirmed to be a pre-ELM, three others could be pre-ELMs, and eleven are  $^3\text{He}$ -enriched), six H-sdOBs (one of them could be a pre-ELM), five H-sdOs (one of them may also be a post-AGB star), three He-sdBs (all of them are intermediate helium-rich, hence they are listed as iHe-sdBs), and eight He-sdOs as well as of three (post-)BHB and six B-type MS stars. The true nature of two program stars remains unclear. Tables 8.1-8.11 provide a detailed overview of all program stars as well as of the respective spectroscopic data used.

In the following, the spectroscopic data (Sect. 8.1), the photometric data (Sect. 8.3), and the astrometric data from *Gaia* (Sect. 8.4) will be presented for the program stars. Section 8.2 provides a brief introduction to spectroscopic data processing, including calibration and reduction as well as telluric absorption correction, co-addition, channel merging, and normalization. Moreover, the spectral line identification will be discussed in this section.

---

<sup>81</sup>Extremely low-mass helium-core white dwarfs (ELMs) are primarily believed to be the product of binary evolution (Marsh et al., 1995), that is, CE evolution or stable RLOF mass transfer in a low-mass X-ray binary or in a cataclysmic variable system. This is because the vast majority of ELMs are found in binary systems with carbon-oxygen WD, A-type star (Maxted et al., 2014), or neutron star (van Kerkwijk et al., 2005) companions. In fact, most ELMs are observed as short-period binaries. ELM masses are typically below  $0.20\text{-}0.30 M_{\odot}$  but their surface gravities of  $5.0 \lesssim \log(g) \lesssim 7.0$  (Brown et al., 2013) often coincide with those of hot subdwarf stars. ELMs have been observed in the Galactic disk as well as in open and globular clusters (see, for instance, Rivera-Sandoval et al. 2015 or Cadelano et al. 2015). Hence, they must have been formed from progenitor stars with very different metallicities. It is also known that the ELM mass strongly depends on the metallicity (Serenelli et al., 2002; Nelson et al., 2004). As a matter of fact, the term ‘pre-ELM’ will be used throughout this work in order to describe objects that are possible progenitors of ELMs. For instance, this can be low-mass hot subdwarf stars (Heber et al., 2003a; Kawka et al., 2015).

## 8.1. Spectroscopic Data

### 8.1.1. The XSHOOTER Reference Sample

As outlined in Sect. 7.3, the uncertainties on the atmospheric parameters that result from quantitative spectral analyses will be the limiting factors when it comes to the determination of the fundamental stellar parameters of this work's program stars. In particular, the uncertainty on the stellar mass strongly depends on the precision of the surface gravity. In order to cope with the precise and accurate trigonometric parallaxes available in *Gaia* DR2, the precision of the atmospheric parameters therefore needs to be improved. This calls for an in-depth investigation of spectral diagnostics in general. Furthermore, the impact of the quality and the wavelength coverage of spectroscopic data needs to be investigated. High-quality, that is, high-resolution and high S/N spectra are not only necessary for the interesting group of (intermediate) helium-rich hot subdwarfs, but also for their well-studied hydrogen-rich counterparts because in terms of effective temperatures and surface gravities the published results from quantitative spectral analyses of the same hot subdwarf B star typically agree to 10% and 0.2 dex only.

Thus, the reference sample of this work, which has been taken with the XSHOOTER Echelle spectrograph installed at the ESO VLT on Cerro Paranal (Vernet et al., 2011), is defined as a spectroscopic calibration sample of 17 bright ( $8.9 \text{ mag} \lesssim G_{\text{Gaia}} \lesssim 14.4 \text{ mag}$ ) hot subdwarf O and B stars covering the wide parameter range in effective temperature, surface gravity, and helium abundance observed for this spectral class. The three different XSHOOTER channels (arms) used for the reference sample have resolutions of  $R \sim 9700$  (UVB, slit width: 0.5"),  $R \sim 18400$  (VIS, slit width: 0.4"), and  $R \sim 11600$  (NIR, slit width: 0.4"). In total, medium-resolution spectra of outstanding quality (34 hours of integration time resulting in S/N ratios of several hundreds after co-adding the single exposures) and with wide wavelength coverage ( $\sim 3000\text{-}25\,000 \text{ \AA}$ ) have been obtained for seven H-sdBs (one of them is confirmed to be a pre-ELM and two are  $^3\text{He}$ -enriched), three H-sdOBs, two iHe-sdBs, and five He-sdOs. Typically, seven single exposures in the individual XSHOOTER channels have been taken in service mode for each target. The calibration and the reduction of the data (a general introduction to data processing will be given in Sect. 8.2) was carried out by the ESO team within the XSHOOTER pipeline (Ballester et al., 2020), which is a subsystem of the VLT Data Flow System. Tables 8.1-8.3 provide a detailed overview of the spectroscopic data of the XSHOOTER reference sample. This sample serves as a perfect starting point for detailed quantitative spectral analyses, which make use of the sophisticated model atmospheres, synthetic spectra, and fitting procedures described in Chs. 6 and 7.

Table 8.1.: Spectroscopic data of the XSHOOTER reference sample.

Object <i>Gaia</i> DR2 Source ID	Nature <sup>a</sup>	Channel <sup>b</sup>	No. Spec.	S/N	$G_{\text{Gaia}}$ [mag]	$P_{\text{orb}}$ [d]	Ref.	Other Names
HD 4539 <sup>c</sup> 2582106305103802880	H-sdB	UVB	7	478	10.2602	-	[1]	PG 0044+097
		VIS	7	360				GALEX J004729.4+095855
		NIR	7	92				TYC 604-109-1
PG 1432+004 3653238674478903040	H-sdB	UVB	7	322	12.7468	-	-	GALEX J143519.8+001352
		VIS	7	205				TYC 325-452-1
		NIR	7	52				
GALEX J104148.9-073031 3762736048191497472	H-sdB	UVB	7	406	11.6490	-	-	TYC 5492-642-1
		VIS	7	307				
		NIR	7	66				
Feige 38 3817717887347994112	<sup>3</sup> He H-sdB	UVB	7	242	13.0048	-	-	PG 1114+073
		VIS	7	154				GALEX J111649.3+065932
		NIR	7	27				

**Notes:**

- (<sup>a</sup>) Hydrogen-rich hot subdwarf O and B stars (H-sdBs, H-sdOBs, H-sdOs), intermediate helium-rich hot subdwarf B stars (iHe-sdBs), helium-rich hot subdwarf O stars, that is, carbon (C), nitrogen (N), and carbon-nitrogen (CN) enriched He-sdOs, <sup>3</sup>He-enriched hydrogen-rich hot subdwarf B stars (<sup>3</sup>He H-sdBs), (post-)blue horizontal branch stars ((post-)BHBs), (post-)asymptotic giant branch stars ((post-)AGBs), B-type main-sequence stars (B MSs), unknown (?), white dwarfs (WDs), main-sequence stars (MSs), low-mass main-sequence stars (dMs), substellar objects (SOs). The given companion types (WD, MS, dM, or SO) of binary systems are either extracted from literature or are constrained from SED fitting in this work (see Ch. 12 for details).
- (<sup>b</sup>) The three different XSHOOTER channels (arms) have medium resolutions of  $R \sim 9700$  (UVB),  $R \sim 18\,400$  (VIS), and  $R \sim 11\,600$  (NIR).
- (<sup>c</sup>) Pulsating star.
- (<sup>d</sup>) RV-variable star.
- (<sup>e</sup>) Rotating star.
- (<sup>f</sup>) The star is a pre-ELM (see Ch. 13 for details).
- (<sup>g</sup>) Within the framework of this thesis, HD 149382 is listed as a single H-sdOB star. It has a background red giant that contributes to the flux in the IR (see Sect. 12.3 for further details).

**References:**

- (1) Silvotti et al. (2019); (2) Geier et al. (2011b); (3) Kawka et al. (2015); (4) Jeffery et al. (2017).

Table 8.2.: Table 8.1 continued.

Object <i>Gaia</i> DR2 Source ID	Nature <sup>a</sup>	Channel <sup>b</sup>	No. Spec.	S/N	$G_{\text{Gaia}}$ [mag]	$P_{\text{orb}}$ [d]	Ref.	Other Names
EC 03591-3232 4883474679951350656	<sup>3</sup> He H-sdB	UVB VIS NIR	7 7 7	345 317 65	11.1601	-	-	CD-32° 1567 GALEX J040105.3-322348 TYC 7030-240-1
PG 1136-003 <sup>d</sup> 3794197787442075008	H-sdB+WD	UVB VIS	7 7	94 47	14.4396	$0.207536 \pm 0.000002$	[2]	FBS 1136-003 SDSS J113840.68-003531.7
GALEX J080510.9-105834 <sup>d e f</sup> 3037891155139776128	H-sdB + SO/dM	UVB VIS NIR	7 7 7	490 277 53	12.2470	$0.173703 \pm 0.000002$	[3]	TYC 5417-2552-1
PG 1505+074 1160486522563096192	H-sdOB	UVB VIS NIR	7 7 7	405 278 53	12.3706	-	-	[CW83] 1505+07 GALEX J150821.2+071313 TYC 347-166-1
EC 13047-3049 6181058207869535872	H-sdOB	UVB VIS NIR	7 7 7	342 169 31	12.7857	-	-	GALEX J130730.9-310500
HD 149382 4354377620100892416	H-sdOB <sup>g</sup>	UVB VIS NIR	9 9 9	376 375 177	8.8900	-	-	BD-03° 3967, LS IV -03° 1 PG 1631-039 TYC 5056-274-1
[CW83] 0825+15 <sup>c</sup> 651745279826458112	iHe-sdB	UVB VIS NIR	7 7 7	244 296 57	11.6376	-	[4]	GALEX J082832.7+145204 TYC 808-490-1
[CW83] 0512-08 3206674676854713344	iHe-sdB	UVB VIS NIR	7 7 7	263 311 62	11.1782	-	-	TYC 5331-1560-1

Table 8.3.: Table 8.1 continued.

Object <i>Gaia</i> DR2 Source ID	Nature <sup>a</sup>	Channel <sup>b</sup>	No. Spec.	S/N	$G_{\text{Gaia}}$ [mag]	$P_{\text{orb}}$ [d]	Ref.	Other Names
GALEX J075807.5-043203 3068507812327598208	He-sdO (C)	UVB	7	270	13.0611	-	-	TYC 4841-1870-1
		VIS	7	155				
		NIR	7	43				
GALEX J042034.8+012041 3255780171819962496	He-sdO (C)	UVB	7	320	12.3175	-	-	GALEX J042034.8+012042
		VIS	7	192				
		NIR	7	66				
HZ 1 3406506723313874688	He-sdO (N)	UVB	7	275	12.5888	-	-	CI* Melotte 25° HZ 1 TYC 1284-314-1
		VIS	7	211				
		NIR	7	56				
GALEX J095256.6-371940 <sup>e</sup> 5433906762213163392	He-sdO (CN)	UVB	7	257	13.2607	-	-	TYC 7180-740-1
		VIS	6	138				
		PG 0314+146 30269452033850624	He-sdO (CN)	UVB				
VIS	7	174						
		NIR	7	37				

Table 8.4.: Spectroscopic data of the high-resolution sample. Given natures are described in Table 8.1.

Object <i>Gaia</i> DR2 Source ID	Nature	Instr.	$R$	No. Spec.	S/N	$G_{\text{Gaia}}$ [mag]	$P_{\text{orb}}$ [d]	Ref.	Other Names
PHL 25 6834927258827406720	$^3\text{He}$ BHB	HRS	60 000	2	40	10.8898	-	[1]	TYC 6365-74-1
PHL 382 <sup>a</sup> 2597188787138939520	$^3\text{He}$ post-BHB	FEROS	48 000	7	88	11.3146	-	[1]	TYC 5818-926-1
BD+48° 2721 2120323958447382272	$^3\text{He}$ BHB	FOCES	40 000	1	84	10.6625	-	[1]	TYC 3531-1327-1
PG 0342+026 <sup>b</sup> 3271319569656254464	H-sdB	FEROS	48 000	4	135	10.9089	-	[2]	TYC 68-204-1
HD 4539 <sup>b</sup> 2582106305103802880	H-sdB	FEROS	48 000	3	71	10.2602	-	[1,3]	see Table 8.1
CD-35° 15910 <sup>b</sup> 2312392250224668288	H-sdB	FEROS	48 000	2	56	10.9201	-	[1,4]	SB 815 HE 2341-3443 GALEX J234422.0-342700 TYC 7518-873-1
EC 03263-6403 4673903262571018240	$^3\text{He}$ H-sdB	FEROS	48 000	2	23	13.4326	-	[1]	GALEX J032710.2-635255
EC 03591-3232 4883474679951350656	$^3\text{He}$ H-sdB	FEROS	48 000	2	65	11.1601	-	[1]	see Table 8.2

**Notes:**

- (a) Rotating star.  
(b) Pulsating star.  
(c) The star is most likely a pre-ELM. For further information, see Sect. 12.2.  
(d) RV-variable star.

**References:**

(1) Schneider et al. (2018); (2) Sahoo et al. (2020); (3) Silvotti et al. (2019); (4) Holdsworth et al. (2017); (5) Saffer et al. (1998); (6) Moran et al. (1999).

Table 8.5.: Table 8.4 continued.

Object <i>Gaia</i> DR2 Source ID	Nature	Instr.	$R$	No. Spec.	S/N	$G_{\text{Gaia}}$ [mag]	$P_{\text{orb}}$ [d]	Ref.	Other Names
EC 12234-2607 3476365637693166208	$^3\text{He}$ H-sdB	FEROS	48 000	4	28	13.7841	-	[1]	GALEX J122606.2-262413
EC 14338-1445 6286983543181717120	$^3\text{He}$ H-sdB	FEROS	48 000	3	38	13.5487	-	[1]	GALEX J143633.6-145801
Feige 38 3817717887347994112	$^3\text{He}$ H-sdB	FEROS	48 000	5	69	13.0048	-	[1]	see Table 8.2
PG 1710+490 1414187320160273024	$^3\text{He}$ H-sdB	FOCES	40 000	1	27	12.8505	-	[1]	GALEX J171218.5+485835 TYC 3504-599-1
SB 290 <sup>a</sup> 5000760581717433088	$^3\text{He}$ H-sdB+MS	FEROS	48 000	2	68	10.4251	-	[1]	CD-38° 222 EC 00405-3824 TYC 7532-1061-1
Feige 36 <sup>c,d</sup> 3995631994142136576	$^3\text{He}$ H-sdB+MS	HIRES	36 000	1	116	12.7678	$0.35386 \pm 0.00014$	[1,5,6]	[CW83] 1101+24 PG 1101+249 TYC 1978-294-1

Table 8.6.: Spectroscopic data of the UVES<sup>a</sup> medium-resolution sample. Given natures are described in Table 8.1.

Object <i>Gaia</i> DR2 Source ID	Nature	No. Spec.	S/N	$G_{\text{Gaia}}$ [mag]	$P_{\text{orb}}$ [d]	Ref.	Other Names
HE 0929-0424 <sup>b</sup> 3824889589379453312	<sup>3</sup> He H-sdB+WD	2	22	16.1966	$0.4400 \pm 0.0002$	[1,2]	GALEX J093202.1-043735
HE 1047-0436 <sup>b</sup> 3777025198226679808	<sup>3</sup> He H-sdB+WD	4	25	15.0022	$1.21325 \pm 0.00001$	[1,3]	PG 1047-046 GALEX J105026.8-045234
HD 149382 4354377620100892416	H-sdOB <sup>c</sup>	1	291	8.8900	-	-	see Table 8.2

**Notes:**

(<sup>a</sup>) The UVES spectra have a resolution of  $R \sim 18\,500$ .

(<sup>b</sup>) RV-variable star.

(<sup>c</sup>) Within the framework of this thesis, HD 149382 is listed as a single H-sdOB star. It has a background red giant that contributes to the flux in the IR (see Sect. 12.3 for further details).

**References:**

(1) Schneider et al. (2018); (2) Karl et al. (2006); (3) Napiwotzki et al. (2001a).

### 8.1.2. Increasing the Sample Size: High-Quality Optical Spectra from Other Instruments

As described in the previous section, the XSHOOTER reference sample offers medium-resolution data of outstanding quality. With 17 hot subdwarf stars only, however, its sample size is very limited. Making use of the reference sample only, meaningful statistics for hot subdwarf stars in terms of atmospheric and fundamental stellar parameters therefore cannot be achieved. Consequently, low, medium, and high-resolution optical spectra from other instruments (see also Sect. 4.4), which have decent S/N (preferably  $\gtrsim 50$ ), are added. In the following, these data will be presented individually in order of decreasing spectral resolution.

#### High-Resolution Data from FEROS, FOCES, HIRES, and HRS

High-resolution data from different Echelle spectrographs, that is, FEROS (Kaufer et al., 1999) mounted at the ESO/MPI<sup>82</sup> 2.2 m telescope in La Silla, Chile, FOCES (Pfeiffer et al., 1998) mounted at the CAHA 2.2 m telescope, HIRES (Vogt et al., 1994) mounted at the Keck 10 m telescope, and HRS (Tull, 1998) mounted at the HET, which is part of the McDonald Observatory, are added to the sample. These data were presented and used in Schneider (2017), Schneider et al. (2017), and Schneider et al. (2018), respectively. In total, the high-resolution sample consists of 14 bright stars with magnitudes of  $10.3 \text{ mag} \lesssim G_{\text{Gaia}} \lesssim 13.8 \text{ mag}$ : three (post-)BHBs and eleven H-sdBs (one of them is probably a pre-ELM). The (post-)BHBs and eight of the H-sdBs are <sup>3</sup>He-enriched. The total number of single spectra obtained for each individual target as well as the quality in terms of S/N of the resulting co-added spectra strongly differ (see Tables 8.4 and 8.5). The FEROS ( $R \sim 48\,000$ , 3530-9200 Å) and FOCES ( $R \sim 40\,000$ , 3800-7000 Å) data were provided by S. Geier. They were calibrated and reduced with the ESO MIDAS package. The HRS spectra of PHL 25 ( $R \sim 60\,000$ , 3660-9950 Å) were obtained, calibrated and reduced by H. Edelmann in July 2006, whereas the HIRES data for Feige 36 ( $R \sim 36\,000$ , 4270-6720 Å) were taken and processed by T. Kupfer in 2017.

#### Medium-Resolution Data from UVES

Data from the ESO SPY project (Napiwotzki et al., 2001a), that is the most comprehensive and homogeneous sample of hot subdwarf stars for which high-quality spectra are currently available, are added to the sample for three program stars: two medium-bright <sup>3</sup>He-enriched H-sdBs with  $G_{\text{Gaia}} \sim 15.0 \text{ mag}$  and  $G_{\text{Gaia}} \sim 16.2 \text{ mag}$ , respectively, and one bright H-sdOB with  $G_{\text{Gaia}} \sim 8.9 \text{ mag}$ . These medium-resolution data ( $R \sim 18\,500$ , 3290-6640 Å, slit width: 2.1") have been obtained with the UVES spectrograph at the ESO VLT (Dekker et al., 2000). They were calibrated and reduced by Karl (2004). U. Heber provided them for the purpose of this work. Two thirds of the medium-resolution data were presented and used in Schneider (2017), Schneider et al. (2017), and Schneider et al. (2018), respectively. As in the case of

---

<sup>82</sup>MPI stands for Max Planck Institute for Astronomy/Max-Planck-Institut für Astronomie.

Table 8.7.: Spectroscopic data of the CAFOS<sup>a</sup> low-resolution sample. Given natures are described in Table 8.1.

Object <i>Gaia</i> DR2 Source ID	Nature	No. Spec.	S/N	$G_{\text{Gaia}}$ [mag]	$P_{\text{orb}}$ [d]	Ref.	Other Names
HIP 67513 1500403089207449856	?	1	226	11.7899	-	-	Balloon 82100002 GALEX J135001.6+410650 TYC 3030-93-1
BD+49° 2226 1552549558458503808	?	1	316	10.2757	-	-	Balloon 82000002 TYC 3466-192-1
FBS 1850+443 2106845182841339264	B MS	1	251	12.1902	-	-	TYC 3131-321-2
FBS 2158+373 1955711708967243136	B MS	1	187	12.2826	-	-	GALEX J220036.0+373330 TYC 3198-103-1
FBS 2204+364 1954666210848854784	B MS	1	177	11.8730	-	-	GALEX J220613.8+364041 TYC 2732-1197-1
HD 4539 <sup>b</sup> 2582106305103802880	H-sdB	1	293	10.2602	-	[1]	see Table 8.1
BD+42° 3250 <sup>c</sup> 2105469320138052864	H-sdB	1	210	10.5933	-	-	TYC 3128-248-1
Balloon 90100001 <sup>b</sup> 2846162921688127360	H-sdB	1	204	12.0984	-	[2]	V* V585 Peg GALEX J231521.4+290502 TYC 2248-1751-1
FBS 0102+362 369576820516013824	H-sdB	1	192	12.3984	-	-	TYC 2290-938-1

**Notes:**

- (a) The CAFOS spectra have a resolution of  $\Delta\lambda \approx 5.26 \text{ \AA}$ .  
(b) Pulsating star.  
(c) The star could be/is most likely a pre-ELM (see Ch. 13 for details).  
(d) RV-variable star.

**References:**

- (1) Silvotti et al. (2019); (2) Oreiro et al. (2004); (3) Kawka et al. (2012); (4) Moran et al. (1999); (5) Randall et al. (2005);  
(6) Geier et al. (2008).

Table 8.8.: Table 8.7 continued.

Object <i>Gaia</i> DR2 Source ID	Nature	No. Spec.	S/N	$G_{\text{Gaia}}$ [mag]	$P_{\text{orb}}$ [d]	Ref.	Other Names
Feige 14 2467789050372181760	H-sdB	1	231	12.7726	-	-	GALEX J014803.4-055545 TYC 4688-2166-1
GALEX J210332.4+303538 1852616039853485824	H-sdB	1	141	12.9515	-	-	TYC 2701-1209-1
FBS 2347+385 <sup>d</sup> 2881551562420806784	H-sdB+WD	1	217	11.7316	$0.462516 \pm 0.000005$	[3]	GALEX J234947.5+384440 TYC 3232-1319-1
PG 0101+039 <sup>b,d</sup> 2551900379931546240	H-sdB+WD	1	255	12.0466	$0.569899 \pm 0.000001$	[4,5,6]	Feige 11 GALEX J010421.5+041340 TYC 22-821-1
PG 1635+414 <sup>c</sup> 1356777767921294976	H-sdOB	1	246	13.9548	-	-	GALEX J163705.3+411539 FBS 1635+413
LS IV +10° 9 3206674676854713344	He-sdO (CN)	1	266	11.9747	-	-	GALEX J204302.4+103427 TYC 1093-369-1

Table 8.9.: Spectroscopic data of the IDS<sup>a</sup> low-resolution sample. Given natures are described in Table 8.1.

Object <i>Gaia</i> DR2 Source ID	Nature	No. Spec.	S/N	$G_{\text{Gaia}}$ [mag]	$P_{\text{orb}}$ [d]	Ref.	Other Names
PG 2219+094 <sup>b</sup> 2723329360986655616	B MS	1	152	11.9028	-	-	GALEX J222159.1+093728 TYC 1142-503-1
SB 395 2357245800583630720	B MS	1	110	12.5253	-	-	GALEX J005911.5-181800
KUV 03591+0457 <sup>b</sup> 3272871049282275328	B MS	1	129	12.3617	-	-	TYC 79-569-1
HE 0247-0418 <sup>c</sup> 5185394353824729856	H-sdB	1	119	13.0230	-	-	PB 9286 GALEX J025023.8-040611 TYC 4703-810-1
GALEX J203913.4+201309 <sup>b</sup> 1817266534856772096	H-sdB	1	130	12.9870	-	-	-
GALEX J202332.7+013618 4230984141696772864	H-sdB	1	129	12.8931	-	-	TYC 497-63-1
GALEX J172445.5+113224 4492298675061523712	H-sdB	1	127	12.5910	-	-	TYC 999-2458-1
PG 2313-021 <sup>d</sup> 2638589797971367936	H-sdB+WD	1	138	12.9980	$8.7465 \pm 0.0010$	[1]	Feige 108 FBS 2313-021
KUV 16256+4034 <sup>d</sup> 1332896306646572160	H-sdB+WD	1	99	12.5582	$0.4776 \pm 0.0008$	[2]	GALEX J162716.4+402728 TYC 3066-1421-1 FBS 1625+407

**Notes:**

- (a) The IDS spectra have a resolution of  $\Delta\lambda \approx 2.82 \text{ \AA}$ .  
(b) Rotating star.  
(c) The star could be a pre-ELM (see Ch. 13 for details).  
(d) RV-variable star.  
(e) Pulsating star.  
(f) It is not possible to determine from SED fitting whether the secondary is a WD or an MS star (see Sect. 12.3 for details).

**References:**

(1) Edelmann et al. (2004); (2) Copperwheat et al. (2011); (3) Edelmann et al. (2005); (4) Kawka et al. (2012); (5) Østensen et al. (2010a); (6) Kilkenny et al. (2009).

Table 8.10.: Table 8.9 continued.

Object <i>Gaia</i> DR2 Source ID	Nature	No. Spec.	S/N	$G_{\text{Gaia}}$ [mag]	$P_{\text{orb}}$ [d]	Ref.	Other Names
PG 0133+114 <sup>d</sup> 2585744516065582848	<sup>3</sup> He H-sdB+WD	1	166	12.2983	$1.23787 \pm 0.00003$	[3]	Balloon 92627001 GALEX J013626.0+113932
GALEX J032139.8+472718 <sup>d</sup> 435211617384833536	H-sdB+WD/MS <sup>f</sup>	1	153	11.5664	$0.265856 \pm 0.000003$	[4]	CI* Melotte 20° 488 TYC 3315-1807-1
2M1938+4603 <sup>de</sup> 2080063931448749824	H-sdB+dM	1	166	12.1376	$0.125765300 \pm 0.000000021$	[5]	TYC 3556-3568-1 Kepler-451
FB 29 488017140776849664	H-sdOB	1	156	12.7298	-	-	LS I +63° 198 TYC 4070-2419-1
EC 01541-1409 <sup>e</sup> 5149241067178231552	H-sdOB+MS	1	159	12.2677	-	[6]	GALEX J015631.9-135427
FBS 0654+366 940739915343553664	iHe-sdB	1	105	11.9964	-	-	GALEX J065802.1+363019 TYC 2449-1411-1
[CW83] 0512-08 3206674676854713344	iHe-sdB	1	138	11.1782	-	-	see Table 8.2
GALEX J175548.5+501210 1364478541203752192	He-sdO (N)	1	107	12.8823	-	-	TYC 3519-907-1
PG 0314+146 30269452033850624	He-sdO (CN)	1	102	12.5187	-	-	see Table 8.3
FBS 0224+330 326527401235564672	He-sdO (new)	1	122	13.2067	-	-	GALEX J022705.2+331545 TYC 2327-1408-1

Table 8.11.: Spectroscopic data from literature. These data are not analyzed in this work. However, the spectroscopic results (effective temperatures, surface gravities, and helium abundances) from the given references are used (see also Table A.19). Given natures are described in Table 8.1.

Object <i>Gaia</i> DR2 Source ID	Nature	Instr.	$R$	No. Spec.	S/N	$G_{\text{Gaia}}$ [mag]	$P_{\text{orb}}$ [d]	Ref.	Other Names
BD+28° 4211 1897151272994229120	H-sdO/post-AGB	FUSE & STIS (HST) BOK, MMT & UVES	[1] [2]	[1] [2]	[1] [2]	10.4589	-	[1] [2]	TYC 2214-1198-1
AGK+81° 266 <sup>a</sup> 1144974578159253632	H-sdO	CAFOS	[3]	[3]	[3]	11.8797	-	[3]	FBS 0913+819 GALEX J092120.8+814327 TYC 4547-1009-1
LS II +18° 9 <sup>a</sup> 1824221903674415360	H-sdO	CAFOS	[3]	[3]	[3]	12.0438	-	[3]	HD 350426 TYC 1606-367-1
Feige 67 <sup>a</sup> 3935488605023787392	H-sdO	BOK	[3]	[3]	[3]	11.7697	-	[3]	BD+18° 2647 PG 1239+178 GALEX J124151.8+173118 TYC 1446-2473-1
Feige 34 <sup>a</sup> 781164326766404736	H-sdO+MS	BOK, MMT & ISIS	[3]	[3]	[3]	11.1072	-	[3]	PG 1036+433 [CW83] 1036+43 TYC 3008-452-1

**Notes:**

<sup>(a)</sup> Rotating star.

**References:**

(1) Latour et al. (2013); (2) Latour et al. (2015); (3) Latour et al. (2018).

## 8.2. Data Processing and Preparation

---

the high-resolution data, the number of single exposures as well as the quality of the individual co-added spectra strongly differ (see Table 8.6).

### Low-Resolution Data from CAFOS and IDS

Low-resolution data for 34 bright program stars with  $10.3 \text{ mag} \lesssim G_{\text{Gaia}} \lesssim 14.0 \text{ mag}$  have been obtained with two long-slit spectrographs: CAFOS on the 2.2 m telescope at Calar Alto (Meisenheimer, 1998) and IDS on the 2.5 m Isaac Newton Telescope on La Palma<sup>83</sup>. For the CAFOS data, the blue-100 and red-100 grisms with a slit width of  $100 \mu\text{m}$  were used. This results in a resolution of  $\Delta\lambda \approx 5.26 \text{ \AA}$ . The CAFOS spectra cover the  $3600\text{-}9000 \text{ \AA}$  range and were obtained in 2016. They were calibrated and reduced with the IRAF (Image Reduction and Analysis Facility) package written at the National Optical Astronomy Observatory (NOAO) and were provided by M. Latour. For the IDS data, the EEV10 detector together with the R400B grating was used. This results in a resolution of  $\Delta\lambda \approx 2.82 \text{ \AA}$ . The IDS spectra cover the  $3500\text{-}7000 \text{ \AA}$  range and date back to 2017. They were processed with MIDAS and were provided by S. Geier.

All in all, the low-resolution sample consists of six B-type MS, 17 H-sdB (two of them could be pre-ELMs and one is <sup>3</sup>He-enriched), three H-sdOB (one of them could be a pre-ELM), two iHe-sdB, and four He-sdO stars. Furthermore, two objects, for which the nature remains unclear (see Ch. 13 for further information), are included. For all stars, single exposures with high S/N ( $\gtrsim 100$ ) have been obtained (see Tables 8.7-8.10).

### Spectroscopic Data from Literature

In addition to the samples described above, this work makes use of the spectroscopic results from literature (effective temperatures, surface gravities, and helium abundances) for five H-sdOs (one of them - BD+28° 4211 - may also be a post-AGB star; see also Sect. 3.3). The respective stars are relatively bright ( $10.5 \text{ mag} \lesssim G_{\text{Gaia}} \lesssim 12.0 \text{ mag}$ ; see also Table 8.11). A detailed description of the data used to derive the corresponding spectroscopic results (the individual instruments used, the data quality, the number of analyzed spectra, and the data processing) can be found in the following publications: Latour et al. (2013), Latour et al. (2015), and Latour et al. (2018).

## 8.2. Data Processing and Preparation

The steps in spectroscopic data processing are called calibration and reduction. For instance, data processing can be performed making use of the MIDAS or IRAF packages. During calibration, the individual diffraction orders and their positions on the CCD detector are identified. Furthermore, the dispersion relation is determined, meaning that different

---

<sup>83</sup><http://www.ing.iac.es/astronomy/instruments/ids/>, last called on 12th May 2021

wavelength points  $\lambda$  are assigned to individual pixel positions  $x$  by means of a comparison spectrum. For example, such a comparison spectrum can be taken with a thorium-argon (ThAr) comparison lamp for which the wavelengths of the emission lines are well known. In this context, the spectral resolution of the respective spectrograph used and, therefore, of the spectrum in question can also be determined. For this, the quotient of the central wavelength of a known emission line and the measured full width at half maximum of a Gaussian profile fitted to the respective line needs to be calculated (see also Sect. 6.5.2; Drechsel et al. 2020). The reduction of the raw data generally consists of different steps that have to be carried out separately one after the other. These individual steps are the removal of cosemics, the removal of scattered light, the subtraction of the dark current, the subtraction of the bias frame, the flat field correction, the rebinning, and the order merging. For instance, a detailed description of the general data reduction process in the case of an Echelle spectrograph can be found in Drechsel et al. (2020).

As presented in Sect. 8.1, the stellar spectra analyzed in this work have already been processed beforehand. Nevertheless, additional steps apart from the ones of the general reduction process should be performed in order to facilitate the subsequent spectroscopic analyses. For the present work, these additional steps include the telluric absorption correction (Sect. 8.2.1), the RV correction and the subsequent co-addition of the single spectra (Sect. 8.2.2), the channel merging (Sect. 8.2.3), the normalization (Sect. 8.2.4) as well as the spectral line identification (Sect. 8.2.5).

### 8.2.1. Telluric Absorption Correction with Molecfit

The optical spectral range ( $\sim 3500\text{-}7500\text{ \AA}$ ) is best suited for the spectroscopic analysis of hot (blue) stars of spectral types O and B because of the availability of the hydrogen Balmer series and several neutral helium lines (see also Sect. 7.1.1 and Table 8.12). Yet, modern spectrographs focus more and more on the NIR. Examples include the CARMENES<sup>84</sup> ( $\sim 5200\text{-}17\,100\text{ \AA}$ ) spectrograph at the Calar Alto 3.5 m telescope, the XSHOOTER<sup>85</sup> ( $\sim 3000\text{-}25\,000\text{ \AA}$ ) and MUSE<sup>86</sup> ( $\sim 4650\text{-}9300\text{ \AA}$ ) spectrographs at the ESO VLT, or the upcoming WEAVE<sup>87</sup> ( $\sim 3700\text{-}9600\text{ \AA}$ ) spectrograph at the 4.2 m William Herschel Telescope (WHT) at the Observatorio del Roque de los Muchachos on La Palma. The NIR wavelength regime has untapped potential in terms of the determination of the atmospheric parameters because of the hydrogen Paschen series (see Table 8.12). However, it strongly suffers from scattering and

<sup>84</sup>More information on CARMENES (Calar Alto High-Resolution Search for M Dwarfs with Exoearths with Near-Infrared and Optical Echelle Spectrographs) can be found at <https://carmenes.caha.es/ext/instrument/index.html> (last called on 13th May 2021).

<sup>85</sup>More information on XSHOOTER can be found at <https://www.eso.org/sci/facilities/paranal/instruments/xshooter/overview.html> (last called on 13th May 2021).

<sup>86</sup>More information on MUSE (Multi Unit Spectroscopic Explorer) can be found at <https://www.eso.org/sci/facilities/develop/instruments/muse.html> (last called on 13th May 2021).

<sup>87</sup>More information on WEAVE (WHT Enhanced Area Velocity Explorer) can be found at <https://ingconfluence.ing.iac.es:8444/confluence//display/WEAV/Instrument+Page> (last called on 13th May 2021).

## 8.2. Data Processing and Preparation

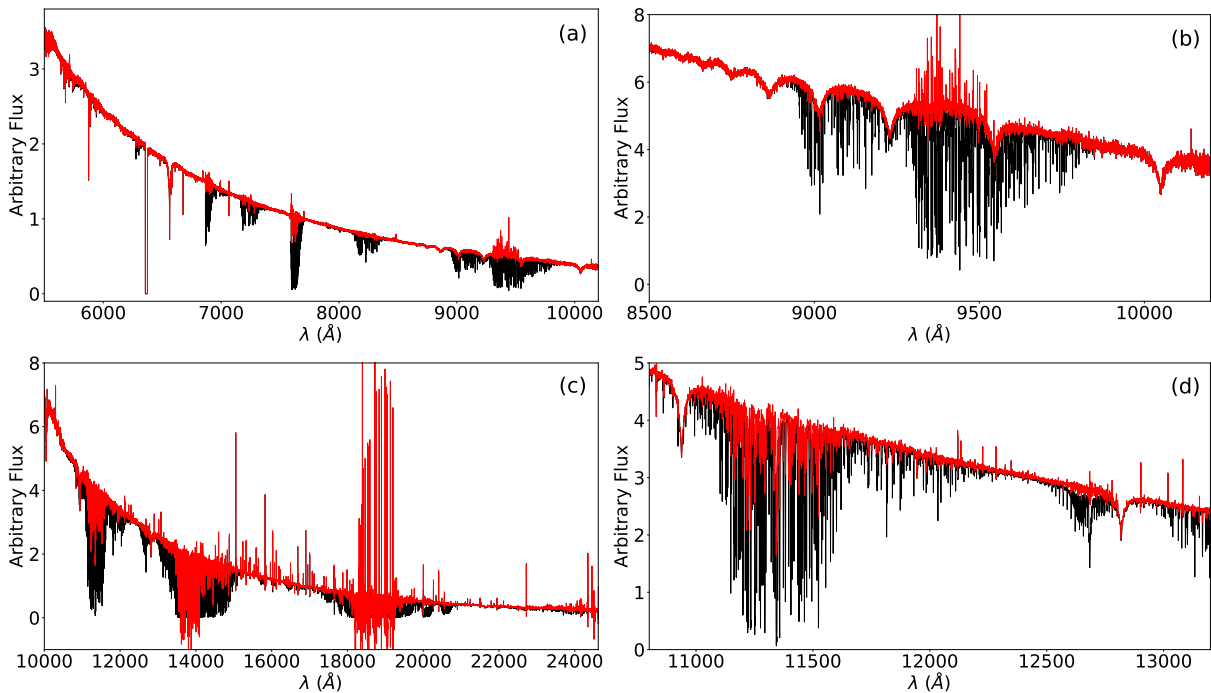


Figure 8.2.1.: Quality of the telluric absorption correction for the VIS and NIR channels of the XSHOOTER spectrum of the H-sdB program star HD 4539. The telluric absorption corrected spectrum (red) is shown in comparison to the original spectrum (black). Note that the fluxes are scaled for illustrative purposes. (a) Full VIS channel. (b) Spectral range of the hydrogen Paschen series. (c) Full NIR channel. (d) Spectral range between 10 800 and 13 200 Å.

absorption processes in the Earth's atmosphere, which cause *telluric absorption bands* that have a negative impact on the quality of the data obtained from ground-based astronomical observations. Being only relatively weak in the region of  $\sim 5800\text{--}6800$  Å, the telluric bands become stronger and stronger the further the spectral coverage in the NIR (see Fig. 8.2.1). The most important molecules that contribute to the greenhouse effect and, hence, cause telluric absorption lines are water ( $\text{H}_2\text{O}$ ), carbon dioxide ( $\text{CO}_2$ ), methane ( $\text{CH}_4$ ), nitrous oxide ( $\text{N}_2\text{O}$ ), and ozone ( $\text{O}_3$ ). As water is the main contributor to the NIR atmospheric spectra, its abundance (the air humidity) is the most essential quantity to be known. The dynamics of changing weather conditions, seasonal effects, or climate change leading to the variability of the individual molecular abundances, in particular that of water, make it extremely difficult to correct for telluric absorption features. Consequently, any data calibration usually needs supplementary calibration frames of bright and hot telluric standard stars (TSSs) observed at a similar time, airmass, and line of sight as the respective scientific target. In addition, the TSSs must have relatively smooth continua with only a few, well-known intrinsic spectral features. Since these data should be taken directly before or after the actual science frame, this approach is very expensive in terms of telescope time. Even in the best case scenario, where such observations are available, the telluric absorption correction with TSSs is tricky to perform in the

near-IR and mid-IR because there is almost no region with negligible atmospheric absorptions present. Thus, a reliable shape of the unabsorbed continuum is very difficult to determine via interpolation methods. This calls for a realistic modelling of the atmospheric absorption for given observing conditions, which not only makes the telluric absorption correction more reliable, but also avoids supplementary observations of TSSs (ESO, 2019; Smette et al., 2015; Kausch et al., 2015).

As a matter of fact, the ESO team developed `molecfit`, a software tool to correct astronomical observations for atmospheric absorption features. It is perfectly suited for the scientific case of VLT/XSHOOTER spectra such as the ones of this work's reference sample (see Sect. 8.1.1). `Molecfit` is based on fitting synthetic transmission spectra calculated by the radiative transfer code LBLRTM<sup>88</sup> (Line-by-line Radiative Transfer Model; Clough et al. 2005) to the respective astronomical data. LBLRTM uses the spectral line parameter database `aer` (Atmospheric and Environmental Research Inc.), which is based on the High-resolution TRANsmiSSion molecular absorption database HITRAN<sup>89</sup> (Rothman et al., 2009). Figures 8.2.2 and 8.2.3 show schematic graphs of the basic functionality of the `molecfit` software. These graphs are discussed in detail in ESO (2019). Here, only a brief explanation of the software workflow shall be given. The `molecfit` code reads the science spectrum and an additional driver parameter file that contains user given input. A single atmospheric profile is compiled from the data of three independent sources: an atmospheric profile, which is created from a standard atmosphere for a given climate zone (containing on-site information on the height, the pressure, the temperature, and the chemical composition for general tropical environments up to 120 km), an appropriate meteorological GDAS (Global Data Assimilation System) data model (containing on-site information on the pressure, the temperature, and the relative humidity for elevations up to  $\sim 25$  km) as well as ground-based on-site meteorological measurements provided by the ESO Meteo Monitor (EMM). The radiative transfer code LBLRTM uses the resulting merged atmospheric profile with possible preselected relevant molecules as well as the target airmass at the time of observation as input. The `mpfit` (Bevington & Robinson, 1992) fit algorithm, which makes use of  $\chi^2$ -minimization based on the Levenberg-Marquardt technique (Press et al., 1986), then tries to obtain a model spectrum that matches the observed science spectrum. For this, the code also optimizes the flux scaling, the wavelength grid, and the resolution of the model spectrum. However, running the radiative transfer code for a wide wavelength range is very time consuming. Thus, the user has to preselect several well-defined narrow wavelength ranges beforehand. The fitting procedure then is performed for the chosen ranges only. In combination with the same parameter file as used for `molecfit`, the executable `calctrans` takes care of the actual telluric absorption correction. In order to do so, it calculates the atmospheric transmission function for the full wavelength range of the input spectrum and applies it to the science frame. By using the executable `corrfilelist`, it is also possible to correct more than one science frame with the same correction function (ESO, 2019; Smette et al., 2015; Kausch et al., 2015).

For the telluric absorption correction of the NIR channels of the XSHOOTER reference data analyzed in this work, most of the parameters (the relative molecular column densities, the

<sup>88</sup>[http://rtweb.aer.com/lblrtm\\_frame.html](http://rtweb.aer.com/lblrtm_frame.html), last called on 13th May 2021

<sup>89</sup><https://www.cfa.harvard.edu/hitran/>, last called on 13th May 2021

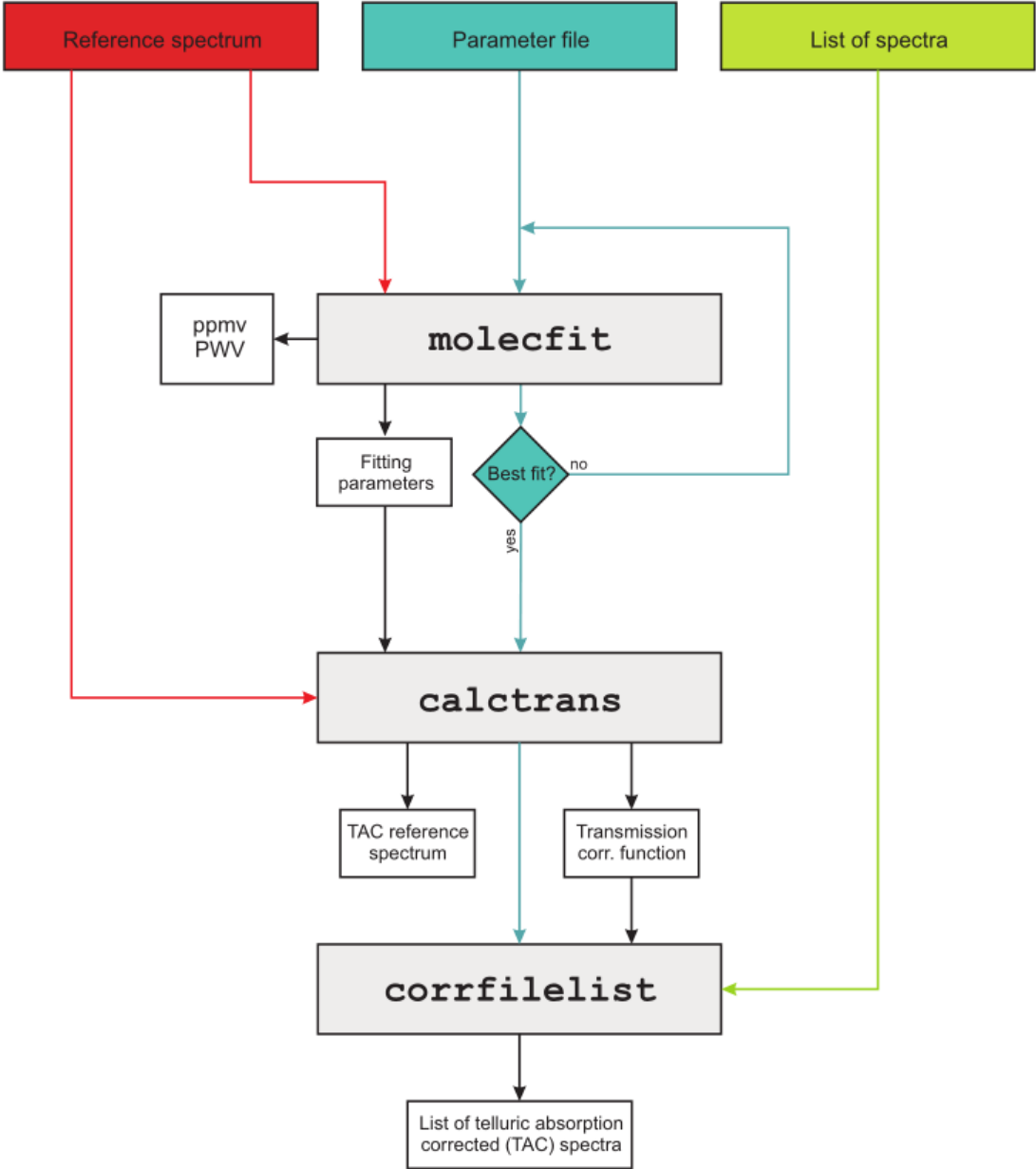
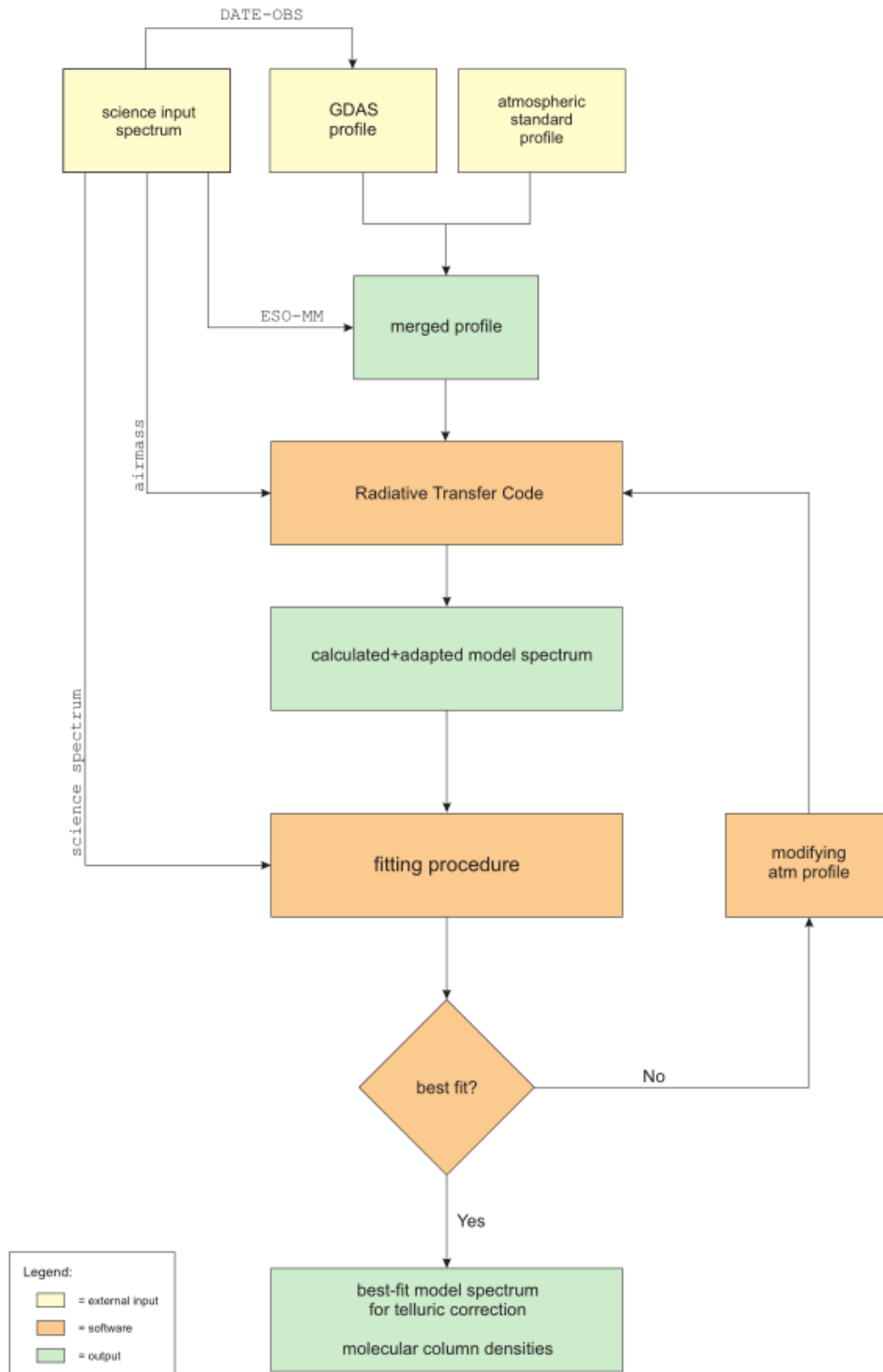


Figure 8.2.2.: Overview of the telluric absorption correction software workflow of molecfit. The input and the output of the three executables molecfit, calctrans, and corrfilelist as well as the connections between these routines are shown. Adopted from ESO (2019).

Figure 8.2.3.: Workflow of the `molecfit` routine. Adopted from ESO (2019).

## 8.2. Data Processing and Preparation

---

degree of the polynomial used for the continuum fit, etc.) as presented in Table 3 of Kausch et al. (2015) are used. However, the list of molecules included in the model is extended to H<sub>2</sub>O, CO<sub>2</sub>, CH<sub>4</sub>, N<sub>2</sub>O, O<sub>3</sub>, O<sub>2</sub>, and CO. The VIS-channel data are treated similarly, but only H<sub>2</sub>O, CO<sub>2</sub>, and O<sub>2</sub> are included in the model. As an example, Fig. 8.2.1 shows a comparison of the original and the telluric absorption corrected XSHOOTER VIS and NIR-channel data in the case of the H-sdB program star HD 4539. As can be seen, the quality of the telluric correction is sufficient in order to make additional use of the hydrogen Paschen and Brackett series for the subsequent quantitative spectral analysis. This additional spectral information is not only useful in the case of HD 4539, but can be utilized for all cool XSHOOTER program stars that show these two series.

In this work, the telluric absorption correction with `molecfit` is only applied to the XSHOOTER data. All other data are not corrected for telluric bands. Hence, the bands are excluded from the spectral fits in the latter cases.

### 8.2.2. Radial Velocity Correction and Co-Addition

After the successful telluric absorption correction of the individual XSHOOTER VIS and NIR channels, all single spectra from all instruments are RV-corrected. Thereby, the different XSHOOTER channels are treated separately. RV measurements are taken with SPAS according to the description in Sect. 7.1.2<sup>90</sup>. Accurate (non-barycentric corrected) RVs are measured by means of sharp metal absorption lines, whereas much broader lines belonging to the hydrogen Balmer, Paschen, and Brackett series are avoided (a selection of identified sharp metal lines used for the RV measurements can be found in Tables 8.12, 8.13, and 8.14). Moreover, broader helium (He I/He II) absorption lines available in the optical wavelength regime are also avoided<sup>91</sup>. In order to achieve RV-corrected spectra for the <sup>3</sup>He program stars of this work, the sharp metal lines used are fully adequate. This is fortunate since for these special stars accurate RVs cannot be determined with SPAS making use of neutral helium lines. This is because of the isotopic shifts that result from the <sup>3</sup>He enrichment (see Sect. 3.3) and the fact that no synthetic spectra based on a detailed <sup>3</sup>He model atom are used in SPAS in order to determine the RVs (see Sect. 7.1.2). For <sup>3</sup>He stars, however, very accurate RVs are necessary for the illustration of the isotopic shifts due to <sup>3</sup>He and for an accurate measurement of the isotopic abundance ratio (<sup>4</sup>He/<sup>3</sup>He). In this work (see Ch. 10), this is ensured by the global analysis strategy described in Sect. 7.1.2 and the detailed <sup>3</sup>He model atom included in the hybrid LTE/NLTE analysis approach (see Sect. 6.8).

In order to achieve the highest possible data quality in terms of S/N, the RV-corrected single spectra are co-added. S/N usually describes the ratio of the mean signal to the standard deviation over some considered continuum spectral range with very few absorption and emission

---

<sup>90</sup>The RV values determined with SPAS are not barycentric corrected RVs, but combine the season-dependent component caused by Earth's rotation and its motion around the barycentre ( $v_{\text{bary}}$ ) as well as the actual RV ( $v_{\text{rad}}$ ; see also Sect. 7.1.1). As this work does not focus on the determination of RV curves, however, this is fully adequate.

<sup>91</sup>In particular, helium dominates for the hotter He-sdO program stars, for which the Pickering series of He II overlaps with the hydrogen Balmer series (see also Table 8.12).

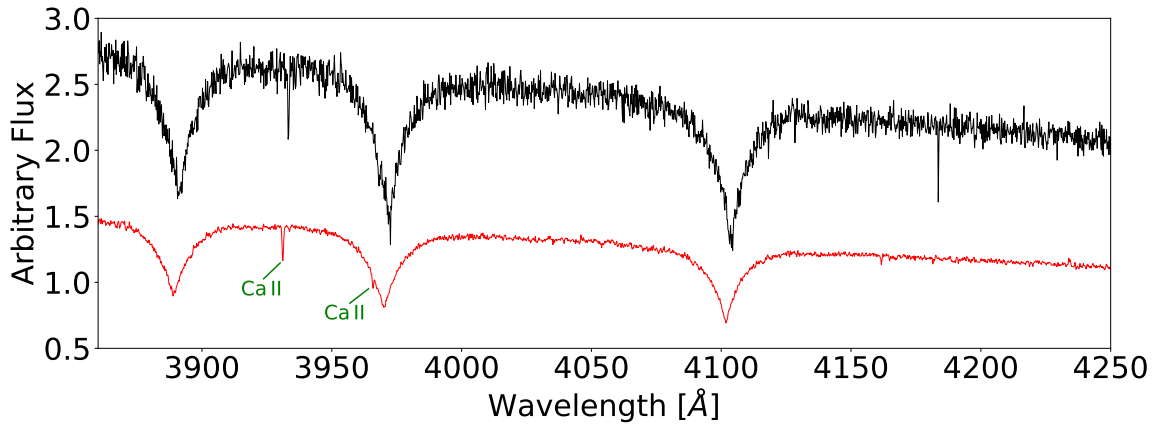


Figure 8.2.4.: Comparison of a single and non-normalized XSHOOTER spectrum of the H-sdB program star PG 1136-003 (black) to the corresponding co-added one (red) for a selected wavelength region. Note that the single spectrum is scaled by a factor of  $10^{15}$  for illustrative purposes. Spectral line identification is much more difficult in the case of the single spectrum because of its much lower signal-to-noise ratio ( $S/N = 38$ ) compared to that of the co-added one ( $S/N = 94$ ). In total, seven single spectra have been co-added in order to achieve the data quality of the red spectrum (see also Table 8.2).

lines. Co-added spectra consist of an addition of single spectra, whereby a weighted average of the input fluxes is taken. For this, the individual  $S/N$  ratios of the single spectra serve as weights. In this way, the individual exposure times are also taken into account because shorter/longer exposures typically lead to lower/higher  $S/N$  of the data obtained. For a successful co-addition, the single spectra also have to be roughly normalized. This is usually achieved by dividing them by their respective median value. As a matter of fact, the  $S/N$  ratio of a co-added spectrum is significantly higher than that of the single spectra. This allows for a more detailed spectral line identification and, hence, for a more sophisticated quantitative spectral analysis of the individual program stars (in particular, in terms of metal abundances; see also Ch. 11). In Fig. 8.2.4, a single XSHOOTER spectrum of the H-sdB program star PG 1136-003 is compared to the corresponding co-added spectrum. The increase in data quality is clearly visible.

Tables 8.1-8.11 list the individual  $S/N$  ratios of the (co-added) spectra analyzed in this work. Note that the different channels available for the XSHOOTER program stars have been treated (co-added) separately.

### 8.2.3. Channel Merging

The XSHOOTER reference data have been obtained in three different overlapping channels: UVB ( $\sim 3000$ - $5560$  Å), VIS ( $\sim 5335$ - $10\,200$  Å), and NIR ( $\sim 9940$ - $24\,790$  Å). Therefore, the individual co-added channels need to be merged in order to create continuous spectra for

## 8.2. Data Processing and Preparation

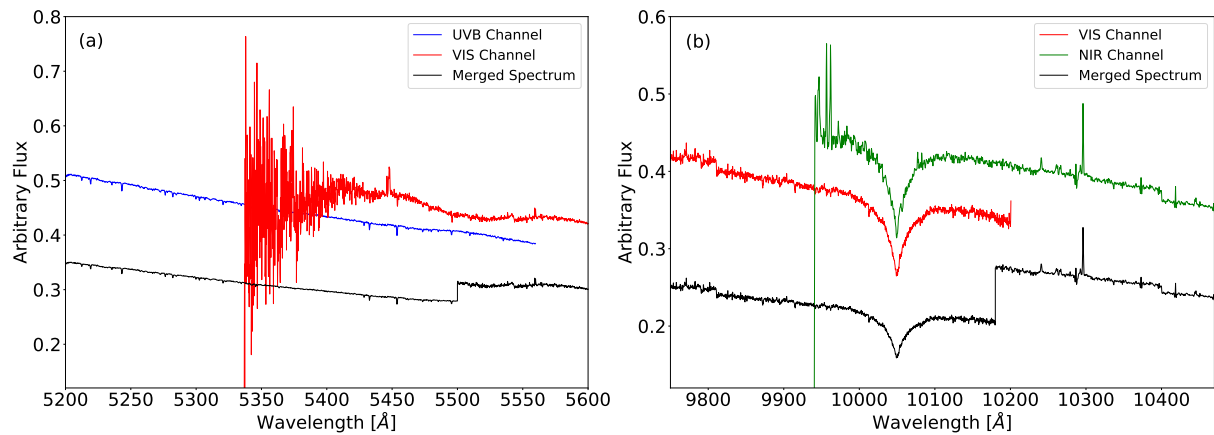


Figure 8.2.5.: Channel merging carried out for the co-added XSHOOTER spectrum of the H-sdB program star HD 4539. Note that the fluxes are scaled for illustrative purposes. (a) UVB channel (blue), VIS channel (red), and merged spectrum (black). (b) VIS channel (red), NIR channel (green), and merged spectrum (black).

the respective program stars. For this, usually the same approach as for order merging is used, namely that a weighted mean is determined at the edges of the neighboring channels. For the purpose of this work, however, it is sufficient to merge the overlapping XSHOOTER channels always at the following fixed wavelength positions:  $\lambda_1 = 5500 \text{ \AA}$  for the UVB/VIS and  $\lambda_2 = 10180 \text{ \AA}$  for the VIS/NIR channels. Certainly, this introduces small jumps at the chosen wavelength positions. However, these jumps can be excluded later on from the spectral fitting. Figure 8.2.5 shows the principle of the XSHOOTER channel merging in the case of the co-added spectrum of the H-sdB program star HD 4539.

In this work, channel merging has to be applied to XSHOOTER data only. This is only because of this instrument's special set-up (see also Sect. 4.4).

### 8.2.4. Normalization

In this step, the (co-added) spectra are normalized, meaning that the continuum regions (without absorption and emission lines) are approximately set to unity (ideally exactly to unity). The normalization step is not necessary, but very useful in order to be able to compare different stellar spectra. Yet, it has to be said that normalization may lead to errors because it is not always obvious where to set the stellar continuum. Particularly, the O and B-type stars investigated in this work have broad hydrogen Balmer, Paschen, and Brackett lines, for which it is extremely difficult to judge the curve of the continuum within the far line wings (see also Fig. 8.2.6). An alternative way of spectral fitting would make use of flux-calibrated spectra whose individual intensity profiles reflect the emitted stellar spectra. Flux-calibrated spectra are obtained in particular from space because in this case no stellar radiation is absorbed by the Earth's atmosphere. For ground-based data such as the spectra analyzed in this work,

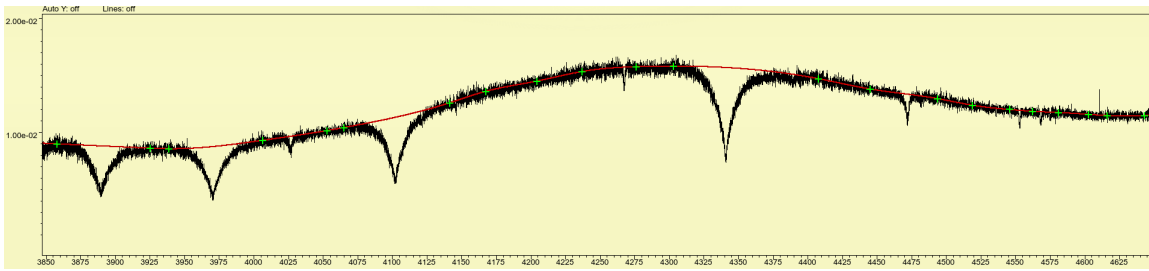


Figure 8.2.6.: Selected wavelength region ( $3850 \text{ \AA} \lesssim \lambda \lesssim 4650 \text{ \AA}$ ) of a single and non-normalized FEROS spectrum of the  ${}^3\text{He}$  H-sdB program star SB 290 (black line) in SPAS. The continuum is assumed to follow the spline function (red line) which is defined by setting numerous anchor points (green crosses) by eye. Note that in the present work this normalization procedure is applied only after the co-addition of the available single spectra. Adopted from Schneider (2017).

however, a spectrophotometric standard star is needed in order to flux calibrate the data. Due to the enormous efforts coming along with flux-calibrated data and ground-based instruments and because of the fact that the comparison of the stellar spectra of the individual program stars is a central part of this work, the normalization approach is chosen here.

The XSHOOTER, FEROS, HRS, HIRES, UVES, CAFOS, and IDS data are normalized by means of the analysis program SPAS (see Sect. 7.1.2). For this, numerous anchor points are set by eye where the continuum in the spectrum to be normalized is assumed. In this way, a spline function that describes the approximate stellar continuum is formed (see Fig. 8.2.6). The normalized spectrum then is determined by dividing the original spectrum by this spline function (see also Fig. 8.2.7). Certainly, this procedure is prone to errors because the continuum is mostly set by eye. However, this normalization process can be reconstructed and/or re-performed, if needed. This is not the case for the provided FOCES data, which have already been normalized beforehand. Hence, a wrong determination of the stellar continuum cannot be excluded for these data.

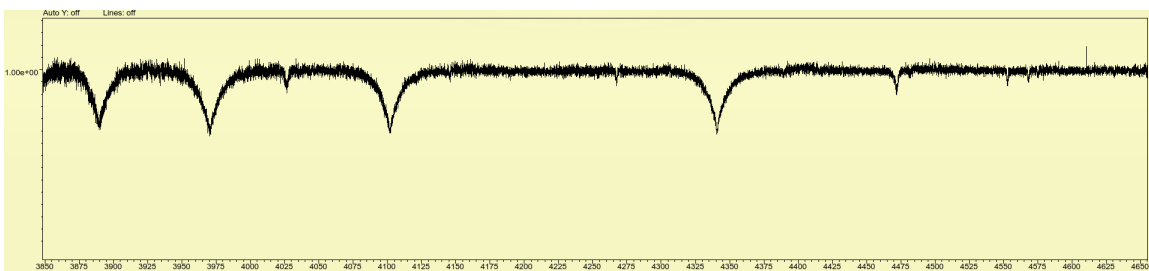


Figure 8.2.7.: Same selected wavelength region of the single but normalized FEROS spectrum of the  ${}^3\text{He}$  H-sdB program star SB 290 in SPAS as displayed in Fig. 8.2.6. The normalized spectrum has been derived by dividing the original non-normalized spectrum by the red spline function shown in Fig. 8.2.6. Note that in the present work this normalization procedure is applied only after the co-addition of the available single spectra. Adopted from Schneider (2017).

### 8.2.5. Spectral Line Identification

Spectral absorption (and emission) lines resulting from numerous different atoms and ions can be detected in the (co-added) spectra of the individual program stars. For this, atomic data are needed because spectral lines are generally identified as specific transitions of chemical elements in different ionization stages (see also Sect. 6.5). In consequence, the textbook “*A multiplet table of astrophysical interest. Part 1*” of Moore (1959) and the spectral data base of NIST<sup>92</sup> are used as sources for spectral line identification. Making use of their contained atomic transition data, observed spectral lines can be associated with chemical elements and their respective ionization stages.

The most prominent lines that are observed for the vast majority of the O and B-type program stars analyzed in this work are those of neutral hydrogen (H I). The optical wavelength regime is dominated by the Balmer series (from H $\alpha$  = 6562.790 Å over H $\beta$  = 4861.350 Å, H $\gamma$  = 4340.472 Å, H $\delta$  = 4101.734 Å, H $\epsilon$  = 3970.075 Å down to H14 = 3721.946 Å and H15 = 3711.978 Å in the case of the coolest program stars), which is associated with atomic transitions from the energy level with principal quantum number  $n = 2$  towards higher levels. On the other hand, the NIR is covered by the Paschen ( $n = 3$ ) and Brackett ( $n = 4$ ) series. Apart from hydrogen, most of the program stars also show prominent helium lines that result from the neutral (He I) and the singly-ionized (He II) stages. He I lines are observed for the major part of the program stars with  $T_{\text{eff}} \lesssim 35\,000$  K. The first He II line that becomes prominent at  $T_{\text{eff}} \sim 35\,000$  K is He II 4686 Å. This is followed by He II 5412 Å at even higher effective temperatures. For the hot He-sdO program stars, the hydrogen Balmer series overlaps with the He II Pickering series. For some of these stars, the helium-to-hydrogen abundance ratio is so high such that the Balmer lines can only be detected as weak blends to the Pickering series (see also Sect. 9.1). For others, the Balmer lines are not visible at all.

In addition, various metal lines can be identified in the spectra of the program stars. Their ionization stages and line strengths differ from star to star because both strongly depend on the individual spectral type (effective temperature), on the stellar evolution as well as on possible atmospheric diffusion processes. Nearly all of the program stars have carbon (C II/III), nitrogen (N II/III), oxygen (O I/II), silicon (Si II/III/IV), and sulfur (S II/III) in their atmospheres. Magnesium (Mg II), aluminum (Al II/III), and iron (Fe II/III) are also detected in most cases. Moreover, the stellar atmospheres of selected program stars contain noble gases such as neon (Ne I/II), argon (Ar II), chlorine (Cl II), and krypton (Kr II) as well as additional metals such as phosphorus (P II), calcium (Ca II), titanium (Ti II), strontium (Sr II), and zirconium (Zr II). Metal abundances will be derived in Ch. 11 based on the hybrid LTE/NLTE approach, which was presented in Sect. 6.8. Many of the lines associated with carbon, nitrogen, oxygen, neon, magnesium, aluminum, silicon, sulfur, argon, and iron are included in the NLTE model atoms used (see Sect. 6.8), which enables a sophisticated NLTE abundance study for these elements. However, NLTE model atoms are not available for all of the chemical elements observed. This includes phosphorus, calcium, titanium, strontium, and zirconium, which will therefore be treated in LTE. The abundances of chlorine and krypton will not be determined because of a lack of appropriate atomic data. Furthermore, it has to

---

<sup>92</sup>[https://physics.nist.gov/PhysRefData/ASD/lines\\_form.html](https://physics.nist.gov/PhysRefData/ASD/lines_form.html), last called on 13th February 2021

## 8. Observations and Data Preparation

Ion	$\lambda_0$ [Å]	Ion	$\lambda_0$ [Å]	Ion	$\lambda_0$ [Å]	Ion	$\lambda_0$ [Å]	Ion	$\lambda_0$ [Å]
H I	3711.978	He I	4437.553	C II	6461.95	C III	8341.60	N II	5001.47
H I	3721.946	He I	4471.470	C II	6578.05	C III	8347.95	N II	5005.15
H I	3734.369	He I	4713.139	C II	6582.88	C III	8500.32	N II	5007.33
H I	3750.151	He I	4921.931	C II	6779.94	C III	9701.10	N II	5010.62
H I	3770.633	He I	5015.678	C II	6780.59	C III	9705.41	N II	5045.10
H I	3797.909	He I	5047.739	C II	6783.91	C III	9715.09	N II	5073.59
H I	3835.397	He I	5875.625	C II	6791.47	N II	3330.32	N II	5495.65
H I	3889.064	He I	6678.152	C II	6800.69	N II	3331.31	N II	5666.63
H I	3970.075	He I	7065.215	C II	7231.33	N II	3437.14	N II	5676.02
H I	4101.734	He I	7281.351	C II	7236.42	N II	3994.997	N II	5679.56
H I	4340.472	He I	10138.424	C II	7237.17	N II	4035.080	N II	5686.21
H I	4861.35	He I	10830.340	C III	3608.778	N II	4041.310	N II	5710.77
H I	6562.79	He I	11969.12	C III	3609.071	N II	4043.530	N II	5927.81
H I	8545.38	He I	12527.52	C III	3609.676	N II	4176.16	N II	5931.78
H I	8598.39	He I	12845.96	C III	3883.816	N II	4199.98	N II	5940.24
H I	8665.02	He I	12968.45	C III	3885.938	N II	4227.74	N II	5941.65
H I	8750.46	He I	12984.89	C III	4056.061	N II	4237.05	N II	5952.39
H I	8862.89	He II	4025.600	C III	4067.940	N II	4241.76	N II	5954.28
H I	9015.3	He II	4100.040	C III	4068.916	N II	4432.74	N II	6150.75
H I	9229.7	He II	4199.830	C III	4070.260	N II	4433.48	N II	6482.05
H I	9546.2	He II	4338.670	C III	4121.845	N II	4447.03	N II	6610.56
H I	10049.8	He II	4541.590	C III	4152.514	N II	4601.48	N III	4634.13
H I	10938.17	He II	4685.682	C III	4156.504	N II	4601.69	N III	4640.64
H I	12818.07	He II	4859.323	C III	4162.877	N II	4607.15	N III	4641.85
H I	16406.88	He II	5411.524	C III	4186.9	N II	4613.87	N III	4895.12
H I	16806.51	He II	6560.100	C III	4515.811	N II	4621.39	O I	7771.94
H I	17362.14	He II	10123.6	C III	4516.788	N II	4630.54	O I	7774.17
He I	3819.607	He II	11626.4	C III	4647.418	N II	4643.09	O I	7775.39
He I	3867.484	C II	3918.97	C III	4650.246	N II	4654.53	O I	8446.25
He I	3888.649	C II	3920.68	C III	4651.473	N II	4779.72	O I	8446.36
He I	3964.729	C II	4267.00	C III	5695.920	N II	4780.44	O I	8446.76
He I	4009.257	C II	4267.26	C III	6727.48	N II	4781.19	O II	3390.21
He I	4026.184	C II	5132.95	C III	6731.04	N II	4788.14	O II	3712.74
He I	4120.811	C II	5133.28	C III	6744.39	N II	4803.29	O II	3727.32
He I	4143.759	C II	5145.16	C III	7486.56	N II	4987.38	O II	3749.48
He I	4168.971	C II	6151.265	C III	7578.15	N II	4994.36	O II	3911.96
He I	4387.929	C II	6151.534	C III	8332.99	N II	5001.13	O II	3912.12

Table 8.12.: List of selected spectral lines observed in the (co-added) spectra of the program stars analyzed in this work. The given rest-frame wavelengths  $\lambda_0$  are extracted from the *Atomic Spectra Database* of the National Institute of Standards and Technology (NIST; [https://physics.nist.gov/PhysRefData/ASD/lines\\_form.html](https://physics.nist.gov/PhysRefData/ASD/lines_form.html), last called on 13th February 2021). Note that no abundances for chlorine and krypton are measured in this work because of a lack of appropriate atomic data. For a selection of metal line fits performed for some of the program stars, see Ch. 11.

## 8.2. Data Processing and Preparation

Ion	$\lambda_0$ [Å]	Ion	$\lambda_0$ [Å]	Ion	$\lambda_0$ [Å]	Ion	$\lambda_0$ [Å]	Ion	$\lambda_0$ [Å]
O II	4069.62	Ne II	4233.847	Si II	4200.658	Si IV	7718.79	S II	5142.322
O II	4069.88	Ne II	4284.836	Si II	4200.887	Si IV	7723.82	S II	5201.027
O II	4072.16	Ne II	4284.944	Si II	4200.898	S II	3931.918	S II	5201.379
O II	4075.86	Ne II	4391.990	Si II	4621.418	S II	3932.286	S II	5212.62
O II	4119.22	Ne II	4413.105	Si II	4621.696	S II	3933.264	S II	5320.723
O II	4132.80	Ne II	4413.126	Si II	4621.722	S II	3979.825	S II	5345.712
O II	4185.44	Ne II	4413.215	Si II	5041.026	S II	3990.908	S II	5428.655
O II	4189.58	Ne II	4428.520	Si II	5055.981	S II	3993.502	S II	5432.797
O II	4189.79	Ne II	4428.636	Si II	5056.314	S II	3998.759	S II	5453.855
O II	4366.89	Ne II	4430.902	Si II	5185.535	S II	4003.874	S II	5473.614
O II	4395.93	Ne II	4430.942	Si II	5466.461	S II	4028.75	S II	5639.977
O II	4414.46	Ne II	4502.754	Si II	5466.849	S II	4032.768	S II	5640.346
O II	4414.90	Ne II	4502.873	Si II	5466.894	S II	4142.259	S II	5819.254
O II	4416.97	Ne II	4534.525	Si II	5957.561	S II	4145.06	S II	6384.893
O II	4452.38	Ne II	4534.643	Si II	5978.929	S II	4153.068	S II	6397.355
O II	4590.97	Ne II	4553.171	Si II	6239.63	S II	4162.665	S II	6398.014
O II	4595.96	Mg II	4481.126	Si II	6347.103	S II	4168.384	S II	6413.711
O II	4596.18	Mg II	4481.15	Si II	6371.359	S II	4189.681	S III	3632.024
O II	4638.86	Mg II	4481.325	Si III	3590.465	S II	4217.182	S III	3656.603
O II	4641.81	Mg II	7877.054	Si III	3806.526	S II	4267.762	S III	3662.008
O II	4649.13	Mg II	7896.04	Si III	3806.7	S II	4269.725	S III	3709.366
O II	4650.84	Mg II	7896.366	Si III	3806.779	S II	4278.506	S III	3710.431
O II	4661.63	Al II	4663.056	Si III	3924.468	S II	4282.593	S III	3717.771
O II	4676.23	Al III	3601.630	Si III	4552.622	S II	4294.402	S III	3747.885
O II	4698.44	Al III	3612.355	Si III	4567.84	S II	4318.643	S III	3750.737
O II	4699.01	Al III	3713.123	Si III	4574.757	S II	4524.675	S III	3774.526
O II	4699.22	Al III	4149.913	Si III	4716.654	S II	4524.941	S III	3778.903
O II	4705.35	Al III	4149.968	Si III	4813.333	S II	4552.41	S III	3831.861
O II	4941.07	Al III	4150.173	Si III	4819.631	S II	4656.757	S III	3837.796
O II	4943.01	Al III	4479.885	Si III	4819.712	S II	4716.271	S III	3838.312
Ne I	5852.488	Al III	4479.971	Si III	4819.814	S II	4815.552	S III	3860.695
Ne I	5944.834	Al III	4480.000	Si III	4828.95	S II	4885.648	S III	3899.296
Ne I	6074.338	Al III	4512.565	Si III	4829.03	S II	4917.198	S III	3920.345
Ne I	6096.163	Al III	4528.945	Si III	4829.111	S II	4924.11	S III	3928.595
Ne I	6143.063	Al III	4529.189	Si III	4829.214	S II	4925.343	S III	3983.766
Ne I	6266.495	Al III	5696.604	Si III	5696.49	S II	4942.473	S III	3985.963
Ne I	6334.428	Al III	5722.730	Si III	5739.73	S II	4991.969	S III	4253.589
Ne I	6382.991	Si II	3853.665	Si III	5898.79	S II	4993.497	S III	4284.979
Ne I	6402.247	Si II	3856.018	Si IV	4088.862	S II	5009.567	S III	4332.692
Ne I	6506.528	Si II	3862.595	Si IV	4116.103	S II	5014.042	S III	4354.566
Ne I	7032.413	Si II	4075.452	Si IV	4212.397	S II	5027.203	S III	4361.527
Ne II	3694.214	Si II	4076.78	Si IV	4212.414	S II	5032.434	S III	4364.747
Ne II	3713.082	Si II	4128.067	Si IV	4631.24	S II	5047.277	S III	4418.836
Ne II	4219.745	Si II	4130.893	Si IV	4654.32	S II	5103.332	S III	4439.844

Table 8.13.: Table 8.12 continued.

Ion	$\lambda_0$ [Å]	Ion	$\lambda_0$ [Å]	Ion	$\lambda_0$ [Å]	Ion	$\lambda_0$ [Å]	Ion	$\lambda_0$ [Å]
S III	4467.756	Ar II	4965.079	Fe II	5169.033	Fe III	4419.596	Fe III	7921.500
S III	4478.474	Ar II	5009.334	Fe II	5197.577	Fe III	4649.271	Fe III	7921.814
S III	4499.245	Ar II	5062.037	Fe II	5234.625	Fe III	5063.421	Cl II	4785.364
S III	4527.911	Ar II	6114.923	Fe II	5272.397	Fe III	5073.903	Cl II	4794.550
S III	4613.487	Ar II	6172.278	Fe II	5276.002	Fe III	5086.701	Cl II	4810.060
S III	4677.657	Ar II	6638.220	Fe II	5316.615	Fe III	5194.160	Cl II	4819.470
Ar II	3603.904	Ar II	6639.740	Fe II	5362.869	Fe III	5272.369	Kr II	4355.477
Ar II	3729.308	Ar II	6643.697	Fe II	5427.826	Fe III	5272.900	Kr II	4658.876
Ar II	3729.345	Ar II	6684.293	Fe II	5534.847	Fe III	5272.975	Kr II	4739.001
Ar II	3780.840	Fe II	3906.035	Fe II	6238.392	Fe III	5276.476	int. Na I	5889.95
Ar II	3850.581	Fe II	3922.004	Fe II	6247.557	Fe III	5282.297	int. Na I	5895.92
Ar II	3868.528	Fe II	3935.962	Fe III	3600.943	Fe III	5284.827	int. Ca II	3933.663
Ar II	3928.623	Fe II	4024.547	Fe III	3603.890	Fe III	5288.887	int. Ca II	3968.469
Ar II	3944.271	Fe II	4173.461	Fe III	3611.736	Fe III	5289.304	P II	4499.230
Ar II	3946.097	Fe II	4233.172	Fe III	3999.325	Fe III	5290.071	P II	4589.846
Ar II	4013.856	Fe II	4273.326	Fe III	4000.518	Fe III	5293.780	P II	4602.069
Ar II	4033.809	Fe II	4296.572	Fe III	4005.573	Fe III	5295.027	P II	6043.08
Ar II	4038.804	Fe II	4303.176	Fe III	4137.130	Fe III	5298.114	Ca II	8498.02
Ar II	4072.004	Fe II	4351.768	Fe III	4139.350	Fe III	5299.926	Ca II	8542.09
Ar II	4072.325	Fe II	4416.830	Fe III	4140.482	Fe III	5302.602	Ca II	8662.14
Ar II	4072.384	Fe II	4489.183	Fe III	4164.916	Fe III	5306.757	Ca II	8912.07
Ar II	4255.603	Fe II	4491.405	Fe III	4194.051	Fe III	5310.337	Ca II	8927.36
Ar II	4277.528	Fe II	4508.247	Fe III	4210.674	Fe III	5340.535	Ti II	3685.189
Ar II	4371.329	Fe II	4515.339	Fe III	4222.271	Fe III	5363.764	Ti II	3685.204
Ar II	4372.095	Fe II	4520.224	Fe III	4248.773	Fe III	5375.566	Ti II	3759.296
Ar II	4379.666	Fe II	4541.524	Fe III	4261.391	Fe III	5535.475	Ti II	3761.323
Ar II	4545.052	Fe II	4549.192	Fe III	4273.372	Fe III	5573.424	Sr II	4077.71
Ar II	4579.349	Fe II	4549.474	Fe III	4273.409	Fe III	5813.302	Sr II	4215.52
Ar II	4609.567	Fe II	4555.893	Fe III	4286.091	Fe III	5833.938	Zr II	3391.982
Ar II	4657.901	Fe II	4576.340	Fe III	4286.128	Fe III	5848.744	Zr II	3437.136
Ar II	4726.868	Fe II	4582.835	Fe III	4286.164	Fe III	5920.394	Zr II	3438.226
Ar II	4735.905	Fe II	4583.837	Fe III	4296.814	Fe III	6032.673	Zr II	3556.585
Ar II	4764.864	Fe II	4629.339	Fe III	4296.851	Fe III	7320.230	Zr II	3709.266
Ar II	4806.020	Fe II	4635.316	Fe III	4304.748	Fe III	7920.559	Zr II	3745.966
Ar II	4847.997	Fe II	4923.927	Fe III	4304.767	Fe III	7920.872	Zr II	3751.606
Ar II	4879.863	Fe II	5018.440	Fe III	4310.355	Fe III	7921.186	Zr II	3766.795

Table 8.14.: Table 8.12 continued.

### 8.3. Photometric Data

---

be noted that chemical elements and corresponding ionization stages cannot be assigned to all detected spectral lines. The respective lines are caused by elements that are not included in the analysis. Thus, these lines will be excluded from the spectral fits. No metal abundances will be derived for the H-sdO and the He-sdO program stars since for the former no spectra are analyzed (see Sect. 8.1.2) and for the latter the TLUSTY/SYNSPEC approach with fixed metal abundances for carbon, nitrogen, and oxygen only is used (see Sect. 6.9).

Last but not least, a word about the *interstellar medium* (ISM) and *interstellar lines*. Emitted light from a stellar surface travels through the ISM, that is, the matter and the radiation that exists in the space between the star systems in a galaxy. The ISM is composed of various different elements (mostly hydrogen, followed by helium with trace amounts of carbon, nitrogen, and oxygen). But also sodium (Na) and calcium are constituents of the “molecular clouds” of the ISM. As the light passes these clouds of various different compositions, part of it is absorbed and, eventually, re-emitted in other frequencies and into other directions. Depending on the actual line of sight to the object of interest, this interstellar absorption can cause several different interstellar lines in the stellar spectrum obtained. The strength of these lines depends on the exact amount of ISM absorber material on the light path to Earth. If the ISM material that causes the absorption additionally moves with respect to the line of sight, interstellar lines may also be shifted compared to their rest-frame wavelengths measured in laboratories. Examples for imprints of the ISM in the spectra of this work’s program stars are the Na I doublet at  $\sim 5890 \text{ \AA}$  and  $\sim 5896 \text{ \AA}$  as well as the Ca II H and K lines at  $\sim 3968 \text{ \AA}$  and  $\sim 3934 \text{ \AA}$ , respectively. Due to the fact that no model for interstellar absorption is used for the quantitative spectral analyses performed in this work, the interstellar lines are excluded from the spectral fitting.

Tables 8.12, 8.13, and 8.14 show a shortened list of selected spectral lines associated with the different chemical elements observed in the (co-added) spectra of the analyzed program stars.

## 8.3. Photometric Data

As described in Sects. 7.2 and 7.3, the stellar angular diameter  $\theta$  of the program stars will be determined from SED fitting to appropriate photometric data in order to subsequently derive the individual fundamental stellar parameters (radius  $R$ , luminosity  $L$ , and mass  $M$ ). For the SED fits, magnitudes and colors from different wavelength filters ranging from the UV to the IR are compiled from various photometric catalogs that are publicly available. For this, the VizieR<sup>93</sup> Service for Astronomical Catalogues provided by the Centre de données astronomiques de Strasbourg (CDS) is used. While querying the individual program stars in the VizieR catalogs, photometric data that belong to nearby sources other than the target stars are excluded. Furthermore, data with missing statistical uncertainties or for which the statistical uncertainties are zero are omitted. The same applies to obviously flawed magnitudes and colors.

---

<sup>93</sup><https://vizier.u-strasbg.fr/viz-bin/VizieR>, last called on 20th May 2021

Table 8.15.: Photometric filter systems used for the SED fitting performed in Ch. 12.

System	Passband	Type	Reference/Catalog
IUE box	1300-1800 Å	magnitude	Wamsteker et al. 2000, INES: VI/110/inescat
IUE box	2000-2500 Å	magnitude	Wamsteker et al. 2000, INES: VI/110/inescat
IUE box	2500-3000 Å	magnitude	Wamsteker et al. 2000, INES: VI/110/inescat
TD1	1565	magnitude	Thompson et al. 1978, TD1: II/59B/catalog
TD1	1965	magnitude	Thompson et al. 1978, TD1: II/59B/catalog
TD1	2365	magnitude	Thompson et al. 1978, TD1: II/59B/catalog
TD1	2740	magnitude	Thompson et al. 1978, TD1: II/59B/catalog
GALEX	FUV	magnitude	Bianchi et al. 2017, Revised GALEX UV (GUVcat_AIS GR6+7): II/335/galex_ais; corrected according to Wall et al. (2019)
GALEX	NUV	magnitude	Bianchi et al. 2017, Revised GALEX UV (GUVcat_AIS GR6+7): II/335/galex_ais; corrected according to Wall et al. (2019)
Johnson-Cousins	V	magnitude	Kilkenny et al. 2017: J/MNRAS/459/4343/table3
Johnson-Cousins	B-V	color	Kilkenny et al. 2017: J/MNRAS/459/4343/table3
Johnson-Cousins	U-B	color	Kilkenny et al. 2017: J/MNRAS/459/4343/table3
Johnson-Cousins	B	magnitude	Henden et al. 2016, APASS DR9: II/336/apass9
Johnson-Cousins	V	magnitude	Henden et al. 2016, APASS DR9: II/336/apass9
Johnson-Cousins	V	magnitude	Kilkenny et al. 2015: J/MNRAS/453/1879/table2
Johnson-Cousins	B-V	color	Kilkenny et al. 2015: J/MNRAS/453/1879/table2
Johnson-Cousins	U-B	color	Kilkenny et al. 2015: J/MNRAS/453/1879/table2
Johnson-Cousins	V	magnitude	Mermilliod 2006: II/168/ubvmeans
Johnson-Cousins	B-V	color	Mermilliod 2006: II/168/ubvmeans
Johnson-Cousins	U-B	color	Mermilliod 2006: II/168/ubvmeans
Johnson-Cousins	B	magnitude	Lamontagne et al. 2000: J/AJ/119/241/table2
Johnson-Cousins	U-B	color	Lamontagne et al. 2000: J/AJ/119/241/table2
Johnson-Cousins	V	magnitude	Norris et al. 1999: J/ApJS/123/639/ubv
Johnson-Cousins	B-V	color	Norris et al. 1999: J/ApJS/123/639/ubv
Johnson-Cousins	U-B	color	Norris et al. 1999: J/ApJS/123/639/ubv
Johnson-Cousins	V	magnitude	Kilkenny et al. 1997: J/MNRAS/287/867/table1
Johnson-Cousins	B-V	color	Kilkenny et al. 1997: J/MNRAS/287/867/table1
Johnson-Cousins	U-B	color	Kilkenny et al. 1997: J/MNRAS/287/867/table1
Johnson-Cousins	U	magnitude	Morel & Magnenat 1978, UBVRIJKLMNH: II/7A/catalog
Johnson-Cousins	B	magnitude	Morel & Magnenat 1978, UBVRIJKLMNH: II/7A/catalog
Johnson-Cousins	V	magnitude	Morel & Magnenat 1978, UBVRIJKLMNH: II/7A/catalog
Johnson-Cousins	R	magnitude	Morel & Magnenat 1978, UBVRIJKLMNH: II/7A/catalog
<i>Tycho</i>	B <sub>T</sub>	magnitude	Høg et al. 2000, <i>Tycho-2</i> : I/259/tyc2
<i>Tycho</i>	V <sub>T</sub>	magnitude	Høg et al. 2000, <i>Tycho-2</i> : I/259/tyc2
HIPPARCOS	H <sub>p</sub>	magnitude	van Leeuwen 2007, HIPPARCOS, the New Reduction: I/311/hip2

**Notes:**(a) Extracted from <http://skyserver.sdss.org/dr14/en/tools/chart/navi.aspx> (last called on 20th May 2021).(b) Extracted from <http://horus.roe.ac.uk/vsa/index.html> (last called on 20th May 2021).(c) More information on VIKING can be found at [https://www.eso.org/sci/observing/phase3/data\\_releases/viking\\_dr1.pdf](https://www.eso.org/sci/observing/phase3/data_releases/viking_dr1.pdf) (last called on 20th May 2021).

Table 8.16.: Table 8.15 continued.

System	Passband	Type	Reference/Catalog
Stroemgren	y	magnitude	Paunzen 2015, Stroemgren-Crawford uvby $\beta$ : J/A+A/580/A23/catalog
Stroemgren	b-y	color	Paunzen 2015, Stroemgren-Crawford uvby $\beta$ : J/A+A/580/A23/catalog
Stroemgren	m <sub>1</sub>	color	Paunzen 2015, Stroemgren-Crawford uvby $\beta$ : J/A+A/580/A23/catalog
Stroemgren	c <sub>1</sub>	color	Paunzen 2015, Stroemgren-Crawford uvby $\beta$ : J/A+A/580/A23/catalog
Stroemgren	H $\beta$ -B	color	Paunzen 2015, Stroemgren-Crawford uvby $\beta$ : J/A+A/580/A23/catalog
Stroemgren	H $\beta$ -AF	color	Paunzen 2015, Stroemgren-Crawford uvby $\beta$ : J/A+A/580/A23/catalog
Stroemgren	y	magnitude	Lamontagne et al. 2000: J/AJ/119/241/table2
Stroemgren	b-y	color	Lamontagne et al. 2000: J/AJ/119/241/table2
Stroemgren	u-b	color	Lamontagne et al. 2000: J/AJ/119/241/table2
Stroemgren	y	magnitude	Hauck & Mermilliod 1998, uvby-beta: II/215/catalog
Stroemgren	b-y	color	Hauck & Mermilliod 1998, uvby-beta: II/215/catalog
Stroemgren	m <sub>1</sub>	color	Hauck & Mermilliod 1998, uvby-beta: II/215/catalog
Stroemgren	c <sub>1</sub>	color	Hauck & Mermilliod 1998, uvby-beta: II/215/catalog
Stroemgren	H $\beta$ -B	color	Hauck & Mermilliod 1998, uvby-beta: II/215/catalog
Stroemgren	H $\beta$ -AF	color	Hauck & Mermilliod 1998, uvby-beta: II/215/catalog
Geneva	V	magnitude	Rufener 1988, Geneva: II/169/main
Geneva	U-B	color	Rufener 1988, Geneva: II/169/main
Geneva	B <sub>1</sub> -B	color	Rufener 1988, Geneva: II/169/main
Geneva	B <sub>2</sub> -B	color	Rufener 1988, Geneva: II/169/main
Geneva	V <sub>1</sub> -B	color	Rufener 1988, Geneva: II/169/main
Geneva	V-B	color	Rufener 1988, Geneva: II/169/main
Geneva	G-B	color	Rufener 1988, Geneva: II/169/main
Gaia	G	magnitude	Gaia Collaboration et al. 2018; Evans et al. 2018, <i>Gaia</i> DR2: I/345/gaia2; corrected according to Maíz Apellániz & Weiler (2018)
Gaia	G <sub>BP</sub>	magnitude	Gaia Collaboration et al. 2018; Evans et al. 2018, <i>Gaia</i> DR2: I/345/gaia2; corrected according to Maíz Apellániz & Weiler (2018)
Gaia	G <sub>RP</sub>	magnitude	Gaia Collaboration et al. 2018; Evans et al. 2018, <i>Gaia</i> DR2: I/345/gaia2; corrected according to Maíz Apellániz & Weiler (2018)
SDSS	u	magnitude	Alam et al. 2015, SDSS DR12: V/147/sdss12; Abolfathi et al. 2018, SDSS DR14 <sup>a</sup>
SDSS	g	magnitude	Henden et al. 2016, APASS DR9: II/336/apass9; Alam et al. 2015, SDSS DR12: V/147/sdss12; Abolfathi et al. 2018, SDSS DR14 <sup>a</sup>
SDSS	r	magnitude	Henden et al. 2016, APASS DR9: II/336/apass9; Alam et al. 2015, SDSS DR12: V/147/sdss12; Abolfathi et al. 2018, SDSS DR14 <sup>a</sup>
SDSS	i	magnitude	Henden et al. 2016, APASS DR9: II/336/apass9; Alam et al. 2015, SDSS DR12: V/147/sdss12; Abolfathi et al. 2018, SDSS DR14 <sup>a</sup>
SDSS	z	magnitude	Alam et al. 2015, SDSS DR12: V/147/sdss12; Abolfathi et al. 2018, SDSS DR14 <sup>a</sup>
SkyMapper	u	magnitude	Wolf et al. 2018, SkyMapper DR1: II/358/smss
SkyMapper	v	magnitude	Wolf et al. 2018, SkyMapper DR1: II/358/smss
SkyMapper	g	magnitude	Wolf et al. 2018, SkyMapper DR1: II/358/smss
SkyMapper	r	magnitude	Wolf et al. 2018, SkyMapper DR1: II/358/smss
SkyMapper	i	magnitude	Wolf et al. 2018, SkyMapper DR1: II/358/smss
SkyMapper	z	magnitude	Wolf et al. 2018, SkyMapper DR1: II/358/smss

Table 8.17.: Table 8.15 continued.

System	Passband	Type	Reference/Catalog
VST	u	magnitude	de Jong et al. 2017, KiDS-ESO-DR3: II/347/kids_dr3
VST	g	magnitude	de Jong et al. 2017, KiDS-ESO-DR3: II/347/kids_dr3
VST	r	magnitude	de Jong et al. 2017, KiDS-ESO-DR3: II/347/kids_dr3
VST	i	magnitude	de Jong et al. 2017, KiDS-ESO-DR3: II/347/kids_dr3
VST	u	magnitude	Shanks et al. 2015, VST ATLAS DR3: II/350/vstatlas
VST	g	magnitude	Shanks et al. 2015, VST ATLAS DR3: II/350/vstatlas
VST	r	magnitude	Shanks et al. 2015, VST ATLAS DR3: II/350/vstatlas
VST	i	magnitude	Shanks et al. 2015, VST ATLAS DR3: II/350/vstatlas
VST	z	magnitude	Shanks et al. 2015, VST ATLAS DR3: II/350/vstatlas
PanSTARRS	g	magnitude	Chambers et al. 2017, PanSTARRS DR1: II/349/ps1
PanSTARRS	r	magnitude	Chambers et al. 2017, PanSTARRS DR1: II/349/ps1
PanSTARRS	i	magnitude	Chambers et al. 2017, PanSTARRS DR1: II/349/ps1
PanSTARRS	z	magnitude	Chambers et al. 2017, PanSTARRS DR1: II/349/ps1
PanSTARRS	y	magnitude	Chambers et al. 2017, PanSTARRS DR1: II/349/ps1
2MASS	J	magnitude	Cutri et al. 2003, 2MASS: II/246/out
2MASS	H	magnitude	Cutri et al. 2003, 2MASS: II/246/out
2MASS	K	magnitude	Cutri et al. 2003, 2MASS: II/246/out
DENIS	I	magnitude	DENIS Consortium 2005, DENIS: B/denis/denis
DENIS	J	magnitude	DENIS Consortium 2005, DENIS: B/denis/denis
DENIS	K	magnitude	DENIS Consortium 2005, DENIS: B/denis/denis
UKIDSS	Z	magnitude	Lawrence et al. 2007; 2013, UKIDSS DR9: II/319/gcs9
UKIDSS	Y	magnitude	Lawrence et al. 2007; 2013, UKIDSS DR9: II/319/gcs9
UKIDSS	J	magnitude	Lawrence et al. 2007; 2013, UKIDSS DR9: II/319/gcs9
UKIDSS	H	magnitude	Lawrence et al. 2007; 2013, UKIDSS DR9: II/319/gcs9
UKIDSS	K	magnitude	Lawrence et al. 2007; 2013, UKIDSS DR9: II/319/gcs9
UKIDSS	Y	magnitude	Lawrence et al. 2007; 2013, UKIDSS DR9: II/319/las9
UKIDSS	J	magnitude	Lawrence et al. 2007; 2013, UKIDSS DR9: II/319/las9
UKIDSS	H	magnitude	Lawrence et al. 2007; 2013, UKIDSS DR9: II/319/las9
UKIDSS	K	magnitude	Lawrence et al. 2007; 2013, UKIDSS DR9: II/319/las9
UKIDSS	K	magnitude	Lawrence et al. 2007; Lucas et al. 2008; UKIDSS Consortium 2012 UKIDSS DR6: II/316/gps6
VISTA	Z	magnitude	VIKING DR4 <sup>bc</sup> : VIKING_DR4
VISTA	Y	magnitude	VIKING DR4 <sup>bc</sup> : VIKING_DR4
VISTA	J	magnitude	VIKING DR4 <sup>bc</sup> : VIKING_DR4
VISTA	H	magnitude	VIKING DR4 <sup>bc</sup> : VIKING_DR4
VISTA	K	magnitude	VIKING DR4 <sup>bc</sup> : VIKING_DR4
VISTA	Y	magnitude	McMahon et al. 2013, VHS DR6 <sup>b</sup> : VHS_DR6
VISTA	J	magnitude	McMahon et al. 2013, VHS DR6 <sup>b</sup> : VHS_DR6
VISTA	H	magnitude	McMahon et al. 2013, VHS DR6 <sup>b</sup> : VHS_DR6
VISTA	K	magnitude	McMahon et al. 2013, VHS DR6 <sup>b</sup> : VHS_DR6
VISTA	Y	magnitude	Cioni et al. 2011, VMC DR4 <sup>b</sup> : II/351/vmc_dr4
VISTA	J	magnitude	Cioni et al. 2011, VMC DR4 <sup>b</sup> : II/351/vmc_dr4
VISTA	K	magnitude	Cioni et al. 2011, VMC DR4 <sup>b</sup> : II/351/vmc_dr4
AllWISE	W <sub>1</sub>	magnitude	Cutri et al. 2014, AllWISE: II/328/allwise
AllWISE	W <sub>2</sub>	magnitude	Cutri et al. 2014, AllWISE: II/328/allwise
AllWISE	W <sub>3</sub>	magnitude	Cutri et al. 2014, AllWISE: II/328/allwise
unWISE	W <sub>1</sub>	magnitude	Schlafly et al. 2019, unWISE: II/363/unwise
unWISE	W <sub>2</sub>	magnitude	Schlafly et al. 2019, unWISE: II/363/unwise

### 8.3. Photometric Data

---

The Balmer jump is the most important diagnostic tool that can be used in order to constrain the atmospheric parameters (the effective temperature and the surface gravity) of O and B-type stars by means of SED fitting. Consequently, the focus is on measurements of optical, NUV, and FUV photometry. If available, low-resolution, large-aperture, and flux-calibrated UV observations from the International Ultraviolet Explorer (IUE; Wamsteker et al. 2000) are included. The low-resolution large-aperture setup is mainly chosen in order to benefit from the more accurate flux calibration rather than from more detailed spectra. To derive appropriate UV magnitudes from the individual IUE spectra, a suitable set of box filters is defined, whereby the spectral ranges of 1300-1800 Å, 2000-2500 Å, and 2500-3000 Å are used. In this way, the impact of the increasing noise level at the boundaries of the short and long-wavelength IUE regimes can be minimized. At the same time, the interstellar reddening parameter can still be derived from the UV absorption bump at  $\sim 2200$  Å which results from interstellar gas absorption. Moreover, by defining the box filters like this, the region around the Lyman-alpha line ( $\sim 1215.67$  Å) is explicitly excluded because of the contribution by interstellar gas absorption. In addition, data from the catalog of stellar UV fluxes obtained by the Thor-Delta 1A satellite (TD1; Thompson et al. 1978) as well as FUV and NUV magnitudes from the revised catalog of GALEX UV sources (Bianchi et al., 2017) are used, if available. The latter two are corrected according to Equation 5 in Wall et al. (2019).

As presented in Heber et al. (2018), available UV data are combined with intermediate and broad-band optical and IR photometry. In this work, the visual range is covered by the following photometric filter systems:

- **Johnson-Cousins:** Magnitudes (U, B, V, R) and colors (B-V, U-B) are collected from various different catalogs. This includes data release 9 of the AAVSO<sup>94</sup> Photometric All Sky Survey (APASS; Henden et al. 2016), the Catalog of Homogeneous Means in the UBV System (Mermilliod, 2006), the UBVRIJKLMNH Photoelectric Catalogue (Morel & Magnenat, 1978), the Edinburgh-Cape Blue Object Survey (Kilkenny et al., 1997, 2015, 2017), the catalog of Montreal-Cambridge-Tololo (MCT) objects in the south Galactic cap region (Lamontagne et al., 2000), and the catalog of UBV photometry of metal-weak candidates (Norris et al., 1999).
- **Tycho:** Magnitudes ( $B_T$ ,  $V_T$ ) from the *Tycho-2* Catalogue (Høg et al., 2000) are included.
- **HIPPARCOS:** Magnitudes ( $H_p$ ) extracted from the HIPPARCOS Catalogue (New Reduction; van Leeuwen 2007) are included.
- **Stroemgren:** Magnitudes ( $y$ ) and colors ( $b-y$ ,  $u-b$ ,  $m_1$ ,  $c_1$ ,  $H\beta-B$ ,  $H\beta-AF$ ) are collected from three different catalogs: the uvby-beta Catalogue (Hauck & Mermilliod, 1998), the Stroemgren-Crawford uvby $\beta$  photometry catalog (Paunzen, 2015), and the catalog of MCT objects in the south Galactic cap region (Lamontagne et al., 2000).
- **Geneva:** Magnitudes ( $V$ ) and colors (U-B,  $B_1-B$ ,  $B_2-B$ ,  $V_1-B$ , V-B, G-B) from Observations in the Geneva Photometric System 4 (Rufener, 1988) are included.

---

<sup>94</sup>AAVSO stands for American Association of Variable Star Observers.

- **Gaia:** *Gaia* data release 2 (Gaia Collaboration et al., 2018; Evans et al., 2018) magnitudes ( $G$ ,  $G_{BP}$ ,  $G_{RP}$ ), corrected and calibrated according to Maíz Apellániz & Weiler (2018), are used.
- **SDSS:** Magnitudes ( $u$ ,  $g$ ,  $r$ ,  $i$ ,  $z$ ) from data release 9 of APASS (Henden et al., 2016) as well as from data releases 12 (Alam et al., 2015) and 14 (Abolfathi et al., 2018) of the Sloan Digital Sky Survey are included. The latter are extracted from <http://skyserver.sdss.org/dr14/en/tools/chart/navi.aspx> (last called on 20th May 2021).
- **SkyMapper:** SkyMapper magnitudes ( $u$ ,  $v$ ,  $g$ ,  $r$ ,  $i$ ,  $z$ ) from data release 1 (Wolf et al., 2018) are used.

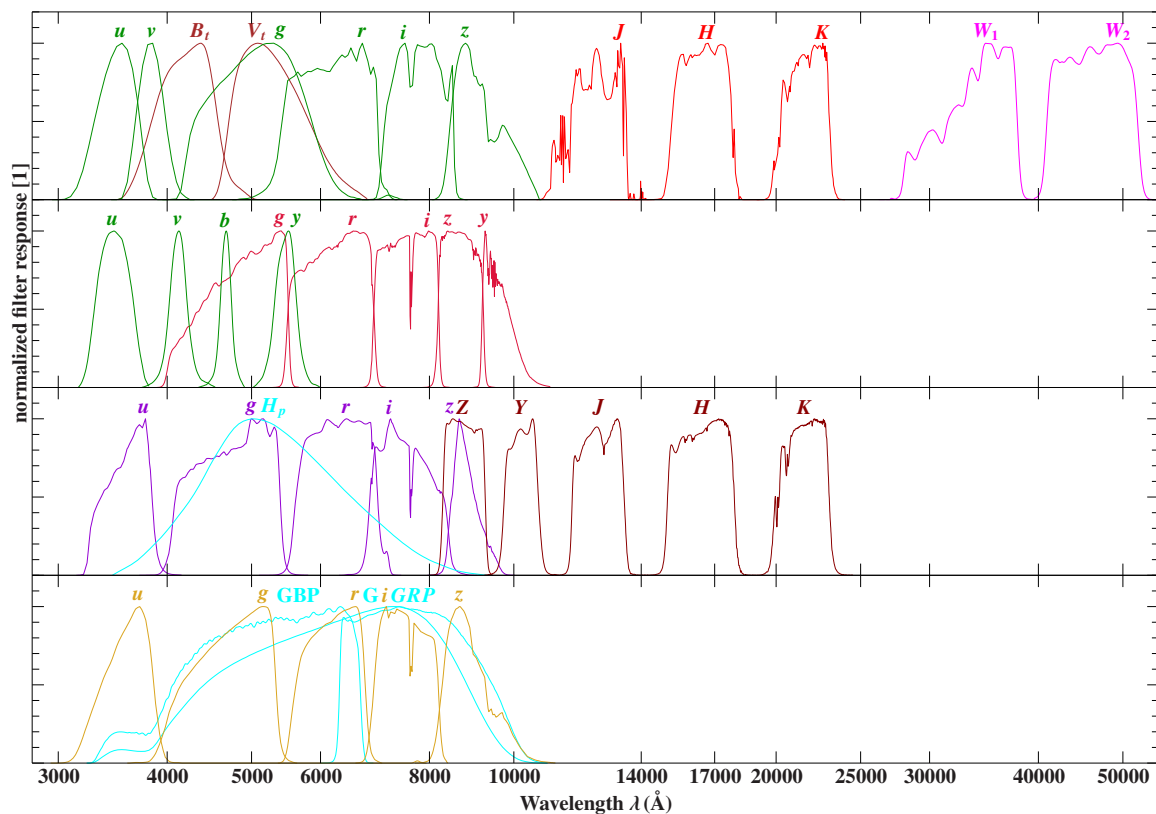


Figure 8.3.1.: Normalized filter response as a function of wavelength for some of the various different photometric filter systems used for the SED fitting performed in Ch. 12. *Upper panel:* SkyMapper (green), *Tycho* (wine red), 2MASS (light red), and AllWISE (magenta). *Upper-middle panel:* Stroemgren (green) and PanSTARRS (dark red). *Lower-middle panel:* VST (violet), HIPPARCOS (turquoise), and VISTA (brown). *Lower panel:* SDSS (yellow) and *Gaia* (turquoise). Modified version of Figure 5.1 in Hämmerich (2020).

### 8.3. Photometric Data

---

- **VST:** VLT Survey Telescope (VST) magnitudes (u, g, r, i, z) from the ATLAS survey (Shanks et al., 2015) and from the KiDS-ESO-DR3 multi-band source catalog (de Jong et al., 2017) of the Kilo-Degree Survey (KiDS) are included.
- **PanSTARRS:** Magnitudes (g, r, i, z, y) from data release 1 of the Panoramic Survey Telescope and Rapid Response System (PanSTARRS; Chambers et al. 2017) are used.

The IR range is covered by the following photometric filter systems:

- **2MASS:** Magnitudes (J, H, K) from the Two Micron All Sky Survey (2MASS; Cutri et al. 2003) are included.
- **DENIS:** Magnitudes (I, J, K) from the database of the Deep Near Infrared Survey (DENIS; DENIS Consortium 2005) of the Southern Sky are used.
- **UKIDSS:** Magnitudes (Z, Y, J, H, K) from data release 6 of the Galactic Plane Survey (Lucas et al., 2008; UKIDSS Consortium, 2012) and from data releases 9 of the Large Area Survey (Lawrence et al., 2013) and the Galactic Clusters Survey (Lawrence et al., 2013) of the UKIRT<sup>95</sup> Infrared Deep Sky Survey (UKIDSS; Lawrence et al. 2007) are included.
- **VISTA<sup>96</sup>:** Magnitudes (Z, Y, J, H, K) from data release 6 of the VISTA Hemisphere Survey (VHS<sup>97</sup>; McMahon et al. 2013) and from data releases 4 of the VISTA Kilo-Degree Infrared Galaxy Survey (VIKING<sup>97 98</sup>) and the VISTA Magellanic Survey (VMC<sup>97</sup>; Cioni et al. 2011) are used.
- **AllWISE/unWISE:** Magnitudes ( $W_1, W_2, W_3$ ) taken with the Wide-field Infrared Survey Explorer (WISE) spacecraft are included. Data from the older AllWISE (Cutri et al., 2014) and the latest unWISE (Schlafly et al., 2019) catalog are compiled. However, the majority of the data used are taken from AllWISE.

By means of the photometric filter systems in the IR, it can be searched for possible IR excesses. Inter alia, this allows to distinguish the hot subdwarf binary systems with cool MS companions from the ones with WDs or from single hot subdwarf stars.

Tables 8.15, 8.16, and 8.17 provide an overview of the various different photometric filter systems used in this work. Note that the photometric data sets are rather inhomogeneous, both with respect to accuracy and bandwidth. This can also be seen in Fig. 8.3.1, where the normalized response curves for some of the aforementioned filter systems are displayed. On the other hand, however, this figure also shows how well the different wavelength regimes are sampled by the photometric data used.

---

<sup>95</sup>UKIRT stands for United Kingdom Infrared Telescope.

<sup>96</sup>VISTA stands for Visible and Infrared Survey Telescope for Astronomy.

<sup>97</sup>Extracted from <http://horus.roe.ac.uk/vsa/index.html> (last called on 20th May 2021).

<sup>98</sup>More information on VIKING can be found at [https://www.eso.org/sci/observing/phase3/data\\_releases/viking\\_dr1.pdf](https://www.eso.org/sci/observing/phase3/data_releases/viking_dr1.pdf) (last called on 20th May 2021).

## 8.4. Astrometric Data

Apart from the spectrophotometric data, precise distance/parallax measurements are needed in order to derive the fundamental stellar parameters (see Sect. 7.3). In this work, the astrometric data from *Gaia* DR2 are primarily used. These data are accessible via the *Gaia* data Archive<sup>99</sup>. Since most of the program stars of this work are nearby, their *Gaia* parallaxes should be reliable. Tables 8.18 and 8.19 list the *Gaia* parallaxes (and the distances) as well as the relative statistical uncertainties of the *Gaia* parallaxes (the apparent fractional parallax uncertainties)  $\Delta\varpi_{\text{Gaia}}/\varpi_{\text{Gaia}}$  for all program stars. Indeed, the astrometric data are precise for most stars because the respective measured statistical errors do not make up more than 20% of the individual parallax values. Tables 8.18 and 8.19 also list the renormalised unit weight error (RUWE) derived from *Gaia* astrometry. According to Lindegren et al. 2018<sup>100 101</sup>, this parameter is a recommended goodness of fit indicator for *Gaia* DR2 astrometry, in particular for bright and blue objects such as the ones investigated in this work. Although directly accessible through the *Gaia* Archive, the RUWE parameter can be computed from the archive quantities  $\chi^2$  (astrometric\_chi2\_al; the astrometric goodness-of-fit in the along-scan direction),  $N$  (astrometric\_n\_good\_obs\_al; the number of along-scan observations that are not strongly downweighted in the astrometric solution of the source),  $G$  (phot\_g\_mean\_mag; the mean magnitude in the  $G$  band), and  $C$  (bp\_rp; the color  $C := G_{\text{BP}} - G_{\text{RP}}$ ) via:

$$\text{RUWE} := \frac{\text{UWE}}{u_0(G, C)} = \frac{\sqrt{\chi^2/(N-5)}}{u_0(G, C)}. \quad (8.1)$$

$\text{UWE} := \sqrt{\chi^2/(N-5)}$  is the unit weight error and  $u_0(G, C)$  is an empirical normalisation factor, which is provided as a lookup table on the ESA *Gaia* DR2 Known issues webpage<sup>102</sup>. The RUWE value should lie between  $\sim 1.00$  and  $\sim 1.40$ , if the *Gaia* five-parameter astrometric solution (position, parallax, proper motion) is appropriate. This applies to nearly all of the program stars. The sole evident exceptions are SB 290 and EC 01541-1409, which interestingly turned out to be binaries (see Ch. 12 for details). For Feige 36, no *Gaia*  $G_{\text{BP}}$  and  $G_{\text{RP}}$  magnitudes and, hence, no color  $C := G_{\text{BP}} - G_{\text{RP}}$  are available in *Gaia* DR2. Therefore, Feige 36 lacks the RUWE parameter. As will be shown in Sect. 12.2, this program star is in fact a very interesting object.

The fact that the target sample mostly consists of stellar objects that exhibit accurate astrometric solutions ( $1.00 \lesssim \text{RUWE} \lesssim 1.40$ ) and non-negative parallaxes with low apparent fractional parallax uncertainties ( $\Delta\varpi_{\text{Gaia}}/\varpi_{\text{Gaia}} < 20\%$ ) justifies working in the space of astrophysical variables rather than in the data space (Luri et al., 2018). In fact,  $\Delta\varpi_{\text{Gaia}}/\varpi_{\text{Gaia}}$  is  $< 5\%$  for the XSHOOTER reference sample, with EC 13047-3049 ( $\Delta\varpi_{\text{Gaia}}/\varpi_{\text{Gaia}} = 5.92$ ) and PG 1136-003 ( $\Delta\varpi_{\text{Gaia}}/\varpi_{\text{Gaia}} = 7.28$ ) being the sole exceptions. In the complete sample, only five

<sup>99</sup><https://gea.esac.esa.int/archive/>, last called on 21st May 2021

<sup>100</sup>[http://www.rssd.esa.int/doc\\_fetch.php?id=3757412](http://www.rssd.esa.int/doc_fetch.php?id=3757412), last called on 21st May 2021

<sup>101</sup>[https://www.cosmos.esa.int/documents/29201/1770596/Lindegren\\_GaiaDR2\\_Astrometry\\_extended.pdf/1ebddb25-f010-6437-cb14-0e360e2d9f09](https://www.cosmos.esa.int/documents/29201/1770596/Lindegren_GaiaDR2_Astrometry_extended.pdf/1ebddb25-f010-6437-cb14-0e360e2d9f09), last called on 21st May 2021

<sup>102</sup><https://www.cosmos.esa.int/web/gaia/dr2-known-issues>, last called on 21st May 2021

## 8.4. Astrometric Data

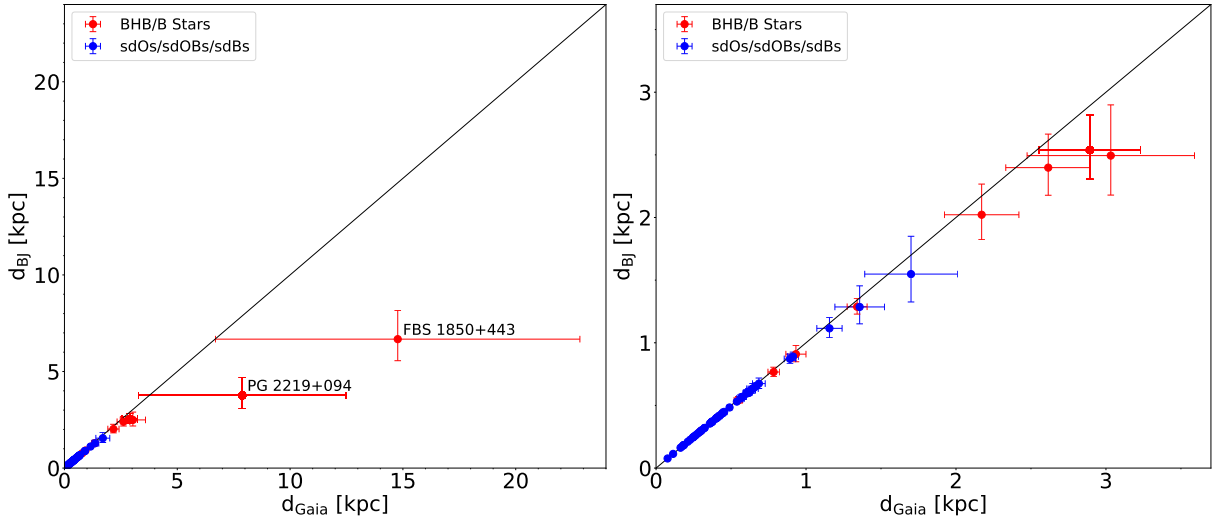


Figure 8.4.1.: *Left-hand panel*: Distances  $d_{\text{BJ}}$  derived from Bayesian methods (Bailer-Jones et al., 2018) vs. distances  $d_{\text{Gaia}}$  determined by the *Gaia* satellite within DR2 for all program stars. Hot subdwarf stars from the target sample are represented by blue data points, whereas potential (post-)BHB and B-type MS stars are shown in red. Note that the distances from Bailer-Jones et al. (2018) have asymmetric statistical uncertainties compared to the *Gaia* measurements (see also Tables 8.18 and 8.19). This is because Bailer-Jones et al. (2018) provide the mode and the highest-density interval (HDI; see also Sect. 5.5.3). The solid black line represents the bisector. In the case of the two most distant objects of the sample (FBS 1850+443 and PG 2219+094),  $d_{\text{BJ}}$  and  $d_{\text{Gaia}}$  strongly deviate from each other. In addition, the apparent fractional parallax uncertainty in *Gaia* DR2 is above 50% for both stars (see Table 8.19). *Right-hand panel*: Same as the left-hand panel, but enlarged.

stars have apparent fractional parallax uncertainties of  $5\% \leq \Delta\varpi_{\text{Gaia}}/\varpi_{\text{Gaia}} \leq 10\%$  and eight stars exceed the 10% mark (see Tables 8.18 and 8.19).

As discussed in Sect. 5.5.1, it is known that there is a global parallax zero point offset of *Gaia* DR2 data, which has been estimated to be around  $-0.029$  mas by means of an examination of quasar parallaxes (Lindgren et al., 2018). This means that the *Gaia* DR2 Catalogue parallaxes are too small such that the distances are systematically overestimated by  $\sim 1\%$  on average, if the usual relation  $d = 1/\varpi$  is adopted. Due to the reasons outlined in Sect. 5.5.1, however, the *Gaia* DR2 parallaxes used in this work are not corrected for the zero point. As a matter of fact, this is also recommended by Lindgren et al. (2018) and Arenou et al. (2018) for single targets in the field such as the ones analyzed in this work.

Furthermore, it is known that the *Gaia* parallax measurements suffer from additional large and small-scale variations (Lindgren et al., 2018). Due to the fact that these variations are rather difficult to determine for single objects (see the descriptions in Sect. 5.5.1), however, they are also not taken into account for the present analysis.

As outlined in Sects. 5.5.3 and 5.5.4, the *Gaia* collaboration recommends users of DR2 data

to not simply estimate distances by inverting parallaxes, but to rather stick to Bayesian methods. For comparison reasons, the distances and the maximum<sup>103</sup> relative statistical distance uncertainties according to the Bayesian approach of Bailer-Jones et al. (2018) therefore are also listed in Tables 8.18 and 8.19 for all program stars. Figure 8.4.1 shows the distances  $d_{\text{BJ}}$  according to Bailer-Jones et al. (2018) plotted against the respective *Gaia* distances  $d_{\text{Gaia}}$ . As expected, the results derived from the Bayesian methods are in good agreement with the *Gaia* DR2 measurements, except for the most distant objects with high apparent fractional parallax uncertainties. For these objects, the usual relation  $d = 1/\varpi$  is inaccurate. Of course, this distance discrepancy also affects the fundamental stellar parameters of the relevant objects. This will be discussed in Sect. 13.4. Note, however, that  $d_{\text{BJ}}$  and  $d_{\text{Gaia}}$  strongly deviate from each other in the case of the two most extreme objects of the sample (FBS 1850+443 and PG 2219+094; see Fig. 8.4.1). Moreover, the apparent fractional parallax uncertainty in *Gaia* DR2 is above 50% for both stars (see Table 8.19). Thus, no fundamental stellar parameters based on the *Gaia* DR2 parallaxes will be determined for FBS 1850+443 and PG 2219+094 in Ch. 13 because using the corresponding parallaxes as presented in Sect. 7.3 would result in completely unreliable radii, luminosities, and masses. In fact, the same applies to the fundamental stellar parameters derived from the respective Bailer-Jones distances. Hence, in this work no radii, luminosities, and masses at all are determined for FBS 1850+443 and PG 2219+094.

---

<sup>103</sup>Compared to the *Gaia* measurements, the distances from Bailer-Jones et al. (2018) have asymmetric statistical uncertainties (see Tables 8.18 and 8.19). This is because Bailer-Jones et al. (2018) provide the mode and the highest-density interval (HDI; see also Sect. 5.5.3).

Table 8.18.: Comparison of *Gaia* DR2 distances ( $d_{\text{Gaia}}$ ) and parallaxes ( $\varpi_{\text{Gaia}}$ ) to distances ( $d_{\text{BJ}}$ ) according to Bailer-Jones et al. (2018) for the program stars of this work. In addition, the relative statistical parallax uncertainties (the apparent fractional parallax uncertainties)  $\Delta\varpi_{\text{Gaia}}/\varpi_{\text{Gaia}}$ , the maximum relative statistical distance uncertainties  $\max(\Delta d_{\text{BJ}})/d_{\text{BJ}}$  as well as the renormalised unit weight errors (RUWE) derived from *Gaia* astrometry are listed (see the text for details).

Object	$d_{\text{Gaia}} \pm \Delta d_{\text{Gaia}}$ [pc]	$\varpi_{\text{Gaia}} \pm \Delta\varpi_{\text{Gaia}}^{\text{a}}$ [mas]	$[\Delta\varpi_{\text{Gaia}}/\varpi_{\text{Gaia}}] \cdot 100$ [%]	$d_{\text{BJ}} \pm \Delta d_{\text{BJ}}$ [pc]	$[\max(\Delta d_{\text{BJ}})/d_{\text{BJ}}] \cdot 100$ [%]	RUWE
HD 4539	185.729 ± 4.557	5.3842 ± 0.1321	2.45	184.898 <sup>+4.663</sup> <sub>-4.442</sub>	2.52	1.2681860
PG 1432+004	578.402 ± 24.088	1.7289 ± 0.0720	4.16	570.083 <sup>+24.554</sup> <sub>-22.639</sub>	4.31	1.2929015
GALEX J104148.9-073031	258.091 ± 5.429	3.8746 ± 0.0815	2.10	256.331 <sup>+5.507</sup> <sub>-5.284</sub>	2.15	1.2068472
Feige 38	443.636 ± 16.789	2.2541 ± 0.0853	3.78	438.544 <sup>+17.143</sup> <sub>-15.922</sub>	3.91	1.0197470
EC 03591-3232	183.170 ± 1.879	5.4594 ± 0.0560	1.03	182.231 <sup>+1.892</sup> <sub>-1.854</sub>	1.04	1.1459038
PG 1136-003	1156.203 ± 84.219	0.8649 ± 0.0630	7.28	1115.302 <sup>+85.519</sup> <sub>-74.413</sub>	7.67	1.1026739
GALEX J080510.9-105834	211.385 ± 2.315	4.7307 ± 0.0518	1.09	210.139 <sup>+2.328</sup> <sub>-2.278</sub>	1.11	1.1671984
PG 1505+074	563.000 ± 27.704	1.7762 ± 0.0874	4.92	555.673 <sup>+29.046</sup> <sub>-26.340</sub>	5.23	1.1066365
EC 13047-3049	643.294 ± 38.073	1.5545 ± 0.0920	5.92	634.088 <sup>+40.246</sup> <sub>-35.785</sub>	6.35	1.2862605
HD 149382	76.826 ± 0.470	13.0164 ± 0.0796	0.61	76.661 <sup>+0.475</sup> <sub>-0.469</sub>	0.62	1.2232592
[CW83] 0825+15	278.676 ± 5.126	3.5884 ± 0.0660	1.84	276.565 <sup>+5.179</sup> <sub>-4.995</sub>	1.87	1.0517213
[CW83] 0512-08	184.577 ± 2.944	5.4178 ± 0.0864	1.59	183.670 <sup>+2.981</sup> <sub>-2.889</sub>	1.62	1.2055103
GALEX J075807.5-043203	603.391 ± 23.957	1.6573 ± 0.0658	3.97	594.018 <sup>+24.331</sup> <sub>-22.519</sub>	4.10	1.0192862
GALEX J042034.8+012041	410.728 ± 10.409	2.4347 ± 0.0617	2.53	406.146 <sup>+10.506</sup> <sub>-9.998</sub>	2.59	0.9860619
HZ 1	322.924 ± 6.998	3.0967 ± 0.0671	2.17	320.141 <sup>+7.077</sup> <sub>-6.782</sub>	2.21	1.0654064
GALEX J095256.6-371940	892.857 ± 38.346	1.1200 ± 0.0481	4.29	871.583 <sup>+38.351</sup> <sub>-35.302</sub>	4.40	1.2146384
PG 0314+146	453.803 ± 18.988	2.2036 ± 0.0922	4.18	448.496 <sup>+19.462</sup> <sub>-17.935</sub>	4.34	1.2913771
PHL 25	548.306 ± 27.930	1.8238 ± 0.0929	5.09	541.534 <sup>+29.377</sup> <sub>-26.547</sub>	5.42	1.2051342
PHL 382	932.575 ± 67.054	1.0723 ± 0.0771	7.18	909.402 <sup>+69.888</sup> <sub>-60.759</sub>	7.69	1.1646906
BD+48° 2721	294.221 ± 3.576	3.3988 ± 0.0413	1.21	291.802 <sup>+3.578</sup> <sub>-3.494</sub>	1.23	1.0930834
PG 0342+026	163.074 ± 3.285	6.1322 ± 0.1235	2.01	162.407 <sup>+3.350</sup> <sub>-3.220</sub>	2.06	1.2811337
CD-35° 15910	245.537 ± 5.445	4.0727 ± 0.0903	2.22	243.982 <sup>+5.535</sup> <sub>-5.299</sub>	2.27	1.2282195
EC 03263-6403	654.922 ± 12.482	1.5269 ± 0.0291	1.90	642.867 <sup>+12.304</sup> <sub>-11.859</sub>	1.91	1.1174277
EC 12234-2607	667.869 ± 23.463	1.4973 ± 0.0526	3.51	655.911 <sup>+23.590</sup> <sub>-22.034</sub>	3.60	1.0134631
EC 14338-1445	634.558 ± 28.187	1.5759 ± 0.0700	4.44	624.701 <sup>+28.785</sup> <sub>-26.396</sub>	4.61	1.2642223
PG 1710+490	448.009 ± 9.354	2.2321 ± 0.0466	2.09	442.478 <sup>+9.001</sup> <sub>-8.376</sub>	2.12	1.2172823
SB 290	175.131 ± 5.917	5.7100 ± 0.1929	3.38	174.567 <sup>+6.130</sup> <sub>-5.734</sub>	3.51	3.1773758
Feige 36	433.351 ± 12.057	2.3076 ± 0.0642	2.78	428.246 <sup>+12.183</sup> <sub>-11.538</sub>	2.84	-
HE 0929-0424	1700.102 ± 308.690	0.5882 ± 0.1068	18.14	1548.348 <sup>+301.742</sup> <sub>-222.578</sub>	19.49	1.0240189
HE 1047-0436	1357.589 ± 165.138	0.7366 ± 0.0896	12.16	1286.076 <sup>+168.466</sup> <sub>-134.844</sub>	13.10	1.1844882

## Notes:

<sup>(a)</sup> No corrections for the global zero point offset and the large and small-scale spatial variations of *Gaia* are considered (see also Sect. 5.5.1).

Table 8.19.: Table 8.18 continued.

Object	$d_{\text{Gaia}} \pm \Delta d_{\text{Gaia}}$ [pc]	$\varpi_{\text{Gaia}} \pm \Delta \varpi_{\text{Gaia}}^a$ [mas]	$[\Delta \varpi_{\text{Gaia}} / \varpi_{\text{Gaia}}] \cdot 100$ [%]	$d_{\text{BJ}} \pm \Delta d_{\text{BJ}}$ [pc]	$[\max(\Delta d_{\text{BJ}}) / d_{\text{BJ}}] \cdot 100$ [%]	RUWE
HIP 67513	1340.662 ± 66.503	0.7459 ± 0.0370	4.95	1287.640 <sup>+64.432</sup> <sub>-58.692</sub>	5.00	1.0698814
BD+49° 2226	783.945 ± 37.858	1.2756 ± 0.0616	4.83	766.786 <sup>+38.186</sup> <sub>-34.791</sub>	4.98	1.0012963
FBS 1850+443	14 771.049 ± 8072.804	0.0677 ± 0.0370	54.64	6675.199 <sup>+1488.507</sup> <sub>-1116.261</sub>	22.30	1.1734486
FBS 2158+373	2615.063 ± 283.117	0.3824 ± 0.0414	10.82	2397.989 <sup>+267.552</sup> <sub>-220.447</sub>	11.16	1.1484578
FBS 2204+364	2171.081 ± 248.407	0.4606 ± 0.0527	11.44	2021.882 <sup>+244.859</sup> <sub>-198.715</sub>	12.11	1.4883481
BD+42° 3250	248.188 ± 2.310	4.0292 ± 0.0375	0.93	246.449 <sup>+2.311</sup> <sub>-2.299</sub>	0.94	1.1394260
Balloon 90100001	365.631 ± 8.570	2.7350 ± 0.0641	2.34	362.046 <sup>+8.556</sup> <sub>-8.268</sub>	2.39	1.1896087
FBS 0102+362	368.650 ± 10.669	2.7126 ± 0.0785	2.89	365.099 <sup>+10.845</sup> <sub>-10.247</sub>	2.97	1.2062991
Feige 14	403.975 ± 13.317	2.4754 ± 0.0816	3.30	399.659 <sup>+13.561</sup> <sub>-12.714</sub>	3.39	1.2854053
GALEX J210332.4+303538	376.648 ± 7.448	2.6550 ± 0.0525	1.98	372.813 <sup>+7.499</sup> <sub>-7.214</sub>	2.01	1.0957806
FBS 2347+385	249.526 ± 3.979	4.0076 ± 0.0639	1.59	247.827 <sup>+4.017</sup> <sub>-3.893</sub>	1.62	1.3568570
PG 0101+039	376.478 ± 17.292	2.6562 ± 0.1220	4.59	373.139 <sup>+17.915</sup> <sub>-16.372</sub>	4.80	1.2183964
PG 1635+414	913.159 ± 35.439	1.0951 ± 0.0425	3.88	890.290 <sup>+35.181</sup> <sub>-32.649</sub>	3.95	1.2178105
LS IV +10° 9	489.956 ± 15.076	2.0410 ± 0.0628	3.08	483.752 <sup>+15.271</sup> <sub>-14.379</sub>	3.16	1.1006023
PG 2219+094	7880.221 ± 4601.453	0.1269 ± 0.0741	58.37	3762.937 <sup>+916.591</sup> <sub>-677.322</sub>	24.36	1.0698879
SB 395	3032.141 ± 558.069	0.3298 ± 0.0607	18.39	2494.040 <sup>+404.764</sup> <sub>-315.118</sub>	16.23	1.1995420
KUV 03591+0457	2892.682 ± 337.215	0.3457 ± 0.0403	11.66	2538.152 <sup>+280.941</sup> <sub>-233.074</sub>	11.07	1.1264296
HE 0247-0418	420.858 ± 18.758	2.3761 ± 0.1059	4.46	416.414 <sup>+19.328</sup> <sub>-17.714</sub>	4.64	1.1902770
GALEX J203913.4+201309	609.088 ± 27.750	1.6418 ± 0.0748	4.55	600.216 <sup>+28.407</sup> <sub>-25.990</sub>	4.73	1.2219675
GALEX J202332.7+013618	399.600 ± 13.941	2.5025 ± 0.0873	3.49	395.794 <sup>+14.268</sup> <sub>-13.324</sub>	3.60	1.1898408
GALEX J172445.5+113224	323.593 ± 6.137	3.0903 ± 0.0586	1.89	320.781 <sup>+6.185</sup> <sub>-5.959</sub>	1.93	1.2120310
PG 2313-021	401.639 ± 15.600	2.4898 ± 0.0967	3.88	397.676 <sup>+16.012</sup> <sub>-14.839</sub>	4.03	1.3567860
KUV 16256+4034	412.643 ± 7.407	2.4234 ± 0.0435	1.79	407.928 <sup>+7.420</sup> <sub>-7.164</sub>	1.82	1.1947138
PG 0133+114	298.329 ± 10.289	3.3520 ± 0.1156	3.45	296.162 <sup>+10.569</sup> <sub>-9.877</sub>	3.57	1.2137033
GALEX J032139.8+472718	265.767 ± 4.090	3.7627 ± 0.0579	1.54	263.839 <sup>+4.124</sup> <sub>-4.001</sub>	1.56	1.1955140
2M1938+4603	400.769 ± 6.489	2.4952 ± 0.0404	1.62	396.332 <sup>+6.490</sup> <sub>-6.288</sub>	1.64	1.1499184
FB 29	358.269 ± 5.186	2.7912 ± 0.0404	1.45	354.706 <sup>+5.193</sup> <sub>-5.048</sub>	1.46	1.1138959
EC 01541-1409	368.922 ± 17.884	2.7106 ± 0.1314	4.85	365.818 <sup>+18.917</sup> <sub>-14.317</sub>	5.17	1.8926908
FBS 0654+366	685.683 ± 42.127	1.4584 ± 0.0896	6.14	674.400 <sup>+39.280</sup> <sub>-39.280</sub>	6.58	1.1774765
GALEX J175548.5+501210	538.706 ± 11.028	1.8563 ± 0.0380	2.05	530.666 <sup>+11.000</sup> <sub>-10.570</sub>	2.07	1.1348749
FBS 0224+330	614.704 ± 28.869	1.6268 ± 0.0764	4.70	604.740 <sup>+29.463</sup> <sub>-26.893</sub>	4.87	1.1352317
BD+28° 4211	113.608 ± 1.402	8.8022 ± 0.1086	1.23	113.266 <sup>+1.421</sup> <sub>-1.387</sub>	1.25	1.1335678
AGK+81° 266	287.902 ± 3.639	3.4734 ± 0.0439	1.26	285.581 <sup>+3.649</sup> <sub>-3.560</sub>	1.28	1.0946660
LS II +18° 9	300.147 ± 8.226	3.3317 ± 0.0913	2.74	297.954 <sup>+8.395</sup> <sub>-7.954</sub>	2.82	1.2252269
Feige 67	306.607 ± 8.903	3.2615 ± 0.0947	2.90	304.241 <sup>+9.093</sup> <sub>-8.589</sub>	2.99	1.3430942
Feige 34	227.330 ± 5.251	4.3989 ± 0.1016	2.31	226.003 <sup>+5.349</sup> <sub>-5.111</sub>	2.37	1.5599100

## 9. Quantitative Spectral Analysis

For all program stars, the effective temperature  $T_{\text{eff}}$ , the surface gravity  $\log(g)$ , and the helium abundance  $\log n(\text{He}) := \log n(^4\text{He} + ^3\text{He})$  are determined by fitting calculated model spectra to the hydrogen and helium lines of the (co-added) spectra of Tables 8.1-8.10<sup>104</sup>. If possible, each star is analyzed spectroscopically by means of the three different model atmosphere approaches presented in Sects. 6.7, 6.8, and 6.9: LTE, hybrid LTE/NLTE (ADS), and NLTE (TLUSTY/SYNSPEC)<sup>105</sup>. In addition, the two different categories of analysis strategies presented in Sect. 7.1.2 are used: the selective (SPAS and FITPROF) and the global (ISIS) approach<sup>106</sup>. In total, the following combinations of models and analysis strategies are investigated: ADS + Global, ADS + SPAS, LTE + SPAS, TLUSTY/SYNSPEC + SPAS, ADS + FITPROF, LTE + FITPROF, and TLUSTY/SYNSPEC + FITPROF. These abbreviations will be used throughout this chapter. In the case of the hybrid LTE/NLTE models in combination with the global analysis strategy (ADS + Global) also metals are investigated. Therefore, the corresponding sharp spectral lines can be used to additionally constrain the projected rotational velocities  $v \sin i$  of the individual program stars. It is indicated throughout this chapter, where metals are fitted in the case of ADS + Global<sup>107</sup>: C, N, O, Ne, Mg, Al, Si, S, Ar, and Fe in NLTE as well as P, Ca, Ti, Sr, and Zr in LTE (NLTE + LTE metals); C, N, O, Ne, Mg, Al, Si, S, Ar, and Fe in NLTE and no other metals (NLTE metals)<sup>108</sup>. Furthermore, the isotopic helium

<sup>104</sup>Table 8.11 also lists five H-sdO/post-AGB program stars. For these stars, however, no spectroscopic data are analyzed within the framework of this thesis. Therefore, these objects will not be dealt with in Sect. 9.2, where the results derived from the different model atmosphere approaches and analysis strategies used in this work will be compared. Nevertheless, spectroscopic results from literature (effective temperatures, surface gravities, and helium abundances) will be used to derive the stellar angular diameters and, hence, the fundamental stellar parameters of these stars (see also Tables A.19 and 13.12).

<sup>105</sup>For the He-sdO program stars, the departures from LTE are large. Thus, these objects are only analyzed in NLTE making use of TLUSTY/SYNSPEC. As stated in Sect. 6.9, the NLTE model grid calculated with TLUSTY/SYNSPEC only covers program stars with  $T_{\text{eff}} \gtrsim 30\,000$  K (see also Table 6.4). As mentioned in Sect. 6.7, the LTE model grids used in this work are based on solar and supersolar (10 times solar) metallicity. While the solar metallicity grid is chosen for program stars with  $T_{\text{eff}} \lesssim 30\,000$  K, the hotter H-sdOBs are fitted with supersolar metallicity. Some program stars are not covered by either of the two LTE grids shown in Table 6.2. Hence, these objects lack LTE analyses. For a detailed description of the metallicities used for the LTE, hybrid LTE/NLTE, and NLTE models, see the respective Sects. 6.7, 6.8, and 6.9.

<sup>106</sup>SPAS and FITPROF are combined with all model atmosphere approaches available, whereas the global analysis strategy (ISIS) is used in combination with the hybrid LTE/NLTE models only.

<sup>107</sup>The results of the metal abundance analyses based on the hybrid model atmosphere approach and the global analysis strategy (ADS + Global) will be presented in Ch. 11.

<sup>108</sup>Metal lines are only investigated for medium and high-resolution spectra. Moreover, the chemical elements P, Ca, Ti, Sr, and Zr, which are treated in LTE, are only analyzed for the program stars of the XSHOOTER reference sample (see Tables 8.1-8.3).

abundances  $\log n(^4\text{He})$  and  $\log n(^3\text{He})$  as well as the isotopic abundance ratios  $n(^4\text{He})/n(^3\text{He})$  are derived for the  $^3\text{He}$  program stars of this work. For this, the hybrid LTE/NLTE models and the global analysis strategy (ADS + Global) are also used because the necessary  $^3\text{He}$  model atom is only implemented for this model atmosphere approach (see Sect. 6.8) and SPAS and FITPROF are not suited for the analysis of  $^3\text{He}$  stars (see Sect. 7.1.2). The results for  $\log n(^4\text{He})$ ,  $\log n(^3\text{He})$ , and  $n(^4\text{He})/n(^3\text{He})$  for the relevant program stars are not dealt with in this chapter but will be presented in Ch. 10, which focuses exclusively on the spectroscopic analysis of the  $^3\text{He}$  anomaly.

## 9.1. Spectral Line Fits

In order to provide an insight into the quality of the spectroscopic fits on which the results of this chapter are based, Figs. 9.1.1-9.1.10 display selected line fits to the observed spectra of some of the program stars. This includes the co-added XSHOOTER spectra of the H-sdB HD 4539, the H-sdOB PG 1505+074, and the He-sdO HZ 1 as well as the IDS spectrum of the iHe-sdB FBS 0654+366. HD 4539 is selected because for this star the published atmospheric parameters differ considerably. PG 1505+074 is selected because of the discrepancy between the hydrogen Balmer line strength and the He I/He II ionization equilibrium (see the discussion below). FBS 0654+366 is a new member of the interesting group of intermediate He-sdBs. Last but not least, HZ 1 is a well-known He-sdO star and, hence, ideal for testing the synthetic NLTE spectra calculated with TLUSTY/SYNSPEC.

Due to the successful telluric absorption correction of the XSHOOTER spectra (see Sect. 8.2.1), these data allow to extensively analyze the NIR, including part of the hydrogen Paschen and Brackett series as well as additional He I/He II lines such as He I 10 830 Å, which is an important indicator for  $^3\text{He}$  (see also Table 3.2). Therefore, the present quantitative spectral analyses of the XSHOOTER data are clearly superior to previous ones that are mostly based on blue spectra only. However, it has to be mentioned that artefacts still remain after the telluric corrections with `molecfit`. For instance, such artefacts can be seen in Figs. 9.1.9 and 9.1.10. For the sake of clarity, the spectral regions that still strongly suffer from telluric lines after the applied corrections are excluded in Figs. 9.1.1 and 9.1.2. In the following, the goodness of the spectral line fits performed for each of the aforementioned program stars shall be presented.

- **HD 4539:** The ADS + Global (NLTE + LTE metals) fit of all suitable hydrogen and He I absorption lines in the co-added XSHOOTER spectrum of the H-sdB HD 4539 is almost perfect (see Fig. 9.1.1). The Paschen series is fitted very accurately. The residuals only show small line mismatches between the fit and the observed spectrum in the case of the Balmer lines  $H\alpha$ ,  $H\beta$ ,  $H\gamma$ ,  $H\delta$ , and  $H\epsilon$  (these lines are slightly too weak in the model, hence suggesting a cooler effective temperature for the star) as well as in the case of neutral helium lines such as He I 4026 Å, He I 4472 Å, He I 4922 Å, He I 6678 Å, or He I 10 830 Å (some of these lines are slightly too weak in the model, whereas others are modelled slightly too strong). Note, however, that the residuals in

## 9.1. Spectral Line Fits

---

Fig. 9.1.1 show deviations in terms of  $\sigma$ . This means that a deviation of  $\pm 1\sigma$ , that is  $\chi = \pm 1$ , only corresponds to  $\sim 0.2\%$  and  $\sim 0.4\%$  of the flux in the UVB and the VIS XSHOOTER channel, respectively.

- **PG 1505+074:** For the co-added XSHOOTER spectrum of the H-sdOB PG 1505+074, the ADS + Global (NLTE + LTE metals) fit of the hydrogen Paschen series has the same quality as for HD 4539 (see Fig. 9.1.2). However, mismatches are visible for the line cores of  $H\alpha$ - $H\epsilon$ , which are too weak in the model, thus suggesting a cooler surface temperature for the star. Yet, the effective temperature of the star is high enough such that He II 4686 Å is visible in the spectrum. This line is predicted too weak by the model. On the other hand, the He I 5875 Å absorption line is modelled clearly too strong. This points towards a higher effective temperature based on the He I/He II ionization equilibrium only. Consequently, no effective temperature can be found in order to simultaneously match the hydrogen Balmer and the He I/He II lines. In fact, this temperature discrepancy has already been reported for the H-sdB star PG 1219+534 by Heber et al. (2000). Later, O’Toole & Heber (2006) observed a similar discrepancy for another star (the H-sdOB CD-24° 731). The authors found that the temperature discrepancy is not related to NLTE because for PG 1219+534 and CD-24° 731 the Balmer lines and He II 4686 Å could be matched simultaneously making use of LTE models with supersolar (10 times solar) metallicity. In both cases, however, the metal-enriched models of O’Toole & Heber (2006) were not able to reproduce the line cores of the strongest He I lines (He I 4472 Å, He I 4713 Å, and He I 5875 Å). In principle, such an analysis that makes use of models with supersolar metallicity instead of models based on the mean metallicity for H-sdBs/H-sdOBs (Naslim et al., 2013) also is possible with ADS. Due to time restrictions, however, this work dispenses with a further ADS analysis for PG 1505+074 based on supersolar metallicity. Nevertheless, the star is also analyzed with LTE + SPAS and LTE + FITPROF, whereby in both cases metal-enriched models with supersolar metallicity are used. As a matter of fact, the Balmer lines and He II 4686 Å are modelled very accurately in this way, whereas mismatches can still be observed for He I 4472 Å, He I 5875 Å, and, to a lesser extent, also for He I 4713 Å. Therefore, the results of this work for PG 1505+074 resemble those of O’Toole & Heber (2006) for PG 1219+534 and CD-24° 731.

In addition, PG 1505+074 shows another special feature, which is helium emission at the position of the He I 6678 Å line<sup>109</sup>. In fact, this emission is predicted by the ADS models, although it is modelled a bit too strong (see Fig. 9.1.2). On the other hand, LTE models (LTE + SPAS and LTE + FITPROF) are not able to reproduce the emission. The star’s atmospheric parameters ( $T_{\text{eff}} = 40\,654 \pm 26$  K and  $\log g = 5.6192^{+0.0025}_{-0.0021}$ ;  $1\sigma$  statistical single parameter errors) strongly support NLTE effects. As the He I 6678 Å line is highly affected by this (see Sect. 6.4), it is safe to say that the observed emission can be explained by occupation numbers that depart from usual LTE. In consequence,

---

<sup>109</sup>He I 6678 Å emission is also observed for another program star (the H-sdOB EC 13047-3049). As in the case of PG 1505+074, the emission can be reproduced if statistical equilibrium is taken into account (see Sect. 6.4).

the hypothesis of Heber et al. (2003b), who argued for a stellar wind as a possible cause of the emission, can be rejected.

- **FBS 0654+366:** The ADS + FITPROF fit of the IDS spectrum of FBS 0654+366 also is of outstanding quality (see Figs. 9.1.3-9.1.5). Besides the usual strong hydrogen Balmer line series, the star shows numerous pronounced He I lines. Only a few mismatches between the model and the observation are observed (for instance, in the line cores of  $H\alpha$ , He I 5015 Å, and He I 5875 Å). The fit parameters ( $T_{\text{eff}} = 24\,642 \pm 174$  K,  $\log g = 4.732 \pm 0.025$ ,  $\log n(\text{He}) = -0.666 \pm 0.013$ ;  $1\sigma$  statistical single parameter errors) suggest that FBS 0654+366 belongs to the small group of iHe-sdBs that are located in the cooler effective temperature regime of normal H-sdBs, that is, between  $\sim 22\,000$  K and  $\sim 32\,000$  K (see Sect. 3.2 and Fig. 3.2.1). Thus, this object is very interesting.
- **HZ 1:** For the He-sdO star HZ 1, numerous He I/He II lines in the NIR can be used for the TLUSTY/SYNSPEC + FITPROF fit (see Figs. 9.1.6-9.1.10). Together with the classical helium lines in the optical, this enables an unprecedented spectral analysis for the star. Most of the analyzed lines are fitted very accurately. The most prominent mismatches are observed for He I 10 138 Å and He I 10 830 Å as well as for the forbidden components of He I 4472 Å and He I 4922 Å. The Balmer lines introduce small asymmetries to every second line of the He II Pickering series (see also Table 8.12) because of the low hydrogen content of the star ( $\log n(\text{He}) = 2.762 \pm 0.119$ ;  $1\sigma$  statistical single parameter errors). In fact, the TLUSTY/SYNSPEC models are able to predict the observed emissions for  $H\alpha$  and He II 6560 Å at the appropriate helium-to-hydrogen ratio, although the line wings of the  $H\alpha$ /He II blend cannot be reproduced with the same quality due to normalization issues (see Fig. 9.1.8). As a matter of fact, the fit of the  $H\alpha$ /He II blend for HZ 1 resembles that for the He-sdO CD-31° 4800 (Schindewolf et al. 2018; Figure 2 therein). This is not least because of the sophisticated telluric corrections with `molecfit`, thanks to which possible contamination affecting the  $H\alpha$ /He II line near the predicted  $H\alpha$  emission component (see, for instance, the spectroscopic analyses of the He-sdOs LSS 1274 and [CW83] 0904-02 performed by Schindewolf et al. 2018; Figures 2 and A.1 therein) can be avoided.

## 9.1. Spectral Line Fits

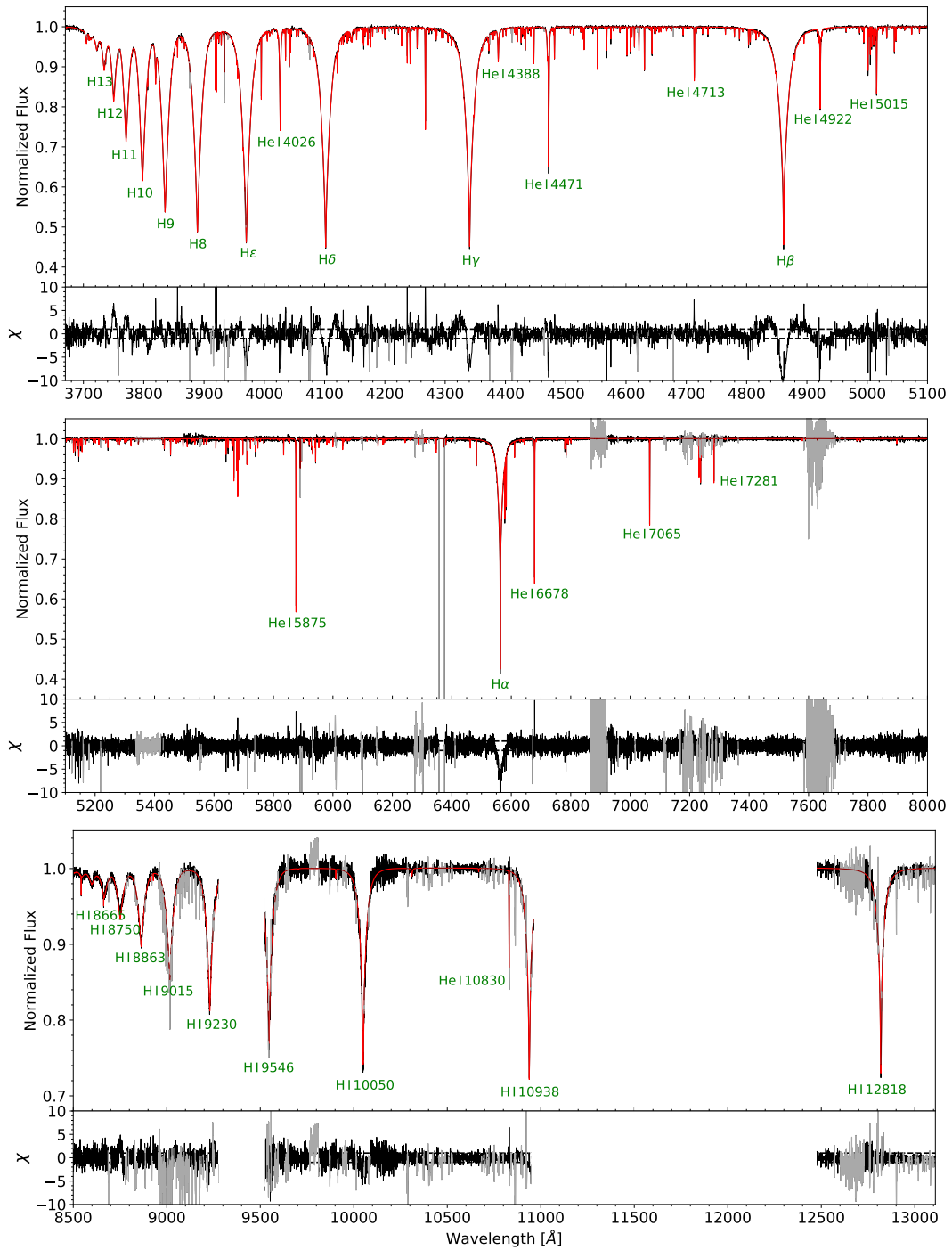


Figure 9.1.1.: Comparison of the observation (solid black line) to the global best fit (solid red line) of the co-added XSHOOTER spectrum of the H-sdB star HD 4539 for selected spectral ranges. The fit ( $T_{\text{eff}} = 23\,971 \pm 14$  K,  $\log g = 5.2971^{+0.0015}_{-0.0013}$ ,  $\log n(\text{He}) = -2.2406^{+0.0023}_{-0.0026}$ ;  $1\sigma$  statistical single parameter errors) is based on the hybrid LTE/NLTE model atmosphere approach and the global analysis strategy (ADS + Global (NLTE + LTE metals); see Sects. 6.8 and 7.1.2), whereby the mean abundances for H-sdBs/H-sdOBs according to Naslim et al. (2013) are used as metallicity. Prominent hydrogen and helium lines are marked by green labels. The residuals for each spectral range are shown in the bottom panels, whereby the dashed horizontal lines mark deviations of  $\pm 1\sigma$ , that is, values of  $\chi = \pm 1$  (corresponding to  $\sim 0.2\%$  of the flux in the UVB and to  $\sim 0.4\%$  of the flux in the VIS channel, respectively). Additional absorption lines are caused by metals. Spectral regions that are excluded from the fit are marked in gray (observation) and dark red (model), respectively. As the ranges between H I 9230 Å and H I 9546 Å as well as between H I 10938 Å and H I 12818 Å strongly suffer from telluric lines (even after the telluric correction with `moIecfit`; see Sect. 8.2.1), they are excluded from the figure.

## 9. Quantitative Spectral Analysis

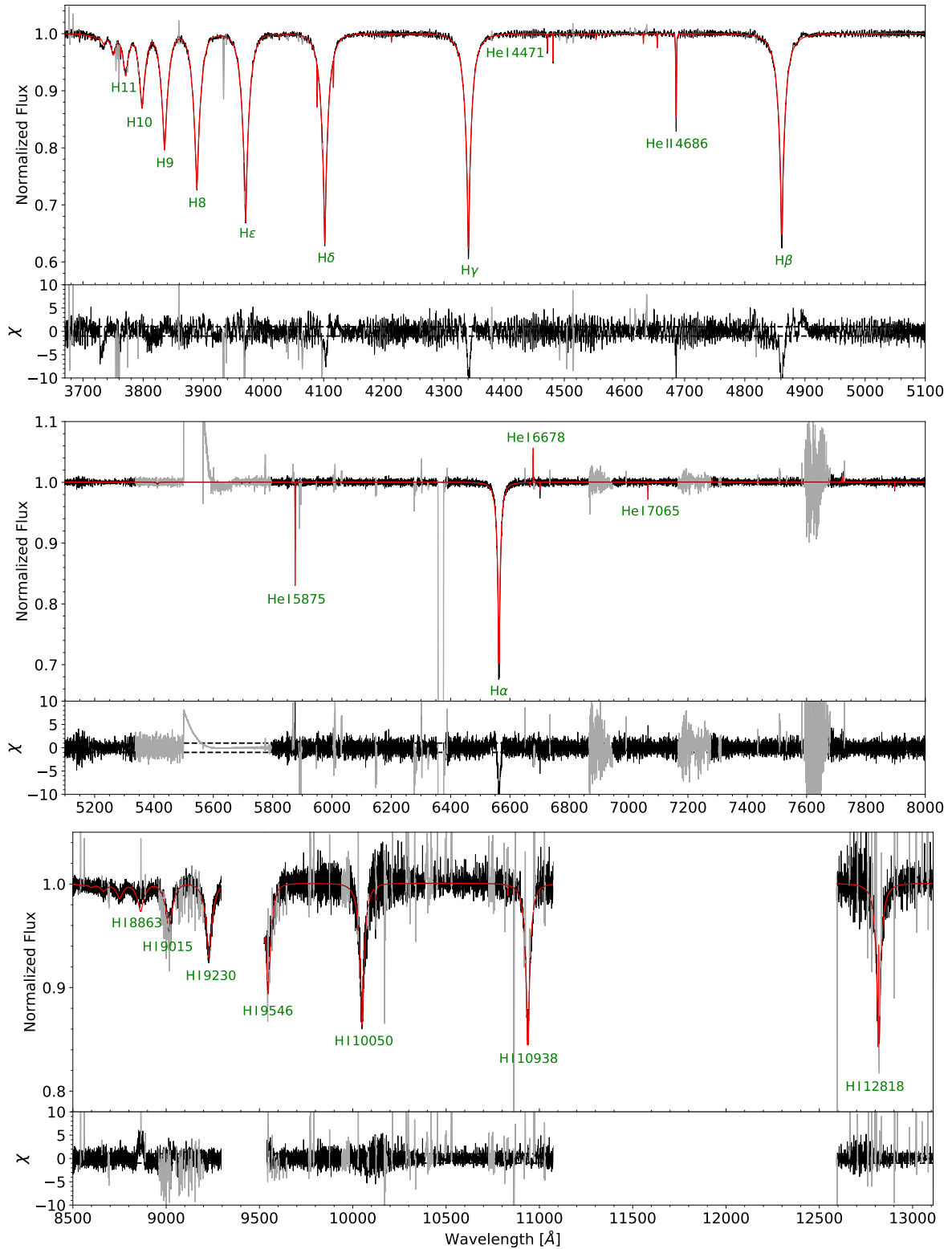


Figure 9.1.2.: Same as Fig. 9.1.1, but showing the comparison of the observation to the global best fit ( $T_{\text{eff}} = 40\,654 \pm 26$  K,  $\log g = 5.6192_{-0.0021}^{+0.0025}$ ,  $\log n(\text{He}) = -3.194_{-0.012}^{+0.011}$ ;  $1\sigma$  statistical single parameter errors) of the co-added XSHOOTER spectrum of the H-sdOB star PG 1505+074 for selected spectral ranges.

## 9.1. Spectral Line Fits

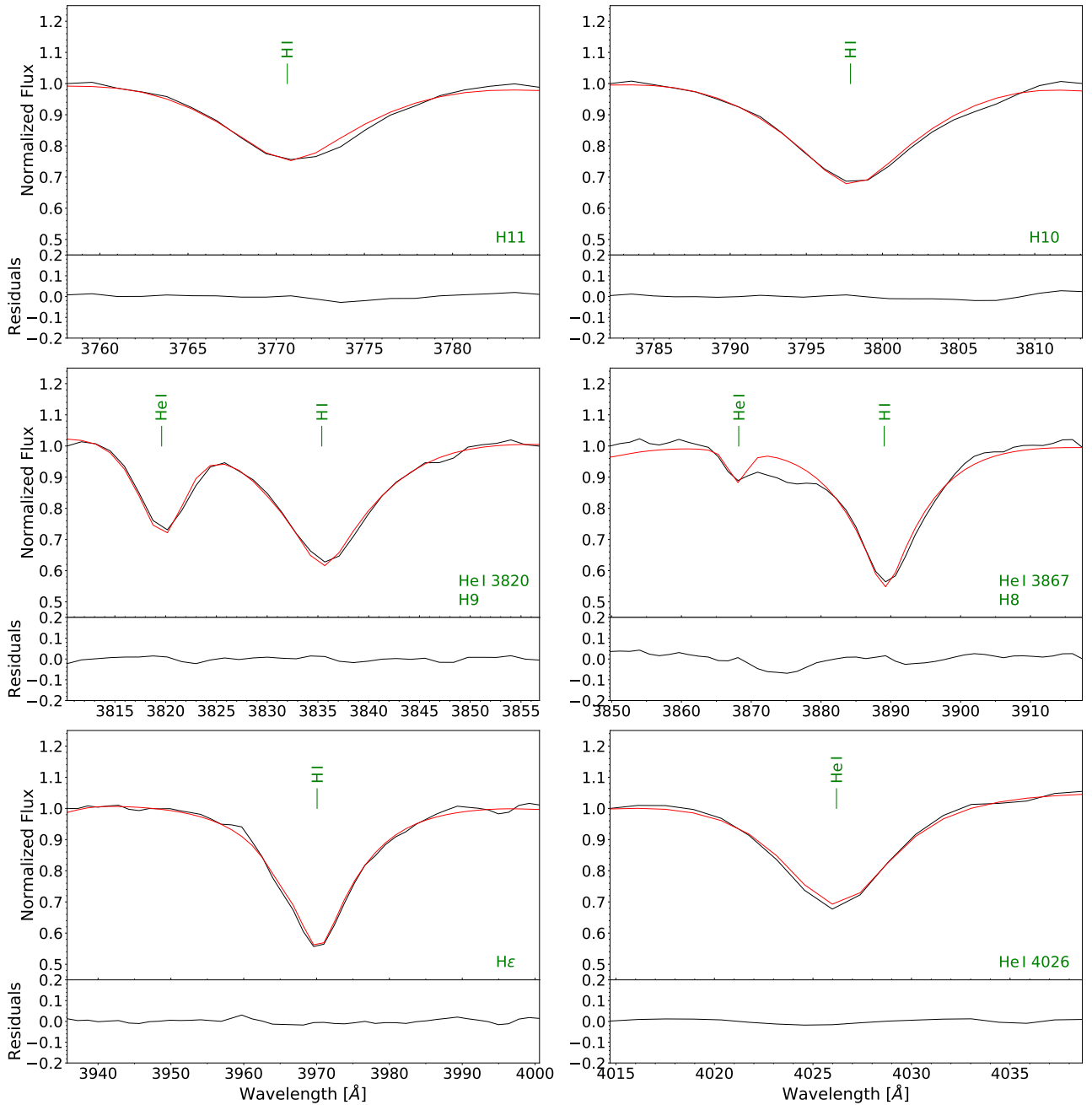


Figure 9.1.3.: Selected hydrogen and helium lines in the IDS spectrum of the iHe-sdB star FBS 0654+366. The top panel of each subpanel shows the comparison of the observed spectrum (solid black line) to the best fit (solid red line). Solid green vertical lines/labels mark the central wavelength positions and the ionization stages of the individual spectral lines. The residuals (observation - model) for each spectral range are shown in the bottom panel of each subpanel. The fit ( $T_{\text{eff}} = 24\,642 \pm 174$  K,  $\log g = 4.732 \pm 0.025$ ,  $\log n(\text{He}) = -0.666 \pm 0.013$ ;  $1\sigma$  statistical single parameter errors) is based on the hybrid LTE/NLTE model atmosphere approach and the selective analysis strategy with FITPROF (ADS + FITPROF; see Sects. 6.8 and 7.1.2). No metals are synthesized but the model atmosphere is based on the mean metallicity of H-sdBs/H-sdOBs according to Naslim et al. (2013).

## 9. Quantitative Spectral Analysis

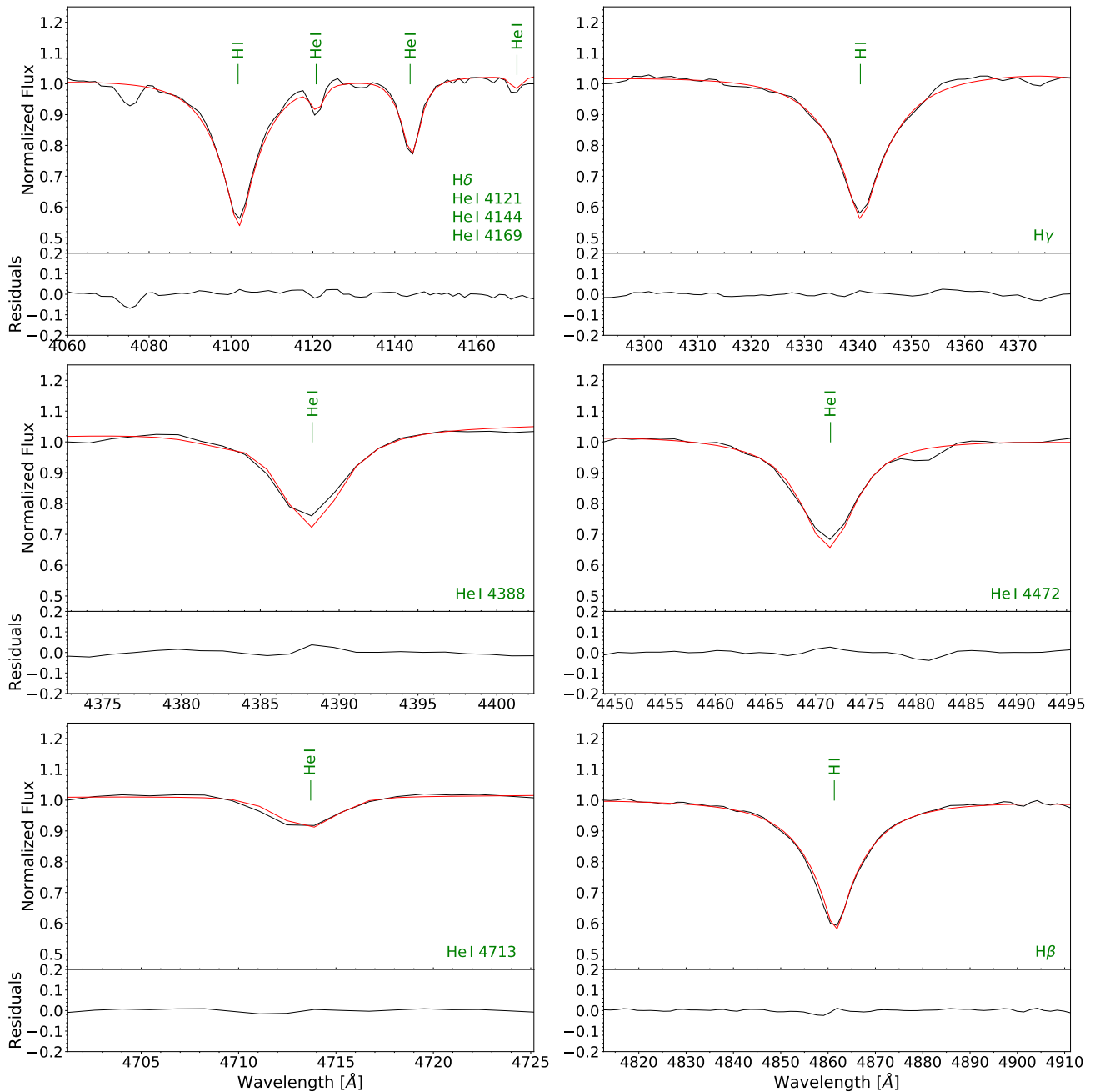


Figure 9.1.4.: Same as Fig. 9.1.3, but showing additional hydrogen and helium lines in the IDS spectrum of the iHe-sdB star FBS 0654+366.

## 9.1. Spectral Line Fits

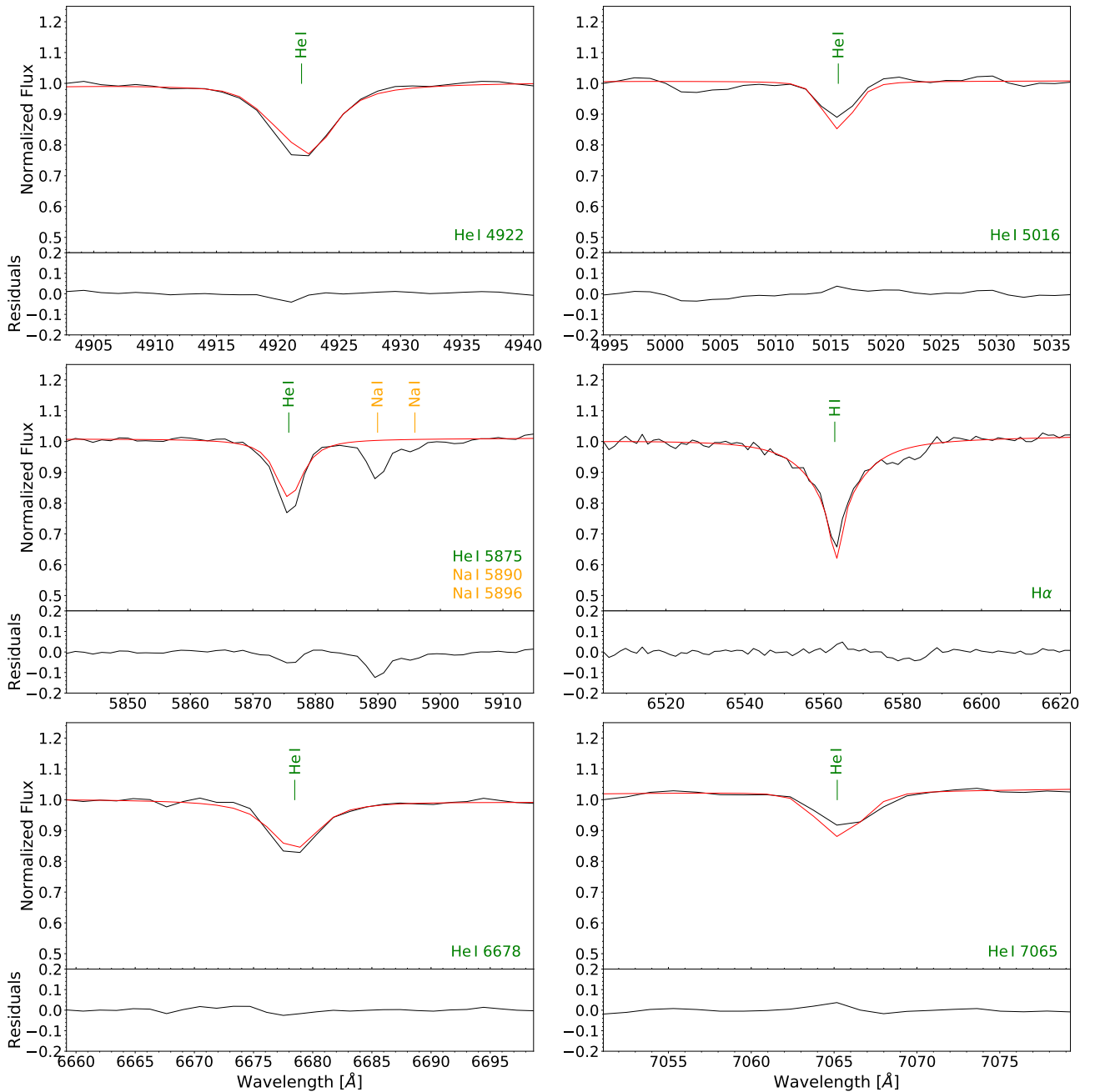


Figure 9.1.5.: Same as Fig. 9.1.3, but showing additional hydrogen and helium lines in the IDS spectrum of the iHe-sdB star FBS 0654+366. The spectrum shows pronounced Na I interstellar lines at  $\lambda 5890 \text{ \AA}$  and  $\lambda 5896 \text{ \AA}$ , respectively (solid orange vertical line markers).

## 9. Quantitative Spectral Analysis

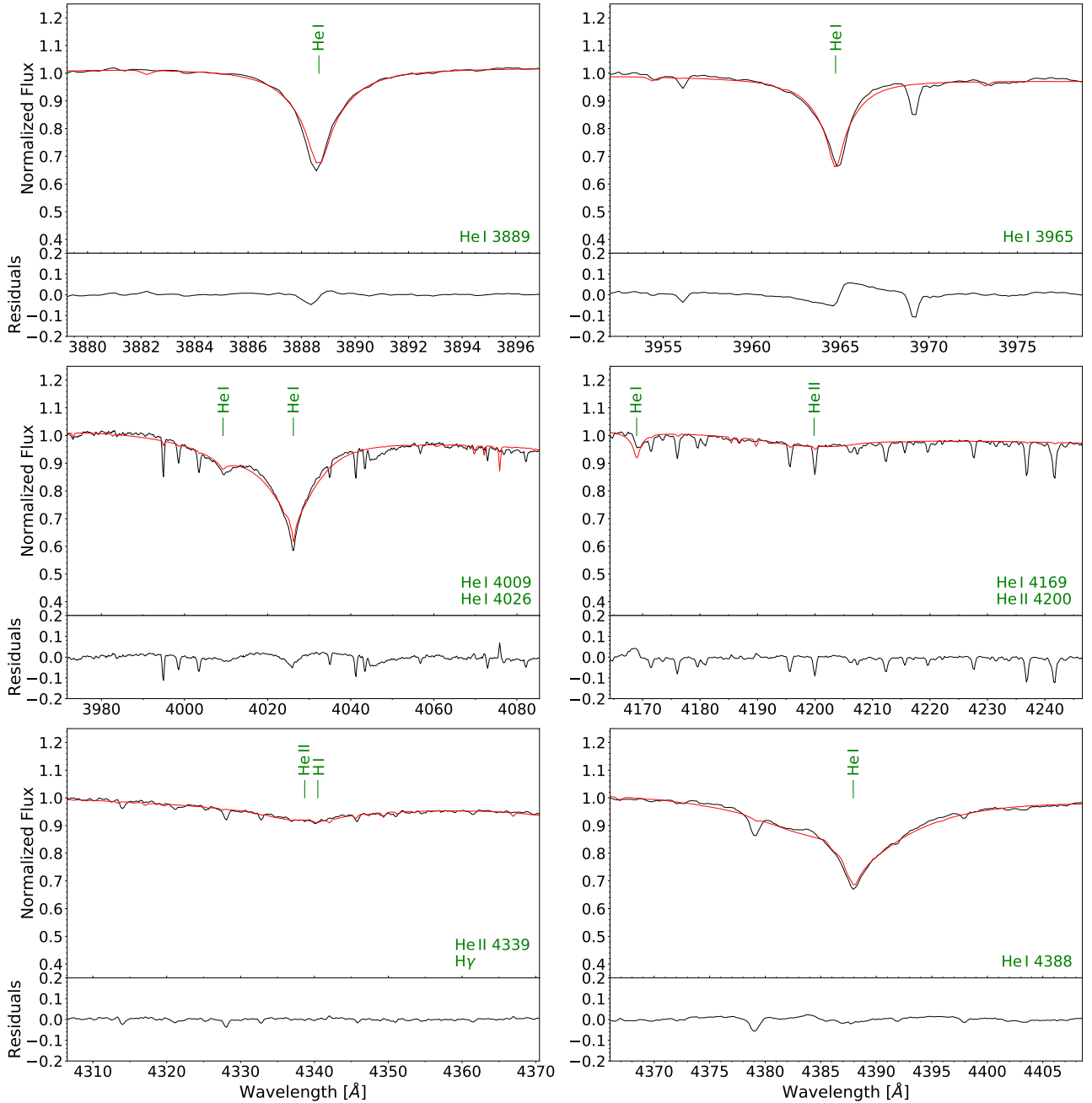


Figure 9.1.6.: Selected helium lines as well as the H $\gamma$ /He II blend in the co-added XSHOOTER spectrum of the He-sdO star HZ 1. The top panel of each subpanel shows the comparison of the observed spectrum (solid black line) to the best fit (solid red line). Solid green vertical lines/labels mark the central wavelength positions and the ionization stages of the individual spectral lines. The residuals (observation - model) for each spectral range are shown in the bottom panel of each subpanel. The fit ( $T_{\text{eff}} = 40\,598 \pm 53$  K,  $\log g = 5.699 \pm 0.024$ ,  $\log n(\text{He}) = 2.762 \pm 0.119$ ;  $1\sigma$  statistical single parameter errors) is based on TLUSTY/SYNSPEC and the selective analysis strategy with FITPROF (TLUSTY/SYNSPEC + FITPROF; see Sects. 6.9 and 7.1.2). The model atmosphere and the synthetic spectrum are based on the mean metal abundances for carbon, oxygen, and nitrogen, as observed for H-sdBs/H-sdOBs (Naslim et al., 2013).

## 9.1. Spectral Line Fits

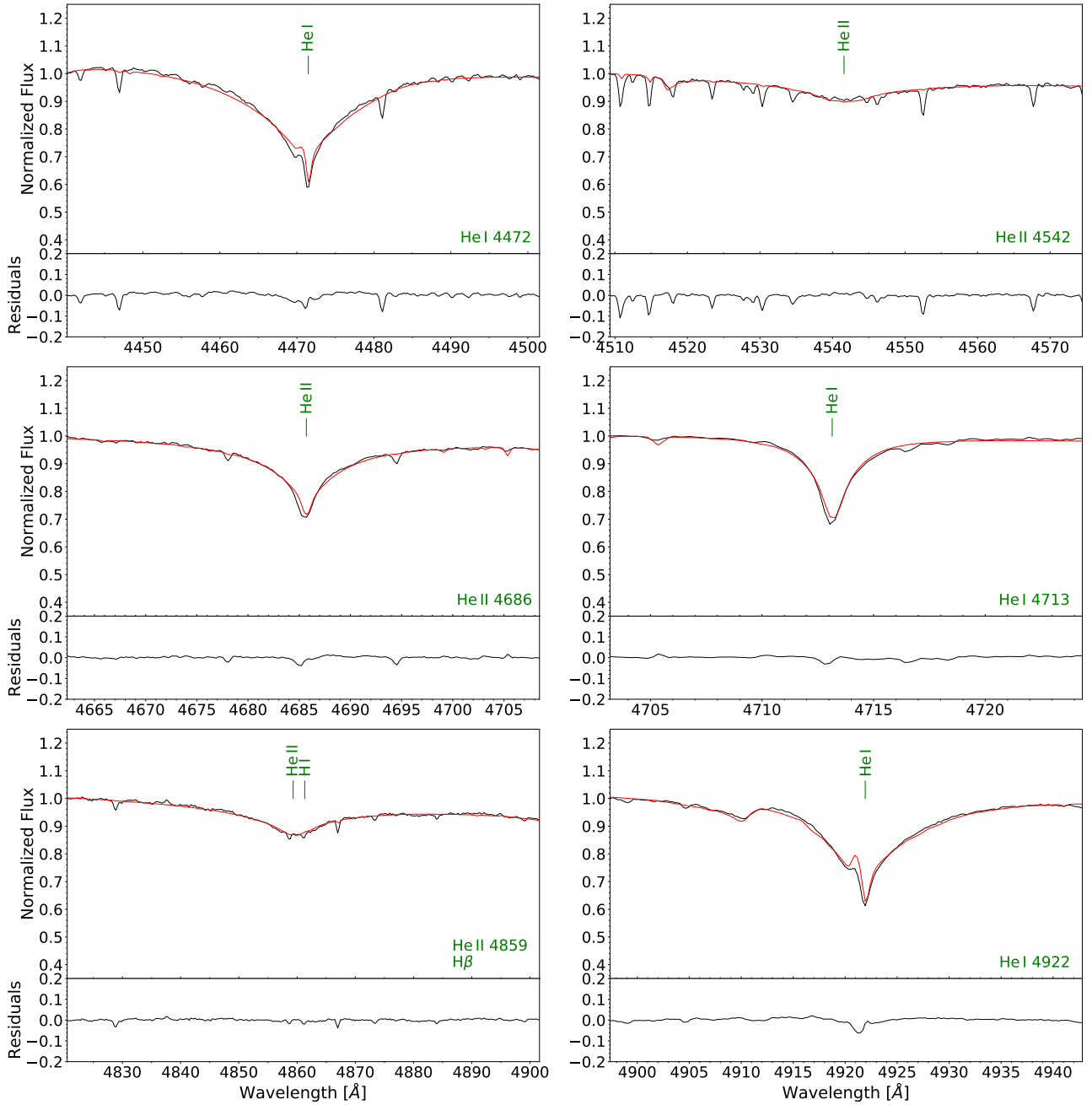


Figure 9.1.7.: Same as Fig. 9.1.6, but showing additional helium lines as well as the H $\beta$ /He II blend in the co-added XSHOOTER spectrum of the He-sdO star HZ 1.

## 9. Quantitative Spectral Analysis

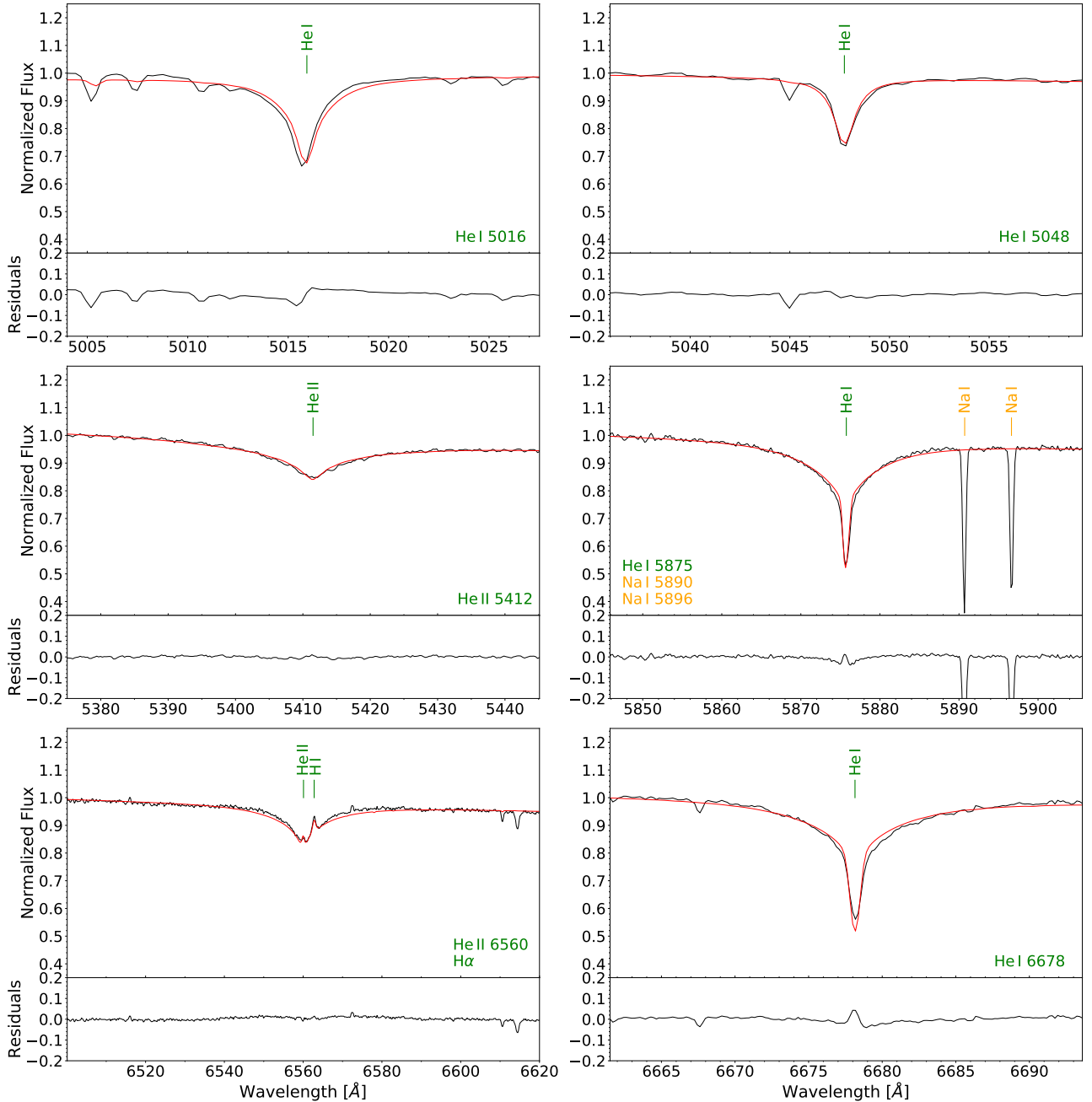


Figure 9.1.8.: Same as Fig. 9.1.6, but showing additional helium lines as well as the H $\alpha$ /He II blend in the co-added XSHOOTER spectrum of the He-sdO star HZ 1. The spectrum shows pronounced Na I interstellar lines at  $\lambda 5890 \text{ \AA}$  and  $\lambda 5896 \text{ \AA}$ , respectively (solid orange vertical line markers).

## 9.1. Spectral Line Fits

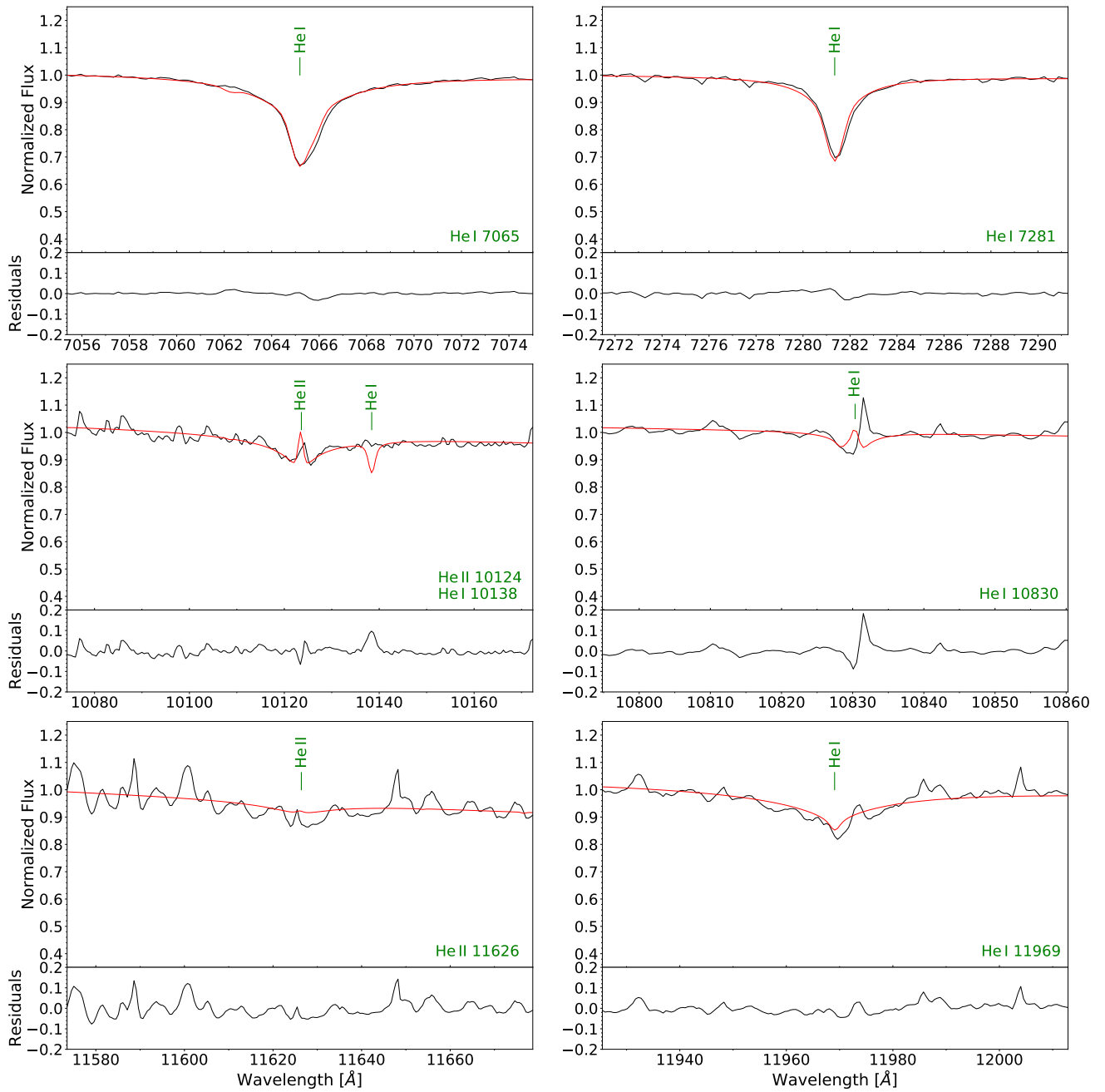


Figure 9.1.9.: Same as Fig. 9.1.6, but showing additional helium lines in the NIR of the co-added XSHOOTER spectrum of the He-sdO star HZ 1.

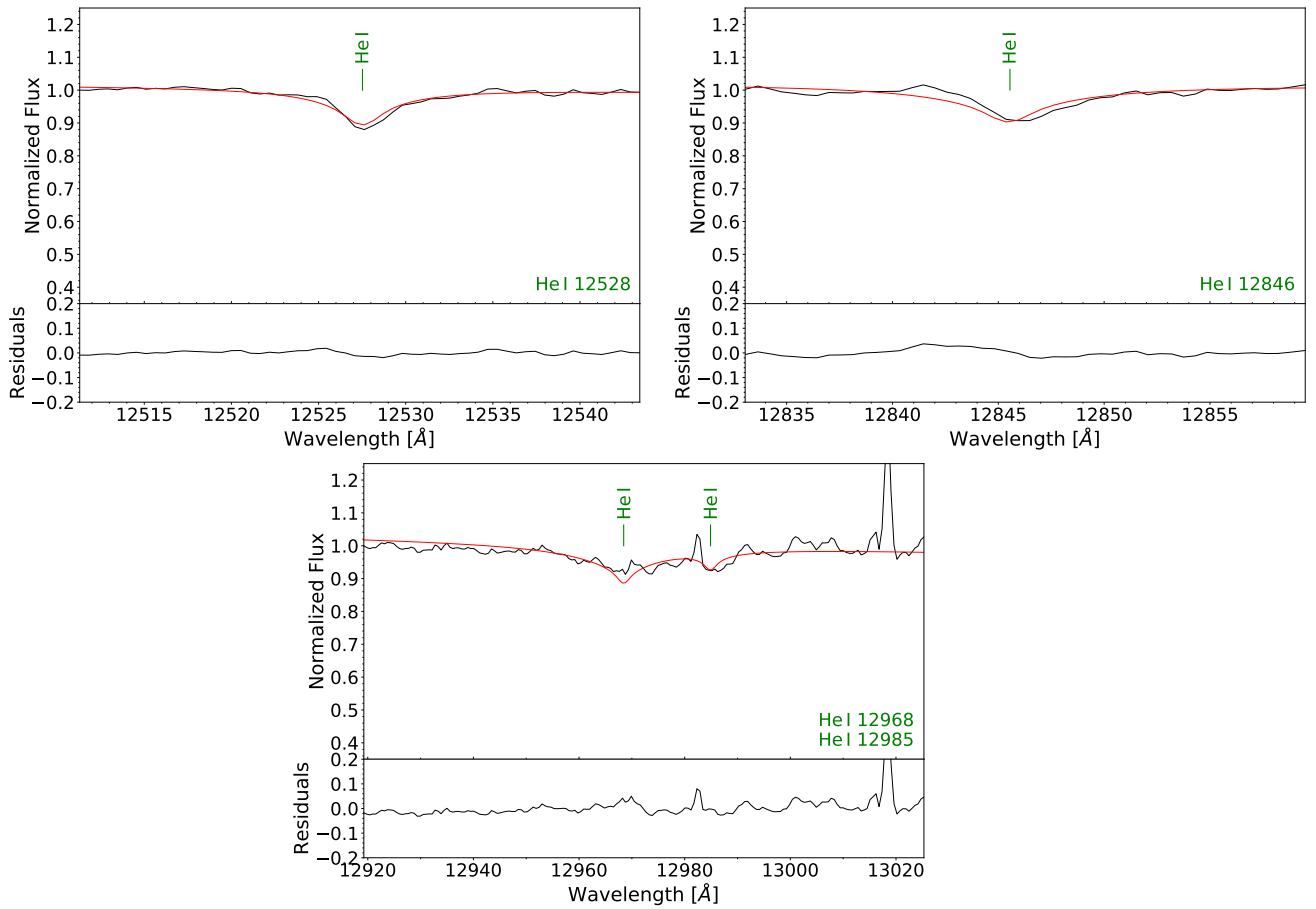


Figure 9.1.10.: Same as Fig. 9.1.6, but showing additional helium lines in the NIR of the co-added XSHOOTER spectrum of the He-sdO star HZ 1.

## 9.2. Detailed Comparison of Different Model Atmosphere Approaches and Analysis Strategies

In terms of the atmospheric parameters derived, this section shall compare the different model atmosphere approaches (LTE vs. hybrid LTE/NLTE with and without fitted metals vs. NLTE) and spectroscopic analysis techniques (global vs. selective) mentioned at the beginning of this chapter. This comparative analysis will provide deep insights into the global systematic uncertainties of the three quantities  $T_{\text{eff}}$ ,  $\log(g)$ , and  $\log n(\text{He}) := \log n(^4\text{He} + ^3\text{He})$ . Particularly, the global systematics need to be known for  $T_{\text{eff}}$  and  $\log(g)$  in order to derive meaningful radii, luminosities, and masses for the individual program stars. As discussed in Sect. 7.3, the global systematic uncertainty on  $\log(g)$  is of special interest for the program stars of this work because it affects the resulting mass ranges the most.

As presented in Sect. 8.1, the spectroscopic data analyzed in this work are very inhomogeneous. This applies to the S/N, to the resolution (low, medium, high) as well as to the wavelength coverage of the spectra used. For the following comparisons, I refrain from tailoring the individual spectra to a uniform spectral range that is covered by all of them. Admittedly, this comes at the expense of comparability of the results obtained, meaning that the statistics for the derived atmospheric parameters will obviously be better for spectra with larger wavelength coverage (particularly, this applies to the stars of the XSHOOTER reference sample) because in these cases more data (in particular, more hydrogen and helium lines) can be investigated. Moreover, the sole influence of the different spectral resolutions on the atmospheric parameters derived cannot be investigated in this way. On the other hand, however, the uniform approach would also have severe disadvantages for this work's target sample. First, the different spectra used in this work exhibit gaps at different wavelength regimes (for instance, the HIRES spectrum of Feige 36 does not cover the important He I 5875 Å line). Second, several spectra such as the analyzed UVES ones of HE 0929-0424 and HE 1047-0436 only range until H $\alpha$  such that another important line (He I 6678 Å) is not covered. These are only a few examples. Using the overlap of all spectra as a uniform wavelength range therefore would result in the fact that none of these lines can be analyzed in any of the spectra available. Unfortunately, omitting those stars for the comparative analysis, for which certain lines are not covered by the individual spectra, is also not an option since with 66 program stars only, the size of the entire sample is not that large anyway (see Ch. 8). Furthermore, the aim should be to get the best out of the data available. Consequently, the following approach is applied: If possible, all hydrogen and helium lines available in the full wavelength range of the spectrum in question are analyzed in order to derive  $T_{\text{eff}}$ ,  $\log(g)$ , and  $\log n(\text{He})$  for the respective program star, regardless of which analysis strategy is used.

Tables A.1-A.18 of appendix A summarize the overall results of the comparative analysis. Therein,  $1\sigma$  statistical single parameter errors are given for  $T_{\text{eff}}$ ,  $\log(g)$ , and  $\log n(\text{He})$  (in the case of SPAS, they are bootstrapped; see Sect. 7.1.2). The number of program stars that are observed with multiple instruments is rather low. This subsample only includes the following six stars: the H-sdBs HD 4539, Feige 38, and EC 03591-3232, the H-sdOB HD 149382, the iHe-sdB [CW83] 0512-08, and the He-sdO PG 0314+146. For these objects, weighted aver-

ages for the individual atmospheric parameters are calculated. This is done for all combinations of model atmosphere approaches and analysis strategies used (see Tables A.20-A.23). In order to calculate the weighted averages, the reciprocals of the individual maximum variances, that is  $\frac{1}{(\max[\text{uncertainty}])^2}$ , are used as weights.

The results of the comparative analysis for the hot subdwarf program sample<sup>110</sup> are visualized in the  $T_{\text{eff}}$  vs.  $T_{\text{eff}}$ ,  $\log(g)$  vs.  $\log(g)$ , and  $\log n(\text{He})$  vs.  $\log n(\text{He})$  planes of Figs. 9.2.1-9.2.12. The objects that are observed multiple times are marked with different symbols in these figures: pentagons (PG 0314+146), asterisks (HD 149382), crosses ([CW83] 0512-08), triangles (Feige 38), squares (EC 03591-3232), and diamonds (HD 4539).

The following subsections present different aspects of the detailed comparisons.

### 9.2.1. SPAS vs. FITPROF

Comparing the overall results for the atmospheric parameters based on the selective analysis strategy with SPAS to those of the global one determined with ISIS, the significantly larger statistical uncertainties in the case of SPAS become obvious. The same is true if the results of SPAS are compared to the ones of the other selective approach used (FITPROF), however to a lesser extent. Figures 9.2.13-9.2.15 show part of the comparisons of the maximum  $1\sigma$  statistical uncertainties on  $T_{\text{eff}}$ ,  $\log(g)$ , and  $\log n(\text{He})$  determined for the hot subdwarf program stars of this work. Therein, the following combinations of model atmosphere approaches and analysis strategies are compared: ADS + SPAS vs. ADS + Global, ADS + FITPROF vs. ADS + Global, LTE + SPAS vs. ADS + Global, and LTE + FITPROF vs. ADS + Global (in all cases, no metals are fitted with the ADS models). As described in Sect. 7.1.2, the uncertainties of SPAS result from bootstrapping, whereas the ones of FITPROF and ISIS are derived from  $\chi^2$ -statistics. This is the crucial factor as it is clearly visible from Figs. 9.2.13-9.2.15 that the FITPROF errors are in much better agreement with the ISIS ones. Yet, small differences in the error sizes can still be observed in this case.

The detailed comparisons indicate that the error determination in SPAS via the bootstrapping method is unreliable. It is absolutely not clear whether the given bootstrapped errors are indeed  $1\sigma$  or something else. This together with the fact that the FITPROF uncertainties are of somewhat similar size than the ISIS ones is the reason why the SPAS results are discarded and will not be considered anymore in the further course of this thesis. Instead, the focus will be on FITPROF and the global analysis approach.

### 9.2.2. LTE vs. Hybrid LTE/NLTE

As mentioned in Sect. 6.7, the LTE models used in this work have been successfully applied to several hundreds of hot subdwarf stars within a time period of more than 20 years. However,

<sup>110</sup>The five H-sdO/post-AGB program stars listed in Table 8.11 are not considered here because no spectroscopic data are analyzed for these objects within the framework of this thesis (see the corresponding footnote at the beginning of Ch. 9).

## 9.2. Detailed Comparison of Different Model Atmosphere Approaches and Analysis Strategies

more and more of these stars are nowadays analyzed with ADS models in hybrid LTE/NLTE and/or with TLUSTY/SYNSPEC models in NLTE. Hence, it is interesting to see how the “old” LTE models perform against the “new” ADS and TLUSTY/SYNSPEC models. For a meaningful sample of program stars, such a detailed comparison study in terms of atmospheric parameters derived is still missing. This shall be made up for at this point. First, a comparison of the results derived from the LTE and the ADS models (without synthesized metals) shall be given. Later (in Sect. 9.2.4), the LTE results will also be compared to the NLTE ones determined with the TLUSTY/SYNSPEC models.

The differences for  $T_{\text{eff}}$ ,  $\log(g)$ , and  $\log n(\text{He})$  derived from the LTE and the ADS models are most likely to show up if both model atmosphere approaches are combined with the same analysis strategy. In this work, this has to be FITPROF because the LTE models are only used in combination with the selective approach (in fact, this is also the case for the numerous LTE results from literature) and the SPAS results have to be discarded because of the unreliable bootstrapped errors. The upper left-hand panels of Figs. 9.2.1, 9.2.5, and 9.2.9 show the relevant comparisons for the hot subdwarf program stars of this work. The optimum effective temperature regime for the LTE models is between  $\sim 25\,000\text{ K}$  and  $\sim 32\,000\text{ K}$  (see the upper left-hand panel of Fig. 9.2.1). For lower and in particular higher temperatures, NLTE effects prevail. Interestingly, the ADS models result, on average, in higher surface gravities compared to LTE ( $\gtrsim 0.10$  dex at  $\log g \sim 5.00$  and  $\lesssim 0.05$  dex at  $\log g \sim 6.00$ ; see the upper left-hand panel of Fig. 9.2.5). At the same time, the helium abundances derived from the ADS models are somehow lower than the ones derived from LTE, at least for the majority of the program stars. Although this observation is significantly more difficult to quantify (see the upper left-hand panel of Fig. 9.2.9), it is in good agreement with the measured surface gravities for both models because it is known that  $\log(g)$  and  $\log n(\text{He})$  somehow anti-correlate: If  $\log(g)$  is higher, less helium is necessary to match the observed helium line profiles (in particular, the line wings) and vice versa. The upper left-hand panels of Figs. 9.2.16, 9.2.17, and 9.2.18 reveal the star-by-star changes of the atmospheric parameters derived from the ADS and the LTE models in the  $T_{\text{eff}}\text{-}\log(g)$ ,  $T_{\text{eff}}\text{-}\log n(\text{He})$ , and  $\log(g)\text{-}\log n(\text{He})$  planes, respectively. These diagrams overall confirm the results discussed.

In the upper left-hand panels of Figs. 9.2.1, 9.2.5, and 9.2.9, the data points are also fitted with polynomial functions. This results in the following regression curves ( $x$  denotes  $T_{\text{eff}}$  [1000 K] /  $\log(g)$  /  $\log n(\text{He})$  determined with LTE + FITPROF;  $f(x)$  denotes  $T_{\text{eff}}$  [1000 K] /  $\log(g)$  /  $\log n(\text{He})$  determined with ADS + FITPROF):

$$f(x) = 0.008 \cdot x^2 + 0.549 \cdot x + 6.694 \quad \text{for } T_{\text{eff}} [1000\text{ K}] \quad (9.1)$$

$$f(x) = 0.924 \cdot x + 0.508 \quad \text{for } \log(g) \quad (9.2)$$

$$f(x) = 0.956 \cdot x - 0.116 \quad \text{for } \log n(\text{He}) . \quad (9.3)$$

The uncertainties on the individual regression coefficients are given in the captions of Figs. 9.2.1, 9.2.5, and 9.2.9, respectively. Equations (9.1-9.3) describe how the atmospheric parameters derived from the “old” LTE models transfer into the “new” ones based on ADS. In principle, this allows to convert the published LTE result for any hot subdwarf star in the covered  $T_{\text{eff}}$ ,  $\log(g)$ , and  $\log n(\text{He})$  regimes into a corresponding result based on ADS, whereby

the actual ADS analysis does not have to be performed anymore. This saves plenty of hours of work time. However, performing this conversion for the several hundreds of hot subdwarfs, for which LTE results can be found in literature, is not one of the goals of this work. Nonetheless, future studies dedicated to this task surely will follow.

### 9.2.3. Global vs. Selective

Another important aspect to investigate is the influence of the analysis method on the atmospheric parameters derived. In order to properly compare the global analysis strategy (ISIS) to the selective one with FITPOF, the same model atmosphere approach should be considered. In this work, the hybrid LTE/NLTE ADS models are used for this comparison because these models are the only ones that are combined with the global analysis strategy. In the following, only ADS models without synthesized metals are considered.

The middle left-hand panels of Figs. 9.2.1, 9.2.5, and 9.2.9 show the relevant  $T_{\text{eff}}$  vs.  $T_{\text{eff}}$ ,  $\log(g)$  vs.  $\log(g)$ , and  $\log n(\text{He})$  vs.  $\log n(\text{He})$  comparison plots. As can be seen, the ADS models yield consistent results for the atmospheric parameters, regardless of whether the selective or the global approach is used. No trend is seen in none of the panels and the scattering of the data points around the bisectors is rather low for all three parameters. This is also recorded in the upper right-hand panels of Figs. 9.2.16, 9.2.17, and 9.2.18, which show the corresponding star-by-star changes of the atmospheric parameters in the  $T_{\text{eff}}\text{-}\log(g)$ ,  $T_{\text{eff}}\text{-}\log n(\text{He})$ , and  $\log(g)\text{-}\log n(\text{He})$  planes, respectively.

The lower panels of Figs. 9.2.19, 9.2.20, and 9.2.21 display histogram distributions of the deviations of  $T_{\text{eff}}$ ,  $\log(g)$ , and  $\log n(\text{He})$  based on the middle left-hand panels of Figs. 9.2.1, 9.2.5, and 9.2.9. In the case of  $T_{\text{eff}}$ , percentage deviations are determined in order to derive the relevant histogram. For all three histogram distributions, a Gaussian function is fitted to the data (represented by the solid red line in the respective panel). The resulting fit parameters (the mean values  $\mu$  and the standard deviations  $\sigma$ ) are summarized in Table 9.1. In all cases,  $\mu$  and  $\sigma$  are well defined as the corresponding standard errors are small. The Gaussian fits show that the individual histograms are barely shifted with respect to zero and that the variance is smallest for  $\log(g)$ .

Histogram Distribution for	$\mu$	$\sigma$
$T_{\text{eff}}$ (percentage)	$-0.320 \pm 0.066$	$0.869 \pm 0.066$
$\log(g)$	$-0.001 \pm 0.001$	$0.043 \pm 0.002$
$\log n(\text{He})$	$-0.003 \pm 0.004$	$0.059 \pm 0.004$

Table 9.1.: Mean values  $\mu$  and standard deviations  $\sigma$  of the Gaussian functions fitted to the histogram data shown in the lower panels of Figs. 9.2.19, 9.2.20, and 9.2.21.

### 9.2.4. LTE vs. NLTE

In this section, the comparison between the “old” LTE models and the NLTE ones calculated with TLUSTY/SYNSPEC shall be discussed in terms of the atmospheric parameters derived. In order to do so, the same analysis approach needs to be considered. As in Sect. 9.2.2, this will be FITPROF. Due to the fact that the NLTE model grid used in this work covers program stars with  $T_{\text{eff}} \gtrsim 30\,000$  K only (see Table 6.4) and since the He-sdOs that are known to show large departures from LTE are not analyzed in LTE, the sample size for the LTE vs. NLTE comparison is significantly smaller compared to that of the previous sections.

The middle right-hand panel of Fig. 9.2.3 shows the relevant  $T_{\text{eff}}$  vs.  $T_{\text{eff}}$  comparison plot for the analyzed program stars. It is striking that there is a small systematic trend observed towards higher effective temperatures. While the results derived from both models seem to match at  $T_{\text{eff}} \sim 30\,000$  K, the NLTE models calculated with TLUSTY/SYNSPEC yield significantly higher effective temperature values (up to  $\sim 1700$  K) for the hotter stars. Apart from NLTE effects, this trend can mainly be explained by the backwarming effect, which has been discussed in the context of metal line-blanketing (see Sect. 6.6). At the hydrogen and helium line-forming regions, the less metal line-blanketed NLTE model atmospheres (only carbon, nitrogen, and oxygen based on the mean metal abundances for H-sdB/H-sdOB stars according to Naslim et al. 2013 are implemented as metallicity; see Sect. 6.9) are cooler than the fully line-blanketed LTE models, which are even based on supersolar metallicity at  $T_{\text{eff}} \gtrsim 30\,000$  K (see Sect. 6.7). Compensating for this temperature difference leads to higher  $T_{\text{eff}}$  values derived from the NLTE models.

In contrast to  $T_{\text{eff}}$ , no clear trends are observed for  $\log(g)$  and  $\log n(\text{He})$ , respectively (see the middle right-hand panels of Figs. 9.2.7 and 9.2.11). Yet, the results for  $\log(g)$  and  $\log n(\text{He})$  derived from the LTE and the NLTE models differ significantly for some of the program stars.

### 9.2.5. Hybrid LTE/NLTE vs. NLTE

The comparison between the hybrid LTE/NLTE models calculated in ADS (without synthesized metals) and the NLTE models calculated with TLUSTY/SYNSPEC is also best conducted if the same analysis approach (FITPROF) is considered. Again, it has to be mentioned that the sample size is rather small for this comparison because of the effective temperature coverage of the NLTE model grid (see Table 6.4) and since the He-sdOs that are known to show large departures from LTE are not analyzed in hybrid LTE/NLTE.

The upper right-hand panel of Fig. 9.2.1 shows the relevant  $T_{\text{eff}}$  vs.  $T_{\text{eff}}$  comparison plot. As in the case of LTE vs. NLTE, the consequences of the backwarming effect (and possible NLTE effects) become evident. On average, the NLTE models result in higher effective temperatures (up to  $\sim 2000$  K) compared to the hybrid models. The latter also use the mean metal abundances for H-sdB/H-sdOB stars (Naslim et al., 2013) as metallicity. However, not only carbon, nitrogen, and oxygen are implemented therein, as is the case for the NLTE models. Also other metals such as iron and nickel, which are known to have a strong impact on the atmospheric temperature-density stratification, are incorporated (see Fig. 3.3.2 and Table 3.1).

Interestingly, the  $\log(g)$  vs.  $\log(g)$  comparison plot reveals that, on average, the hybrid models also result in higher surface gravities compared to the NLTE models ( $\lesssim 0.08$  dex at  $\log g \sim 5.50$  and  $\lesssim 0.15$  dex at  $\log g \sim 5.80$ ; see the upper right-hand panel of Fig. 9.2.5). However, the helium abundances derived from both model atmosphere approaches are rather similar, at least for stars with  $\log n(\text{He}) \lesssim -1.70$  (see the upper right-hand panel of Fig. 9.2.9). This is why the anti-correlation between  $\log(g)$  and  $\log n(\text{He})$  cannot serve as the sole explanation in this case. Hence, either NLTE effects significantly affect the temperature-density stratification (although this should not be the case due to the high surface gravities of the analyzed stars, which is also why the hybrid approach should be appropriate; see the discussion in Sect. 6.8) or metal line-blanketing is responsible. The latter seems to be more realistic because the surface gravity difference somehow seems to vanish if the NLTE results are compared to the LTE ones, which are derived from models with even higher metallicity (see the results of the previous section as well as the middle right-hand panel of Fig. 9.2.7). Nevertheless, it remains an open question why a higher metallicity does not increase the observed difference, but instead reduces it.

The analyzed program stars with  $\log n(\text{He}) \gtrsim -1.70$  seem to be slightly shifted towards higher helium abundances in the case of the NLTE models (see the upper right-hand panel of Fig. 9.2.9). This potential trend definitely needs to be confirmed by a larger sample. For the relevant stars, however, the higher helium abundances in the case of the NLTE models explain why the hybrid models result in higher surface gravities.

### 9.2.6. Influence of Metals in Spectral Synthesis

As explained in Sect. 7.1.1, the effective temperature (and the surface gravity) of a star can be derived from the ionization equilibrium of spectral lines associated with two or more ionization stages of the same chemical element. The influence of metals on the atmospheric parameters derived hence is an important source of systematics that needs to be investigated. This section shall shed light on this aspect. In this work, metal lines are only investigated for medium and high-resolution spectra making use of the ADS models and the global analysis approach with ISIS. In consequence, the following discussions refer to the results of ADS + Global (with metals), meaning that metal lines are added in the spectral synthesis, versus ADS + Global (without metals), meaning that metal lines are neglected in the spectral synthesis.

The middle left-hand panels of Figs. 9.2.2, 9.2.6, and 9.2.10 show the relevant  $T_{\text{eff}}$  vs.  $T_{\text{eff}}$ ,  $\log(g)$  vs.  $\log(g)$ , and  $\log n(\text{He})$  vs.  $\log n(\text{He})$  comparison plots, whereby in these cases NLTE and LTE metals are considered for the program stars of the XSHOOTER reference sample whereas for all other objects only NLTE metals are analyzed (see the introduction of Ch. 9 for further information on which elements are treated in NLTE and which are treated in LTE). On the other hand, the middle right-hand panels of Figs. 9.2.2, 9.2.6, and 9.2.10 display the results for which only NLTE metals are investigated in all cases. As can be seen, the analyzed LTE metals have no additional significant impact on the atmospheric parameters derived for the XSHOOTER program stars, if the NLTE metals are already implemented in the models. Generally, the scattering of the data points around the respective bisectors is rather

## 9.2. Detailed Comparison of Different Model Atmosphere Approaches and Analysis Strategies

Histogram Distribution for	$\mu$	$\sigma$	Comments
$T_{\text{eff}}$ (percentage)	$-0.308 \pm 0.073$	$0.550 \pm 0.073$	NLTE + LTE metals for XSHOOTER stars, otherwise NLTE metals only
$\log(g)$	$-0.003 \pm 0.001$	$0.035 \pm 0.001$	NLTE + LTE metals for XSHOOTER stars, otherwise NLTE metals only
$\log n(\text{He})$	$-0.009 \pm 0.002$	$0.047 \pm 0.002$	NLTE + LTE metals for XSHOOTER stars, otherwise NLTE metals only
$T_{\text{eff}}$ (percentage)	$-0.100 \pm 0.050$	$0.677 \pm 0.050$	NLTE metals only
$\log(g)$	$0.001 \pm 0.001$	$0.035 \pm 0.001$	NLTE metals only
$\log n(\text{He})$	$0.002 \pm 0.004$	$0.040 \pm 0.004$	NLTE metals only

Table 9.2.: Mean values  $\mu$  and standard deviations  $\sigma$  of the Gaussian functions fitted to the histogram data shown in the upper panels of Figs. 9.2.19, 9.2.20, and 9.2.21.

low. This means that the ionization equilibria for the investigated metals only marginally affect the effective temperatures, the surface gravities, and the helium abundances. All three parameters are already well defined by the numerous hydrogen and helium lines available in the spectra. The lower panels of Figs. 9.2.16, 9.2.17, and 9.2.18 overall confirm these results. Thus, it can safely be assumed that the previous results of the LTE vs. hybrid LTE/NLTE (Sect. 9.2.2), the LTE vs. NLTE (Sect. 9.2.4), and the hybrid LTE/NLTE vs. NLTE (Sect. 9.2.5) comparisons do not change significantly, if metals are added to the respective models. The upper panels of Figs. 9.2.19, 9.2.20, and 9.2.21 display histogram distributions of the deviations of  $T_{\text{eff}}$  (percentage),  $\log(g)$ , and  $\log n(\text{He})$  based on the middle panels of Figs. 9.2.2, 9.2.6, and 9.2.10. Again, a Gaussian function is fitted to the individual histogram data. The results of these fits are summarized in Table 9.2. Interestingly,  $\log(g)$  is least affected by the added metals because the Gaussians fitted to the corresponding distributions have the lowest standard deviations  $\sigma$ .

### 9.2.7. Total Uncertainties of the Atmospheric Parameters

Due to the fact that most of the analyzed program stars lie in the effective temperature regime of  $20\,000\text{ K} \lesssim T_{\text{eff}} \lesssim 40\,000\text{ K}$ , well covered by the hybrid LTE/NLTE models calculated in ADS, the results derived from these models are used in order to estimate the systematic uncertainties of the atmospheric parameters. For this, the results of the comparison between the global and the selective approach (Sect. 9.2.3) are considered. On the other hand, the influence of metals (Sect. 9.2.6) shall be taken into account.

The relevant histogram distributions of Figs. 9.2.19, 9.2.20, and 9.2.21 are barely shifted with respect to zero (see also Tables 9.1 and 9.2). Therefore, it is feasible to derive the global systematic uncertainties on  $T_{\text{eff}}$ ,  $\log(g)$ , and  $\log n(\text{He})$  from the standard deviations of the Gaussian functions fitted to the individual histogram data (regarding the influence of metals, the results of the upper left-hand panels of Figs. 9.2.19, 9.2.20, and 9.2.21 shall be considered). The total (statistical + systematic) uncertainties of the atmospheric parameters of a given program star hence are given by:

$$\Delta T_{\text{eff, total}} = \sqrt{(\Delta T_{\text{eff, stat.}})^2 + \left(\frac{0.550}{100} \cdot T_{\text{eff}}\right)^2 + \left(\frac{0.869}{100} \cdot T_{\text{eff}}\right)^2} \quad (9.4)$$

$$\Delta \log (g)_{\text{total}} = \sqrt{(\Delta \log (g)_{\text{stat.}})^2 + 0.035^2 + 0.043^2} \quad (9.5)$$

$$\Delta \log n(\text{He})_{\text{total}} = \sqrt{(\Delta \log n(\text{He})_{\text{stat.}})^2 + 0.047^2 + 0.059^2}. \quad (9.6)$$

Here,  $\Delta T_{\text{eff,stat.}}$ ,  $\Delta \log (g)_{\text{stat.}}$ , and  $\Delta \log n(\text{He})_{\text{stat.}}$  are the respective statistical uncertainties derived for the object in question and  $T_{\text{eff}}$  denotes the measured effective temperature. For the  ${}^3\text{He}$  program stars of this work (see Ch. 10), it seems reasonable to assume that the global systematic uncertainties of the isotopic helium abundances  $\log n({}^4\text{He})$  and  $\log n({}^3\text{He})$  correspond to that of  $\log n(\text{He})$ . Therefore,  $\Delta \log n({}^4\text{He})_{\text{total}}$  and  $\Delta \log n({}^3\text{He})_{\text{total}}$  are also given by Eq. (9.6), whereby the respective statistical uncertainties  $\Delta \log n({}^4\text{He})_{\text{stat.}}$  and  $\Delta \log n({}^3\text{He})_{\text{stat.}}$  need to be used. Since the program stars of this work have atmospheric parameters for which the statistical uncertainties are rather low (see Tables A.1-A.23), the error budget in Eqs. (9.4-9.6) is clearly dominated by the systematic uncertainties.

Certainly, there are numerous other causes of systematic effects apart from the influence of metals as well as the different spectroscopic analysis strategies and their different treatments of the continuum normalization (global vs. selective), which are considered here. For instance, the different resolutions of the spectrographs used, the choice/availability of hydrogen and helium lines to be fitted with the synthetic spectra, or the model spectra themselves are additional sources of systematic effects that are not treated here. A possible solution to the systematics coming along with the different optical resolving powers may be the calculation of distributions such as the ones shown in Figs. 9.2.19, 9.2.20, and 9.2.21, but for the different resolutions/instruments used. Then, the respective systematic uncertainties derived from the Gaussian fits could be applied individually to the atmospheric parameters derived from spectra of the corresponding instruments. However, this would lead to biased results because the number of low, medium, and high-resolution spectra in the sample of the present work significantly differs. Apart from the different coverages (and gaps) of the analyzed spectra, which depend on the different instruments used and which have already been discussed at the beginning of Sect. 9.2, it is simply not possible to always use the same helium lines for the quantitative spectral analyses of all program stars because the individual helium line strength depends on the atmospheric parameters of the star in question. Consequently, one helium line or the other is intrinsically missing in the spectra of some of the helium-poor program stars. Last but not least, it is rather difficult to estimate the internal systematic effect resulting from the models used, as outlined in Sect. 7.1.2. The comparison between the LTE, the hybrid LTE/NLTE, and the NLTE models presented in this chapter also does not provide remedy here because the number of program stars that are analyzed with one of the three model types differs.

Despite all of this, it seems reasonable to assume that the combined effect of all the yet unconsidered additional systematic aspects is of minor size. Thus, the systematics in Eqs. (9.4-9.6) should not be considerably affected.

## 9.2. Detailed Comparison of Different Model Atmosphere Approaches and Analysis Strategies

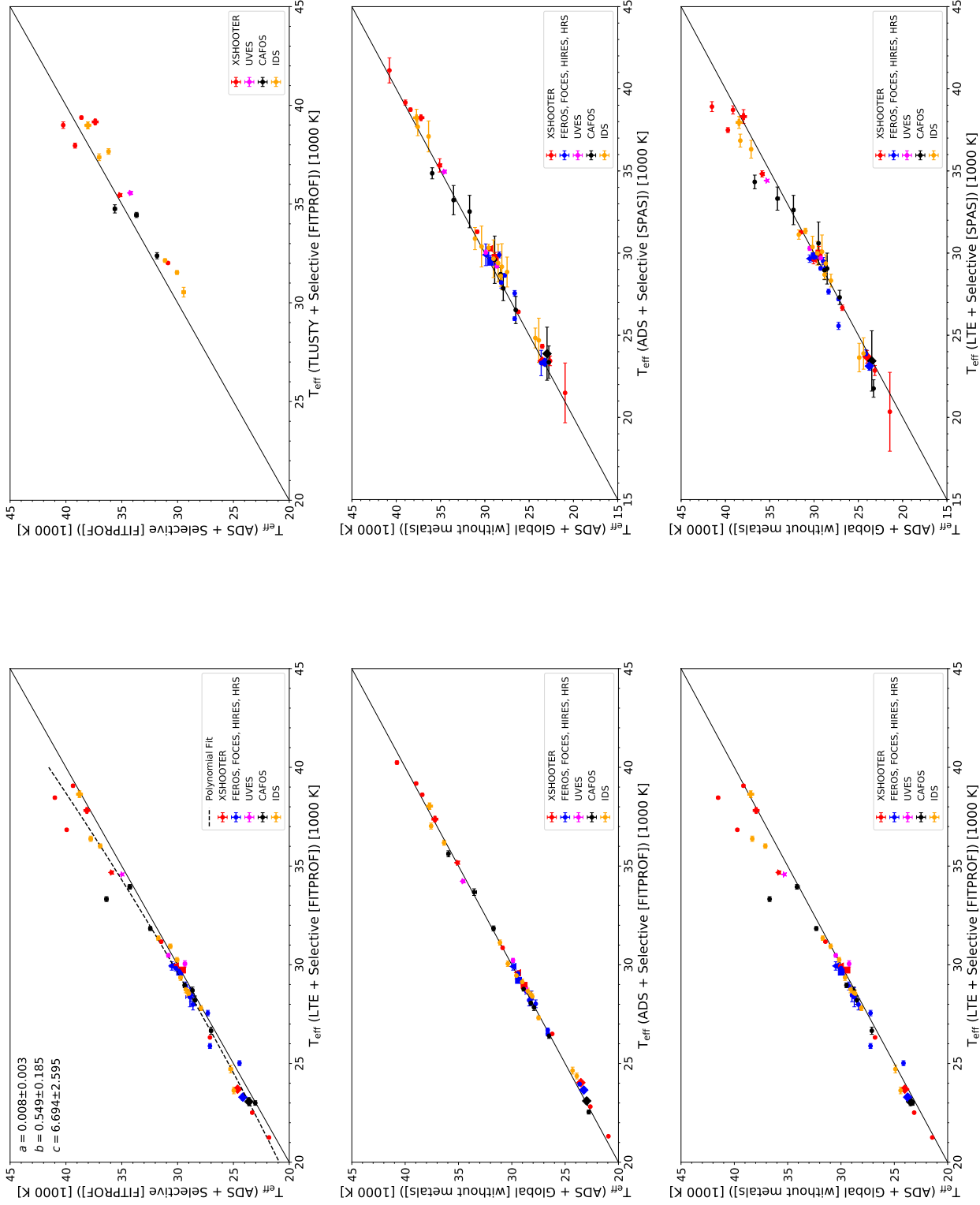


**Figure 9.2.1.:**  $T_{\text{eff}}$  vs.  $T_{\text{eff}}$  comparison plots for the different model atmosphere approaches and spectroscopic analysis techniques used to analyze the hot subdwarf program stars of this work (see Tables A.1-A.18 and A.20-A.23; the results of Table A.19 are not included here; see the text for details). The solid black lines represent the bisectors. Different colors represent different instruments: XSHOOTER (red), FEROS, FOCES, HIRES, and HRS (blue), UVES (magenta), CAFOS (black), and IDS (yellow). Pentagons (PG 0314+146), asterisks (HD 149382), crosses ([CW83] 0512-08), triangles (Feige 38), squares (EC 03591-3232), and diamonds (HD 4539) mark objects that are observed with multiple instruments. Error bars represent  $1\sigma$  statistical single parameter errors (in the case of SPAS, they are bootstrapped; see Sect. 7.1.2). The data points in the upper left-hand panel are fitted with a second order polynomial of the form  $ax^2 + bx + c$  ( $a = 0.008 \pm 0.003$ ,  $b = 0.549 \pm 0.185$ ,  $c = 6.694 \pm 2.595$ ), as displayed by the dashed black line. For a detailed explanation why the different panels do not include the same number of data points, see the introduction (the footnotes) of Ch. 9.

## 9. Quantitative Spectral Analysis

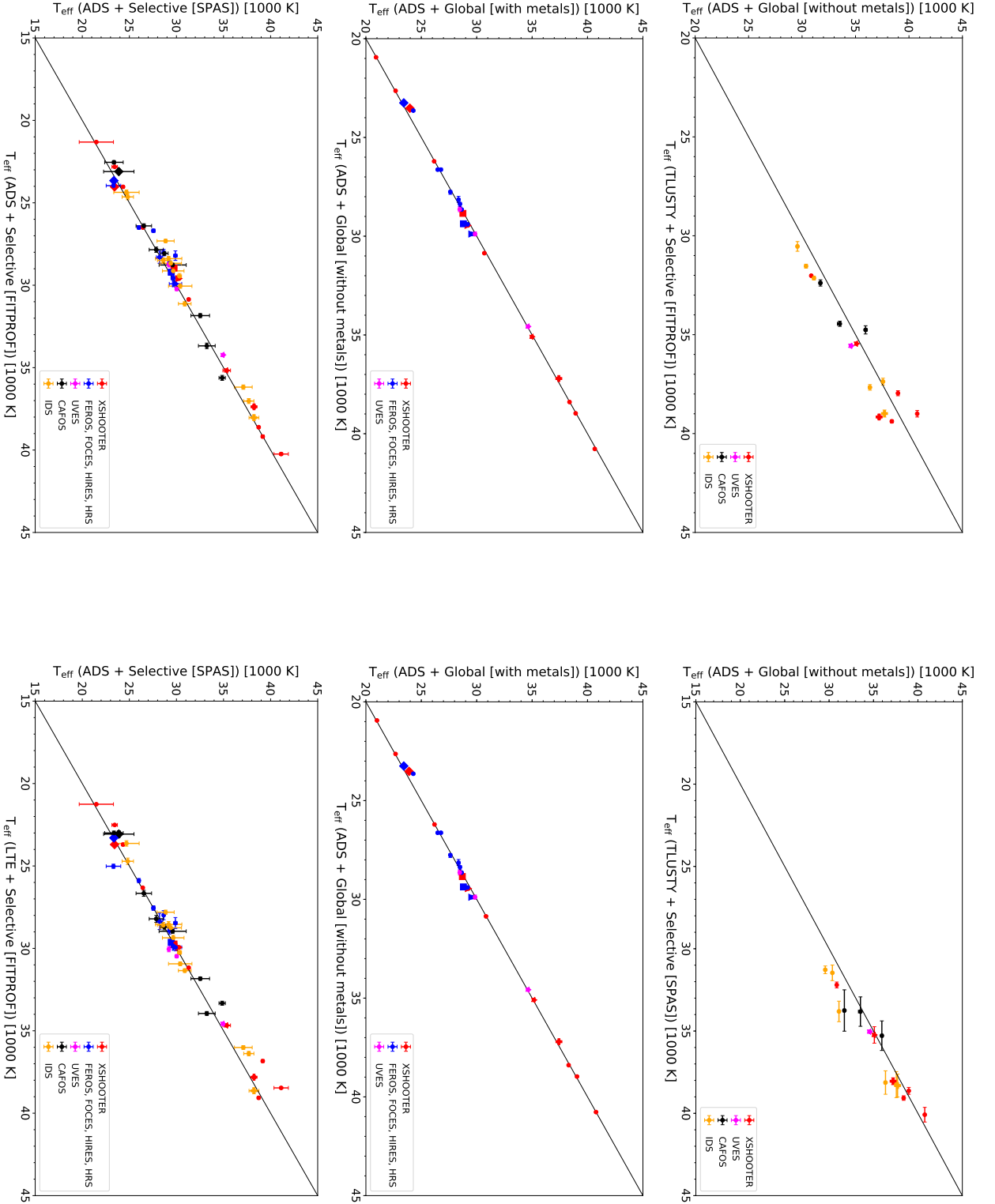


**Figure 9.2.2.:** Figure 9.2.1 continued. Note that the two middle panels both show the comparison of ADS + Global (with metals) vs. ADS + Global (without metals) and that these panels do not include the results of the low-resolution CAFOS and IDS samples. For the middle right-hand panel, only NLTE metals are analyzed in all cases. For the middle left-hand panel, NLTE and LTE metals are considered for the program stars of the XSHOOTER reference sample, whereas for all other objects only NLTE metals are analyzed (see the introduction of Ch. 9 and the corresponding footnotes therein for further information).

## 9.2. Detailed Comparison of Different Model Atmosphere Approaches and Analysis Strategies

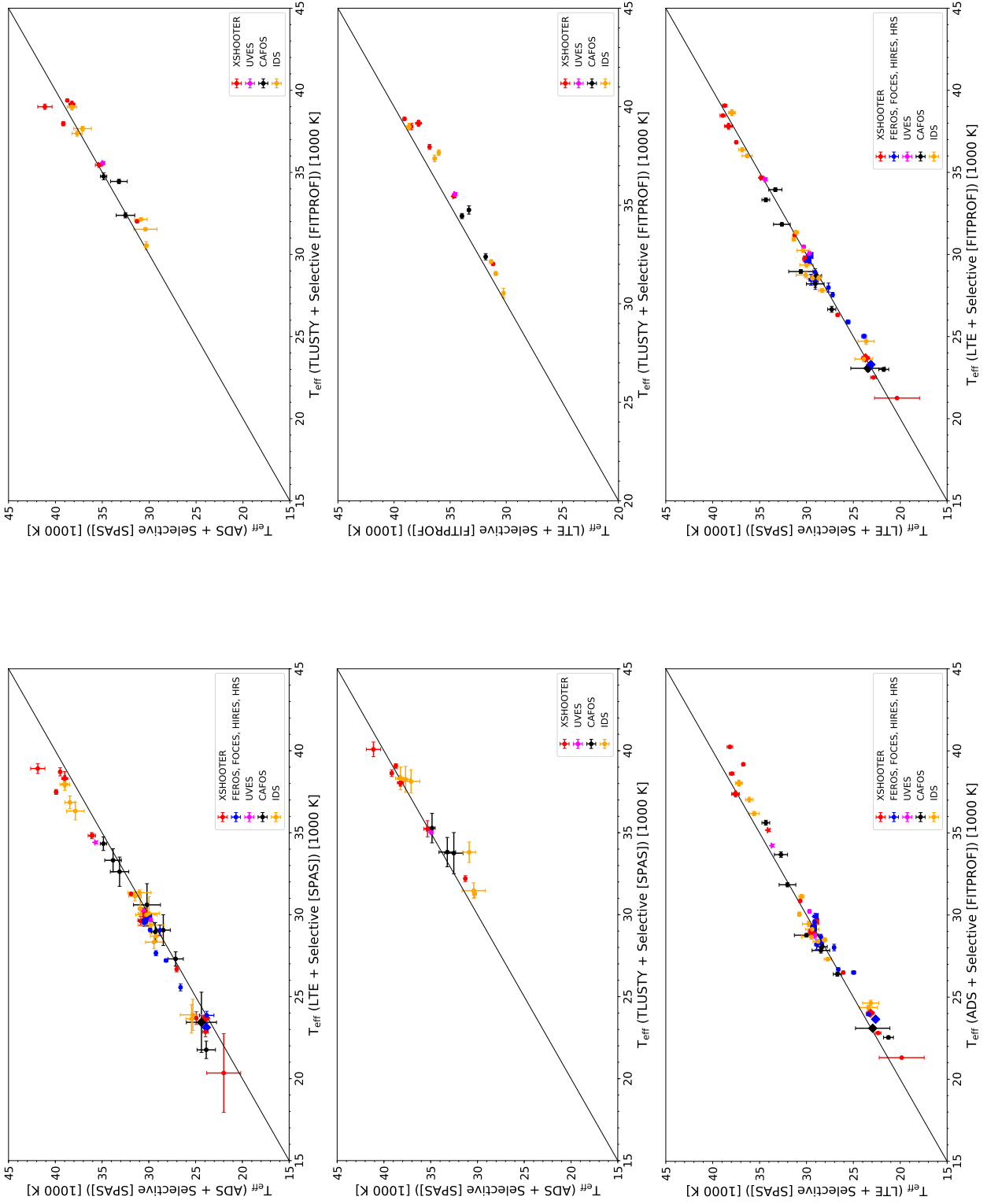


Figure 9.2.3.: Figure 9.2.1 continued.

## 9. Quantitative Spectral Analysis

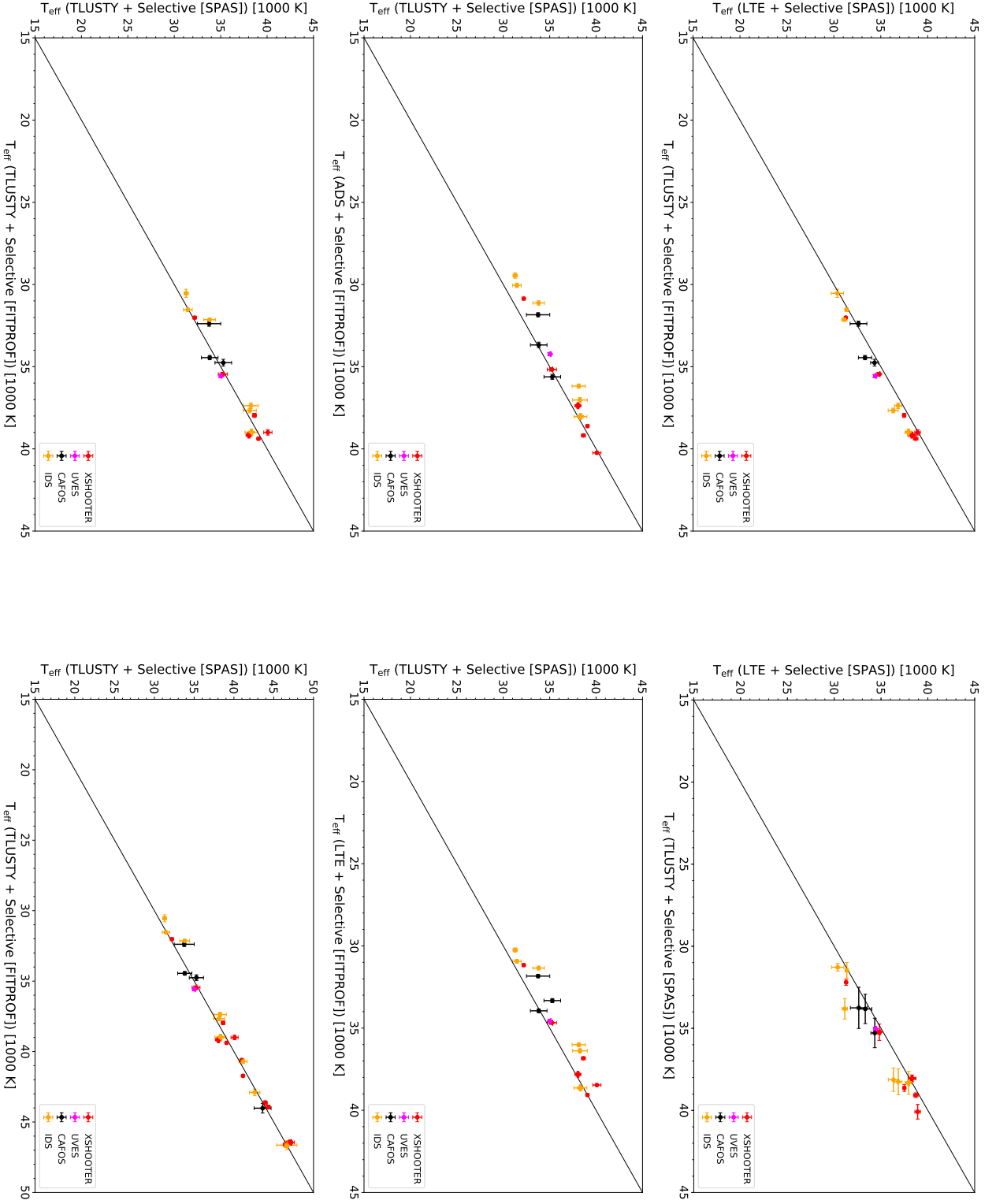
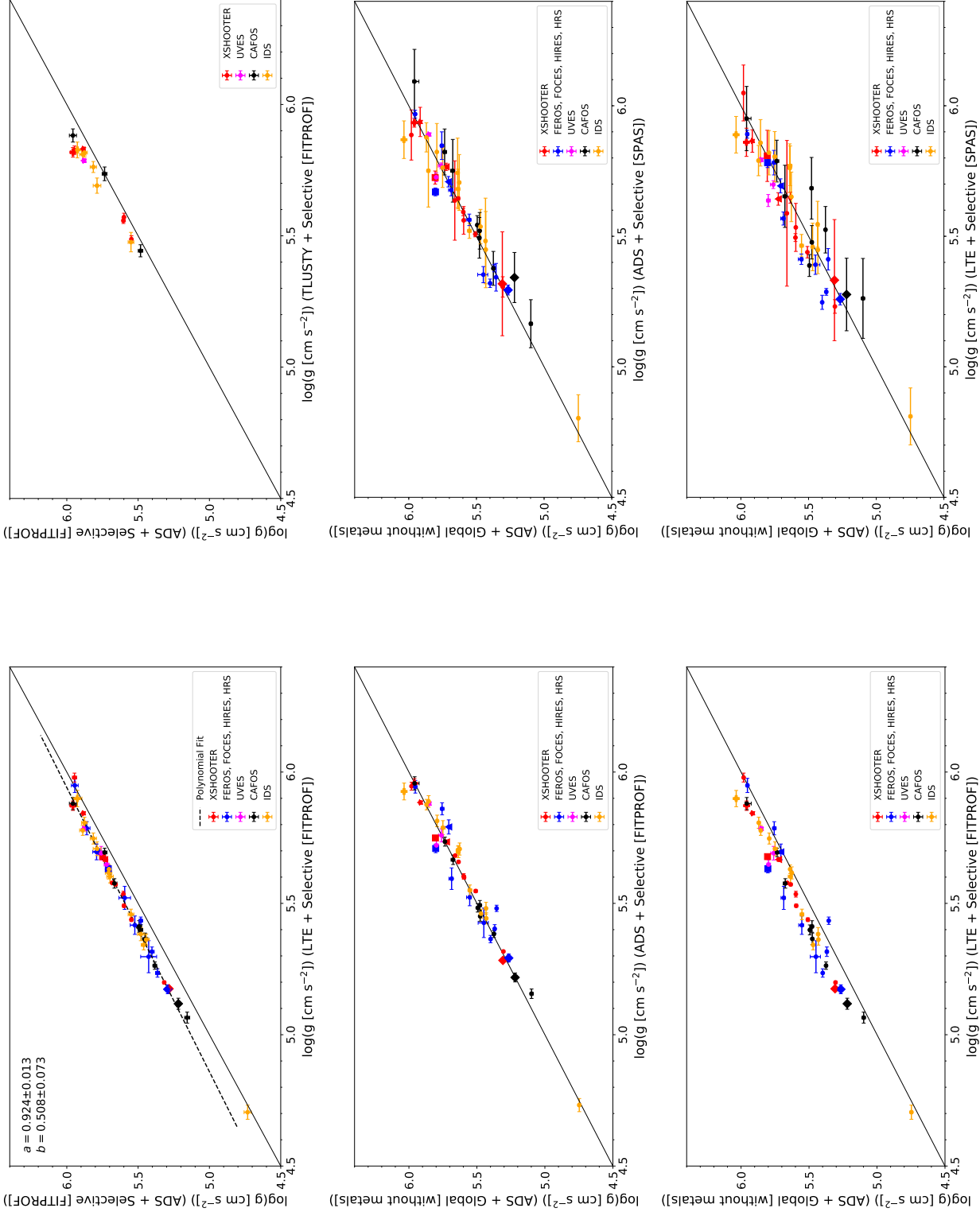


Figure 9.2.4.: Figure 9.2.1 continued. Note that the two lower panels both show the comparison of TLUSTY/SYNSPEC + SPAS vs. TLUSTY/SYNSPEC + FITPROF but have different ranges for the abscissa and the ordinate. In the lower right-hand panel, the He-sdO program stars are included, whereas this is not the case for the lower left-hand panel.

## 9.2. Detailed Comparison of Different Model Atmosphere Approaches and Analysis Strategies



**Figure 9.2.5.:**  $\log(g)$  vs.  $\log(g)$  comparison plots for the different model atmosphere approaches and spectroscopic analysis techniques used to analyze the hot subdwarf program stars of this work (see Tables A.1-A.18 and A.20-A.23; the results of Table A.19 are not included here; see the text for details). The solid black lines represent the bisectors. Different colors represent different instruments: XSHOOTER (red), FEROS, FOCES, HRS, and HRS (blue), UVES (magenta), CAFOs (black), and IDS (yellow). Pentagons (PG 0314+146), asterisks (HD 149382), crosses ([CW83] 0512-08), triangles (Feige 38), squares (EC 03591-3232), and diamonds (HD 4539) mark objects that are observed with multiple instruments. Error bars represent  $1\sigma$  statistical single parameter errors (in the case of SPAS, they are bootstrapped; see Sect. 7.1.2). The data points in the upper left-hand panel are fitted with a first order polynomial of the form  $ax + b$  ( $a = 0.924 \pm 0.013$ ,  $b = 0.508 \pm 0.073$ ), as displayed by the dashed black line. For a detailed explanation why the different panels do not include the same number of data points, see the introduction (the footnotes) of Ch. 9.

## 9. Quantitative Spectral Analysis

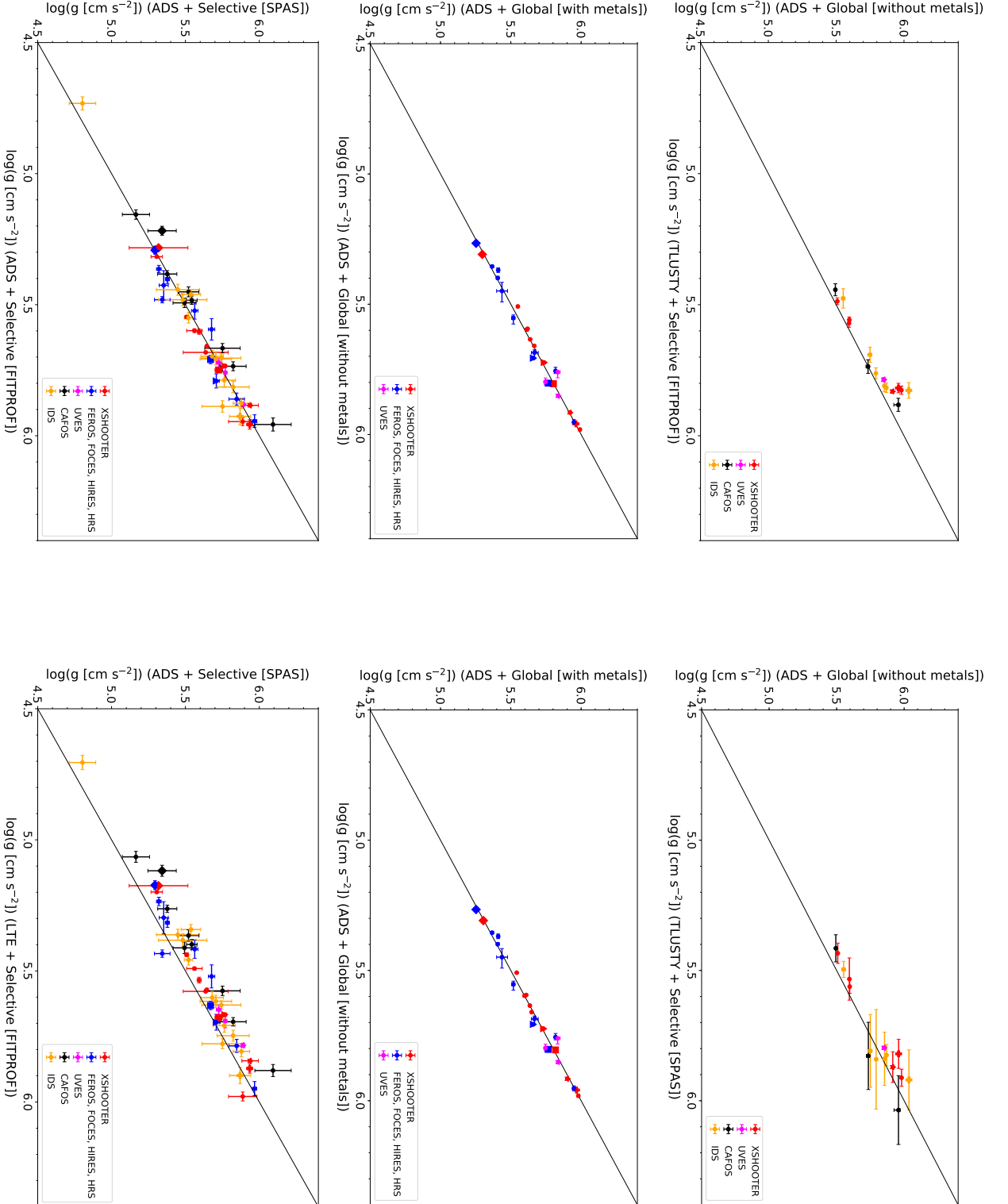


**Figure 9.2.6.:** Figure 9.2.5 continued. Note that the two middle panels both show the comparison of ADS + Global (with metals) vs. ADS + Global (without metals) and that these panels do not include the results of the low-resolution CAFOS and IDS samples. For the middle right-hand panel, only NLTE metals are analyzed in all cases. For the middle left-hand panel, NLTE and LTE metals are considered for the program stars of the XSHOOTER reference sample, whereas for all other objects only NLTE metals are analyzed (see the introduction of Ch. 9 and the corresponding footnotes therein for further information).

## 9.2. Detailed Comparison of Different Model Atmosphere Approaches and Analysis Strategies

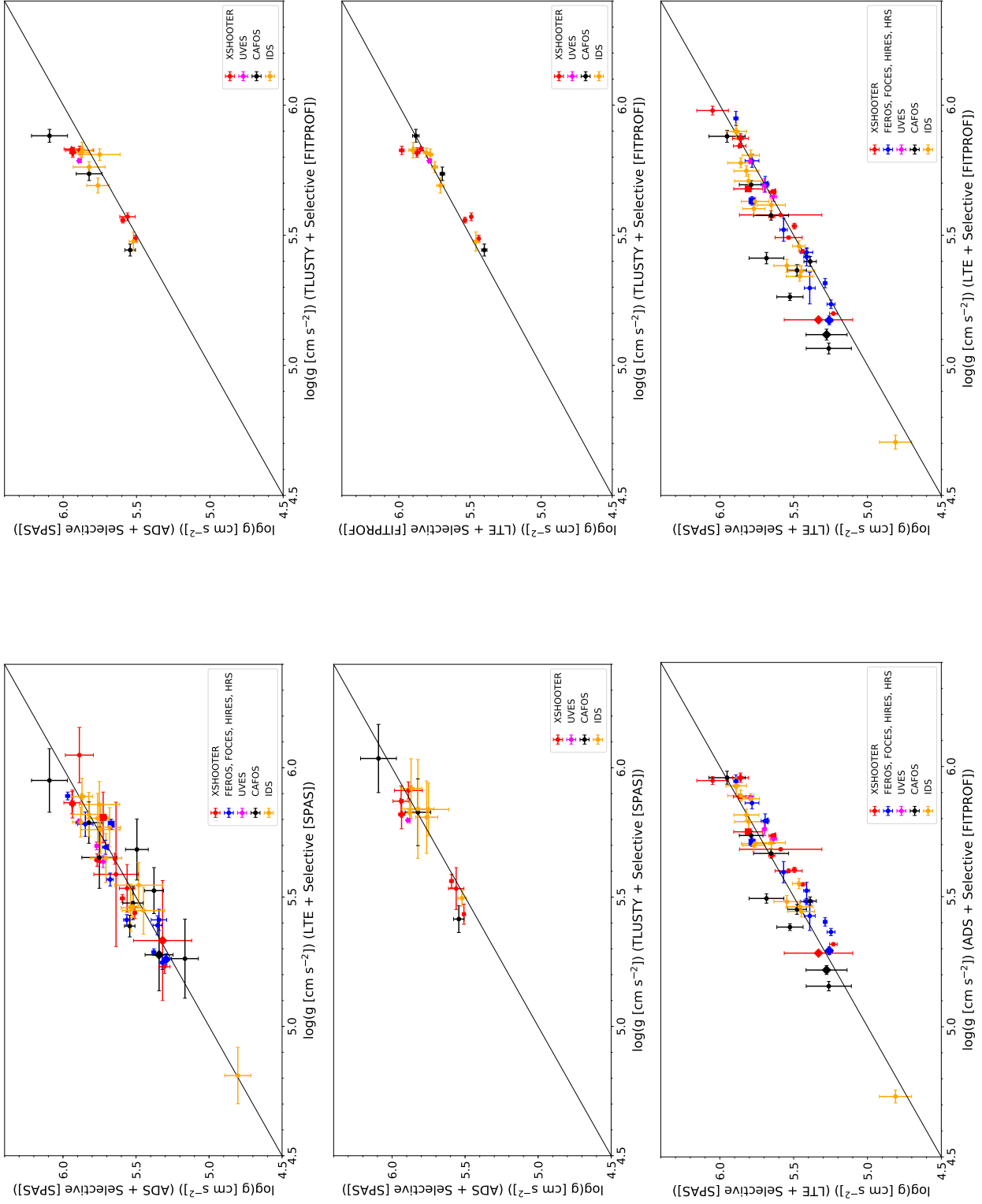


Figure 9.2.7.: Figure 9.2.5 continued.

## 9. Quantitative Spectral Analysis

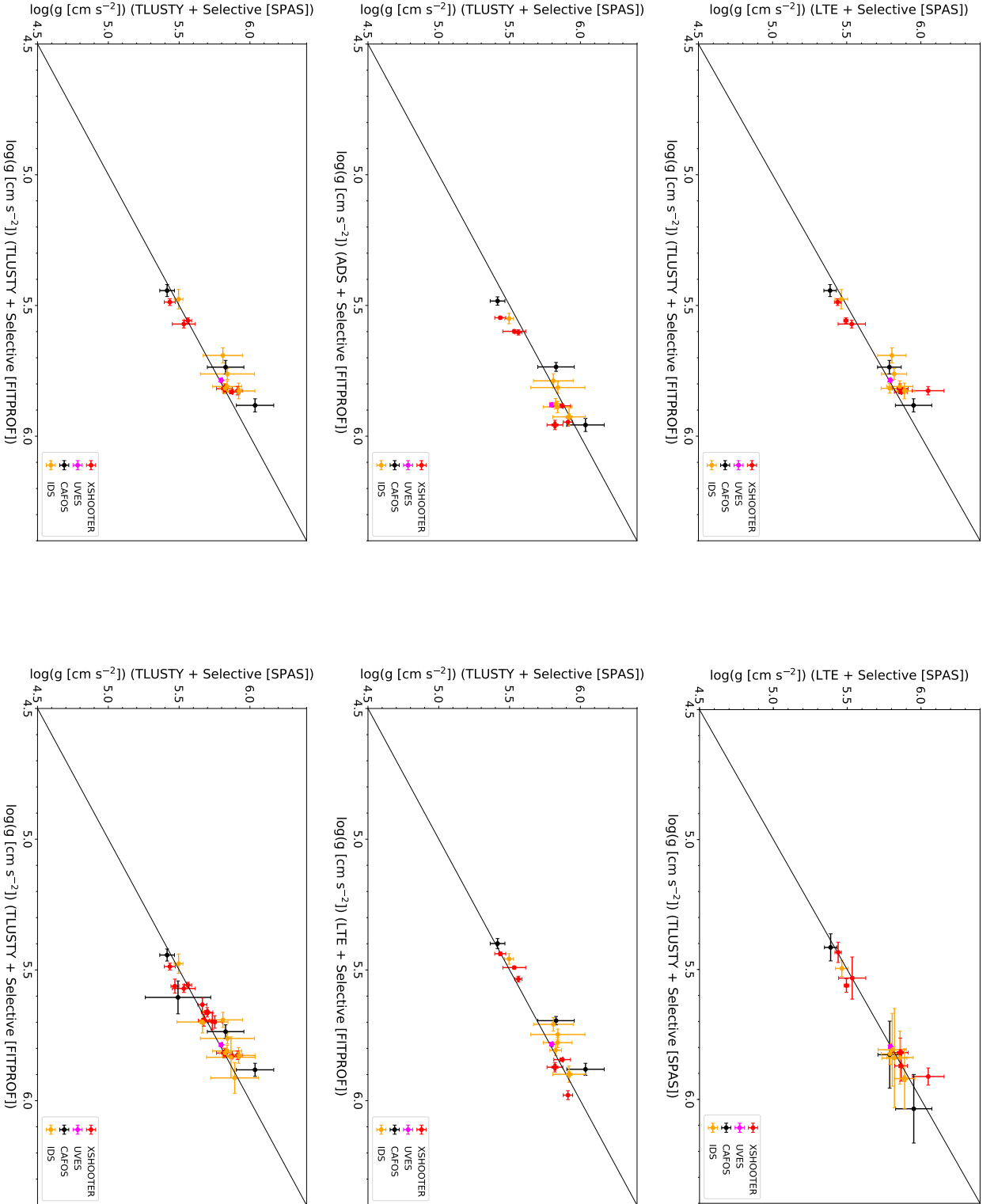
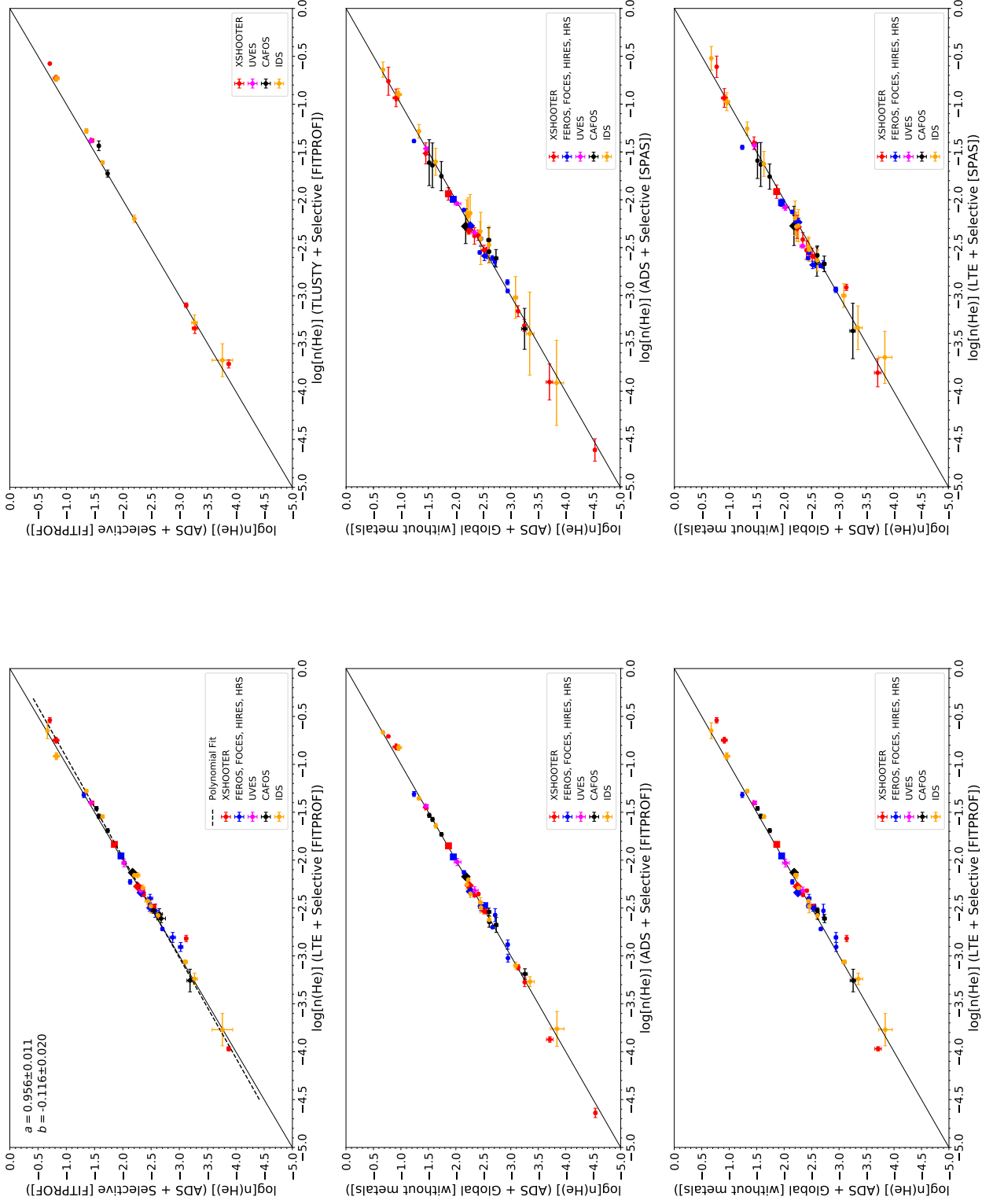


Figure 9.2.8.: Figure 9.2.5 continued. Note that the two lower panels both show the comparison of TLUSTY/SYNSPEC + SPAS vs. TLUSTY/SYNSPEC + FITPROF. In the lower right-hand panel, the He-sdO program stars are included, whereas this is not the case for the lower left-hand panel.

## 9.2. Detailed Comparison of Different Model Atmosphere Approaches and Analysis Strategies



**Figure 9.2.9.:**  $\log m(\text{He})$  vs.  $\log n(\text{He})$  comparison plots for the different model atmosphere approaches and spectroscopic analysis techniques used to analyze the hot subdwarf program stars of this work (see Tables A.1-A.18 and A.20-A.23; the results of Table A.19 are not included here; see the text for details). No derived upper and lower limits and no fixed values are plotted. The solid black lines represent the bisectors. Different colors represent different instruments: XSHOOTER (red), FEROS, FOCES, HIRES, and HRS (blue), UVES (magenta), CAFOS (black), and IDS (yellow). Pentagons (PG 0314+146), asterisks (HD 149382), crosses ([CW83] 0512-08), triangles (Feige 38), squares (EC 03591-3232), and diamonds (HD 4539) mark objects that are observed with multiple instruments. Error bars represent  $1\sigma$  statistical single parameter errors (in the case of SPAS, they are bootstrapped; see Sect. 7.1.2). The data points in the upper left-hand panel are fitted with a first order polynomial of the form  $ax + b$  ( $a = 0.956 \pm 0.011$ ,  $b = -0.116 \pm 0.020$ ), as displayed by the dashed black line. For a detailed explanation why the different panels do not include the same number of data points, see the introduction (the footnotes) of Ch. 9.

## 9. Quantitative Spectral Analysis

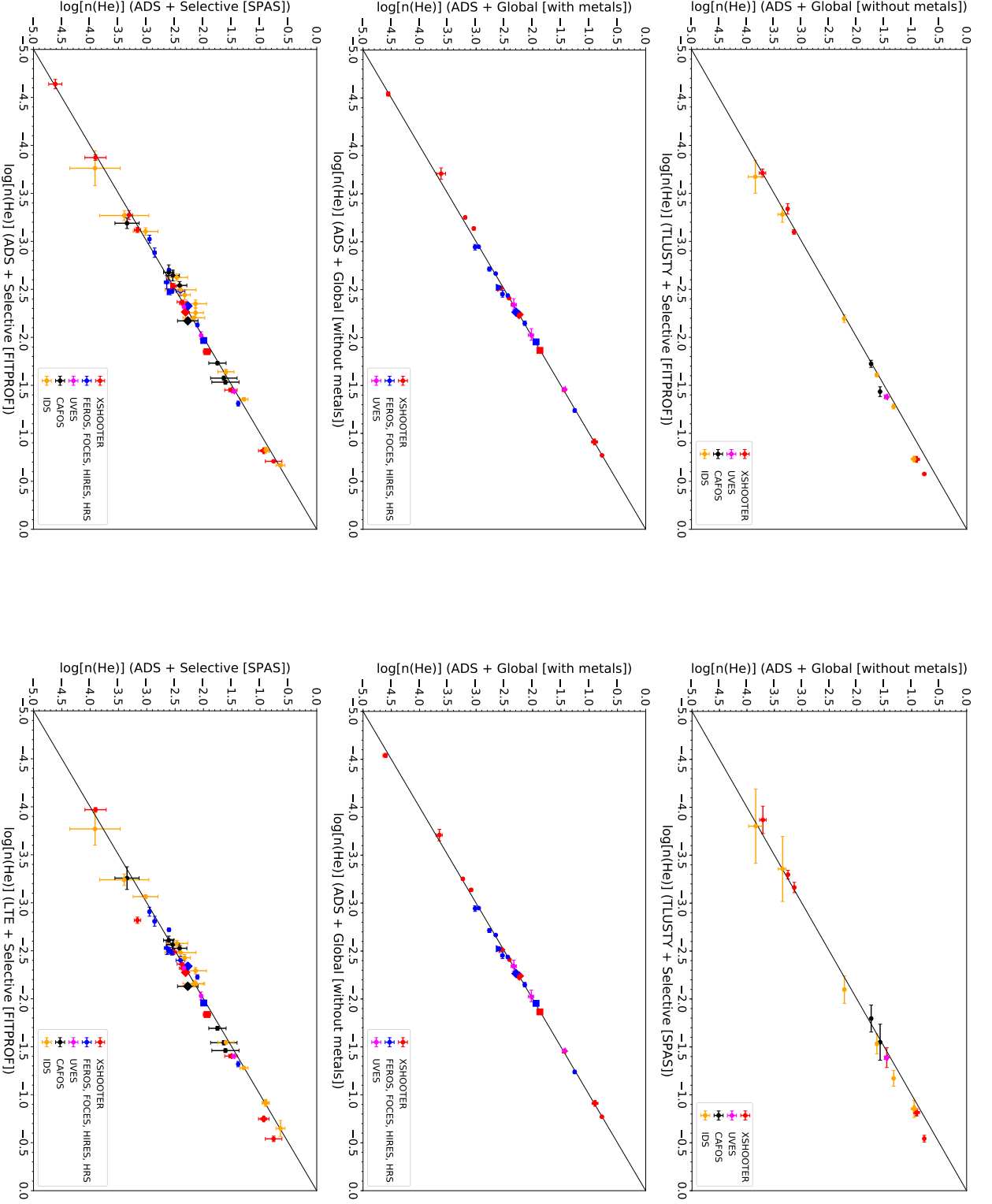


**Figure 9.2.10.:** Figure 9.2.9 continued. Note that the two middle panels both show the comparison of ADS + Global (with metals) vs. ADS + Global (without metals) and that these panels do not include the results of the low-resolution CAFOS and IDS samples. For the middle right-hand panel, only NLTE metals are analyzed in all cases. For the middle left-hand panel, NLTE and LTE metals are considered for the program stars of the XSHOOTER reference sample, whereas for all other objects only NLTE metals are analyzed (see the introduction of Ch. 9 and the corresponding footnotes therein for further information).

## 9.2. Detailed Comparison of Different Model Atmosphere Approaches and Analysis Strategies

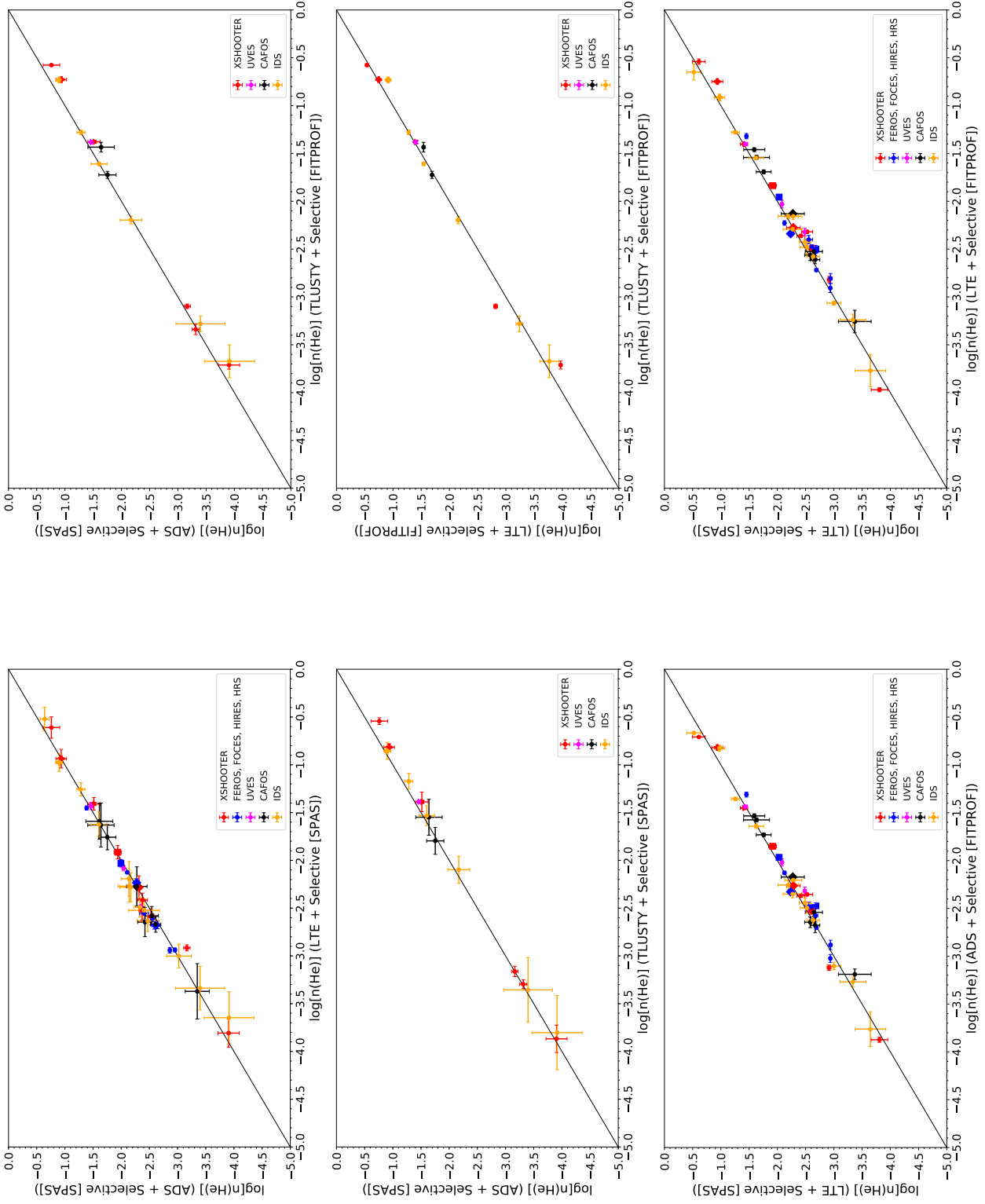


Figure 9.2.11.: Figure 9.2.9 continued.

## 9. Quantitative Spectral Analysis

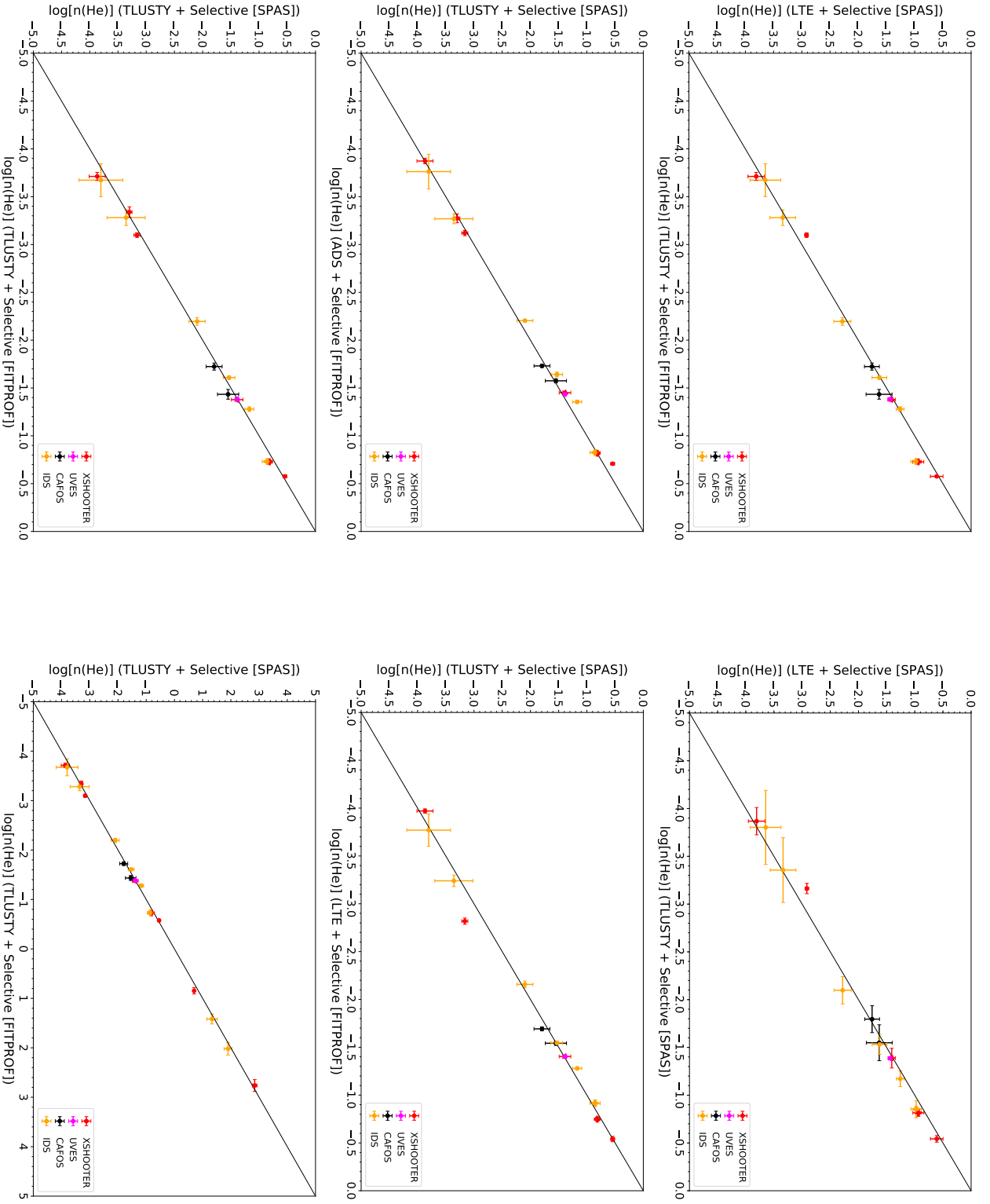


Figure 9.2.12.: Figure 9.2.9 continued. Note that the two lower panels both show the comparison of TLUSTY/SYNSPEC + SPAS vs. TLUSTY/SYNSPEC + FITPROF but have different ranges for the abscissa and the ordinate. In the lower right-hand panel, the He-sdO program stars are included, whereas this is not the case for the lower left-hand panel.

## 9.2. Detailed Comparison of Different Model Atmosphere Approaches and Analysis Strategies

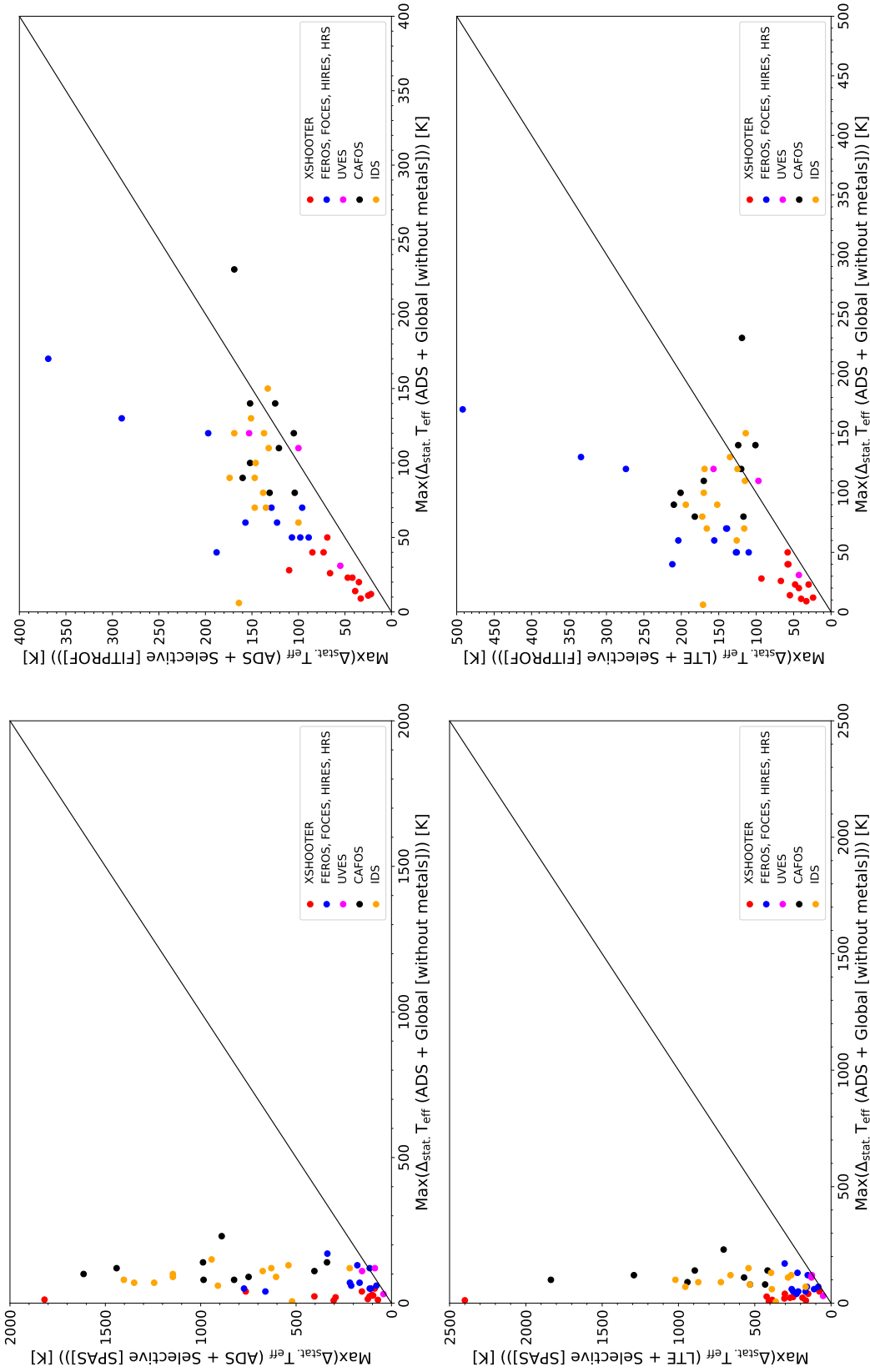


Figure 9.2.13.: Comparisons of the maximum  $1\sigma$  statistical uncertainties on  $T_{\text{eff}}$  determined for the hot subdwarf program stars of this work (in the case of SPAS, the uncertainties are bootstrapped; see Sect. 7.1.2). The data are extracted from Tables A.1-A.18 and A.20-A.23 (the results of Table A.19 are not included here; see the text for details). In all four panels, the abscissa shows the results for ADS + Global (without metals). Note, however, that the ordinate is always different: ADS + SPAS (upper left-hand panel), ADS + FITPROF (upper right-hand panel), LTE + SPAS (lower left-hand panel), and LTE + FITPROF (lower right-hand panel). The solid black lines represent the bisectors. Different colors represent different instruments: XSHOOTER (red), FEROS, FOCES, HIRES, and HRS (blue), UVES (magenta), CAFOS (black), and IDS (yellow).

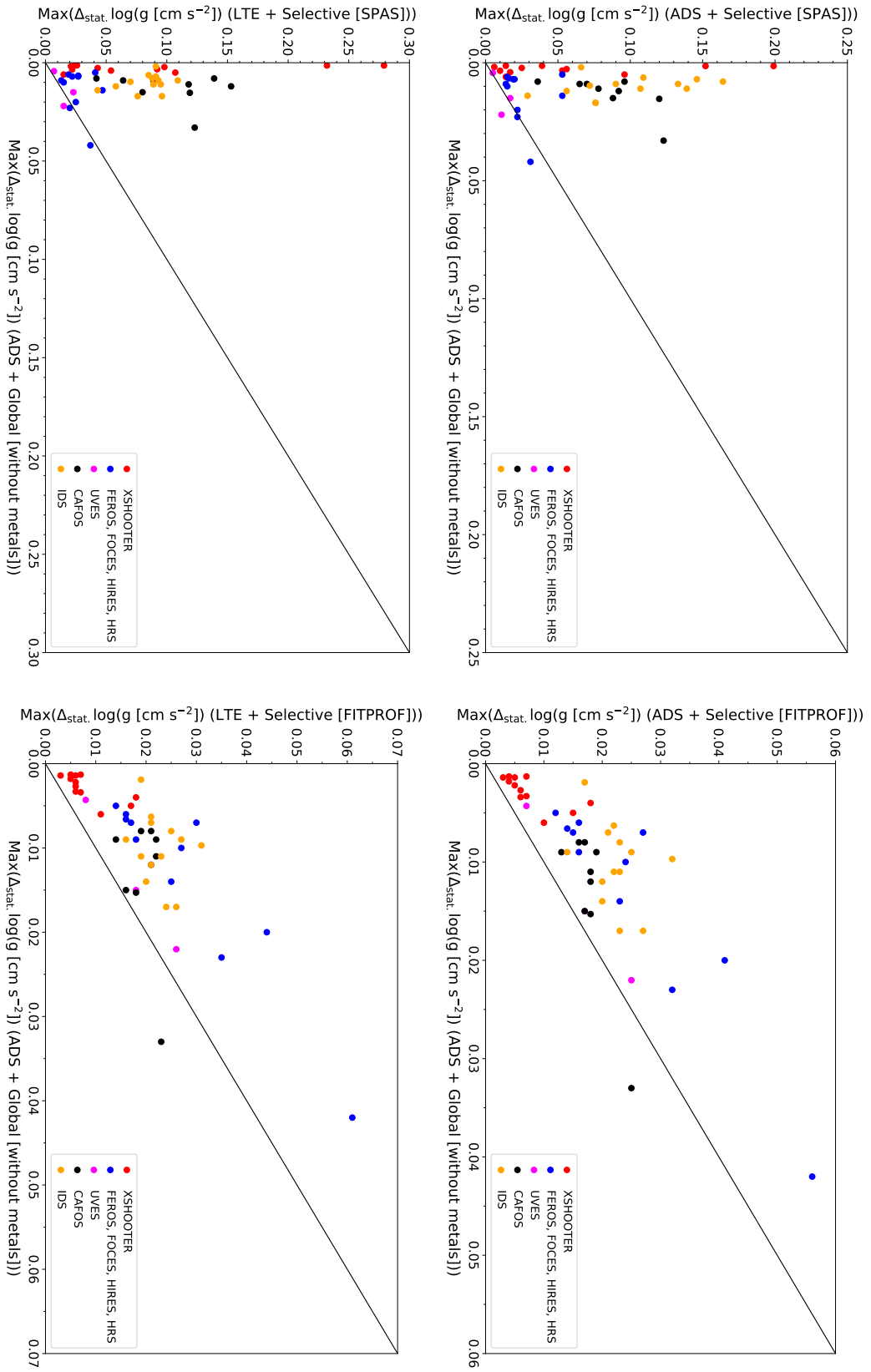


Figure 9.2.14.: Same as Fig. 9.2.13, but for  $\log(g)$ .

## 9.2. Detailed Comparison of Different Model Atmosphere Approaches and Analysis Strategies

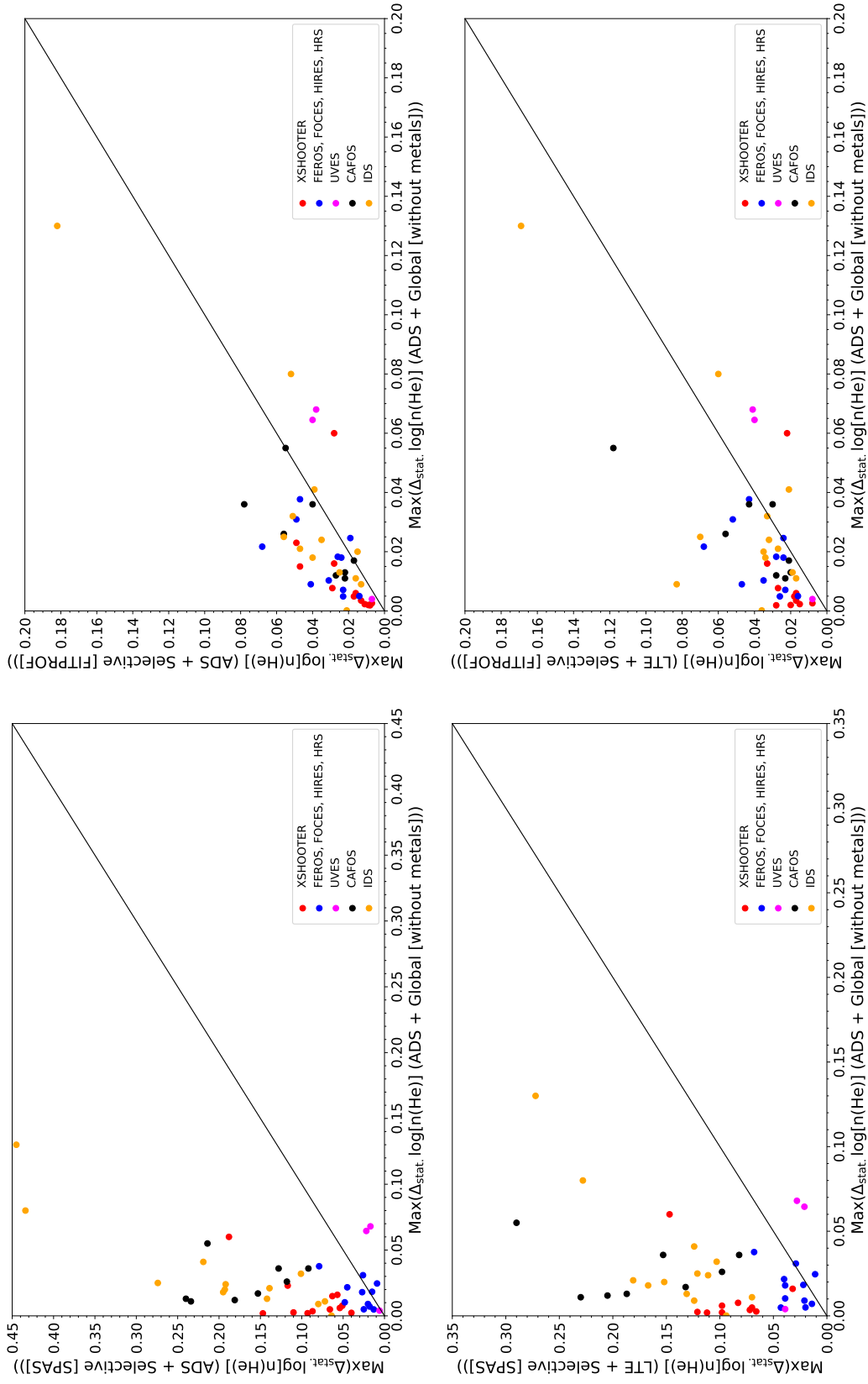


Figure 9.2.15.: Same as Fig. 9.2.13, but for  $\log n(\text{He})$ . No results for program stars with fixed values of  $\log n(\text{He})$  or with upper or lower limits on  $\log n(\text{He})$  are plotted.

## 9. Quantitative Spectral Analysis

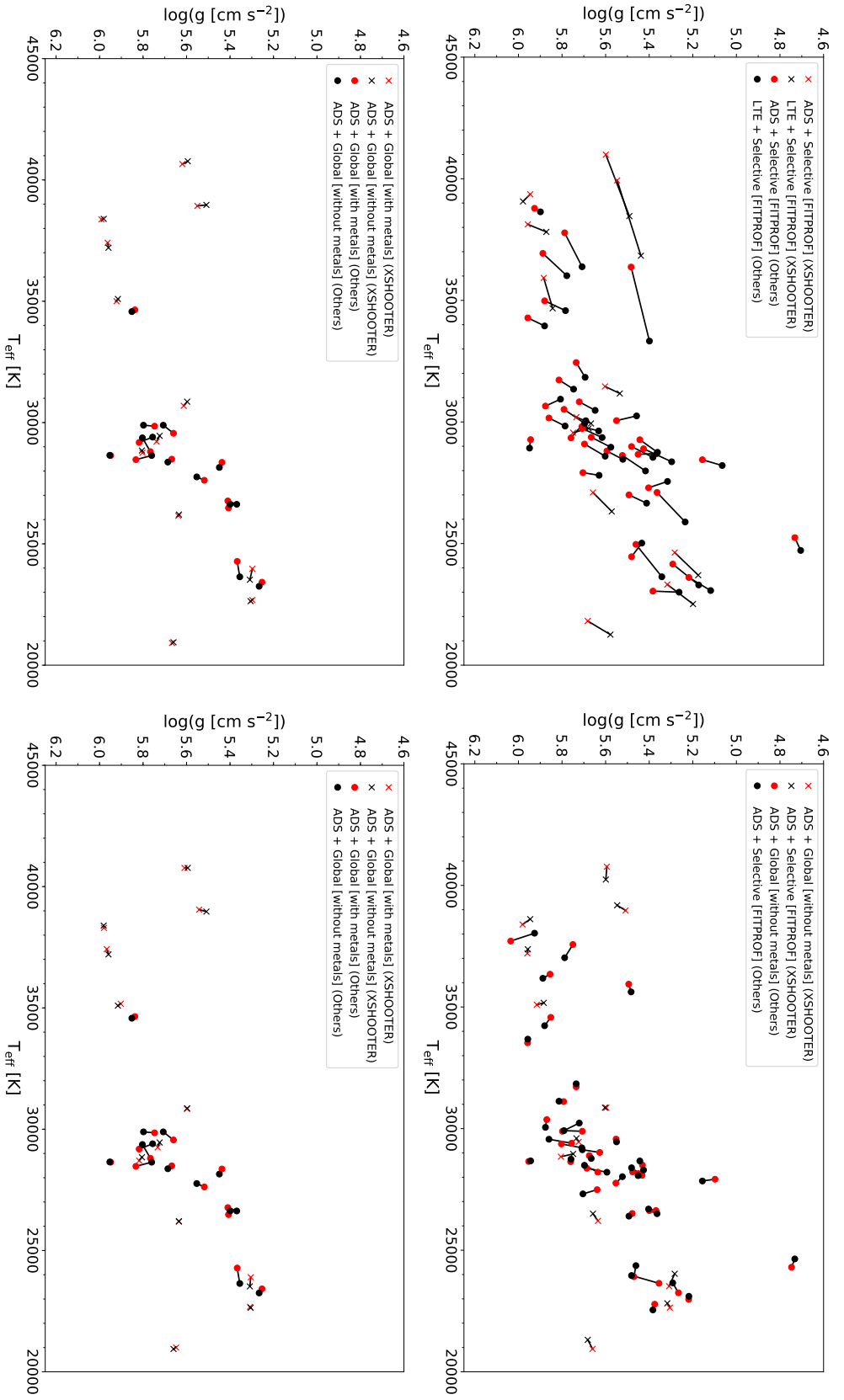


Figure 9.2.16.:  $T_{\text{eff}}\text{-}\log(g)$  diagrams (Kiel diagrams) for the hot subdwarf program stars of this work (see Tables A.1-A.18 and A.20-A.23, the results of Table A.19 are not included here; see the text for details) comparing the results of ADS + FITPROF to LTE + FITPROF (upper left-hand panel), of ADS + Global (without metals) to ADS + FITPROF (upper right-hand panel) as well as of ADS + Global (with metals) to ADS + Global (without metals) (lower panels). Note that the two lower panels do not include the results of the low-resolution CAFOS and IDS samples. For the lower right-hand panel, only NLTE metals are analyzed in all cases. For the lower left-hand panel, NLTE and LTE metals are considered for the program stars of the XSHOOTER reference sample, whereas for all other objects only NLTE metals are analyzed (see the introduction of Ch. 9 and the corresponding footnotes therein for further information). For the sake of clarity, no error bars are plotted. Red and black data points indicate the different combinations investigated (see the respective legends). Results based on XSHOOTER data are marked by crosses. Lines connect data points associated with the same stars and, hence, make shifts visible.

## 9.2. Detailed Comparison of Different Model Atmosphere Approaches and Analysis Strategies

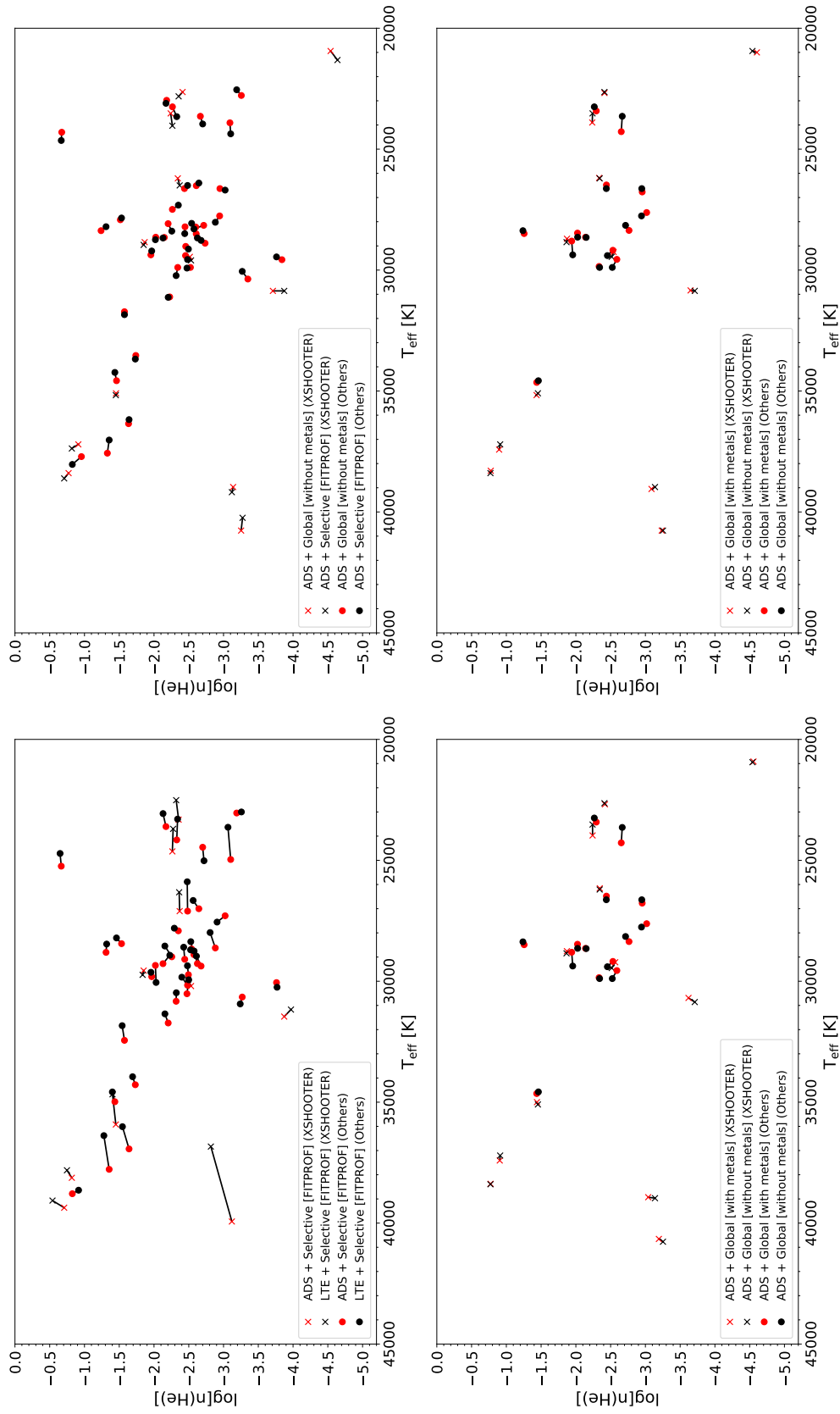


Figure 9.2.17.: Same as Fig. 9.2.16, but showing the corresponding  $T_{\text{eff}}\text{-}\log n(\text{He})$  diagrams. No results for program stars with fixed values of  $\log n(\text{He})$  or with upper or lower limits on  $\log n(\text{He})$  are plotted.

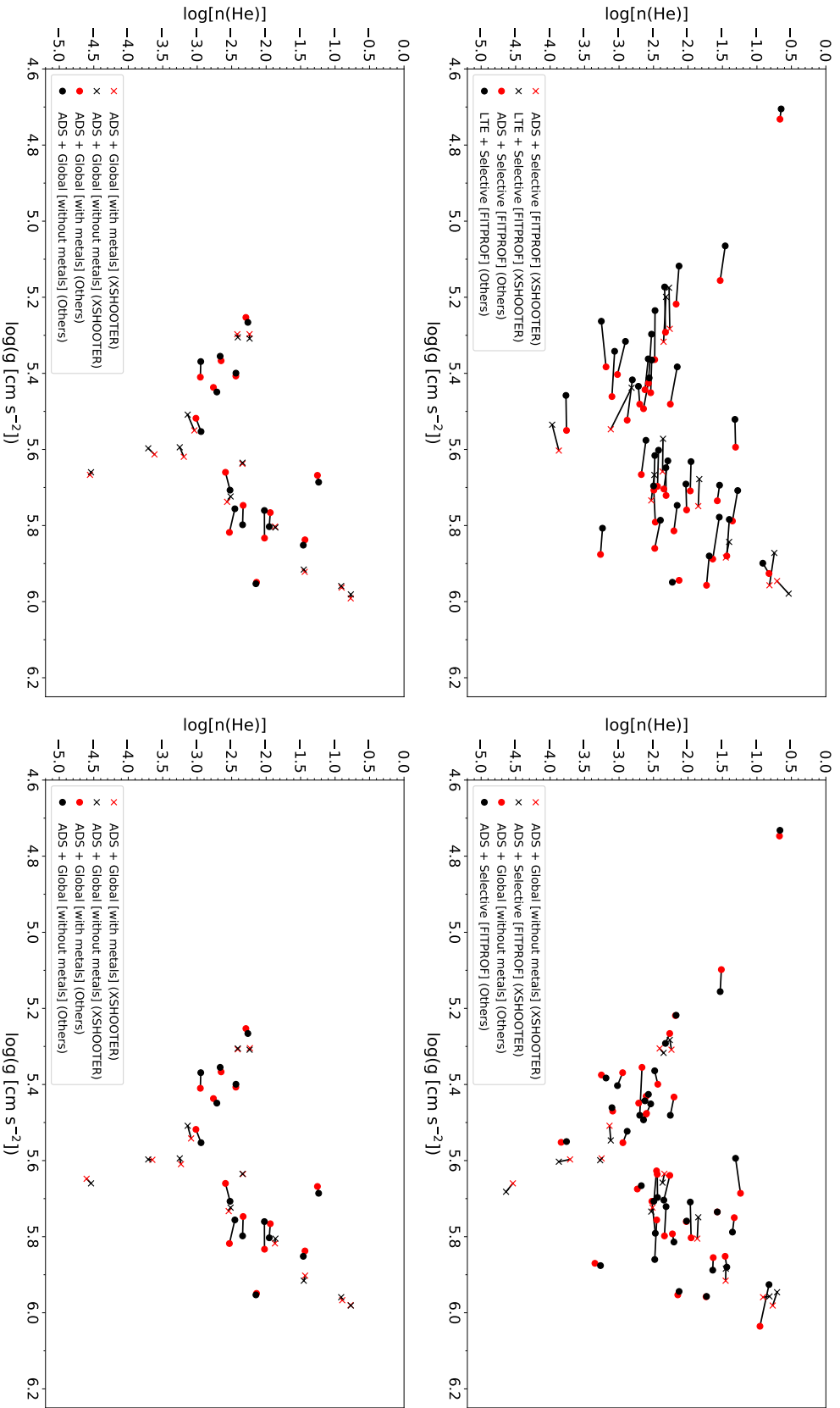
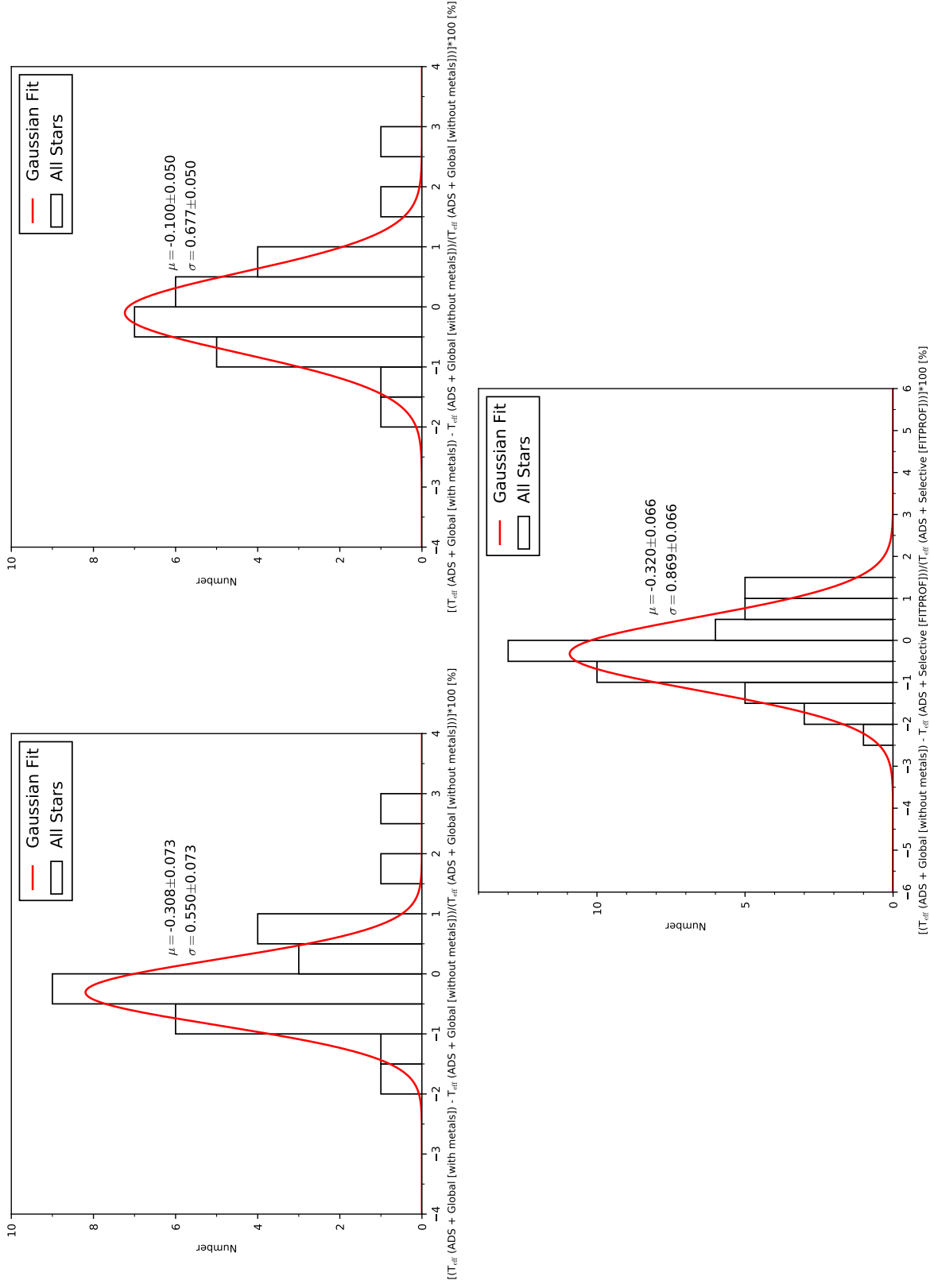


Figure 9.2.18.: Same as Fig. 9.2.16, but showing the corresponding  $\log(g)$ - $\log n(\text{He})$  diagrams. No results for program stars with fixed values of  $\log n(\text{He})$  or with upper or lower limits on  $\log n(\text{He})$  are plotted.

## 9.2. Detailed Comparison of Different Model Atmosphere Approaches and Analysis Strategies



**Figure 9.2.19.:** Histogram distributions of the deviations of  $T_{\text{eff}}$  derived from the middle left-hand panel of Fig. 9.2.2 (upper left-hand panel), from the middle right-hand panel of Fig. 9.2.2 (upper right-hand panel) as well as from the middle left-hand panel of Fig. 9.2.1 (lower panel). Note that only hot subdwarf program stars are considered (see Tables A.1-A.18 and A.20-A.23; the results of Table A.19 are not included here; see the text for details), that the two upper panels do not include the results of the low-resolution CAFOS and IDS samples, and that all histograms are derived from percentage deviations (see the respective abscissae). The given mean values  $\mu$  and standard deviations  $\sigma$  as well as their individual standard errors result from Gaussian fits (represented by the solid red line in all three panels) performed on the full data of the individual histograms. The two upper panels are both based on the comparison of ADS + Global (with metals) vs. ADS + Global (without metals). For the upper right-hand panel, only NLTE metals are analyzed in all cases. For the upper left-hand panel, NLTE and LTE metals are considered for the program stars of the XSHOOTER reference sample, whereas for all other objects only NLTE metals are analyzed (see the introduction of Ch. 9 and the corresponding footnotes therein for further information).

## 9. Quantitative Spectral Analysis

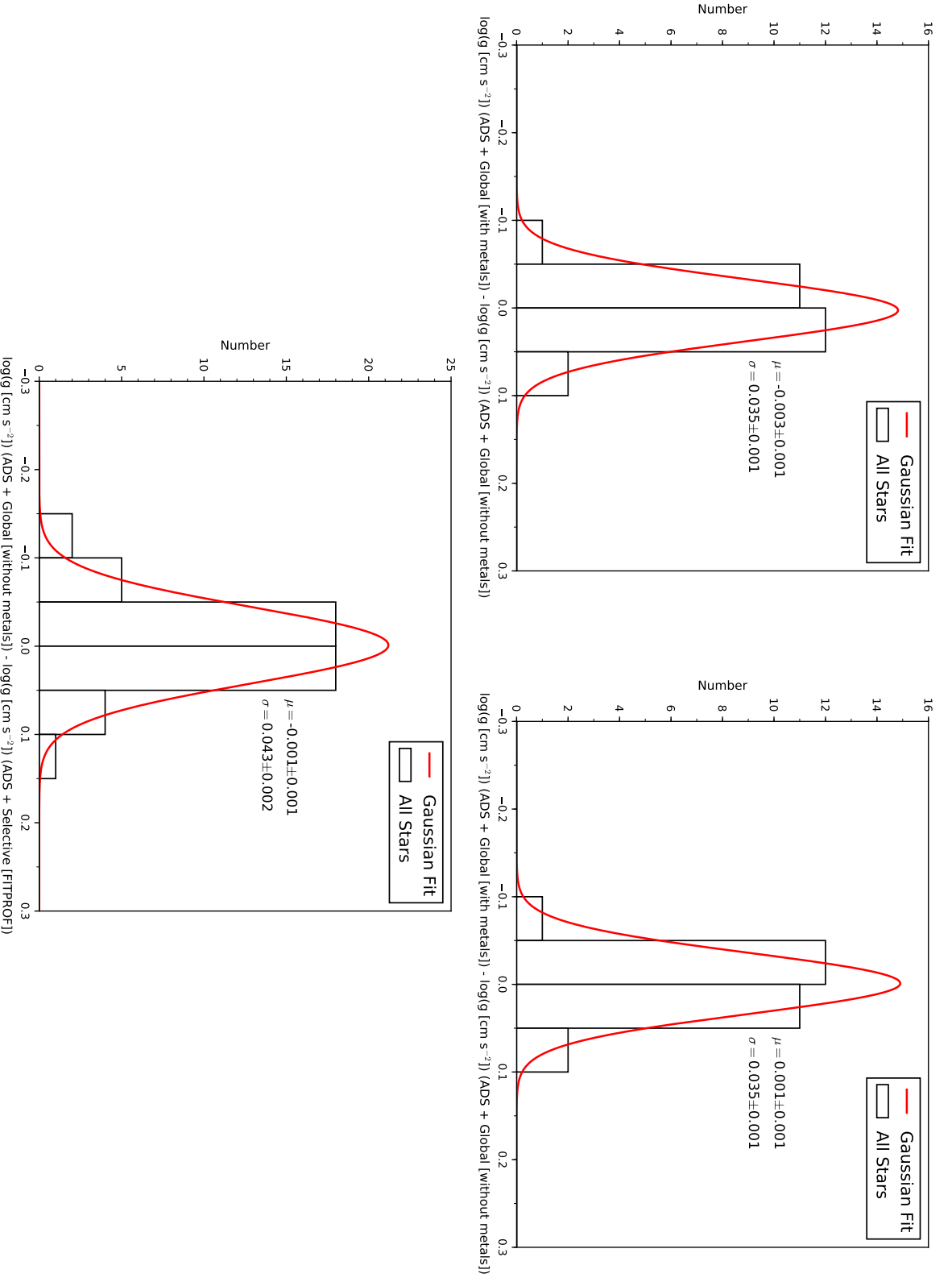


**Figure 9.2.20.:** Histogram distributions of the deviations of  $\log(g)$  derived from the middle left-hand panel of Fig. 9.2.6 (upper left-hand panel), from the middle right-hand panel of Fig. 9.2.6 (upper right-hand panel) as well as from the middle left-hand panel of Fig. 9.2.5 (lower panel). Note that only hot subdwarf program stars are considered (see Tables A.1-A.18 and A.20-A.23; the results of Table A.19 are not included here; see the text for details) and that the two upper panels do not include the results of the low-resolution CAFOS and IDS samples. The given mean values  $\mu$  and standard deviations  $\sigma$  as well as their individual standard errors result from Gaussian fits (represented by the solid red line in all three panels) performed on the full data of the individual histograms. The two upper panels are both based on the comparison of ADS + Global (with metals) vs. ADS + Global (without metals). For the upper right-hand panel, only NLTE metals are analyzed in all cases. For the upper left-hand panel, NLTE and LTE metals are considered for the program stars of the XSHOOTER reference sample, whereas for all other objects only NLTE metals are analyzed (see the introduction of Ch. 9 and the corresponding footnotes therein for further information).

## 9.2. Detailed Comparison of Different Model Atmosphere Approaches and Analysis Strategies

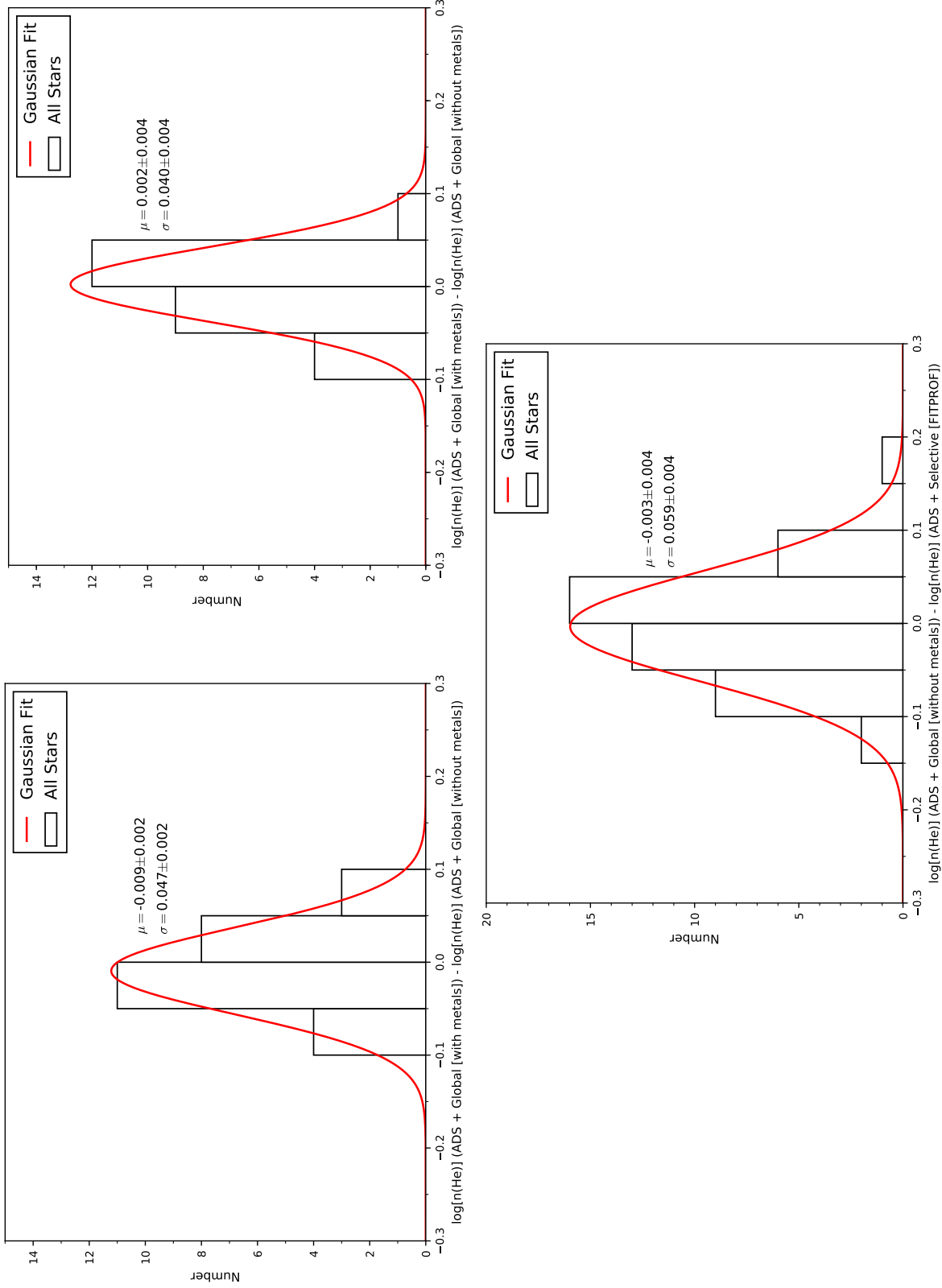


**Figure 9.2.21.:** Histogram distributions of the deviations of  $\log n(\text{He})$  derived from the middle left-hand panel of Fig. 9.2.10 (upper left-hand panel), from the middle right-hand panel of Fig. 9.2.10 (upper right-hand panel) as well as from the middle left-hand panel of Fig. 9.2.9 (lower panel). Note that only hot subdwarf program stars are considered (see Tables A.1-A.18 and A.20-A.23; the results of Table A.19 are not included here; see the text for details), that the two upper panels do not include the results of the low-resolution CAFOS and IDS samples, and that no results for program stars with fixed values of  $\log n(\text{He})$  or with upper or lower limits on  $\log n(\text{He})$  are used for all histograms. The given mean values  $\mu$  and standard deviations  $\sigma$  as well as their individual standard errors result from Gaussian fits (represented by the solid red line in all three panels) performed on the full data of the individual histograms. The two upper panels are both based on the comparison of ADS + Global (with metals) vs. ADS + Global (without metals). For the upper right-hand panel, only NLTE metals are analyzed in all cases. For the upper left-hand panel, NLTE and LTE metals are considered for the program stars of the XSHOOTER reference sample, whereas for all other objects only NLTE metals are analyzed (see the introduction of Ch. 9 and the corresponding footnotes therein for further information).

### 9.3. Influence of the Hydrogen Paschen Series

The previous section provided a detailed comparison of the results derived from the different model atmosphere approaches and analysis strategies used to spectroscopically analyze the individual program stars. Here, another important aspect shall be investigated, which is the influence of the NIR spectral range on the atmospheric parameters derived. In other words: Are the atmospheric parameters of hot subdwarf stars already well constrained by the hydrogen Paschen series and the helium lines in the IR? In order to investigate this, three XSHOOTER program stars (the H-sdBs HD 4539, GALEX J104148.9-073031, and Feige 38) in the effective temperature regime of  $20\,000\text{ K} \lesssim T_{\text{eff}} \lesssim 30\,000\text{ K}$  (where the Paschen lines are sufficiently strong) are selected. Their atmospheric parameters  $T_{\text{eff}}$ ,  $\log(g)$ , and  $\log n(\text{He})$  are derived in three different ways: I) via the complete spectrum (full); II) via the spectral range up to and including He I 6678 Å (blue); III) via the NIR spectral range from 7000 Å onwards (NIR). In all three cases, the hybrid LTE/NLTE model atmosphere approach and the global analysis strategy (ADS + Global) are used, whereby the mean abundances for H-sdB/H-sdOB stars according to Naslim et al. (2013) are implemented as metallicity. No metals are fitted. Table 9.3 summarizes the results of the investigations. In the following, three different aspects shall be detailed.

First, the determined statistical uncertainties of the atmospheric parameters are smallest if the full spectra are analyzed. This is simply because the number of analyzed data points (the number of hydrogen and helium lines from which  $T_{\text{eff}}$ ,  $\log g$ , and  $\log n(\text{He})$  are derived) is largest in this case. Interestingly, the uncertainties only slightly increase if the analyzed spectral range is limited to the blue. However, the uncertainties become significantly larger if only the NIR spectral range is used. Generally, this is due to the fact that the statistical uncertainties derived are linked to the S/N of the data used (see Sect. 7.1.2), which have the worst S/N in the NIR (see Tables 8.1-8.3 as well as Figs. 9.1.1 and 9.1.2). For  $\log n(\text{He})$ , however, another aspect comes into play, which is the small number of pronounced neutral helium lines available in the NIR. The only prominent NIR He I lines that are observed for hot subdwarf stars in the considered effective temperature regime are He I 7065 Å, He I 7281 Å, and He I 10830 Å. Obviously, this deficiency is reflected in the statistical errors.

Second, the results of the atmospheric parameters derived from the blue spectra are in good agreement with those derived from the full spectra. This shows once again why this wavelength regime with the hydrogen Balmer (and the He II Pickering) series as well as with numerous other He I/II lines (see Table 8.12) is so important for the analysis of hot subdwarfs.

Third, the atmospheric parameters are already quite well determined if only the NIR range is used. In fact, this shows how much impact the hydrogen Paschen series has on the determination of  $T_{\text{eff}}$ ,  $\log(g)$ , and  $\log n(\text{He})$ . Of course,  $\log n(\text{He})$  is worst determined from the NIR because of the few helium lines available in this wavelength regime. For  $T_{\text{eff}}$  and  $\log(g)$ , however, the NIR spectral range is very promising, at least for hot subdwarf stars in the appropriate effective temperature regime of  $20\,000\text{ K} \lesssim T_{\text{eff}} \lesssim 30\,000\text{ K}$ . This is excellent because many of the current (for instance, XSHOOTER and CARMENES) and future (for instance, WEAVE) spectrographs are explicitly configured for this wavelength regime. The usual analyses of blue spectra for cool H-sdBs can therefore be extended to the NIR. In the

## 9.4. Final Atmospheric Results and Projected Rotational Velocities

Object	$T_{\text{eff}}$ [K]	$\log(g[\text{cm s}^{-2}])$	$\log n(\text{He})$	Comment
HD 4539	$23\,521 \pm 14$	$5.3086 \pm 0.0014$	$-2.2398 \pm 0.0023$	full
	$23\,693^{+21}_{-13}$	$5.3013^{+0.0026}_{-0.0011}$	$-2.2370^{+0.0032}_{-0.0025}$	blue
	$23\,710^{+50}_{-40}$	$5.312 \pm 0.060$	$-2.255^{+0.106}_{-0.111}$	NIR
GALEX J104148.9-073031	$26\,208 \pm 11$	$5.6349^{+0.0015}_{-0.0018}$	$-2.3423^{+0.0035}_{-0.0023}$	full
	$26\,138 \pm 12$	$5.6371^{+0.0016}_{-0.0020}$	$-2.3434^{+0.0031}_{-0.0028}$	blue
	$26\,310^{+40}_{-80}$	$5.671^{+0.060}_{-0.050}$	$-2.396^{+0.109}_{-0.118}$	NIR
Feige 38	$29\,453^{+13}_{-23}$	$5.7236^{+0.0013}_{-0.0011}$	$-2.5154^{+0.0077}_{-0.0049}$	full
	$29\,232^{+25}_{-20}$	$5.7259^{+0.0029}_{-0.0035}$	$-2.5319^{+0.0077}_{-0.0068}$	blue
	$29\,710^{+90}_{-70}$	$5.753^{+0.032}_{-0.038}$	$-2.6054^{+0.0513}_{-0.0636}$	NIR

Table 9.3.: The atmospheric parameters of the H-sdB stars HD 4539, GALEX J104148.9-073031, and Feige 38 that are derived from the respective co-added XSHOOTER spectra in three different ways: I) via the complete spectrum (full); II) via the spectral range up to and including He I 6678 Å (blue); III) via the NIR spectral range from 7000 Å onwards (NIR). In all cases,  $1\sigma$  statistical single parameter errors are given for  $T_{\text{eff}}$ ,  $\log(g)$ , and  $\log n(\text{He})$ . All results are based on the hybrid LTE/NLTE model atmosphere approach and the global analysis strategy (ADS + Global), whereby the mean abundances for H-sdB/H-sdOB stars according to Naslim et al. (2013) are implemented as metallicity. No metals are fitted.

long run, the analyses of these stars based on blue spectra may even be replaced by the NIR. It has to be pointed out, however, that the hydrogen Paschen series is not observed for the hotter H-sdO and He-sdO stars. These stars benefit from several helium lines in the NIR (see Table 8.12 as well as Figs. 9.1.9 and 9.1.10), but a supplement by the hydrogen Balmer and He II Pickering series as well as by other He I/II lines in the blue remains indispensable. This is not least due to the fact that the line-broadening theory for He I lines in the NIR is still incomplete.

## 9.4. Final Atmospheric Results and Projected Rotational Velocities

This section shall present the final atmospheric parameters (Sect. 9.4.1) and the projected rotational velocities (Sect. 9.4.2) for the 66 program stars of this work. The vast majority of the program stars are indeed analyzed in this work, hence their final atmospheric parameters are derived from the results of the different model atmosphere approaches and analysis strategies listed in Tables A.1-A.18 and A.20-A.23, respectively. For five H-sdOs/post-AGBs only, literature values for  $T_{\text{eff}}$ ,  $\log(g)$ , and  $\log n(\text{He})$  are used (see Tables 8.11 and A.19). The final atmospheric results for the analyzed He-sdOs are based on TLUSTY/SYNSPEC + FITPROF (thus, no metals are analyzed in these cases), whereas the ones for all other program stars

(except for the aforementioned H-sdOs/post-AGBs) result from ADS + Global (+ NLTE (+ LTE) metals)<sup>111</sup>. HD 4539, Feige 38, EC 03591-3232, HD 149382, [CW83] 0512-08, and PG 0314+146 are observed multiple times such that for these objects weighted averages are defined as the final atmospheric results (see Tables A.20-A.23)<sup>112</sup>.

It shall be noted that Tables A.1-A.18 also provide different atmospheric results from literature for the individual program stars. These results are mainly based on LTE models. In consequence, deviations from the results of the present work are to be expected. However, they will not be discussed in the following subsections.

### 9.4.1. Effective Temperatures, Surface Gravities and Helium Content

Figures 9.4.1-9.4.4 show different versions of the Kiel diagram for the analyzed sample. Plotted error bars combine the  $1\sigma$  statistical single parameter errors (listed in Tables A.1-A.23) and the global systematic errors derived in Sect. 9.2.7. The atmospheric results are compared to predictions of evolutionary models for the HB/EHB and beyond (Dorman et al., 1993). The ZAHB and the TAHB are shown for a canonical mass hot subdwarf (core mass:  $0.47 M_{\odot}$ ) with solar metallicity. The displayed evolutionary tracks are all based on the same metallicity and the same core mass of  $0.47 M_{\odot}$  but vary in hydrogen-envelope masses of  $0.001 M_{\odot}$ ,  $0.003 M_{\odot}$ ,  $0.005 M_{\odot}$ ,  $0.010 M_{\odot}$ ,  $0.015 M_{\odot}$ , and  $0.020 M_{\odot}$ , respectively. In addition, two evolutionary tracks for (pre-)ELMs from Istrate et al. (2016) are displayed in Figs. 9.4.1-9.4.4. Both are based on solar metallicity and include element diffusion as well as rotational mixing. The considered ELM masses are  $0.206 M_{\odot}$  and  $0.234 M_{\odot}$ , respectively. The ZAMS and the TAMS for solar metallicity stars are also plotted (Schaller et al., 1992). Last but not least, the HeMS according to Dorman et al. (1993) is shown. Evolutionary tracks for post-AGB stars are not displayed in Figs. 9.4.1-9.4.4, however, because the vast majority of the program stars are less luminous than observed for this particular evolutionary stage (see the results of Ch. 13). The sole exceptions to this are BD+28° 4211 (see also Sect. 3.3) and the MS candidates, which will be discussed in the later course of this section.

Most of the analyzed objects (H-sdB, H-sdOB, and BHB stars) are located in the canonical BHB/EHB band. The He-sdOs lie within the  $T_{\text{eff}}\text{-}\log(g)$  regime that can be explained by the

<sup>111</sup>For program stars that are neither H-sdOs/post-AGBs nor He-sdOs, ADS + Global (+ NLTE (+ LTE) metals) as the final atmospheric result has to be interpreted as follows. Low-resolution spectra of the relevant stars are not analyzed in terms of metals. The final atmospheric results for the respective objects are therefore based on ADS + Global. Medium and high-resolution spectra (except for the ones of the XSHOOTER reference sample) of program stars that are neither H-sdOs/post-AGBs nor He-sdOs are investigated in terms of C, N, O, Ne, Mg, Al, Si, S, Ar, and Fe (all in NLTE). For these cases, the final atmospheric parameters result from ADS + Global (NLTE metals). Program stars of the XSHOOTER reference sample that are neither H-sdOs/post-AGBs nor He-sdOs are additionally analyzed in terms of P, Ca, Ti, Sr, and Zr (all in LTE). The final  $T_{\text{eff}}$ ,  $\log(g)$ , and  $\log n(\text{He})$  values derived for the relevant objects of the XSHOOTER reference sample are thus based on ADS + Global (NLTE + LTE metals).

<sup>112</sup>For HD 4539, Feige 38, EC 03591-3232, HD 149382, and [CW83] 0512-08, the final results are derived from the weighted averages of the ADS + Global (+ NLTE (+ LTE) metals) measurements. For the He-sdO PG 0314+146, however, the final values for  $T_{\text{eff}}$ ,  $\log(g)$ , and  $\log n(\text{He})$  result from the weighted averages of the corresponding TLUSTY/SYNSPEC + FITPROF measurements.

## 9.4. Final Atmospheric Results and Projected Rotational Velocities

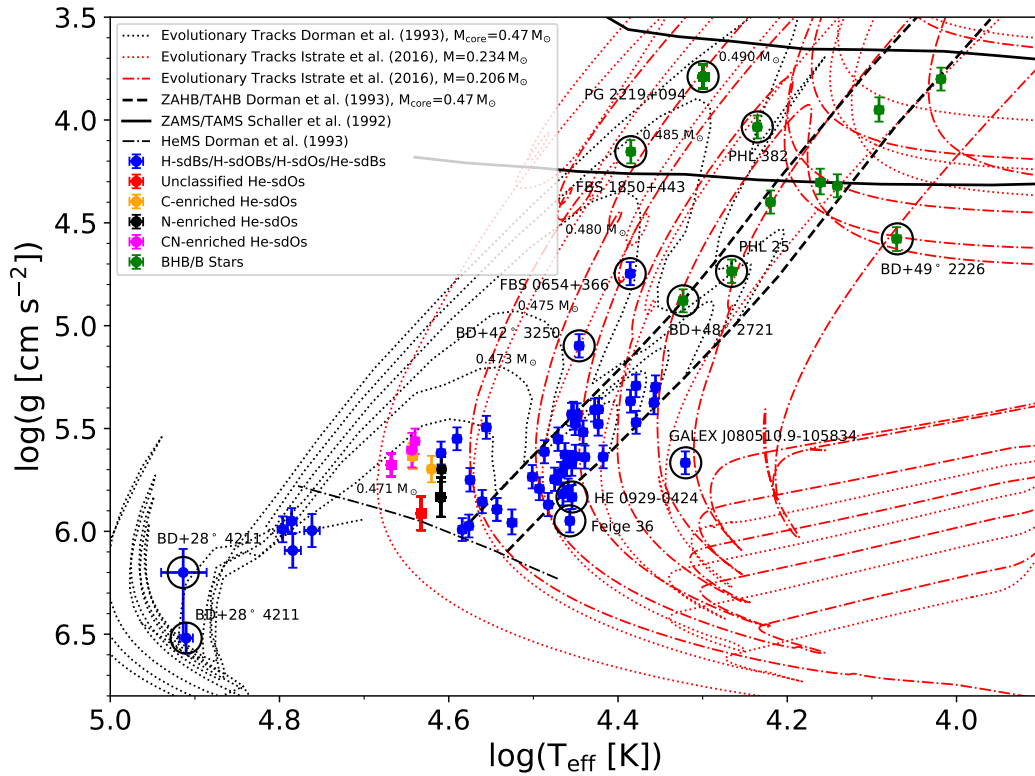


Figure 9.4.1.: Distribution of the program stars in the  $\log(T_{\text{eff}})$ - $\log(g)$  plane (Kiel diagram). Interesting objects are highlighted with solid black circles. H-sdBs/H-sdOBs/H-sdOs/He-sdBs are marked in blue, whereas green dots represent potential (post-)BHB and B-type MS stars (based on their positions, Feige 36, BD+49° 2226, and HE 0929-0424 could be pre-ELMs; see Sect. 12.2 and Ch. 13 for further information; GALEX J080510.9-105834 is a known pre-ELM; see the text for further details). In addition, the different types of He-sdOs are characterized by different colors: carbon-enriched (orange), nitrogen-enriched (black), and carbon-nitrogen-enriched (magenta). The red dot represents the newly found He-sdO FBS 0224+330, for which only a low-resolution IDS spectrum is analyzed such that an assignment to C, CN, or N-type He-sdOs is not possible. The zero-age (ZAHB) and the terminal-age horizontal branch (TAHB) for a canonical mass hot subdwarf (core mass:  $0.47 M_{\odot}$ ) with solar metallicity from Dorman et al. (1993) are plotted as dashed black lines. Evolutionary tracks from Dorman et al. (1993) for the same canonical hot subdwarf but with different hydrogen-envelope masses (in ascending order from bottom to top:  $0.001 M_{\odot}$ ,  $0.003 M_{\odot}$ ,  $0.005 M_{\odot}$ ,  $0.010 M_{\odot}$ ,  $0.015 M_{\odot}$ , and  $0.020 M_{\odot}$ ) are shown with dotted black lines. Additionally, two evolutionary tracks for a  $0.206 M_{\odot}$  and a  $0.234 M_{\odot}$  (pre-)ELM with solar metallicity (element diffusion and rotational mixing included; Istrate et al. 2016) are plotted as red dashed-dotted and red dotted lines, respectively. Note that these tracks exhibit several loops. The zero-age (ZAMS) and the terminal-age main sequence (TAMS) for solar metallicity stars from Schaller et al. (1992) are displayed with solid black lines. The helium main sequence (HeMS) according to Dorman et al. (1993) is plotted as a dashed-dotted black line. Plotted error bars combine the  $1\sigma$  statistical single parameter errors (listed in Tables A.1-A.23) and the global systematic errors derived in Sect. 9.2.7. For details on what results from Tables A.1-A.23 are plotted, see the introduction (the footnotes) of Sect. 9.4.

double HeWD merger scenario (compare Figure 16 in Zhang & Jeffery 2012 to the results of Figs. 9.4.1-9.4.4). The same is true for the iHe-sdBs [CW83] 0512-08 and [CW83] 0825+15 (see Figure 17 in Zhang & Jeffery 2012), but not for the newly found cool iHe-sdB FBS 0654+366 (see also Sect. 9.1 and Figs. 9.1.3-9.1.5). It is confirmed that the carbon-enriched He-sdOs tend to be hotter than their nitrogen-enriched siblings, as has been reported by Hirsch (2009). Several hydrogen-rich program stars lie above the canonical EHB, including BD+42° 3250, EC 01541-1409, EC 13047-3049, PG 1635+414, PG 1505+074, and FB 29. The same

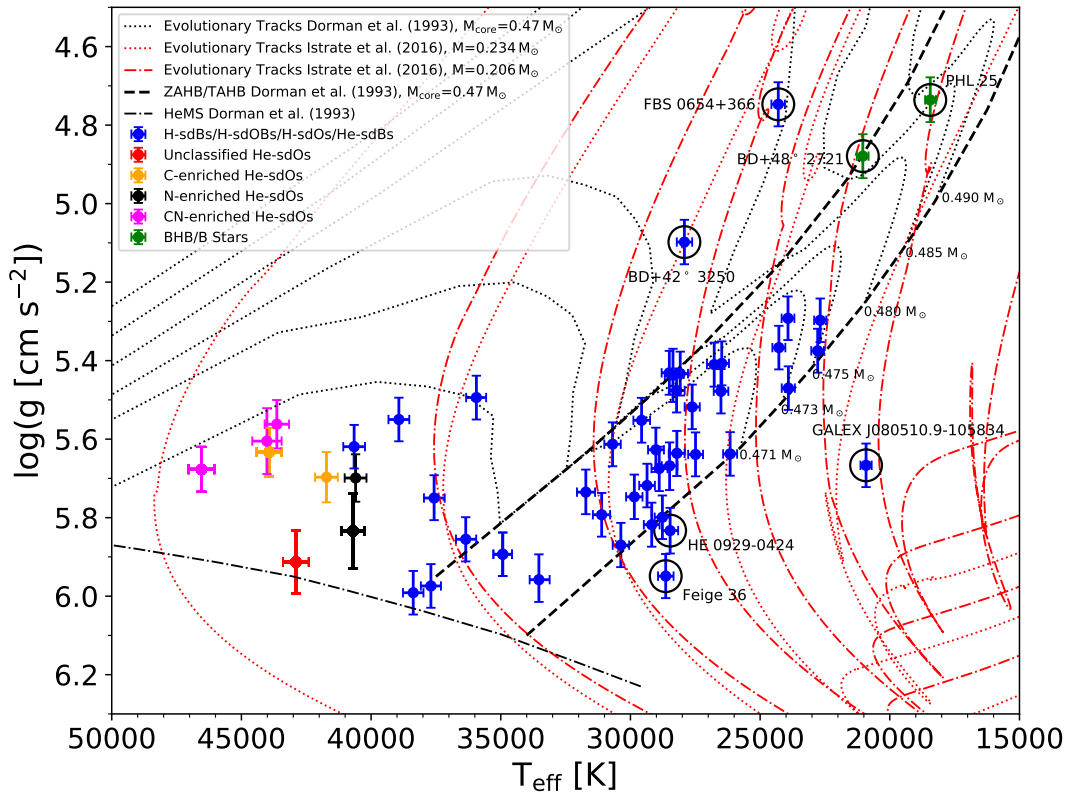


Figure 9.4.2.: Same as Fig. 9.4.1, but enlarged. Note that in comparison to Fig. 9.4.1, the abscissa is not logarithmic either.

holds for FBS 0654+366. Following the post-EHB evolutionary tracks from Dorman et al. (1993), all of these objects may have already left the core helium-burning phase. This also applies to the hot and compact H-sdOs of Table A.19 (note again that no spectra are analyzed for these stars within the framework of this thesis).

Schneider et al. (2018) found the  $^3\text{He}$  H-sdB EC 03263-6403 and PHL 382 to be located above the canonical HB. For PHL 382, this is confirmed here such that this object has most likely evolved beyond the core helium-burning phase, representing a post-BHB star<sup>113</sup>. However,

<sup>113</sup>Both an MS and a pre-ELM nature of PHL 382 can be excluded because of the fundamental stellar parameters of the star (see also Ch. 13). The final atmospheric parameters for PHL 382 derived in this work ( $T_{\text{eff}} = 17195^{+26}_{-28}$  K and  $\log g = 4.034^{+0.004}_{-0.006}$ ,  $1\sigma$  statistical errors) are close to  $T_{\text{eff}} = 17903 \pm 190$  K and  $\log(g) = 4.08 \pm 0.05$  determined by Hämmerich (2020). Apart from the post-BHB nature of PHL

#### 9.4. Final Atmospheric Results and Projected Rotational Velocities

EC 03263-6403 now has a significantly higher surface gravity (compare  $\log g = 5.21 \pm 0.02$  determined by Schneider et al. 2018 to  $\log g = 5.437^{+0.040}_{-0.038}$  derived in this work;  $1\sigma$  statistical errors in both cases) such that its position still matches the canonical EHB. In fact, the new result is in good agreement with the LTE study of Geier et al. (2013a) who determined  $\log(g) = 5.48 \pm 0.14$ . Consequently, it is very likely that EC 03263-6403 still burns helium in its core.

Furthermore, it is worthwhile to note that four program stars lie below the ZAHB: Feige

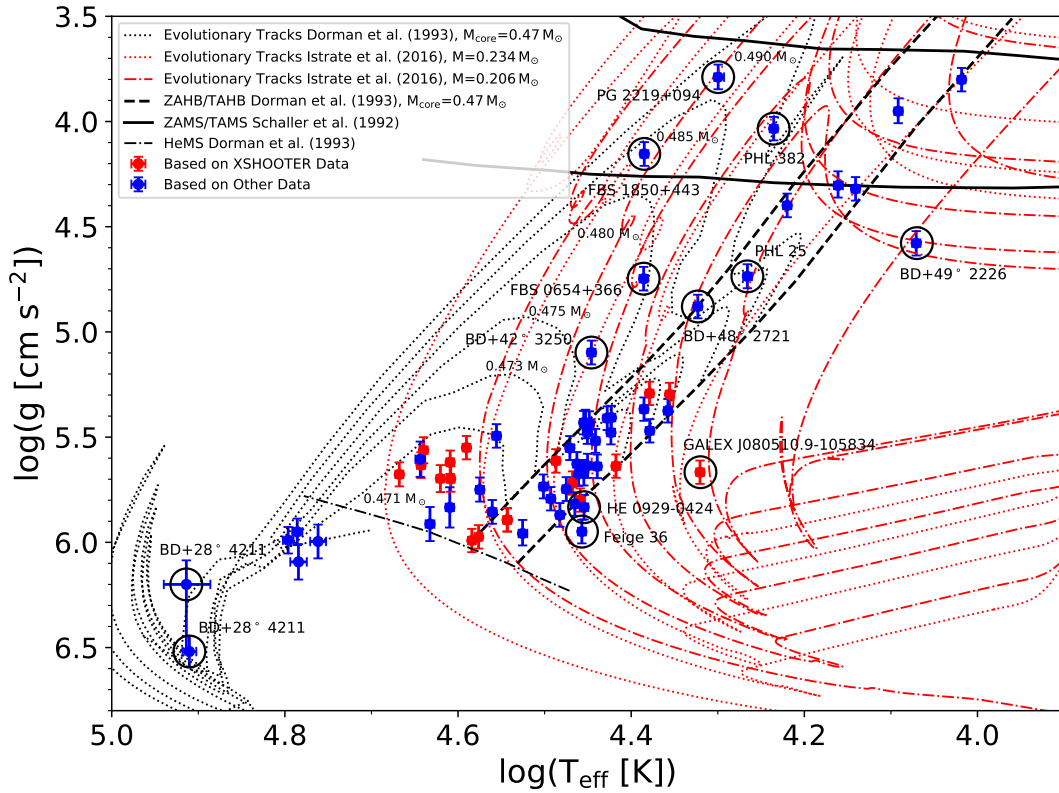


Figure 9.4.3.: Same as Fig. 9.4.1, but distinguishing between the XSHOOTER reference sample (red dots) and other program stars (blue dots).

36 at  $T_{\text{eff}} = 28\,640^{+40}_{-70}$  K and  $\log(g) = 5.949^{+0.008}_{-0.010}$ , HE 0929-0424 at  $T_{\text{eff}} = 28\,470^{+110}_{-100}$  K and  $\log(g) = 5.833^{+0.018}_{-0.017}$ , GALEX J080510.9-105834 at  $T_{\text{eff}} = 20\,915^{+10}_{-15}$  K and  $\log(g) = 5.6667^{+0.0015}_{-0.0016}$  as well as BD+49° 2226 at  $T_{\text{eff}} = 11\,770^{+40}_{-50}$  K and  $\log(g) = 4.578^{+0.020}_{-0.013}$  ( $1\sigma$  statistical errors in each case). In principle, this may be explained by a lower-than-canonical mass of the respective stars. Interestingly, the position of HE 0929-0424 still matched the canonical EHB regime in the study of Schneider et al. (2018) who determined  $T_{\text{eff}} = 29\,300 \pm 100$  K and

382, Hämmerich (2020) suggested that the star could still be a core helium-burning object, if it belonged to a helium-enhanced population (see Section 9.6 in their work). Multiple and possibly helium-enhanced populations are observed in globular clusters, but it is not yet fully understood how these populations may have formed. In any case, the atmospheric parameters derived in the present work make this also a plausible explanation for the nature of PHL 382. Nevertheless, the star is considered a post-BHB object in this work because this scenario is more natural.

$\log(g) = 5.65 \pm 0.01$  for the star. On the other hand, Feige 36 exhibited  $T_{\text{eff}} = 29\,400 \pm 100$  K and  $\log(g) = 5.97 \pm 0.01$  in the study of Schneider et al. (2018), which also located the star below the canonical EHB. From the analysis of the present work, it is rather unlikely that GALEX J080510.9-105834 and BD+49° 2226 are really related to the HB because both objects are located far away from it. However, their positions can be explained by the evolutionary tracks of Istrate et al. (2016) such that a pre-ELM nature seems reasonable for them. As a matter of fact, this has been concluded in literature for GALEX J080510.9-105834 (see the works of Vennes et al. 2011 and Kawka et al. 2015). Of course, a pre-ELM nature might

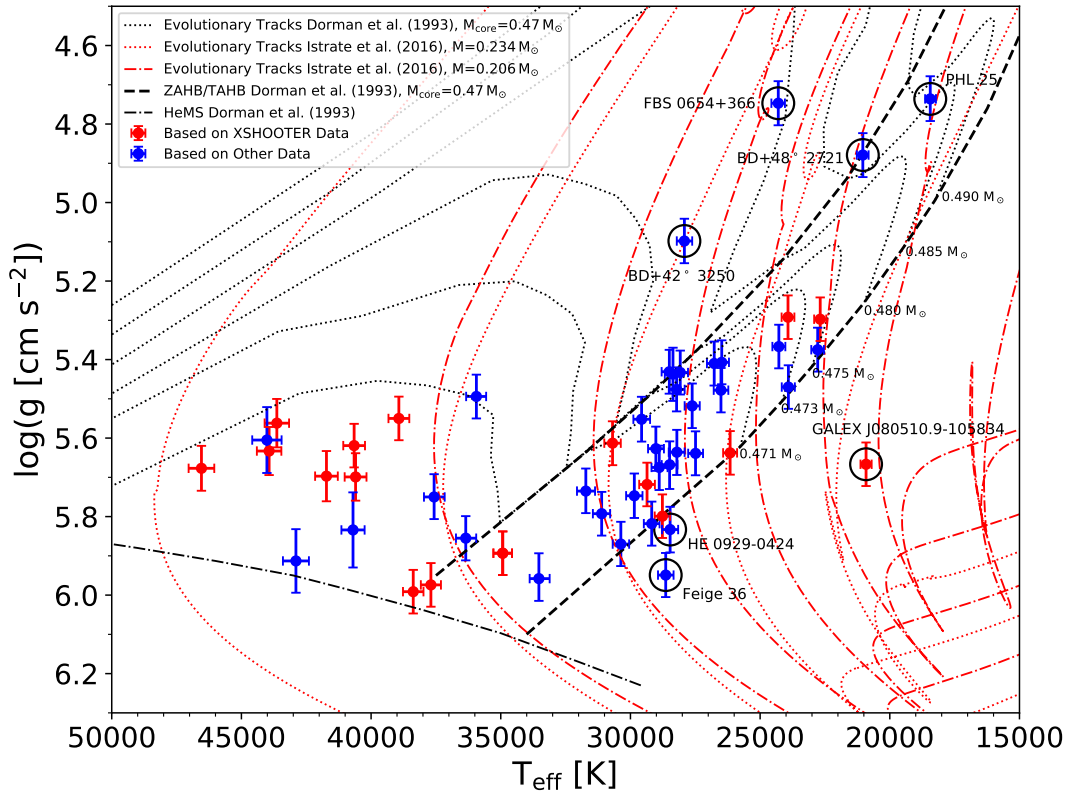


Figure 9.4.4.: Same as Fig. 9.4.2, but distinguishing between the XSHOOTER reference sample (red dots) and other program stars (blue dots).

also be a valid option for Feige 36 and HE 0929-0424. GALEX J080510.9-105834, BD+49° 2226, and HE 0929-0424 will be further discussed in Ch. 13, where their fundamental stellar parameters will be taken into account. Feige 36 is a very unique object indeed, which will be discussed in Sect. 12.2.

Another very interesting object is BD+48° 2721, which, based on the LTE results ( $T_{\text{eff}} = 24\,800 \pm 1100$  K,  $\log g = 5.38 \pm 0.14$ ) of Geier et al. (2013a), has been considered a H-sdB star for several years. However, the atmospheric parameters of  $T_{\text{eff}} = 21\,040_{-50}^{+80}$  K and  $\log(g) = 4.879_{-0.006}^{+0.009}$  ( $1\sigma$  statistical errors) derived in the present work are drastically lower, even though the same FOCES spectrum as used by Geier et al. (2013a) is analyzed. The new result barely matches the canonical HB. Yet, it is quite similar to the one determined

#### 9.4. Final Atmospheric Results and Projected Rotational Velocities

---

by Schneider et al. (2018):  $T_{\text{eff}} = 20\,700_{-200}^{+100}$  K and  $\log(g) = 4.81 \pm 0.02$ . Because of its similarity in terms of atmospheric parameters to another BHB star (PHL 25; also one of the program stars of this work), Schneider et al. (2018) suggested to consider BD+48° 2721 no longer a H-sdB star, but to rather allocate the object to the BHB. Although the similarity to PHL 25 is not as striking as before, the results of the present work can confirm this allocation. In consequence, BD+48° 2721 is listed as a BHB star in this thesis<sup>114</sup>.

Additionally, several other objects are found at the cool end of the HB or in the  $T_{\text{eff}}\text{-}\log(g)$  regime for MS stars. These objects are FBS 1850+443, HIP 67513, FBS 2158+373, FBS 2204+364, PG 2219+094, SB 395, and KUV 03591+0457. According to its atmospheric parameters, SB 395 most likely belongs to the BHB, whereas FBS 1850+443 is most likely a B-type MS star<sup>115</sup>. The latter is also true for PG 2219+094<sup>116</sup>, which is in good agreement with literature (see, for instance, the results of Ramspeck et al. 2001). For HIP 67513, FBS 2158+373, FBS 2204+364, and KUV 03591+0457, however, a clear assignment based on the atmospheric parameters alone is not possible. This will further be investigated in Ch. 13, where the fundamental stellar parameters of the respective stars will be considered. In this way, it should also be possible to clarify a potential pre-ELM nature.

Figures 9.4.5-9.4.8 show different versions of the  $T_{\text{eff}}\text{-}\log n(\text{He})$  diagram for the analyzed sample. Again, plotted error bars combine the  $1\sigma$  statistical single parameter errors (listed in Tables A.1-A.23) and the global systematic errors derived in Sect. 9.2.7.

All hydrogen-rich hot subdwarf program stars are helium-deficient compared to the solar helium abundance of  $\log n(\text{He}) = -1.07$  (Asplund et al., 2009), with the H-sdO BD+28° 4211 being the sole exception. Its helium content is about solar. As stated in Sect. 3.3, however, BD+28° 4211 may also be a post-AGB star. The bulk of the program stars exhibit helium abundances of  $-3.00 \lesssim \log n(\text{He}) \lesssim -2.00$ , which is typical for hydrogen-rich sdBs/sdOBs. In fact, the linear correlation between  $T_{\text{eff}}$  and  $\log n(\text{He})$  (see Sect. 3.2), discovered for H-sdBs/H-sdOBs by Edelman et al. (2003), is confirmed here. Moreover, the sequences described by Eqs.

<sup>114</sup>A pre-ELM nature of BD+48° 2721 and PHL 25 can be excluded because of the fundamental stellar parameters of both stars (see Ch. 13).

<sup>115</sup>For FBS 1850+443, the parallax and the proper motion based on the results of *Gaia* DR2 transfer into a transverse velocity of  $\gtrsim 600 \text{ km s}^{-1}$ . The RV derived from the analyzed CAFOS spectrum is  $\sim 30 \text{ km s}^{-1}$ . Therefore, the total space velocity of FBS 1850+443 is high enough such that the object is not bound to the Galaxy. Hence, it is highly likely that FBS 1850+443 is a runaway B star. No fundamental stellar parameters based on the *Gaia* DR2 parallax will be determined for FBS 1850+443 in Ch. 13 because the corresponding apparent fractional parallax uncertainty is above 50% (see Table 8.19) and  $d_{\text{Gaia}}$  (the *Gaia* distance) and  $d_{\text{BJ}}$  (the distance according to Bailer-Jones et al. 2018) strongly deviate from each other (see Fig. 8.4.1). Using the *Gaia* parallax as presented in Sect. 7.3 would result in a completely unreliable radius, luminosity, and mass for the star. The same applies to the fundamental stellar parameters derived from the corresponding Bailer-Jones distance, which is why in this work no radius, no luminosity, and no mass at all is determined for FBS 1850+443.

<sup>116</sup>No fundamental stellar parameters based on the *Gaia* DR2 parallax will be determined for PG 2219+094 in Ch. 13 because the corresponding apparent fractional parallax uncertainty is above 50% (see Table 8.19) and  $d_{\text{Gaia}}$  (the *Gaia* distance) and  $d_{\text{BJ}}$  (the distance according to Bailer-Jones et al. 2018) strongly deviate from each other (see Fig. 8.4.1). Using the *Gaia* parallax as presented in Sect. 7.3 would result in a completely unreliable radius, luminosity, and mass for the star. The same applies to the fundamental stellar parameters derived from the corresponding Bailer-Jones distance, which is why in this work no radius, no luminosity, and no mass at all is determined for PG 2219+094.

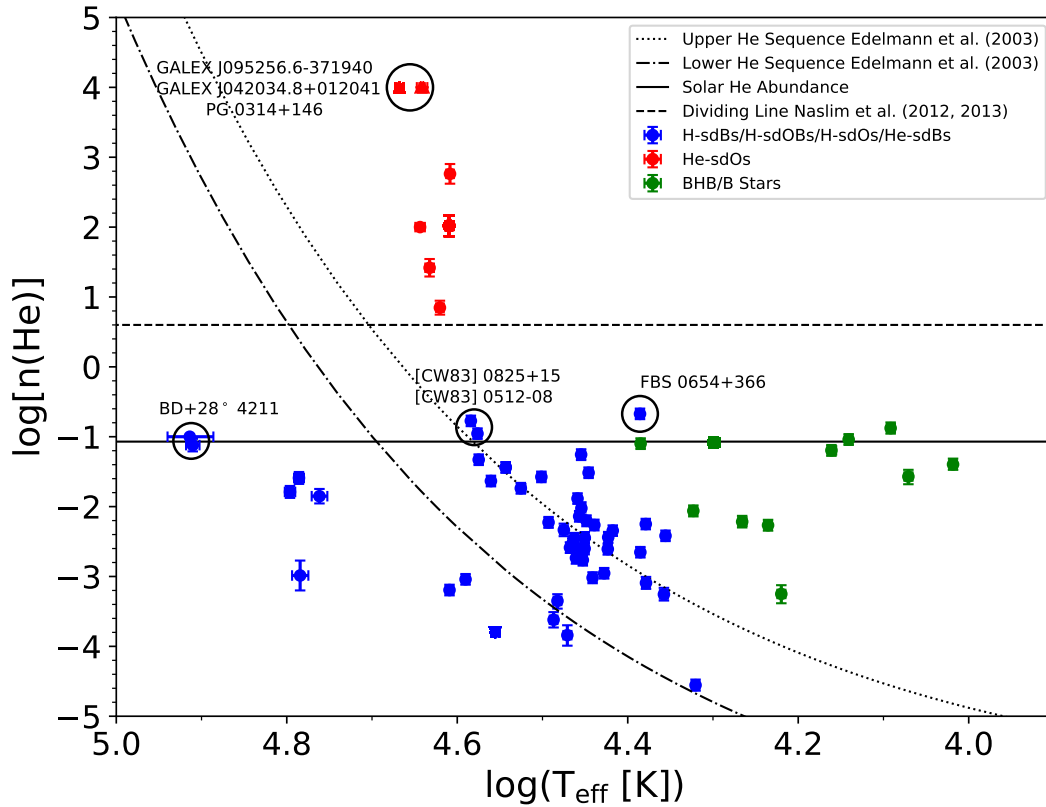


Figure 9.4.5.: Distribution of the program stars in the  $\log(T_{\text{eff}})$ - $\log n(\text{He})$  plane (helium abundance vs. effective temperature). Interesting objects are highlighted with solid black circles. H-sdBs/H-sdOBs/H-sdOs/He-sdBs are marked in blue, whereas green data points represent potential (post-)BHB and B-type MS stars. He-sdOs are characterized by red data points. Program stars with upper and lower limits on  $\log n(\text{He})$  are indicated by downward and upward triangles, respectively. The upper and lower helium sequences of Edelmann et al. (2003) are plotted as dotted and dashed-dotted lines (see Eqs. 3.4 and 3.5). The solid horizontal line marks the solar helium abundance (Asplund et al., 2009). Additionally, the dashed horizontal line marks a helium abundance of  $\log n(\text{He}) = 0.6$ . According to Naslim et al. (2012, 2013), this abundance value can be used in order to separate the intermediate from the extreme He-sdBs/He-sdOs. Plotted error bars combine the  $1\sigma$  statistical single parameter errors (listed in Tables A.1-A.23) and the global systematic errors derived in Sect. 9.2.7. For details on what results from Tables A.1-A.23 are plotted, see the introduction (the footnotes) of Sect. 9.4.

#### 9.4. Final Atmospheric Results and Projected Rotational Velocities

(3.4) and (3.5) are clearly visible in Figs. 9.4.5-9.4.8, whereby the upper helium sequence is significantly more populated than the lower one. This is also in good agreement with the results of Edelmann et al. (2003).

The iHe-sdBs [CW83] 0512-08, [CW83] 0825+15, and FBS 0654+366 have a slightly supersolar helium content. The helium abundances of the analyzed He-sdOs are even higher. In fact, all of the analyzed He-sdOs belong to the group of extreme He-sdOs and three of them (GALEX J095256.6-371940, GALEX J042034.8+012041, and PG 0314+146) even have  $\log n(\text{He}) \gtrsim 4.00$ , meaning that almost no hydrogen at all can be found in the respective stellar atmospheres.

Eventually, the cooler (post-)BHB and B-type MS candidates of the sample are not directly linked to the other program stars in the  $T_{\text{eff}}\text{-}\log n(\text{He})$  plane. For the majority of these objects (BD+49° 2226, FBS 1850+443, HIP 67513, FBS 2158+373, FBS 2204+364, PG 2219+094, and KUV 03591+0457), the measured helium content is close to that of the Sun. This points towards a B-type MS nature of the respective stars, which (except for FBS 1850+443 and PG 2219+094, for which no fundamental stellar parameters are determined in this work; see Sect. 8.4) will be further discussed in Ch. 13.

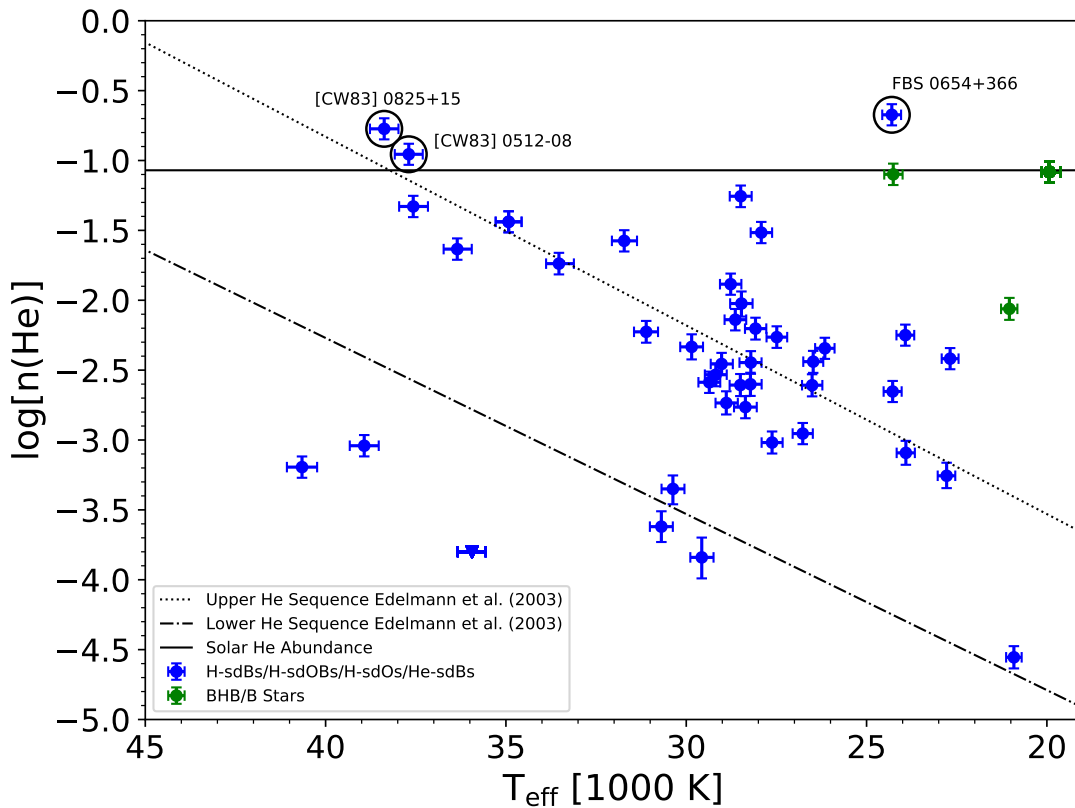


Figure 9.4.6.: Same as Fig. 9.4.5, but enlarged. Note that in comparison to Fig. 9.4.5, the abscissa is not logarithmic either.

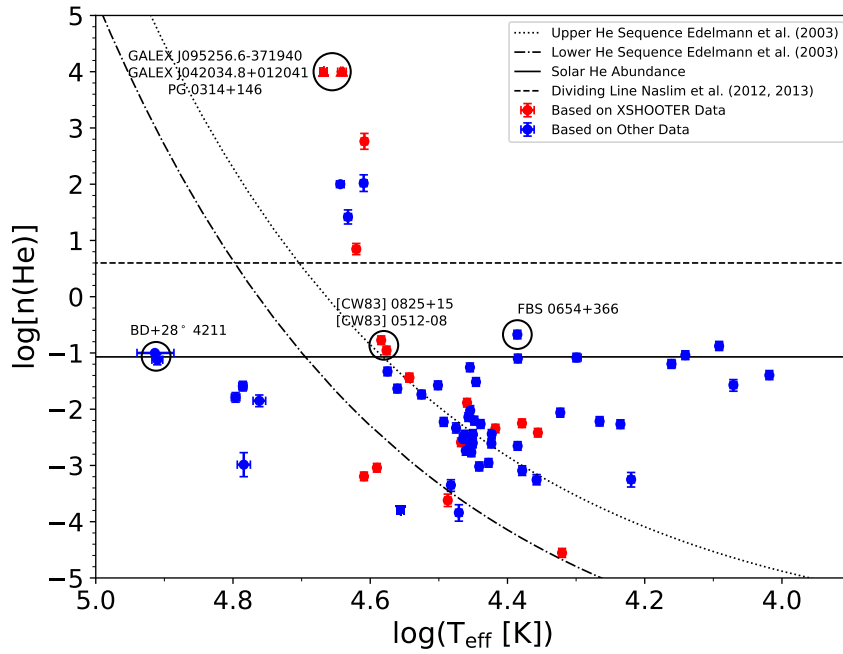


Figure 9.4.7.: Same as Fig. 9.4.5, but distinguishing between the XSHOOTER reference sample (red dots) and other program stars (blue dots).

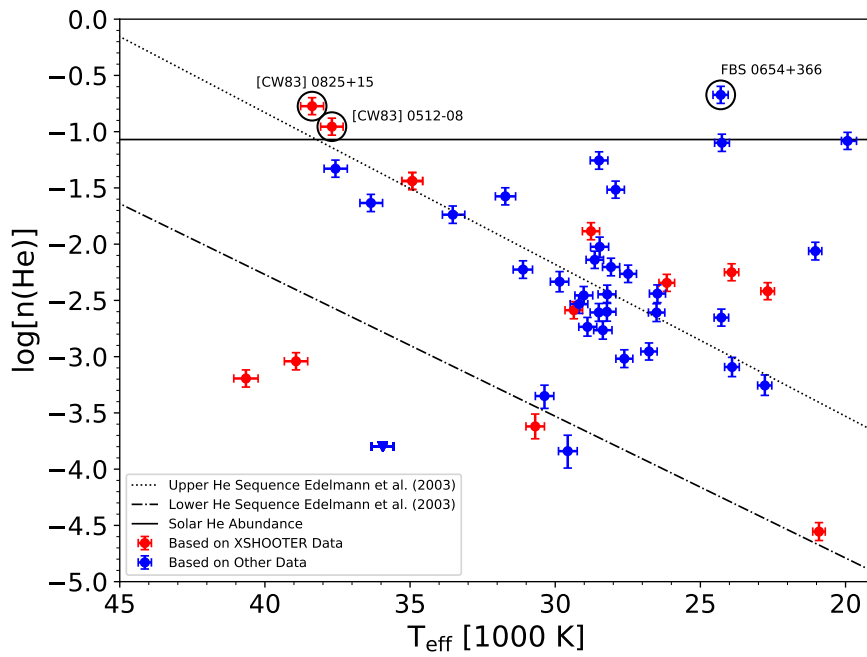


Figure 9.4.8.: Same as Fig. 9.4.6, but distinguishing between the XSHOOTER reference sample (red dots) and other program stars (blue dots).

### 9.4.2. Rotational Broadening

Due to the fact that hot subdwarf O and B stars are usually slow rotators unless they are spun up by a compact companion (see Geier et al. 2010 and Geier & Heber 2012), rotational broadening of the spectral line profiles typically lies below or near the detection limit for these stars<sup>117</sup>. For most of the hot subdwarf program stars of this work, this slow rotation is confirmed from the analysis of metal line profiles (see Ch. 11 for details on the metal abundance analysis based on the hybrid LTE/NLTE approach and the global analysis strategy). For these objects, rotation hence does not affect the modelling of the H I, He I, and He II line profiles. The sole H-sdBs that show significantly rotationally-broadened lines are GALEX J203913.4+201309, SB 290, and GALEX J080510.9-105834, whereby the latter is a known pre-ELM (see the works of Vennes et al. 2011 and Kawka et al. 2015). In addition, significant projected rotational velocities  $v \sin i$  are measured for a single He-sdO (GALEX J095256.6-371940) as well as for the following three objects of the subsample of (post-)BHB and B-type MS stars: PHL 382, PG 2219+094, and KUV 03591+0457. Furthermore, it is known from literature that the four H-sdO program stars AGK+81° 266, LS II +18° 9, Feige 67, and Feige 34 rotate. Spectra of these objects are not analyzed in this work but the spectroscopic results of Latour et al. (2018), who adopted a value of  $v \sin i = 25.0 \text{ km s}^{-1}$  for these four stars, are used. The results for  $v \sin i$  of all rotationally-broadened program stars are summarized in Table 9.4. PHL 382 and SB 290 are known rotators and will be discussed in Ch. 10 because both objects belong to the group of <sup>3</sup>He stars. PG 2219+094 is known to rapidly rotate (see, for instance, the works of Ramspeck et al. 2001 and Behr 2003) and the result of  $v \sin i = 241.9_{-3.3}^{+2.7} \text{ km s}^{-1}$  determined in this work is in good agreement with literature. The He-sdO GALEX J095256.6-371940 is only analyzed by means of the NLTE models calculated with TLUSTY/SYNSPEC (see Sect. 6.9). Thus, no metal lines are used to determine  $v \sin i$ . From the detailed modelling of the numerous helium lines available in the XSHOOTER spectrum, however, a value of  $v \sin i = 21.2 \pm 7.7 \text{ km s}^{-1}$  can be derived. In fact, this is in good agreement with the value of  $v \sin i = 22.0 \pm 3.0 \text{ km s}^{-1}$  determined by Schindewolf (2018), who could make use of isolated and sharp nitrogen lines. The fact that GALEX J080510.9-105834, GALEX J203913.4+201309, and KUV 03591+0457 rotate is a new discovery. GALEX J080510.9-105834 shows a moderate  $v \sin i$  of  $13.5_{-1.0}^{+0.8} \text{ km s}^{-1}$ , whereas the projected rotational velocities of GALEX J203913.4+201309 ( $v \sin i = 142.0_{-11.0}^{+9.0} \text{ km s}^{-1}$ ) and KUV 03591+0457 ( $v \sin i = 231.0 \pm 6.0 \text{ km s}^{-1}$ ) are strikingly high.

The high projected rotational velocity measured for the H-sdB GALEX J203913.4+201309 truly is remarkable. The star even rotates significantly faster than EVR-CB-004 ( $v \sin i = 116.5 \pm 8.1 \text{ km s}^{-1}$ ), which is most likely one of the rare objects that could be observed in the post-BHB evolutionary phase (Ratzloff et al., 2020). Up to now, the only two hot subdwarfs, for which even higher values of  $v \sin i$  than measured for GALEX J203913.4+201309 have been derived, are ZTF J2130+4420 ( $v \sin i = 238 \pm 15 \text{ km s}^{-1}$ ) and ZTF J2055+4651 ( $v \sin i = 201 \pm 30 \text{ km s}^{-1}$ ). Both objects belong to the relatively new class of short-period hot subdwarf stars that have filled their Roche lobes and started mass transfer onto a WD companion

<sup>117</sup>The detection limit depends on the spectral resolution element of the instrumental profile and is typically of the order of  $\sim 5\text{-}8 \text{ km s}^{-1}$ , if high-resolution spectrographs such as FEROS are used.

Object	Nature	$v \sin i$ [km s <sup>-1</sup> ]	Reference
GALEX J080510.9-105834	H-sdB/pre-ELM	13.5 <sup>+0.8</sup> <sub>-1.0</sub>	This work
GALEX J203913.4+201309	H-sdB	142.0 <sup>+9.0</sup> <sub>-11.0</sub>	This work
SB 290	H-sdB	49.4 ± 0.1	This work
AGK+81° 266	H-sdO	25.0 (fixed)	Latour et al. (2018)
LS II +18° 9	H-sdO	25.0 (fixed)	Latour et al. (2018)
Feige 67	H-sdO	25.0 (fixed)	Latour et al. (2018)
Feige 34	H-sdO	25.0 (fixed)	Latour et al. (2018)
GALEX J095256.6-371940	He-sdO	21.2 ± 7.7	This work
PHL 382	post-BHB	13.4 ± 0.1	This work
PG 2219+094	B MS	241.9 <sup>+2.7</sup> <sub>-3.3</sub>	This work
KUV 03591+0457	B MS	231.0 ± 6.0	This work

Table 9.4.: Program stars with significant projected rotational velocities. In all cases,  $1\sigma$  statistical single parameter errors are given.

(Kupfer et al., 2020a,b).

From low-resolution data, Németh et al. (2012) measured a RV above 100 km s<sup>-1</sup> with respect to the kinematic local standard of rest for GALEX J203913.4+201309. However, a long-term RV study for the object is still missing (the present work can also only make use of a single IDS spectrum for which a RV in the regime of 100 km s<sup>-1</sup> is measured; see also Table 8.9). Nonetheless, the large RV measured by Németh et al. (2012) is a hint for a possible companion, which could explain the star’s high rotation from an evolutionary point of view, that is, by tidal interaction<sup>118</sup>. GALEX J203913.4+201309 does not show any signs of an IR excess such that an SB2 system with a cool or giant star companion can be excluded (see the photometric results of Ch. 12). However, the possibility of a single-lined SB1 system with a WD companion still remains. GALEX J203913.4+201309 could also have been formed from a double HeWD merger, which is also able to explain the high rotational velocity. But then the question arises why the star is hydrogen and not helium-rich because double HeWD mergers are believed to produce mainly helium-rich objects (see Sect. 3.4.2). Moreover, GALEX J203913.4+201309 then must have been a triple system if the current binary hypothesis is indeed true.

KUV 03591+0457 does not show any evidence for binarity. No IR excess is observed in the SED (see Ch. 12), the RV determined from the analyzed IDS spectrum is not striking, and, as in the case of GALEX J203913.4+201309, the object also lacks a long-term RV study. Hence, the most plausible explanation for KUV 03591+0457 is that of a young massive B-type MS star because in this case binarity is not required in order to produce such a high observed projected rotational velocity. A potential B-type MS nature would also be in good agreement

<sup>118</sup>As shown by Geier et al. (2010), this would require the orbital period to be less than 1.2 d.

#### 9.4. Final Atmospheric Results and Projected Rotational Velocities

---

with the measured helium content of the star (see Sect. 9.4.1)<sup>119</sup>. In the rather unlikely case that KUV 03591+0457 is a BHB star after all, the high rotation would be very unusual as BHB stars are not known to rotate at such high velocities (Geier & Heber, 2012).

---

<sup>119</sup>As a matter of fact, the B-type MS hypothesis for KUV 03591+0457 is supported by the fundamental stellar parameters of the star (see Ch. 13).



## 10. Spectroscopic Analysis of the $^3\text{He}$ Anomaly Based on the Hybrid LTE/NLTE Approach

This chapter presents the results of the spectroscopic analysis of the  $^3\text{He}$  anomaly. The  $^3\text{He}$  program stars that are analyzed in terms of  $^3\text{He}$  in this work are PHL 25, PHL 382, BD+48° 2721, EC 03263-6403, EC 03591-3232, EC 12234-2607, EC 14338-1445, Feige 38, PG 1710+490, SB 290, Feige 36, HE 0929-0424, and HE 1047-0436<sup>120</sup>. The latter two are new discoveries that are explicitly discussed in Sect. 10.2.2. As in the previous  $^3\text{He}$  study of Schneider et al. (2018), all results presented in this chapter are based on the hybrid LTE/NLTE model atmosphere approach and the global analysis strategy (ADS + Global; see Sects. 6.8 and 7.1.2), whereby the mean metal abundances for H-sdB/H-sdOB stars according to Naslim et al. (2013) are implemented as metallicity (see Fig. 3.3.2 and Table 3.1). All model spectra used are calculated based on a detailed  $^3\text{He}$  model atom that has been successfully applied before by Maza et al. (2014a) or Schneider et al. (2018). In addition to hydrogen and helium, the calculated synthetic spectra include dozens of spectral lines associated with various different metals (see Table 6.3) that are used to measure the radial as well as the projected rotational velocities of the respective program stars very accurately. In particular, the RV has to be determined very accurately because it strongly affects the measured isotopic line shifts (see Sect. 3.3) and, hence, the abundance ratio  $n(^4\text{He})/n(^3\text{He})$  derived. As presented in Sects. 3.3 and 7.1.1 (see also Fig. 7.1.2), the modelling of two lines (He I 6678 Å due to its strong isotopic shift of  $\Delta\lambda \sim 0.50$  Å and He I 5875 Å because it can be used as a reference line) is particularly important for the spectroscopic analysis of  $^3\text{He}$  stars. As first shown by Auer & Mihalas (1973), these two lines are considerably strengthened by departures from LTE (see also Sect. 6.4). This can be seen in Fig. 10.0.1, which shows a comparison between model spectra calculated in LTE and NLTE for the He I 6678 Å line<sup>121</sup>. Hence, the hybrid LTE/NLTE approach is perfectly suited for a sophisticated NLTE analysis of the  $^3\text{He}$  anomaly observed for the relevant program stars of this work. This approach solves the structural equations in LTE, which is sufficient for the  $^3\text{He}$  program stars of this work because the atmospheric temperature-density stratification for the optical depths that are relevant for the formation of the observable line spectra and continua is only marginally affected by departures from LTE in the case of these stars (see Sects. 6.4 and 6.8). Subsequently, however, the hybrid approach is able to derive the occupation numbers of the individual atomic energy levels from statistical

<sup>120</sup>For these stars, medium or high-resolution spectra can be investigated (see Tables 8.1, 8.2, 8.4, 8.5, and 8.6). The  $^3\text{He}$  program star PG 0133+114 is not analyzed in terms of  $^3\text{He}$  in this work because no medium or high-resolution spectra are used for this object. Only a low-resolution IDS spectrum is investigated (see Table 8.10).

<sup>121</sup>Figure 10.0.1 also illustrates the impact of different Stark broadening tables on the modelled line profile of He I 6678 Å.

## 10. Spectroscopic Analysis of the $^3\text{He}$ Anomaly Based on the Hybrid LTE/NLTE Approach

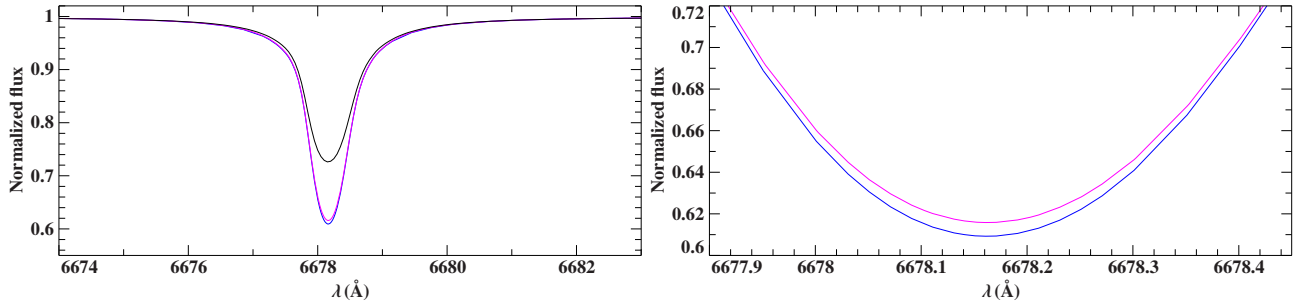


Figure 10.0.1.: *Left-hand panel*: Model spectra for He I 6678 Å calculated in LTE (solid black line) and NLTE (solid magenta and blue lines) for  $T_{\text{eff}} = 28\,000\text{ K}$ ,  $\log(g) = 5.60$ , and  $\log n(\text{He}) = -2.00$  (no  $^3\text{He}$  is synthesized). While the magenta model is based on “old” Stark broadening tables for hydrogen and He I from Dimitrijevic & Sahal-Brechot (1990), the blue model uses “new” broadening tables from Beauchamp et al. (1997). *Right-hand panel*: Same as the left-hand panel, but enlarged. The difference between the “old” (magenta line) and the “new” (blue line) model is marginal but relevant when it comes to a sophisticated determination of the isotopic helium abundances  $\log n(^4\text{He})$  and  $\log n(^3\text{He})$  as well as of the isotopic abundance ratio  $n(^4\text{He})/n(^3\text{He})$ . Modified version of Figure 1 in Schneider et al. (2018).

equilibrium, thus accounting for line strengthening due to NLTE effects. As presented in Sect. 6.8, the  $^3\text{He}$  and  $^4\text{He}$  isotopes are treated simultaneously during the solution of the statistical equilibrium and radiative transfer equations because all of their spectral lines overlap.

### 10.1. Atmospheric Parameters and Projected Rotational Velocities

The determined atmospheric parameters for the  $^3\text{He}$  program stars, for which medium or high-resolution spectra are analyzed in this work, are listed in Tables 10.1 and 10.2. Therein,  $1\sigma$  single parameter errors derived from  $\chi^2$ -statistics (see Sect. 7.1.2) are given for  $T_{\text{eff}}$ ,  $\log(g)$ ,  $\log n(^4\text{He})$ , and  $\log n(^3\text{He})$ . The listed uncertainties on the total helium abundances  $\log n(\text{He}) := \log n(^4\text{He} + ^3\text{He})$  as well as on the isotopic abundance ratios  $n(^4\text{He})/n(^3\text{He})$  result from the given statistical errors on  $\log n(^4\text{He})$  and  $\log n(^3\text{He})$ , whereby Gaussian error propagation is used. The global systematic errors of  $T_{\text{eff}}$ ,  $\log(g)$ , and  $\log n(\text{He})$  are given in Sect. 9.2.7 and the ones of  $\log n(^4\text{He})$  and  $\log n(^3\text{He})$  are considered equal to that of  $\log n(\text{He})$ . In the case of the two  $^3\text{He}$  program stars EC 03591-3232 and Feige 38, multiple spectra are analyzed. Thus, the adopted atmospheric parameter values for these two objects represent weighted averages, whereby the reciprocals of the individual maximum variances, that is  $\frac{1}{(\max[\text{uncertainty}])^2}$ , are used as weights.

Table 10.1.: Effective temperatures  $T_{\text{eff}}$ , surface gravities  $\log(g)$ , and (isotopic) helium abundances  $\log n(^4\text{He})$ ,  $\log n(^3\text{He})$ , and  $\log n(\text{He}) := \log n(^4\text{He} + ^3\text{He})$  of the  $^3\text{He}$  program stars, for which medium or high-resolution spectra are analyzed. Isotopic abundance ratios  $n(^4\text{He})/n(^3\text{He})$  are also given. All results are based on the hybrid LTE/NLTE model atmosphere approach and the global analysis strategy (ADS + Global). The results of this work are compared to the ones of Schneider et al. (2018).

Object	Instrument	$T_{\text{eff}}$ [K]	$\log(g[\text{cm s}^{-2}])$	$\log n(^4\text{He})$	$\log n(^3\text{He})$	$\log n(\text{He})$	$\frac{n(^4\text{He})}{n(^3\text{He})}$	Ref.
PHL 25 <sup>a</sup>	HRS	$18\,440^{+60}_{-110}$	$4.736^{+0.010}_{-0.016}$	$-2.525^{+0.053}_{-0.042}$	$-2.51 \pm 0.05$	$-2.2164^{+0.0365}_{-0.0328}$	$0.97^{+0.17}_{-0.15}$	This work [1]
		$19\,500 \pm 100$	$4.77^{+0.01}_{-0.02}$	$-2.75 \pm 0.03$	$-2.69 \pm 0.03$	$-2.42 \pm 0.03$	$0.87 \pm 0.09$	
PHL 382 <sup>a,b</sup>	FEROS	$17\,195^{+26}_{-28}$	$4.034^{+0.004}_{-0.006}$	$-2.66 \pm 0.04$	$-2.492^{+0.018}_{-0.014}$	$-2.2669^{+0.0195}_{-0.0183}$	$0.68 \pm 0.07$	This work [1]
		$17\,600 \pm 100$	$3.92 \pm 0.01$	$-3.25 \pm 0.05$	$-2.63 \pm 0.02$	$-2.54 \pm 0.02$	$0.240 \pm 0.030$	
BD+48° 2721 <sup>a</sup>	FOCES	$21\,040^{+80}_{-50}$	$4.879^{+0.009}_{-0.006}$	$-2.75^{+0.06}_{-0.09}$	$-2.161^{+0.021}_{-0.018}$	$-2.0614^{+0.0208}_{-0.0234}$	$0.26^{+0.04}_{-0.06}$	This work [1]
		$20\,700^{+100}_{-200}$	$4.81 \pm 0.02$	$-3.34^{+0.09}_{-0.11}$	$-2.57^{+0.09}_{-0.11}$	$-2.51^{+0.08}_{-0.10}$	$0.17^{+0.05}_{-0.07}$	
EC 03263-6403	FEROS	$28\,360 \pm 120$	$5.437^{+0.040}_{-0.038}$	$-4.121^{+0.180}_{-0.334}$	$-2.784^{+0.022}_{-0.023}$	$-2.7645^{+0.0225}_{-0.0265}$	$0.046^{+0.020}_{-0.040}$	This work [1]
		$29\,000 \pm 200$	$5.21 \pm 0.02$	$-4.75^{+0.29}_{-0.32}$	$-2.85^{+0.03}_{-0.02}$	$-2.84 \pm 0.03$	$0.013^{+0.009}_{-0.010}$	
EC 03591-3232 <sup>a</sup>	XSHOOTER	$28\,757^{+15}_{-24}$	$5.8027^{+0.0020}_{-0.0017}$	$-3.01^{+0.05}_{-0.08}$	$-1.904^{+0.007}_{-0.006}$	$-1.8712^{+0.0075}_{-0.0081}$	$0.078^{+0.010}_{-0.015}$	This work
	FEROS	$28\,800 \pm 40$	$5.766^{+0.006}_{-0.005}$	$-2.363 \pm 0.030$	$-2.146 \pm 0.018$	$-1.9401 \pm 0.0160$	$0.61 \pm 0.05$	This work
Weighted average for EC 03591-3232		$28\,768 \pm 21$	$5.7990 \pm 0.0019$	$-2.443 \pm 0.029$	$-1.936 \pm 0.007$	$-1.885 \pm 0.008$	$0.122 \pm 0.015$	This work [1]
		$28\,700 \pm 100$	$5.61 \pm 0.01$	$-3.51^{+0.14}_{-0.19}$	$-2.11 \pm 0.01$	$-2.09 \pm 0.02$	$0.040^{+0.013}_{-0.018}$	

**Notes:** For the results of this work,  $1\sigma$  single parameter errors derived from  $\chi^2$ -statistics are given for  $T_{\text{eff}}$ ,  $\log(g)$ ,  $\log n(^4\text{He})$ , and  $\log n(^3\text{He})$  (see Sect. 7.1.2). The listed uncertainties on  $\log n(\text{He})$  as well as on  $n(^4\text{He})/n(^3\text{He})$  result from the given statistical errors on  $\log n(^4\text{He})$  and  $\log n(^3\text{He})$ , whereby Gaussian error propagation is used. The global systematic errors of  $T_{\text{eff}}$ ,  $\log(g)$ , and  $\log n(\text{He})$  are given in Sect. 9.2.7 and the ones of  $\log n(^4\text{He})$  and  $\log n(^3\text{He})$  are considered equal to that of  $\log n(\text{He})$ . In order to calculate the listed weighted averages, the reciprocals of the individual maximum variances, that is  $\frac{1}{(\max[\text{uncertainty}])^2}$ , are used as weights.

(a) Anomalous helium line profiles (see Sect. 10.2.3). Therefore, the isotopic helium abundances  $\log n(^4\text{He})$  and  $\log n(^3\text{He})$ , the total helium abundance  $\log n(\text{He})$ , and the isotopic abundance ratio  $n(^4\text{He})/n(^3\text{He})$  are uncertain, as indicated by colons.

(b) Rotating star.

(c) The star is most likely a pre-ELM. For further information, see Sect. 12.2.

(d) RV-variable star.

**References:** (1) Schneider et al. (2018).

Table 10.2.: Table 10.1 continued.

Object	Instrument	$T_{\text{eff}}$ [K]	$\log(g[\text{cm s}^{-2}])$	$\log n(^4\text{He})$	$\log n(^3\text{He})$	$\log n(\text{He})$	$\frac{n(^4\text{He})}{n(^3\text{He})}$	Ref.
EC 12234-2607 <sup>a</sup>	FEROS	$28\,490 \pm 80$	$5.668^{+0.027}_{-0.022}$	$-1.442^{+0.012}_{-0.016}$	$-1.71373^{+0.15038}_{-0.20251}$	$-1.2559^{+0.0530}_{-0.0714}$	$1.9^{+0.7}_{-0.9}$	This work
		$28\,900 \pm 100$	$5.62 \pm 0.02$	$-1.65^{+0.03}_{-0.02}$	$-2.14 \pm 0.05$	$-1.53^{+0.03}_{-0.02}$	$3.1^{+0.5}_{-0.4}$	[1]
EC 14338-1445	FEROS	$27\,620^{+60}_{-70}$	$5.518^{+0.011}_{-0.013}$	$-3.89^{+0.05}_{-0.06}$	$-3.081^{+0.027}_{-0.023}$	$-3.0183^{+0.0244}_{-0.0215}$	$0.155^{+0.021}_{-0.023}$	This work
		$27\,900 \pm 100$	$5.46^{+0.01}_{-0.02}$	$-3.75^{+0.07}_{-0.08}$	$-3.10 \pm 0.03$	$-3.01 \pm 0.03$	$0.22^{+0.04}_{-0.05}$	[1]
Feige 38	XSHOOTER	$29\,214^{+25}_{-15}$	$5.7377^{+0.0026}_{-0.0029}$	$-3.37^{+0.08}_{-0.19}$	$-2.640^{+0.032}_{-0.016}$	$-2.5658^{+0.0298}_{-0.0328}$	$0.19^{+0.04}_{-0.09}$	This work
	FEROS	$29\,557 \pm 29$	$5.660 \pm 0.005$	$-3.596^{+0.062}_{-0.059}$	$-2.635^{+0.009}_{-0.011}$	$-2.5899^{+0.0102}_{-0.0115}$	$0.109 \pm 0.016$	This work
Weighted average for Feige 38		$29\,360 \pm 19$	$5.7182 \pm 0.0026$	$-3.574 \pm 0.059$	$-2.636 \pm 0.011$	$-2.587 \pm 0.011$	$0.111 \pm 0.016$	This work
		$28\,200 \pm 100$	$5.61 \pm 0.01$	$-3.48^{+0.08}_{-0.11}$	$-2.78 \pm 0.02$	$-2.70 \pm 0.03$	$0.20^{+0.04}_{-0.06}$	[1]
PG 1710+490	FOCES	$29\,180^{+50}_{-40}$	$5.818^{+0.008}_{-0.009}$	$-3.440^{+0.107}_{-0.114}$	$-2.590^{+0.023}_{-0.036}$	$-2.5326^{+0.0242}_{-0.0346}$	$0.14 \pm 0.04$	This work
		$29\,200 \pm 100$	$5.72 \pm 0.02$	$-3.67^{+0.05}_{-0.04}$	$-2.70 \pm 0.01$	$-2.66^{+0.02}_{-0.01}$	$0.107^{+0.013}_{-0.011}$	[1]
SB 290 <sup>ab</sup>	FEROS	$26\,480^{+40}_{-60}$	$5.407^{+0.007}_{-0.008}$	$-4.20^{+0.46}_{-0.29}$	$-2.447^{+0.014}_{-0.016}$	$-2.4394^{+0.0160}_{-0.0166}$	$0.018^{+0.019}_{-0.012}$	This work
		$26\,600 \pm 100$	$5.42 \pm 0.01$	$-3.73^{+0.12}_{-0.11}$	$-2.73 \pm 0.02$	$-2.69 \pm 0.03$	$0.100^{+0.029}_{-0.026}$	[1]
Feige 36 <sup>cd</sup>	HIRES	$28\,640^{+40}_{-70}$	$5.949^{+0.008}_{-0.010}$	$-2.450^{+0.014}_{-0.015}$	$-2.4305^{+0.0320}_{-0.0322}$	$-2.1391^{+0.0178}_{-0.0181}$	$0.96 \pm 0.08$	This work
		$29\,400 \pm 100$	$5.97 \pm 0.01$	$-2.49^{+0.04}_{-0.06}$	$-2.48^{+0.04}_{-0.06}$	$-2.18^{+0.03}_{-0.05}$	$0.98^{+0.13}_{-0.20}$	[1]
HE 0929-0424 <sup>d</sup>	UVES	$28\,470^{+110}_{-100}$	$5.833^{+0.018}_{-0.017}$	$-2.101^{+0.039}_{-0.044}$	$-2.81^{+0.16}_{-0.25}$	$-2.0235^{+0.0419}_{-0.0551}$	$5.1^{+2.0}_{-3.0}$	This work
		$29\,300 \pm 100$	$5.65 \pm 0.01$	$-2.10 \pm 0.03$	$-2.50 \pm 0.06$	$-1.95 \pm 0.03$	$2.5 \pm 0.4$	[1]
HE 1047-0436 <sup>d</sup>	UVES	$29\,850^{+80}_{-70}$	$5.747^{+0.011}_{-0.012}$	$-2.650^{+0.054}_{-0.077}$	$-2.62^{+0.08}_{-0.06}$	$-2.3337^{+0.0490}_{-0.0485}$	$0.93 \pm 0.21$	This work
		$29\,800 \pm 100$	$5.65 \pm 0.01$	$-2.76 \pm 0.04$	$-2.72 \pm 0.03$	$-2.44 \pm 0.03$	$0.91 \pm 0.11$	[1]

In the following, the atmospheric parameters derived for the  ${}^3\text{He}$  program stars, for which medium or high-resolution spectra are analyzed, shall be discussed in detail, whereby the focus is on  $T_{\text{eff}}$ ,  $\log(g)$ , and  $\log n(\text{He})$ <sup>122</sup>. In this context, the results of this work shall also be compared to the ones of the  ${}^3\text{He}$  study of Schneider et al. (2018), who also chose the hybrid LTE/NLTE approach and the global analysis strategy (ADS + Global) and, for most of the analyzed objects, also used the same observed spectra as the present work. As described in Sects. 6.8 and 7.1.2, however, small improvements and differences have been implemented into the respective models and analysis procedures since then (for instance, level dissolution or the local normalization procedure). These features could not be used by Schneider et al. (2018), which makes a reanalysis of the relevant objects as well as a comparison worthwhile.

### 10.1.1. Effective Temperatures, Surface Gravities and Helium Content

As for the other program stars investigated in this work (see Ch. 9), the statistical uncertainties of the atmospheric parameters derived for the  ${}^3\text{He}$  stars are small. The error budget is dominated by the systematic uncertainties derived in Sect. 9.2.7. The analyzed  ${}^3\text{He}$  stars are helium-deficient compared to the solar helium abundance of  $-1.07$  (Asplund et al., 2009) and most of them show typical total helium abundances of  $-3.00 \lesssim \log n(\text{He}) \lesssim -2.00$ . However, there are two notable exceptions (EC 03591-3232 and EC 12234-2607) that have  $\log n(\text{He}) > -2.00$ .

Figure 10.1.1 shows the  $T_{\text{eff}}\text{-}\log(g)$  diagram for the analyzed  ${}^3\text{He}$  stars. Plotted error bars combine the  $1\sigma$  statistical single parameter errors (listed in Tables 10.1 and 10.2) and the global systematic errors derived in Sect. 9.2.7.

Most importantly, all analyzed  ${}^3\text{He}$  H-sdBs cluster in a narrow temperature strip between  $\sim 26\,000\text{ K}$  and  $\sim 30\,000\text{ K}$ , very similar to what has been reported previously (Geier et al. 2013a and Schneider et al. 2018; see Sect. 3.3). Moreover, many of the  ${}^3\text{He}$  stars lie within the HB band, as expected. The only outliers are PHL 382, Feige 36, and HE 0929-0424. Further interesting objects are BD+48° 2721 and EC 03263-6403. All of them have already been discussed in Sect. 9.4.1.

When comparing the results of this work to the ones of Schneider et al. (2018) in great detail, it becomes evident that the improved models and more sophisticated analysis procedures have affected the atmospheric parameters of the  ${}^3\text{He}$  stars quite a lot because the deviations are striking (see Tables 10.1 and 10.2). In terms of the effective temperature  $T_{\text{eff}}$ , the most significant deviations are measured for PHL 25 (now  $\sim 1100\text{ K}$  cooler), EC 03263-6403 (now  $\sim 600\text{ K}$  cooler), Feige 38 (now  $\sim 1200\text{ K}$  hotter), Feige 36 (now  $\sim 800\text{ K}$  cooler), and HE 0929-0424 (now  $\sim 800\text{ K}$  cooler). Furthermore, the following stars are heavily affected in terms of the surface gravity  $\log(g)$ : EC 03263-6403 and EC 03591-3232 (both now  $\sim 0.20$  dex higher) as well as HE 0929-0424 (now  $\sim 0.18$  dex higher). However, the deviations are most evident for the determined total helium abundances  $\log n(\text{He})$  because several  ${}^3\text{He}$  stars are now significantly more abundant in helium: PHL 25 (by  $\sim +0.20$  dex), PHL 382 (by  $\sim +0.27$  dex), BD+48°

<sup>122</sup>The results for  $\log n({}^4\text{He})$ ,  $\log n({}^3\text{He})$ , and  $n({}^4\text{He})/n({}^3\text{He})$  will be discussed in Sect. 10.2.

## 10. Spectroscopic Analysis of the $^3\text{He}$ Anomaly Based on the Hybrid LTE/NLTE Approach

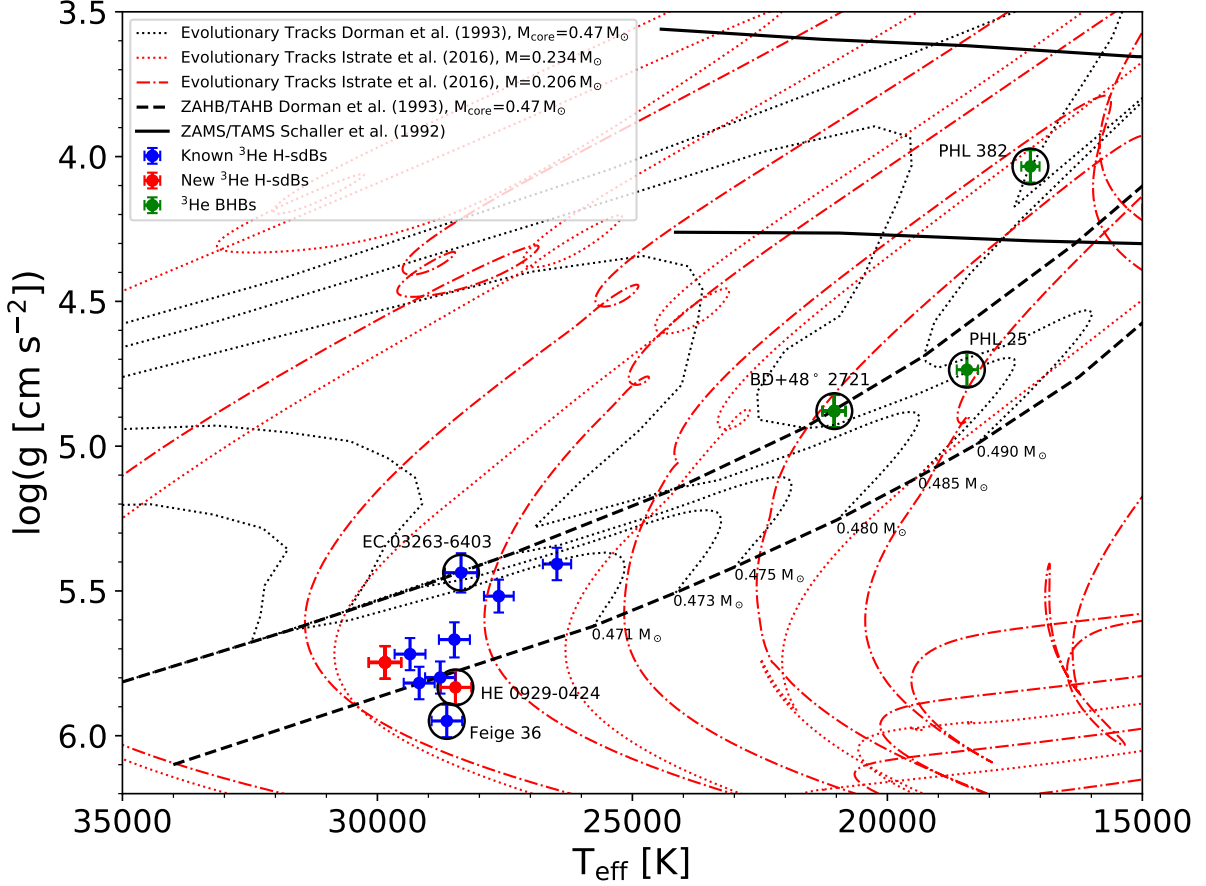


Figure 10.1.1.: Distribution of the  $^3\text{He}$  program stars, for which medium or high-resolution spectra are analyzed, in the  $T_{\text{eff}}\text{-log}(g)$  plane (Kiel diagram). The results are based on the hybrid LTE/NLTE model atmosphere approach and the global analysis strategy (ADS + Global; see Sects. 6.8 and 7.1.2). Interesting objects are highlighted with solid black circles. Known  $^3\text{He}$  H-sdBs are marked in blue, whereas the red dots represent the two new  $^3\text{He}$  H-sdBs from the ESO SPY project (HE 0929-0424 and HE 1047-0436; see Sect. 10.2.2). The green dots at the cool end of the temperature sequence shown represent the three  $^3\text{He}$  (post-)BHB stars PHL 25, PHL 382, and BD+48° 2721. Plotted models and evolutionary tracks are described in Fig. 9.4.1. Plotted error bars combine the  $1\sigma$  statistical single parameter errors (listed in Tables 10.1 and 10.2) and the global systematic errors derived in Sect. 9.2.7. In the case of the two  $^3\text{He}$  program stars EC 03591-3232 and Feige 38, multiple spectra are analyzed. Thus, the adopted (plotted) atmospheric parameter values for these two objects represent weighted averages, whereby the reciprocals of the individual maximum variances, that is  $\frac{1}{(\max[\text{uncertainty}])^2}$ , are used as weights.

## 10.1. Atmospheric Parameters and Projected Rotational Velocities

---

2721 (by  $\sim +0.45$  dex), EC 03591-3232 (by  $\sim +0.20$  dex), EC 12234-2607 (by  $\sim +0.27$  dex), PG 1710+490 (by  $\sim +0.13$  dex), and SB 290 (by  $\sim +0.25$  dex).

Hämmerich (2020) performed a quantitative spectral analysis of PHL 25 and PHL 382 (see Table 16 in their work) that included the improvements of the hybrid approach as well as of the global analysis strategy described in Sects. 6.8 and 7.1.2. The author also made use of the same observed spectra as used in the present work and as used by Schneider et al. (2018). In fact, Hämmerich (2020) also found deviations from the results of Schneider et al. (2018) in both cases:

- **PHL 25:** Compare  $T_{\text{eff}} = 17\,585 \pm 200$  K,  $\log(g) = 4.57 \pm 0.05$ , and  $\log n(\text{He}) = -2.194^{+0.008}_{-0.050}$  derived by Hämmerich (2020) to  $T_{\text{eff}} = 19\,500 \pm 100$  K,  $\log(g) = 4.77^{+0.01}_{-0.02}$ , and  $\log n(\text{He}) = -2.42 \pm 0.03$  determined by Schneider et al. (2018).
- **PHL 382:** Compare  $T_{\text{eff}} = 17\,903 \pm 190$  K,  $\log(g) = 4.08 \pm 0.05$ , and  $\log n(\text{He}) = -2.368 \pm 0.022$  (Hämmerich, 2020) to  $T_{\text{eff}} = 17\,600 \pm 100$  K,  $\log(g) = 3.92 \pm 0.01$ , and  $\log n(\text{He}) = -2.54 \pm 0.02$  (Schneider et al., 2018).

For both stars, Hämmerich (2020) therefore also measured significantly higher total helium abundances, which, in terms of absolute values, are rather similar to what is found in the present work. For PHL 382, the atmospheric parameters derived in this work are close to the ones of Hämmerich (2020), although the star is a bit cooler (by  $\sim 700$  K) and has a bit more helium ( $\sim +0.10$  dex) here. In the case of PHL 25,  $T_{\text{eff}}$  derived in this work is hotter (by  $\sim 850$  K) and  $\log(g)$  is higher (by  $\sim 0.17$  dex) compared to Hämmerich (2020). On the one hand, this may be explained by two solutions with similar  $\chi^2$  values. On the other hand, however, it has to be mentioned that both analyses are not fully comparable to each other because Hämmerich (2020) also fitted the microturbulence  $\xi$  as well as the macroturbulence  $\zeta$ , both of which are set to zero within the framework of this thesis. Thus, this may also be a plausible explanation for the measured deviations in the case of PHL 25, even though Hämmerich (2020) did not determine any unusual values for  $\xi$  and  $\zeta$  for this star (see Table 17 in their work). Certainly, the smaller deviations in the case of PHL 382 may also be related to  $\xi$  and  $\zeta$ .

### 10.1.2. Rotational Broadening

For most of the  $^3\text{He}$  stars known today, literature values of the projected rotational velocities  $v \sin i$  have been reported to be low. The quantitative spectral analyses of the  $^3\text{He}$  stars performed in this work overall confirm the slow rotation<sup>123</sup>. Hence, this implies that rotation is irrelevant for the modelling of the relevant helium line profiles, from which the isotopic abundances as well as the abundance ratios are determined. However, there are two notable exceptions that have already been mentioned in Sect. 9.4.2 (see Table 9.4): the H-sdB SB 290 ( $v \sin i = 49.4 \pm 0.1 \text{ km s}^{-1}$ ) and the post-BHB star PHL 382 ( $v \sin i = 13.4 \pm 0.1 \text{ km s}^{-1}$ ). SB 290 has been known to be a rapid rotator since the study of Geier et al. (2013b), who

---

<sup>123</sup>In order to constrain  $v \sin i$  for the  $^3\text{He}$  program stars, various different sharp metal line profiles are analyzed. This will be demonstrated in Ch. 11.

determined the projected rotational velocity by means of metal lines to be  $v \sin i = 48.0 \pm 2.0 \text{ km s}^{-1}$ , that is, similar to the result of the present work. The authors noted, however, that the observed helium lines require a higher rotational broadening of  $v \sin i = 58.0 \pm 1.0 \text{ km s}^{-1}$  to be matched by synthetic spectra. This discrepancy is confirmed here and it will be further discussed in Sect. 10.2.3. The fact that PHL 382 rotates is also well known and the result derived in this work is in good agreement with literature (for instance, compare the result of this work to those of Schneider et al. 2018 and Hämmerich 2020).

## 10.2. Isotopic Helium Abundances

Making use of the calculated model spectra presented in Sect. 6.8, selected He I lines in the optical and NIR spectral ranges (see Table 8.12) are investigated for the analyzed  $^3\text{He}$  program stars. The selection criterion for each neutral helium line under investigation is its respective strength, which obviously depends on the helium abundance. In consequence, the abundance analyses for the individual stars do not rely on the same He I lines. The analyses focus on detailed syntheses of the composite helium line profiles in order to derive both isotopic abundances  $\log n(^3\text{He})$  and  $\log n(^4\text{He})$  as well as the abundance ratio  $n(^4\text{He})/n(^3\text{He})$ . Unfortunately, He I 7281 Å, one of the lines with the largest observable isotopic line shift ( $\Delta\lambda \sim 0.55 \text{ Å}$ ; see Table 3.2), cannot add much to the analyses in most cases. This is because it is not covered in the spectral ranges of the Echelle spectrographs used (this is the case for FOCES, HIRES, and UVES spectra) or because it is truncated due to the different diffraction orders (HRS spectra). If covered (XSHOOTER and FEROS spectra), He I 7281 Å is often too weak to be useful. In order to study the  $^3\text{He}$  anomaly in most of the  $^3\text{He}$  program stars, the analyses therefore have to rely on the strong He I 6678 Å and He I 4922 Å lines, which are the most important signatures for  $n(^4\text{He})/n(^3\text{He})$  remaining in the optical spectral range.  $^3\text{He}$  program stars of the XSHOOTER reference sample (Feige 38 and EC 03591-3232; see Tables 8.1 and 8.2) additionally benefit from the He I 10 830 Å line in the NIR, which is known to show the largest isotopic line shift ( $\Delta\lambda \sim 1.32 \text{ Å}$ ; see Table 3.2). The influence of this line shall be investigated in detail in the later course of this chapter (Sect. 10.2.4).

Figure 10.2.1 (and the two upper panels of Fig. 11.1.1 in Ch. 11) show the isotopic helium abundances of the analyzed  $^3\text{He}$  program stars in a  $T_{\text{eff}}\text{-}\log n(^3\text{He})$  as well as in a  $T_{\text{eff}}\text{-}\log n(^4\text{He})$  diagram. While all measured  $^4\text{He}$  abundances are clearly subsolar (solar  $^4\text{He}$  abundance:  $\log n(^4\text{He}) = -1.07$ ), the  $^3\text{He}$  abundances are strongly overabundant compared to the solar value of  $\log n(^3\text{He}) = -4.85$  (Asplund et al., 2009). This is in good agreement with the  $^3\text{He}$  study of Schneider et al. (2018). However, when comparing the individual isotopic abundances from this work to the ones determined by Schneider et al. (2018), significant deviations become obvious (see also Tables 10.1 and 10.2). In the following, the results of the isotopic abundances and the abundance ratios will first be detailed for the five known  $^3\text{He}$  H-sdBs EC 03263-6403, EC 14338-1445, Feige 38, PG 1710+490, and Feige 36 (Sect. 10.2.1). After that, they will be discussed for the two newly found  $^3\text{He}$  H-sdBs from the ESO SPY survey (HE 0929-0424 and HE 1047-0436; Sect. 10.2.2). Anomalous helium line profiles are observed for the  $^3\text{He}$  (post-)BHB stars PHL 25, PHL 382, and BD+48° 2721 as well as for the three  $^3\text{He}$  H-sdBs

## 10.2. Isotopic Helium Abundances

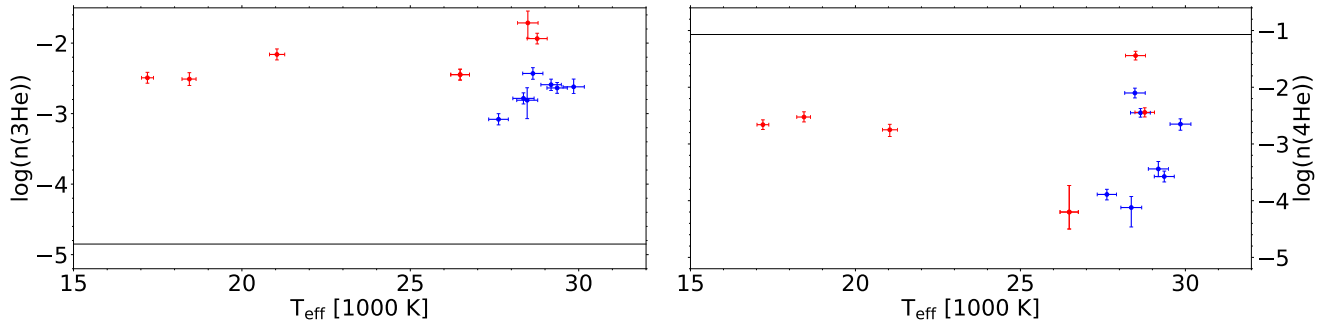


Figure 10.2.1.: *Left-hand panel:*  ${}^3\text{He}$  abundances of the analyzed  ${}^3\text{He}$  program stars plotted against the effective temperature  $T_{\text{eff}}$ . Stars showing anomalous helium line profiles (see Sect. 10.2.3) are marked in red. Blue dots represent  ${}^3\text{He}$  stars for which the helium line profiles can be matched by synthetic spectra. The solid horizontal line marks the solar  ${}^3\text{He}$  abundance of  $\log n({}^3\text{He}) = -4.85$  (Asplund et al., 2009). *Right-hand panel:* Same as the left-hand panel, but showing the corresponding  ${}^4\text{He}$  abundances. Here, the solid horizontal line marks the solar  ${}^4\text{He}$  abundance of  $\log n({}^4\text{He}) = -1.07$  (Asplund et al., 2009).

Note that the abundances are given as base-10 logarithmic particle densities relative to the density of hydrogen. The individual abundance values together with the respective effective temperatures can be found in Tables 10.1 and 10.2. Plotted error bars combine the  $1\sigma$  statistical single parameter errors (listed in Tables 10.1 and 10.2) and the global systematic errors derived in Sect. 9.2.7.

EC 03591-3232, EC 12234-2607, and SB 290. These stars will be discussed in Sect. 10.2.3. Finally, Sect. 10.2.4 will provide a sensitivity study in order to verify the overall results.

### 10.2.1. The ${}^3\text{He}$ Subdwarf B Stars EC 03263-6403, EC 14338-1445, Feige 38, PG 1710+490 and Feige 36

The analyzed  ${}^3\text{He}$  H-sdB stars EC 03263-6403, EC 14338-1445, Feige 38, PG 1710+490, and Feige 36 show helium line fits of good quality. Photospheric  ${}^3\text{He}$  is clearly detectable in these stars, as can be seen from the  ${}^3\text{He}$  and  ${}^4\text{He}$  abundances listed in Tables 10.1 and 10.2. Feige 36 shows a balanced abundance ratio of  $n({}^4\text{He})/n({}^3\text{He}) \sim 0.96$ , whereas for EC 03263-6403, EC 14338-1445, Feige 38, and PG 1710+490  ${}^4\text{He}$  is almost absent, manifesting in  $n({}^4\text{He})/n({}^3\text{He}) < 0.20$ . In fact, these results are rather similar to what has been found by Schneider et al. (2018). Yet, with the exception of EC 14338-1445, helium now is more abundant than in Schneider et al. (2018). Hence, it is not surprising that the majority of the corresponding isotopic helium abundances also have increased. The notable changes compared to Schneider et al. (2018) are as follows: The  ${}^4\text{He}$  abundance of EC 03263-6403 has increased by  $\sim +0.63$  dex, whereas for Feige 38 the  ${}^3\text{He}$  abundance has increased by  $\sim +0.14$  dex. Both isotopic abundances have increased for PG 1710+490 ( ${}^4\text{He}$  by  $\sim +0.23$  dex and  ${}^3\text{He}$  by  $\sim +0.11$  dex). As a matter of fact, a notable decrease of the  ${}^4\text{He}$  abundance (by

## 10. Spectroscopic Analysis of the $^3\text{He}$ Anomaly Based on the Hybrid LTE/NLTE Approach

$\sim -0.14$  dex) is observed for EC 14338-1445. The remaining isotopic abundance changes for the discussed stars are  $\lesssim 0.10$  in absolute terms.

### 10.2.2. The Two New $^3\text{He}$ Subdwarf B Stars from the ESO SPY Project: HE 0929-0424 and HE 1047-0436

The most comprehensive and most homogeneous sample of hot subdwarf B stars for which high-resolution spectra are available emerged from the ESO SPY project. Overall, the sample includes 76 H-sdBs for which UVES spectra at the ESO VLT were obtained (Napiwotzki et al., 2001a). These spectra were analyzed by Lisker et al. (2005), but no search for the  $^3\text{He}$  anomaly was carried out because the UVES spectra do not cover He I 7281 Å or He I 6678 Å. Schneider et al. (2018) revisited the list of classified H-sdBs from ESO SPY in order to spectroscopically study the  $^3\text{He}$  anomaly. The focus had to be on He I 4922 Å, which is the strongest and the most sensitive line for the detection of  $^3\text{He}$  in the spectral range of the available UVES spectra (3290-6640 Å). In a first step, 26 candidates with effective temperatures between  $\sim 26\,000$  K and  $\sim 31\,000$  K, typical for  $^3\text{He}$ -enriched H-sdBs (see Fig. 10.1.1 and the results of Geier et al. 2013a), were preselected. Some of the candidates were too helium-deficient to show He I 4922 Å so that the  $^3\text{He}$  anomaly could not be investigated in these stars. The remaining candidates were spectroscopically analyzed and two of them were identified as  $^3\text{He}$ -enriched H-sdBs by means of their isotopic abundance ratios. These stars (HE 0929-0424 and HE 1047-0436) had been classified as close binaries before by Karl et al. (2006) and Napiwotzki et al. (2001b), respectively. HE 0929-0424 has a semi-amplitude of  $K = 114.3 \pm 1.4$  km s $^{-1}$  and a period of  $P = 0.4400 \pm 0.0002$  d, whereas HE 1047-0436 has  $K = 94.0 \pm 3.0$  km s $^{-1}$  and  $P = 1.21325 \pm 0.00001$  d. With HE 0929-0424 and HE 1047-0436 being short-period H-sdB binaries, the total number of known close H-sdB binaries showing  $^3\text{He}$  has increased to five (PG 1519+640, Feige 36, PG 0133+114, HE 0929-0424, and HE 1047-0436; see also Sect. 3.3).

Two other objects from the ESO SPY project (HE 2156-3927 and HE 2322-0617) were also classified as  $^3\text{He}$ -enriched H-sdBs within the framework of the preliminary studies of Schneider (2017) and Schneider et al. (2017), respectively. However, Lisker et al. (2005) had found that both stars show features of cool companions such as the Mg I triplet between  $\sim 5167$  Å and  $\sim 5184$  Å. In the case of HE 2156-3927, Lisker et al. (2005) had determined the companion type to be K3, whereas the companion of HE 2322-0617 had to be of somewhat earlier spectral type (G9). Since the cool companions therefore already significantly contribute to the total flux at the spectral range of He I 4922 Å, it is not certain that the detection of  $^3\text{He}$  for HE 2156-3927 and HE 2322-0617 is real. Further investigations that make use of He I 6678 Å, He I 7281 Å, and He I 10 830 Å (see Sect. 10.2.4) have to be conducted in order to consolidate the  $^3\text{He}$  hypothesis. For this reason, both objects were not included into the sample of Schneider et al. (2018).

Within the framework of this thesis, the two new  $^3\text{He}$  H-sdBs HE 0929-0424 and HE 1047-0436 are reanalyzed as well. In both cases, the neutral helium lines in the corresponding UVES spectra can be fitted as accurately as in the  $^3\text{He}$  study of Schneider et al. (2018). Based on

## 10.2. Isotopic Helium Abundances

---

the isotopic line shifts observable (in particular for He I 4922 Å and He I 5015 Å; see also Figure 7 in Schneider et al. 2018),  $^3\text{He}$  enrichment is evident. As can be seen from Tables 10.1 and 10.2, HE 0929-0424 and HE 1047-0436 have significantly higher isotopic abundance ratios than the stars discussed in Sect. 10.2.1 (with the exception of Feige 36). Schneider et al. (2018) argued that this could be a selection effect because of the absence of the sensitive He I 6678 Å line in the UVES spectra. This will be further investigated in Sect. 10.2.4. In addition, the S/N ratio could play a role because the analyzed spectra of HE 0929-0424 and HE 1047-0436 have a lower S/N than that measured for the spectra of most other  $^3\text{He}$  program stars (compare the relevant entries in Table 8.6 to the ones in Tables 8.1, 8.2, 8.4, and 8.5).

Interestingly, both isotopic abundances and, hence, also the total helium abundance have increased compared to Schneider et al. (2018) in the case of HE 1047-0436 ( $^4\text{He}$  has increased by  $\sim +0.11$  dex,  $^3\text{He}$  by  $\sim +0.10$  dex, and  $\log n(\text{He})$  by  $\sim +0.11$  dex). However, this is not the case for HE 0929-0424, for which the same amount of  $^4\text{He}$  but less  $^3\text{He}$  (by  $\sim -0.30$  dex) is measured. For this star, the abundance ratio of  $n(^4\text{He})/n(^3\text{He}) = 5.1_{-3.0}^{+2.0}$  derived in this work thus is slightly larger than the one determined by Schneider et al. (2018).

### 10.2.3. Helium Line Profile Anomalies and Vertical Abundance Stratification

The observed helium line profiles of the  $^3\text{He}$  program stars EC 03263-6403, EC 14338-1445, Feige 38, PG 1710+490, Feige 36, HE 0929-0424, and HE 1047-0436 are fitted very accurately. For the other half of the  $^3\text{He}$  sample of this work, however, the helium line profiles cannot be reproduced satisfactorily. This is the case for all three analyzed  $^3\text{He}$  (post-)BHB stars, that is, PHL 25, PHL 382 (see Figs. 10.2.2 and 10.2.3), and BD+48° 2721 as well as for the  $^3\text{He}$  H-sdBs EC 03591-3232 (see Figs. 10.2.4 and 10.2.5), EC 12234-2607, and SB 290. A significant mismatch of the cores of many strong He I lines is obvious, as also observed by Schneider et al. (2018). Only some of the weakest He I lines can be matched satisfactorily by the synthetic spectra. The most prominent discrepancies are found for PHL 25, PHL 382, and BD+48° 2721. The shortcomings are also visible for EC 03591-3232, EC 12234-2607, and SB 290, however to a lesser extent. Due to the high projected rotational velocity of  $\sim 50 \text{ km s}^{-1}$  of SB 290 (see Sect. 10.1.2) and the line broadening coming along with it, a more obvious mismatch as seen for the other relevant stars might be hidden to some extent. To test this, the observed FEROS and the synthetic spectrum of the non-rotating  $^3\text{He}$  H-sdB EC 03591-3232 are convolved with a rotational profile for  $v \sin i \sim 50 \text{ km s}^{-1}$ . In this way, similarly strong mismatches in the broadened helium line profiles of the star as seen for SB 290 can be reproduced. Therefore, it is most likely that the strong line broadening in the case of SB 290 indeed hides greater shortcomings in fitting (see also Schneider et al. 2018). Due to the insufficient line matches in the case of PHL 25, PHL 382, BD+48° 2721, EC 03591-3232, EC 12234-2607, and SB 290, the resulting isotopic abundances, the total helium abundances as well as the isotopic abundance ratios listed in Tables 10.1 and 10.2 are uncertain. Although the same data are analyzed, significant deviations from the results of Schneider et al. (2018) are measured. As already mentioned in Sect. 10.1.1, the relevant

## 10. Spectroscopic Analysis of the $^3\text{He}$ Anomaly Based on the Hybrid LTE/NLTE Approach

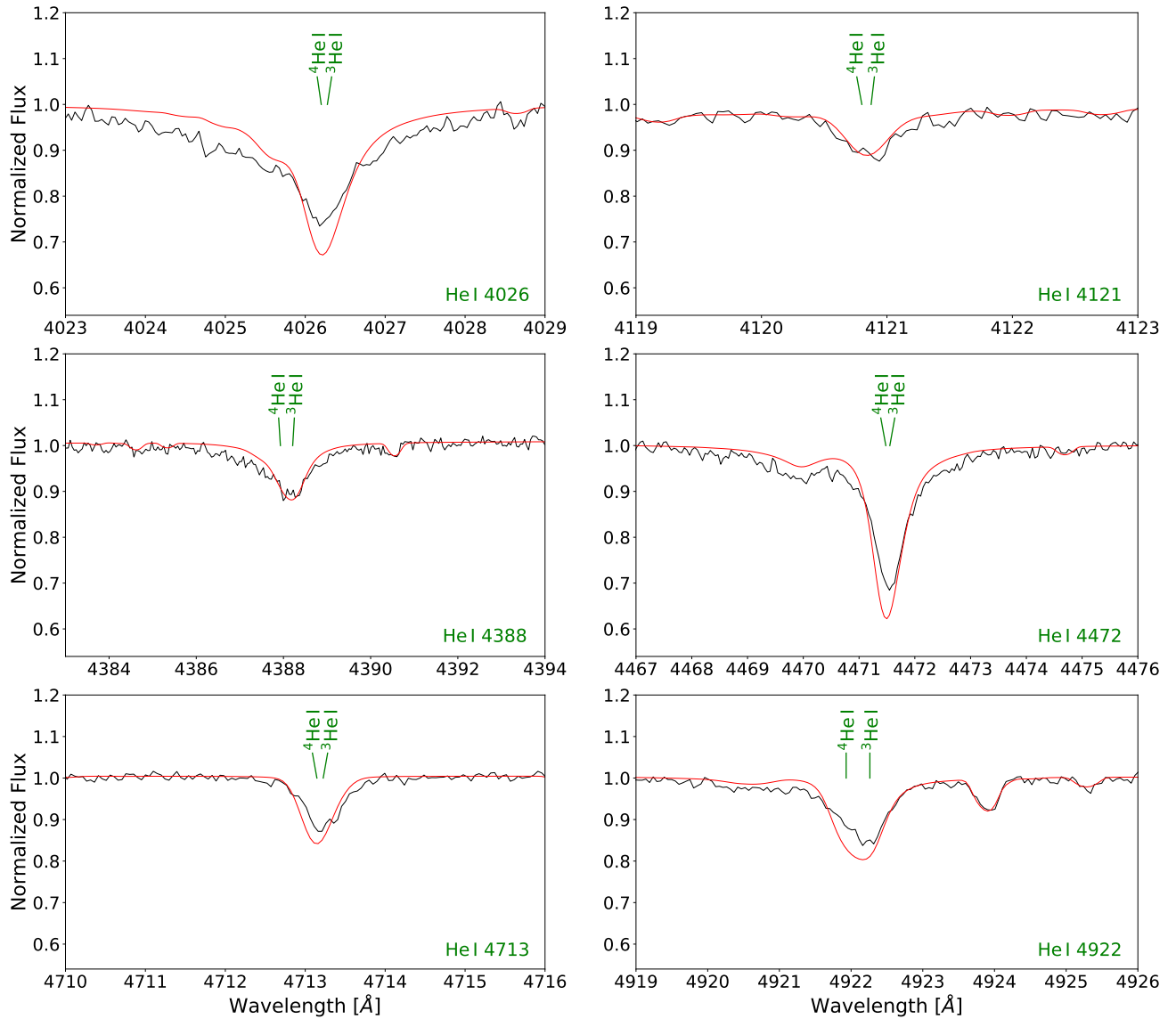


Figure 10.2.2.: Selected He I lines in the FEROS spectrum of the rotating  $^3\text{He}$  post-BHB star PHL 382. The observed spectrum (solid black line) and the best fit (solid red line) are shown. Solid green lines/labels mark the central wavelength positions of the  $^3\text{He}$  and  $^4\text{He}$  components of the individual spectral lines. Additional absorption lines are caused by metals (see Ch. 11), but are not marked. The star shows strong helium stratification, as is obvious from the mismatch of the cores of several He I lines (see the text for details).

## 10.2. Isotopic Helium Abundances

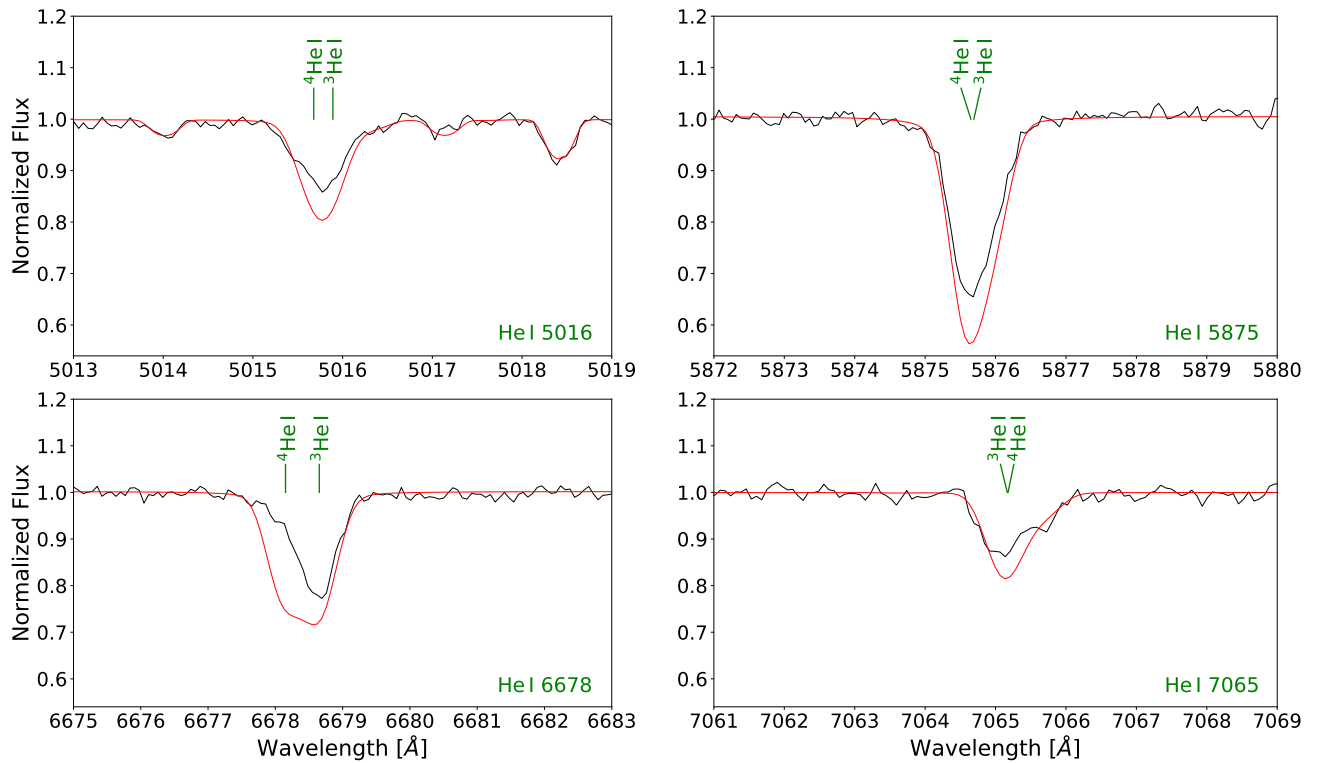


Figure 10.2.3.: Same as Fig. 10.2.2, but showing additional He I lines in the FEROS spectrum of the rotating  ${}^3\text{He}$  post-BHB star PHL 382.

stars now have much more helium in total. This is because the individual isotopic abundances have altered dramatically. The  ${}^3\text{He}$  abundances have increased by  $\sim +0.18$  dex (PHL 25), by  $\sim +0.14$  dex (PHL 382), by  $\sim +0.41$  dex (BD+48° 2721), by  $\sim +0.17$  dex (EC 03591-3232), by  $\sim +0.43$  dex (EC 12234-2607), and by  $\sim +0.28$  dex (SB 290), respectively. The changes of the  ${}^4\text{He}$  abundances are even more dramatic:  $\sim +0.22$  dex (PHL 25),  $\sim +0.60$  dex (PHL 382),  $\sim +0.60$  dex (BD+48° 2721),  $\sim +1.07$  dex (EC 03591-3232),  $\sim +0.21$  dex (EC 12234-2607), and  $\sim -0.47$  dex (SB 290). Accordingly, the respective isotopic abundance ratios have also strongly altered. No evidence that the stars with anomalous helium line profiles have more atmospheric helium than the other  ${}^3\text{He}$  program stars is found, although EC 03591-3232 and EC 12234-2607 are among the most helium-rich  ${}^3\text{He}$  objects analyzed. It can be concluded that  ${}^3\text{He}$  is the dominant isotope in the case of PHL 382, BD+48° 2721, EC 03591-3232, and SB 290, whereas  ${}^4\text{He}$  is more abundant in EC 12234-2607. PHL 25 shows a somewhat balanced  $n({}^4\text{He})/n({}^3\text{He})$  abundance ratio.

As already mentioned in Sect. 10.1.1, PHL 25 and PHL 382 have also been analyzed in a similar way by Hämmerich (2020). For both stars, Table 10.3 compares the isotopic helium abundances derived in this work to the corresponding results of Hämmerich (2020). In fact, the results are rather similar. Only  ${}^4\text{He}$  is significantly discrepant in the case of PHL 382.

The fact that the isotopic abundances, the total helium abundances as well as the isotopic abundance ratios have altered that much for PHL 25, PHL 382, BD+48° 2721, EC 03591-

## 10. Spectroscopic Analysis of the $^3\text{He}$ Anomaly Based on the Hybrid LTE/NLTE Approach

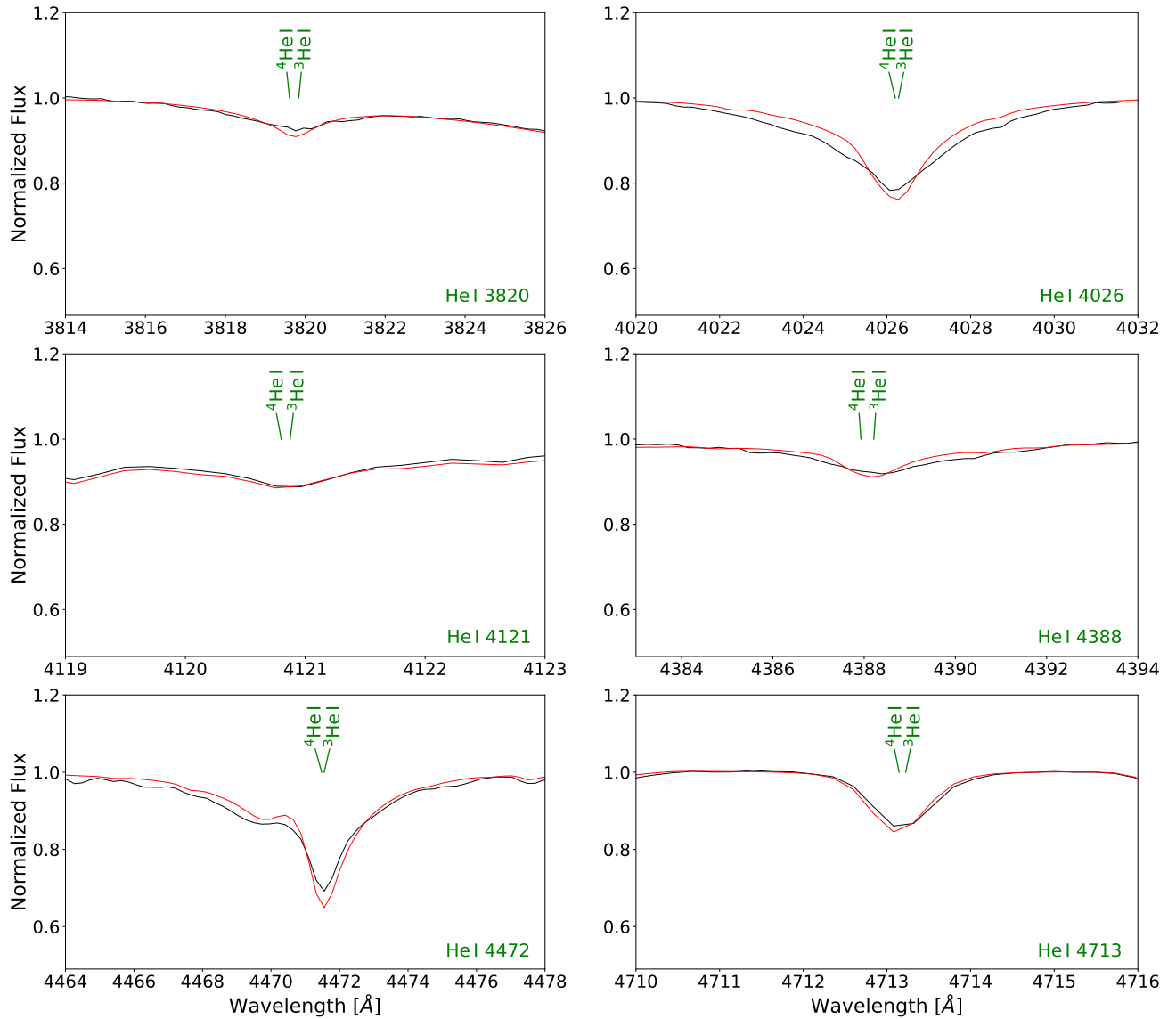


Figure 10.2.4.: Selected He I lines in the XSHOOTER spectrum of the  $^3\text{He}$  H-sdB star EC 03591-3232. The observed spectrum (solid black line) and the best fit (solid red line) are shown. Solid green lines/labels mark the central wavelength positions of the  $^3\text{He}$  and  $^4\text{He}$  components of the individual spectral lines. Additional absorption lines are caused by metals (see Ch. 11), but are not marked. The star shows strong helium stratification, as is obvious from the mismatch of the cores of several He I lines (see the text for details).

## 10.2. Isotopic Helium Abundances

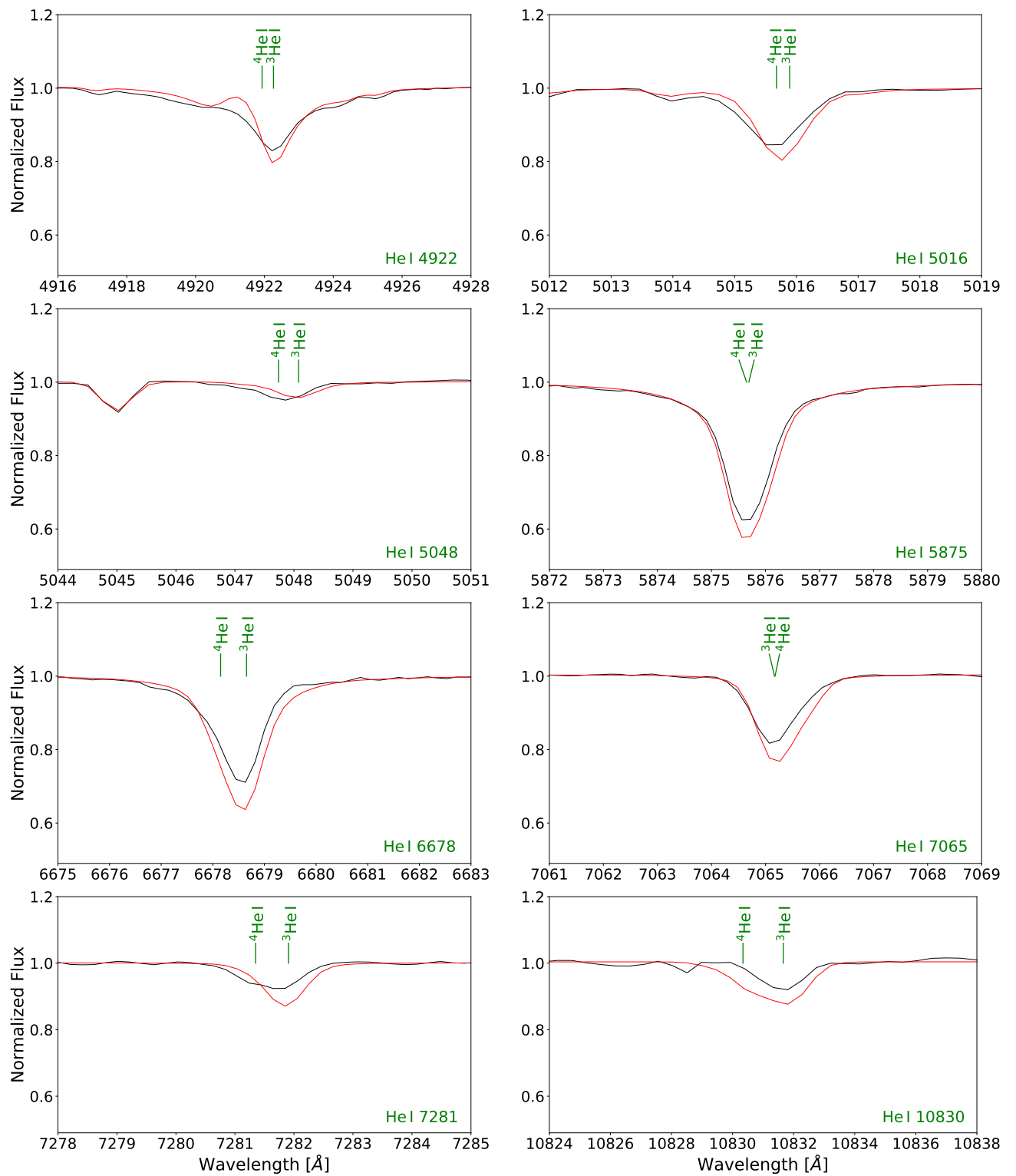


Figure 10.2.5.: Same as Fig. 10.2.4, but showing additional He I lines in the XSHOOTER spectrum of the  $^3\text{He}$  H-sdB star EC 03591-3232.

## 10. Spectroscopic Analysis of the $^3\text{He}$ Anomaly Based on the Hybrid LTE/NLTE Approach

Star	$\log n(^4\text{He})$	$\log n(^3\text{He})$	Reference
PHL 25	$-2.525^{+0.053}_{-0.042}$	$-2.51 \pm 0.05$	This work
PHL 25	$-2.48^{+0.04}_{-0.06}$	$-2.52^{+0.05}_{-0.06}$	Hämmerich (2020)
PHL 382	$-2.66 \pm 0.04$	$-2.492^{+0.018}_{-0.014}$	This work
PHL 382	$-3.19^{+0.07}_{-0.06}$	$-2.439^{+0.022}_{-0.023}$	Hämmerich (2020)

Table 10.3.: Isotopic helium abundances determined for the (post-)BHB stars PHL 25 and PHL 382. The results of this work are compared to those of Hämmerich (2020).

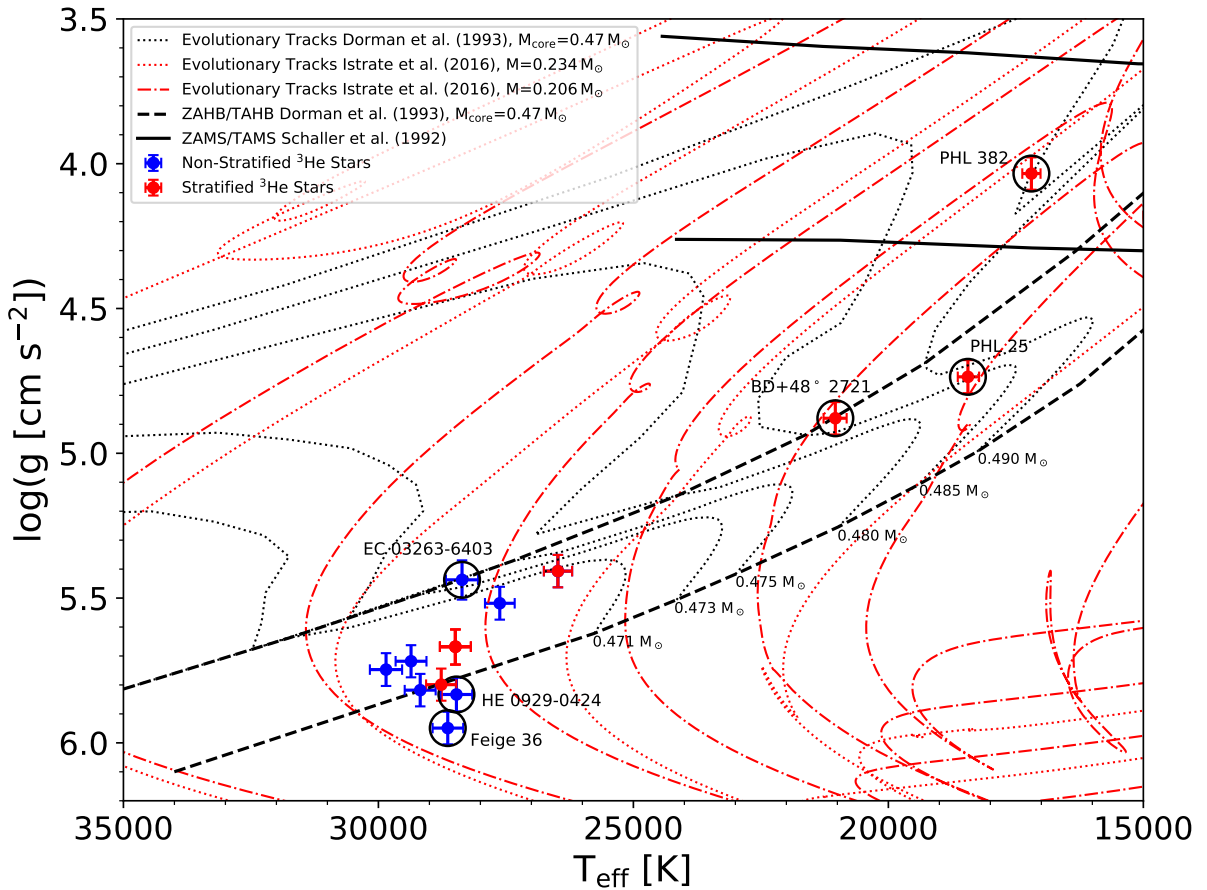


Figure 10.2.6.: Same as Fig. 10.1.1, but distinguishing between  $^3\text{He}$  program stars that show no evidence for helium stratification (blue dots) and stratified ones (red dots). See the text for further information.

## 10.2. Isotopic Helium Abundances

---

3232, EC 12234-2607, and SB 290 compared to Schneider et al. (2018) on the one hand shows how much impact the updated models and the improvements of the analysis procedures have for these stars. On the other hand, the  $\chi^2$ -landscapes are also not well behaved in these cases because of the shortcomings due to the anomalous helium line profiles. In fact, the entire helium line spectrum is calculated for a large variety of helium abundances, but none of them can simultaneously match both the wings and the cores of the analyzed helium absorption lines of the relevant stars, as also realized by Schneider et al. (2018). Specifically, He I 4026 Å and He I 4472 Å exhibit shallow cores in combination with unusually broad wings (see Figs. 10.2.2 and 10.2.4), indicating that helium is not homogeneously distributed throughout the stellar atmosphere, but instead shows a vertical abundance stratification. The observed shallow line cores indicate a lower-than-average helium abundance in the outer atmospheric layers, where the cores are formed. The observed strong line wings require a higher-than-average helium abundance in the deeper atmospheric layers, where the wings are formed. The further out in the stellar atmosphere the particular helium absorption line core is formed, that is, the stronger the respective line, the poorer the reproduction of the observed line core (see Figs. 10.2.2-10.2.5). In addition to  $\lambda 4026$  Å and  $\lambda 4472$  Å, this particularly applies to  $\lambda 4922$  Å,  $\lambda 5016$  Å,  $\lambda 5875$  Å,  $\lambda 6678$  Å,  $\lambda 7065$  Å, and, if available, also to  $\lambda 7281$  Å and  $\lambda 10830$  Å. This indicates that the helium abundance indeed has to be higher in the deeper layers of the atmosphere than in the outer ones (see also Schneider et al. 2018). Thus, the apparent discrepancy in the projected rotational velocities of SB 290 ( $v \sin i$  determined from helium lines is larger than  $v \sin i$  determined from metal lines; see Sect. 10.1.2) can be explained as an effect of the helium abundance stratification. Furthermore, Geier et al. (2013a) were not aware of the helium-stratified atmosphere of BD+48° 2721. This together with a different choice of investigated helium lines for their LTE spectral analysis could be the crucial factor for the deviations of the atmospheric parameters discussed in Sect. 9.4.1.

Helium stratification has been reported for a few  $^3\text{He}$  B-type stars only so far (for instance, see Bohlender 2005). This includes B-type MS stars such as the helium-variable star aCen (Leone & Lanzafame, 1997; Bohlender et al., 2010; Maza et al., 2014b), the prototype HgMn star  $\kappa$  Cancri (Maza et al., 2014a) as well as the chemically peculiar  $^3\text{He}$  star HD 185330 (Niemczura et al., 2018). Helium stratification has also been observed for Feige 86, a well-studied BHB star (Bonifacio et al., 1995; Cowley & Hubrig, 2005; Cowley et al., 2009; Németh, 2017; Hämmerich, 2020), and for other chemically peculiar stars (for instance, see Dworetzky 2004 or Castelli & Hubrig 2007). However, Schneider et al. (2018) detected it for the first time in hot subdwarf B stars. Figure 10.2.6 highlights the stratified program stars of the present work in the  $T_{\text{eff}}\text{-}\log(g)$  plane. As observed by Schneider et al. (2018), these objects populate the whole effective temperature sequence of the HB.

In order to reproduce the observed helium line profiles and to estimate the total helium abundance  $\log n(\text{He})$  in the outer and in the inner parts of the stellar atmospheres of the stratified program stars, a two-component fit is applied. Such a fit has also been realized in the studies of Maza et al. (2014a) and Schneider et al. (2018). To this end, the strong He I lines at  $\lambda 4026$  Å and  $\lambda 4472$  Å are chosen. Their line cores are formed further out in the stellar atmosphere than other, weaker He I lines and the line wings. Trying to match the cores and the wings of both lines individually, four fits by eye are performed for each of the stratified stars, whereby

## 10. Spectroscopic Analysis of the $^3\text{He}$ Anomaly Based on the Hybrid LTE/NLTE Approach

Table 10.4.: Total helium abundances  $\log n(\text{He})$  derived from the fits by eye performed for the line cores and the line wings of He I 4026 Å and He I 4472 Å in the spectra of the helium-stratified  $^3\text{He}$  program stars of this work (see the text for details). In the case of EC 03591-3232, only the available FEROS spectrum is used.

Fitted Line	PHL 25	PHL 382	BD+48° 2721	SB 290	EC 03591-3232	EC 12234-2607
He I 4026 Å core	$-2.35 \pm 0.20$	$-2.40^{+0.15}_{-0.12}$	$-2.10 \pm 0.20$	$-2.25^{+0.20}_{-0.15}$	$-2.00 \pm 0.20$	$-1.55^{+0.30}_{-0.40}$
He I 4026 Å wings	$-1.65^{+0.50}_{-0.30}$	$-1.60^{+0.28}_{-0.32}$	$-1.45 \pm 0.35$	$-2.15^{+0.35}_{-0.25}$	$-1.60^{+0.20}_{-0.35}$	$-1.25^{+0.40}_{-0.35}$
He I 4472 Å core	$-2.85^{+0.10}_{-0.20}$	$-2.50^{+0.25}_{-0.20}$	$-2.40^{+0.25}_{-0.15}$	$-2.55^{+0.15}_{-0.25}$	$-2.25^{+0.30}_{-0.20}$	$-2.10 \pm 0.30$
He I 4472 Å wings	$-1.90^{+0.25}_{-0.15}$	$-1.75^{+0.13}_{-0.18}$	$-1.55 \pm 0.30$	$-2.12^{+0.21}_{-0.32}$	$-1.65^{+0.30}_{-0.20}$	$-1.25^{+0.25}_{-0.32}$

**Notes:**

Given errors result from the fits by eye (see the text for details).

the corresponding effective temperatures, the surface gravities, and the projected rotational velocities are fixed to the values presented in Sects. 10.1.1 and 10.1.2 and only  $\log n(\text{He})$  is fitted. The errors on  $\log n(\text{He})$  are estimated by varying the total helium abundance until clear mismatches in the cores and in the wings become obvious. In the case of EC 03591-3232, for which FEROS and XSHOOTER data are available, the fits by eye are only performed for the FEROS spectrum. Table 10.4 summarizes the results of the fits by eye. As an example, Fig. 10.2.7 shows the fits by eye for He I 4026 Å and He I 4472 Å in the HRS spectrum of PHL 25. As can be seen from the results listed in Table 10.4, the total helium abundance overall increases from the outer to the inner atmospheric layers of the analyzed stars. For He I 4026 Å, the helium abundance increases by  $\sim +0.10$  dex in the case of SB 290 up to  $\sim +0.80$  dex in the case of PHL 382. Derived from He I 4472 Å, the helium abundance increases with depth even more dramatically (by  $\sim +0.43$  dex in the case of SB 290 up to  $\sim +0.95$  dex in the case of PHL 25). Hence, the helium abundance can be estimated to increase by a factor of  $\sim 1.2$ -9.0 from the outer to the inner parts of the atmosphere, depending on the respective stratified star. This is very similar to  $\sim 1.4$ -8.0 determined by Schneider et al. (2018) and a clear indication for an inhomogeneous distribution of helium in the atmospheres of PHL 25, PHL 382, BD+48° 2721, EC 03591-3232, EC 12234-2607, and SB 290. In other words, the atmospheres of these stars show vertical abundance stratification.

The simplest way to carry out a quantitative spectral analysis of the stratification profile would be the usage of a smoothed step function (see Farthmann et al. 1994), which sets the helium abundance in the outer atmospheric layers to a lower level than further in. In this way, the optical depth at which the change in helium abundance occurs could be identified. For instance, successful stratification analyses have been carried out by Khalack et al. (2014) for carbon and nitrogen in the post-HB star HD 76431 or by Khalack et al. (2007, 2008, 2010) and LeBlanc et al. (2010) for nitrogen, sulfur, titanium, and iron in BHB stars. Furthermore, the strategy to determine the stratified helium abundance profile throughout the photosphere by means of the hybrid LTE/NLTE approach used in the present work has been reported in

## 10.2. Isotopic Helium Abundances

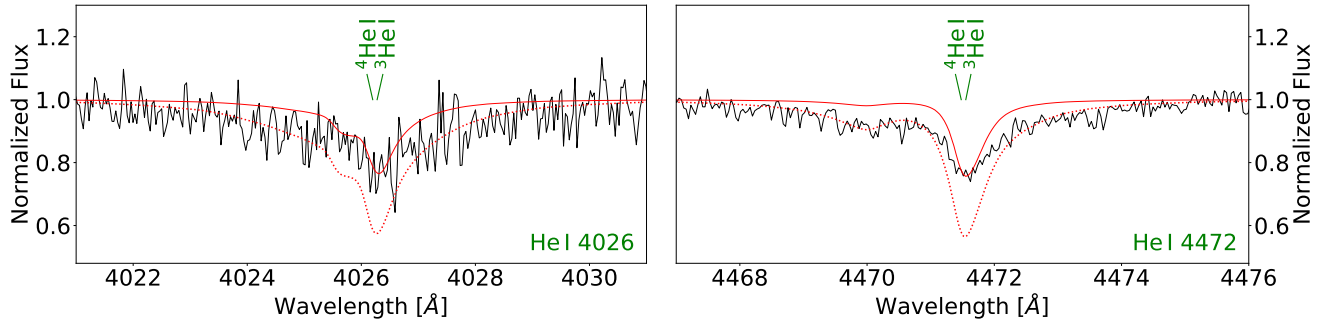


Figure 10.2.7.: *Left-hand panel*: Best fits by eye for the line core (solid red line;  $\log n(\text{He}) = -2.35$ ) and the line wings (dotted red line;  $\log n(\text{He}) = -1.65$ ) of He I 4026 Å in the HRS spectrum of PHL 25 (solid black line). Solid green lines/labels mark the central wavelength positions of the  $^3\text{He}$  and  $^4\text{He}$  component of the spectral line. *Right-hand panel*: Same as the left-hand panel, but for the He I 4472 Å line. Here, the total helium abundances are  $\log n(\text{He}) = -2.85$  (solid red line) and  $\log n(\text{He}) = -1.90$  (dotted red line), respectively.

the study of Maza et al. (2014a), who successfully tested it on  $\kappa$  Cancri. However, such a detailed treatment of the helium abundance is beyond the scope of this work.

### 10.2.4. Sensitivity Study

As described in Sect. 10.2.1, EC 03263-6403, EC 14338-1445, Feige 38, and PG 1710+490 have isotopic abundance ratios of  $n(^4\text{He})/n(^3\text{He}) < 0.20$  (see Tables 10.1 and 10.2). This brings up the following question: Given the range in S/N of the observations, what are the detection limits for  $^4\text{He}$  and  $^3\text{He}$ ?

In order to answer this, Gaussian noise is added to synthetic spectra computed with the spectroscopic parameters and the S/N ratios associated with the following three program stars (see also Tables 10.1, 10.2, 8.4, and 8.6): EC 03263-6403 = Model I, BD+48° 2721 = Model II, and HE 1047-0436 = Model III (Schneider et al., 2018). BD+48° 2721 is chosen because of the relatively high S/N ratio of the corresponding FOCES spectrum ( $\sim 84$ ; see Table 8.4), EC 03263-6403 because of its low isotopic abundance ratio ( $n(^4\text{He})/n(^3\text{He}) \sim 0.05$ ; see Table 10.1), and HE 1047-0436 because it has the lower  $^4\text{He}$  abundance of the two new  $^3\text{He}$  H-sdBs from ESO SPY (for which the sensitive He I 6678 Å line is not observed; see Table 10.2).

According to the methodology presented in Schneider et al. (2018), the Gaussian noise is simulated using samples ( $p$ ) drawn from a parameterized normal distribution centred around zero (mean value  $\mu = 0$ ) and with a standard deviation of one ( $\sigma = 1$ ). The fluxes of the

## 10. Spectroscopic Analysis of the $^3\text{He}$ Anomaly Based on the Hybrid LTE/NLTE Approach

mock spectra at the individual data points  $i$  ( $F_{\text{mock},i}$ ) are calculated from the respective model fluxes ( $F_{\text{model},i}$ ) in the following way:

$$F_{\text{mock},i} = \left( \frac{p}{S/N} \right) \cdot F_{\text{model},i} + F_{\text{model},i}. \quad (10.1)$$

Here,  $S/N$  is the signal-to-noise ratio for which different values are chosen: I) the original  $S/N$  of the observed (co-added) spectra; II)  $S/N = 100$ ; III)  $S/N = 200$ ; and IV)  $S/N = 300$  (in the case of HE 1047-0436 = Model III, only the original  $S/N$  is used). The effective temperature, the surface gravity, and the isotopic helium abundances are fitted simultaneously for the individual mock spectra, whereby the hybrid LTE/NLTE approach and the global analysis strategy are used.

### Detectability and Error Estimation

The results of the sensitivity study for the three models described above are shown in Table 10.5. In the following, three important aspects shall be pointed out.

First, the results of the previous abundance analyses can be reproduced. This confirms that the abundances given in Tables 10.1 and 10.2 are indeed reliable detections of the small traces of  $^4\text{He}$ . The values and the uncertainties for  $\log n(^4\text{He})$  and  $\log n(^3\text{He})$  derived from the mock spectra are overall in good agreement with the observed ones if the same  $S/N$  and the same number of investigated helium lines are used. An increase of the  $S/N$  ratio mainly leads to an improvement in precision.

Second, the observed  $^4\text{He}$  abundance of EC 03263-6403 (and to some extent also that of BD+48° 2721) cannot be reproduced, if the strong and sensitive He I 6678 Å line is ignored. Ignoring this important line particularly results in large statistical uncertainties on  $\log n(^4\text{He})$ , even for better  $S/N$ . Hence, the presence of He I 6678 Å is a necessary requirement in order to determine  $\log n(^4\text{He})$  for stars for which  $^4\text{He}$  is as deficient as in EC 03263-6403.

Last, similar isotopic helium abundances and statistical uncertainties as in the previous abundance analysis are also derived from the mock spectrum of HE 1047-0436 (Model III), that is, for the most  $^4\text{He}$ -deficient but  $^3\text{He}$ -enriched H-sdB from the ESO SPY project. In this case, the analyzed UVES spectrum is simulated, which lacks the He I 6678 Å line as the most important signature for  $n(^4\text{He})/n(^3\text{He})$  in the optical. The result of the sensitivity study for HE 1047-0436 therefore substantiates the discovery of the object as a  $^3\text{He}$ -enriched H-sdB. Yet, it has to be said that observations of He I 6678 Å (and He I 10 830 Å; see the next section) would still significantly improve the accuracy as well as the precision of the corresponding analysis. Moreover, an availability of these two lines for ESO SPY program stars in general could potentially reveal other yet unclassified  $^3\text{He}$  H-sdBs at lower  $n(^4\text{He})/n(^3\text{He})$  ratios.

All three aspects discussed are very similar to what has been found by Schneider et al. (2018) in their sensitivity study, even though the isotopic abundances and the abundance ratios of the three investigated stars have altered. Schneider et al. (2018) also deduced a detection limit for  $^3\text{He}$ . Although He I 6678 Å is not observed for HE 1047-0436 and the  $S/N$

## 10.2. Isotopic Helium Abundances

Table 10.5.: Results of the sensitivity study.

Mock spectrum	S/N	$\log n(^4\text{He})$	$\log n(^3\text{He})$	$\frac{n(^4\text{He})}{n(^3\text{He})}$
Model I+	23	$-4.205^{+0.174}_{-0.329}$	$-2.835 \pm 0.021$	$0.043^{+0.018}_{-0.033}$
Model I+	100	$-4.162^{+0.146}_{-0.273}$	$-2.802 \pm 0.018$	$0.044^{+0.015}_{-0.028}$
Model I+	200	$-4.156^{+0.103}_{-0.238}$	$-2.768^{+0.013}_{-0.012}$	$0.041^{+0.010}_{-0.023}$
Model I+	300	$-4.133^{+0.057}_{-0.171}$	$-2.772 \pm 0.010$	$0.044^{+0.006}_{-0.018}$
EC 03263-6403 <sup>a</sup>	23	$-4.121^{+0.180}_{-0.334}$	$-2.784^{+0.022}_{-0.023}$	$0.046^{+0.020}_{-0.040}$
Model II+	84	$-2.82^{+0.07}_{-0.11}$	$-2.127^{+0.020}_{-0.019}$	$0.20^{+0.04}_{-0.06}$
Model II+	100	$-2.79^{+0.06}_{-0.10}$	$-2.132 \pm 0.017$	$0.22^{+0.04}_{-0.06}$
Model II+	200	$-2.78^{+0.03}_{-0.06}$	$-2.149 \pm 0.009$	$0.23^{+0.02}_{-0.04}$
Model II+	300	$-2.76^{+0.01}_{-0.02}$	$-2.153 \pm 0.005$	$0.25^{+0.01}_{-0.02}$
BD+48° 2721 <sup>a</sup>	84	$-2.75^{+0.06}_{-0.09}$	$-2.161^{+0.021}_{-0.018}$	$0.26^{+0.04}_{-0.06}$
Model III-	25	$-2.670^{+0.061}_{-0.082}$	$-2.66^{+0.06}_{-0.05}$	$0.98^{+0.20}_{-0.22}$
HE 1047-0436 <sup>a</sup>	25	$-2.650^{+0.054}_{-0.077}$	$-2.62^{+0.08}_{-0.06}$	$0.93 \pm 0.21$

**Notes:**

$1\sigma$  single parameter errors derived from  $\chi^2$ -statistics are given for  $\log n(^4\text{He})$  and  $\log n(^3\text{He})$  (see Sect. 7.1.2). The listed uncertainties on  $n(^4\text{He})/n(^3\text{He})$  result from the given statistical errors on  $\log n(^4\text{He})$  and  $\log n(^3\text{He})$ , whereby Gaussian error propagation is used. The global systematic errors of  $\log n(^4\text{He})$  and  $\log n(^3\text{He})$  are considered equal to that of  $\log n(\text{He})$  derived in Sect. 9.2.7. From Tables 10.1 and 10.2: Model I+ ( $T_{\text{eff}} = 28360$  K,  $\log g = 5.437$ ,  $\log n(^4\text{He}) = -4.121$ ,  $\log n(^3\text{He}) = -2.784$ , He I 6678 Å included in the analysis), Model II+ ( $T_{\text{eff}} = 21040$  K,  $\log g = 4.879$ ,  $\log n(^4\text{He}) = -2.75$ ,  $\log n(^3\text{He}) = -2.161$ , He I 6678 Å included in the analysis), and Model III- ( $T_{\text{eff}} = 29850$  K,  $\log g = 5.747$ ,  $\log n(^4\text{He}) = -2.650$ ,  $\log n(^3\text{He}) = -2.62$ , He I 6678 Å excluded from the analysis).

(<sup>a</sup>) Observed spectrum.

ratio of the corresponding UVES spectrum is mediocre (S/N  $\sim 25$ ; see Table 8.6), the authors demonstrated that the  $^3\text{He}$  anomaly is still detectable at an abundance ratio as high as  $n(^4\text{He})/n(^3\text{He}) \sim 0.91$ , even for such poor data. In the present work, the abundance ratio of HE 1047-0436 is even  $\sim 0.93$  (see Table 10.2). In consequence, it can be concluded that all other cases where the abundance ratio is lower than  $\sim 0.93$  are indeed reliable detections of  $^3\text{He}$ , even if the  $^3\text{He}$  abundance is as low as  $\log n(^3\text{He}) \sim -3.08$  (EC 14338-1445). Hence, the latter value is a trustworthy upper limit for the detection limit for  $^3\text{He}$  (see also Schneider et al. 2018). HE 0929-0424 has an even higher abundance ratio ( $n(^4\text{He})/n(^3\text{He}) \sim 5.1$ ) than HE 1047-0436, but at the same time shows significantly more helium in total (see Table 10.2). Thus, the discovery of HE 0929-0424 as a  $^3\text{He}$ -enriched H-sdB is also supported.

After all these findings, another interesting question arises: Is there a potential continuum of  $^3\text{He}$ -enriched H-sdBs/BHBs to be found at higher abundance ratios, for instance, at  $n(^4\text{He})/n(^3\text{He}) \sim 1.0$ -3.0? This could be answered best from a homogeneous sample with excellent data. Such a sample may be the one of Geier et al. (2013a), who investigated 44

## 10. Spectroscopic Analysis of the $^3\text{He}$ Anomaly Based on the Hybrid LTE/NLTE Approach

bright H-sdB stars that were observed at high spectral resolution and good S/N (for instance, FEROS spectra were analyzed which covered He I 6678 Å). The sample is somewhat biased, however, because the previously known  $^3\text{He}$  H-sdBs were included a priori. In fact, most of the new  $^3\text{He}$  H-sdBs found by Geier et al. (2013a), which are also analyzed in the present work (EC 14338-1445, EC 03263-6403, PG 1710+490, and Feige 38), exhibit very low  $^4\text{He}$  abundances ( $\log n(^4\text{He}) \lesssim -3.44$ ; see Tables 10.1 and 10.2). The only two exceptions to this are EC 03591-3232 and EC 12234-2607. Nonetheless, a larger unbiased sample is definitely needed in order to draw sound conclusions about the distribution of  $n(^4\text{He})/n(^3\text{He})$  ratios.

### The Infrared He I 10 830 Å Line

The He I 10 830 Å line in the NIR is known to show the largest isotopic line shift of  $\sim 1.32$  Å, which is more than twice as large as that observed for He I 6678 Å ( $\sim 0.50$  Å; see Table 3.2). Thus, He I 10 830 Å should significantly improve the detectability of  $^3\text{He}$  and, in turn, the sensitivity to  $n(^4\text{He})/n(^3\text{He})$ . Just like He I 5875 Å and He I 6678 Å, the He I 10 830 Å line is strongly affected by departures from LTE. However, the helium model atom used in this work as well as the hybrid LTE/NLTE approach have been shown to be appropriate to match the observed line profiles of He I 10 830 Å in early B-type MS stars well (Przybilla, 2005). For this reason, He I 10 830 Å hence is included into the sensitivity study of this work in the case of BD+48° 2721 (see Table 10.6). In this way, the influence of this important line on the  $n(^4\text{He})/n(^3\text{He})$  abundance ratio derived can be tested (see also Schneider et al. 2018).

As a matter of fact, He I 10 830 Å particularly leads to a better accuracy and precision in determining both isotopic abundances for a given S/N (compare the results of Table 10.6 to those of Table 10.5). Both isotopic abundances are already quite well determined if He I 6678 Å as well as He I 10 830 Å are available and if the S/N ratio is of the order of  $\sim 85$ . An even higher S/N decreases the statistical uncertainties of both isotopic abundances if He I 10 830 Å is included in the analysis. All of these results are in good agreement with the previous ones determined by Schneider et al. (2018).

In fact, the He I 10 830 Å line can also be analyzed in real data in this work, that is, in the XSHOOTER spectra of the two  $^3\text{He}$  program stars Feige 38 and EC 03591-3232 (see Tables 8.1 and 8.2). Although the corresponding line fits of He I 10 830 Å are not very accurate (in particular in the case of EC 03591-3232, which is most likely due to its helium-stratified atmosphere; see Fig. 10.2.5), it turns out that the line has a great impact on the measured isotopic helium abundances. Particularly, the  $^4\text{He}$  abundances derived from the XSHOOTER data largely deviate from those determined from the FEROS data, which do not cover He I 10 830 Å (see Tables 10.1 and 10.2). For EC 03591-3232, compare  $\log n(^4\text{He}) = -3.01^{+0.05}_{-0.08}$  (XSHOOTER) to  $\log n(^4\text{He}) = -2.363 \pm 0.030$  (FEROS) and for Feige 38 compare  $\log n(^4\text{He}) = -3.37^{+0.08}_{-0.19}$  (XSHOOTER) to  $\log n(^4\text{He}) = -3.596^{+0.062}_{-0.059}$  (FEROS). The  $^3\text{He}$  abundance of EC 03591-3232 is also affected by the presence of He I 10 830 Å:  $\log n(^3\text{He}) = -1.904^{+0.007}_{-0.006}$  (XSHOOTER) vs.  $\log n(^3\text{He}) = -2.146 \pm 0.018$  (FEROS). However, this is not the case for the non-stratified star Feige 38:  $\log n(^3\text{He}) = -2.640^{+0.032}_{-0.016}$  (XSHOOTER) vs.  $\log n(^3\text{He}) = -2.635^{+0.009}_{-0.011}$  (FEROS). As a result of all of this, it can be concluded that He I 10 830 Å strongly affects the determined isotopic abundance ratios, in particular that of EC 03591-3232: compare  $n(^4\text{He})/n(^3\text{He}) =$

## 10.2. Isotopic Helium Abundances

Table 10.6.: Influence of the He I 10 830 Å line on the sensitivity study in the case of BD+48° 2721.

Mock spectrum	S/N	$\log n(^4\text{He})$	$\log n(^3\text{He})$	$\frac{n(^4\text{He})}{n(^3\text{He})}$
Model II++	84	$-2.77^{+0.04}_{-0.05}$	$-2.183 \pm 0.013$	$0.26^{+0.03}_{-0.04}$
Model II++	100	$-2.76^{+0.03}_{-0.04}$	$-2.177^{+0.009}_{-0.010}$	$0.26^{+0.02}_{-0.03}$
Model II++	200	$-2.75 \pm 0.02$	$-2.165^{+0.004}_{-0.005}$	$0.26 \pm 0.02$
Model II++	300	$-2.75 \pm 0.01$	$-2.162 \pm 0.002$	$0.26 \pm 0.01$
BD+48° 2721 <sup>a</sup>	84	$-2.75^{+0.06}_{-0.09}$	$-2.161^{+0.021}_{-0.018}$	$0.26^{+0.04}_{-0.06}$

**Notes:**

Given uncertainties are the same as in Table 10.5. From Table 10.1: Model II++ ( $T_{\text{eff}} = 21\,040\text{ K}$ ,  $\log g = 4.879$ ,  $\log n(^4\text{He}) = -2.75$ ,  $\log n(^3\text{He}) = -2.161$ , He I 6678 Å and He I 10 830 Å included in the analysis).

<sup>(a)</sup> Observed spectrum.

$0.078^{+0.010}_{-0.015}$  (XSHOOTER) to  $n(^4\text{He})/n(^3\text{He}) = 0.61 \pm 0.05$  (FEROS). Feige 38 is less affected:  $n(^4\text{He})/n(^3\text{He}) = 0.19^{+0.04}_{-0.09}$  (XSHOOTER) vs.  $n(^4\text{He})/n(^3\text{He}) = 0.109 \pm 0.016$  (FEROS).

## Conclusion and Outlook

As detailed in Sect. 3.3, the  $^3\text{He}$  isotopic anomaly has been considered a rare phenomenon. It has only been detected in less than 20% of the stars analyzed by Geier et al. (2013a). Although many hot subdwarf B stars have been investigated based on high-resolution spectra, observations of the crucial (sensitive) lines He I 6678 Å, He I 7281 Å, and He I 10 830 Å are lacking in many cases. This is particularly true for the largest homogeneous H-sdB sample known today, which has been derived from ESO SPY (Lisker et al., 2005). However, the most recent detections of  $^3\text{He}$  in HE 0929-0424 and HE 1047-0436 show that several other  $^3\text{He}$  H-sdBs could be found among the stars of ESO SPY, if high/medium-resolution spectra that cover these important lines were available for these objects. This would further constrain the fraction of  $^3\text{He}$  stars among H-sdBs. Luckily, observations of the He I 10 830 Å line in the NIR have now become possible with more and more modern spectrographs (for instance, with XSHOOTER or CARMENES). This looks very promising for further detailed investigations of the isotopic anomaly in other potential  $^3\text{He}$  stars.



# 11. Metal Abundance Study Based on the Hybrid LTE/NLTE Approach

The high and medium-resolution spectra of the program stars of this work are analyzed in terms of metals<sup>124</sup>. For this, the hybrid LTE/NLTE model atmosphere approach and the global analysis strategy (ADS + Global; see Sects. 6.8 and 7.1.2) are used. In order to perform the metal abundance analyses in a sophisticated way, the mean metal abundances for H-sdB/H-sdOB stars (see Fig. 3.3.2 and Table 3.1; Naslim et al. 2013) are implemented as metallicity for all calculated models. As described in Sects. 6.8 and 8.2.5, a detailed metal abundance study can be realized for the following chemical elements: carbon (C II/III), nitrogen (N II/III), oxygen (O I/II), neon (Ne I/II), magnesium (Mg II), aluminum (Al II/III), silicon (Si II/III/IV), sulfur (S II/III), argon (Ar II), and iron (Fe II/III). To this end, the sophisticated NLTE model atoms listed in Table 6.3 are used. In addition, phosphorus (P II), calcium (Ca II), titanium (Ti II), strontium (Sr II), and zirconium (Zr II), which are found for some of the XSHOOTER program stars, are treated in LTE (see Sect. 6.8). Consequently, the metal abundance study presented in this chapter represents a detailed analysis of almost all spectral lines detected in the optical as well as in the NIR wavelength regime, with most of the lines being considered in NLTE. This is a major improvement compared to the LTE study of Geier (2013), who only used a semi-automatic analysis pipeline and a small set of selected and representative spectral lines per ion (see Sect. 3.3). As mentioned in Sect. 8.2.5, however, chemical elements and corresponding ionization stages cannot be assigned to all lines detected in the spectra analyzed in this work. The respective lines are caused by elements that are not included in the analysis. Thus, these lines are excluded from the spectral fits. Furthermore, no model for interstellar absorption is used for the present analysis so that interstellar lines such as the Na I doublet at  $\sim 5890 \text{ \AA}$  and  $\sim 5896 \text{ \AA}$  or the Ca II H and K lines at  $\sim 3968 \text{ \AA}$  and  $\sim 3934 \text{ \AA}$  also have to be excluded from the spectral fits.

Figures 11.0.1-11.0.7 show examples for fitted metal lines in the co-added spectra of the H-sdB GALEX J104148.9-073031 (XSHOOTER), of the <sup>3</sup>He post-BHB PHL 382 (FEROS) as well as of the <sup>3</sup>He H-sdB EC 03591-3232 (FEROS). Part of the analyzed lines are listed in Tables 8.12-8.14. The richness of spectral lines for each of the investigated stars strongly depends on the effective temperature. Typically, the following numbers of spectral lines can be analyzed for each metal under investigation:  $\sim 5$ -80 (C),  $\sim 3$ -90 (N),  $\sim 10$ -100 (O),  $\sim 2$ -30 (Ne),  $\sim 3$ -10 (Mg),  $\sim 4$ -10 (Al),  $\sim 6$ -35 (Si), 2 (P),  $\sim 10$ -35 (S),  $\sim 15$ -35 (Ar), 8 (Ca),  $\sim 5$ -15 (Ti),  $\sim 10$ -120 (Fe),  $\sim 2$ -5 (Sr), and  $\sim 10$  (Zr). Obviously, the more lines per element are

<sup>124</sup>No metal abundances are derived for the H-sdO and the He-sdO program stars. For the former, no spectra are analyzed (see Sect. 8.1.2) and for the latter the TLUSTY/SYNSPEC approach with fixed metal abundances for carbon, nitrogen, and oxygen only is used (see Sect. 6.9).

## 11. Metal Abundance Study Based on the Hybrid LTE/NLTE Approach

---

present in a stellar spectrum, the better. This is because the uncertainties in the atomic data, mainly resulting from the individual oscillator strengths, average out if the number of analyzed lines is sufficiently high. As can be seen from Figs. 11.0.1-11.0.7, metal lines associated with different ionization stages of the same elements generally can be fitted similarly well. Therefore, the respective ionization equilibria additionally constrain the effective temperatures (and the surface gravities) of the analyzed stars (see Sect. 7.1.1). However, there is one striking exception (the H-sdB HD 4539), for which Si II and Si III lines cannot be matched simultaneously. This phenomenon was also recently observed by Möller (2021) and it seems to be related to the silicon model atoms used.

Tables 11.1-11.6 summarize the metal abundances derived for the analyzed program stars. Therein, all values are given as base-10 logarithmic particle densities relative to the density of all particles (see Sect. 7.1.1), that is,  $\log n(X) := \log \left[ \frac{N(X)}{N(\text{all elements})} \right]$ , where  $X \in \{\text{C, N, O, Ne, Mg, Al, Si, P, S, Ar, Ca, Ti, Fe, Sr, Zr}\}$  and  $n(X)$  is the ratio of the number density of element X to that of all the elements in the stellar atmosphere. In Figs. 11.1.1, 11.1.2, and 11.2.1, the measured metal abundances are plotted against the corresponding effective temperatures  $T_{\text{eff}}$  of the analyzed stars (the individual values for  $T_{\text{eff}}$  can be found in Tables A.1-A.10 and A.20-A.23). In these figures, the solar abundances (Asplund et al., 2009) as well as the mean abundances for H-sdBs/H-sdOBs (see Fig. 3.3.2 and Table 3.1; Naslim et al. 2013) are marked. In addition, the abundance ranges of Geier (2013) and Naslim et al. (2013) are given therein. The metal abundance errors listed in Tables 11.1-11.6 and plotted in Figs. 11.1.1, 11.1.2, and 11.2.1 combine  $1\sigma$  statistical confidence intervals and the  $1\sigma$  systematic uncertainties described in Sect. 7.1.2. The plotted uncertainties for  $T_{\text{eff}}$  combine the  $1\sigma$  statistical single parameter errors (listed in Tables A.1-A.10 and A.20-A.23) and the global systematic errors derived in Sect. 9.2.7. For the H-sdBs HD 4539, Feige 38, and EC 03591-3232 as well as for the H-sdOB HD 149382, multiple spectra are analyzed. Thus, the adopted (plotted) abundances and effective temperatures for these objects represent weighted averages, whereby the reciprocals of the individual maximum variances, that is  $\frac{1}{(\max[\text{uncertainty}])^2}$ , are used as weights. As can be seen from Tables 11.1-11.6, upper limits are derived for some elements in the case of several program stars. These upper limits are marked by triangles in Figs. 11.1.1 and 11.1.2. In the rare case that only upper limits for a metal abundance result from the multiple spectra available, the highest abundance value is adopted (plotted) as the final upper limit. As a matter of fact, most of the stars analyzed in this chapter belong to the group of hot subdwarf stars. The (post-)BHB stars PHL 25, PHL 382, and BD+48° 2721 are the sole exceptions to this. These three stars are highlighted in Figs. 11.1.1 and 11.1.2.



11. Metal Abundance Study Based on the Hybrid LTE/NLTE Approach

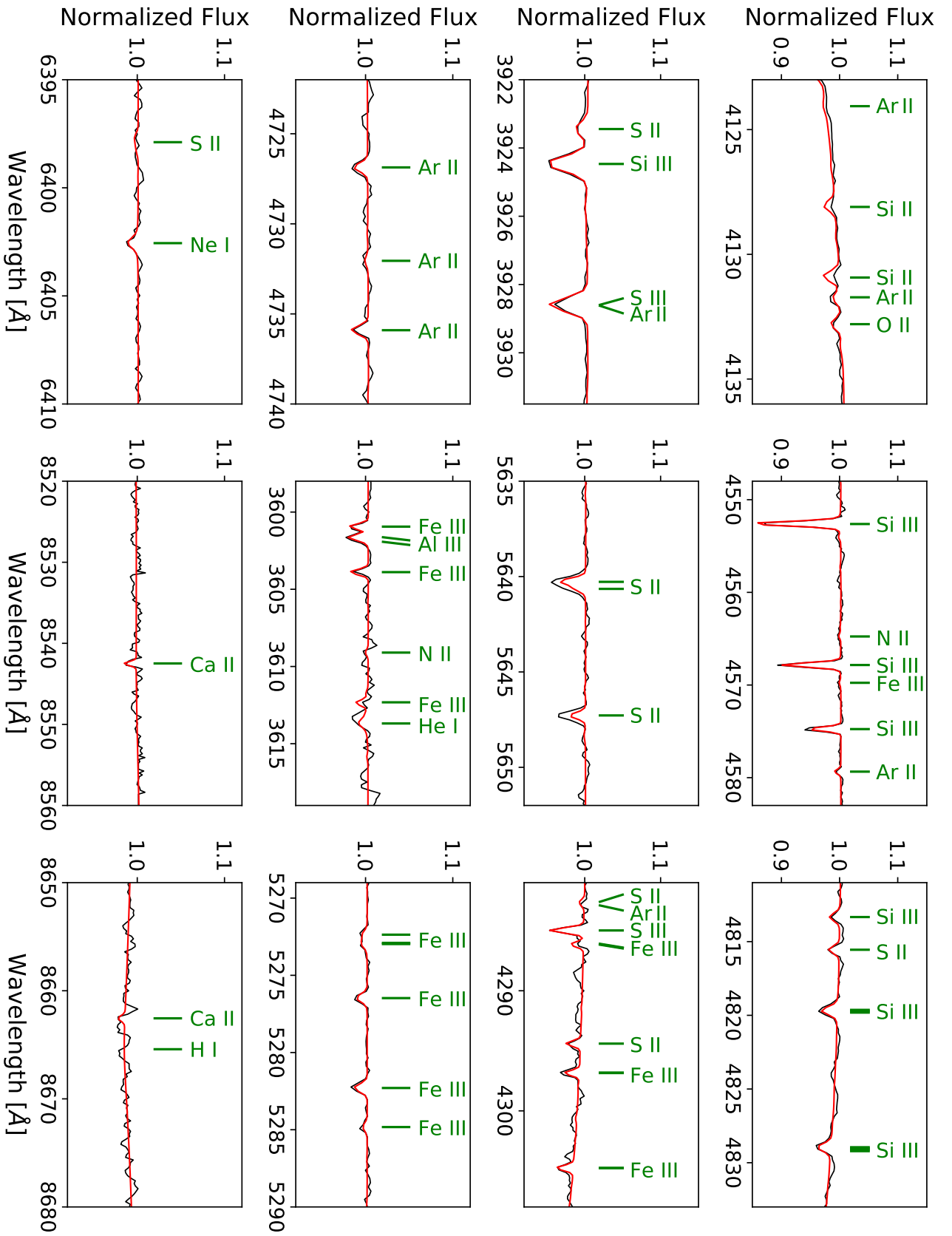


Figure 11.0.2.: Same as Fig. 11.0.1, but showing additional metal (and hydrogen and helium) lines in the co-added XSHOOTER spectrum of the H-sdB star GALEX J104148.9-073031.



11. Metal Abundance Study Based on the Hybrid LTE/NLTE Approach

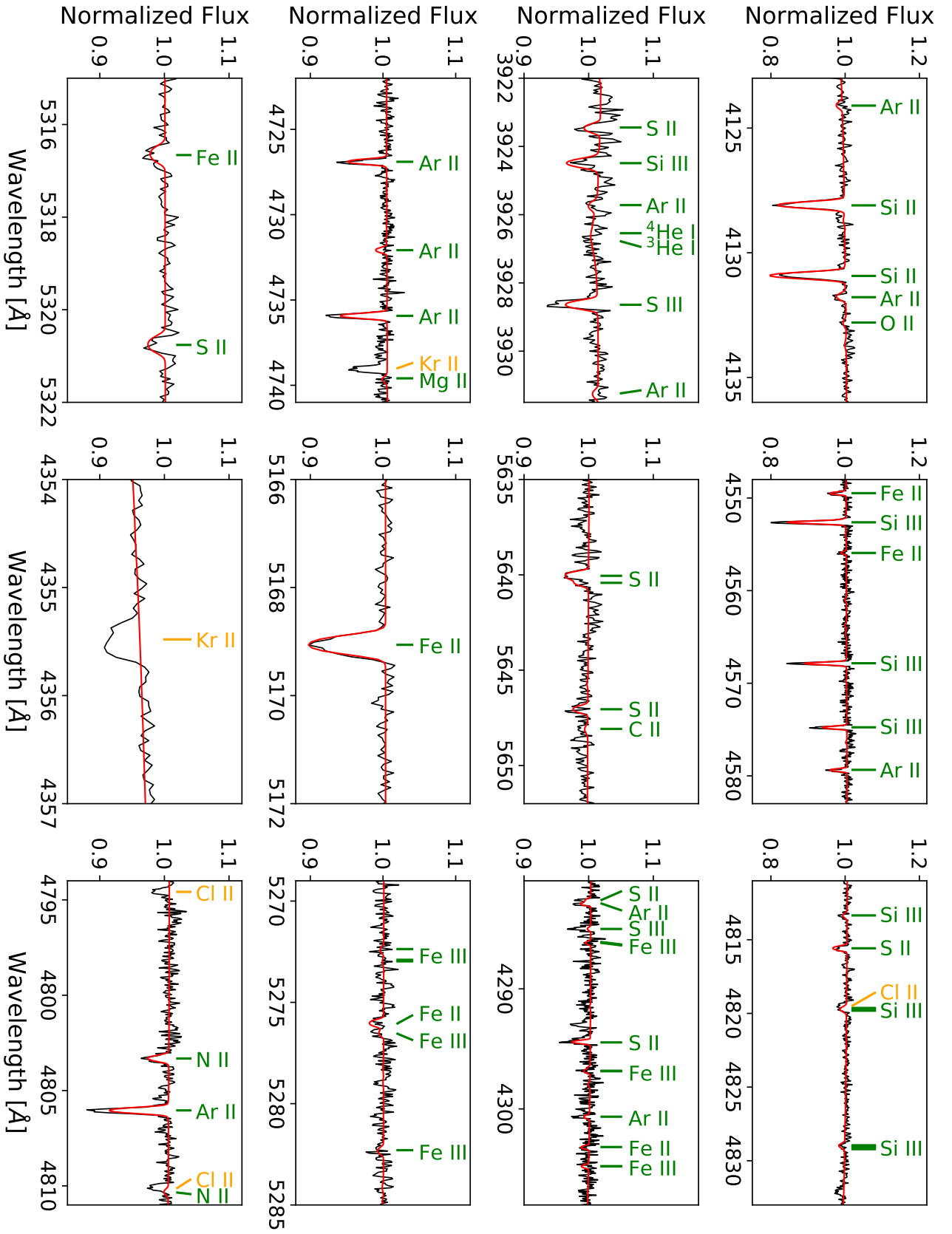


Figure 11.0.4.: Same as Fig. 11.0.3, but showing additional metal (and helium) lines in the co-added FEROS spectrum of the rotating  ${}^3\text{He}$  post-BHB star PHL 382.

## 11. Metal Abundance Study Based on the Hybrid LTE/NLTE Approach

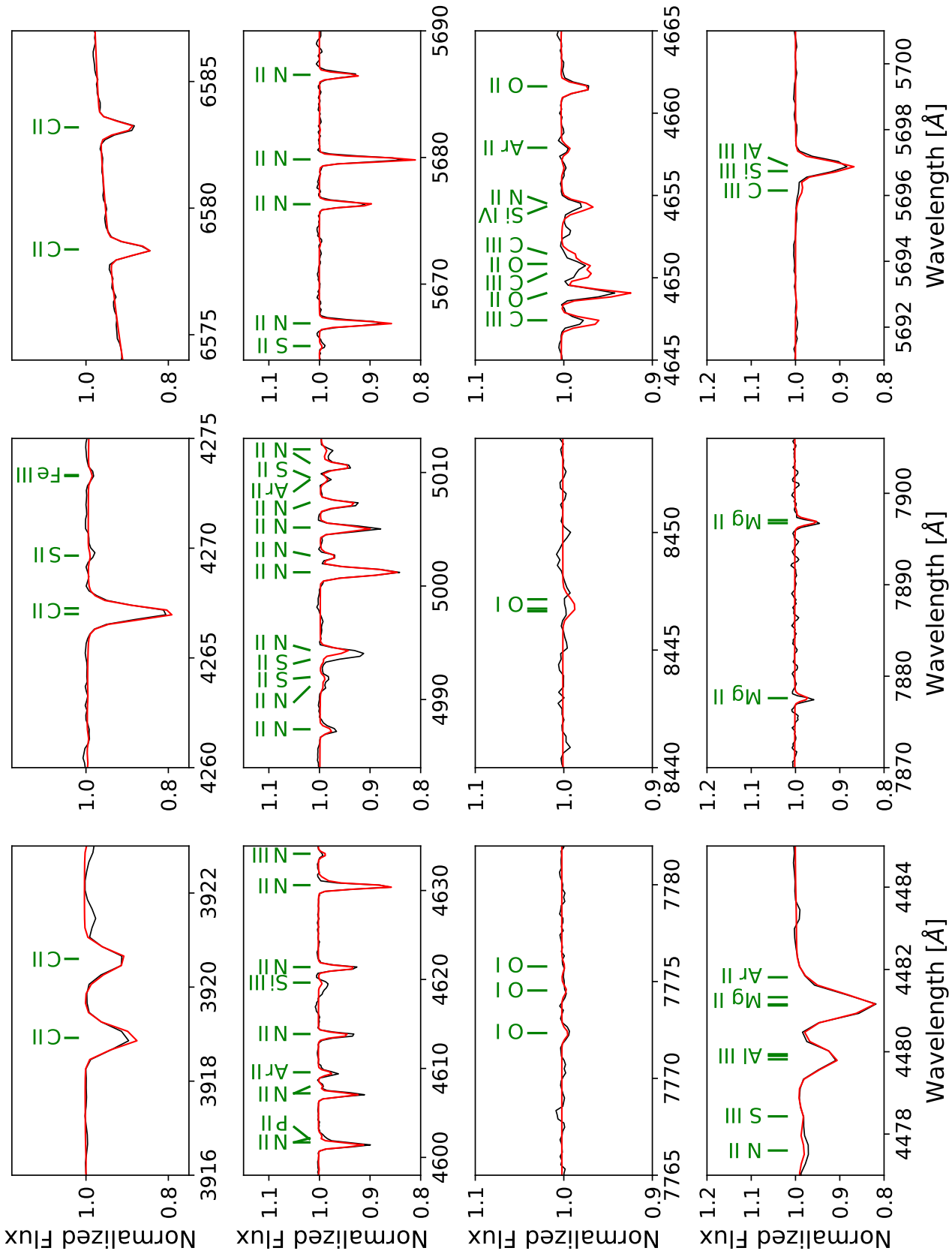


Figure 11.0.5.: Selected metal lines in the co-added FEROS spectrum of the  ${}^3\text{He}$  H-sdB star EC 03591-3232. The observed spectrum (solid black line) and the best fit (solid red line) are shown. Solid green lines/labels mark the central wavelength positions and the ionization stages of the individual spectral lines (see also Tables 8.12-8.14).

11. Metal Abundance Study Based on the Hybrid LTE/NLTE Approach

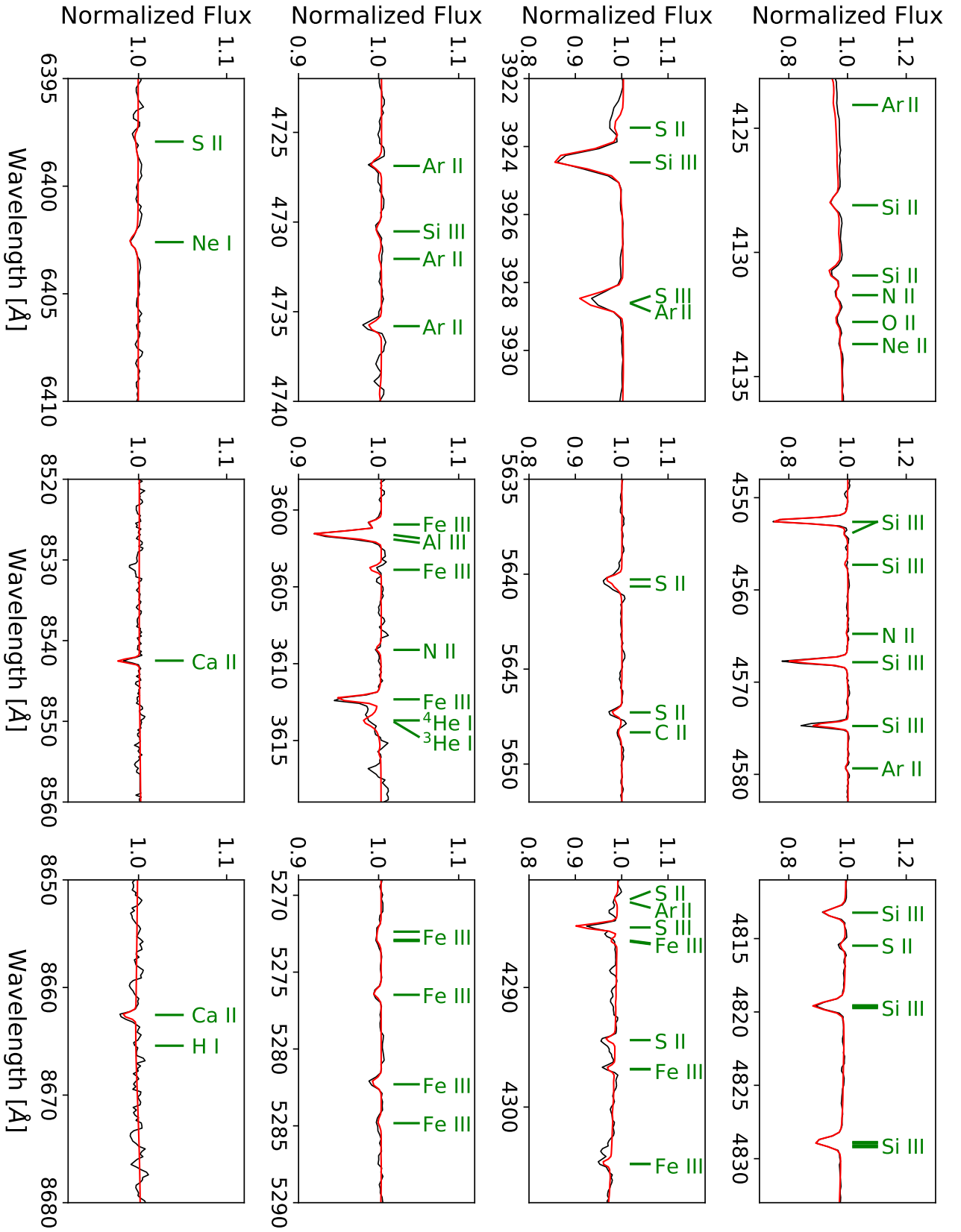


Figure 11.0.6.: Same as Fig. 11.0.5, but showing additional metal (and hydrogen and helium) lines in the co-added FEROS spectrum of the  ${}^3\text{He}$  H-sdB star EC 03591-3232.



Table 11.1.: Carbon to phosphorus metal abundances (listed as base-10 logarithmic particle densities relative to the density of all particles) that are determined from the hybrid LTE/NLTE model atmosphere approach and the global analysis strategy (ADS + Global) for the program stars, for which high and medium-resolution spectra are analyzed (H-sdOs and He-sdOs excluded; see the corresponding footnote at the beginning of Ch. 11 for more information). The results of this work are compared to the ones of the LTE study of Geier (2013) as well as to solar abundances according to Asplund et al. (2009).

Star	Instrument	$\log n(\text{C})$	$\log n(\text{N})$	$\log n(\text{O})$	$\log n(\text{Ne})$	$\log n(\text{Mg})$	$\log n(\text{Al})$	$\log n(\text{Si})$	$\log n(\text{P})$	Ref.
HD 4539 <sup>a</sup>	XSHOOTER	$-3.970^{+0.013}_{-0.009}$	$-3.894^{+0.043}_{-0.033}$	$-4.894 \pm 0.049$	$\leq -6.80^e$	$-5.601^{+0.032}_{-0.037}$	$-6.375^{+0.027}_{-0.019}$	$-5.3880^{+0.0123}_{-0.0138}$	-	This work
	FEROS	$-3.95^{+0.03}_{-0.02}$	$-3.77^{+0.05}_{-0.04}$	$-4.76^{+0.05}_{-0.08}$	$\leq -7.00^e$	$-5.64 \pm 0.05$	$-6.31 \pm 0.04$	$-5.38 \pm 0.03$	-	This work
Adopted		$-3.97 \pm 0.02$	$-3.84 \pm 0.04$	$-4.86 \pm 0.05$	$\leq -6.80^e$	$-5.61 \pm 0.03$	$-6.35 \pm 0.03$	$-5.39 \pm 0.02$	-	This work
		$-3.96 \pm 0.23$	$-4.14 \pm 0.16$	$-5.01 \pm 0.31$	$\leq -3.86^e$	$-5.44 \pm 0.15$	$-6.44 \pm 0.15$	$-5.34 \pm 0.08$	$\leq -7.22^e$	[1]
Feige 38	XSHOOTER	$-4.148^{+0.040}_{-0.037}$	$-3.873^{+0.031}_{-0.026}$	$-4.495^{+0.017}_{-0.016}$	$\leq -5.80^e$	$-4.872 \pm 0.035$	$-6.318^{+0.040}_{-0.036}$	$-4.375 \pm 0.017$	-	This work
	FEROS	$-4.19^{+0.02}_{-0.03}$	$-3.89^{+0.03}_{-0.02}$	$-4.45^{+0.03}_{-0.02}$	$\leq -5.40^e$	$-4.84 \pm 0.04$	$-6.24^{+0.04}_{-0.03}$	$-4.26 \pm 0.02$	-	This work
Adopted		$-4.17 \pm 0.03$	$-3.88 \pm 0.03$	$-4.48 \pm 0.02$	$\leq -5.40^e$	$-4.86 \pm 0.03$	$-6.28 \pm 0.03$	$-4.33 \pm 0.02$	-	This work
		$-4.31 \pm 0.35$	$-4.02 \pm 0.14$	$-4.39 \pm 0.11$	$\leq -4.02^e$	$-4.94 \pm 0.15$	$-6.24 \pm 0.15$	$-4.24 \pm 0.34$	$\leq -7.13^e$	[1]
EC 03591-3232	XSHOOTER	$-4.042^{+0.045}_{-0.040}$	$-3.772^{+0.015}_{-0.012}$	$-4.307 \pm 0.016$	$-4.590^{+0.044}_{-0.074}$	$-4.571^{+0.040}_{-0.037}$	$-5.574^{+0.018}_{-0.017}$	$-4.324 \pm 0.007$	$-6.425^{+0.187}_{-0.444}$	This work
	FEROS	$-4.11 \pm 0.03$	$-3.75 \pm 0.02$	$-4.36 \pm 0.02$	$-4.18^{+0.05}_{-0.06}$	$-4.48 \pm 0.04$	$-5.53 \pm 0.03$	$-4.36 \pm 0.02$	-	This work
Adopted		$-4.09 \pm 0.03$	$-3.76 \pm 0.02$	$-4.33 \pm 0.02$	$-4.34 \pm 0.05$	$-4.53 \pm 0.03$	$-5.56 \pm 0.02$	$-4.33 \pm 0.01$	$-6.425^{+0.187}_{-0.444}$	This work
		$-4.24 \pm 0.32$	$-3.94 \pm 0.16$	$-4.26 \pm 0.29$	-	$-4.74 \pm 0.15$	$-5.64 \pm 0.14$	$-4.13 \pm 0.38$	$\leq -7.21^e$	[1]
PG 1432+004	XSHOOTER	$-4.008^{+0.024}_{-0.023}$	$-3.970 \pm 0.047$	$-4.620^{+0.046}_{-0.053}$	$-4.957^{+0.045}_{-0.044}$	$-5.219^{+0.030}_{-0.032}$	$-6.032^{+0.053}_{-0.052}$	$-5.115^{+0.037}_{-0.044}$	-	This work
		$-3.94 \pm 0.25$	$-4.05 \pm 0.23$	$-4.42 \pm 0.33$	-	$-5.34 \pm 0.15$	$-6.04 \pm 0.15$	$-4.79 \pm 0.13$	$\leq -7.20^e$	[1]
PG 1136-003 <sup>b</sup>	XSHOOTER	$\leq -6.60^e$	$\leq -6.00^e$	$-4.90^{+0.08}_{-0.06}$	$\leq -6.00^e$	$-5.240^{+0.055}_{-0.057}$	$-6.319^{+0.095}_{-0.087}$	$-5.94^{+0.08}_{-0.10}$	-	This work
Solar Abundance		$-3.61 \pm 0.05$	$-4.21 \pm 0.05$	$-3.35 \pm 0.05$	$-4.11 \pm 0.10$	$-4.44 \pm 0.04$	$-5.59 \pm 0.03$	$-4.53 \pm 0.03$	$-6.63 \pm 0.03$	[2]

**Notes:** C, N, O, Ne, Mg, Al, and Si are analyzed in NLTE thanks to the sophisticated NLTE model atoms available, whereas P is treated in LTE (see Sect. 6.8). P is only analyzed for stars of the XSHOOTER reference sample. For the results of this work, the listed errors combine  $1\sigma$  statistical confidence intervals and the  $1\sigma$  systematic uncertainties described in Sect. 7.1.2. For HD 4539, Feige 38, EC 03591-3232, and HD 149382, multiple spectra are analyzed. Thus, the adopted abundances for these objects represent weighted averages, whereby the reciprocals of the individual maximum variances, that is  $\frac{1}{(\max[\text{uncertainty}])^2}$ , are used as weights.

(a) Pulsating star.

(b) RV-variable star.

(c) Rotating star.

(d) The star is (most likely) a pre-ELM. For further information, see Ch. 13. For the very unique object Feige 36, see in particular Sect. 12.2.

(e) Upper limit.

**References:** (1) Geier (2013); (2) Asplund et al. (2009).

Table 11.2.: Table 11.1 continued.

Star	Instrument	$\log n(\text{C})$	$\log n(\text{N})$	$\log n(\text{O})$	$\log n(\text{Ne})$	$\log n(\text{Mg})$	$\log n(\text{Al})$	$\log n(\text{Si})$	$\log n(\text{P})$	Ref.
GALEX J104148.9-073031	XSHOOTER	$-4.783^{+0.028}_{-0.026}$	$-3.966^{+0.020}_{-0.012}$	$-4.122^{+0.030}_{-0.028}$	$-4.73 \pm 0.09$	$-5.204^{+0.030}_{-0.034}$	$-6.390^{+0.017}_{-0.016}$	$-5.068^{+0.020}_{-0.018}$	-	This work
GALEX J080510.9-105834 <sup>bcd</sup>	XSHOOTER	$\leq -6.00^e$	$\leq -7.00^e$	$\leq -6.00^e$	$\leq -7.00^e$	$-5.982^{+0.036}_{-0.032}$	$\leq -7.00^e$	$\leq -7.00^e$	-	This work
PG 1505+074	XSHOOTER	$\leq -7.00^e$ $\leq -5.93^e$	$\leq -7.00^e$ $\leq -5.18^e$	$\leq -6.00^e$ $\leq -5.26^e$	$-4.93^{+0.17}_{-0.21}$ -	$-4.920^{+0.044}_{-0.043}$ $-5.04 \pm 0.15$	$-6.48 \pm 0.11$ $\leq -6.13^e$	$-5.584^{+0.055}_{-0.059}$ $-5.79 \pm 0.07$	-	This work [1]
EC 13047-3049	XSHOOTER	$-5.476^{+0.050}_{-0.048}$ $\leq -4.25^e$	$-5.191^{+0.030}_{-0.045}$ $\leq -4.97^e$	$\leq -6.00^e$ $\leq -4.99^e$	$\leq -7.00^e$ $\leq -4.21^e$	$-5.007^{+0.029}_{-0.035}$ $-5.24 \pm 0.15$	$-6.33 \pm 0.09$ $-5.74 \pm 0.15$	$-5.569^{+0.040}_{-0.032}$ $-5.94 \pm 0.14$	- $\leq -6.20^e$	This work [1]
[CW83] 0825+15 <sup>a</sup>	XSHOOTER	$\leq -6.00^e$	$-3.989^{+0.062}_{-0.068}$	$\leq -6.00^e$	$\leq -7.00^e$	$-5.14 \pm 0.08$	$-6.12 \pm 0.11$	$-5.370^{+0.044}_{-0.060}$	-	This work
[CW83] 0512-08	XSHOOTER	$-3.622 \pm 0.020$ $-3.37 \pm 0.09$	$-3.978^{+0.056}_{-0.062}$ $-4.11 \pm 0.15$	$-5.19^{+0.17}_{-0.20}$ $\leq -4.72^e$	$\leq -7.00^e$ -	$-5.60^{+0.12}_{-0.17}$ -	$-6.30^{+0.12}_{-0.15}$ $\leq -5.18^e$	$-6.45^{+0.15}_{-0.16}$ $-6.54 \pm 0.15$	- $\leq -5.95^e$	This work [1]
HD 149382	XSHOOTER UVES	$-5.423 \pm 0.034$ $-5.18 \pm 0.03$	$-4.214^{+0.046}_{-0.056}$ $-4.07 \pm 0.05$	$\leq -6.00^e$ $\leq -6.00^e$	$\leq -7.00^e$ $\leq -7.00^e$	$\leq -5.80^e$ $\leq -5.80^e$	$\leq -7.00^e$ $\leq -7.00^e$	$\leq -7.00^e$ $\leq -7.00^e$	- -	This work This work
Adopted		$-5.29 \pm 0.03$ $\leq -4.91^e$	$-4.13 \pm 0.04$ $-4.40 \pm 0.11$	$\leq -6.00^e$ $-4.49 \pm 0.21$	$\leq -7.00^e$ $\leq -4.93^e$	$\leq -5.80^e$ $\leq -5.87^e$	$\leq -7.00^e$ $\leq -6.08^e$	$\leq -7.00^e$ $\leq -6.92^e$	- -	This work [1]
CD-35 <sup>o</sup> 15910 <sup>a</sup>	FEROS	$-5.50 \pm 0.06$ $\leq -4.75^e$	$-4.53 \pm 0.02$ $-4.54 \pm 0.15$	$-4.32^{+0.04}_{-0.03}$ $-4.43 \pm 0.17$	$-4.39^{+0.08}_{-0.11}$ -	$-5.69 \pm 0.05$ $-5.34 \pm 0.15$	$-7.10^{+0.11}_{-0.13}$ $\leq -6.25^e$	$-5.65 \pm 0.04$ $\leq -6.10^e$	- $\leq -7.10^e$	This work [1]
PHL 25	HRS	$-5.83^{+0.17}_{-0.25}$	$\leq -6.80^e$	$\leq -6.00^e$	$\leq -7.00^e$	$-5.36^{+0.07}_{-0.09}$	$\leq -8.00^e$	$-4.30 \pm 0.04$	-	This work
PHL 382 <sup>c</sup>	FEROS	$-4.10 \pm 0.05$	$-3.68^{+0.07}_{-0.06}$	$-3.81^{+0.09}_{-0.10}$	$-4.85 \pm 0.05$	$-5.10 \pm 0.03$	$-6.34^{+0.08}_{-0.06}$	$-4.44^{+0.03}_{-0.04}$	-	This work
BD+48 <sup>o</sup> 2721	FOCES	$-5.37 \pm 0.03$ $-5.54 \pm 0.15$	$-4.46 \pm 0.05$ $-4.30 \pm 0.12$	$-4.49^{+0.07}_{-0.06}$ $-4.13 \pm 0.13$	$-4.56 \pm 0.03$ -	$-5.21^{+0.05}_{-0.04}$ $-5.44 \pm 0.15$	$-6.62^{+0.07}_{-0.08}$ $-6.64 \pm 0.15$	$-5.11^{+0.04}_{-0.05}$ $-4.91 \pm 0.21$	- -	This work [1]
SB 290 <sup>c</sup>	FEROS	$-4.61^{+0.03}_{-0.04}$	$-4.76^{+0.03}_{-0.02}$	$-4.48^{+0.06}_{-0.05}$	$\leq -5.90^e$	$-6.02^{+0.10}_{-0.13}$	$-7.05^{+0.16}_{-0.24}$	$-5.11 \pm 0.04$	-	This work
EC 03263-6403	FEROS	$-4.68 \pm 0.06$	$-4.59 \pm 0.04$	$-4.28 \pm 0.03$	$\leq -6.20^e$	$-5.16 \pm 0.06$	$-6.59^{+0.10}_{-0.15}$	$-4.92 \pm 0.04$	-	This work
Solar Abundance		$-3.61 \pm 0.05$	$-4.21 \pm 0.05$	$-3.35 \pm 0.05$	$-4.11 \pm 0.10$	$-4.44 \pm 0.04$	$-5.59 \pm 0.03$	$-4.53 \pm 0.03$	$-6.63 \pm 0.03$	[2]

Table 11.3.: Table 11.1 continued.

Star	Instrument	$\log n(\text{C})$	$\log n(\text{N})$	$\log n(\text{O})$	$\log n(\text{Ne})$	$\log n(\text{Mg})$	$\log n(\text{Al})$	$\log n(\text{Si})$	$\log n(\text{P})$	Ref.
EC 12234-2607	FEROS	$-4.05 \pm 0.05$ $-4.34 \pm 0.26$	$-4.11 \pm 0.02$ $-4.26 \pm 0.18$	$-3.56 \pm 0.04$ $-3.52 \pm 0.23$	$-3.71 \pm 0.05$ -	$-4.75 \pm 0.05$ $-5.04 \pm 0.15$	$-6.34 \pm 0.05$ $\leq -5.95^e$	$-4.65 \pm 0.03$ $-4.75 \pm 0.35$	- $\leq -6.57^e$	This work [1]
EC 14338-1445	FEROS	$-4.77 \pm 0.05$ $-5.04 \pm 0.15$	$-4.19^{+0.02}_{-0.03}$ $-4.42 \pm 0.17$	$-4.53 \pm 0.03$ $-4.53 \pm 0.25$	$\leq -6.00^e$ $\leq -3.43^e$	$-5.47 \pm 0.08$ $-5.54 \pm 0.15$	$-6.26 \pm 0.05$ $\leq -6.08^e$	$-4.72 \pm 0.03$ $-4.67 \pm 0.42$	- $\leq -6.77^e$	This work [1]
PG 1710+490	FOCES	$-4.42 \pm 0.06$ $\leq -5.05^e$	$-3.84 \pm 0.05$ $-4.10 \pm 0.15$	$-4.37^{+0.03}_{-0.04}$ $-4.24 \pm 0.09$	$\leq -5.20^e$ -	$-5.32^{+0.11}_{-0.12}$ $-5.14 \pm 0.15$	$-6.03^{+0.08}_{-0.09}$ $-5.74 \pm 0.15$	$-4.41^{+0.03}_{-0.04}$ $-4.44 \pm 0.20$	- -	This work [1]
Feige 36 <sup>bd</sup>	HIRES	$\leq -6.00^e$ $\leq -4.73^e$	$-4.37 \pm 0.02$ $-4.48 \pm 0.05$	$-4.17 \pm 0.03$ $-4.27 \pm 0.26$	$\leq -6.20^e$ -	$-5.38 \pm 0.05$ $-5.44 \pm 0.15$	$-6.49 \pm 0.04$ $-6.44 \pm 0.15$	$-5.04 \pm 0.02$ $-4.97 \pm 0.06$	- -	This work [1]
HE 0929-0424 <sup>b</sup>	UVES	$\leq -6.00^e$ $\leq -4.51^e$	$-4.10 \pm 0.04$ $-4.34 \pm 0.16$	$-4.16 \pm 0.05$ $-4.40 \pm 0.14$	$\leq -5.20^e$ $-5.04 \pm 0.15$	$-5.10 \pm 0.10$ -	$-5.73 \pm 0.07$ $-6.54 \pm 0.15$	$-5.15 \pm 0.07$ $-5.84 \pm 0.28$	- $\leq -6.87^e$	This work [1]
HE 1047-0436 <sup>b</sup>	UVES	$-4.19^{+0.05}_{-0.07}$ $\leq -4.45^e$	$-3.79^{+0.04}_{-0.03}$ $-4.04 \pm 0.01$	$-4.16 \pm 0.03$ $-4.34 \pm 0.13$	$\leq -5.50^e$ $-5.24 \pm 0.15$	$-5.05 \pm 0.08$ $-5.14 \pm 0.15$	$-6.23^{+0.09}_{-0.13}$ $-6.64 \pm 0.15$	$-4.82 \pm 0.04$ $-5.23 \pm 0.21$	- $\leq -7.02^e$	This work [1]
PG 0342+026 <sup>a</sup>	FEROS	$-4.57 \pm 0.03$ $-4.84 \pm 0.26$	$-3.98 \pm 0.03$ $-4.07 \pm 0.19$	$-4.20 \pm 0.05$ $-4.28 \pm 0.21$	$\leq -6.60^e$ -	$-5.56 \pm 0.03$ $-5.44 \pm 0.15$	$-6.73 \pm 0.03$ $\leq -6.37^e$	$-5.08 \pm 0.04$ $-5.05 \pm 0.18$	- $\leq -7.23^e$	This work [1]
Solar Abundance		$-3.61 \pm 0.05$	$-4.21 \pm 0.05$	$-3.35 \pm 0.05$	$-4.11 \pm 0.10$	$-4.44 \pm 0.04$	$-5.59 \pm 0.03$	$-4.53 \pm 0.03$	$-6.63 \pm 0.03$	[2]

Table 11.4.: Sulfur to zirconium metal abundances (listed as base-10 logarithmic particle densities relative to the density of all particles) that are determined from the hybrid LTE/NLTE model atmosphere approach and the global analysis strategy (ADS + Global) for the program stars, for which high and medium-resolution spectra are analyzed (H-sdOs and He-sdOs excluded; see the corresponding footnote at the beginning of Ch. 11 for more information). The results of this work are compared to the ones of the LTE study of Geier (2013) as well as to solar abundances according to Asplund et al. (2009).

Star	Instrument	$\log n(\text{S})$	$\log n(\text{Ar})$	$\log n(\text{Ca})$	$\log n(\text{Ti})$	$\log n(\text{Fe})$	$\log n(\text{Sr})$	$\log n(\text{Zr})$	Ref.
HD 4539 <sup>a</sup>	XSHOOTER	$-4.976^{+0.026}_{-0.028}$	$-5.109^{+0.040}_{-0.030}$	$-5.799^{+0.092}_{-0.093}$	-	$-4.498^{+0.024}_{-0.022}$	$-7.41^{+0.31}_{-0.61}$	-	This work
	FEROS	$-5.11 \pm 0.04$	$-5.14 \pm 0.02$	-	-	$-4.49 \pm 0.03$	-	-	This work
Adopted		$-5.02 \pm 0.03$	$-5.13 \pm 0.02$	$-5.799^{+0.092}_{-0.093}$	-	$-4.49 \pm 0.02$	$-7.41^{+0.31}_{-0.61}$	-	This work
		$-4.94 \pm 0.14$	$-4.87 \pm 0.15$	-	$-5.79 \pm 0.49$	$-4.66 \pm 0.15$	-	-	[1]
Feige 38	XSHOOTER	$-4.666^{+0.021}_{-0.020}$	$-4.793^{+0.076}_{-0.087}$	-	$-5.75^{+0.25}_{-0.23}$	$-4.929^{+0.051}_{-0.047}$	-	-	This work
	FEROS	$-4.48 \pm 0.03$	$-4.86^{+0.06}_{-0.05}$	-	-	$-4.87 \pm 0.02$	-	-	This work
Adopted		$-4.60 \pm 0.02$	$-4.84 \pm 0.05$	-	$-5.75^{+0.25}_{-0.23}$	$-4.88 \pm 0.02$	-	-	This work
		$-4.78 \pm 0.15$	$-4.94 \pm 0.17$	-	$-5.19 \pm 0.35$	$-4.88 \pm 0.11$	-	-	[1]
EC 03591-3232	XSHOOTER	$-4.533^{+0.021}_{-0.023}$	$-4.800^{+0.068}_{-0.079}$	$-5.27^{+0.09}_{-0.10}$	$-5.90^{+0.19}_{-0.25}$	$-4.809^{+0.013}_{-0.015}$	$-6.35^{+0.41}_{-0.72}$	-	This work
	FEROS	$-4.41^{+0.05}_{-0.04}$	$-4.80 \pm 0.05$	-	-	$-4.89 \pm 0.02$	-	-	This work
Adopted		$-4.51 \pm 0.03$	$-4.80 \pm 0.05$	$-5.27^{+0.09}_{-0.10}$	$-5.90^{+0.19}_{-0.25}$	$-4.84 \pm 0.02$	$-6.35^{+0.41}_{-0.72}$	-	This work
		$-4.93 \pm 0.07$	$-5.01 \pm 0.15$	-	$-5.24 \pm 0.42$	$-5.01 \pm 0.19$	-	-	[1]
PG 1432+004	XSHOOTER	$-4.881^{+0.028}_{-0.027}$	$-5.098^{+0.028}_{-0.026}$	$-5.918^{+0.085}_{-0.081}$	$-6.27 \pm 0.15$	$-4.851^{+0.043}_{-0.039}$	-	-	This work
		$-5.22 \pm 0.09$	$-5.14 \pm 0.17$	-	$-5.79 \pm 0.49$	$-4.90 \pm 0.16$	-	-	[1]
PG 1136-003 <sup>b</sup>	XSHOOTER	$-5.90^{+0.13}_{-0.11}$	$\leq -5.80^e$	-	-	$\leq -6.00^e$	-	-	This work
Solar Abundance		$-4.92 \pm 0.03$	$-5.64 \pm 0.13$	$-5.70 \pm 0.04$	$-7.09 \pm 0.05$	$-4.54 \pm 0.04$	$-9.17 \pm 0.07$	$-9.46 \pm 0.04$	[2]

**Notes:** S, Ar, and Fe are analyzed in NLTE thanks to the sophisticated NLTE model atoms available, whereas Ca, Ti, Sr, and Zr are treated in LTE (see Sect. 6.8). Ca, Ti, Sr, and Zr are only analyzed for stars of the XSHOOTER reference sample. For the results of this work, the listed errors combine  $1\sigma$  statistical confidence intervals and the  $1\sigma$  systematic uncertainties described in Sect. 7.1.2. For HD 4539, Feige 38, EC 03591-3232, and HD 149382, multiple spectra are analyzed. Thus, the adopted abundances for these objects represent weighted averages, whereby the reciprocals of the individual maximum variances, that is  $\frac{1}{(\max[\text{uncertainty}])^2}$ , are used as weights.

(a) Pulsating star.

(b) RV-variable star.

(c) Rotating star.

(d) The star is (most likely) a pre-ELM. For further information, see Ch. 13. For the very unique object Feige 36, see in particular Sect. 12.2.

(e) Upper limit.

**References:** (1) Geier (2013); (2) Asplund et al. (2009).

Table 11.5.: Table 11.4 continued.

Star	Instrument	$\log n(\text{S})$	$\log n(\text{Ar})$	$\log n(\text{Ca})$	$\log n(\text{Ti})$	$\log n(\text{Fe})$	$\log n(\text{Sr})$	$\log n(\text{Zr})$	Ref.
GALEX J104148.9-073031	XSHOOTER	$-4.867^{+0.031}_{-0.032}$	$-4.977^{+0.048}_{-0.047}$	$-5.90^{+0.10}_{-0.11}$	-	$-4.622^{+0.019}_{-0.017}$	-	-	This work
GALEX J080510.9-105834 <sup>bcd</sup>	XSHOOTER	$\leq -7.00^e$	$\leq -7.00^e$	-	-	$-5.29^{+0.20}_{-0.32}$	-	-	This work
PG 1505+074	XSHOOTER	$\leq -7.00^e$ $\leq -6.57^e$	$\leq -7.00^e$ -	- -	$\leq -6.14^e$	$\leq -6.00^e$ $\leq -5.32^e$	-	-	This work [1]
EC 13047-3049	XSHOOTER	$\leq -7.00^e$ $\leq -5.72^e$	$\leq -7.00^e$ $\leq -4.14^e$	- $\leq -4.06^e$	- $\leq -5.39^e$	$\leq -6.00^e$ $-4.64 \pm 0.15$	-	-	This work [1]
[CW83] 0825+15 <sup>a</sup>	XSHOOTER	$-3.928^{+0.087}_{-0.082}$	$\leq -6.00^e$	$-4.54^{+0.09}_{-0.11}$	-	$-4.43 \pm 0.13$	-	$-4.99^{+0.16}_{-0.29}$	This work
[CW83] 0512-08	XSHOOTER	$-4.109^{+0.074}_{-0.069}$ $-3.99 \pm 0.21$	$\leq -6.00^e$ -	$-4.463^{+0.048}_{-0.047}$ $-3.89 \pm 0.07$	- $-4.34 \pm 0.14$	$-4.175^{+0.080}_{-0.087}$ $\leq -4.23^e$	-	-	This work [1]
HD 149382	XSHOOTER UVES	$-4.571^{+0.068}_{-0.077}$ $-4.36 \pm 0.07$	$-4.24^{+0.21}_{-0.26}$ $-4.21^{+0.19}_{-0.17}$	$-4.88^{+0.06}_{-0.08}$ -	- -	$-5.03^{+0.15}_{-0.18}$ $-4.89^{+0.13}_{-0.10}$	-	-	This work This work
Adopted		$-4.46 \pm 0.06$ $-4.69 \pm 0.07$	$-4.22 \pm 0.16$ $-4.34 \pm 0.15$	$-4.88^{+0.06}_{-0.08}$ $-4.14 \pm 0.14$	- $\leq -4.68^e$	$-4.94 \pm 0.11$ $\leq -5.23^e$	-	-	This work [1]
CD-35 <sup>o</sup> 15910 <sup>a</sup>	FEROS	$-5.67 \pm 0.05$ $-6.09 \pm 0.07$	$\leq -6.60^e$ $\leq -5.26^e$	- -	- $\leq -6.35^e$	$-4.42 \pm 0.02$ $-4.48 \pm 0.15$	-	-	This work [1]
PHL 25	HRS	$\leq -7.20^e$	$-5.05^{+0.08}_{-0.05}$	-	-	$-4.74 \pm 0.05$	-	-	This work
PHL 382 <sup>c</sup>	FEROS	$-5.54 \pm 0.02$	$-4.63 \pm 0.04$	-	-	$-4.54^{+0.02}_{-0.03}$	-	-	This work
BD+48 <sup>o</sup> 2721	FOCES	$-5.42 \pm 0.04$ $-6.01 \pm 0.15$	$-5.31 \pm 0.02$ $-5.27 \pm 0.23$	- -	- $\leq -6.66^e$	$-5.26 \pm 0.05$ $-5.04 \pm 0.35$	-	-	This work [1]
SB 290 <sup>c</sup>	FEROS	$-5.36 \pm 0.06$	$-5.37 \pm 0.08$	-	-	$\leq -6.00^e$	-	-	This work
EC 03263-6403	FEROS	$-4.58 \pm 0.04$	$\leq -7.00^e$	-	-	$-4.57 \pm 0.03$	-	-	This work
Solar Abundance		$-4.92 \pm 0.03$	$-5.64 \pm 0.13$	$-5.70 \pm 0.04$	$-7.09 \pm 0.05$	$-4.54 \pm 0.04$	$-9.17 \pm 0.07$	$-9.46 \pm 0.04$	[2]

Table 11.6.: Table 11.4 continued.

Star	Instrument	$\log n(\text{S})$	$\log n(\text{Ar})$	$\log n(\text{Ca})$	$\log n(\text{Ti})$	$\log n(\text{Fe})$	$\log n(\text{Sr})$	$\log n(\text{Zr})$	Ref.
EC 12234-2607	FEROS	$-4.75 \pm 0.03$	$-5.18^{+0.06}_{-0.08}$	-	-	$-4.95^{+0.03}_{-0.04}$	-	-	This work [1]
		$-5.02 \pm 0.05$	$\leq -5.03^e$	-	$\leq -5.60^e$	$-4.94 \pm 0.21$	-	-	
EC 14338-1445	FEROS	$-4.80^{+0.03}_{-0.04}$	$-5.50 \pm 0.10$	-	-	$-4.74 \pm 0.02$	-	-	This work [1]
		$-5.29 \pm 0.07$	$\leq -5.09^e$	-	$-5.49 \pm 0.78$	$-4.79 \pm 0.23$	-	-	
PG 1710+490	FOCES	$-4.33^{+0.04}_{-0.05}$	$-4.69^{+0.12}_{-0.10}$	-	-	$-4.62^{+0.06}_{-0.08}$	-	-	This work [1]
		$\leq -4.56^e$	$\leq -4.98^e$	-	$-4.84 \pm 0.28$	$-4.29 \pm 0.07$	-	-	
Feige 36 <sup>bd</sup>	HIRES	$-5.06 \pm 0.03$	$-5.29 \pm 0.06$	-	-	$-4.94 \pm 0.02$	-	-	This work [1]
		$\leq -5.12^e$	$-5.24 \pm 0.15$	-	$\leq -4.56^e$	$-4.79 \pm 0.21$	-	-	
HE 0929-0424 <sup>b</sup>	UVES	$-4.86^{+0.08}_{-0.07}$	$-5.07^{+0.13}_{-0.16}$	-	-	$\leq -7.00^e$	-	-	This work [1]
		$-5.59 \pm 0.07$	$-4.89 \pm 0.21$	$-3.34 \pm 0.15$	$-4.91 \pm 0.13$	$-4.94 \pm 0.15$	-	-	
HE 1047-0436 <sup>b</sup>	UVES	$-4.27 \pm 0.04$	$-4.76 \pm 0.09$	-	-	$\leq -7.00^e$	-	-	This work [1]
		$-4.89 \pm 0.07$	$-5.00 \pm 0.16$	-	$-5.01 \pm 0.41$	$-5.14 \pm 0.36$	-	-	
PG 0342+026 <sup>a</sup>	FEROS	$-5.18 \pm 0.03$	$-5.36 \pm 0.03$	-	-	$-4.43 \pm 0.03$	-	-	This work [1]
		$-5.21 \pm 0.19$	$-5.24 \pm 0.10$	-	$-5.94 \pm 0.57$	$-4.41 \pm 0.18$	-	-	
Solar Abundance		$-4.92 \pm 0.03$	$-5.64 \pm 0.13$	$-5.70 \pm 0.04$	$-7.09 \pm 0.05$	$-4.54 \pm 0.04$	$-9.17 \pm 0.07$	$-9.46 \pm 0.04$	[2]

## 11.1. NLTE Metal Abundances

In the following, the NLTE metal abundances measured for the analyzed program stars will be presented. First, the metal abundances that are derived from multiple spectra will be compared. Second, the metal abundances derived for the analyzed hot subdwarf program stars will be compared to literature. Third, the abundance patterns determined for the individual objects will be detailed. In this context, the NLTE abundances derived for the (post-)BHB stars PHL 25, PHL 382, and BD+48° 2721 will also be discussed.

Throughout this section, abundance values are defined as discrepant if they do not overlap within the uncertainties listed in Tables 11.1-11.6.

### NLTE Abundances Derived from Multiple Spectra

With a few exceptions, the discrepancies between the NLTE abundances derived from the XSHOOTER and FEROS spectra of HD 4539, Feige 38, and EC 03591-3232 are rather small. However, nitrogen (by  $\sim 0.12$  dex) in the case of HD 4539, neon (by  $\sim 0.41$  dex) in the case of EC 03591-3232, silicon (by  $\sim 0.12$  dex) in the case of Feige 38, and sulfur (HD 4539: by  $\sim 0.13$  dex, Feige 38: by  $\sim 0.19$  dex, EC 03591-3232: by  $\sim 0.12$  dex) are significantly discrepant. HD 149382 is metal-poor (NLTE abundances are only measured for C, N, S, Ar, and Fe, whereas upper limits are derived for O, Ne, Mg, Al, and Si). For this star, the discrepancies between the abundances derived from the XSHOOTER and UVES spectra are quite large in some cases:  $\sim 0.24$  dex (carbon),  $\sim 0.14$  dex (nitrogen), and  $\sim 0.21$  dex (sulfur). It has to be pointed out, however, that further systematic uncertainties that are not considered in the present abundance analyses (for instance, the placement of the continuum) could in principle add up to  $\sim 0.10$  dex. Certainly, this puts the discrepancies measured for HD 4539, Feige 38, EC 03591-3232, and HD 149382 into perspective. Nonetheless, it must be kept in mind that the final results for the metal abundances of these stars (determined from the weighted averages of the single measurements) are affected by the abundance discrepancies.

### NLTE Abundances of the Hot Subdwarf Stars Compared to Literature

The NLTE metal abundances derived for the analyzed hot subdwarf program stars of this work shall be compared to LTE abundances from literature (see Sect. 3.3 and Fig. 3.3.1) determined via the semi-automatic analysis pipeline of Geier (2013). In this regard, the results of the present work shall also be set into the context of the mean metal abundances of H-sdB/H-sdOB stars (see Fig. 3.3.2 and Table 3.1; Naslim et al. 2013). The following discussions specifically refer to the results presented in Tables 11.1-11.6 as well as to those displayed in Figs. 11.1.1 and 11.1.2.

### NLTE vs. LTE

When the measured NLTE metal abundances derived for the analyzed hot subdwarf program stars of this work are compared to the LTE ones determined by Geier (2013), one aspect clearly stands out at first glance: the improved statistics. Due to the much larger number of spectral lines analyzed in this work, the abundances determined for the elements C, N, O, Ne, Mg, Al, Si, S, Ar, and Fe show significantly lower uncertainties. But this is not the only consequence of the more detailed metal abundance analysis compared to Geier (2013). Additionally, parts of the abundances of the individual hot subdwarf program stars have altered and several discrepancies with respect to Geier (2013) are observed. These discrepancies shall be discussed star-by-star below<sup>125</sup>:

- **HD 4539**: HD 4539 is now more abundant in nitrogen (by  $\sim +0.30$  dex) and less abundant in argon (by  $\sim -0.26$  dex).
- **Feige 38**: Feige 38 is now more abundant in sulfur (by  $\sim +0.18$  dex).
- **EC 03591-3232**: EC 03591-3232 now has more magnesium ( $\sim +0.21$  dex), more sulfur ( $\sim +0.42$  dex), and more argon ( $\sim +0.21$  dex).
- **PG 1432+004**: For PG 1432+004, the silicon abundance has decreased by  $\sim -0.33$  dex, whereas the sulfur abundance has increased by  $\sim +0.34$  dex.
- **PG 1505+074**: For PG 1505+074, the silicon abundance has increased by  $\sim +0.21$  dex.
- **EC 13047-3049**: EC 13047-3049 now has more magnesium ( $\sim +0.23$  dex) and silicon ( $\sim +0.37$  dex) but significantly less aluminum ( $\sim -0.59$  dex) and iron ( $\lesssim -1.36$  dex).
- **[CW83] 0512-08**: [CW83] 0512-08 is now less abundant in carbon (by  $\sim -0.25$  dex).
- **HD 149382**: HD 149382 now has more nitrogen ( $\sim +0.27$  dex), more sulfur ( $\sim +0.23$  dex), and more iron ( $\gtrsim +0.29$  dex) but significantly less oxygen ( $\lesssim -1.51$  dex).
- **CD-35° 15910**: For CD-35° 15910, the magnesium abundance has decreased by  $\sim -0.35$  dex, whereas the silicon and sulfur abundances have increased by  $\gtrsim +0.45$  dex and  $\sim +0.42$  dex, respectively.
- **EC 12234-2607**: EC 12234-2607 is now more abundant in magnesium (by  $\sim +0.29$  dex) and sulfur (by  $\sim +0.27$  dex).
- **EC 14338-1445**: EC 14338-1445 is now more abundant in carbon (by  $\sim +0.27$  dex), nitrogen (by  $\sim +0.23$  dex), and sulfur (by  $\sim +0.49$  dex).
- **PG 1710+490**: PG 1710+490 now has more carbon ( $\gtrsim +0.63$  dex), more nitrogen ( $\sim +0.26$  dex), more sulfur ( $\gtrsim +0.23$  dex), and more argon ( $\gtrsim +0.29$  dex) but less oxygen ( $\sim -0.13$  dex), less aluminum ( $\sim -0.29$  dex), and less iron ( $\sim -0.33$  dex).

<sup>125</sup>Although also analyzed by Geier (2013), BD+48° 2721 is not discussed here because the star is treated as a BHB object in this work (see Sect. 9.4.1). Yet, BD+48° 2721 will be topic in the later course of this section.

- **Feige 36:** For Feige 36, the nitrogen abundance has increased by  $\sim +0.11$  dex.
- **HE 0929-0424:** HE 0929-0424 is now more abundant in nitrogen (by  $\sim +0.24$  dex), oxygen (by  $\sim +0.24$  dex), aluminum (by  $\sim +0.81$  dex), silicon (by  $\sim +0.69$  dex), and sulfur (by  $\sim +0.73$  dex). However, it is now less abundant in neon (by  $\lesssim -0.16$  dex) and, more significantly, in iron (by  $\lesssim -2.06$  dex).
- **HE 1047-0436:** HE 1047-0436 now has more carbon ( $\gtrsim +0.26$  dex), more nitrogen ( $\sim +0.25$  dex), more oxygen ( $\sim +0.18$  dex), more aluminum ( $\sim +0.41$  dex), more silicon ( $\sim +0.41$  dex), and more sulfur ( $\sim +0.62$  dex) but less neon ( $\lesssim -0.26$  dex) and, to a much greater extent, less iron ( $\lesssim -1.86$  dex).

The only analyzed hot subdwarf program star, for which no discrepancies are observed, is PG 0342+026. Most of the measured discrepancies can be explained by the much more sophisticated analysis of this work. However, it should also be noted that the abundance errors determined by Geier (2013) are very optimistic for individual stars because they most often represent the standard deviations of a few spectral lines only. As a matter of fact, Geier (2013) could not determine any abundance error at all, if there was only one spectral line available for the analysis of the respective element. This is also why Geier (2013) made use of the results of numerical experiments carried out earlier by Geier et al. (2010) in order to quantify the impact of noise on the results. In fact, 0.3 dex was used by Geier (2013) as the typical statistical uncertainty for their abundance analyses. In some cases, however, the abundance determinations of Geier (2013) are most likely only correct to within  $\pm 0.5$  dex due to peculiar line profiles, as stated by the author. Discrepancies of up to  $\pm 0.5$  dex between the results of this work and the ones of Geier (2013) thus are not surprising at all. In the case of EC 13047-3049, HD 149382, PG 1710+490, HE 0929-0424, and HE 1047-0436, however, the measured discrepancies sometimes exceed this value and, therefore, are strikingly high. This begs the question of whether the semi-automatic analysis procedure of Geier (2013) may have failed for these stars. Another possible explanation could be noise peaks that may have affected the analyses of Geier (2013).

### General Statements on the NLTE Abundances Measured for the Hot Subdwarf Stars

- **Carbon:** The carbon abundances measured for the analyzed hot subdwarf program stars and derived from C II/III lines scatter from  $\sim -3.40$  dex subsolar to about solar (solar abundance:  $-3.61$ ; Asplund et al. 2009). Very similar to the results of Geier (2013), they vary by orders of magnitude from star to star. Not a single analyzed hot subdwarf star shows a supersolar carbon abundance. Furthermore, no trend with effective temperature is visible at all for the analyzed objects. Interestingly, a group of H-sdBs, including most of the analyzed  $^3\text{He}$  ones, has (slightly) higher carbon abundances (up to  $\sim +0.80$  dex) than the mean H-sdB/H-sdOB abundance of  $-4.84$  (see Table 3.1; Naslim et al. 2013). These C-rich stars are found in the effective temperature strip of  $22\,000\text{ K} \lesssim T_{\text{eff}} \lesssim 30\,000\text{ K}$ . Two hot subdwarf program stars (PG 1136-003 and

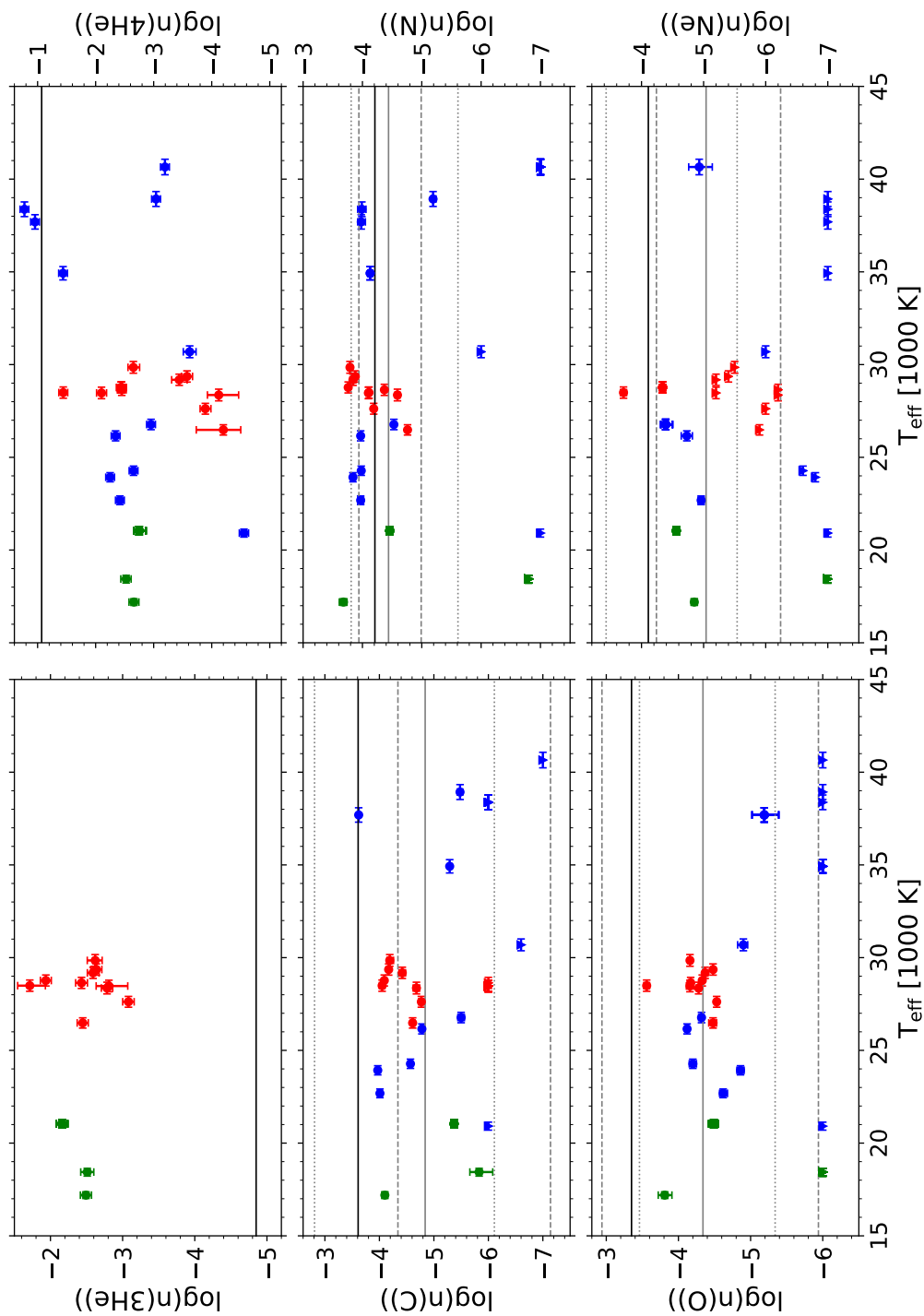


Figure 11.1.1.: Chemical abundances from  ${}^3\text{He}$  to neon plotted against the effective temperature  $T_{\text{eff}}$  for the program stars, for which high and medium-resolution spectra are analyzed (H-sdOs and He-sdOs excluded; see the corresponding footnote at the beginning of Ch. 11 for more information). For  ${}^3\text{He}$  and  ${}^4\text{He}$ , the abundances are given as base-10 logarithmic particle densities relative to the density of hydrogen. For all other elements, they are given relative to the density of all particles. Tables 10.1, 10.2, 11.1, 11.2, and 11.3 list the plotted abundance values, whereas the plotted effective temperature intervals can be found in Tables A.1-A.10 and A.20-A.23. Plotted metal abundance errors combine  $1\sigma$  statistical confidence intervals and the  $1\sigma$  systematic uncertainties described in Sect. 7.1.2. Plotted error bars on  $T_{\text{eff}}$ ,  $\log n({}^4\text{He})$ , and  $\log n({}^3\text{He})$  combine the  $1\sigma$  statistical single parameter errors (listed in Tables A.1-A.10 and A.20-A.23) and the global systematic errors derived in Sect. 9.2.7. While  ${}^3\text{He}$  H-sdBs are plotted in red, blue data points represent He-normal stars. The  ${}^3\text{He}$  (post-)BHB stars PHL 25, PHL 382, and BD+48° 2721 are marked in green. Upper limits are characterized by triangles. Solid black horizontal lines represent the solar abundance levels (Asplund et al., 2009), whereas solid gray horizontal lines mark the mean metal abundances of H-sdBs/H-sdOBs (see Fig. 3.3.2 and Table 3.1; Naslim et al. 2013). Additionally, the abundance ranges of Naslim et al. (2013) and Geier (2013) are given as dashed and dotted gray horizontal lines, respectively.

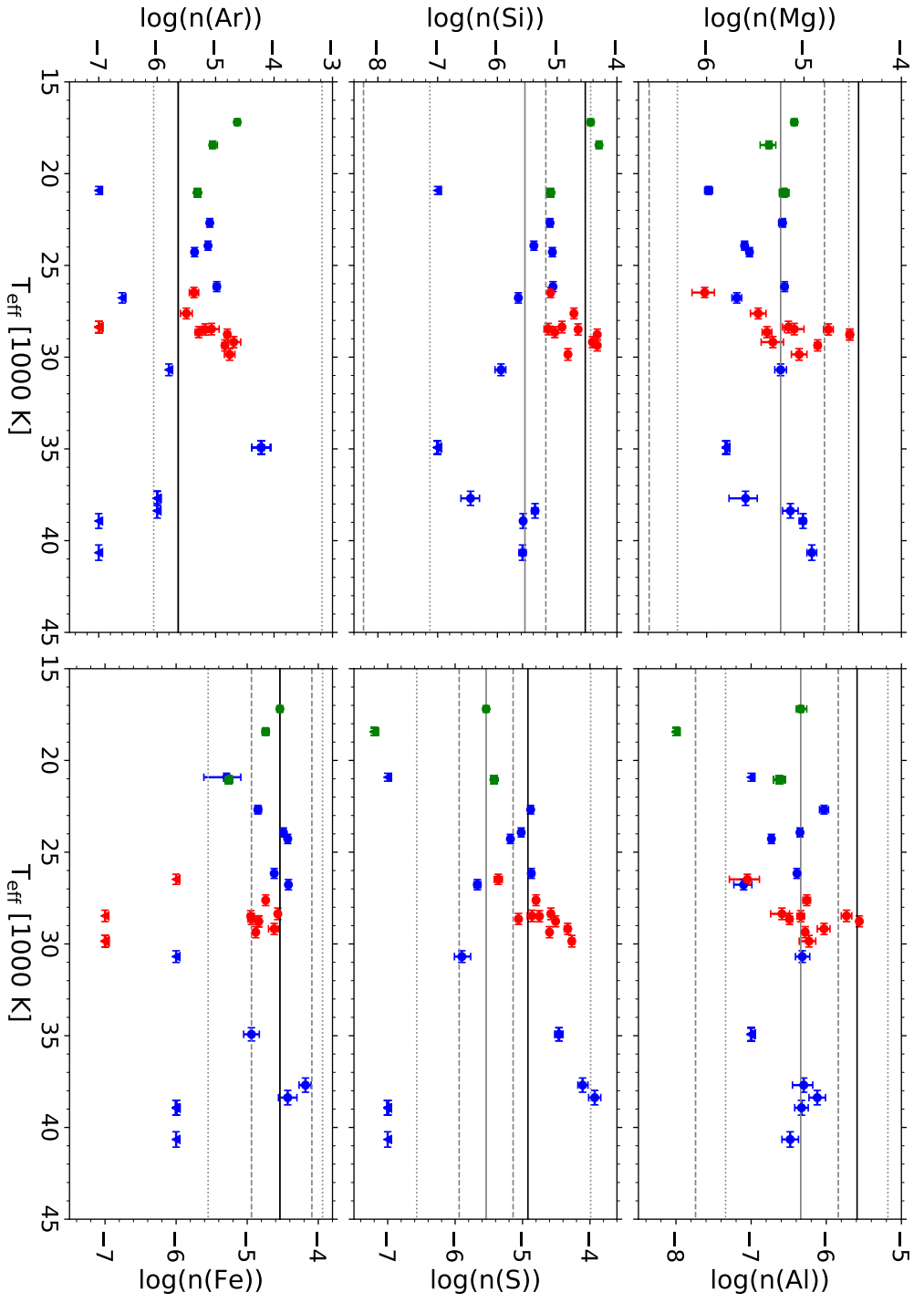


Figure 11.1.2.: Same as Fig. 11.1.1, but showing the chemical abundances from magnesium to iron plotted against the effective temperature  $T_{\text{eff}}$ . Tables 11.1-11.6 list the plotted abundance values, whereas the plotted effective temperatures can be found in Tables A.1-A.10 and A.20-A.23. For argon and iron, the mean abundance for H-sdBs/H-sdOBs is solar (see Table 3.1 and Fig. 3.3.2; Naslim et al. 2013). For argon, no abundance range of Naslim et al. (2013) is plotted because it is not given in the respective study.

## 11.1. NLTE Metal Abundances

---

PG 1505+074) are found below the carbon abundance range of Geier (2013), whereas several other hot subdwarfs (HD 4539, Feige 38, EC 03591-3232, PG 1432+004, EC 12234-2607, HE 1047-0436, and [CW83] 0512-08) are located above the abundance range of Naslim et al. (2013).

- **Nitrogen:** The N<sub>II/III</sub> abundances (solar abundance: -4.21; Asplund et al. 2009) observed for the analyzed hot subdwarf program stars also do not show any trend with temperature. Overall, they range from  $\sim -2.80$  dex subsolar to  $\sim +0.45$  dex supersolar. For the majority of the analyzed hot subdwarfs, however, the nitrogen abundances range from  $\sim -0.55$  dex subsolar to  $\sim +0.45$  dex supersolar, which is consistent with the abundances determined by Geier (2013). In fact, most of the measured nitrogen abundances are located above the mean abundance of -4.44 for H-sdBs/H-sdOBs (see Table 3.1; Naslim et al. 2013). The majority of the investigated program stars therefore are N-rich. This also includes many of the analyzed <sup>3</sup>He H-sdBs. Three hot subdwarf stars (PG 1136-003, GALEX J080510.9-105834, and PG 1505+074) are located below the nitrogen abundance range of Geier (2013). EC 13047-3049 is still covered by Geier (2013) but is located below the abundance range of Naslim et al. (2013). Moreover, a handful of stars (HD 4539, Feige 38, EC 03591-3232, PG 1710+490, and HE 1047-0436) is found slightly above the abundance interval of Naslim et al. (2013).
- **Oxygen:** The oxygen abundances (solar abundance: -3.35; Asplund et al. 2009) measured for the analyzed hot subdwarf program stars and derived from O<sub>I/II</sub> lines range from  $\sim -2.65$  dex to  $\sim -0.21$  dex subsolar. With the exception of GALEX J080510.9-105834, PG 1505+074, EC 13047-3049, [CW83] 0825+15, and HD 149382 (for these objects, only upper limits on the oxygen abundance are determined), all analyzed hot subdwarfs lie within the abundance region of Geier (2013). This means that their individual abundances are one to two orders of magnitude lower than the solar one. At an effective temperature of  $T_{\text{eff}} \gtrsim 30\,000$  K, the measured oxygen abundances seem to be shifted to lower values compared to the cooler stars in the analyzed sample. This potential abundance shift is rather similar to that measured by Geier (2013) but more data points are needed to quantify it. All in all, the oxygen abundances derived for most of the analyzed hot subdwarfs match the mean abundance of -4.34 for H-sdBs/H-sdOBs (see Table 3.1; Naslim et al. 2013). This also includes many of the analyzed <sup>3</sup>He H-sdBs. Only the hot subdwarf program stars, for which upper limits are derived, are located below the abundance range of Naslim et al. (2013).
- **Neon:** Neon is only measured for a small number of analyzed program stars. Most often, only upper limits are derived. Overall, the neon abundances (solar abundance: -4.11; Asplund et al. 2009) measured for the analyzed hot subdwarf program stars and derived from Ne<sub>I/II</sub> lines largely scatter from  $\sim -2.90$  dex subsolar to  $\sim +0.40$  dex supersolar. More than half of the analyzed hot subdwarfs, including PG 1136-003, SB 290, EC 03263-6403, EC 14338-1445, Feige 36, HD 4539, GALEX J080510.9-105834, EC 13047-3049, [CW83] 0825+15, [CW83] 0512-08, HD 149382, and PG 0342+026, are found below the neon abundance range of Geier (2013). In fact, most of the measured neon abundances also lie below the mean abundance of -5.04 for H-sdBs/H-sdOBs (see

## 11. Metal Abundance Study Based on the Hybrid LTE/NLTE Approach

---

Table 3.1; Naslim et al. 2013). This also includes the abundances derived for many of the analyzed  $^3\text{He}$  H-sdBs. Several hot subdwarf stars (HD 4539, GALEX J080510.9-105834, EC 13047-3049, [CW83] 0825+15, [CW83] 0512-08, HD 149382, and PG 0342+026) are even so Ne-poor that they are located below the neon abundance range of Naslim et al. (2013). Finally, EC 12234-2607 is the only analyzed hot subdwarf star that lies above the abundance range of Naslim et al. (2013).

- **Magnesium:** The Mg II abundances (solar abundance: -4.44; Asplund et al. 2009) derived for the analyzed hot subdwarf program stars range from  $\sim -1.60$  dex to  $\sim -0.10$  dex subsolar. They scatter similarly strong as in the sample of Geier (2013). Contrary to the latter, however, no slight subsolar trend with effective temperature is observed. A group of hot subdwarf stars, including the majority of the analyzed  $^3\text{He}$  H-sdBs, clusters around the mean H-sdB/H-sdOB abundance of -5.24 (see Table 3.1; Naslim et al. 2013). Only two hot subdwarf program stars (EC 03591-3232 and EC 12234-2607) are located above the magnesium abundance range of Naslim et al. (2013). However, these two objects are still covered by the abundance range of Geier (2013).
- **Aluminum:** The aluminum abundances measured for the analyzed hot subdwarf program stars and derived from Al II/III lines range from  $\sim -1.50$  dex subsolar to about solar (solar abundance: -5.59; Asplund et al. 2009). The sample size of this work is much smaller than the one of Geier (2013). This is most likely why the slight temperature trend measured by the latter cannot be confirmed here. The vast majority of the analyzed hot subdwarf program stars lie around the mean abundance of -6.34 for H-sdBs/H-sdOBs (see Table 3.1; Naslim et al. 2013). This also includes many of the analyzed  $^3\text{He}$  H-sdBs. Only two hot subdwarf stars (EC 03591-3232 and HE 0929-0424) are located above the aluminum abundance range of Naslim et al. (2013). However, these two objects still lie within the abundance range of Geier (2013).
- **Silicon:** The silicon abundances measured for the analyzed hot subdwarf program stars and derived from Si II/III/IV lines (solar abundance: -4.53; Asplund et al. 2009) show a large scatter similar to what has been observed by Geier (2013). They range from  $\sim -2.50$  dex subsolar to  $\sim +0.20$  dex supersolar. The silicon abundances derived for the analyzed program stars with effective temperatures higher than  $\sim 30\,000$  K appear to be shifted to lower values, as in the case of oxygen. Due to the small sample size, however, this potential silicon abundance drop cannot be quantified. Yet, it is very similar to the one of Geier (2013) observed at  $T_{\text{eff}} \sim 35\,000$  K. All in all, only a small number of the analyzed hot subdwarf stars has a silicon abundance that is lower or near the mean abundance of -5.54 for H-sdBs/H-sdOBs (see Table 3.1; Naslim et al. 2013). Most of the analyzed hot subdwarfs thus are Si-rich. In fact, even more than half of them are found above the silicon abundance range of Naslim et al. (2013). This includes PG 0342+026, PG 1432+004, and GALEX J104148.9-073031 as well as all analyzed  $^3\text{He}$  H-sdBs (Feige 38, EC 03591-3232, SB 290, EC 03263-6403, EC 12234-2607, EC 14338-1445, PG 1710+490, Feige 36, HE 0929-0424, and HE 1047-0436). Feige 38, EC 03591-3232, and PG 1710+490 are even located above the abundance interval of Geier (2013).

## 11.1. NLTE Metal Abundances

---

- **Sulfur:** The sulfur abundances observed for the analyzed hot subdwarf program stars and derived from S II/III lines (solar abundance:  $-4.92$ ; Asplund et al. 2009) show a large scatter between  $\sim -2.10$  dex subsolar and  $\sim +1.00$  dex supersolar. As a matter of fact, the scatter is less strong than the one observed by Geier (2013), if GALEX J080510.9-105834, PG 1505+074, and EC 13047-3049 are excluded (for these three objects, only upper limits on the sulfur abundance are determined). A possible reason for the smaller scattering of the sulfur abundances in this work could be the fact that the results of Geier (2013) are considerably less accurate. Most of the hot subdwarf stars analyzed in the present work belong to the group of S-rich H-sdBs/H-sdOBs because their respective abundances lie well above (up to  $\sim +1.60$  dex) the mean H-sdB/H-sdOB abundance of  $-5.54$  (see Table 3.1; Naslim et al. 2013). In fact, most of the investigated hot subdwarfs (HD 4539, Feige 38, EC 03591-3232, PG 1432+004, GALEX J104148.9-073031, [CW83] 0825+15, [CW83] 0512-08, HD 149382, EC 03263-6403, EC 12234-2607, EC 14338-1445, PG 1710+490, Feige 36, HE 0929-0424, and HE 1047-0436) are even located above the sulfur abundance range of Naslim et al. (2013). This also includes most of the investigated  $^3\text{He}$  H-sdBs. Yet, [CW83] 0825+15 is the only analyzed hot subdwarf star that lies above the abundance interval of Geier (2013). Last but not least, GALEX J080510.9-105834, PG 1505+074, and EC 13047-3049 are so S-poor that they fall below both considered abundance ranges.
- **Argon:** Overall, the argon abundances observed for the analyzed hot subdwarf program stars and derived from Ar II lines strongly scatter between  $\sim -1.40$  dex subsolar and  $\sim +1.40$  dex supersolar (solar abundance:  $-5.64$ ; Asplund et al. 2009). With the exception of PG 1136-003, GALEX J080510.9-105834, PG 1505+074, EC 13047-3049, [CW83] 0825+15, [CW83] 0512-08, CD-35° 15910, and EC 03263-6403 (for these objects, only upper limits on the argon abundance are derived), all analyzed hot subdwarfs show argon abundances that range from about solar to  $\sim +1.40$  dex supersolar. In fact, the measured Ar II abundances tend to increase over the temperature regime between  $\sim 20\,000$  K and  $\sim 35\,000$  K, if the aforementioned stars are excluded. However, more data points are needed at the hot end in order to confirm this potential trend. Yet, this behavior of the argon abundances is rather similar to the results for the larger sample of Geier (2013). Many of the hot subdwarf program stars investigated in this work, including most of the analyzed  $^3\text{He}$  H-sdBs, are Ar-rich because they lie above the mean abundance of  $-5.64$  for H-sdBs/H-sdOBs (for argon, the mean abundance of H-sdBs/H-sdOBs is solar; see Table 3.1; Naslim et al. 2013). Unfortunately, Naslim et al. (2013) does not provide any abundance range for the element argon. Nevertheless, it is worthwhile to note that most of the analyzed hot subdwarf stars lie within the argon abundance range of Geier (2013). The sole exceptions to this are GALEX J080510.9-105834, PG 1505+074, EC 13047-3049, CD-35° 15910, and EC 03263-6403.
- **Iron:** The iron abundances measured for the analyzed hot subdwarf program stars are derived from Fe II/III lines. They lie between  $\sim -2.50$  dex subsolar and  $\sim +0.40$  dex supersolar (solar abundance:  $-4.54$ ; Asplund et al. 2009). With the exception of PG 1136-003, PG 1505+074, EC 13047-3049, SB 290, HE 0929-0424, and HE 1047-0436

(for these objects, only upper limits on the iron abundance are determined), all analyzed hot subdwarfs show iron abundances that range from  $\sim -0.80$  dex subsolar to  $\sim +0.40$  dex supersolar. In fact, the measured Fe II/III abundances stay more or less constant over the investigated temperature range, if the aforementioned stars are excluded. This is in good agreement with the results of Geier (2013), who observed a constant iron abundance with temperature between  $-0.70$  dex subsolar and  $+0.50$  dex supersolar. As a matter of fact, the mean H-sdB/H-sdOB abundance for iron is  $-4.54$ , which is solar (see Table 3.1; Naslim et al. 2013). In consequence, most of the analyzed hot subdwarfs are Fe-poor. PG 1136-003, PG 1505+074, EC 13047-3049, SB 290, HE 0929-0424, and HE 1047-0436 are so Fe-poor that they fall below the abundance ranges of Naslim et al. (2013) and Geier (2013). GALEX J080510.9-105834 is the only analyzed hot subdwarf star that is located in the regime between the lower boundaries of the two considered abundance intervals.

### Chemical Abundance Patterns

Figures 11.1.3 and 11.1.4 show the chemical abundance patterns of selected analyzed program stars relative to the solar abundance level of Asplund et al. (2009). Additionally, the mean abundances for H-sdBs/H-sdOBs according to Naslim et al. (2013) are displayed therein (see also Fig. 3.3.2 and Table 3.1). Several investigated objects are underabundant in carbon and oxygen but overabundant in nitrogen compared to the Sun. Therefore, these objects show the prominent CNO signature as a remnant of the hydrogen core burning through the CNO cycle (during the red giant phase, the hydrogen-burning flame slowly propagates outwards). In most cases, aluminum and the alpha elements neon, magnesium, silicon, and sulfur are underabundant compared to the respective solar abundance values. Thus, these elements largely follow the mean metallicity trend of H-sdBs/H-sdOBs. For most of the analyzed objects, the iron-group elements also lie within the abundance ranges of Naslim et al. (2013). Last but not least, argon is very striking. While this element is enriched compared to the Sun for the vast majority of the analyzed stars, other objects such as the low-metallicity star GALEX J080510.9-105834, the zirconium-rich iHe-sdB [CW83] 0825+15 (for more information, see Sect. 11.2), or the H-sdOB PG 1505+074 show no spectral lines of argon at all. However, this is not the only reason why these three objects are notable exceptions to the generally observed abundance patterns.

### The (Post-)BHB Stars PHL 25, PHL 382 and BD+48° 2721

In terms of their metal compositions, the three analyzed (post-)BHB stars PHL 25, PHL 382, and BD+48° 2721 cannot be lumped together. While the abundance patterns of PHL 382 and BD+48° 2721 are rather similar to the general one observed for most of the analyzed hot subdwarf program stars, the one of PHL 25 is very peculiar (see Fig. 11.1.3). For PHL 25, no nitrogen, oxygen, neon, aluminum, and sulfur are detectable such that only upper limits are

## 11.1. NLTE Metal Abundances

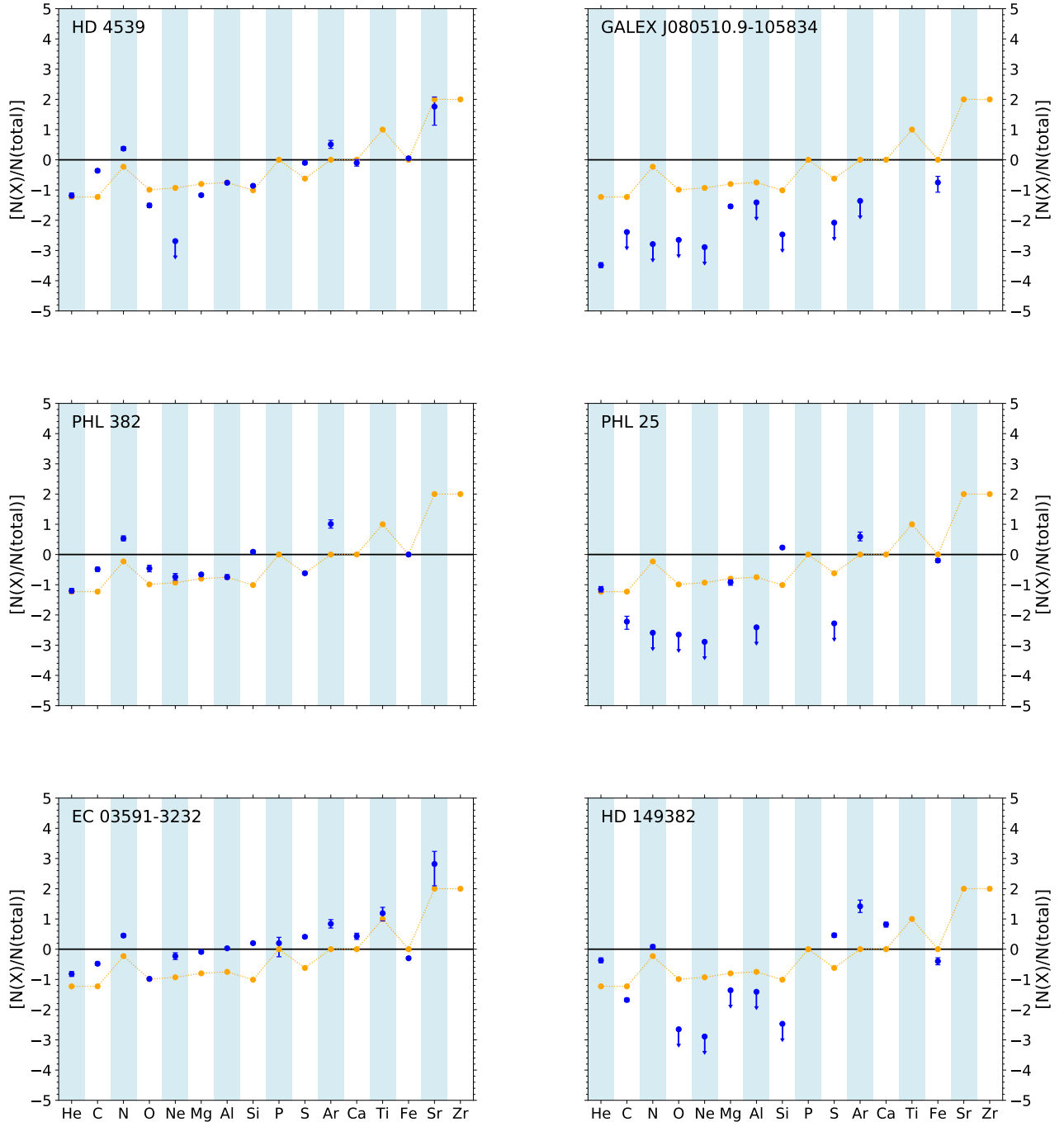


Figure 11.1.3.: The chemical abundance patterns (represented by blue dots) of selected analyzed program stars relative to the solar abundance level of Asplund et al. (2009). In each subpanel, the solar abundance level is represented by the solid black horizontal line, whereas the dotted orange line connects the mean abundances for H-sdBs/H-sdOBs (see Fig. 3.3.2 and Table 3.1; Naslim et al. 2013). Upper limits are marked with downward arrows and  $\left[ \frac{N(X)}{N(\text{total})} \right] := \log_{10} \left\{ \frac{N(X)}{N(\text{total})} \right\} - \log_{10} \left\{ \frac{N(X)}{N(\text{total})} \right\}_{\odot}$ .

## 11. Metal Abundance Study Based on the Hybrid LTE/NLTE Approach

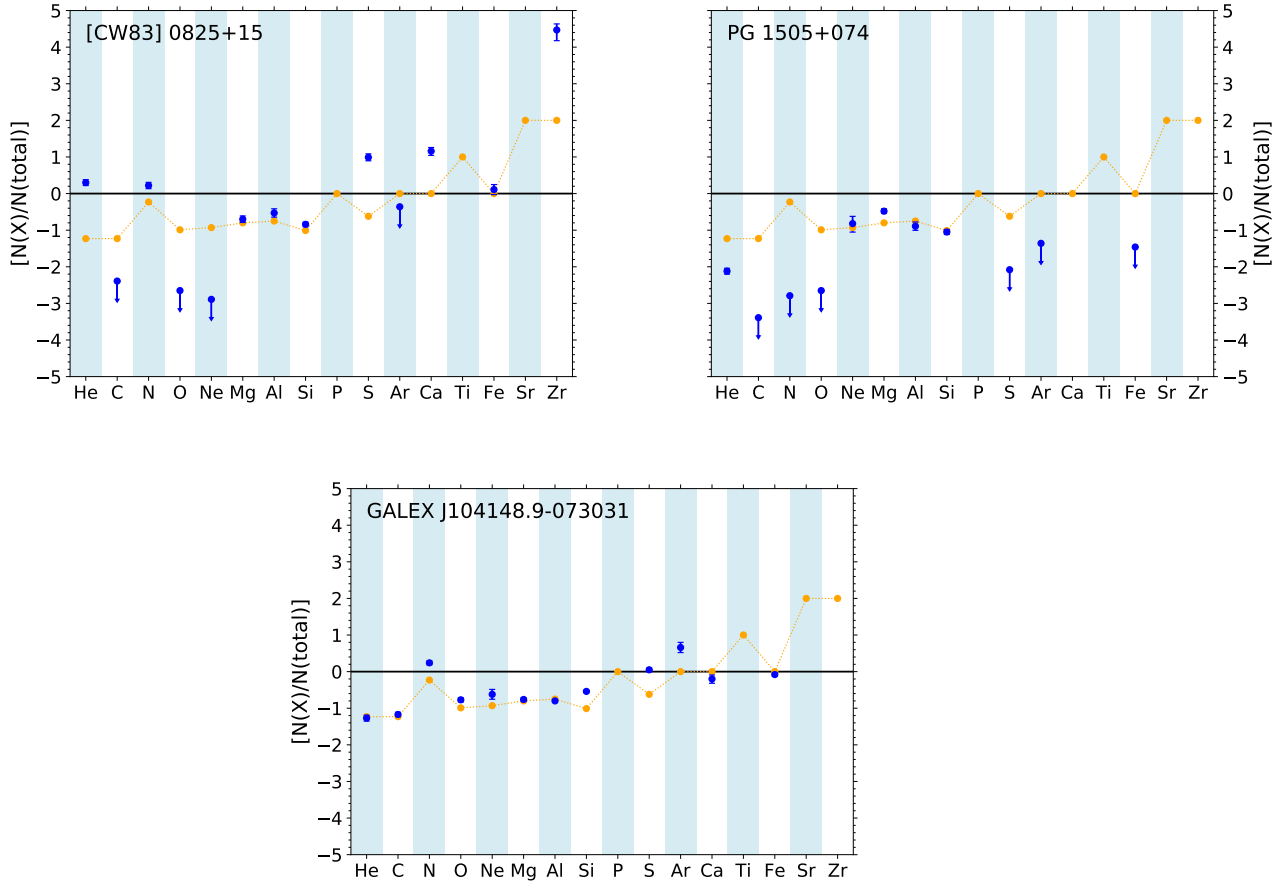


Figure 11.1.4.: Figure 11.1.3 continued.

derived for the abundances of these elements:  $\sim -2.60$  dex subsolar (N),  $\sim -2.70$  dex subsolar (O),  $\sim -2.90$  dex subsolar (Ne),  $\sim -2.40$  dex subsolar (Al), and  $\sim -2.30$  dex subsolar (S). On the other hand, however, the abundances for carbon, magnesium, silicon, argon, and iron measured for PHL 25 are in rather good agreement with the abundance patterns derived for most of the analyzed H-sdBs/H-sdOBs. Consequently, the abundances of these elements seem to match the mean abundances of Naslim et al. (2013).

Recently, Hämmerich (2020) also performed a detailed metal abundance analysis of PHL 25 and PHL 382, whereby the improvements of the hybrid LTE/NLTE model atmosphere approach as well as of the global analysis strategy described in Sects. 6.8 and 7.1.2 (for instance, level dissolution or the local normalization procedure) were implemented. The author also made use of the same observed spectra as the present work. For both stars, a comparison of the results of this work to those of Hämmerich (2020) therefore seems reasonable. It is provided in appendix B.

## 11.2. LTE Metal Abundances Derived from the XSHOOTER Reference Sample

The analyzed program stars of the XSHOOTER reference sample (He-sdOs excluded; see the corresponding footnote at the beginning of Ch. 11) are additionally investigated in terms of phosphorus (P II), calcium (Ca II), titanium (Ti II), strontium (Sr II), and zirconium (Zr II). In contrast to the results presented in Sect. 11.1, however, the abundances of these metals are derived in LTE. In principle, atomic data for higher ionization stages of these chemical elements are desirable for the hot program stars of this work. However, the necessary implementation of these data for the spectral syntheses is not realized in this work because of time restrictions. Hence, the following abundance results are only based on the singly-ionized stages of the respective elements.

The  ${}^3\text{He}$  H-sdB EC 03591-3232 is the only analyzed star that shows P II in its spectrum (see

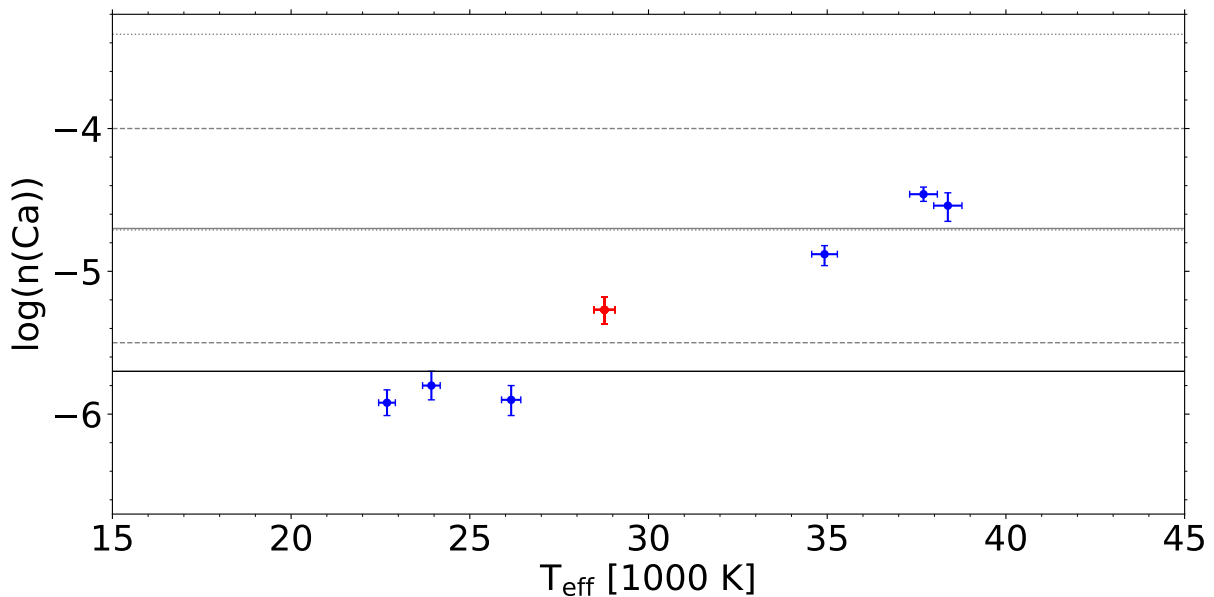


Figure 11.2.1.: Same as Fig. 11.1.1, but showing the measured calcium abundances plotted against the effective temperature  $T_{\text{eff}}$  for the analyzed XSHOOTER program stars (He-sdOs excluded; see the corresponding footnote at the beginning of Ch. 11). Tables 11.4-11.6 list the plotted abundance values, whereas the plotted effective temperatures can be found in Tables A.1-A.5 and A.20-A.23.

Figs. 11.0.5-11.0.7). However, the phosphorus abundance derived ( $-6.425^{+0.187}_{-0.444}$ ) has high uncertainties because only a few very weak spectral lines are investigated (see Table 8.14). Nonetheless, the phosphorus abundance of EC 03591-3232 (see Fig. 11.1.3) matches the mean abundance value of -6.63 for H-sdBs/H-sdOBs, which is solar (see Table 3.1; Naslim et al. 2013; Asplund et al. 2009). It also fits to the corresponding LTE abundances determined by Geier (2013) and displayed in Fig. 3.3.1. As a matter of fact, however, the phosphorus

abundance of EC 03591-3232 has increased significantly (by  $\gtrsim +0.78$  dex; see Table 11.1) compared to Geier (2013).

In contrast to the LTE study of Geier (2013), who could only derive abundances for Ca III in stars with  $T_{\text{eff}} \gtrsim 29\,000$  K, some Ca II lines in the NIR are investigated in this work (see Table 8.14). Thus, it is not surprising that calcium is found in several cooler H-sdB stars that have  $T_{\text{eff}} \lesssim 29\,000$  K. The respective objects are HD 4539, EC 03591-3232 (see Figs. 11.0.5-11.0.7), PG 1432+004, and GALEX J104148.9-073031 (see Figs. 11.0.1 and 11.0.2). Moreover, Ca II lines are observed in the spectra of [CW83] 0825+15, [CW83] 0512-08, and HD 149382 (see Figs. 11.1.3 and 11.1.4). These stars are much hotter ( $T_{\text{eff}} \gtrsim 35\,000$  K) and, hence, do not belong to the group of H-sdBs. Overall, there is a clear calcium abundance trend with effective temperature visible for the analyzed program stars (see Fig. 11.2.1). The measured abundances range from  $\sim -0.20$  dex subsolar at the cool end to  $\sim +1.20$  dex supersolar at the hot end (solar abundance:  $-5.70$ ; Asplund et al. 2009). In consequence, the abundances derived for the hotter stars follow the trend of Geier (2013), although HD 149382 is located slightly below the corresponding abundance range. Interestingly, the calcium abundances of two of the hotter stars have decreased heavily compared to Geier (2013): [CW83] 0512-08 (by  $\sim -0.57$  dex) and HD 149382 (by  $\sim -0.74$  dex; see Table 11.5). In fact, the hotter objects scatter around the mean calcium abundance of  $-4.70$  for H-sdBs/H-sdOBs (see Table 3.1; Naslim et al. 2013). On the other hand, the cooler stars are located well below the calcium abundance range of Geier (2013) and also have abundances that are well below the mean abundance of H-sdBs/H-sdOBs. Three of them (HD 4539, PG 1432+004, and GALEX J104148.9-073031) even have subsolar calcium abundances and lie below the abundance range of Naslim et al. (2013). EC 03591-3232 is the only analyzed cool star that is located within the abundance interval of Naslim et al. (2013).

Ti II lines are found in the following three H-sdB program stars of the XSHOOTER reference sample: Feige 38, EC 03591-3232 (see Figs. 11.0.5-11.0.7 and Fig. 11.1.3), and PG 1432+004. These objects are strongly Ti-enriched compared to the Sun (see Table 11.4; solar abundance:  $-7.09$ ; Asplund et al. 2009). In fact, this matches the observation of Geier (2013), who also found a strong titanium enhancement for their analyzed H-sdBs/H-sdOBs (ranging from  $\sim +1.0$  dex to  $\sim +3.0$  dex supersolar; see Fig. 3.3.1). In terms of absolute titanium abundances, only one of the three stars is discrepant compared to Geier (2013), which is EC 03591-3232. Its abundance has decreased by  $\sim -0.66$  dex (see Table 11.4). As is the case for Feige 38 and PG 1432+004, the titanium abundance of EC 03591-3232 scatters around the mean abundance of  $-6.09$  for H-sdBs/H-sdOBs (see Table 3.1; Naslim et al. 2013).

Sr II lines are observed for the H-sdB program stars HD 4539 and EC 03591-3232 (see Figs. 11.0.5-11.0.7). It has to be noted, however, that the uncertainties of the determined strontium abundances are very large ( $-7.41^{+0.31}_{-0.61}$  and  $-6.35^{+0.41}_{-0.72}$ ; see Table 11.4). This is because only a few weak Sr II lines are analyzed (see Table 8.14). Interestingly, both abundance values lie well above the solar strontium abundance of  $-9.17$  (Asplund et al., 2009). The strontium abundance of HD 4539 is slightly lower (by  $\sim -0.24$  dex) than the mean H-sdB/H-sdOB abundance of  $-7.17$  (see Table 3.1; Naslim et al. 2013). On the other hand, EC 03591-3232 is Sr-enriched (see Fig. 11.1.3). Unfortunately, a comparison to the LTE results of Geier (2013) is not possible for both objects because no strontium abundances have been derived in their

## 11.2. LTE Metal Abundances Derived from the XSHOOTER Reference Sample

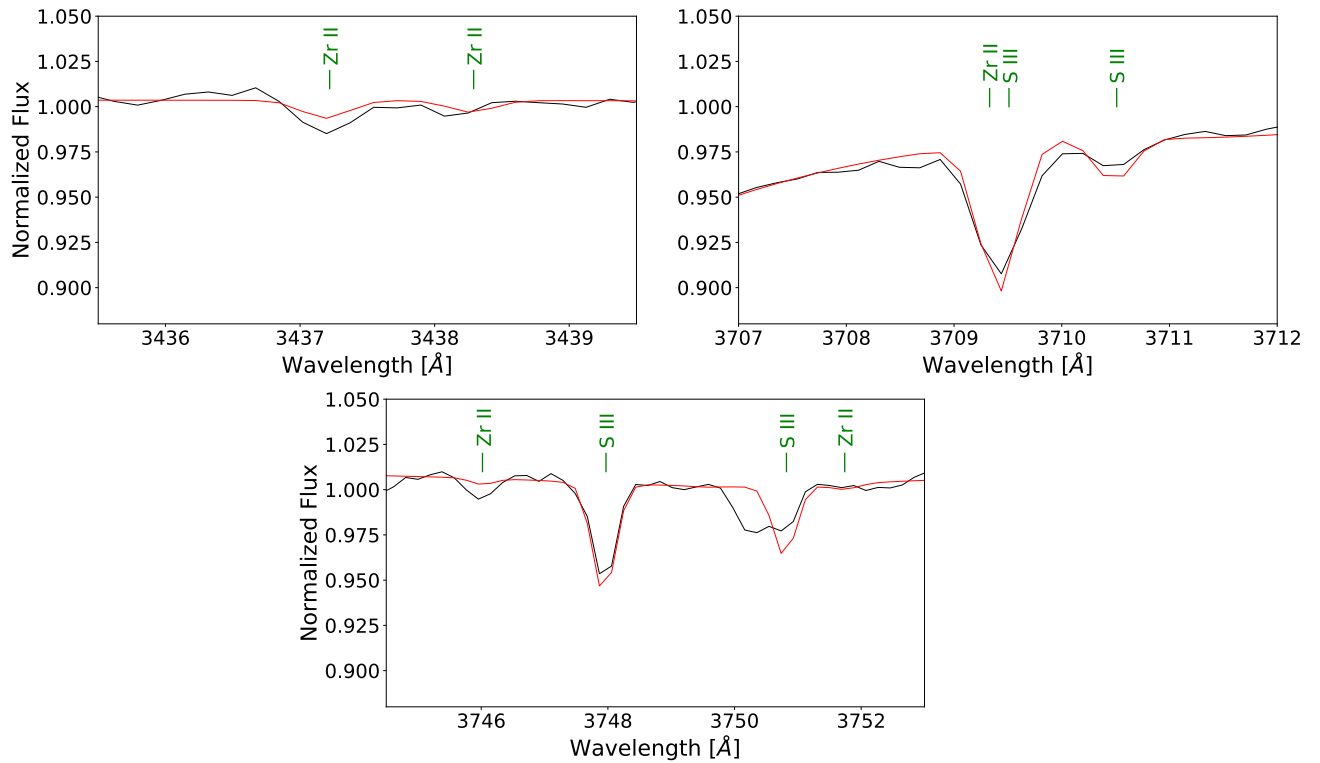


Figure 11.2.2.: Selected metal lines in the co-added XSHOOTER spectrum of the iHe-sdB star [CW83] 0825+15. The observed spectrum (solid black line) and the best fit (solid red line) are shown. Solid green vertical lines/labels mark the central wavelength positions and the ionization stages of the individual spectral lines (see also Tables 8.12-8.14). The star is strongly enriched in zirconium. In this work, however, only a few weak Zr II lines are analyzed (see the text for details).

study.

Last but not least, several spectral lines associated with Zr II are analyzed for the iHe-sdB [CW83] 0825+15 (see Fig. 11.2.2 and Table 8.14). In fact, this object is heavily enriched in zirconium (see Fig. 11.1.4) because the abundance of the element ( $-4.99^{+0.16}_{-0.29}$ ; see Table 11.5) is more than 10 000 times higher than the solar one of  $-9.46$  (Asplund et al., 2009) and more than 100 times higher than the mean abundance of  $-7.46$  for H-sdBs/H-sdOBs (see Table 3.1; Naslim et al. 2013). As a matter of fact, such a high zirconium abundance is also not covered by the abundance range for usual H-sdBs/H-sdOBs (see Fig. 3.3.2; Naslim et al. 2013). A comparison to Geier (2013) is not possible for [CW83] 0825+15 because no zirconium abundances have been derived in their study in general and the star is also not included in their sample. However, the object has been analyzed by Jeffery et al. (2017). In their work, the authors determined an upper limit on the zirconium abundance of  $\leq -6.74$ , whereby several pronounced Zr IV lines were investigated. This upper limit is significantly lower (by  $\sim -1.75$  dex) than the zirconium abundance measured in the present work. It has to

be pointed out, however, that only a few weak Zr II lines are analyzed for [CW83] 0825+15 in this thesis. No Zr III and, in particular, no Zr IV lines are investigated due to time restrictions. Hence, the comparison to Jeffery et al. (2017) may be misleading. Since the abundance study of Jeffery et al. (2017), [CW83] 0825+15 has been listed as a heavy-metal star (see Sect. 3.3), also showing pronounced lead lines. This is confirmed in the present work because lots of spectral lines associated with trans-iron elements such as germanium, yttrium, or even lead are excluded from the spectral fit due to a lack of appropriate atomic data.

### 11.3. Detection of Chlorine and Krypton

Apart from the metal abundance results already discussed, some of the analyzed program stars also show even more exotic chemical species, among them chlorine (Cl) and krypton (Kr).

The analyzed co-added FEROS spectrum of the rotating <sup>3</sup>He post-BHB star PHL 382 shows Cl II and Kr II lines (see Figs. 11.0.3 and 11.0.4). In fact, the two chemical elements can be assigned to the following absorption lines: Cl II 4785.364 Å, Cl II 4794.550 Å, Cl II 4810.060 Å, Cl II 4819.470 Å, Kr II 4355.477 Å, Kr II 4658.876 Å, and Kr II 4739.001 Å (see Table 8.14). While Kr II lines have already been detected by Schneider (2017), Cl II is a new discovery.

For the <sup>3</sup>He BHB star PHL 25, Heber (1991) and Schneider (2017) detected spectral lines of Cl II. This is confirmed in this work, whereby the following absorption lines are observed in the analyzed co-added HRS spectrum: Cl II 4785.364 Å, Cl II 4794.550 Å, Cl II 4810.060 Å, and Cl II 4819.470 Å. However, no krypton is detected in the respective spectrum.

Eventually, the analyzed co-added XSHOOTER spectrum of the H-sdB PG 1432+004 also shows chlorine lines: Cl II 4785.364 Å, Cl II 4794.550 Å, Cl II 4810.060 Å, and Cl II 4819.470 Å. As in the case of PHL 25, however, no krypton lines are found.

In all three cases, the relevant Cl II and Kr II lines are excluded from the spectral fits because of a lack of appropriate atomic data. Therefore, no abundances of chlorine and krypton are determined for the three program stars in question.

### 11.4. Detection of Silicon Line Emission

Silicon (Si II/III/IV) emission lines are detected in the red and NIR spectra of several program stars, including the <sup>3</sup>He H-sdBs Feige 38 and EC 03591-3232, the H-sdB PG 1432+004, the H-sdOBs EC 13047-3049 and PG 1505+074 as well as the <sup>3</sup>He post-BHB star PHL 382 (see Fig. 11.4.1). Silicon emission was recently reported in B-type MS stars (Sadakane & Nishimura, 2017, 2019) but this is the first time that it is detected in hot subdwarf and (post-)BHB stars<sup>126</sup>. This is not least due to the fact that the observed emission lines are very weak. All in all, the following lines are affected in the respective program stars: 1)

<sup>126</sup>As a matter of fact, Hämmerich (2020) investigated the same FEROS spectrum of PHL 382 as analyzed in the present work. The author also detected the Si II-emission line at 6239.63 Å (compare subpanel c of Fig. 11.4.1 to Figure 9.5 in Hämmerich 2020).

## 11.4. Detection of Silicon Line Emission

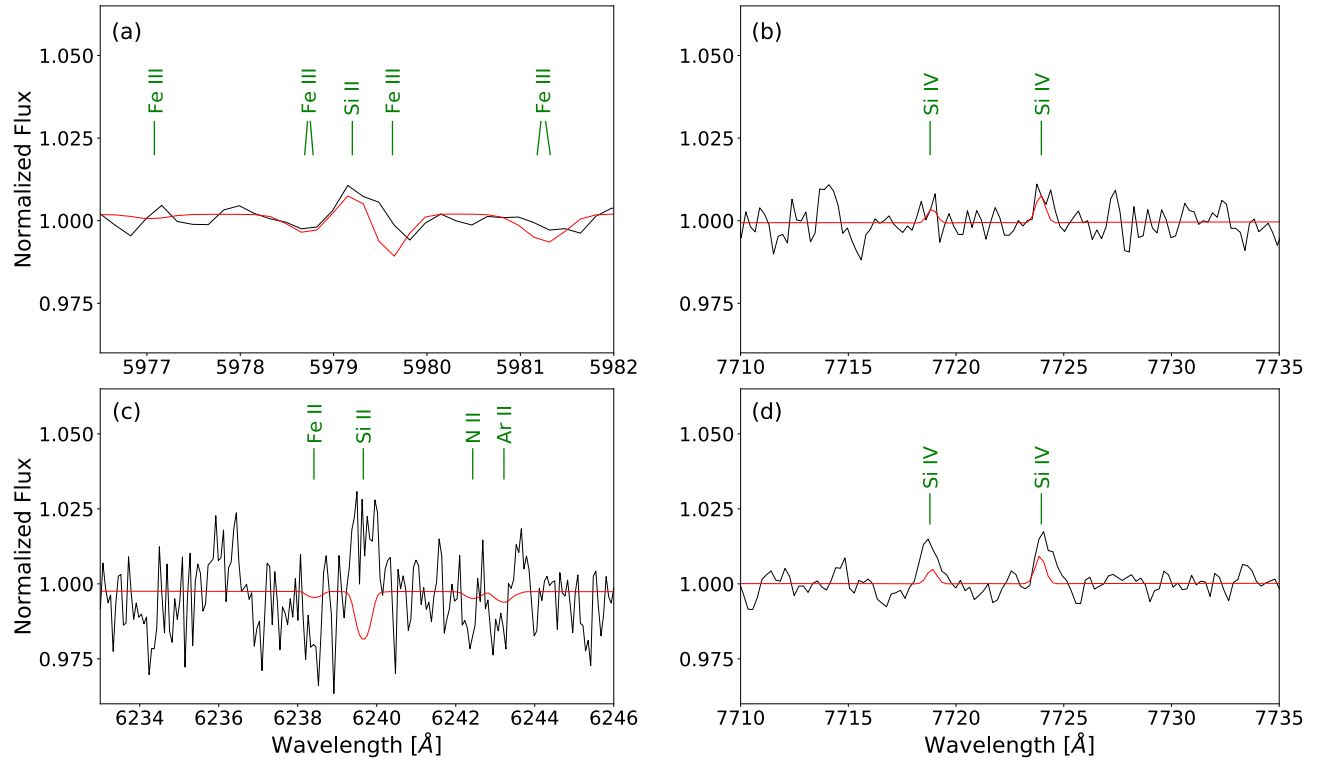


Figure 11.4.1.: Selected silicon emission (and other metal) lines in the co-added spectra of four analyzed program stars. The observed spectra (solid black lines) and the best fits (solid red lines) are shown. Solid green lines/labels mark the central wavelength positions and the ionization stages of the individual spectral lines (see also Tables 8.12-8.14). (a)  ${}^3\text{He}$  H-sdB EC 03591-3232 (XSHOOTER spectrum); (b) H-sdOB EC 13047-3049 (XSHOOTER spectrum); (c)  ${}^3\text{He}$  post-BHB PHL 382 (FEROS spectrum); (d) H-sdOB PG 1505+074 (XSHOOTER spectrum).

Si II: 5957.561 Å, 5978.929 Å, 6239.63 Å, and the triplet consisting of 7848.82 Å, 7849.62 Å, and 7849.72 Å; II) Si III: the doublet consisting of 8102.86 Å and 8103.45 Å as well as the triplet consisting of 8190.43 Å, 8191.16 Å, and 8191.68 Å; III) Si IV: the triplet consisting of 7718.79 Å, 7723.82 Å, and 7725.64 Å, whereby the latter component is not visible in most cases. For some of the detected silicon emission lines, the model also predicts emission at the respective wavelength positions but the modelled lines are often too weak (for instance, see subpanel d of Fig. 11.4.1). As it is likely that the emission is caused by departures from LTE, a possible reason for the mismatches between the model and the observation could be shortcomings in the silicon model atoms used. This is also supported by the fact that the model predicts an absorption at the respective wavelength position for other lines, which is not seen in the observed data (for instance, see subpanel c of Fig. 11.4.1). In B-type MS stars, however, the observed silicon emission most likely arises from the outermost layers of the stellar atmosphere, which cover the whole stellar surface and co-rotate with the respective

## 11. Metal Abundance Study Based on the Hybrid LTE/NLTE Approach

---

star (Sadakane & Nishimura, 2017). In principle, this is also a valid option for the affected program stars of the present work such that insufficient model atoms do not necessarily have to be the cause of the mismatches between the model and the observation<sup>127</sup>. A circumstellar disk around the stars as a potential source of emission, however, can rather be excluded (see also Sadakane & Nishimura 2017).

Due to the fact that similar findings of silicon emission have not been reported in other EHB/BHB stars yet, Feige 38, EC 03591-3232, PG 1432+004, EC 13047-3049, PG 1505+074, and PHL 382 are very interesting targets for further spectroscopic observations in the future.

---

<sup>127</sup>Note, however, that insufficient silicon model atoms are most likely also responsible for the mismatches of Si II and Si III lines in the analyzed co-added XSHOOTER and FEROS spectra of the H-sdB HD 4539 (see the beginning of Ch. 11).

## 12. Photometric Results

According to the methodology described in Sect. 7.2.3, the calculated ATLAS12 and TLUSTY/SYNSPEC models (see Sects. 7.2.1 and 7.2.2) are used to perform SED fits for all program stars. To this end, the photometric filter systems described in Sect. 8.3 (see Tables 8.15-8.17) and the spectroscopic results derived from one combination of model atmosphere approach and quantitative spectral analysis strategy are used. The respective spectroscopic parameters can be found in Tables A.1-A.23. These tables also list the angular diameters  $\theta$  and the monochromatic color excesses  $E(44 - 55)$  derived from the individual SED fits. The majority of the determined angular diameters are small ( $\theta \sim 10^{-11} - 10^{-12}$  rad), as expected for the distances to the objects (see Tables 8.18 and 8.19). HD 149382 is the only analyzed program star whose distance is below 100 pc such that its angular diameter is larger ( $\theta \sim 10^{-10}$  rad). For each star, the measured monochromatic color excess is checked against the reddening maps of Schlegel et al. (1998) and Schlafly & Finkbeiner (2011). As a matter of fact, most of the measured  $E(44 - 55)$  values are lower than the ones derived from the respective reddening maps. Only about two handfuls of program stars exhibit significant reddening values of  $E(44 - 55) \gtrsim 0.10$  mag. These stars are: HZ 1, PG 0314+146, PG 0342+026, EC 14338-1445, FBS 2158+373, FBS 2204+364, FBS 2347+385, KUV 03591+0457, GALEX J172445.5+113224, GALEX J032139.8+472718, and FB 29.

Binary SED fits (with fixed atmospheric parameters for the primaries; see Sect. 7.2.3) are performed for program stars, for which a priori a clear IR excess is visible or for which  $E(44 - 55)$  lies distinctly above the expectations for a single SED fit, which is also a clear indication for a cool companion. The analyzed program stars with visible MS companions are SB 290, Feige 36, and EC 01541-1409 (these three objects are new discoveries) as well as Feige 34, which is already known (Latour et al., 2018). The color excesses derived from the individual binary SED fits are trustworthy because they are lower than or near the values of Schlegel et al. (1998) and Schlafly & Finkbeiner (2011).

As an example, Figs. 12.0.1-12.0.4 show the single SED fit for the H-sdB PG 1432+004 as well as the binary SED fits for the H-sdOB EC 01541-1409, the  $^3\text{He}$  H-sdB SB 290, and the RV-variable star Feige 36, respectively. In almost all cases, the absolute values for the residuals of the synthetic and the observed magnitudes lie below  $|\chi| = 2$ , meaning that the residuals do not exceed  $2\sigma$  in absolute values. The IR excesses are clearly visible for EC 01541-1409 and SB 290, which, apart from their rapid pulsation (EC 01541-1409; Kilkenney et al. 2009) and rapid rotation (SB 290; Geier et al. 2013b; Schneider et al. 2018; see also Sect. 10.1.2), makes these two objects even more interesting for future studies.

The orbital period of SB 290 (not determined within the framework of this thesis because only two high-resolution FEROS spectra are used; see Table 8.5) could provide information on whether the star has been spun-up by tidal interaction with the current companion (for this,

the orbital period has to be less than 1.2 d; Geier et al. 2010) or whether it has been spun-up during a potential double HeWD merger (see Sect. 3.4.2). The latter scenario, however, is less likely because it would mean that SB 290 used to be a triple system. Moreover, double HeWD mergers are believed to produce mainly helium-rich objects, which is not the case for SB 290.

The very unique system of Feige 36 will be discussed in detail in Sect. 12.2.

## 12. Photometric Results

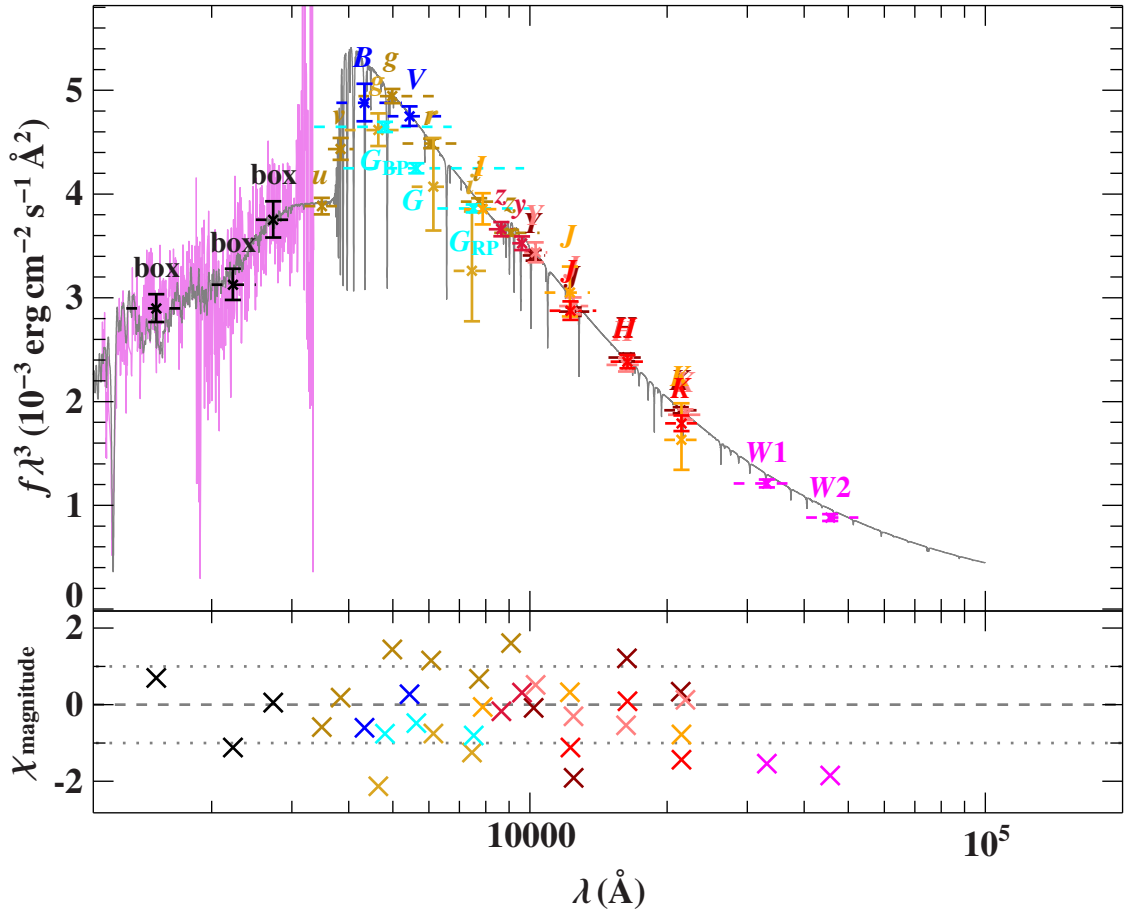


Figure 12.0.1.: Comparison of the smoothed final synthetic spectrum of the H-sdB PG 1432+004 (solid gray line) to photometric data (spectral energy distribution; SED). The synthetic spectrum is based on the atmospheric parameters derived from the hybrid LTE/NLTE model atmosphere approach and the global analysis strategy (ADS + Global). The three black data points labelled “box” are binned fluxes from an IUE spectrum (Wamsteker et al., 2000) that is plotted as a solid magenta line. Filter-averaged fluxes that are converted from observed magnitudes are shown as colored data points (the colored dashed horizontal lines indicate the respective filter widths). The residual panel at the bottom shows the differences between the synthetic and the observed magnitudes, whereby the dotted gray horizontal lines mark deviations of  $\pm 1\sigma$ , that is, values of  $\chi = \pm 1$ . The  $\chi = 0$  level is marked by the dashed gray horizontal line. The following color codes are used to identify the individual photometric filter systems: SDSS (yellow; Henden et al. 2016), SkyMapper DR1 (golden; Wolf et al. 2018), PanSTARRS DR1 (dark red; Chambers et al. 2017), Johnson-Cousins (blue; Henden et al. 2016), Gaia DR2 (turquoise; Gaia Collaboration et al. 2018), VISTA (brown; McMahon et al. 2013; extracted from <http://horus.roe.ac.uk/vsa/index.html>, last called on 20th May 2021), DENIS (orange; DENIS Consortium 2005), 2MASS (light red; Cutri et al. 2003), UKIDSS (rose; Lawrence et al. 2013), and AllWISE (magenta; Cutri et al. 2014). In order to eliminate the steep slope of the constructed SED over the displayed broad wavelength range, the flux density times the wavelength to the power of three ( $f_\lambda \lambda^3$ ) is chosen as the ordinate in the upper panel of the figure.

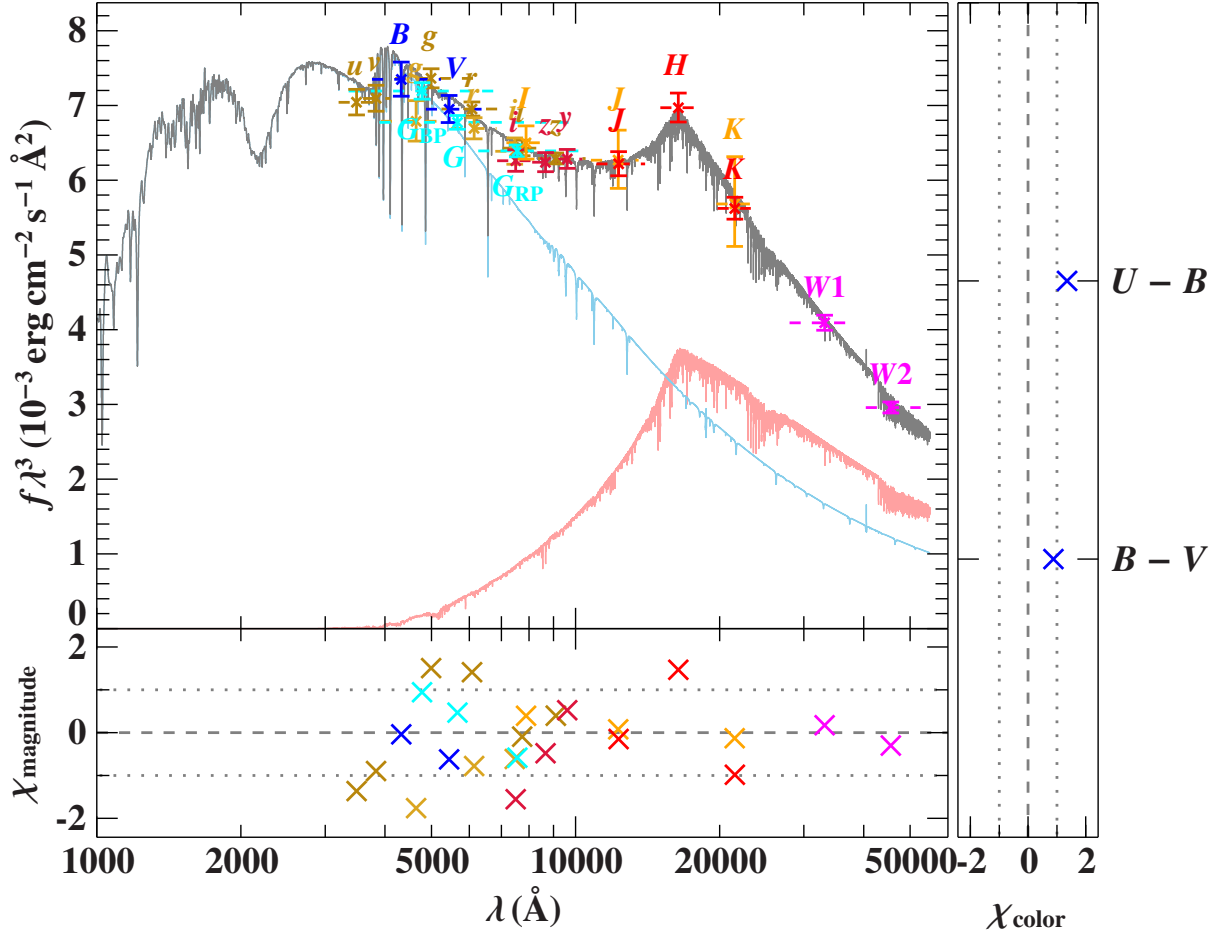


Figure 12.0.2.: Same as Fig. 12.0.1, but showing the binary SED fit for the rapidly pulsating H-sdOB EC 01541-1409. The contribution of the primary H-sdOB to the total SED flux is shown as a solid light blue line. The star shows an IR excess because of the presence of a cool MS companion, as can be seen from the solid light red line. The residual panels at the bottom and on the right-hand side show the differences between the synthetic and the observed magnitudes and colors, respectively, whereby the dotted gray horizontal lines mark deviations of  $\pm 1\sigma$ , that is, values of  $\chi = \pm 1$ . The  $\chi = 0$  levels are marked by the dashed gray horizontal lines. The following color codes are used to identify the individual photometric filter systems: SDSS (yellow; Henden et al. 2016), SkyMapper DR1 (golden; Wolf et al. 2018), PanSTARRS DR1 (dark red; Chambers et al. 2017), Johnson-Cousins (blue; Henden et al. 2016; Kilkenny et al. 2017), *Gaia* DR2 (turquoise; Gaia Collaboration et al. 2018), DENIS (orange; DENIS Consortium 2005), 2MASS (light red; Cutri et al. 2003), and unWISE (magenta; Schlafly et al. 2019).

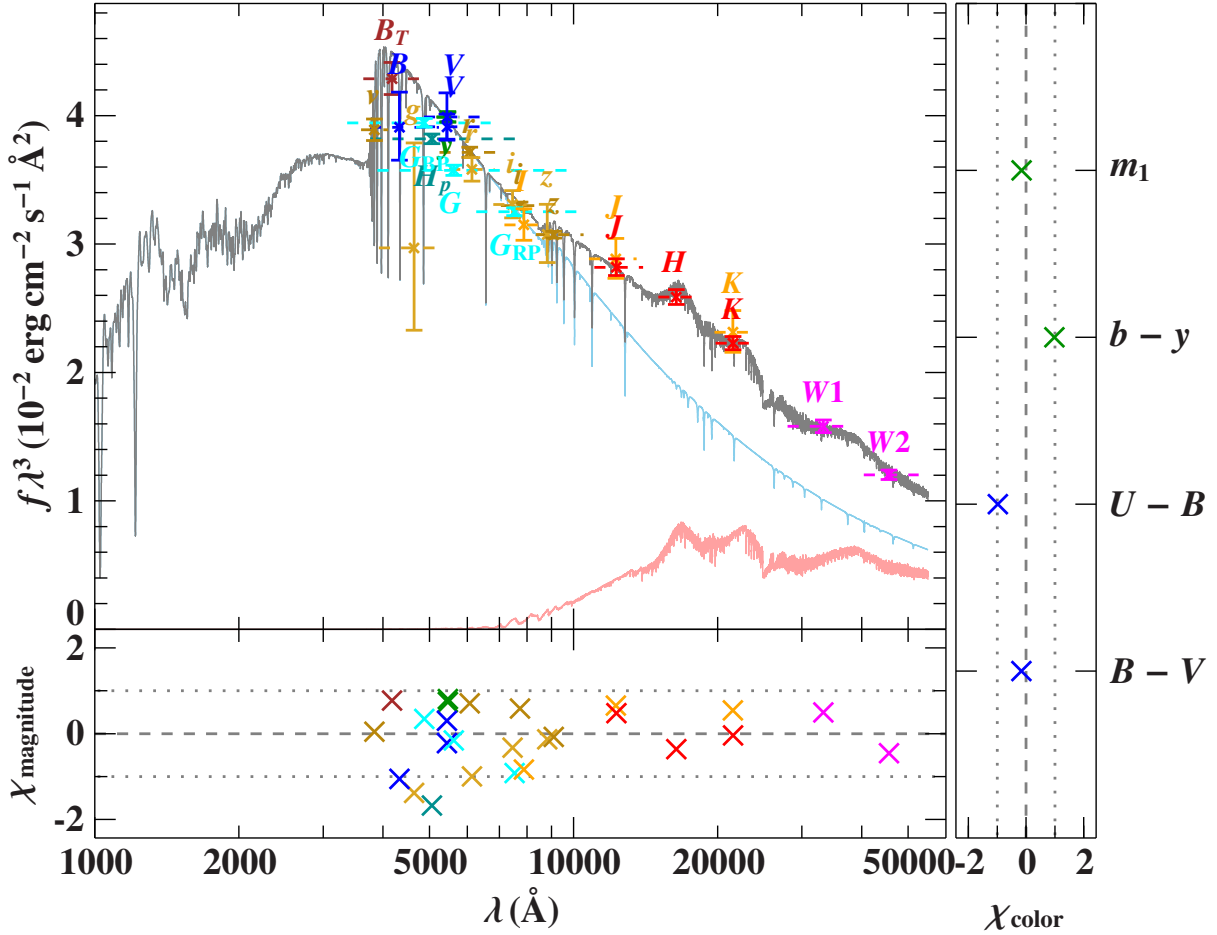


Figure 12.0.3.: Same as Fig. 12.0.1, but showing the binary SED fit for the rapidly rotating  ${}^3\text{He}$  H-sdB SB 290. The contribution of the primary H-sdB to the total SED flux is shown as a solid light blue line. The star shows an IR excess because of the presence of a cool MS companion, as can be seen from the solid light red line. The residual panels at the bottom and on the right-hand side show the differences between the synthetic and the observed magnitudes and colors, respectively, whereby the dotted gray horizontal lines mark deviations of  $\pm 1\sigma$ , that is, values of  $\chi = \pm 1$ . The  $\chi = 0$  levels are marked by the dashed gray horizontal lines. The following color codes are used to identify the individual photometric filter systems: SDSS (yellow; Henden et al. 2016), SkyMapper DR1 (golden; Wolf et al. 2018), HIPPARCOS (dark turquoise; van Leeuwen 2007), *Tycho* (wine red; Høg et al. 2000), Stroemgren (green; Hauck & Mermilliod 1998; Paunzen 2015), Johnson-Cousins (blue; Henden et al. 2016; Kilkeny et al. 2017), *Gaia* DR2 (light turquoise; Gaia Collaboration et al. 2018), DENIS (orange; DENIS Consortium 2005), 2MASS (light red; Cutri et al. 2003), and AllWISE (magenta; Cutri et al. 2014).

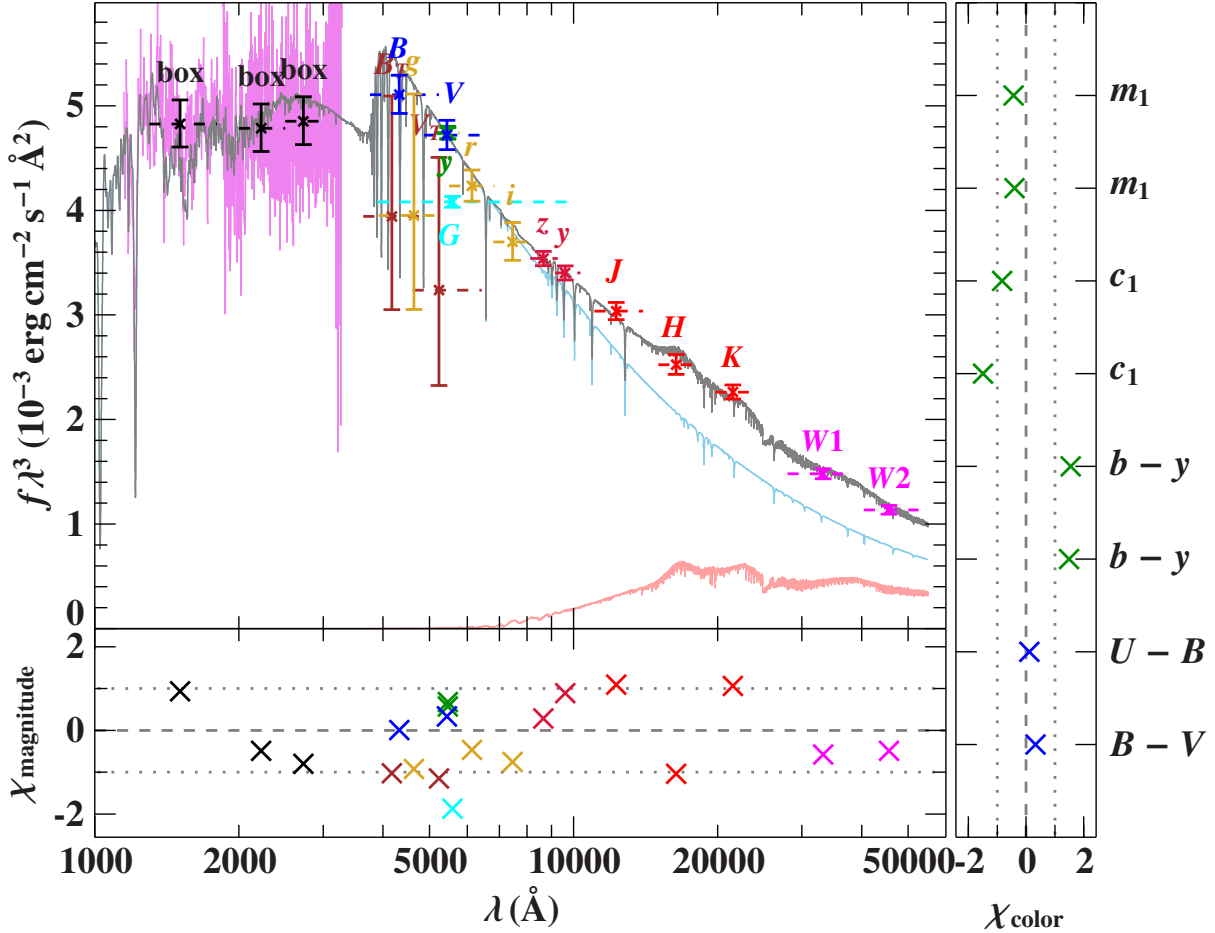


Figure 12.0.4.: Same as Fig. 12.0.1, but showing the binary SED fit for the RV-variable star Feige 36. The contribution of the primary to the total SED flux is shown as a solid light blue line. The star shows an IR excess because of the presence of a cool MS companion, as can be seen from the solid light red line. The residual panels at the bottom and on the right-hand side show the differences between the synthetic and the observed magnitudes and colors, respectively, whereby the dotted gray horizontal lines mark deviations of  $\pm 1\sigma$ , that is, values of  $\chi = \pm 1$ . The  $\chi = 0$  levels are marked by the dashed gray horizontal lines. The following color codes are used to identify the individual photometric filter systems: SDSS (yellow; Henden et al. 2016), PanSTARRS DR1 (dark red; Chambers et al. 2017), *Tycho* (wine red; Høg et al. 2000), Stroemgren (green; Hauck & Mermilliod 1998; Paunzen 2015), Johnson-Cousins (blue; Mermilliod 2006; Henden et al. 2016), *Gaia* DR2 (turquoise; Gaia Collaboration et al. 2018), 2MASS (light red; Cutri et al. 2003), and AllWISE (magenta; Cutri et al. 2014).

**Table 12.1.:** Parameters of the spectroscopic binary systems with main-sequence companions analyzed in this work. The listed atmospheric parameters of the primary stars ( $T_{\text{eff,pri}}$ ,  $\log g_{\text{pri}}$ ) are extracted from Tables A.9, A.18, and A.19. They are derived from spectroscopy via the hybrid LTE/NLTE model atmosphere approach and the global analysis strategy (ADS + Global; see Sects. 6.8 and 7.1.2). Together with the determined helium abundances (not listed here), the values of  $T_{\text{eff,pri}}$  and  $\log(g_{\text{pri}})$  are used as input for the performed binary SED fits (see Sect. 7.2). The listed radii  $R_{\text{pri}}$  and masses  $M_{\text{pri}}$  of the primaries can also be found in Tables 13.5, 13.10, and 13.12. They are determined as presented in Sect. 7.3 and are based on *Gaia* DR2 parallaxes (Gaia Collaboration et al., 2018) and Bailer-Jones distances (Bailer-Jones et al., 2018), respectively. The column labelled “ $T_{\text{eff,sec}}$ ” lists the effective temperatures of the individual companions, whereas the column labelled “ $S$ ” provides the surface ratios defined as  $S := A_{\text{sec}}/A_{\text{pri}}$ . These two parameters are derived from the performed binary SED fits (see Sect. 7.2.3). The columns labelled “ $R_{\text{sec}}$ ” and “ $M_{\text{sec}}$ ” list the radii and the masses derived for the individual companions. Additionally, the spectral types of the companions are given in the last column. Due to the fact that the surface gravity of the secondary ( $\log g_{\text{sec}}$ ) is usually unconstrained in the case of binary SED fits, it is fixed to a value of 4.50, typical for main-sequence stars (see Sect. 7.2.3). The sole exception to this is Feige 34, for which the result of Latour et al. (2018) is used (see the corresponding footnote below).

Primary Star	$T_{\text{eff,pri}}$ [K]	$\log(g_{\text{pri}})$ [ $\text{cm s}^{-2}$ ]	$R_{\text{pri}}$ [ $R_{\odot}$ ]	$M_{\text{pri}}$ [ $M_{\odot}$ ]	$S$	$T_{\text{eff,sec}}$ [K]	$R_{\text{sec}}^{\text{a}}$ [ $R_{\odot}$ ]	$M_{\text{sec}}^{\text{b}}$ [ $M_{\odot}$ ]	$R_{\text{sec}}^{\text{c}}$ [ $R_{\odot}$ ]	$M_{\text{sec}}^{\text{c}}$ [ $M_{\odot}$ ]	Sp. Type Comp. <sup>d</sup>
EC 01541-1409 <sup>e</sup>	$37\,570^{+60}_{-130}$	$5.750^{+0.010}_{-0.017}$	$0.15 \pm 0.01$	$0.44 \pm 0.07$	$13.9^{+1.3}_{-0.9}$	$4510 \pm 250$	$0.56 \pm 0.05$	$0.51 \pm 0.05$	$\sim 0.74$	$\sim 0.69$	K4
Feige 34 <sup>f</sup>	$62\,550 \pm 600^{\text{i}}$	$5.99 \pm 0.03^{\text{i}}$	$0.10 \pm 0.01^{\text{i}}$	$0.36 \pm 0.06^{\text{j}}/0.37 \pm 0.06^{\text{i}}$	$23.5 \pm 2.0^{\text{i}}$	$3848^{+214}_{-309}$	$0.48 \pm 0.06^{\text{i}}$	$0.43 \pm 0.06^{\text{i}}$	$\sim 0.60^{\text{i}}$	$\sim 0.51^{\text{i}}$	M0 <sup>i</sup>
SB 290 <sup>f</sup>	$26\,480^{+40}_{-60}$	$5.407^{+0.007}_{-0.008}$	j	j	$6.2^{+1.6}_{-1.0}$	$3260^{+340}_{-280}$	j	j	$\sim 0.35$	$\sim 0.27$	M4
Feige 36 <sup>g,h</sup>	$28\,640^{+40}_{-70}$	$5.949^{+0.008}_{-0.010}$	$0.17 \pm 0.01$	$0.90^{+0.12}_{-0.13}/0.91^{+0.12}_{-0.13}$	$4.6^{+1.4}_{-1.2}$	$3400^{+800}_{-400}$	$0.36 \pm 0.06$	$0.32 \pm 0.06$	$\sim 0.42$	$\sim 0.33$	M3

**Notes:** For the results of this work,  $1\sigma$  single parameter errors derived from  $\chi^2$ -statistics are given for  $T_{\text{eff,pri}}$ ,  $\log(g_{\text{pri}})$ ,  $T_{\text{eff,sec}}$ , and  $S$  (see Sects. 7.1.2 and 7.2.3). The listed uncertainties on  $R_{\text{pri}}$  and  $M_{\text{pri}}$  result from Gaussian error propagation according to Eqs. (7.10) and (7.12). The given errors on  $R_{\text{sec}}$  are also derived from Gaussian error propagation, whereby the statistical uncertainties of  $S$  as well as the given errors on  $R_{\text{pri}}$  are used. Last but not least, the given errors on  $M_{\text{sec}}$  also result from Gaussian error propagation.

(a) Determined from  $S$  and  $R_{\text{pri}}$ .

(b) Determined from the mass-radius relation for low-mass main-sequence stars from Demircan & Kahraman (1991) applied to the radii  $R_{\text{sec}}$  given in the eighth column of this table. The values for  $R_{\text{sec}}$  are determined from  $S$  and  $R_{\text{pri}}$ .

(c) Derived for main-sequence stars making use of  $T_{\text{eff,sec}}$  as well as of Tables 15.7 and 15.8 in Cox (2000). Solar metallicity is assumed.

(d) Derived from  $T_{\text{eff,sec}}$  and Table 15.7 in Cox (2000).

(e) Pulsating star.

(f) Rotating star.

(g) The star is most likely a pre-ELM. For further information, see Sect. 12.2.

(h) RV-variable star.

(i) Adopted from/based on Latour et al. (2018). For the binary SED fit of Feige 34, the authors used the surface gravity of the secondary ( $\log g_{\text{sec}}$ ) as a free parameter and derived a value of  $\log(g_{\text{sec}}) = 5.4^{+0.1}_{-1.3}$ .

(j) SB 290 has a renormalised unit weight error (RUWE) larger than three derived from *Gaia* DR2 data (see Sect. 8.4 and Table 8.18). This is a strong indicator for a flawed *Gaia* parallax, which also affects the derived Bailer-Jones distance (Bailer-Jones et al., 2018). Hence, no fundamental stellar parameters are determined for SB 290 in this work. This is also why the radius  $R_{\text{sec}}$  and the mass  $M_{\text{sec}}$  for the main-sequence companion of SB 290 are not determined via the surface ratio  $S$ , the radius of the primary  $R_{\text{pri}}$ , and the mass-radius relation for low-mass main-sequence stars from Demircan & Kahraman (1991).

## 12.1. Spectroscopic Binary Systems with Main-Sequence Companions

The properties of the four spectroscopic binary systems with MS companions analyzed in this work (EC 01541-1409, Feige 34, SB 290, and Feige 36) are summarized in Table 12.1. Therein, the individual surface ratios  $S := A_{\text{sec}}/A_{\text{pri}}$  and effective temperatures of the companions  $T_{\text{eff,sec}}$  (both derived from the performed binary SED fits) are listed in the sixth and seventh columns. As described in Sect. 7.2.3, the surface gravity of the secondary ( $\log g_{\text{sec}}$ ) is fixed to 4.50 for the SED fits (except for Feige 34 for which the result of Latour et al. 2018 is used; see the corresponding footnote in Table 12.1) because this is a typical value for MS stars and  $\log(g_{\text{sec}})$  is usually unconstrained in the case of binary SED fits. From  $T_{\text{eff,sec}}$  and Table 15.7 in Cox (2000), the spectral types of the individual companion stars can be derived. In the MK classification scheme, they are (see Table 12.1): K4 (EC 01541-1409), M0 (Feige 34), M4 (SB 290), and M3 (Feige 36). As these cool late-type MS companions do not significantly contribute to the total flux in the optical spectral range, the atmospheric parameters of the corresponding primary stars ( $T_{\text{eff,pri}}$  and  $\log g_{\text{pri}}$ ; both derived from spectroscopy and also listed in Table 12.1) are not compromised. According to Eqs. (7.7) and (7.10), the radii of the primaries  $R_{\text{pri}}$  can be determined from the results of the SED fits (from the angular diameters  $\theta$ ) and the corresponding parallaxes  $\varpi$ /distances  $d$ . The resulting values for  $R_{\text{pri}}$  are also listed in Table 12.1, at least for EC 01541-1409, Feige 34, and Feige 36<sup>128</sup>. In fact, the values are pretty much the same for the *Gaia* DR2 parallaxes (Gaia Collaboration et al., 2018) and the Bailer-Jones distances (Bailer-Jones et al., 2018) used, which is why a distinction in that regard is not necessary (see Ch. 13 and, in particular, Sect. 13.4 for details on the comparison between the fundamental stellar parameters derived from *Gaia* DR2 parallaxes and Bailer-Jones distances for all of the program stars analyzed in this work). Knowing the individual values for  $R_{\text{pri}}$ , the radii of the secondary stars ( $R_{\text{sec}}$ ) can be calculated from the respective surface ratios  $S$  in the following way:

$$R_{\text{sec}} = R_{\text{pri}} \cdot \sqrt{S}. \quad (12.1)$$

As a result, the masses of the secondaries ( $M_{\text{sec}}$ ) can also be estimated. In this work, this is done via the mass-radius relation for low-mass MS stars from Demircan & Kahraman (1991), which is given by:

$$\frac{R_{\text{sec}}}{R_{\odot}} = 1.06 \cdot \left( \frac{M_{\text{sec}}}{M_{\odot}} \right)^{0.945} \quad \text{for } M_{\text{sec}} < 1.66 M_{\odot}. \quad (12.2)$$

For EC 01541-1409, Feige 34, and Feige 36, the resulting values for  $R_{\text{sec}}$  and  $M_{\text{sec}}$  are listed in the eighth and ninth columns of Table 12.1<sup>129</sup>. In addition,  $R_{\text{sec}}$  and  $M_{\text{sec}}$  are derived from

<sup>128</sup>SB 290 has a renormalised unit weight error (RUWE) larger than three derived from *Gaia* DR2 data (see Sect. 8.4 and Table 8.18). This is a strong indicator for a flawed *Gaia* parallax, which also affects the derived Bailer-Jones distance (Bailer-Jones et al., 2018). Hence, no fundamental stellar parameters are determined for SB 290 in this work. This is also why no value for  $R_{\text{pri}}$  is given in Table 12.1.

<sup>129</sup>For SB 290,  $R_{\text{sec}}$  and  $M_{\text{sec}}$  are not determined via the surface ratio  $S$ , the radius of the primary  $R_{\text{pri}}$ , and the mass-radius relation for low-mass MS stars from Demircan & Kahraman (1991) because no fundamental

## 12.2. The Peculiar System of Feige 36

---

Table 15.8 in Cox (2000). For this, solar metallicity is assumed and Table 15.7 in Cox (2000) is used, whereby the determined values for  $T_{\text{eff,sec}}$  are taken into account. In this case,  $R_{\text{sec}}$  and  $M_{\text{sec}}$  can also be estimated for the system of SB 290 (see the respective entries in columns ten and eleven of Table 12.1).

Interestingly,  $R_{\text{sec}}$  and  $M_{\text{sec}}$  (derived from  $S$ ,  $R_{\text{pri}}$ , and the mass-radius relation) are systematically lower compared to the respective values derived from Cox (2000), which are based on  $T_{\text{eff,sec}}$  and solar metallicity. It has to be pointed out, however, that no uncertainties can be determined for the Cox (2000) values. Nonetheless, the discrepancy between  $R_{\text{sec}}$  and  $M_{\text{sec}}$  (derived from  $S$ ,  $R_{\text{pri}}$ , and the mass-radius relation) and the spectral types of the companions derived from Cox (2000) cannot be dismissed in the case of EC 01541-1409 and Feige 34. Only for Feige 36,  $R_{\text{sec}}$  and  $M_{\text{sec}}$  (derived from  $S$ ,  $R_{\text{pri}}$ , and the mass-radius relation) match the values of Cox (2000), if the uncertainties are taken into account. In fact, the discrepancies in the case of EC 01541-1409 and Feige 34 could indicate metallicities below the solar one for the respective MS companions.

Last but not least, a word about the surface gravities of the secondary stars ( $\log g_{\text{sec}}$ ), which can be determined from  $R_{\text{sec}}$  and  $M_{\text{sec}}$  via the known relation:

$$g_{\text{sec}} = \frac{GM_{\text{sec}}}{R_{\text{sec}}^2}. \quad (12.3)$$

Using the values listed in columns eight and nine of Table 12.1 for  $R_{\text{sec}}$  and  $M_{\text{sec}}$ , the following results for  $\log(g_{\text{sec}})$  can be derived:  $4.65 \pm 0.09$  (EC 01541-1409),  $4.71 \pm 0.13$  (Feige 34), and  $4.83 \pm 0.17$  (Feige 36). For EC 01541-1409 and Feige 36, the determined surface gravities of the secondaries are (slightly) higher than the fixed value of 4.50 used to perform the binary SED fits for the respective objects. However, the calculated surface gravities agree with a value of 4.50 within  $2\sigma$ . For the system of Feige 34, the calculated value for  $\log(g_{\text{sec}})$  matches the result of  $\log(g_{\text{sec}}) = 5.4_{-1.3}^{+0.1}$  determined by Latour et al. (2018), if the uncertainties are taken into account.

## 12.2. The Peculiar System of Feige 36

Among the RV-variable program stars with MS companions analyzed in this work, orbital parameters are only known for Feige 36 (orbital period  $P = 0.35386 \pm 0.00014$  d, RV semi-amplitude  $K = 134.59 \pm 1.31$  km s<sup>-1</sup>, systemic velocity  $\gamma = -0.84 \pm 0.94$  km s<sup>-1</sup>; Moran et al. 1999). Knowing the orbital period and the RV semi-amplitude of this system, allows

---

stellar parameters are derived for this object in this work. This is because SB 290 has a renormalised unit weight error (RUWE) larger than three derived from *Gaia* DR2 data (see Sect. 8.4 and Table 8.18), which is a strong indicator for a flawed *Gaia* parallax that also affects the derived Bailer-Jones distance (Bailer-Jones et al., 2018).

to calculate the mass of the primary star ( $M_{\text{pri}}$ ) for a certain inclination angle  $i$ . This can be achieved via the binary mass function:

$$f(M_{\text{pri}}, M_{\text{sec}}) = \frac{M_{\text{sec}}^3 \sin^3 i}{(M_{\text{pri}} + M_{\text{sec}})^2} = \frac{PK^3}{2\pi G}. \quad (12.4)$$

Assuming a mass of  $M_{\text{sec}} \sim 0.33 M_{\odot}$  for the M3 MS companion in the system of Feige 36 (see the results of Table 12.1 and the binary SED fit displayed in Fig. 12.0.4), an upper limit of  $M_{\text{pri}} \lesssim 0.30 M_{\odot}$  can be obtained. The exact value of  $M_{\text{pri}}$  depends on the inclination of the system but the determined upper limit is nowhere near the canonical mass of core helium-burning hot subdwarf O and B stars, which lies around  $\sim 0.46\text{--}0.48 M_{\odot}$  (see Ch. 3). For a hot subdwarf star, a mass of  $M_{\text{pri}} \lesssim 0.30 M_{\odot}$  could possibly be accomplished by the first stable RLOF channel (see Fig. 3.4.4 and Table 3.3). However, such a low mass is also rather unlikely for this scenario. Moreover, the first stable RLOF channel mainly produces long-period binary systems with  $0.50 \text{ d} \lesssim P \lesssim 1600 \text{ d}$  (see Sect. 3.4.1). This is clearly at odds with the orbital period of  $P = 0.35386 \pm 0.00014 \text{ d}$  observed by Moran et al. (1999). Consequently, it can be ruled out that the primary star in the system of Feige 36 is a core helium-burning EHB object. As a matter of fact, a mass of  $M_{\text{pri}} \lesssim 0.30 M_{\odot}$  is in good agreement with the position of Feige 36 below the canonical EHB in the  $T_{\text{eff}}\text{--}\log(g)$  plane (see Sect. 9.4.1), which indeed favors a lower than canonical mass for the primary. The position of Feige 36 in the  $T_{\text{eff}}\text{--}\log(g)$  plane is also crossed by evolutionary tracks for (pre-)ELMs (see Fig. 9.4.1). In fact, ELM masses may lie in a range of  $\sim 0.16\text{--}0.30 M_{\odot}$  (for instance, see Istrate et al. 2016). From this perspective, the most plausible explanation for the primary star in the system of Feige 36 hence seems to be that of a pre-ELM.

Strikingly, the spectroscopic mass of Feige 36 determined in this work and based on the *Gaia* DR2 parallax (Gaia Collaboration et al., 2018) is  $0.90^{+0.12}_{-0.13} M_{\odot}$ . This result and the similarly high spectroscopic mass of  $0.91^{+0.12}_{-0.13} M_{\odot}$  derived from the Bailer-Jones distance (Bailer-Jones et al., 2018) are listed in the fifth column of Table 12.1. Such high masses for Feige 36 suggest a position of the object in the  $T_{\text{eff}}\text{--}\log(g)$  diagram that lies above the canonical horizontal branch. However, this is in complete contradiction to the results derived from the quantitative spectral analysis as well as to the upper limit of  $\lesssim 0.30 M_{\odot}$  determined from the binary mass function. The high spectroscopic masses are also clearly at odds with the nature of pre-ELMs. As described in Sect. 7.3, the spectroscopic mass of Feige 36 is derived from a combination of the following three parameters: the angular diameter  $\theta$ , the surface gravity  $\log(g)$ , and the parallax  $\varpi$ /distance  $d$  (see Eqs. 7.9 and 7.12).  $\theta$  can be excluded as a potential source of error because Feige 36 is similarly distant than other analyzed program stars (see Tables 8.18 and 8.19) and the value of  $\theta = 1.7378^{+0.0091}_{-0.0092} \cdot 10^{-11} \text{ rad}$  (see Table A.9) perfectly matches the order of magnitude of  $10^{-11} - 10^{-12} \text{ rad}$  derived for almost all investigated objects. Furthermore, it is highly unlikely that the determined value for the surface gravity ( $\log g = 5.949^{+0.008}_{-0.010}$ ; see Table A.9) is responsible for a falsely derived spectroscopic mass because this result is in good agreement with the previous ones of Schneider et al. (2018) and Edelmann et al. (1999), which are  $5.97 \pm 0.01$  and  $5.97 \pm 0.02$ , respectively. Thus, the measured *Gaia* DR2 parallax  $\varpi_{\text{Gaia}}$  and the Bailer-Jones distance derived from it remain. In fact, Feige 36 is the only program star analyzed in this work, for

## 12.2. The Peculiar System of Feige 36

---

which no *Gaia*  $G_{BP}$  and  $G_{RP}$  magnitudes and, hence, no RUWE parameter are available in DR2, as already presented in Sect. 8.4 (see Tables 8.18 and 8.19). In addition, the poor unit weight error of UWE  $\sim 2.26$  ( $> 1$ ), which results from the archive quantities `astrometric_chi2_al` = 625.7668 and `astrometric_n_good_obs_al` = 128, points towards a poor astrometric solution, even though the corresponding apparent fractional parallax uncertainty is low ( $\Delta\varpi_{Gaia}/\varpi_{Gaia} < 0.03$ ;  $\varpi_{Gaia} = 2.3076 \pm 0.0642$  mas; see Table 8.18). In consequence, there is indeed a chance that the *Gaia* DR2 parallax is wrong. Although this thesis is based solely on *Gaia* DR2 data, the results of EDR3 (Gaia Collaboration et al., 2020) were made publicly available during the writing phase. A quick look at these data reveals  $\varpi_{Gaia} = 2.3116 \pm 0.0435$  mas, which is consistent with the DR2 parallax, and RUWE = 0.948328 ( $\sim 1$ ), which points towards a trustworthy astrometric solution. Additionally, the flags `ipd_gof_harmonic_phase`  $\sim 113$ , `ipd_frac_multi_peak` = 0, and `ipd_frac_odd_win` = 0, which, in general, may indicate whether a source is one of a close pair (possibly a binary) or whether the data suffers from nearby disturbing sources (see Gaia Collaboration et al. 2020 for further information), are not striking at all. However, the binarity flag `ipd_gof_harmonic_amplitude`  $\sim 0.34$  ( $> 0.1$ ) is a possible hint for a marginally-resolved binary according to El-Badry et al. (2021). Therefore, it is possible that even the EDR3 data are not trustworthy for Feige 36 such that  $\varpi_{Gaia}$  (and the Bailer-Jones distance derived from it) remain the main responsible parameters for the falsely determined spectroscopic masses.

As a matter of fact, the small change of the *Gaia* parallax coming along with EDR3 compared to DR2 does not result in any significant difference in the derived mass. If the high spectroscopic masses calculated for Feige 36 were correct and the star were a hot subdwarf after all, the double HeWD merger channel would be the only evolutionary scenario that could potentially explain such high masses (see Fig. 3.4.4 and Table 3.3). However, the fact that Feige 36 has a cool MS companion makes it rather unlikely that the primary star has been formed from the merger channel because this would mean that Feige 36 used to be a triple system. And even in the unlikely case that the primary star actually emerged from the coalescence of two HeWDs, the question arises why Feige 36 is hydrogen and not helium-rich because the latter is expected from the merger scenario (see Sect. 3.4.2).

Last but not least, the system of Feige 36 is also covered by the ongoing mission of the TESS satellite. In fact, the measured light curve shows a variation with a period of  $\sim 7.6$  d (see Fig. 12.2.1). This is significantly larger than the orbital period of  $P = 0.35386 \pm 0.00014$  d measured by Moran et al. (1999). Surprisingly, no variation at all is observed in the TESS light curve for the latter. This together with the detected IR excess (see Fig. 12.0.4) is a possible hint that the  $\sim 7.6$  d reflection effect<sup>130</sup> could be caused by an additional third body in the

---

<sup>130</sup>Reflection effects can be observed for close binary systems in which the primary star has a significantly higher effective temperature than the companion. Due to this difference in temperature, the hemisphere of the cooler component that faces the hotter primary is heated up by the radiation of the latter. Because of the fact that the intensity and the temperature are highly correlated (see Eq. 6.7), the radiation from the heated side of the secondary is more intense, meaning that the more of the heated half of the companion becomes visible to the observer, the higher the measured flux. This leads to a continually changing periodic reflection effect that is visible in the light curve of the system. Due to the origin of the reflection effect, its period corresponds to the orbital one. As a matter of fact, a prominent reflection effect requires a huge secondary with a large surface that can be heated up by the radiation of the primary. For instance,

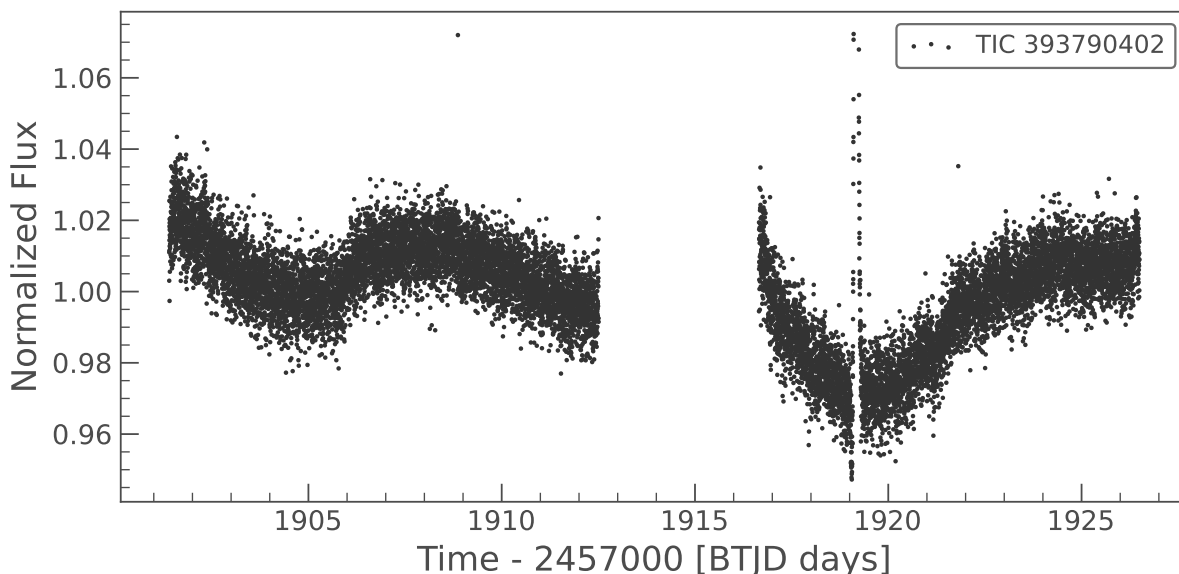


Figure 12.2.1.: TESS light curve observed for Feige 36 (TIC 393790402). The observed variation indicates a reflection effect with a period of  $\sim 7.6$  d, which is significantly larger than the orbital period of  $P = 0.35386 \pm 0.00014$  d measured by Moran et al. (1999). Surprisingly, no variation at all is observed in the light curve for the latter. This combined with the IR excess detected for Feige 36 (see Fig. 12.0.4) is a possible hint that the  $\sim 7.6$  d reflection effect could be caused by an additional third body in the system (see the text for more details). Produced by V. Schaffenroth and shared via private communication.

system, although the amplitude observed in Fig. 12.2.1 is quite large for such a long period. Since the *Gaia* satellite is generally not able to provide reliable astrometric solutions for triple systems, a third body would also explain why the spectroscopic mass of Feige 36 based on the measured *Gaia* parallax (as well as on the derived Bailer-Jones distance) differs so much from the upper limit of  $M_{\text{pri}} \lesssim 0.30 M_{\odot}$  determined from the binary mass function and favoring a pre-ELM nature of the primary<sup>131</sup>. In fact, a primary mass below  $0.30 M_{\odot}$  could well be achieved in a triple system. Unfortunately, the observed TESS light curve is based on data of a single observation sector only such that an instrumental effect for the measured  $\sim 7.6$  d variation cannot be ruled out at the moment. What is also striking is the fact that the second minimum observed in the TESS data is lower than the first one (see Fig. 12.2.1). However, it should not be interpreted too much into this at the moment because TESS data are known to show trends quite often. In any case, further observations from more sectors are needed.

this is fulfilled in HW Vir systems (see Schaffenroth et al. 2019 and references therein) but it has to be mentioned that the modelling of the reflection effect is only feasible if the RV curve of the companion is known. Unfortunately, this is quite often not the case.

<sup>131</sup>If the third body in the system of Feige 36 is indeed real, it is even more unlikely that the primary star was formed from a double HeWD merger because this would mean that the system used to be a quadruple system.

Taking all of the above considerations into account, a current triple system for Feige 36 and a pre-ELM nature for the primary feel most likely. However, the validity of the observed TESS light curve can be questioned. As a result, only one thing is clear: The system of Feige 36 is very peculiar and unique, making future observations necessary and exciting at the same time.

## 12.3. The Objects HD 149382 and GALEX J032139.8+472718

The SEDs of two hot subdwarf program stars cannot be fitted satisfactorily, neither by a single nor by a binary fit. These objects are the H-sdOB HD 149382 and the H-sdB GALEX J032139.8+472718. While GALEX J032139.8+472718 is a known RV-variable star (Kawka et al., 2012) for which the companion type is still unknown, imaging via adaptive optics has potentially revealed a visual, stellar companion of HD 149382, which is  $\sim 1''$  (corresponding to  $\sim 75$  AU at a distance of  $\sim 75$  pc; see Table 8.18) away from the primary (Østensen et al., 2005). This orbital separation corresponds to a period of at least  $\sim 530$  years according to Kepler’s third law and Newton’s law of universal gravitation, if a canonical hot subdwarf mass of  $\sim 0.50 M_{\odot}$  and a mass of  $\sim 1.00 M_{\odot}$  are assumed for the primary and the red star companion, respectively. In fact, Jacobs et al. (2011) did not find any significant RV variations with semi-amplitudes higher than  $0.79 \text{ km s}^{-1}$  on periods shorter than 50 d for HD 149382. At first glance, this supports a large orbital separation of the system. However, the observed visual component may not be gravitationally bound to HD 149382 at all. Unfortunately, the *Gaia* DR2 data, including the negative parallax value of  $\varpi_{\text{Gaia}} = -0.3634 \pm 0.2734$  mas for the possible companion, do not provide any further insights into this interesting system. If it was reliable, the measured DR2 parallax for the possible companion would place the red star far behind the hot subdwarf primary. A quick look at the EDR3 data (Gaia Collaboration et al., 2020) reveals a positive parallax of  $\varpi_{\text{Gaia}} = 0.1613 \pm 0.1164$  mas for the possible companion. The large apparent fractional parallax uncertainty of  $\Delta\varpi_{\text{Gaia}}/\varpi_{\text{Gaia}} \sim 0.72$  shows that this astrometric solution has to be treated with a certain grain of salt. However, the measured value definitely rules out a physical companion because the minimum distance to the secondary is  $1/0.2777 \sim 3.60$  kpc, which is significantly larger than the distance to HD 149382 derived from the corresponding DR2 ( $d_{\text{Gaia}} = 76.826 \pm 0.470$  pc; see Table 8.18) and EDR3 ( $d_{\text{Gaia}} = 75.525 \pm 0.324$  pc) parallaxes. Thus, it can be concluded that the visible companion of HD 149382 is a background red giant. Within the framework of this thesis, HD 149382 therefore is listed as a single H-sdOB star.

Figures 12.3.1 and 12.3.2 show the single and binary SED fits for HD 149382 and GALEX J032139.8+472718, respectively. In the case of HD 149382, a possible IR excess because of the background red giant is visible from a combination of 2MASS (K), DENIS (K), and unWISE (W1/W2) photometry. Appropriate IUE spectra and TD1 photometry are used in order to constrain the monochromatic color excess  $E(44 - 55)$ . The binary SED fit for HD 149382 (see the right-hand panel of Fig. 12.3.1) results in  $E(44 - 55) = 0.038 \pm 0.005$  mag

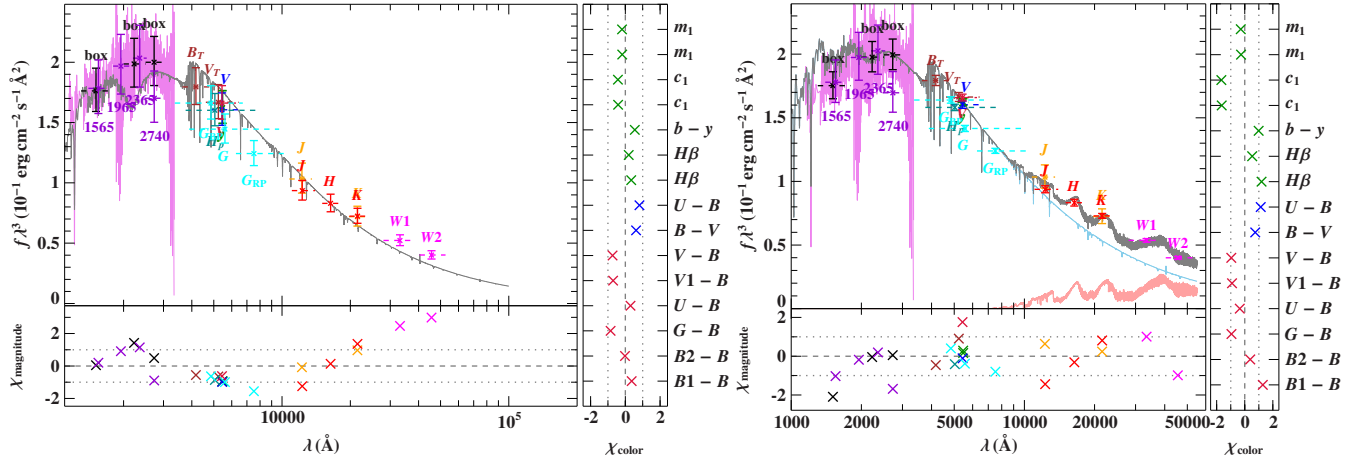


Figure 12.3.1.: *Left-hand panel*: Same as Fig. 12.0.1, but showing the single SED fit for the H-sdOB HD 149382. *Right-hand panel*: Same as the left-hand panel, but showing the corresponding binary SED fit. The contribution of the primary H-sdOB to the total SED flux is shown as a solid light blue line. The star possibly shows an IR excess because of the presence of a background red giant, as can be seen from the solid light red line (see the text for details).

The residual panels at the bottom and on the right-hand side show the differences between the synthetic and the observed magnitudes and colors, respectively, whereby the dotted gray horizontal lines mark deviations of  $\pm 1\sigma$ , that is, values of  $\chi = \pm 1$ . The  $\chi = 0$  levels are marked by the dashed gray horizontal lines. The following color codes are used to identify the individual photometric filter systems: TD1 (purple; Thompson et al. 1978), HIPPARCOS (dark turquoise; van Leeuwen 2007), *Tycho* (wine red; Høg et al. 2000), Stroemgren (green; Hauck & Mermilliod 1998; Paunzen 2015), Johnson-Cousins (blue; Mermilliod 2006), Geneva (dark red; Rufener 1988), *Gaia* DR2 (light turquoise; Gaia Collaboration et al. 2018), DENIS (orange; DENIS Consortium 2005), 2MASS (light red; Cutri et al. 2003), and unWISE (magenta; Schlafly et al. 2019).

and in an upper limit of  $T_{\text{eff,sec}} \leq 2865$  K for the effective temperature of the background red giant. In fact, the best fit even suggests  $T_{\text{eff,sec}} < 2300$  K, which is lower than the lower limit of the PHOENIX model grid used (see Sect. 7.2.1). The derived surface ratio of  $S = 19.7^{+1.8}_{-9.1}$  is not matched at all by a typical canonical hot subdwarf radius of  $R_{\text{pri}} \sim 0.10\text{-}0.30 R_{\odot}$  and a secondary radius of  $R_{\text{sec}} \sim 0.10\text{-}0.15 R_{\odot}$ , which can be assumed for a late M-type MS star (M7/M8) with solar metallicity based on the determined value for  $T_{\text{eff,sec}}$  (see Tables 15.7 and 15.8 in Cox 2000). This is another indication that the observed IR excess indeed does not result from a physical companion of HD 149382. The single SED fit for HD 149382 (see the left-hand panel of Fig. 12.3.1) results in  $E(44 - 55) = 0.081 \pm 0.008$  mag, which is, as in the case of the binary fit, in good agreement with  $E(B - V) = 0.318 \pm 0.013$  mag and  $E(B - V) = 0.274 \pm 0.011$  mag suggested by the reddening maps of Schlegel et al. (1998)

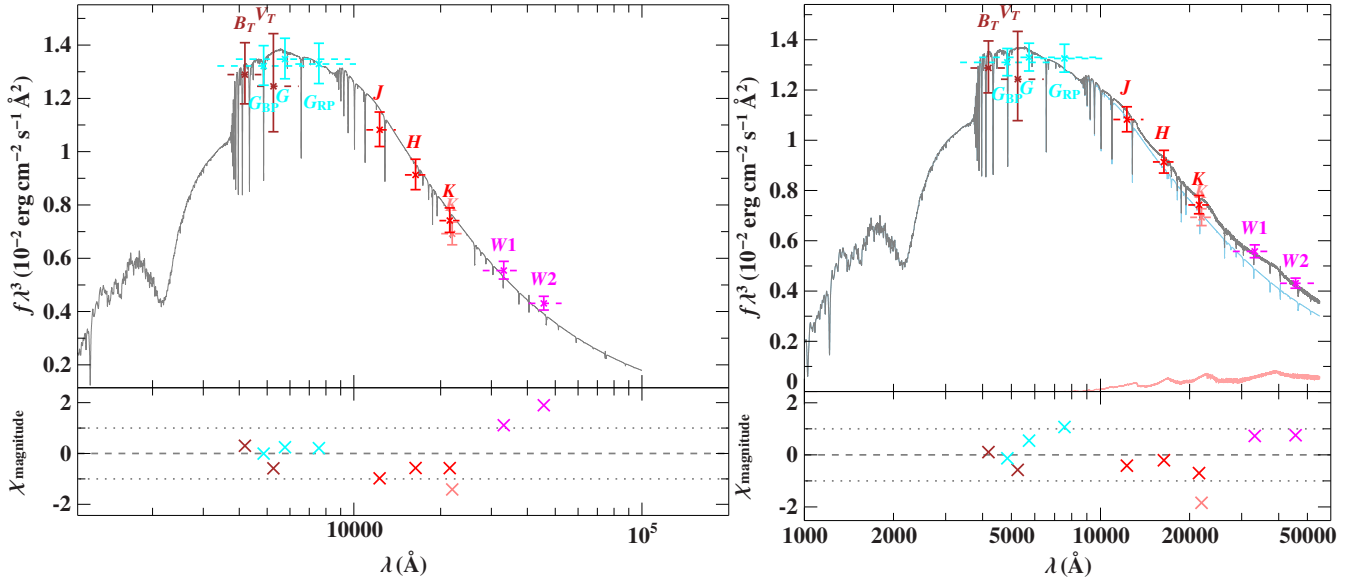


Figure 12.3.2.: *Left-hand panel*: Same as Fig. 12.0.1, but showing the single SED fit for the H-sdB GALEX J032139.8+472718. *Right-hand panel*: Same as the left-hand panel, but showing the corresponding binary SED fit. The contribution of the primary H-sdB to the total SED flux is shown as a solid light blue line. The star possibly shows an IR excess because of the presence of a cool MS companion, as can be seen from the solid light red line (see the text for details).

The residual panels at the bottom show the differences between the synthetic and the observed magnitudes, whereby the dotted gray horizontal lines mark deviations of  $\pm 1\sigma$ , that is, values of  $\chi = \pm 1$ . The  $\chi = 0$  levels are marked by the dashed gray horizontal lines. The following color codes are used to identify the individual photometric filter systems: *Tycho* (wine red; Høg et al. 2000), *Gaia* DR2 (turquoise; Gaia Collaboration et al. 2018), 2MASS (light red; Cutri et al. 2003), UKIDSS (rose; Lawrence et al. 2013), and unWISE (magenta; Schlafly et al. 2019).

and Schlafly & Finkbeiner (2011), respectively<sup>132</sup>. However, the single SED fit is not able to sufficiently reproduce the observed magnitudes in the IR, including the aforementioned ones of 2MASS (K), DENIS (K), and unWISE (W1/W2).

For GALEX J032139.8+472718, a possible IR excess may be visible from the unWISE (W1/W2) magnitudes. On the other hand, the photometric data from 2MASS (JHK) and UKIDSS (K) are also matched by a single SED fit (see the residuals in Fig. 12.3.2). The single SED fit (see the left-hand panel of Fig. 12.3.2) results in a monochromatic color excess of  $E(44 - 55) = 0.210 \pm 0.015$  mag, which is quite high and might therefore indicate a potential MS companion. However, Schlegel et al. (1998) and Schlafly & Finkbeiner (2011) suggest even

<sup>132</sup>As already described in Sect. 7.2.3,  $E(44 - 55)$  and  $E(B - V)$  are identical for high effective temperatures of  $T_{\text{eff}} \gtrsim 20000$  K and low interstellar extinction values of  $E(44 - 55) \lesssim 0.50$  mag, which can be seen from Table 4 in Fitzpatrick et al. (2019).

higher values of  $E(B - V) = 0.593 \pm 0.015$  mag and  $E(B - V) = 0.510 \pm 0.013$  mag, respectively. Unfortunately, no reliable UV photometry can be used for GALEX J032139.8+472718 in order to constrain the color excess. The binary SED fit (see the right-hand panel of Fig. 12.3.2) results in  $E(44 - 55) = 0.184 \pm 0.018$  mag and in an upper limit of  $T_{\text{eff,sec}} \leq 2709$  K for the effective temperature of the possible MS companion. As in the case of HD 149382, the best fit even suggests  $T_{\text{eff,sec}} < 2300$  K, which is again lower than the lower limit of the PHOENIX model grid used. In addition, a surface ratio of  $S = 3.5^{+1.1}_{-1.5}$  is derived. The determined value for  $T_{\text{eff,sec}}$  suggests a rather late M-type MS companion for GALEX J032139.8+472718 (see Table 15.7 in Cox 2000). However, this does not match the measured surface ratio, which should be  $\lesssim 1$  if a canonical hot subdwarf radius of  $R_{\text{pri}} \sim 0.10\text{-}0.30 R_{\odot}$  for the primary and  $R_{\text{sec}} \lesssim 0.10 R_{\odot}$  (typical for late M dwarfs with solar metallicity; see Table 15.8 in Cox 2000) for the secondary are assumed.

Due to all of the above considerations, HD 149382 and GALEX J032139.8+472718 are not listed in Table 12.1. It can safely be assumed that the possible late-type MS companion of GALEX J032139.8+472718 and the background red giant of HD 149382 do not contribute to the total flux in the optical spectral range. Hence, the atmospheric parameters of both primary stars derived from spectroscopy and used as input for the performed SED fits are trustworthy. The results derived from the single and binary SED fits for HD 149382 and GALEX J032139.8+472718 will be used in order to determine the fundamental stellar parameters (radius  $R$ , luminosity  $L$ , and mass  $M$ ) of both objects. This will be presented in the next chapter.

## 13. Fundamental Stellar Parameters

This chapter presents the results of the fundamental stellar parameters (radius  $R$ , luminosity  $L$ , and mass  $M$ ) of the program stars. As outlined in Sect. 7.3, these parameters are derived from the respective *Gaia* DR2 parallaxes  $\varpi_{\text{Gaia}}$ <sup>133</sup>, the atmospheric parameters  $T_{\text{eff}}$  and  $\log(g)$  determined from spectroscopy, and the angular diameters  $\theta$  derived from the SED fits. For the vast majority of the program stars, the results of this chapter are based on the spectroscopic results of one combination of model atmosphere approach and analysis strategy, namely the one whose results are used as input for the respective SED fit (see Tables A.1-A.18 and A.20-A.23 for details). For five H-sdOs/post-AGBs only, literature values for  $T_{\text{eff}}$  and  $\log(g)$  are used on the basis of which the corresponding SEDs are also generated (see Tables 8.11 and A.19). Tables 13.2-13.13 summarize the results of the fundamental stellar parameters derived for the individual program stars. The listed uncertainties on the individual radii, luminosities, and masses result from Gaussian error propagation according to Eqs. (7.10), (7.11), and (7.12), whereby the total errors on the respective quantities  $\varpi_{\text{Gaia}}$ ,  $\theta$ ,  $T_{\text{eff}}$ , and  $\log(g)$  are taken into account<sup>134</sup>. HD 4539, Feige 38, EC 03591-3232, HD 149382, [CW83] 0512-08, and PG 0314+146 are observed multiple times such that for these objects the weighted averages of the atmospheric parameters given in Tables A.20-A.23 are used in order to determine the fundamental stellar parameters<sup>135</sup>. In *Gaia* DR2, SB 290 has a RUWE parameter that is larger than three (see Sect. 8.4 and Table 8.18). This is a strong indicator for a flawed *Gaia* parallax. Hence, no fundamental stellar parameters are determined for this object in this work. The same also applies to FBS 1850+443 and PG 2219+094, for which the apparent fractional parallax uncertainty in *Gaia* DR2 is above 50 % (see Table 8.19), because using the corresponding parallaxes as presented in Sect. 7.3 would result in completely unreliable radii, luminosities, and masses for both objects.

<sup>133</sup>Reminder: During the writing phase of this thesis, the results of *Gaia* Early Data Release 3 (EDR3; Gaia Collaboration et al. 2020) were made publicly available. However, the results of this work are mainly based on DR2 data (Gaia Collaboration et al., 2018) because the parallaxes from both data releases differ only slightly for the analyzed nearby program stars. Nonetheless, EDR3 data are additionally used in some cases. It is explicitly described in the text where this is the case.

<sup>134</sup>Tables 8.18 and 8.19 list the statistical uncertainties used for  $\varpi_{\text{Gaia}}$ . No systematics (no corrections for the global zero point offset and the large and small-scale spatial variations of *Gaia*) are considered for  $\varpi_{\text{Gaia}}$  (see also Sect. 5.5.1). Tables A.1-A.23 list the total uncertainties on  $\theta$  as well as the statistical ones used for  $T_{\text{eff}}$  and  $\log(g)$ . The results derived in Sect. 9.2.7 are used as global systematic errors on  $T_{\text{eff}}$  and  $\log(g)$ .

<sup>135</sup>For HD 4539, Feige 38, EC 03591-3232, HD 149382, and [CW83] 0512-08, the fundamental stellar parameters are based on the weighted averages of the atmospheric parameters derived from the ADS + Global (+ NLTE (+ LTE) metals) measurements. The radius, the luminosity, and the mass of the He-sdO PG 0314+146, however, are derived from the weighted averages of the corresponding TLUSTY/SYNSPEC + FITPROF measurements (see Table 13.13).

The radii, luminosities, and masses of all program stars are also derived from the distances determined by Bailer-Jones et al. (2018), who used Bayesian statistical methods (see Sect. 5.5.4). For all investigated objects, the Bailer-Jones distances are presented in Sect. 8.4 (see also Tables 8.18 and 8.19 as well as Fig. 8.4.1). As a matter of fact, Bailer-Jones et al. (2018) already applied the global parallax zero point offset of 0.029 mas measured in *Gaia* DR2 data (Lindgren et al., 2018) before determining their distances based on the Bayesian approach. However, this offset is not applied to the *Gaia* DR2 parallaxes used in this thesis, as already presented in Sects. 5.5.1 and 8.4, respectively. In order to ensure the comparability between the fundamental stellar parameters derived from the Bailer-Jones distances and the ones based on the parallaxes from *Gaia* DR2, the distances of Bailer-Jones et al. (2018) are corrected for the zero point offset after the conversion to parallaxes has been performed in the classical way, that is, via the usual relation  $\varpi = 1/d$ <sup>136</sup>. The radii, luminosities, and masses derived from the distances of Bailer-Jones et al. (2018) are also determined according to the methodology presented in Sect. 7.3. The results obtained are listed in Tables 13.2-13.13<sup>137</sup>. They will be discussed in detail in Sect. 13.4, where a comparison to the fundamental stellar parameters derived from the *Gaia* DR2 parallaxes is given. In the following Sects. 13.1-13.3, however, the *Gaia*-based results shall be presented first.

## 13.1. Radii

### 13.1.1. Hydrogen-Rich Hot Subdwarf Stars

The radius distribution for the hydrogen-rich hot subdwarf program stars of this work (H-sdBs, H-sdOBs, and H-sdOs) based on the *Gaia* DR2 parallaxes is shown in Fig. 13.1.1. The histogram distribution is subdivided into single and binary stars (upper left-hand panel of Fig. 13.1.1), into pulsating and non-pulsating stars (upper right-hand panel of Fig. 13.1.1) as well as into stars belonging to the upper and the lower helium sequence of Edelman et al. (2003) (lower panel of Fig. 13.1.1; see also Eqs. 3.4 and 3.5). Furthermore, the distribution for the H-sdO program stars is implemented in the lower panel of Fig. 13.1.1. The plotted results for stars, for which multiple spectra are analyzed, are given in Table 13.13. The H-sdB GALEX J032139.8+472718 and the H-sdOB HD 149382 are two times accounted for (see Tables 13.10 and 13.13) because of the reasons discussed in Sect. 12.3. For the H-sdO/post-AGB BD+28° 4211, both the spectroscopic results of Latour et al. (2013) and Latour et al. (2015) are initially considered. However, the low-gravity solution of Latour et al. (2013) results in a mass that is significantly lower than the canonical one (this will be detailed in Sect. 13.3.2).

<sup>136</sup>Consequently, a value of 0.029 mas is subtracted from the inferred parallaxes. As a matter of fact, the usual relation  $\varpi = 1/d$  is a valid option for the conversion to parallaxes in most cases. This is due to the low apparent fractional parallax uncertainties measured for most of the program stars (see Tables 8.18 and 8.19 as well as the example shown in Fig. 5.5.4). For more information, see Sect. 13.4.

<sup>137</sup>This excludes SB 290, FBS 1850+443, and PG 2219+094 because of the aforementioned reasons and because of the fact that Bailer-Jones et al. (2018) used the measured *Gaia* DR2 parallaxes in order to determine the distances based on the Bayesian approach.

## 13.1. Radii

---

On the other hand, the high-gravity solution of Latour et al. (2015) yields an almost canonical mass for the star (see Table 13.12). This is why the fundamental stellar parameters based on the high-gravity solution are favored and used for BD+28° 4211, whereas those of the low-gravity solution are discarded. Consequently, only the high-gravity solution for BD+28° 4211 contributes to the determined radius distribution. Last but not least, note again that no fundamental stellar parameters are derived for the <sup>3</sup>He H-sdB SB 290 in this work because of the star's poor RUWE parameter in *Gaia* DR2 (see Sect. 8.4 and Table 8.18). Thus, SB 290 is not included in Fig. 13.1.1. In the following, three aspects of the radius distribution determined for the hydrogen-rich hot subdwarf program stars shall be discussed.

First, the radius distribution is consistent with predictions of canonical evolutionary models for hot subdwarf stars, meaning that most of the analyzed objects have radii of  $0.10 R_{\odot} \lesssim R \lesssim 0.30 R_{\odot}$  (see also Sect. 3.2). Interestingly, the three objects below the hotter end of the ZAHB in the  $T_{\text{eff}}\text{-}\log(g)$  plane (GALEX J080510.9-105834, Feige 36, and HE 0929-0424; see Sect. 9.4.1 and Fig. 9.4.1) also have canonical radii. The post-EHB H-sdO program stars of this work generally tend to have the smallest radii in the analyzed sample (see the lower panel of Fig. 13.1.1). In fact, one of them barely scratches the typical radius regime of  $0.10 R_{\odot} \lesssim R \lesssim 0.30 R_{\odot}$  (AGK+81° 266;  $0.09 \pm 0.01 R_{\odot}$ ; see Table 13.12). Another one does not match it at all (BD+28° 4211;  $0.06 \pm 0.01 R_{\odot}$ ). As already discussed in Sect. 3.3, however, BD+28° 4211 may also be a post-AGB star because of its high effective temperature of  $T_{\text{eff}} \sim 81000$  K and high surface gravity of  $\log(g) \sim 6.5^{138}$ . This, together with the fact that it has a solar helium content (see Sect. 9.4.1), makes the star not comparable to the other H-sdOs analyzed in this work.

Second, the radius distribution is of bimodal shape. This can be seen from the bimodal Gaussian fit (represented by the solid red line in all three panels of Fig. 13.1.1) performed on the full histogram data. The mean values  $\mu$  and the standard deviations  $\sigma$  resulting from this fit as well as their individual standard errors are listed in Table 13.1. The radius distribution has two well-defined peaks at  $\mu_1 = 0.138 \pm 0.001 R_{\odot}$  and  $\mu_2 = 0.205 \pm 0.002 R_{\odot}$ , respectively. Third, there is no systematic difference at all between single and binary as well as between pulsating and non-pulsating stars. The same also applies to upper and lower helium-sequence stars. However, it has to be noted that this could possibly change in all three cases if a larger sample of hydrogen-rich hot subdwarf stars than analyzed in the present work was considered.

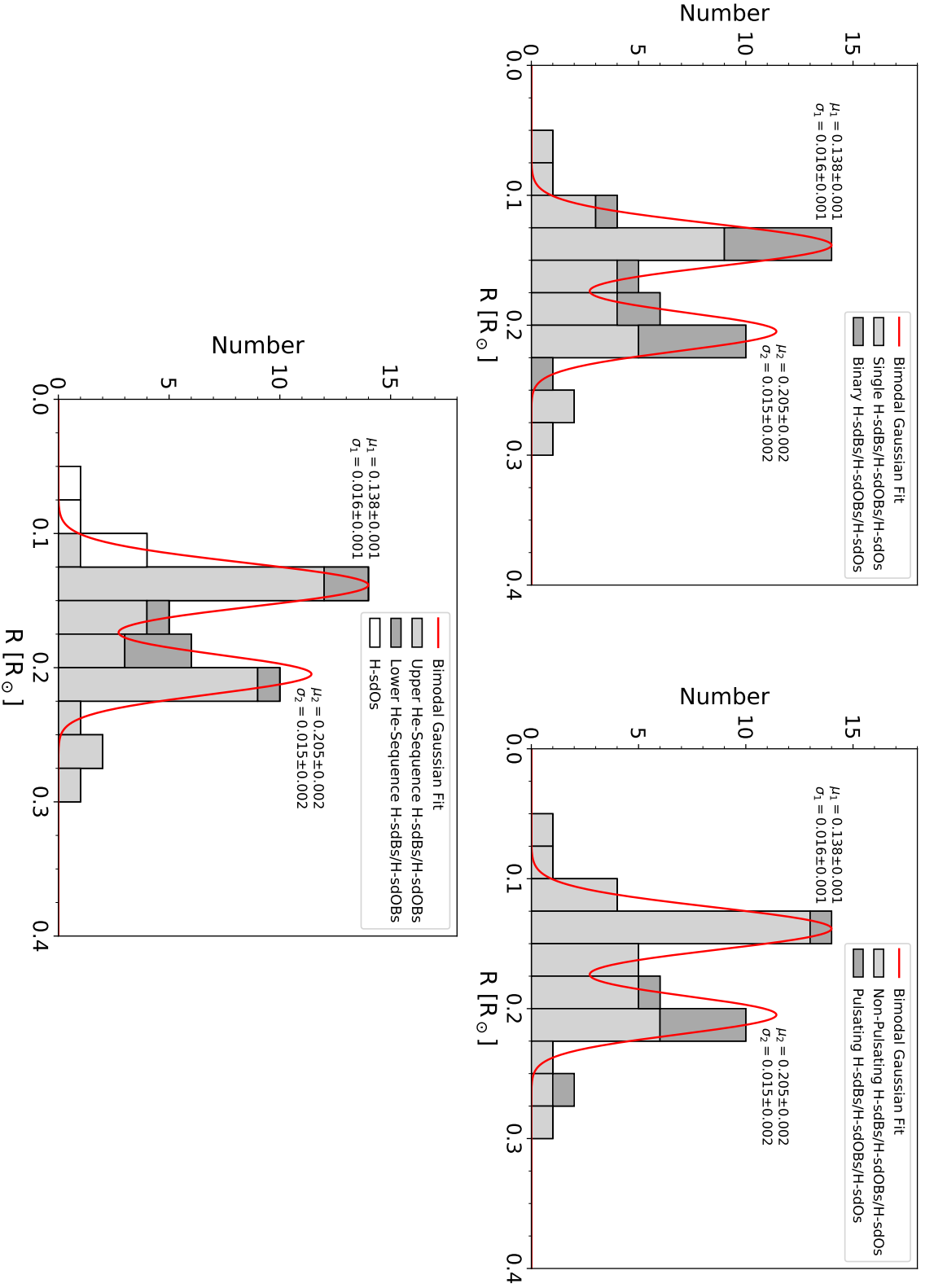
### 13.1.2. Helium-Rich Hot Subdwarf Stars

The iHe-sdB program stars [CW83] 0825+15 and [CW83] 0512-08 have typical canonical radii of  $0.13 \pm 0.01 R_{\odot}$  and  $0.12 \pm 0.01 R_{\odot}$ , respectively (see Tables 13.3 and 13.13). However, the newly discovered cool iHe-sdB FBS 0654+366 has a radius of  $0.45 \pm 0.03 R_{\odot}$  (see Table 13.10), which is clearly too large for a usual hot subdwarf star.

The radii determined for all eight analyzed He-sdO program stars (GALEX J075807.5-043203,

---

<sup>138</sup>The low-gravity solution of Latour et al. (2013) for BD+28° 4211 can be considered obsolete because of the aforementioned reasons.


**Figure 13.1.1.:**

Radius distribution for the hydrogen-rich hot subdwarf program stars of this work (H-sdBS, H-sdOBs, and H-sdOs) based on the *Gaia* DR2 parallaxes (see Tables 13.2-13.13). The distribution is 'barstacked', meaning that multiple data are stacked on top of each other. The histogram distribution is subdivided into single and binary stars (upper left-hand panel), into pulsating and non-pulsating stars (upper right-hand panel) as well as into stars belonging to the upper and the lower helium sequence of Edelmann et al. (2003) (lower panel; see also Eqs. 3.4 and 3.5). The distribution for the H-sdO program stars is also implemented in the lower panel. The plotted results for stars, for which multiple spectra are analyzed, are given in Table 13.13. The H-sdB GALEX J032139.8+472718 and the H-sdOB HD 149382 are two times accounted for (see Tables 13.10 and 13.13) because of the reasons discussed in Sect. 12.3. For the H-sdO/post-AGB BD+28° 4211, only the result based on the favored high-gravity solution of Latour et al. (2015) is plotted. In contrast to the low-gravity solution of Latour et al. (2013), this solution yields an almost canonical mass for the star (this is detailed in Sect. 13.3.2). Also note that the <sup>3</sup>He H-sdB SB 290 is not included in this figure since no fundamental stellar parameters are derived for this star in this work because of its poor RUWE parameter in *Gaia* DR2 (see Sect. 8.4 and Table 8.18). The given mean values  $\mu$  and standard deviations  $\sigma$  as well as their individual standard errors result from a bimodal Gaussian fit (represented by the solid red line in all three panels) performed on the full histogram data.

## 13.1. Radii

---

GALEX J042034.8+012041, GALEX J095256.6-371940, GALEX J175548.5+501210, HZ 1, PG 0314+146, LS IV +10° 9, and FBS 0224+330) lie in the canonical regime of  $0.10 R_{\odot} \lesssim R \lesssim 0.30 R_{\odot}$ .

### 13.1.3. Other Program Stars

Most of the other analyzed objects (PHL 382, BD+49° 2226, HIP 67513, FBS 2158+373, FBS 2204+364, SB 395, and KUV 03591+0457) are significantly larger ( $R \gtrsim 1.0 R_{\odot}$ ) than the hot subdwarf program stars. In fact, the radii derived for these objects do not match the (post-)EHB, the (post-)BHB, and the pre-ELM evolutionary phases. The photometric data and the atmospheric parameters that are used for the SED fits in order to derive the respective angular diameters  $\theta$  can most likely be ruled out as possible causes of the large radii. As can be seen from Tables 8.18 and 8.19, however, flawed *Gaia* parallaxes could be an issue, at least for FBS 2158+373, FBS 2204+364, SB 395, and KUV 03591+0457. This is because the apparent fractional parallax uncertainty in *Gaia* DR2 is large in these cases ( $\Delta\varpi_{\text{Gaia}}/\varpi_{\text{Gaia}} > 10\%$ ), whereas it is low(er) for PHL 382 ( $\sim 7\%$ ), BD+49° 2226 ( $\sim 5\%$ ), and HIP 67513 ( $\sim 5\%$ ). It has to be noted, however, that other program stars such as PG 1136-003, HE 0929-0424, or HE 1047-0436, which have apparent fractional parallax uncertainties of  $\Delta\varpi_{\text{Gaia}}/\varpi_{\text{Gaia}} \sim 7\text{--}18\%$ , show radii in the expected range of hot subdwarf stars ( $0.10 R_{\odot} \lesssim R \lesssim 0.30 R_{\odot}$ ). This is why the hypothesis that flawed *Gaia* parallaxes are responsible for the large radii of FBS 2158+373, FBS 2204+364, SB 395, and KUV 03591+0457 does not necessarily have to be true.

In fact, stars like HIP 67513, FBS 2158+373, FBS 2204+364, or KUV 03591+0457 could seriously be considered MS stars based on their radii. An MS nature would also be in good agreement with the solar-like helium abundances as well as with the surface gravities measured for these objects (see Sect. 9.4.1).

Certainly, the radius determined for SB 395 ( $2.08 \pm 0.39 R_{\odot}$ ) also matches the B-type MS. However, the helium abundance of  $\log n(\text{He}) = -3.25^{+0.10}_{-0.11}$  is too low and the surface gravity of  $\log(g) = 4.399^{+0.007}_{-0.010}$  is too high for a usual B-type MS star.

In principle, the radius of BD+49° 2226 ( $2.12 \pm 0.11 R_{\odot}$ ) would also match the MS. However, the atmospheric parameters of the star are too far off from it (see Fig. 9.4.1). The hypothesis of a pre-ELM that could explain the position of the star in the  $T_{\text{eff}}\text{-}\log(g)$  plane also has to be discarded because the determined radius is clearly too large for this evolutionary phase.

As discussed in Sect. 9.4.1, PHL 382 is most likely a post-BHB object. In fact, its enhanced radius of  $1.08 \pm 0.08 R_{\odot}$  agrees well with the result of Hämmerich (2020) and is clearly too large for the canonical HB. This supports the post-BHB hypothesis.

Last but not least, the stars PHL 25 and BD+48° 2721, which have not yet been addressed and are believed to be BHB objects (see Sect. 9.4.1), exhibit radii of  $0.42 \pm 0.03 R_{\odot}$  and  $0.39 \pm 0.01 R_{\odot}$ , respectively. These values perfectly match the BHB band, also considering the effective temperatures and the surface gravities of both objects.

## 13.2. Luminosities

### 13.2.1. Hertzsprung-Russell Diagram

The  $\log(T_{\text{eff}})$ - $\log(L/L_{\odot})$  diagram (Hertzsprung-Russell diagram) for the program stars of this work is shown in Fig. 13.2.1. Therein, the results of this work are compared to predictions of evolutionary models for the HB/EHB and beyond (Dorman et al., 1993), which are also used in Figs. 9.4.1-9.4.4, 10.1.1, and 10.2.6, respectively. Additionally, Fig. 13.2.1 contains two evolutionary tracks for (pre-)ELMs with masses of  $0.206 M_{\odot}$  and  $0.279 M_{\odot}$  (element diffusion and rotational mixing included, solar metallicity; Istrate et al. 2016). As shown by Han et al. (2003), the position of hot subdwarf stars in the  $\log(T_{\text{eff}})$ - $\log(L/L_{\odot})$  plane depends not only on the effective temperature but also on the individual formation channel from which these objects result (see Fig. 13.2.2). As can be seen from Fig. 13.2.1, most of the hot subdwarf program stars analyzed in this work lie in or near the canonical HB/EHB band indicated by the Dorman models. Therefore, the positions of these stars are in good agreement with the theoretical predictions of the first and second CE ejection channels as well as with those of the first stable RLOF channel (compare the results of Fig. 13.2.1 to subpanels a, b, and c of Fig. 13.2.2). Since the evolutionary tracks for (pre-)ELMs from Istrate et al. (2016) also cross the HB location in the  $\log(T_{\text{eff}})$ - $\log(L/L_{\odot})$  plane, however, a distinction between hot subdwarfs and pre-ELMs solely based on the position in the HRD is not possible. Due to their higher effective temperatures, the post-EHB H-sdOs as well as the He-sdOs have higher luminosity. The double HeWD merger channel is able to explain the position of the He-sdOs in the HRD (compare the results of Fig. 13.2.1 to subpanel d of Fig. 13.2.2). This also applies to the two investigated iHe-sdBs [CW83] 0512-08 and [CW83] 0825+15. The position of the newly found cool iHe-sdB FBS 0654+366 in the HRD, however, is not matched by the simulations of Han et al. (2003) for the merger channel. The analyzed H-sdOs have most likely formed from the CE ejection channels or from stable RLOF. It can be assumed that they evolved further away from the canonical EHB after their formation<sup>139</sup>. Interestingly, a single star (GALEX J080510.9-105834) is located well below the canonical HB in the HRD (see Fig. 13.2.1). In principle, however, its position can still be explained by the first stable RLOF channel (see subpanel b of Fig. 13.2.2). Nevertheless, it is confirmed from literature that GALEX J080510.9-105834 is in fact a pre-ELM (see the works of Vennes et al. 2011 and Kawka et al. 2015). The pre-ELM nature is also able to explain the position of the star in the  $T_{\text{eff}}$ - $\log(g)$  plane, which is well below the canonical HB (see Fig. 9.4.1).

### 13.2.2. Hydrogen-Rich Hot Subdwarf Stars

The luminosity distribution (with abscissa  $\log L/L_{\odot}$ ) for the hydrogen-rich hot subdwarf program stars of this work (H-sdBs, H-sdOBs, and H-sdOs) based on the *Gaia* DR2 parallaxes

<sup>139</sup>The scenario described here does not necessarily have to be true for BD+28° 4211 because this star may also be a post-AGB object instead of a H-sdO (see Sects. 3.3 and 9.4.1).

## 13.2. Luminosities

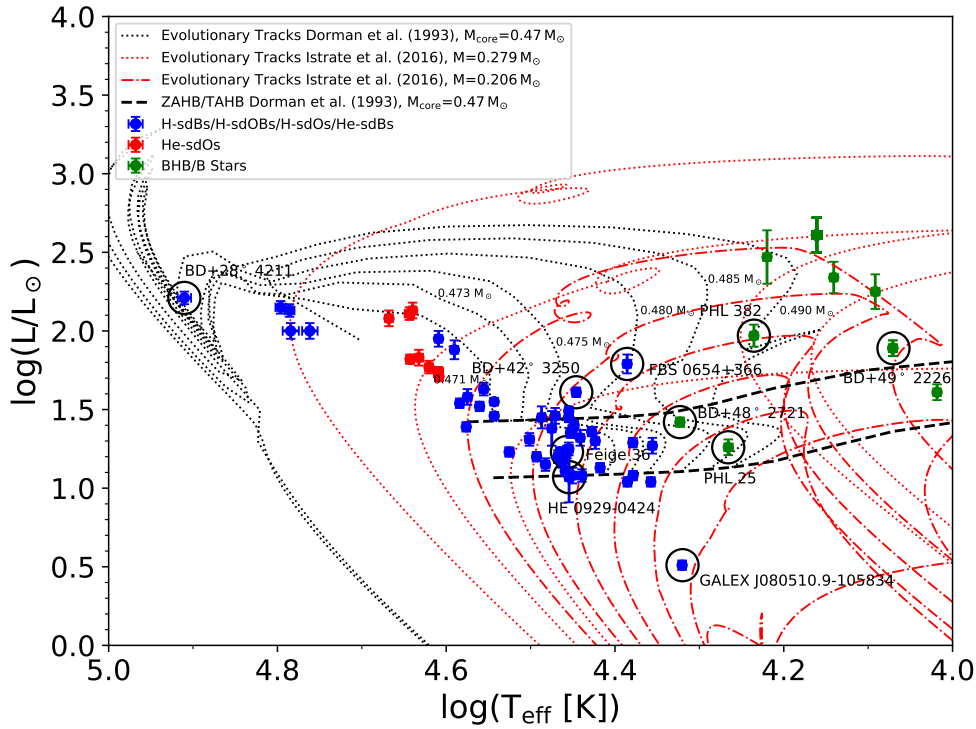


Figure 13.2.1.: Distribution of the program stars in the  $\log(T_{\text{eff}})$ - $\log(L/L_{\odot})$  plane (Hertzsprung-Russell diagram). Interesting objects are highlighted with solid black circles. While H-sdBs/H-sdOBs/H-sdOs/He-sdBs are marked in blue, green dots represent potential (post-)BHB and B-type MS stars. He-sdOs are characterized by red data points. The zero-age (ZAHB) and the terminal-age horizontal branch (TAHB) for a canonical mass hot subdwarf (core mass:  $0.47 M_{\odot}$ ) with solar metallicity from Dorman et al. (1993) are plotted as dashed black lines. Evolutionary tracks from Dorman et al. (1993) for the same canonical hot subdwarf but with different hydrogen-envelope masses (in ascending order from left to right:  $0.001 M_{\odot}$ ,  $0.003 M_{\odot}$ ,  $0.005 M_{\odot}$ ,  $0.010 M_{\odot}$ ,  $0.015 M_{\odot}$ , and  $0.020 M_{\odot}$ ) are shown with dotted black lines. Additionally, two evolutionary tracks for a  $0.206 M_{\odot}$  and a  $0.279 M_{\odot}$  (pre-)ELM with solar metallicity (element diffusion and rotational mixing included; Istrate et al. 2016) are plotted as red dashed-dotted and red dotted lines, respectively. Note that these tracks exhibit several loops. Plotted uncertainties on  $\log(T_{\text{eff}})$  result from the  $1\sigma$  statistical single parameter errors (listed in Tables A.1-A.23) and the global systematic errors derived in Sect. 9.2.7. Plotted uncertainties on  $\log(L/L_{\odot})$  are given in Tables 13.2-13.13 (see the entries labelled “Based on *Gaia*”). The plotted  $\log(L/L_{\odot})$  values for stars, for which multiple spectra are analyzed, are given in Table 13.13 (see also the entries labelled “Based on *Gaia*”). The H-sdB GALEX J032139.8+472718 and the H-sdOB HD 149382 are two times accounted for (see Tables 13.10 and 13.13) because of the reasons discussed in Sect. 12.3. For the H-sdO/post-AGB BD+28° 4211, only the result based on the favored high-gravity solution of Latour et al. (2015) is plotted. In contrast to the low-gravity solution of Latour et al. (2013), this solution yields an almost canonical mass for the star (this is detailed in Sect. 13.3.2). Also note that the  $^3\text{He}$  H-sdB SB 290 is not included in this figure since no fundamental stellar parameters are derived for this star in this work because of its poor RUWE parameter in *Gaia* DR2 (see Sect. 8.4 and Table 8.18). The same also applies to the objects FBS 1850+443 and PG 2219+094, for which the apparent fractional parallax uncertainty in *Gaia* DR2 is above 50% (see Table 8.19). For further details on what results from Tables A.1-A.23 and 13.2-13.13 are plotted, see the introduction (the footnotes) of Ch. 13.

is shown in Fig. 13.2.3. It is created in the same way as the radius distribution displayed in Fig. 13.1.1. As in the case of the latter, no systematic difference between single and binary (upper left-hand panel of Fig. 13.2.3), pulsating and non-pulsating (upper right-hand panel of Fig. 13.2.3), and upper and lower helium-sequence (lower panel of Fig. 13.2.3) stars is

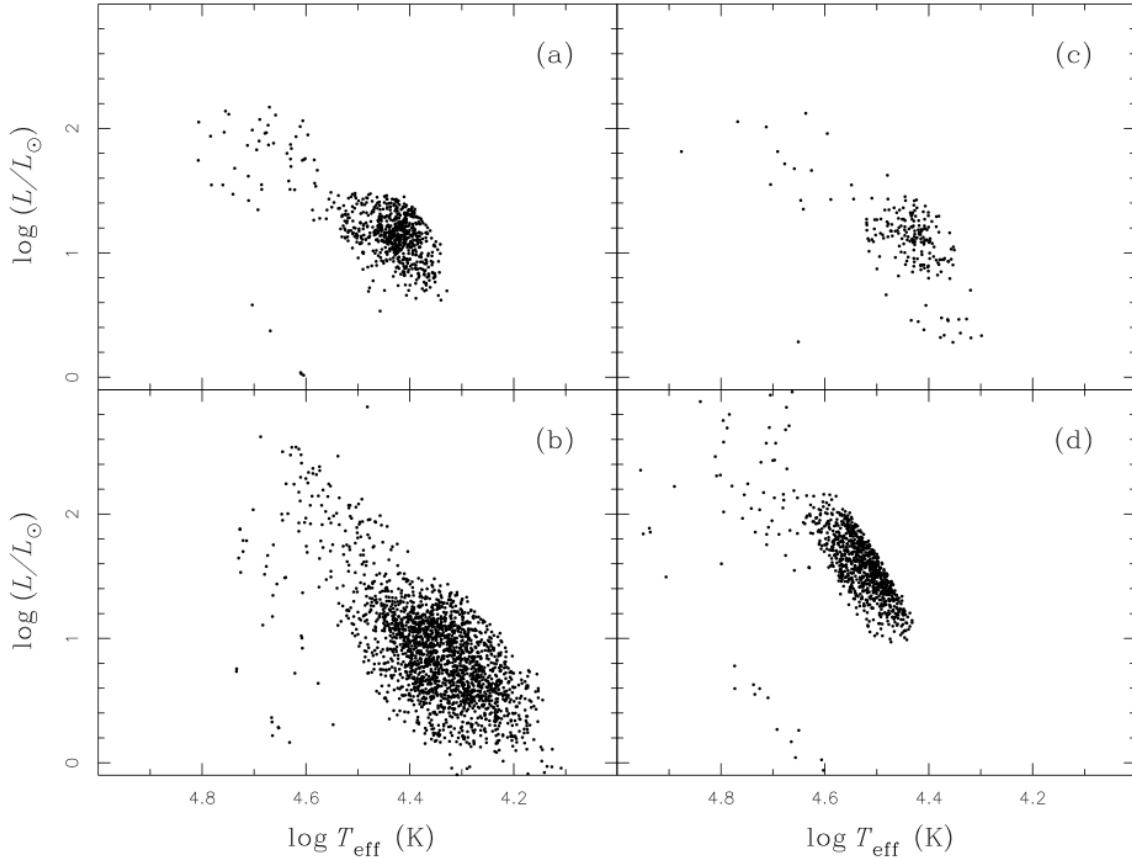


Figure 13.2.2.:  $\log(T_{\text{eff}})$ - $\log(L/L_{\odot})$  diagrams (Hertzsprung-Russell diagrams) for hot subdwarf stars from parameter set 2 (the best-choice model; see Sect. 3.4.4) of Han et al. (2003). The subpanels (a)-(d) represent the results for the formation channels of the first CE ejection, the first stable RLOF, the second CE ejection, and the double HeWD merger, respectively. For this figure, Han et al. (2003) assumed that hot subdwarf stars resulting from the CE ejection channels have hydrogen-envelope masses between 0.0 and  $0.006 M_{\odot}$ , that subdwarfs from the stable RLOF channel have envelope masses between 0.0 and  $0.012 M_{\odot}$ , and that subdwarfs from the merger channel have envelope masses between 0.0 and  $0.002 M_{\odot}$ . Adopted from Han et al. (2003).

found. However, this could be different for a larger sample of hydrogen-rich hot subdwarf stars than analyzed in this work. Interestingly, the luminosity distribution is also of bimodal shape, peaking at  $\mu_1 = 1.291 \pm 0.016$  and  $\mu_2 = 2.090 \pm 0.046$ , respectively (see Table 13.1). The smaller second peak at higher luminosity results mainly from the post-EHB H-sdOs (see the

lower panel of Fig. 13.2.3), which have higher effective temperatures than the investigated H-sdBs and H-sdOBs. The potential post-AGB star BD+28° 4211 ( $\log L/L_{\odot} = 2.21 \pm 0.04$ ) is also part of the second peak. GALEX J080510.9-105834 ( $\log L/L_{\odot} = 0.51 \pm 0.03$ ) is the least luminous star in the analyzed sample. Feige 36 and HE 0929-0424, which, like GALEX J080510.9-105834, are located below the hotter end of the ZAHB in the  $T_{\text{eff}}\text{-}\log(g)$  plane (see Fig. 9.4.1), have usual luminosities of  $\log(L/L_{\odot}) = 1.23 \pm 0.04$  and  $\log(L/L_{\odot}) = 1.07 \pm 0.16$ , respectively.

### 13.2.3. Helium-Rich Hot Subdwarf Stars

The iHe-sdB program stars [CW83] 0825+15 and [CW83] 0512-08 have typical luminosities of  $\log(L/L_{\odot}) = 1.54 \pm 0.03$  and  $\log(L/L_{\odot}) = 1.39 \pm 0.03$ , respectively (see Tables 13.3 and 13.13). The cool iHe-sdB FBS 0654+366, however, is more luminous ( $\log L/L_{\odot} = 1.79 \pm 0.06$ ) because of its exceptionally large radius (see Table 13.10).

Due to their higher effective temperatures, the analyzed He-sdO program stars are generally more luminous ( $1.70 \lesssim \log L/L_{\odot} \lesssim 2.15$ ) than their H-sdB/H-sdOB siblings. As a matter of fact, the most luminous He-sdOs in the analyzed sample are about as bright as the hot H-sdO program stars (see Fig. 13.2.1).

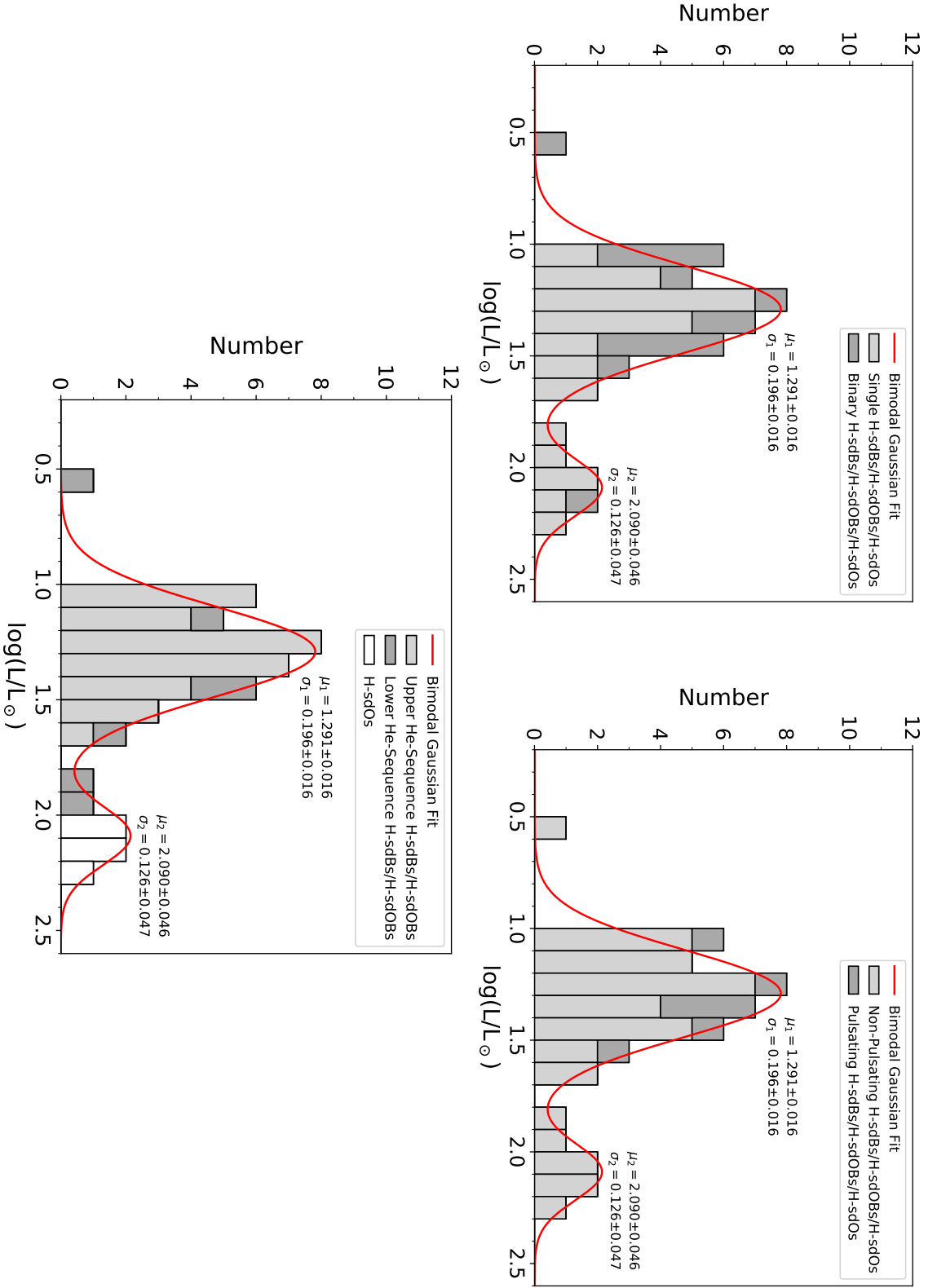
### 13.2.4. Other Program Stars

With  $\log(L/L_{\odot}) = 2.47 \pm 0.17$ ,  $\log(L/L_{\odot}) = 2.34 \pm 0.10$ ,  $\log(L/L_{\odot}) = 2.25 \pm 0.11$ , and  $\log(L/L_{\odot}) = 2.61 \pm 0.11$ , respectively, an MS nature seems reasonable for SB 395, FBS 2158+373, FBS 2204+364, and KUV 03591+0457. Remember, however, that the surface gravity of SB 395 is too high and that the star has too little helium in its atmosphere to be a usual MS object.

The coolest star in the analyzed sample (HIP 67513) has a rather moderate luminosity of  $\log(L/L_{\odot}) = 1.61 \pm 0.05$ . This is also in good agreement with a potential MS nature.

In addition to the radius, the luminosity of BD+49° 2226 ( $\log L/L_{\odot} = 1.89 \pm 0.05$ ) also matches the MS. As stated earlier in Sect. 13.1.3, however, a potential MS nature is not covered by the star's atmospheric parameters (see Fig. 9.4.1). As can be seen from Fig. 13.2.1, evolutionary tracks for (pre-)ELMs are in principle able to explain the luminosity derived for BD+49° 2226. Nonetheless, the determined radius of  $2.12 \pm 0.11 R_{\odot}$  remains clearly too large for this evolutionary phase.

PHL 25 ( $\log L/L_{\odot} = 1.26 \pm 0.05$ ) and BD+48° 2721 ( $\log L/L_{\odot} = 1.42 \pm 0.03$ ) have luminosities that agree well with the BHB. On the other hand, PHL 382 is more luminous ( $\log L/L_{\odot} = 1.97 \pm 0.07$ ). However, this is expected for a post-BHB object (see Fig. 13.2.1).


**Figure 13.2.3.:**

Luminosity distribution for the hydrogen-rich hot subdwarf program stars of this work (H-sdbs, H-sdOBs, and H-sdOs) based on the *Gaia* DR2 parallaxes (see Tables 13.2-13.13). The distribution is ‘barstacked’, meaning that multiple data are stacked on top of each other. The histogram distribution is subdivided into single and binary stars (upper left-hand panel), into pulsating and non-pulsating stars (upper right-hand panel) as well as into stars belonging to the upper and the lower helium sequence of Edelman et al. (2003) (lower panel; see also Eqs. 3.4 and 3.5). The distribution for the H-sdO program stars is also implemented in the lower panel. The plotted results for stars, for which multiple spectra are analyzed, are given in Table 13.13. The H-sdB GALEX J032139.8+472718 and the H-sdOB HD 149382 are two times accounted for (see Tables 13.10 and 13.13) because of the reasons discussed in Sect. 12.3. For the H-sdO/post-AGB BD+28° 4211, only the result based on the favored high-gravity solution of Latour et al. (2015) is plotted. In contrast to the low-gravity solution of Latour et al. (2013), this solution yields an almost canonical mass for the star (this is detailed in Sect. 13.3.2). Also note that the <sup>3</sup>He H-sdB SB 290 is not included in this figure since no fundamental stellar parameters are derived for this star in this work because of its poor RUWE parameter in *Gaia* DR2 (see Sect. 8.4 and Table 8.18). The given mean values  $\mu$  and standard deviations  $\sigma$  as well as their individual standard errors result from a bimodal Gaussian fit (represented by the solid red line in all three panels) performed on the full histogram data.

### 13.3. Masses

Histogram Distribution for	$\mu_1$	$\sigma_1$	$\mu_2$	$\sigma_2$
$R [R_\odot]$	$0.138 \pm 0.001$	$0.016 \pm 0.001$	$0.205 \pm 0.002$	$0.015 \pm 0.002$
$\log(L/L_\odot)$	$1.291 \pm 0.016$	$0.196 \pm 0.016$	$2.090 \pm 0.046$	$0.126 \pm 0.047$
$M [M_\odot]$	$0.465 \pm 0.012$	$0.102 \pm 0.012$	-	-

Table 13.1.: Mean values  $\mu$  and standard deviations  $\sigma$  of the (bimodal) Gaussian functions fitted to the histogram data shown in Figs. 13.1.1, 13.2.3, and 13.3.5.

## 13.3. Masses

### 13.3.1. Mass vs. Effective Temperature and Mass vs. Surface Gravity Diagrams

Figures 13.3.1-13.3.4 show the distribution of the program stars in the  $\log(T_{\text{eff}})$ - $M$  (mass vs. effective temperature) and  $\log(g)$ - $M$  (mass vs. surface gravity) planes. As can be seen, no correlation between the determined masses and the two atmospheric parameters is found for the analyzed sample.

The program stars FBS 2158+373 ( $5.13 \pm 0.87 M_\odot$ ), FBS 2204+364 ( $2.77^{+0.49}_{-0.51} M_\odot$ ), SB 395 ( $3.95 \pm 0.89 M_\odot$ ), and KUV 03591+0457 ( $7.65^{+1.36}_{-1.49} M_\odot$ ) have large masses. In consequence, the (post-)BHB and pre-ELM evolutionary phases can be clearly discarded for these four objects. At the same time, however, a B-type MS nature is quite likely. Yet, it has to be noted that the mass uncertainty for all four stars is rather large due to the relatively high apparent fractional parallax uncertainties (see Table 8.19).

The coolest star in the analyzed sample (HIP 67513) has a mass of  $0.88 \pm 0.13 M_\odot$ . This is way too low for a potential B-type MS nature of the star. Instead, the mass derived for HIP 67513 indicates a solar-like star of spectral type G, which, in turn, contradicts the determined radius ( $1.95 \pm 0.10 R_\odot$ ) and luminosity ( $\log L/L_\odot = 1.61 \pm 0.05$ ). Since a pre-ELM can also be excluded, the real nature of HIP 67513 remains hidden for now.

BD+49° 2226, which could be a pre-ELM because of its position in the  $T_{\text{eff}}$ - $\log(g)$  diagram (see Fig. 9.4.1), is extremely massive ( $6.23^{+0.91}_{-0.88} M_\odot$ ). Just like the radius of  $2.12 \pm 0.11 R_\odot$ , such a high mass rules out the pre-ELM scenario and instead favors an MS nature of the star. The latter, however, is at odds with the atmospheric parameters derived for BD+49° 2226. As in the case of HIP 67513, the true nature of the star hence remains unclear.

Finally, PHL 382 ( $0.46 \pm 0.07 M_\odot$ ), PHL 25 ( $0.35^{+0.05}_{-0.06} M_\odot$ ), and BD+48° 2721 ( $0.41 \pm 0.06 M_\odot$ ) have masses that match the (post-)BHB, as also suggested by their respective atmospheric parameters, radii, and luminosities.

### 13.3.2. Hydrogen-Rich Hot Subdwarf Stars

The mass distribution for the hydrogen-rich hot subdwarf program stars of this work (H-sdBs, H-sdOBs, and H-sdOs) based on the *Gaia* DR2 parallaxes is shown in Fig. 13.3.5. It is created in the same way as the radius and luminosity distribution displayed in Figs. 13.1.1 and 13.2.3,

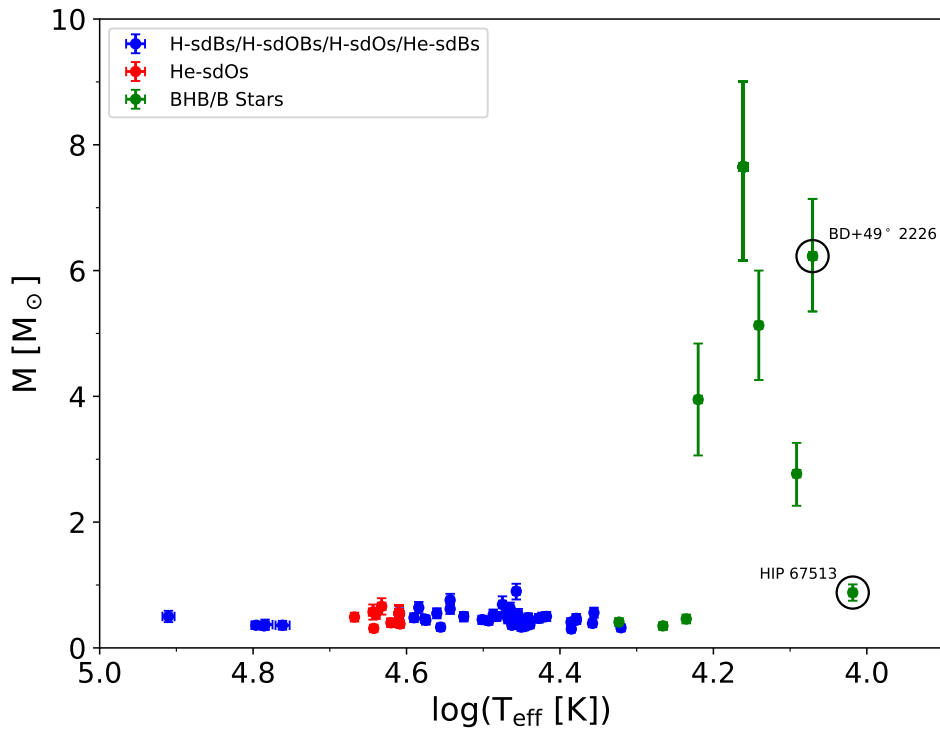


Figure 13.3.1.: Distribution of the program stars in the  $\log(T_{\text{eff}})$ - $M$  plane (mass vs. effective temperature diagram). The interesting objects BD+49° 2226 and HIP 67513 are highlighted with solid black circles. H-sdBs/H-sdOBs/H-sdOs/He-sdBs are marked in blue, whereas green dots represent potential (post-)BHB and B-type MS stars. He-sdOs are characterized by red data points. Plotted uncertainties on  $\log(T_{\text{eff}})$  result from the  $1\sigma$  statistical single parameter errors (listed in Tables A.1-A.23) and the global systematic errors derived in Sect. 9.2.7. Plotted uncertainties on  $M$  are given in Tables 13.2-13.13 (see the entries labelled “Based on *Gaia*”). The plotted mass values for stars, for which multiple spectra are analyzed, are given in Table 13.13 (see also the entries labelled “Based on *Gaia*”). The H-sdB GALEX J032139.8+472718 and the H-sdOB HD 149382 are two times accounted for (see Tables 13.10 and 13.13) because of the reasons discussed in Sect. 12.3. For the H-sdO/post-AGB BD+28° 4211, only the result based on the favored high-gravity solution of Latour et al. (2015) is plotted. In contrast to the low-gravity solution of Latour et al. (2013), this solution yields an almost canonical mass for the star (this is detailed in Sect. 13.3.2). Also note that the  $^3\text{He}$  H-sdB SB 290 is not included in this figure since no fundamental stellar parameters are derived for this star in this work because of its poor RUWE parameter in *Gaia* DR2 (see Sect. 8.4 and Table 8.18). The same also applies to the objects FBS 1850+443 and PG 2219+094, for which the apparent fractional parallax uncertainty in *Gaia* DR2 is above 50% (see Table 8.19). For further details on what results from Tables A.1-A.23 and 13.2-13.13 are plotted, see the introduction (the footnotes) of Ch. 13.

respectively. As in the case of the latter two, no systematic difference between single and binary (upper left-hand panel of Fig. 13.3.5), pulsating and non-pulsating (upper right-hand panel of Fig. 13.3.5), and upper and lower helium-sequence (lower panel of Fig. 13.3.5) stars

### 13.3. Masses

is found. Remember, however, that this could be different for a larger sample size. Unlike the radius and luminosity distribution, the mass distribution can be described by a single Gaussian that peaks at  $\mu = 0.465 \pm 0.012 M_{\odot}$  and has a standard deviation of  $\sigma = 0.102 \pm 0.012 M_{\odot}$  (see Table 13.1). This is consistent with predictions of canonical evolutionary models for hot subdwarf stars (see Fig. 3.4.4 and Table 3.3), in particular if the determined value for  $\sigma$  is taken into account. In Figs. 13.3.2 and 13.3.4, it can be seen that most of the analyzed H-sdBs, H-sdOBs, and H-sdOs scatter around the canonical mass regime of  $\sim 0.46$ - $0.48 M_{\odot}$ . Therefore, most of these objects can be explained well by the EHF scenario, by the first and

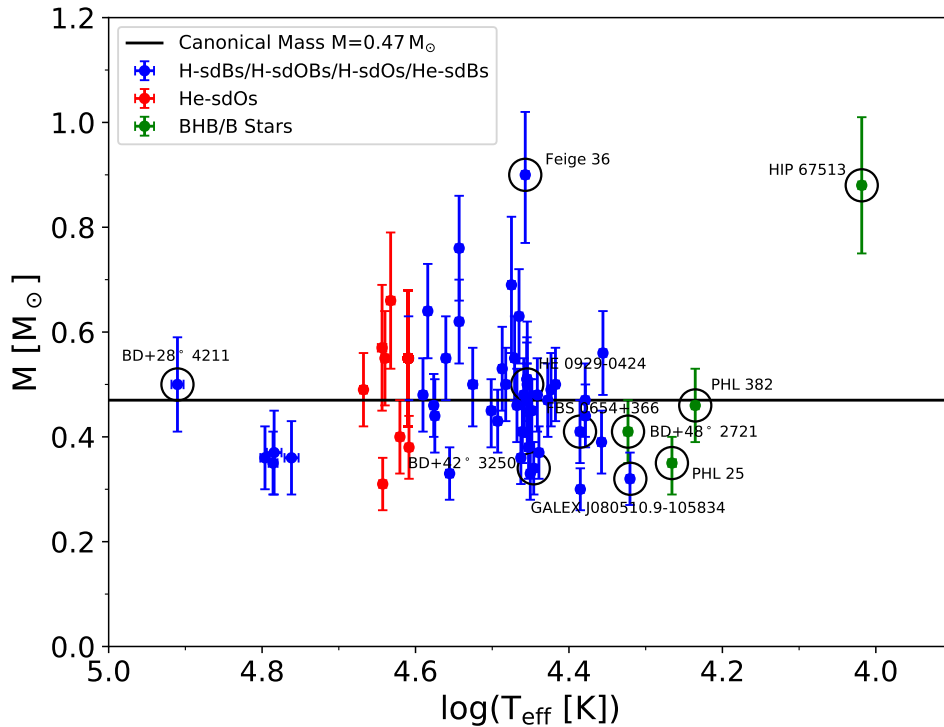


Figure 13.3.2.: Same as Fig. 13.3.1, but enlarged. The solid black horizontal line marks a canonical hot subdwarf mass of  $0.47 M_{\odot}$  (see also Fig. 3.4.4 and Table 3.3). Interesting objects are highlighted with solid black circles.

second CE ejection channels, or by the first stable RLOF channel.

Although the mass distribution determined for the hydrogen-rich hot subdwarf program stars is overall consistent with predictions of canonical models, different outliers at the low and high-mass end are visible. One of them (Feige 36) at the high-mass end has already been discussed in Sect. 12.2.

The H-sdOB HD 149382, which has a background red giant as discussed in Sect. 12.3, exhibits a spectroscopic mass in the range of  $\sim 0.54$ - $0.86 M_{\odot}$ , depending on whether the result for the angular diameter derived from the single or the binary SED fit is applied (see Table 13.13). In particular, the mass based on the result of the single SED fit ( $0.76 \pm 0.10 M_{\odot}$ ) lies significantly

above the canonical mass regime of  $\sim 0.46\text{-}0.48 M_{\odot}$ . Due to the fact that HD 149382 is a single object, the only formation scenario that is able to explain the nature of this star is the double HeWD merger channel, although it is believed to produce mainly helium-rich objects (see Sect. 3.4.2).

PG 1710+490 and HE 1047-0436 are two more hydrogen-rich hot subdwarf stars that, based

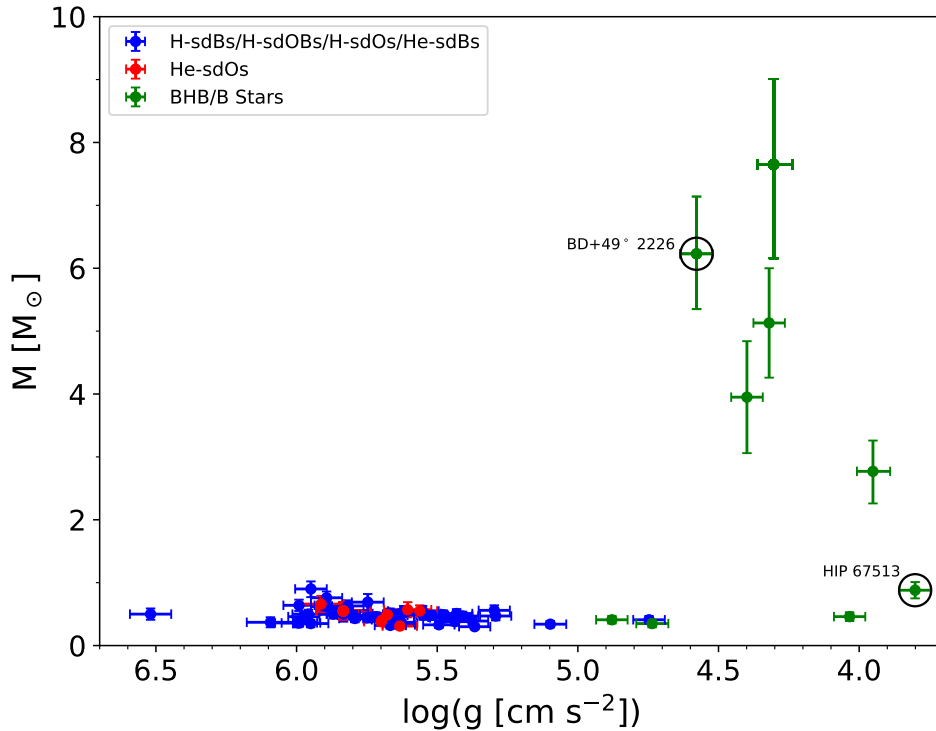


Figure 13.3.3.: Distribution of the program stars in the  $\log(g)$ - $M$  plane (mass vs. surface gravity diagram). The interesting objects BD+49° 2226 and HIP 67513 are highlighted with solid black circles. H-sdBs/H-sdOBs/H-sdOs/He-sdBs are marked in blue, whereas green dots represent potential (post-)BHB and B-type MS stars. He-sdOs are characterized by red data points. Plotted uncertainties on  $\log(g)$  result from the  $1\sigma$  statistical single parameter errors (listed in Tables A.1-A.23) and the global systematic errors derived in Sect. 9.2.7. Plotted uncertainties on  $M$  are given in Tables 13.2-13.13 (see the entries labelled “Based on *Gaia*”). The plotted mass values for stars, for which multiple spectra are analyzed, are given in Table 13.13 (see also the entries labelled “Based on *Gaia*”). The H-sdB GALEX J032139.8+472718 and the H-sdOB HD 149382 are two times accounted for (see Tables 13.10 and 13.13) because of the reasons discussed in Sect. 12.3. For the H-sdO/post-AGB BD+28° 4211, only the result based on the favored high-gravity solution of Latour et al. (2015) is plotted. In contrast to the low-gravity solution of Latour et al. (2013), this solution yields an almost canonical mass for the star (this is detailed in Sect. 13.3.2). Also note that the  $^3\text{He}$  H-sdB SB 290 is not included in this figure since no fundamental stellar parameters are derived for this star in this work because of its poor RUWE parameter in *Gaia* DR2 (see Sect. 8.4 and Table 8.18). The same also applies to the objects FBS 1850+443 and PG 2219+094, for which the apparent fractional parallax uncertainty in *Gaia* DR2 is above 50% (see Table 8.19). For further details on what results from Tables A.1-A.23 and 13.2-13.13 are plotted, see the introduction (the footnotes) of Ch. 13.

on the masses derived from the *Gaia* DR2 parallaxes, have most likely formed from the merger channel. The individual masses of both objects are  $0.63 \pm 0.09 M_{\odot}$  (PG 1710+490) and  $0.69 \pm 0.13 M_{\odot}$  (HE 1047-0436), respectively. In fact, HE 1047-0436 is a H-sdB+WD binary. Therefore, this system must have been a triple system in the past if the primary star was

### 13.3. Masses

indeed formed from a double HeWD merger<sup>140</sup>.

Having a mass of  $0.30 \pm 0.04 M_{\odot}$ , the pulsating H-sdB PG 0342+026 is the least massive object in the analyzed sample. In fact, this star is exactly at the limit of the canonical formation channels of hot subdwarf stars, which hardly predict objects below  $\sim 0.30 M_{\odot}$  (see Fig. 3.4.4 and Table 3.3).

As already mentioned in Sect. 13.1.1, the low-gravity solution of Latour et al. (2013) for

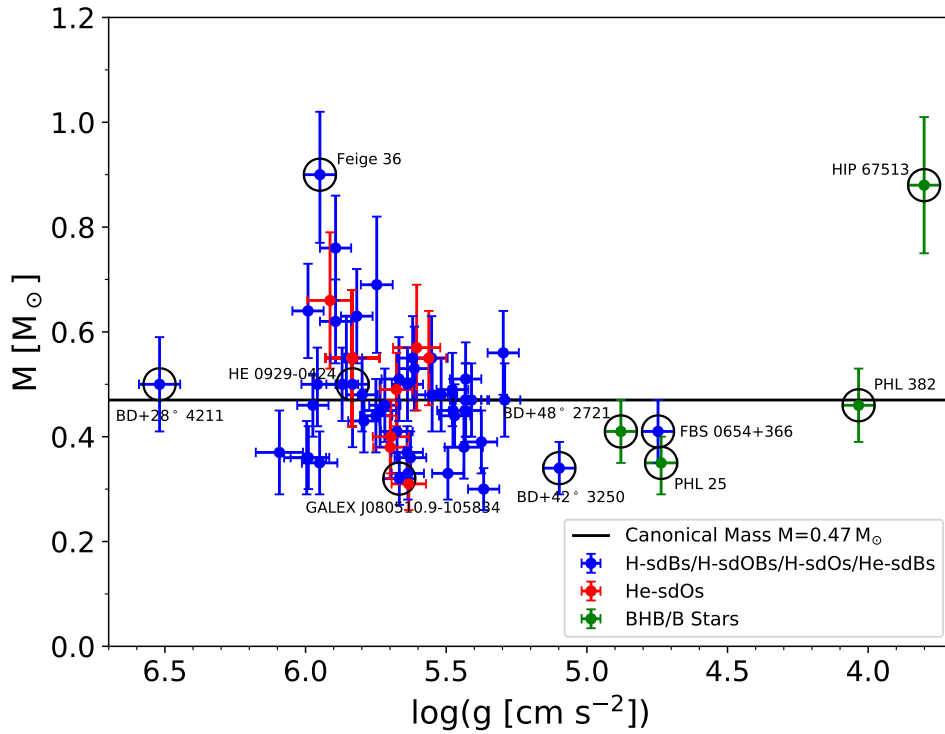


Figure 13.3.4.: Same as Fig. 13.3.3, but enlarged. The solid black horizontal line marks a canonical hot subdwarf mass of  $0.47 M_{\odot}$  (see also Fig. 3.4.4 and Table 3.3). Interesting objects are highlighted with solid black circles.

BD+28° 4211 results in a mass that is significantly lower than the canonical one, namely  $0.24_{-0.07}^{+0.17} M_{\odot}$ . On the other hand, the spectroscopic results of Latour et al. (2015), the high-gravity solution, result in a mass of  $0.50 \pm 0.09 M_{\odot}$  for the star, which matches the canonical mass regime. Thus, the low-gravity solution of Latour et al. (2013) for BD+28° 4211 can be

<sup>140</sup>A quick look at the *Gaia* EDR3 data (Gaia Collaboration et al., 2020) reveals  $\varpi_{\text{Gaia}} = 0.9564 \pm 0.0592$  mas for HE 1047-0436. This parallax value is significantly higher than that measured in DR2 ( $\varpi_{\text{Gaia}} = 0.7366 \pm 0.0896$  mas; see Table 8.18). Based on the values of  $T_{\text{eff}}$ ,  $\log(g)$ , and  $\theta$  determined for HE 1047-0436 in this work, the EDR3 parallax results in  $R = 0.14 \pm 0.01 R_{\odot}$ ,  $\log(L/L_{\odot}) = 1.15 \pm 0.06$ , and  $M = 0.41 \pm 0.06 M_{\odot}$ . The new mass is significantly lower than that derived from the DR2 parallax and, in fact, can be reconciled with evolutionary models for hot subdwarf stars other than the double HeWD merger scenario. Hence, HE 1047-0436 must not have been a triple system in the past.

considered obsolete and the fundamental stellar parameters derived from it are discarded. Other hydrogen-rich hot subdwarf program stars that have masses below  $\sim 0.35 M_{\odot}$  are PG 1635+414 ( $0.33 \pm 0.05 M_{\odot}$ ), HE 0247-0418 ( $0.33 \pm 0.05 M_{\odot}$ ), and Feige 67 ( $0.35 \pm 0.06 M_{\odot}$ ). In consequence, these three stars may also be difficult to reconcile with the canonical formation channels of hot subdwarf stars. The best explanation for the formation of these objects would be the first stable RLOF channel (see Fig. 3.4.4), but PG 1635+414, HE 0247-0418, and Feige 67 are most likely single stars. Consequently, RLOF is most likely not an option. It is certain that the H-sdO Feige 67 has evolved away from the canonical EHB. The same could also apply to PG 1635+414, which is located above the canonical EHB in the  $T_{\text{eff}}\text{-}\log(g)$  plane (see Sect. 9.4.1 and Fig. 9.4.1). However, its position can also be explained by evolutionary tracks for (pre-)ELMs. Moreover, a pre-ELM nature of PG 1635+414 would also match the determined mass. Yet, it has to be noted again that the star does not show any signs of binarity and that, with a few exceptions only, ELMs are found in short-period binaries. This makes a pre-ELM nature of PG 1635+414 rather unlikely. In principle, a pre-ELM nature is also able to explain the position of HE 0247-0418 in the  $T_{\text{eff}}\text{-}\log(g)$  plane because the (pre-)ELM tracks of Istrate et al. (2016) also cross the canonical HB where the star is located (see Fig. 9.4.1). But also in this case, no close companion has been detected so far.

GALEX J080510.9-105834, HE 0929-0424, and BD+42° 3250 are also very interesting objects. GALEX J080510.9-105834 is located well below the canonical HB in the  $T_{\text{eff}}\text{-}\log(g)$  and  $\log(T_{\text{eff}})\text{-}\log(L/L_{\odot})$  planes (see Figs. 9.4.1 and 13.2.1), suggesting a lower than canonical mass for the star. In fact, this is in good agreement with the determined spectroscopic mass of  $0.32 \pm 0.05 M_{\odot}$ . On the other hand, the radius of  $0.14 \pm 0.01 R_{\odot}$  matches that of usual hot subdwarfs. Based on both the atmospheric as well as the fundamental stellar parameters, the low-mass H-sdB star GALEX J080510.9-105834 therefore is confirmed to be a pre-ELM, as already found by Vennes et al. (2011) and Kawka et al. (2015), respectively. HE 0929-0424 has an almost canonical mass of  $0.50 \pm 0.12 M_{\odot}$  but is located below the canonical HB in the  $T_{\text{eff}}\text{-}\log(g)$  diagram (see Fig. 9.4.1). This does not match, at least not if solar metallicity is assumed. However, the HB band in the  $T_{\text{eff}}\text{-}\log(g)$  plane of Fig. 9.4.1 is shifted to the right for metallicities higher than the solar one. In this way, HE 0929-0424 would be covered by the HB. A pre-ELM nature of the star can be clearly ruled out based on the determined mass. Based on *Gaia* DR2, it hence feels likely that HE 0929-0424 is a hot subdwarf star<sup>141</sup>. On the other hand, BD+42° 3250 is located above the canonical HB in the  $T_{\text{eff}}\text{-}\log(g)$  diagram (see Fig. 9.4.1) but has a spectroscopic mass of  $0.34 \pm 0.05 M_{\odot}$ . In this case, however, the determined mass does not preclude a pre-ELM nature of the star. As a matter of fact, the position of BD+42° 3250 in the  $T_{\text{eff}}\text{-}\log(g)$  and  $\log(T_{\text{eff}})\text{-}\log(L/L_{\odot})$  planes can be explained

<sup>141</sup>A quick look at the *Gaia* EDR3 data (Gaia Collaboration et al., 2020) reveals  $\varpi_{\text{Gaia}} = 0.4654 \pm 0.0621$  mas for HE 0929-0424. This parallax value is lower than that measured in DR2 ( $\varpi_{\text{Gaia}} = 0.5882 \pm 0.1068$  mas; see Table 8.18), even though the values agree with each other within the given error limits. Based on the values of  $T_{\text{eff}}$ ,  $\log(g)$ , and  $\theta$  determined for HE 0929-0424 in this work, the EDR3 parallax results in  $R = 0.18 \pm 0.03 R_{\odot}$ ,  $\log(L/L_{\odot}) = 1.28 \pm 0.12$ , and  $M = 0.80 \pm 0.16 M_{\odot}$ . The new mass is significantly larger than that derived from the DR2 parallax and, in fact, is extremely difficult to reconcile with the canonical HB band in the  $T_{\text{eff}}\text{-}\log(g)$  plane, even for higher metallicities than the solar one. Hence, the hot subdwarf nature of HE 0929-0424 based on *Gaia* DR2 is not set in stone yet. Further spectrophotometric analyses based on future data releases of the *Gaia* satellite are required in order to manifest it.

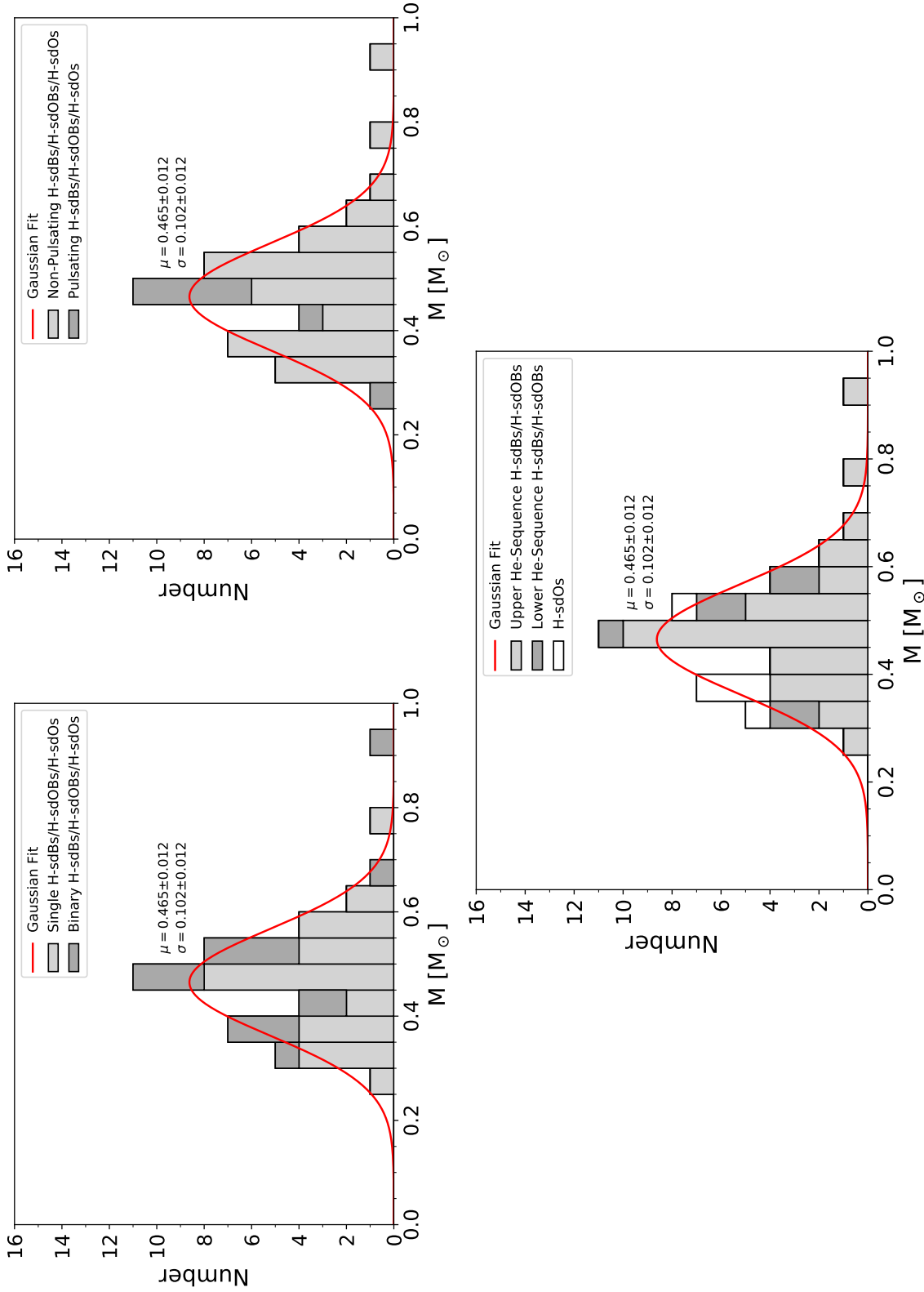


**Figure 13.3.5.:** Mass distribution for the hydrogen-rich hot subdwarf program stars of this work (H-sdBs, H-sdOBs, and H-sdOs) based on the *Gaia* DR2 parallaxes (see Tables 13.2-13.13). The distribution is ‘barstacked’, meaning that multiple data are stacked on top of each other. The histogram distribution is subdivided into single and binary stars (upper left-hand panel), into pulsating and non-pulsating stars (upper right-hand panel) as well as into stars belonging to the upper and the lower helium sequence of Edelmann et al. (2003) (lower panel; see also Eqs. 3.4 and 3.5). The distribution for the H-sdO program stars is also implemented in the lower panel. The plotted results for stars, for which multiple spectra are analyzed, are given in Table 13.13. The H-sdB GALEX J032139.8+472718 and the H-sdOB HD 149382 are two times accounted for (see Tables 13.10 and 13.13) because of the reasons discussed in Sect. 12.3. For the H-sdO/post-AGB BD+28° 4211, only the result based on the favored high-gravity solution of Latour et al. (2015) is plotted. In contrast to the low-gravity solution of Latour et al. (2013), this solution yields an almost canonical mass for the star (this is detailed in Sect. 13.3.2). Also note that the  $^3\text{He}$ -H-sdB SB 290 is not included in this figure since no fundamental stellar parameters are derived for this star in this work because of its poor RUWE parameter in *Gaia* DR2 (see Sect. 8.4 and Table 8.18). The given mean values  $\mu$  and standard deviations  $\sigma$  as well as their individual standard errors result from a Gaussian fit (represented by the solid red line in all three panels) performed on the full histogram data.

by evolutionary tracks for (pre-)ELMs (see Figs. 9.4.1 and 13.2.1). A possible future discovery of a close companion for BD+42° 3250 could thus indeed confirm the pre-ELM nature of the star.

As already presented in Sect. 9.4.1, EC 01541-1409, EC 13047-3049, PG 1505+074, and FB 29 are located above the canonical EHB in the  $T_{\text{eff}}\text{-}\log(g)$  diagram. The masses of all four objects are similar to the canonical one. Therefore, it is very likely that these H-sdOB stars are post-EHB objects.

In contrast to the study of Schneider et al. (2018), EC 03263-6403 is located on the canonical EHB in the  $T_{\text{eff}}\text{-}\log(g)$  plane in the present work (see Sect. 9.4.1). Furthermore, the star has a spectroscopic mass of  $0.38_{-0.06}^{+0.07} M_{\odot}$ . In principle, this EHB mass is best explained by binary interaction processes such as the first stable RLOF channel or the first and second CE ejection channels (see Fig. 3.4.4). However, EC 03263-6403 is a single star such that it cannot have emerged from these formation channels. The most likely explanation for the core helium-burning nature of EC 03263-6403 therefore remains an EHF, although the mass determined for the star seems to be slightly too small for this scenario (see Table 3.3).

### 13.3.3. Helium-Rich Hot Subdwarf Stars

The masses determined for many of the analyzed He-sdO program stars can be explained well by the double HeWD merger channel or by the late hot flasher scenario (see Figs. 13.3.2 and 13.3.4 as well as Table 3.3). GALEX J042034.8+012041, however, is quite striking because its mass of  $0.31 \pm 0.05 M_{\odot}$  is close to the limit for which core helium burning is still possible. It is highly unlikely that such a low-mass He-sdO star was produced by a late hot flasher. Yet, there is still a chance that GALEX J042034.8+012041 was formed from a merger of two ELMs with individual masses of  $\sim 0.15 M_{\odot}$ .

The iHe-sdB program stars [CW83] 0825+15 and [CW83] 0512-08 have spectroscopic masses of  $0.64 \pm 0.09 M_{\odot}$  and  $0.46 \pm 0.06 M_{\odot}$ , respectively (see Tables 13.3 and 13.13). Consequently, [CW83] 0825+15 has most likely been formed via the merger channel, whereas [CW83] 0512-08 could have emerged from a late hot flasher. In fact, it is also highly likely that a late hot flasher has produced the cool iHe-sdB FBS 0654+366, which has a mass of  $0.41 \pm 0.06 M_{\odot}$  (see Table 13.10).

## 13.4. Comparison to Bayesian Methods

As discussed in Sect. 5.5.4, the distance inference problem for observed *Gaia* parallaxes, which arises for poorly determined ones from a simple conversion according to the usual relation  $d = 1/\varpi$  (see Sect. 5.5.3), can be bypassed by means of Bayesian statistical methods. In fact, such methods for converting the measured parallaxes are even recommended by the *Gaia* collaboration. For this reason, the radii, luminosities, and masses of all analyzed program

## 13.4. Comparison to Bayesian Methods

---

stars<sup>142</sup> determined from the distances derived from Bayesian methods (Bailer-Jones et al., 2018) shall be presented here. For a detailed description on how the fundamental stellar parameters are derived from the distances determined by Bailer-Jones et al. (2018), see again the introduction of Ch. 13.

For the vast majority of the analyzed program stars, the Bailer-Jones distance does not differ significantly from that measured by the *Gaia* satellite. Moreover, the apparent fractional parallax/distance uncertainty measured for most objects is low (see Tables 8.18 and 8.19 as well as Fig. 8.4.1). Thus, the non-linearity of the usual relation  $d = 1/\varpi$  and the asymmetry of the resulting probability distribution vanish in most cases (see the example shown in Fig. 5.5.4). Hence, it is not surprising that the radii, luminosities, and masses derived from the *Gaia* DR2 parallaxes are rather similar to those derived from the Bailer-Jones distances, at least for most of the investigated objects.

As expected, the largest deviations in terms of the fundamental stellar parameters are found for the most distant program stars with the smallest parallaxes and the highest apparent fractional parallax uncertainties. This includes the objects FBS 2158+373, FBS 2204+364, SB 395, KUV 03591+0457, HE 0929-0424, and HE 1047-0436. For these stars, the difference between the *Gaia* and the Bailer-Jones distance is also largest (excluding FBS 1850+443 and PG 2219+094, which are the two most extreme objects in the analyzed sample and for which no fundamental stellar parameters are determined in this work; see Sect. 8.4). Since the parallaxes inferred from the Bailer-Jones distances are larger than those measured by the *Gaia* satellite in the case of FBS 2158+373, FBS 2204+364, SB 395, KUV 03591+0457, HE 0929-0424, and HE 1047-0436 (see Fig. 8.4.1), the Bailer-Jones values for the radii, the luminosities, and the masses of these stars are lower than the ones resulting from the *Gaia* parallaxes (for the dependence of the fundamental stellar parameters on the parallax, see Eqs. 7.7-7.9). In the case of the MS candidates SB 395 and KUV 03591+0457 in particular, this leads to significantly lower and, therefore, more realistic fundamental stellar parameters (see Table 13.9).

---

<sup>142</sup>This excludes SB 290, FBS 1850+443, and PG 2219+094 because of the reasons discussed in the introduction of Ch. 13 and because of the fact that Bailer-Jones et al. (2018) used the measured *Gaia* DR2 parallaxes in order to determine the distances based on the Bayesian approach.

Table 13.2.: Fundamental stellar parameters (radius  $R$ , luminosity  $L$ , and mass  $M$ ) of the analyzed XSHOOTER program stars based on measured *Gaia* DR2 parallaxes (“Based on *Gaia*”; Gaia Collaboration et al. 2018) and determined Bailer-Jones distances (“Based on Bailer-Jones”; Bailer-Jones et al. 2018). The respective parallaxes and distances used are listed in Tables 8.18 and 8.19. For each star, the given fundamental stellar parameters are based on the spectroscopic results of one combination of model atmosphere approach and analysis strategy, namely the one whose results are used as input for the respective SED fit, from which the corresponding angular diameter  $\theta$  is derived (see Tables A.1-A.5 for details). The natures of the individual program stars can be found in Tables 8.1-8.3.

Object	$R$ [ $R_{\odot}$ ]	$\log(L/L_{\odot})$	$M$ [ $M_{\odot}$ ]	Comments
HD 4539 <sup>a</sup>	$0.26 \pm 0.01$	$1.29 \pm 0.03$	$0.48 \pm 0.07$	Based on <i>Gaia</i> , ADS + Global (NLTE + LTE metals)
	$0.26 \pm 0.01$	$1.29 \pm 0.03$	$0.48 \pm 0.07$	Based on Bailer-Jones, ADS + Global (NLTE + LTE metals)
PG 1432+004	$0.28 \pm 0.02$	$1.27 \pm 0.05$	$0.56 \pm 0.08$	Based on <i>Gaia</i> , ADS + Global (NLTE + LTE metals)
	$0.28 \pm 0.02$	$1.27^{+0.05}_{-0.04}$	$0.57 \pm 0.08$	Based on Bailer-Jones, ADS + Global (NLTE + LTE metals)
GALEX J104148.9-073031	$0.18 \pm 0.01$	$1.13 \pm 0.03$	$0.50 \pm 0.07$	Based on <i>Gaia</i> , ADS + Global (NLTE + LTE metals)
	$0.18 \pm 0.01$	$1.13 \pm 0.03$	$0.50 \pm 0.07$	Based on Bailer-Jones, ADS + Global (NLTE + LTE metals)
Feige 38	$0.16 \pm 0.01$	$1.20 \pm 0.04$	$0.48 \pm 0.07$	Based on <i>Gaia</i> , ADS + Global (NLTE + LTE metals)
	$0.16 \pm 0.01$	$1.20 \pm 0.04$	$0.48 \pm 0.07$	Based on Bailer-Jones, ADS + Global (NLTE + LTE metals)

**Notes:** The listed uncertainties of the individual values result from Gaussian error propagation according to Eqs. (7.10), (7.11), and (7.12), whereby the total errors on the respective angular diameters  $\theta$ , effective temperatures  $T_{\text{eff}}$ , surface gravities  $\log(g)$ , and parallaxes  $\varpi_{\text{Gaia}}$ /distances  $d_{\text{Bailer-Jones}}$  ( $d_{\text{BJ}}$ ) are taken into account. Tables 8.18 and 8.19 list the statistical uncertainties used for  $\varpi_{\text{Gaia}}$  and  $d_{\text{BJ}}$ . No systematics (no corrections for the global zero point offset and the large and small-scale spatial variations of *Gaia*) are considered for  $\varpi_{\text{Gaia}}$  (see also Sect. 5.5.1). A value of 0.029 mas (corresponding to the global *Gaia* parallax zero point offset measured by Lindegren et al. 2018) is subtracted from the parallaxes inferred from the Bayesian distance measurements ( $d_{\text{BJ}}$ ) of Bailer-Jones et al. (2018). For more information on this, see the introduction of Ch. 13. Tables A.1-A.5 list the total uncertainties on  $\theta$  as well as the statistical ones used for  $T_{\text{eff}}$  and  $\log(g)$ . The results derived in Sect. 9.2.7 are used as global systematic errors on  $T_{\text{eff}}$  and  $\log(g)$ .

- (a) Pulsating star.
- (b) RV-variable star.
- (c) Rotating star.
- (d) The star is a pre-ELM (see Ch. 13 for details).
- (e) Based on the result for the angular diameter derived from the single SED fit.
- (f) Based on the result for the angular diameter derived from the binary SED fit.
- (g) He I 6678 Å included in spectral analysis fit.
- (h) He I 6678 Å not included in spectral analysis fit.

Table 13.3.: Table 13.2 continued.

Object	$R$ [ $R_{\odot}$ ]	$\log(L/L_{\odot})$	$M$ [ $M_{\odot}$ ]	Comments
EC 03591-3232	$0.14 \pm 0.01$ $0.14 \pm 0.01$	$1.11 \pm 0.03$ $1.11 \pm 0.03$	$0.49 \pm 0.07$ $0.49 \pm 0.07$	Based on <i>Gaia</i> , ADS + Global (NLTE + LTE metals) Based on Bailer-Jones, ADS + Global (NLTE + LTE metals)
PG 1136-003 <sup>b</sup>	$0.19 \pm 0.02$ $0.19 \pm 0.02$	$1.45 \pm 0.07$ $1.44^{+0.08}_{-0.07}$	$0.53 \pm 0.08$ $0.52 \pm 0.08$	Based on <i>Gaia</i> , ADS + Global (NLTE + LTE metals) Based on Bailer-Jones, ADS + Global (NLTE + LTE metals)
GALEX J080510.9-105834 <sup>bcd</sup>	$0.14 \pm 0.01$ $0.14 \pm 0.01$	$0.51 \pm 0.03$ $0.51 \pm 0.03$	$0.32 \pm 0.05$ $0.32 \pm 0.05$	Based on <i>Gaia</i> , ADS + Global (NLTE + LTE metals) Based on Bailer-Jones, ADS + Global (NLTE + LTE metals)
PG 1505+074	$0.19 \pm 0.01$ $0.19^{+0.02}_{-0.01}$	$1.95 \pm 0.05$ $1.95 \pm 0.05$	$0.55 \pm 0.08$ $0.56 \pm 0.08$	Based on <i>Gaia</i> , ADS + Global (NLTE + LTE metals) Based on Bailer-Jones, ADS + Global (NLTE + LTE metals)
EC 13047-3049	$0.19 \pm 0.02$ $0.19 \pm 0.02$	$1.88 \pm 0.06$ $1.89 \pm 0.06$	$0.48 \pm 0.07$ $0.48 \pm 0.07$	Based on <i>Gaia</i> , ADS + Global (NLTE + LTE metals) Based on Bailer-Jones, ADS + Global (NLTE + LTE metals)
HD 149382	$0.16 \pm 0.01^e, 0.15 \pm 0.01^f$ $0.16 \pm 0.01^e, 0.15 \pm 0.01^f$	$1.55 \pm 0.02^e, 1.47 \pm 0.02^f$ $1.55 \pm 0.02^e, 1.47 \pm 0.02^f$	$0.81 \pm 0.11^e, 0.66 \pm 0.09^f$ $0.81 \pm 0.11^e, 0.66 \pm 0.09^f$	Based on <i>Gaia</i> , ADS + Global (NLTE + LTE metals) Based on Bailer-Jones, ADS + Global (NLTE + LTE metals)
[CW83] 0825+15 <sup>a</sup>	$0.13 \pm 0.01$ $0.13 \pm 0.01$	$1.54 \pm 0.03$ $1.54 \pm 0.03$	$0.64 \pm 0.09$ $0.64 \pm 0.09$	Based on <i>Gaia</i> , ADS + Global (NLTE + LTE metals) Based on Bailer-Jones, ADS + Global (NLTE + LTE metals)
[CW83] 0512-08	$0.12 \pm 0.01$ $0.12 \pm 0.01$	$1.38 \pm 0.03$ $1.38 \pm 0.03$	$0.45 \pm 0.06$ $0.45 \pm 0.06$	Based on <i>Gaia</i> , ADS + Global (NLTE + LTE metals) Based on Bailer-Jones, ADS + Global (NLTE + LTE metals)
GALEX J075807.5-043203	$0.15 \pm 0.01$ $0.15 \pm 0.01$	$1.77 \pm 0.04$ $1.77^{+0.05}_{-0.04}$	$0.40 \pm 0.07$ $0.40 \pm 0.07$	Based on <i>Gaia</i> , TLUSTY/SYNSPEC + FITPROF Based on Bailer-Jones, TLUSTY/SYNSPEC + FITPROF
GALEX J042034.8+012041	$0.14 \pm 0.01$ $0.14 \pm 0.01$	$1.82 \pm 0.03$ $1.82 \pm 0.03$	$0.31 \pm 0.05$ $0.31 \pm 0.05$	Based on <i>Gaia</i> , TLUSTY/SYNSPEC + FITPROF Based on Bailer-Jones, TLUSTY/SYNSPEC + FITPROF
HZ 1	$0.14 \pm 0.01$ $0.14 \pm 0.01$	$1.71 \pm 0.03$ $1.71 \pm 0.03$	$0.38 \pm 0.06$ $0.38 \pm 0.06$	Based on <i>Gaia</i> , TLUSTY/SYNSPEC + FITPROF Based on Bailer-Jones, TLUSTY/SYNSPEC + FITPROF
GALEX J095256.6-371940 <sup>c</sup>	$0.20 \pm 0.01$ $0.20 \pm 0.01$	$2.13 \pm 0.05$ $2.13 \pm 0.05$	$0.55 \pm 0.09$ $0.55 \pm 0.09$	Based on <i>Gaia</i> , TLUSTY/SYNSPEC + FITPROF Based on Bailer-Jones, TLUSTY/SYNSPEC + FITPROF
PG 0314+146	$0.17 \pm 0.01^g, 0.17 \pm 0.01^h$ $0.17 \pm 0.01^g, 0.17 \pm 0.01^h$	$2.08 \pm 0.05^g, 2.08 \pm 0.05^h$ $2.08 \pm 0.05^g, 2.08 \pm 0.05^h$	$0.51 \pm 0.08^g, 0.48 \pm 0.07^h$ $0.51 \pm 0.08^g, 0.48 \pm 0.07^h$	Based on <i>Gaia</i> , TLUSTY/SYNSPEC + FITPROF Based on Bailer-Jones, TLUSTY/SYNSPEC + FITPROF

Table 13.4.: Same as Table 13.2, but showing the fundamental stellar parameters (radius  $R$ , luminosity  $L$ , and mass  $M$ ) of the program stars, which are analyzed by means of high-resolution data from FEROS, FOCES, HIRES, and HRS. For each star, the given fundamental stellar parameters are based on the spectroscopic results of one combination of model atmosphere approach and analysis strategy, namely the one whose results are used as input for the respective SED fit, from which the corresponding angular diameter  $\theta$  is derived (see Tables A.6-A.9 for details). The natures of the individual program stars can be found in Tables 8.4 and 8.5.

Object	$R$ [ $R_{\odot}$ ]	$\log(L/L_{\odot})$	$M$ [ $M_{\odot}$ ]	Comments
PHL 25	$0.42 \pm 0.03$	$1.26 \pm 0.05$	$0.35^{+0.05}_{-0.06}$	Based on <i>Gaia</i> , ADS + Global (NLTE metals)
	$0.42 \pm 0.03$	$1.27^{+0.06}_{-0.05}$	$0.35^{+0.05}_{-0.06}$	Based on Bailer-Jones, ADS + Global (NLTE metals)
PHL 382 <sup>a</sup>	$1.08 \pm 0.08$	$1.97 \pm 0.07$	$0.46 \pm 0.07$	Based on <i>Gaia</i> , ADS + Global (NLTE metals)
	$1.09^{+0.09}_{-0.08}$	$1.97^{+0.08}_{-0.07}$	$0.47^{+0.08}_{-0.07}$	Based on Bailer-Jones, ADS + Global (NLTE metals)
BD+48 <sup>c</sup> 2721	$0.39 \pm 0.01$	$1.42 \pm 0.03$	$0.41 \pm 0.06$	Based on <i>Gaia</i> , ADS + Global (NLTE metals)
	$0.39 \pm 0.01$	$1.42 \pm 0.03$	$0.41 \pm 0.06$	Based on Bailer-Jones, ADS + Global (NLTE metals)
PG 0342+026 <sup>b</sup>	$0.19 \pm 0.01$	$1.04 \pm 0.03$	$0.30 \pm 0.04$	Based on <i>Gaia</i> , ADS + Global (NLTE metals)
	$0.19 \pm 0.01$	$1.04 \pm 0.03$	$0.30 \pm 0.04$	Based on Bailer-Jones, ADS + Global (NLTE metals)

**Notes:** The listed uncertainties of the individual values result from Gaussian error propagation according to Eqs. (7.10), (7.11), and (7.12), whereby the total errors on the respective angular diameters  $\theta$ , effective temperatures  $T_{\text{eff}}$ , surface gravities  $\log(g)$ , and parallaxes  $\varpi_{\text{Gaia}}$ /distances  $d_{\text{Bailer-Jones}}$  ( $d_{\text{BJ}}$ ) are taken into account. Tables 8.18 and 8.19 list the statistical uncertainties used for  $\varpi_{\text{Gaia}}$  and  $d_{\text{BJ}}$ . No systematics (no corrections for the global zero point offset and the large and small-scale spatial variations of *Gaia*) are considered for  $\varpi_{\text{Gaia}}$  (see also Sect. 5.5.1). A value of 0.029 mas (corresponding to the global *Gaia* parallax zero point offset measured by Lindegren et al. 2018) is subtracted from the parallaxes inferred from the Bayesian distance measurements ( $d_{\text{BJ}}$ ) of Bailer-Jones et al. (2018). For more information on this, see the introduction of Ch. 13. Tables A.6-A.9 list the total uncertainties on  $\theta$  as well as the statistical ones used for  $T_{\text{eff}}$  and  $\log(g)$ . The results derived in Sect. 9.2.7 are used as global systematic errors on  $T_{\text{eff}}$  and  $\log(g)$ .

(a) Rotating star.

(b) Pulsating star.

(c) The star is most likely a pre-ELM. For further information, see Sect. 12.2.

(d) RV-variable star.

(e) SB 290 has a renormalised unit weight error (RUWE) larger than three derived from *Gaia* DR2 data (see Sect. 8.4 and Table 8.18). This is a strong indicator for a flawed *Gaia* parallax, which also affects the derived Bailer-Jones distance (Bailer-Jones et al., 2018). Hence, no fundamental stellar parameters are determined for SB 290 in this work.

Table 13.5.: Table 13.4 continued.

Object	$R$ [ $R_{\odot}$ ]	$\log(L/L_{\odot})$	$M$ [ $M_{\odot}$ ]	Comments
HD 4539 <sup>b</sup>	$0.26 \pm 0.01$	$1.26 \pm 0.03$	$0.44 \pm 0.06$	Based on <i>Gaia</i> , ADS + Global (NLTE metals)
	$0.26 \pm 0.01$	$1.26 \pm 0.03$	$0.45 \pm 0.06$	Based on Bailer-Jones, ADS + Global (NLTE metals)
CD-35° 15910 <sup>b</sup>	$0.22 \pm 0.01$	$1.36 \pm 0.03$	$0.47 \pm 0.07$	Based on <i>Gaia</i> , ADS + Global (NLTE metals)
	$0.22 \pm 0.01$	$1.36 \pm 0.03$	$0.47 \pm 0.07$	Based on Bailer-Jones, ADS + Global (NLTE metals)
EC 03263-6403	$0.20 \pm 0.01$	$1.35 \pm 0.03$	$0.38^{+0.07}_{-0.06}$	Based on <i>Gaia</i> , ADS + Global (NLTE metals)
	$0.20 \pm 0.01$	$1.35 \pm 0.03$	$0.38^{+0.07}_{-0.06}$	Based on Bailer-Jones, ADS + Global (NLTE metals)
EC 03591-3232	$0.14 \pm 0.01$	$1.11 \pm 0.03$	$0.44 \pm 0.06$	Based on <i>Gaia</i> , ADS + Global (NLTE metals)
	$0.14 \pm 0.01$	$1.11 \pm 0.03$	$0.45 \pm 0.06$	Based on Bailer-Jones, ADS + Global (NLTE metals)
EC 12234-2607	$0.17 \pm 0.01$	$1.25 \pm 0.04$	$0.51 \pm 0.08$	Based on <i>Gaia</i> , ADS + Global (NLTE metals)
	$0.17 \pm 0.01$	$1.25 \pm 0.04$	$0.51 \pm 0.08$	Based on Bailer-Jones, ADS + Global (NLTE metals)
EC 14338-1445	$0.20 \pm 0.01$	$1.32 \pm 0.05$	$0.48 \pm 0.07$	Based on <i>Gaia</i> , ADS + Global (NLTE metals)
	$0.20 \pm 0.01$	$1.32 \pm 0.05$	$0.48 \pm 0.07$	Based on Bailer-Jones, ADS + Global (NLTE metals)
Feige 38	$0.15 \pm 0.01$	$1.21 \pm 0.04$	$0.40 \pm 0.06$	Based on <i>Gaia</i> , ADS + Global (NLTE metals)
	$0.15 \pm 0.01$	$1.21 \pm 0.04$	$0.40 \pm 0.06$	Based on Bailer-Jones, ADS + Global (NLTE metals)
PG 1710+490	$0.16 \pm 0.01$	$1.23 \pm 0.03$	$0.63 \pm 0.09$	Based on <i>Gaia</i> , ADS + Global (NLTE metals)
	$0.16 \pm 0.01$	$1.23 \pm 0.03$	$0.63 \pm 0.09$	Based on Bailer-Jones, ADS + Global (NLTE metals)
SB 290 <sup>a</sup>	e	e	e	Based on <i>Gaia</i> , ADS + Global (NLTE metals)
	e	e	e	Based on Bailer-Jones, ADS + Global (NLTE metals)
Feige 36 <sup>c d</sup>	$0.17 \pm 0.01$	$1.23 \pm 0.04$	$0.90^{+0.12}_{-0.13}$	Based on <i>Gaia</i> , ADS + Global (NLTE metals)
	$0.17 \pm 0.01$	$1.23 \pm 0.04$	$0.91^{+0.12}_{-0.13}$	Based on Bailer-Jones, ADS + Global (NLTE metals)

Table 13.6.: Same as Table 13.2, but showing the fundamental stellar parameters (radius  $R$ , luminosity  $L$ , and mass  $M$ ) of the program stars, which are analyzed by means of medium-resolution data from UVES. For each star, the given fundamental stellar parameters are based on the spectroscopic results of one combination of model atmosphere approach and analysis strategy, namely the one whose results are used as input for the respective SED fit, from which the corresponding angular diameter  $\theta$  is derived (see Table A.10 for details). The natures of the individual program stars can be found in Table 8.6.

Object	$R$ [ $R_{\odot}$ ]	$\log(L/L_{\odot})$	$M$ [ $M_{\odot}$ ]	Comments
HE 0929-0424 <sup>a</sup>	$0.14 \pm 0.03$	$1.07 \pm 0.16$	$0.50 \pm 0.12$	Based on <i>Gaia</i> , ADS + Global (NLTE metals)
	$0.13 \pm 0.03$	$1.03^{+0.18}_{-0.14}$	$0.45^{+0.12}_{-0.10}$	Based on Bailer-Jones, ADS + Global (NLTE metals)
HE 1047-0436 <sup>a</sup>	$0.18 \pm 0.03$	$1.38 \pm 0.11$	$0.69 \pm 0.13$	Based on <i>Gaia</i> , ADS + Global (NLTE metals)
	$0.18^{+0.03}_{-0.02}$	$1.37^{+0.12}_{-0.10}$	$0.66^{+0.13}_{-0.12}$	Based on Bailer-Jones, ADS + Global (NLTE metals)
HD 149382	$0.16 \pm 0.01^b, 0.15 \pm 0.01^c$	$1.54 \pm 0.02^b, 1.45 \pm 0.02^c$	$0.68 \pm 0.09^b, 0.55 \pm 0.08^c$	Based on <i>Gaia</i> , ADS + Global (NLTE metals)
	$0.16 \pm 0.01^b, 0.15 \pm 0.01^c$	$1.54 \pm 0.02^b, 1.45 \pm 0.02^c$	$0.68 \pm 0.09^b, 0.55 \pm 0.08^c$	Based on Bailer-Jones, ADS + Global (NLTE metals)

**Notes:** The listed uncertainties of the individual values result from Gaussian error propagation according to Eqs. (7.10), (7.11), and (7.12), whereby the total errors on the respective angular diameters  $\theta$ , effective temperatures  $T_{\text{eff}}$ , surface gravities  $\log(g)$ , and parallaxes  $\varpi_{\text{Gaia}}$ /distances  $d_{\text{Bailer-Jones}}$  ( $d_{\text{BJ}}$ ) are taken into account. Tables 8.18 and 8.19 list the statistical uncertainties used for  $\varpi_{\text{Gaia}}$  and  $d_{\text{BJ}}$ . No systematics (no corrections for the global zero point offset and the large and small-scale spatial variations of *Gaia*) are considered for  $\varpi_{\text{Gaia}}$  (see also Sect. 5.5.1). A value of 0.029 mas (corresponding to the global *Gaia* parallax zero point offset measured by Lindegren et al. 2018) is subtracted from the parallaxes inferred from the Bayesian distance measurements ( $d_{\text{BJ}}$ ) of Bailer-Jones et al. (2018). For more information on this, see the introduction of Ch. 13. Table A.10 lists the total uncertainties on  $\theta$  as well as the statistical ones used for  $T_{\text{eff}}$  and  $\log(g)$ . The results derived in Sect. 9.2.7 are used as global systematic errors on  $T_{\text{eff}}$  and  $\log(g)$ .

<sup>(a)</sup> RV-variable star.

<sup>(b)</sup> Based on the result for the angular diameter derived from the single SED fit.

<sup>(c)</sup> Based on the result for the angular diameter derived from the binary SED fit.

Table 13.7.: Same as Table 13.2, but showing the fundamental stellar parameters (radius  $R$ , luminosity  $L$ , and mass  $M$ ) of the program stars, which are analyzed by means of low-resolution data from CAFOS. For each star, the given fundamental stellar parameters are based on the spectroscopic results of one combination of model atmosphere approach and analysis strategy, namely the one whose results are used as input for the respective SED fit, from which the corresponding angular diameter  $\theta$  is derived (see Tables A.11-A.14 for details). The natures of the individual program stars can be found in Tables 8.7 and 8.8.

Object	$R$ [ $R_{\odot}$ ]	$\log(L/L_{\odot})$	$M$ [ $M_{\odot}$ ]	Comments
HIP 67513	$1.95 \pm 0.10$	$1.61 \pm 0.05$	$0.88 \pm 0.13$	Based on <i>Gaia</i> , ADS + Global
	$1.94^{+0.11}_{-0.10}$	$1.60 \pm 0.05$	$0.87^{+0.13}_{-0.12}$	Based on Bailer-Jones, ADS + Global
BD+49° 2226	$2.12 \pm 0.11$	$1.89 \pm 0.05$	$6.23^{+0.91}_{-0.88}$	Based on <i>Gaia</i> , ADS + Global
	$2.12^{+0.11}_{-0.10}$	$1.89 \pm 0.05$	$6.24^{+0.91}_{-0.88}$	Based on Bailer-Jones, ADS + Global
FBS 1850+443	d	d	d	Based on <i>Gaia</i> , ADS + Global
	d	d	d	Based on Bailer-Jones, ADS + Global
FBS 2158+373	$2.59 \pm 0.29$	$2.34 \pm 0.10$	$5.13 \pm 0.87$	Based on <i>Gaia</i> , ADS + Global
	$2.55^{+0.31}_{-0.26}$	$2.33^{+0.11}_{-0.09}$	$4.98^{+0.88}_{-0.81}$	Based on Bailer-Jones, ADS + Global

**Notes:** The listed uncertainties of the individual values result from Gaussian error propagation according to Eqs. (7.10), (7.11), and (7.12), whereby the total errors on the respective angular diameters  $\theta$ , effective temperatures  $T_{\text{eff}}$ , surface gravities  $\log(g)$ , and parallaxes  $\varpi_{\text{Gaia}}$ /distances  $d_{\text{Bailer-Jones}}$  ( $d_{\text{BJ}}$ ) are taken into account. Tables 8.18 and 8.19 list the statistical uncertainties used for  $\varpi_{\text{Gaia}}$  and  $d_{\text{BJ}}$ . No systematics (no corrections for the global zero point offset and the large and small-scale spatial variations of *Gaia*) are considered for  $\varpi_{\text{Gaia}}$  (see also Sect. 5.5.1). A value of 0.029 mas (corresponding to the global *Gaia* parallax zero point offset measured by Lindegren et al. 2018) is subtracted from the parallaxes inferred from the Bayesian distance measurements ( $d_{\text{BJ}}$ ) of Bailer-Jones et al. (2018). For more information on this, see the introduction of Ch. 13. Tables A.11-A.14 list the total uncertainties on  $\theta$  as well as the statistical ones used for  $T_{\text{eff}}$  and  $\log(g)$ . The results derived in Sect. 9.2.7 are used as global systematic errors on  $T_{\text{eff}}$  and  $\log(g)$ .

(a) Pulsating star.

(b) The star could be/is most likely a pre-ELM (see Ch. 13 for details).

(c) RV-variable star.

(d) No fundamental stellar parameters are determined for FBS 1850+443 because the corresponding apparent fractional parallax uncertainty in *Gaia* DR2 is above 50% (see Table 8.19). Using this parallax as presented in Sect. 7.3 would result in a completely unreliable radius, luminosity, and mass for the star.

Table 13.8.: Table 13.7 continued.

Object	$R$ [ $R_{\odot}$ ]	$\log(L/L_{\odot})$	$M$ [ $M_{\odot}$ ]	Comments
FBS 2204+364	$2.91 \pm 0.34$	$2.25 \pm 0.11$	$2.77^{+0.49}_{-0.51}$	Based on <i>Gaia</i> , ADS + Global
	$2.88^{+0.38}_{-0.31}$	$2.24^{+0.12}_{-0.10}$	$2.71^{+0.50}_{-0.48}$	Based on Bailer-Jones, ADS + Global
HD 4539 <sup>a</sup>	$0.27 \pm 0.01$	$1.25 \pm 0.03$	$0.43 \pm 0.06$	Based on <i>Gaia</i> , ADS + Global
	$0.27 \pm 0.01$	$1.25 \pm 0.03$	$0.43 \pm 0.06$	Based on Bailer-Jones, ADS + Global
BD+42° 3250 <sup>b</sup>	$0.27 \pm 0.01$	$1.61 \pm 0.03$	$0.34 \pm 0.05$	Based on <i>Gaia</i> , ADS + Global
	$0.27 \pm 0.01$	$1.61 \pm 0.03$	$0.34 \pm 0.05$	Based on Bailer-Jones, ADS + Global
Balloon 90100001 <sup>a</sup>	$0.20 \pm 0.01$	$1.37 \pm 0.03$	$0.45^{+0.06}_{-0.07}$	Based on <i>Gaia</i> , ADS + Global
	$0.20 \pm 0.01$	$1.38 \pm 0.03$	$0.46^{+0.06}_{-0.07}$	Based on Bailer-Jones, ADS + Global
FBS 0102+362	$0.15 \pm 0.01$	$1.31 \pm 0.04$	$0.45^{+0.06}_{-0.07}$	Based on <i>Gaia</i> , ADS + Global
	$0.15 \pm 0.01$	$1.31 \pm 0.04$	$0.45^{+0.06}_{-0.07}$	Based on Bailer-Jones, ADS + Global
Feige 14	$0.15 \pm 0.01$	$1.18 \pm 0.04$	$0.41 \pm 0.06$	Based on <i>Gaia</i> , ADS + Global
	$0.15 \pm 0.01$	$1.18 \pm 0.04$	$0.41 \pm 0.06$	Based on Bailer-Jones, ADS + Global
GALEX J210332.4+303538	$0.12 \pm 0.01$	$1.23 \pm 0.03$	$0.50^{+0.07}_{-0.08}$	Based on <i>Gaia</i> , ADS + Global
	$0.12 \pm 0.01$	$1.23 \pm 0.03$	$0.50^{+0.07}_{-0.08}$	Based on Bailer-Jones, ADS + Global
FBS 2347+385 <sup>c</sup>	$0.21 \pm 0.01$	$1.04 \pm 0.03$	$0.39 \pm 0.06$	Based on <i>Gaia</i> , ADS + Global
	$0.21 \pm 0.01$	$1.04 \pm 0.03$	$0.39 \pm 0.06$	Based on Bailer-Jones, ADS + Global
PG 0101+039 <sup>a,c</sup>	$0.21 \pm 0.01$	$1.30 \pm 0.05$	$0.49 \pm 0.07$	Based on <i>Gaia</i> , ADS + Global
	$0.21^{+0.02}_{-0.01}$	$1.30 \pm 0.05$	$0.49 \pm 0.07$	Based on Bailer-Jones, ADS + Global
PG 1635+414 <sup>b</sup>	$0.17 \pm 0.01$	$1.63 \pm 0.04$	$0.33 \pm 0.05$	Based on <i>Gaia</i> , ADS + Global
	$0.17 \pm 0.01$	$1.64^{+0.05}_{-0.04}$	$0.33 \pm 0.05$	Based on Bailer-Jones, ADS + Global
LS IV +10° 9	$0.20 \pm 0.01$	$2.11 \pm 0.04$	$0.57 \pm 0.12$	Based on <i>Gaia</i> , TLUSTY/SYNSPEC + FITPROF
	$0.20 \pm 0.01$	$2.11 \pm 0.04$	$0.57 \pm 0.12$	Based on Bailer-Jones, TLUSTY/SYNSPEC + FITPROF

Table 13.9.: Same as Table 13.2, but showing the fundamental stellar parameters (radius  $R$ , luminosity  $L$ , and mass  $M$ ) of the program stars, which are analyzed by means of low-resolution data from IDS. For each star, the given fundamental stellar parameters are based on the spectroscopic results of one combination of model atmosphere approach and analysis strategy, namely the one whose results are used as input for the respective SED fit, from which the corresponding angular diameter  $\theta$  is derived (see Tables A.15-A.18 for details). The natures of the individual program stars can be found in Tables 8.9 and 8.10.

Object	$R$ [ $R_{\odot}$ ]	$\log(L/L_{\odot})$	$M$ [ $M_{\odot}$ ]	Comments
PG 2219+094 <sup>a</sup>	e	e	e	Based on <i>Gaia</i> , ADS + Global
	e	e	e	Based on Bailer-Jones, ADS + Global
SB 395	$2.08 \pm 0.39$	$2.47 \pm 0.17$	$3.95 \pm 0.89$	Based on <i>Gaia</i> , ADS + Global
	$1.84^{+0.33}_{-0.26}$	$2.36^{+0.16}_{-0.12}$	$3.10^{+0.68}_{-0.59}$	Based on Bailer-Jones, ADS + Global
KUV 03591+0457 <sup>a</sup>	$3.22 \pm 0.38$	$2.61 \pm 0.11$	$7.65^{+1.36}_{-1.49}$	Based on <i>Gaia</i> , ADS + Global
	$3.05^{+0.37}_{-0.31}$	$2.57^{+0.11}_{-0.09}$	$6.86^{+1.23}_{-1.27}$	Based on Bailer-Jones, ADS + Global

**Notes:** The listed uncertainties of the individual values result from Gaussian error propagation according to Eqs. (7.10), (7.11), and (7.12), whereby the total errors on the respective angular diameters  $\theta$ , effective temperatures  $T_{\text{eff}}$ , surface gravities  $\log(g)$ , and parallaxes  $\varpi_{\text{Gaia}}$ /distances  $d_{\text{Bailer-Jones}}$  ( $d_{\text{BJ}}$ ) are taken into account. Tables 8.18 and 8.19 list the statistical uncertainties used for  $\varpi_{\text{Gaia}}$  and  $d_{\text{BJ}}$ . No systematics (no corrections for the global zero point offset and the large and small-scale spatial variations of *Gaia*) are considered for  $\varpi_{\text{Gaia}}$  (see also Sect. 5.5.1). A value of 0.029 mas (corresponding to the global *Gaia* parallax zero point offset measured by Lindegren et al. 2018) is subtracted from the parallaxes inferred from the Bayesian distance measurements ( $d_{\text{BJ}}$ ) of Bailer-Jones et al. (2018). For more information on this, see the introduction of Ch. 13. Tables A.15-A.18 list the total uncertainties on  $\theta$  as well as the statistical ones used for  $T_{\text{eff}}$  and  $\log(g)$ . The results derived in Sect. 9.2.7 are used as global systematic errors on  $T_{\text{eff}}$  and  $\log(g)$ .

(a) Rotating star.

(b) The star could be a pre-ELM (see Ch. 13 for details).

(c) RV-variable star.

(d) Pulsating star.

(e) No fundamental stellar parameters are determined for PG 2219+094 because the corresponding apparent fractional parallax uncertainty in *Gaia* DR2 is above 50 % (see Table 8.19). Using this parallax as presented in Sect. 7.3 would result in a completely unreliable radius, luminosity, and mass for the star.

(f) Based on the result for the angular diameter derived from the single SED fit.

(g) Based on the result for the angular diameter derived from the binary SED fit.

Table 13.10.: Table 13.9 continued.

Object	$R$ [ $R_{\odot}$ ]	$\log(L/L_{\odot})$	$M$ [ $M_{\odot}$ ]	Comments
HE 0247-0418 <sup>b</sup>	$0.15 \pm 0.01$ $0.15 \pm 0.01$	$1.08 \pm 0.05$ $1.08 \pm 0.05$	$0.33 \pm 0.05$ $0.33 \pm 0.05$	Based on <i>Gaia</i> , ADS + Global Based on Bailer-Jones, ADS + Global
GALEX J203913.4+201309 <sup>a</sup>	$0.20 \pm 0.01$ $0.21 \pm 0.01$	$1.46 \pm 0.05$ $1.46 \pm 0.05$	$0.55 \pm 0.08$ $0.55 \pm 0.08$	Based on <i>Gaia</i> , ADS + Global Based on Bailer-Jones, ADS + Global
GALEX J202332.7+013618	$0.15 \pm 0.01$ $0.15 \pm 0.01$	$1.17 \pm 0.04$ $1.17 \pm 0.04$	$0.36 \pm 0.05$ $0.36 \pm 0.05$	Based on <i>Gaia</i> , ADS + Global Based on Bailer-Jones, ADS + Global
GALEX J172445.5+113224	$0.14 \pm 0.01$ $0.14 \pm 0.01$	$1.20 \pm 0.03$ $1.20 \pm 0.03$	$0.43 \pm 0.06$ $0.43 \pm 0.06$	Based on <i>Gaia</i> , ADS + Global Based on Bailer-Jones, ADS + Global
PG 2313-021 <sup>c</sup>	$0.14 \pm 0.01$ $0.14 \pm 0.01$	$1.15 \pm 0.04$ $1.15 \pm 0.04$	$0.50 \pm 0.07$ $0.50 \pm 0.07$	Based on <i>Gaia</i> , ADS + Global Based on Bailer-Jones, ADS + Global
KUV 16256+4034 <sup>c</sup>	$0.20 \pm 0.01$ $0.20 \pm 0.01$	$1.08 \pm 0.03$ $1.08 \pm 0.03$	$0.44 \pm 0.06$ $0.44 \pm 0.06$	Based on <i>Gaia</i> , ADS + Global Based on Bailer-Jones, ADS + Global
PG 0133+114 <sup>c</sup>	$0.15 \pm 0.01$ $0.15 \pm 0.01$	$1.08 \pm 0.04$ $1.08 \pm 0.04$	$0.37 \pm 0.05$ $0.37 \pm 0.05$	Based on <i>Gaia</i> , ADS + Global Based on Bailer-Jones, ADS + Global
GALEX J032139.8+472718 <sup>c</sup>	$0.23 \pm 0.01^f$ , $0.22 \pm 0.01^g$ $0.23 \pm 0.01^f$ , $0.22 \pm 0.01^g$	$1.49 \pm 0.03^f$ , $1.45 \pm 0.03^g$ $1.49 \pm 0.03^f$ , $1.45 \pm 0.03^g$	$0.51 \pm 0.07^f$ , $0.47 \pm 0.07^g$ $0.51 \pm 0.07^f$ , $0.47 \pm 0.07^g$	Based on <i>Gaia</i> , ADS + Global Based on Bailer-Jones, ADS + Global
2M1938+4603 <sup>c,d</sup>	$0.21 \pm 0.01$ $0.21 \pm 0.01$	$1.40 \pm 0.03$ $1.40 \pm 0.03$	$0.45 \pm 0.06$ $0.45 \pm 0.06$	Based on <i>Gaia</i> , ADS + Global Based on Bailer-Jones, ADS + Global
FB 29	$0.14 \pm 0.01$ $0.14 \pm 0.01$	$1.52 \pm 0.03$ $1.52 \pm 0.03$	$0.55 \pm 0.08$ $0.55 \pm 0.08$	Based on <i>Gaia</i> , ADS + Global Based on Bailer-Jones, ADS + Global
EC 01541-1409 <sup>d</sup>	$0.15 \pm 0.01$ $0.15 \pm 0.01$	$1.58 \pm 0.05$ $1.59 \pm 0.05$	$0.44 \pm 0.07$ $0.44 \pm 0.07$	Based on <i>Gaia</i> , ADS + Global Based on Bailer-Jones, ADS + Global
FBS 0654+366	$0.45 \pm 0.03$ $0.45^{+0.04}_{-0.03}$	$1.79 \pm 0.06$ $1.80^{+0.07}_{-0.06}$	$0.41 \pm 0.06$ $0.41 \pm 0.06$	Based on <i>Gaia</i> , ADS + Global Based on Bailer-Jones, ADS + Global
[CW83] 0512-08	$0.12 \pm 0.01$ $0.12 \pm 0.01$	$1.39 \pm 0.03$ $1.39 \pm 0.03$	$0.53 \pm 0.07$ $0.53 \pm 0.07$	Based on <i>Gaia</i> , ADS + Global Based on Bailer-Jones, ADS + Global

Table 13.11.: Table 13.9 continued.

Object	$R$ [ $R_{\odot}$ ]	$\log(L/L_{\odot})$	$M$ [ $M_{\odot}$ ]	Comments
GALEX J175548.5+501210	$0.15 \pm 0.01$	$1.74 \pm 0.03$	$0.55 \pm 0.13$	Based on <i>Gaia</i> , TLUSTY/SYNSPEC + FITPROF
	$0.15 \pm 0.01$	$1.74 \pm 0.03$	$0.55 \pm 0.13$	Based on Bailer-Jones, TLUSTY/SYNSPEC + FITPROF
PG 0314+146	$0.17 \pm 0.01$	$2.08 \pm 0.05$	$0.52 \pm 0.09$	Based on <i>Gaia</i> , TLUSTY/SYNSPEC + FITPROF
	$0.17 \pm 0.01$	$2.08 \pm 0.05$	$0.52 \pm 0.09$	Based on Bailer-Jones, TLUSTY/SYNSPEC + FITPROF
FBS 0224+330	$0.15 \pm 0.01$	$1.83 \pm 0.05$	$0.66 \pm 0.13$	Based on <i>Gaia</i> , TLUSTY/SYNSPEC + FITPROF
	$0.15 \pm 0.01$	$1.83 \pm 0.05$	$0.66 \pm 0.13$	Based on Bailer-Jones, TLUSTY/SYNSPEC + FITPROF

Table 13.12.: Same as Table 13.2, but showing the fundamental stellar parameters (radius  $R$ , luminosity  $L$ , and mass  $M$ ) of the program stars from literature, for which no spectra are analyzed in this work. For each star, the given fundamental stellar parameters are based on the corresponding results listed in Table A.19. The natures of the individual program stars can be found in Table 8.11.

Object	$R$ [ $R_{\odot}$ ]	$\log(L/L_{\odot})$	$M$ [ $M_{\odot}$ ]	Comments
BD+28° 4211	$0.06 \pm 0.01^b$ , $0.06 \pm 0.01^c$	$2.22 \pm 0.12^b$ , $2.21 \pm 0.04^c$	$0.24^{+0.17}_{-0.07}^b$ , $0.50 \pm 0.09^c$	Based on <i>Gaia</i>
	$0.06 \pm 0.01^b$ , $0.06 \pm 0.01^c$	$2.22 \pm 0.12^b$ , $2.21 \pm 0.04^c$	$0.24^{+0.17}_{-0.07}^b$ , $0.50 \pm 0.09^c$	Based on Bailer-Jones
AGK+81° 266 <sup>a</sup>	$0.09 \pm 0.01^d$	$2.00 \pm 0.05^d$	$0.37 \pm 0.08^d$	Based on <i>Gaia</i>
	$0.09 \pm 0.01^d$	$2.00 \pm 0.05^d$	$0.37 \pm 0.08^d$	Based on Bailer-Jones
LS II +18° 9 <sup>a</sup>	$0.10 \pm 0.01^d$	$2.00 \pm 0.05^d$	$0.36 \pm 0.07^d$	Based on <i>Gaia</i>
	$0.10 \pm 0.01^d$	$2.00 \pm 0.05^d$	$0.36 \pm 0.07^d$	Based on Bailer-Jones
Feige 67 <sup>a</sup>	$0.10 \pm 0.01^d$	$2.13 \pm 0.04^d$	$0.35 \pm 0.06^d$	Based on <i>Gaia</i>
	$0.10 \pm 0.01^d$	$2.13 \pm 0.04^d$	$0.35 \pm 0.06^d$	Based on Bailer-Jones
Feige 34 <sup>a</sup>	$0.10 \pm 0.01^d$	$2.15 \pm 0.04^d$	$0.36 \pm 0.06^d$	Based on <i>Gaia</i>
	$0.10 \pm 0.01^d$	$2.15 \pm 0.04^d$	$0.37 \pm 0.06^d$	Based on Bailer-Jones

**Notes:** The listed uncertainties of the individual values result from Gaussian error propagation according to Eqs. (7.10), (7.11), and (7.12), whereby the total errors on the respective angular diameters  $\theta$ , effective temperatures  $T_{\text{eff}}$ , surface gravities  $\log(g)$ , and parallaxes  $\varpi_{\text{Gaia}}$ /distances  $d_{\text{Bailer-Jones}}$  ( $d_{\text{BJ}}$ ) are taken into account. Tables 8.18 and 8.19 list the statistical uncertainties used for  $\varpi_{\text{Gaia}}$  and  $d_{\text{BJ}}$ . No systematics (no corrections for the global zero point offset and the large and small-scale spatial variations of *Gaia*) are considered for  $\varpi_{\text{Gaia}}$  (see also Sect. 5.5.1). A value of 0.029 mas (corresponding to the global *Gaia* parallax zero point offset measured by Lindegren et al. 2018) is subtracted from the parallaxes inferred from the Bayesian distance measurements ( $d_{\text{BJ}}$ ) of Bailer-Jones et al. (2018). For more information on this, see the introduction of Ch. 13. Table A.19 lists the total uncertainties on  $\theta$  as well as the statistical ones used for  $T_{\text{eff}}$  and  $\log(g)$ . The results derived in Sect. 9.2.7 are used as global systematic errors on  $T_{\text{eff}}$  and  $\log(g)$ .

(<sup>a</sup>) Rotating star.

(<sup>b</sup>) Based on the spectroscopic results of Latour et al. (2013). The listed fundamental stellar parameters are discarded due to the extremely low mass derived (see Sect. 13.3.2 for details).

(<sup>c</sup>) Based on the spectroscopic results of Latour et al. (2015). The listed fundamental stellar parameters are favored and used due to the almost canonical mass derived (see Sect. 13.3.2 for details).

(<sup>d</sup>) Based on the spectroscopic results of Latour et al. (2018).

Table 13.13.: Same as Table 13.2, but showing the fundamental stellar parameters (radius  $R$ , luminosity  $L$ , and mass  $M$ ) of the program stars, for which spectra from multiple spectrographs are analyzed. For each star, the given fundamental stellar parameters are based on the weighted averages of the spectroscopic results for one combination of model atmosphere approach and analysis strategy, namely the one whose averaged results are used as input for the respective SED fit, from which the corresponding angular diameter  $\theta$  is derived (see Tables A.20-A.23 for details). The natures of the individual program stars can be found in Tables 8.1-8.3.

Object	$R$ [ $R_{\odot}$ ]	$\log(L/L_{\odot})$	$M$ [ $M_{\odot}$ ]	Comments
HD 4539 <sup>a</sup>	$0.26 \pm 0.01$	$1.29 \pm 0.03$	$0.47 \pm 0.07$	Based on <i>Gaia</i> , ADS + Global
	$0.26 \pm 0.01$	$1.29 \pm 0.03$	$0.47 \pm 0.07$	Based on Bailer-Jones, ADS + Global
Feige 38	$0.15 \pm 0.01$	$1.20 \pm 0.04$	$0.46 \pm 0.07$	Based on <i>Gaia</i> , ADS + Global
	$0.15 \pm 0.01$	$1.20 \pm 0.04$	$0.46 \pm 0.07$	Based on Bailer-Jones, ADS + Global
EC 03591-3232	$0.14 \pm 0.01$	$1.11 \pm 0.03$	$0.48 \pm 0.07$	Based on <i>Gaia</i> , ADS + Global
	$0.14 \pm 0.01$	$1.11 \pm 0.03$	$0.48 \pm 0.07$	Based on Bailer-Jones, ADS + Global
[CW83] 0512-08	$0.12 \pm 0.01$	$1.39 \pm 0.03$	$0.46 \pm 0.06$	Based on <i>Gaia</i> , ADS + Global
	$0.12 \pm 0.01$	$1.39 \pm 0.03$	$0.46 \pm 0.06$	Based on Bailer-Jones, ADS + Global
PG 0314+146	$0.17 \pm 0.01$	$2.08 \pm 0.05$	$0.49 \pm 0.07$	Based on <i>Gaia</i> , TLUSTY/SYNSPEC + FITPROF
	$0.17 \pm 0.01$	$2.08^{+0.05}_{-0.04}$	$0.50 \pm 0.07$	Based on Bailer-Jones, TLUSTY/SYNSPEC + FITPROF
HD 149382	$0.16 \pm 0.01^b, 0.15 \pm 0.01^c$	$1.55 \pm 0.02^b, 1.46 \pm 0.02^c$	$0.76 \pm 0.10^b, 0.62 \pm 0.08^c$	Based on <i>Gaia</i> , ADS + Global
	$0.16 \pm 0.01^b, 0.15 \pm 0.01^c$	$1.55 \pm 0.02^b, 1.46 \pm 0.02^c$	$0.76 \pm 0.10^b, 0.62 \pm 0.08^c$	Based on Bailer-Jones, ADS + Global

**Notes:** The listed uncertainties of the individual values result from Gaussian error propagation according to Eqs. (7.10), (7.11), and (7.12), whereby the total errors on the respective angular diameters  $\theta$ , effective temperatures  $T_{\text{eff}}$ , surface gravities  $\log(g)$ , and parallaxes  $\varpi_{\text{Gaia}}$ /distances  $d_{\text{Bailer-Jones}}$  ( $d_{\text{BJ}}$ ) are taken into account. Tables 8.18 and 8.19 list the statistical uncertainties used for  $\varpi_{\text{Gaia}}$  and  $d_{\text{BJ}}$ . No systematics (no corrections for the global zero point offset and the large and small-scale spatial variations of *Gaia*) are considered for  $\varpi_{\text{Gaia}}$  (see also Sect. 5.5.1). A value of 0.029 mas (corresponding to the global *Gaia* parallax zero point offset measured by Lindegren et al. 2018) is subtracted from the parallaxes inferred from the Bayesian distance measurements ( $d_{\text{BJ}}$ ) of Bailer-Jones et al. (2018). For more information on this, see the introduction of Ch. 13. Tables A.20-A.23 list the total uncertainties on  $\theta$  as well as the statistical ones used for  $T_{\text{eff}}$  and  $\log(g)$ . The results derived in Sect. 9.2.7 are used as global systematic errors on  $T_{\text{eff}}$  and  $\log(g)$ .

<sup>(a)</sup> Pulsating star.

<sup>(b)</sup> Based on the result for the angular diameter derived from the single SED fit.

<sup>(c)</sup> Based on the result for the angular diameter derived from the binary SED fit.



## 14. Summary and Outlook

The spectral class of hot subdwarf stars (sdOs/sdBs) covers a wide range of objects of different subtypes showing a variety of different properties. This class may therefore be considered a stellar zoo. It is general consensus that hot subdwarfs are highly evolved objects that are in the core helium-burning phase or beyond. Several evolutionary links between the subtypes and other classes of stars have been proposed so far, involving binary interaction processes such as Roche-lobe overflow (RLOF), common-envelope (CE) ejection, or the coalescence of two helium white dwarfs (HeWDs). Furthermore, internal mixing in the so-called hot flasher scenario (early hot flashers, EHF; shallow and deep mixing) is considered a possible option for the formation of sdOs/sdBs. However, various investigations are lacking to fully resolve the issue on how these remarkable objects form.

To this end, the present work presented an in-depth fundamental stellar analysis of a carefully chosen set of 63 known and candidate hot subdwarf stars that represented all relevant subtypes of sdOs/sdBs. The sample covered the full range of atmospheric parameters ( $T_{\text{eff}}$ ,  $\log g$ , and  $\log n(\text{He})$ ) of single and binary stars, pulsating and non-pulsating objects, and stars with particularly peculiar abundance anomalies (for instance, that of  $^3\text{He}$ ). In addition to the 63 stars, three known (post-)blue horizontal branch ((post-)BHB) objects were included for comparison, leading to a total sample size of 66 program stars.

The aim of the project was twofold:

- 1.) Precise and accurate atmospheric parameters derived from spectroscopy are prerequisites in order to understand the nature and the evolution of the various subtypes of hot subdwarf stars. However, sophisticated spectroscopic analyses require spectra of excellent quality (signal-to-noise, spectral resolution, and wavelength coverage). In the real world, only very few observations fulfill such optimum conditions. A first important goal of the present work hence was the investigation of the impact of the data quality of spectroscopic observations on the derived atmospheric parameters. For this purpose, data obtained with different instruments were analyzed, whereby a sample of 17 program stars with optimum data quality (XSHOOTER) served as a reference.

Apart from high-quality observations, sophisticated model atmospheres are required in order to derive meaningful atmospheric parameters. Since sdOs/sdBs are hot objects, departures from the local thermodynamic equilibrium (LTE) approximation commonly used in the context of stellar atmosphere modelling affect the occupation numbers of the atomic energy levels of the atoms/ions present in the atmospheres of these stars. In addition to that, these so-called non-LTE (NLTE) effects may significantly influence the temperature-density stratification of the stellar atmospheres of these stars, although in principle this should be counteracted by the predominant high atmospheric particle densities. The large range of effective temperatures and

surface gravities observed for sdOs/sdBs called for a detailed investigation. The very peculiar metal-rich chemical composition of sdOs/sdBs implies that metal line-blanketing is another important ingredient. As a matter of fact, no currently available stellar atmosphere code is able to fully meet all of the requirements needed to model the atmospheres of hot subdwarf stars. Thus, the following three sets of model atmospheres that cover the parameter space observed for sdOs/sdBs were used in this work in order to study the impact of the relevant effects in great detail: I) classical metal line-blanketed LTE models of Heber et al. (2000), which have been successfully utilized for many published studies, II) NLTE model atmospheres with limited metal line-blanketing, and III) hybrid models that allowed to treat NLTE effects and extensive metal line-blanketing.

Additionally, the impact of the analysis method used on the derived atmospheric parameters was investigated in this work. To this end, the following two analysis strategies were compared: I) the classical selective approach where only preselected wavelength ranges were analyzed, which covered the most important hydrogen and helium lines, and II) the global approach where the whole spectrum was fitted at once and only obvious outliers were excluded.

Inter alia, the resulting sophisticated comparative analysis lead to a deeper understanding of the caveats of modern spectroscopic analyses of hot subdwarf stars.

2.) A consistent comparison to theoretical evolutionary models for hot subdwarf stars required the knowledge of the fundamental stellar parameters (radius  $R$ , luminosity  $L$ , and mass  $M$ ) of the program stars. The precise parallax measurements, published within the second data release (DR2) of the *Gaia* satellite, made it possible for the very first time for such a large hot subdwarf sample to reliably convert atmospheric parameters into fundamental ones. However, this required the determination of the angular diameters of the program stars from spectral energy distribution (SED) fitting to appropriate photometric data. Therefore, the second part of the present work dealt with the construction and the analysis of SEDs as well as with the subsequent derivation of the fundamental stellar parameters by means of parallaxes from *Gaia* DR2.

## Main Findings

### Model Atmospheres and Analysis Strategies

- **LTE vs. hybrid LTE/NLTE vs. NLTE:**

1.) The optimum effective temperature regime for the LTE models is between  $\sim 25\,000$  K and  $\sim 32\,000$  K. For lower and in particular higher temperatures, NLTE effects prevail. On average, the hybrid models resulted in higher surface gravities compared to LTE ( $\gtrsim 0.10$  dex at  $\log g \sim 5.00$  and  $\lesssim 0.05$  dex at  $\log g \sim 6.00$ ), but at the same time the corresponding helium abundances have been observed to be lower. This can be explained by the anti-correlation between  $\log(g)$  and  $\log n(\text{He})$ .

2.) The results derived from the LTE and the NLTE models seem to match at a

## 14. Summary and Outlook

---

temperature of  $T_{\text{eff}} \sim 30\,000\text{ K}$ . However, the NLTE models yielded significantly higher effective temperature values (up to  $\sim 1700\text{ K}$ ) for the hotter stars. Apart from NLTE effects, this trend can mainly be explained by the limited metal line-blanketing of these models (backwarming effect). The same applies to the comparison between the hybrid and the NLTE models for which differences of up to  $\sim 2000\text{ K}$  have been measured for individual program stars. Interestingly, the hybrid models also resulted, on average, in higher surface gravities compared to the NLTE models ( $\lesssim 0.08\text{ dex}$  at  $\log g \sim 5.50$  and  $\lesssim 0.15\text{ dex}$  at  $\log g \sim 5.80$ ). In this case, however, the anti-correlation between  $\log(g)$  and  $\log n(\text{He})$  cannot serve as the sole explanation because the helium abundances derived from both model atmosphere approaches have been found to be rather similar, at least for stars with  $\log n(\text{He}) \lesssim -1.70$ . Therefore, it is again highly likely that metal line-blanketing is responsible for the observed surface gravity difference.

3.) For hot subdwarf stars in the temperature regime of  $20\,000\text{ K} \lesssim T_{\text{eff}} \lesssim 40\,000\text{ K}$ , the hybrid models have been found to be best suited because these models yielded consistent results, regardless of whether the selective or the global analysis approach was used.

4.) For several hundreds of hot subdwarf stars from literature, the determined regression curves of Eqs. (9.1-9.3) allow to convert the published atmospheric parameters that are based on old LTE models into new ones based on state-of-the-art models, without having to actually perform the respective spectroscopic analyses with the new hybrid LTE/NLTE approach. In this way, plenty of hours of work time will be saved for future studies on hot subdwarf stars.

- **Systematic uncertainties:** The detailed comparison of different model atmosphere approaches and analysis strategies performed in this work resulted in the following global systematic uncertainties of the atmospheric parameters of a given program star:
  - $T_{\text{eff}}$ : 0.550 % and 0.869 %
  - $\log(g)$ : 0.035 and 0.043
  - $\log n(\text{He})$ : 0.047 and 0.059.

For each parameter, the first value considers the results of the comparison between the global and the selective analysis approach, whereas the second value takes the influence of metals in the spectral synthesis into account. In order to get the total uncertainty of an atmospheric parameter of a given program star, the first and second value needed to be combined with the respective measured statistical uncertainty. This was done via addition in quadrature.

- **Impact of the hydrogen Paschen series:** In literature, the hydrogen Paschen lines have very rarely been used as a diagnostic tool for hot subdwarf stars. Instead, the Balmer lines are often used. For the program stars of this work that lie in the effective temperature regime of  $20\,000\text{ K} \lesssim T_{\text{eff}} \lesssim 30\,000\text{ K}$ , the atmospheric parameters derived from the Paschen series have been found to be largely consistent with those derived from the Balmer series and the full spectrum. This shows that the Paschen series is indeed a reliable diagnostic tool, which is very promising because many of the current and future

spectrographs (for instance, XSHOOTER, CARMENES, or WEAVE) are configured for the near-infrared (NIR) wavelength regime with the Paschen series. Hence, it will be possible for future studies on cool hydrogen-rich sdB stars to extend the usual analyses of blue spectra to the NIR. In the long run, the analyses of these stars based on blue spectra may even be replaced by the NIR. However, this will not be possible for the hotter hydrogen and helium-rich sdOs, which, on the one hand, benefit from several helium lines in the NIR, but for which the hydrogen Paschen series is not observed. Not least due to the fact that the line-broadening theory for He I lines in the NIR is still incomplete, the hydrogen Balmer and He II Pickering series as well as other He I/II lines in the blue remain indispensable for the spectroscopic analyses of these stars.

## Evolutionary Status, Chemical Composition, Rotational Velocities and Atmospheric and Fundamental Stellar Parameters

### Evolutionary Status, Chemical Composition and Atmospheric Parameters

- **Spectral type:** Two thirds ( $\sim 67\%$ ) of all analyzed program stars belong to the group of hydrogen-rich hot subdwarfs. At the same time, their (intermediate) helium-rich siblings make up  $\sim 17\%$ .
- **Evolutionary status:**
  - 1.) A comparison of the atmospheric parameters determined for the program stars to evolutionary tracks in the  $T_{\text{eff}}\text{-}\log(g)$  plane (Kiel diagram) revealed that the majority of the analyzed stars ( $\sim 62\%$ , helium-rich sdOs included) are core helium-burning objects that are located on the extreme horizontal branch (EHB). Another  $\sim 17\%$  are more evolved post-EHB objects for which core helium burning has already ceased.  $\sim 9\%$  of the analyzed program stars turned out to be B-type main-sequence stars and  $\sim 5\%$  are (post-)BHB objects. The nature of two stars remains unclear, which corresponds to about  $3\%$  of the total analyzed sample. One object (GALEX J080510.9-105834) is confirmed to be a progenitor of an extremely low-mass helium-core white dwarf (pre-ELM), whereas for two other stars (Feige 36 and BD+42° 3250) a pre-ELM nature seems highly likely. Thus, the total pre-ELM percentage in the analyzed sample is  $\sim 5\%$ . Furthermore, it is possible (but less likely) that two more objects are pre-ELMs. Last but not least, one star may also be a post-asymptotic giant branch (post-AGB) object.
  - 2.) The observed SEDs could be matched with single model atmospheres for all but four targets, which showed clear infrared excesses indicating the presence of a cool companion. The spectral types of the individual companions have been determined to be M4 (SB 290), M3 (Feige 36), M0 (Feige 34), and K4 (EC 01541-1409). In fact, the binarities of SB 290, Feige 36, and EC 01541-1409 are new discoveries.
- **$^3\text{He}$  anomaly and atmospheric stratification:** The analyzed  $^3\text{He}$  hydrogen-rich sdB program stars have been found to cluster in a narrow temperature strip between

$\sim 26\,000\text{ K}$  and  $\sim 30\,000\text{ K}$ . For these stars, a detailed comparison of the results derived in the present work to those determined by Schneider et al. (2018) lead to strikingly high deviations in terms of  $T_{\text{eff}}$  (up to  $\sim 1200\text{ K}$ ),  $\log(g)$  (up to  $\sim 0.20\text{ dex}$ ), and  $\log n(\text{He})$  (up to  $\sim 0.45\text{ dex}$ ). Similar deviations have also been observed for the individual  $^4\text{He}$  and  $^3\text{He}$  isotopic abundances as well as for the isotopic abundance ratios  $n(^4\text{He})/n(^3\text{He})$ . The deviations can be partially explained by the small improvements and differences that have been implemented into the respective models and analysis procedures (for instance, level dissolution or the local normalization procedure), which were not yet available for Schneider et al. (2018). Moreover, anomalous helium line profiles, which have been observed for about half of the analyzed  $^3\text{He}$  program stars, could be responsible for the large measured deviations. The unusually broad wings and shallow cores of the spectral lines of the relevant stars indicate that helium is not homogeneously distributed throughout the stellar atmosphere, but instead shows a vertical abundance stratification that has not been considered by the models used in this work. Yet, by means of the available models, it could be estimated that the total helium abundance increases by factors of up to  $\sim 9.0$  (PHL 25) from the outer to the inner atmospheric layers.

- **Metal abundances:** For the metal abundance study presented in this work, almost all lines detected in the optical and NIR wavelength regime of the investigated high and medium-resolution spectra could be used. The abundances of the chemical elements C, N, O, Ne, Mg, Al, Si, S, Ar, and Fe were analyzed in NLTE. In addition, P, Ca, Ti, Sr, and Zr lines were found for some program stars of the XSHOOTER reference sample and were analyzed in LTE. In consequence, the metal abundance study of this work represents a major improvement over previous LTE studies such as that of Geier (2013), who only used a semi-automatic analysis pipeline and a small set of selected and representative spectral lines per ion. Not least because of that, the metal abundances derived for a bunch of program stars changed dramatically. At the same time, significantly lower uncertainties for the individual abundances could be determined.

### Rotational Velocities and Fundamental Stellar Parameters

- **Rotational velocities:** The analyses of the sharp metal line profiles also allowed for an accurate determination of the projected rotational velocities. As expected, most of the program stars turned out to be slow rotators. However, eleven stars have been found to show significant rotation, including three new discoveries. The exceptionally high projected rotational velocity of  $v \sin i = 142.0_{-11.0}^{+9.0} \text{ km s}^{-1}$  measured for the hydrogen-rich sdB star GALEX J203913.4+201309 is truly remarkable given the fact that faster rotation has only been reported for hot subdwarf stars that have filled their Roche lobes and started mass transfer onto a white dwarf companion (Kupfer et al., 2020a,b).
- **Radius and luminosity distribution:** The radius distribution determined for the hydrogen-rich hot subdwarf program stars has been found to be consistent with predictions of canonical evolutionary models, meaning that most program stars have radii of  $0.10 R_{\odot} \lesssim R \lesssim 0.30 R_{\odot}$ . Surprisingly, the radius distribution is of bimodal shape,

showing two well-defined peaks at  $R_1 = 0.138 R_\odot$  and  $R_2 = 0.205 R_\odot$ . In fact, the same has been found for the corresponding luminosity distribution (with abscissa  $\log L/L_\odot$ ), which peaks at  $L_1 = 1.291$  and  $L_2 = 2.090$ , respectively.

- **Mass distribution:** The mass distribution determined for the hydrogen-rich hot subdwarf program stars has also been found to be largely consistent with predictions of canonical evolutionary models. It could be described by a single Gaussian peaking at  $M_p = 0.465 M_\odot$ . This means that most of the analyzed program stars can be explained well by the EHF scenario, by RLOF, or by CE ejection. Nevertheless, several outliers at the low and high-mass end of the mass distribution were observed. While the latter could in principle be explained by the merger of two HeWDs, the former are rather difficult to reconcile with any of the formation channels of hot subdwarf stars known today.

## Outlook

With about 70 analyzed objects, the statistics of the present work are rather low. A larger number of analyzed hot subdwarf stars would significantly increase the validity of the derived radius, luminosity, and mass distribution. Additionally, it would also provide meaningful distributions for (intermediate) helium-rich objects. From this perspective, the results of the present work serve as a basis for future studies on hot subdwarf stars because the results of the detailed comparison of different model atmosphere approaches and analysis strategies provide a good estimate for the magnitude of the systematic uncertainties of the atmospheric parameters for program stars in future projects. The hybrid LTE/NLTE approach used in this work should be considered the new standard for hot subdwarf stars with effective temperatures of  $20\,000\text{ K} \lesssim T_{\text{eff}} \lesssim 40\,000\text{ K}$  and the determined regression curves of Eqs. (9.1-9.3) allow to update the published atmospheric parameters for several hundreds of these objects from literature, which have only been analyzed by means of old LTE models. In this way, larger statistics in terms of reliable fundamental stellar parameters will be achieved, which is not least supported by the more and more precise trigonometric parallaxes available in future data releases of the *Gaia* satellite. Certainly, the updated parallaxes will also improve the error budget of the resulting radii, luminosities, and masses. Hence, the golden age of thorough fundamental stellar analyses of large samples of hot subdwarf stars has only just begun. A bright future with lots of remarkable discoveries in this very interesting field of research lies upon us!

## **A. Atmospheric and Photometric Results of the Analyzed Program Stars**

**Table A.1.:** Effective temperatures  $T_{\text{eff}}$ , surface gravities  $\log(g)$ , helium abundances  $\log n(\text{He}) := \log n(^4\text{He} + ^3\text{He})$ , angular diameters  $\theta$ , and monochromatic color excesses  $E(44 - 55)$  of the analyzed XSHOOTER program stars compared to literature values. If possible, each star is analyzed spectroscopically making use of three different model atmosphere approaches (LTE, ADS, and TLUSTY/SYNSPEC; see Sects. 6.7, 6.8, and 6.9). In addition, two different analysis strategies (global with ISIS and selective with SPAS and FITPROF; see Sect. 7.1.2) are used. If metals are fitted, it is indicated: C, N, O, Ne, Mg, Al, Si, S, Ar, and Fe in NLTE as well as P, Ca, Ti, Sr, and Zr in LTE (NLTE + LTE metals); C, N, O, Ne, Mg, Al, Si, S, Ar, and Fe in NLTE and no other metals (NLTE metals).  $\theta$  and  $E(44 - 55)$  are derived from SED fitting to photometric data (see Sect. 7.2) and are only listed for one model atmosphere approach and analysis strategy combination. The listed  $\theta$  values together with the corresponding spectroscopic parameters are used to derive the fundamental stellar parameters (radius, luminosity, mass) according to Sect. 7.3. To this end, the global systematic errors on  $T_{\text{eff}}$  and  $\log(g)$  (not included here) according to the results of Sect. 9.2.7 as well as the parallaxes of Tables 8.18 and 8.19 are taken into account. The natures of the individual program stars can be found in Tables 8.1-8.3.

Object	$T_{\text{eff}}$ [K]	$\log(g[\text{cm s}^{-2}])$	$\log n(\text{He})$	$\theta$ [ $10^{-11}$ rad]	$E(44 - 55)$ [mag]	Comments/Ref.
HD 4539 <sup>a</sup>	$23\,971 \pm 14$	$5.2971^{+0.0015}_{-0.0013}$	$-2.2406^{+0.0023}_{-0.0026}$	$6.2273 \pm 0.0321$	$\leq 0.0049$	ADS + Global (NLTE + LTE metals)
	$23\,897^{+11}_{-16}$	$5.3045^{+0.0010}_{-0.0020}$	$-2.2355^{+0.0023}_{-0.0025}$	-	-	ADS + Global (NLTE metals)
	$23\,521 \pm 14$	$5.3086 \pm 0.0014$	$-2.2398 \pm 0.0023$	-	-	ADS + Global
	$24\,327 \pm 124$	$5.318 \pm 0.199$	$-2.315 \pm 0.040$	-	-	ADS + SPAS
	$23\,694 \pm 386$	$5.332 \pm 0.232$	$-2.283 \pm 0.121$	-	-	LTE + SPAS
	-	-	-	-	-	TLUSTY/SYNSPEC + SPAS
	$24\,031 \pm 39$	$5.283 \pm 0.005$	$-2.264 \pm 0.011$	-	-	ADS + FITPROF
	$23\,700 \pm 55$	$5.175 \pm 0.006$	$-2.275 \pm 0.015$	-	-	LTE + FITPROF
	-	-	-	-	-	TLUSTY/SYNSPEC + FITPROF
	$23\,200 \pm 100$	$5.20 \pm 0.01$	$-2.27 \pm 0.01$	-	-	[1]
$24\,650^{+590}_{-200}$	$5.38^{+0.03}_{-0.05}$	$-2.42^{+0.20}_{-0.07}$	-	-	[2]	

**Notes:** For the results of this work,  $1\sigma$  statistical single parameter errors are given for  $T_{\text{eff}}$ ,  $\log(g)$ ,  $\log n(\text{He})$ , and  $E(44-55)$ . If SPAS is used, the uncertainties on  $T_{\text{eff}}$ ,  $\log(g)$ , and  $\log n(\text{He})$  result from bootstrapping, whereas in all other cases the corresponding errors are derived from  $\chi^2$ -statistics (see Sect. 7.1.2). The latter also applies to all listed  $E(44 - 55)$  values (see Sect. 7.2.3). The listed uncertainties on  $\theta$  result from Eq. (7.17), whereby the total uncertainties on  $T_{\text{eff}}$  derived from spectroscopy (combining the individual listed  $1\sigma$  statistical errors and the global systematic ones from Sect. 9.2.7) are considered. Hence,  $\Delta T_{\text{eff,model}} = \Delta T_{\text{eff,spectr.}} = \sqrt{[\Delta T_{\text{eff,spectr.,stat.}}]^2 + [(0.550/100) \cdot T_{\text{eff}}]^2 + [(0.869/100) \cdot T_{\text{eff}}]^2}$  is used in Eq. (7.17) in order to calculate the individual values of  $\Delta\theta$ .

- (a) Pulsating star.
- (b) RV-variable star.
- (c) Rotating star.
- (d) The star is a pre-ELM (see Ch. 13 for details).
- (e) Derived from the single SED fit.
- (f) Derived from the binary SED fit.
- (g) He I 6678 Å included in spectral analysis fit.
- (h) He I 6678 Å not included in spectral analysis fit.

**References:** (1) Schneider et al. (2018); (2) Németh et al. (2012); (3) Geier et al. (2013a); (4) Geier et al. (2011b); (5) Geier et al. (2009); (6) Jeffery et al. (2017); (7) Schindewolf (2018).

Table A.2.: Table A.1 continued.

Object	$T_{\text{eff}}$ [K]	$\log(g[\text{cm s}^{-2}])$	$\log n(\text{He})$	$\theta$ [ $10^{-11}$ rad]	$E(44 - 55)$ [mag]	Comments/Ref.
PG 1432+004	$22\,683^{+14}_{-16}$	$5.2972^{+0.0015}_{-0.0018}$	$-2.418^{+0.007}_{-0.006}$	$2.1792 \pm 0.0113$	$0.0281 \pm 0.0025$	ADS + Global (NLTE + LTE metals)
	$22\,678^{+19}_{-21}$	$5.3076^{+0.0022}_{-0.0021}$	$-2.412^{+0.006}_{-0.009}$	-	-	ADS + Global (NLTE metals)
	$22\,638^{+11}_{-20}$	$5.3053^{+0.0013}_{-0.0012}$	$-2.411 \pm 0.006$	-	-	ADS + Global
	$23\,440 \pm 293$	$5.306 \pm 0.039$	$-2.370 \pm 0.054$	-	-	ADS + SPAS
	$22\,855 \pm 306$	$5.231 \pm 0.026$	$-2.527 \pm 0.098$	-	-	LTE + SPAS
	-	-	-	-	-	TLUSTY/SYNSPEC + SPAS
	$22\,817 \pm 35$	$5.317 \pm 0.004$	$-2.354 \pm 0.015$	-	-	ADS + FITPROF
	$22\,513 \pm 43$	$5.199 \pm 0.005$	$-2.319 \pm 0.017$	-	-	LTE + FITPROF
	-	-	-	-	-	TLUSTY/SYNSPEC + FITPROF
	$23\,090^{+780}_{-250}$	$5.28 \pm 0.08$	$-2.39^{+0.18}_{-0.20}$	-	-	[2]
GALEX J104148.9-073031	$26\,157^{+16}_{-8}$	$5.6377^{+0.0017}_{-0.0032}$	$-2.344 \pm 0.004$	$3.1182 \pm 0.0161$	$0.019 \pm 0.005$	ADS + Global (NLTE + LTE metals)
	$26\,190 \pm 11$	$5.6354 \pm 0.0018$	$-2.335 \pm 0.004$	-	-	ADS + Global (NLTE metals)
	$26\,208 \pm 11$	$5.6349^{+0.0015}_{-0.0018}$	$-2.3423^{+0.0035}_{-0.0023}$	-	-	ADS + Global
	$26\,426 \pm 71$	$5.645 \pm 0.006$	$-2.378 \pm 0.087$	-	-	ADS + SPAS
	$26\,674 \pm 165$	$5.648 \pm 0.021$	$-2.415 \pm 0.072$	-	-	LTE + SPAS
	-	-	-	-	-	TLUSTY/SYNSPEC + SPAS
	$26\,500 \pm 25$	$5.658 \pm 0.004$	$-2.369 \pm 0.013$	-	-	ADS + FITPROF
	$26\,321 \pm 40$	$5.572 \pm 0.005$	$-2.362 \pm 0.017$	-	-	LTE + FITPROF
	-	-	-	-	-	TLUSTY/SYNSPEC + FITPROF
	$27\,440^{+620}_{-450}$	$5.63^{+0.09}_{-0.06}$	$-2.44^{+0.16}_{-0.23}$	-	-	[2]
Feige 38	$29\,214^{+25}_{-15}$	$5.7377^{+0.0026}_{-0.0029}$	$-2.5658^{+0.0298}_{-0.0328}$	$1.5791 \pm 0.0082$	$0.054 \pm 0.004$	ADS + Global (NLTE + LTE metals)
	$29\,248^{+20}_{-19}$	$5.7328^{+0.0028}_{-0.0029}$	$-2.5429^{+0.0260}_{-0.0465}$	-	-	ADS + Global (NLTE metals)
	$29\,453^{+13}_{-23}$	$5.7236^{+0.0013}_{-0.0011}$	$-2.5154^{+0.0077}_{-0.0049}$	-	-	ADS + Global
	$30\,271 \pm 115$	$5.766 \pm 0.014$	$-2.526 \pm 0.051$	-	-	ADS + SPAS
	$29\,614 \pm 269$	$5.643 \pm 0.024$	$-2.591 \pm 0.083$	-	-	LTE + SPAS
	-	-	-	-	-	TLUSTY/SYNSPEC + SPAS
	$29\,599 \pm 47$	$5.734 \pm 0.007$	$-2.533 \pm 0.029$	-	-	ADS + FITPROF
	$29\,938 \pm 48$	$5.667 \pm 0.007$	$-2.488 \pm 0.027$	-	-	LTE + FITPROF
	-	-	-	-	-	TLUSTY/SYNSPEC + FITPROF
	$28\,200 \pm 100$	$5.61 \pm 0.01$	$-2.70 \pm 0.03$	-	-	[1]
$30\,600 \pm 500$	$5.83 \pm 0.05$	$-2.37 \pm 0.10$	-	-	[3]	
EC 03591-3232	$28\,757^{+15}_{-24}$	$5.8027^{+0.0020}_{-0.0017}$	$-1.8712^{+0.0075}_{-0.0081}$	$3.5662 \pm 0.0184$	$0.024 \pm 0.004$	ADS + Global (NLTE + LTE metals)
	$28\,704 \pm 7$	$5.8177^{+0.0010}_{-0.0012}$	$-1.8720^{+0.0024}_{-0.0060}$	-	-	ADS + Global (NLTE metals)
	$28\,845 \pm 9$	$5.8051^{+0.0012}_{-0.0022}$	$-1.8656^{+0.0046}_{-0.0049}$	-	-	ADS + Global
	$29\,741 \pm 303$	$5.725 \pm 0.025$	$-1.938 \pm 0.066$	-	-	ADS + SPAS
	$30\,001 \pm 408$	$5.808 \pm 0.098$	$-1.915 \pm 0.070$	-	-	LTE + SPAS
	-	-	-	-	-	TLUSTY/SYNSPEC + SPAS
	$28\,959 \pm 33$	$5.749 \pm 0.005$	$-1.851 \pm 0.017$	-	-	ADS + FITPROF
	$29\,734 \pm 33$	$5.678 \pm 0.006$	$-1.836 \pm 0.018$	-	-	LTE + FITPROF
	-	-	-	-	-	TLUSTY/SYNSPEC + FITPROF
	$28\,700 \pm 100$	$5.61 \pm 0.01$	$-2.09 \pm 0.02$	-	-	[1]
$28\,000 \pm 1100$	$5.55 \pm 0.14$	$-2.03 \pm 0.10$	-	-	[3]	

Table A.3.: Table A.1 continued.

Object	$T_{\text{eff}}$ [K]	$\log(g[\text{cm s}^{-2}])$	$\log n(\text{He})$	$\theta$ [ $10^{-11}$ rad]	$E(44 - 55)$ [mag]	Comments/Ref.
PG 1136-003 <sup>b</sup>	30 690 ± 40	5.613 <sup>+0.008</sup> <sub>-0.006</sub>	-3.62 ± 0.08	0.7320 ± 0.0038	0.012 ± 0.004	ADS + Global (NLTE + LTE metals)
	30 840 <sup>+40</sup> <sub>-60</sub>	5.598 <sup>+0.008</sup> <sub>-0.006</sub>	-3.65 <sup>+0.05</sup> <sub>-0.06</sub>	-	-	ADS + Global (NLTE metals)
	30 860 <sup>+30</sup> <sub>-50</sub>	5.597 <sup>+0.006</sup> <sub>-0.005</sub>	-3.71 ± 0.06	-	-	ADS + Global
	31 299 ± 88	5.593 ± 0.014	-3.905 ± 0.188	-	-	ADS + SPAS
	31 269 ± 76	5.495 ± 0.015	-3.808 ± 0.147	-	-	LTE + SPAS
	32 201 ± 178	5.562 ± 0.026	-3.868 ± 0.143	-	-	TLUSTY/SYNSPEC + SPAS
	30 861 ± 69	5.603 ± 0.010	-3.873 ± 0.028	-	-	ADS + FITPROF
	31 171 ± 58	5.535 ± 0.011	-3.970 ± 0.022	-	-	LTE + FITPROF
	32 019 ± 61	5.558 ± 0.011	-3.712 ± 0.042	-	-	TLUSTY/SYNSPEC + FITPROF
	31 200 ± 600	5.54 ± 0.09	-3.00	-	-	[4]
	GALEX J080510.9-105834 <sup>bcd</sup>	20 915 <sup>+10</sup> <sub>-15</sub>	5.6667 <sup>+0.0015</sup> <sub>-0.0016</sub>	-4.555 <sup>+0.026</sup> <sub>-0.025</sub>	2.9410 ± 0.0152	0.030 ± 0.004
21 000.0 <sup>+0.6</sup> <sub>-1.9</sub>		5.6478 <sup>+0.0010</sup> <sub>-0.0019</sub>	-4.604 <sup>+0.029</sup> <sub>-0.044</sub>	-	-	ADS + Global (NLTE metals)
20 942 <sup>+12</sup> <sub>-11</sub>		5.6599 <sup>+0.0014</sup> <sub>-0.0012</sub>	-4.540 <sup>+0.021</sup> <sub>-0.023</sub>	-	-	ADS + Global
21 493 ± 1819		5.637 ± 0.152	-4.615 ± 0.117	-	-	ADS + SPAS
20 343 ± 2400		5.588 ± 0.279	≤ -4.00	-	-	LTE + SPAS
-		-	-	-	-	TLUSTY/SYNSPEC + SPAS
21 315 ± 22		5.682 ± 0.003	-4.639 ± 0.049	-	-	ADS + FITPROF
21 255 ± 24		5.578 ± 0.003	≤ -4.00	-	-	LTE + FITPROF
-		-	-	-	-	TLUSTY/SYNSPEC + FITPROF
22 320 <sup>+330</sup> <sub>-280</sub>		5.68 <sup>+0.03</sup> <sub>-0.06</sub>	≤ -3.44	-	-	[2]
PG 1505+074		40 654 ± 26	5.6192 <sup>+0.0025</sup> <sub>-0.0021</sub>	-3.194 <sup>+0.011</sup> <sub>-0.012</sub>	1.5311 ± 0.0079	0.031 ± 0.005
	40 769 <sup>+38</sup> <sub>-30</sub>	5.6094 <sup>+0.0032</sup> <sub>-0.0026</sub>	-3.235 <sup>+0.015</sup> <sub>-0.014</sub>	-	-	ADS + Global (NLTE metals)
	40 770 ± 40	5.5943 <sup>+0.0029</sup> <sub>-0.0033</sub>	-3.253 <sup>+0.015</sup> <sub>-0.013</sub>	-	-	ADS + Global
	41 121 ± 764	5.561 ± 0.053	-3.315 ± 0.063	-	-	ADS + SPAS
	38 914 ± 303	5.534 ± 0.092	≤ -3.00	-	-	LTE + SPAS
	40 083 ± 446	5.533 ± 0.081	-3.297 ± 0.046	-	-	TLUSTY/SYNSPEC + SPAS
	40 242 ± 85	5.599 ± 0.007	-3.274 ± 0.047	-	-	ADS + FITPROF
	38 464 ± 58	5.491 ± 0.006	≤ -3.00	-	-	LTE + FITPROF
	38 998 ± 165	5.571 ± 0.015	-3.339 ± 0.055	-	-	TLUSTY/SYNSPEC + FITPROF
	37 100 ± 500	5.39 ± 0.05	-2.69 ± 0.10	-	-	[3]
	EC 13047-3049	38 929 <sup>+24</sup> <sub>-38</sub>	5.5500 <sup>+0.0016</sup> <sub>-0.0039</sub>	-3.041 ± 0.012	1.3490 ± 0.0070	0.052 ± 0.004
39 050 ± 40		5.5418 ± 0.0029	-3.088 <sup>+0.014</sup> <sub>-0.015</sub>	-	-	ADS + Global (NLTE metals)
38 970 ± 40		5.5086 <sup>+0.0034</sup> <sub>-0.0027</sub>	-3.138 <sup>+0.016</sup> <sub>-0.015</sub>	-	-	ADS + Global
39 163 ± 155		5.508 ± 0.010	-3.165 ± 0.057	-	-	ADS + SPAS
37 486 ± 150		5.439 ± 0.022	-2.916 ± 0.032	-	-	LTE + SPAS
38 634 ± 209		5.434 ± 0.039	-3.163 ± 0.054	-	-	TLUSTY/SYNSPEC + SPAS
39 183 ± 73		5.547 ± 0.006	-3.120 ± 0.028	-	-	ADS + FITPROF
36 835 ± 57		5.438 ± 0.007	-2.818 ± 0.033	-	-	LTE + FITPROF
37 961 ± 128		5.487 ± 0.013	-3.098 ± 0.024	-	-	TLUSTY/SYNSPEC + FITPROF
34 700 ± 1100		5.35 ± 0.14	-2.57 ± 0.10	-	-	[3]

Table A.4.: Table A.1 continued.

Object	$T_{\text{eff}}$ [K]	$\log(g[\text{cm s}^{-2}])$	$\log n(\text{He})$	$\theta$ [ $10^{-11}$ rad]	$E(44 - 55)$ [mag]	Comments/Ref.	
HD 149382	$35\,000^{+14}_{-11}$	$5.9217 \pm 0.0020$	$-1.4401^{+0.0019}_{-0.0022}$	$9.5719 \pm 0.0493^e, 8.6696 \pm 0.0447^f$	$0.081 \pm 0.008^e, 0.039 \pm 0.005^f$	ADS + Global (NLTE + LTE metals)	
	$35\,169^{+15}_{-17}$	$5.9024 \pm 0.0026$	$-1.4346^{+0.0027}_{-0.0030}$	-	-	ADS + Global (NLTE metals)	
	$35\,094^{+23}_{-15}$	$5.9157^{+0.0018}_{-0.0027}$	$-1.4540^{+0.0026}_{-0.0020}$	-	-	ADS + Global	
	$35\,338 \pm 404$	$5.938 \pm 0.056$	$-1.515 \pm 0.110$	-	-	ADS + SPAS	
	$34\,822 \pm 187$	$5.865 \pm 0.043$	$-1.409 \pm 0.066$	-	-	LTE + SPAS	
	$35\,237 \pm 499$	$5.871 \pm 0.059$	$-1.388 \pm 0.103$	-	-	TLUSTY/SYNSPEC + SPAS	
	$35\,171 \pm 42$	$5.884 \pm 0.006$	$-1.451 \pm 0.007$	-	-	ADS + FITPROF	
	$34\,673 \pm 30$	$5.843 \pm 0.006$	$-1.403 \pm 0.008$	-	-	LTE + FITPROF	
	$35\,454 \pm 30$	$5.831 \pm 0.006$	$-1.378 \pm 0.007$	-	-	TLUSTY/SYNSPEC + FITPROF	
	$35\,500 \pm 500$	$5.80 \pm 0.05$	$-1.44 \pm 0.01$	-	-	[5]	
	[CW83] 0825+15 <sup>a</sup>	$38\,375^{+23}_{-20}$	$5.9913^{+0.0030}_{-0.0036}$	$-0.7734^{+0.0019}_{-0.0016}$	$2.1577 \pm 0.0112$	$0.020 \pm 0.005$	ADS + Global (NLTE + LTE metals)
		$38\,297^{+27}_{-20}$	$5.980^{+0.005}_{-0.003}$	$-0.7758^{+0.0019}_{-0.0021}$	-	-	ADS + Global (NLTE metals)
		$38\,394^{+26}_{-23}$	$5.981^{+0.005}_{-0.004}$	$-0.7714^{+0.0015}_{-0.0014}$	-	-	ADS + Global
$38\,731 \pm 96$		$5.888 \pm 0.096$	$-0.761 \pm 0.147$	-	-	ADS + SPAS	
$38\,714 \pm 249$		$6.049 \pm 0.107$	$-0.610 \pm 0.112$	-	-	LTE + SPAS	
$39\,071 \pm 138$		$5.912 \pm 0.033$	$-0.543 \pm 0.035$	-	-	TLUSTY/SYNSPEC + SPAS	
$38\,613 \pm 66$		$5.946 \pm 0.015$	$-0.708 \pm 0.008$	-	-	ADS + FITPROF	
$39\,068 \pm 67$		$5.979 \pm 0.017$	$-0.540 \pm 0.028$	-	-	LTE + FITPROF	
$39\,382 \pm 76$		$5.826 \pm 0.016$	$-0.576 \pm 0.010$	-	-	TLUSTY/SYNSPEC + FITPROF	
$38\,900 \pm 270$		$5.97 \pm 0.11$	$-0.57 \pm 0.01$	-	-	[6]	
[CW83] 0512-08	$37\,411^{+21}_{-24}$	$5.963 \pm 0.004$	$-0.9051^{+0.0019}_{-0.0018}$	$2.8451 \pm 0.0147$	$0.038 \pm 0.004$	ADS + Global (NLTE + LTE metals)	
	$37\,421^{+25}_{-26}$	$5.967 \pm 0.004$	$-0.8963 \pm 0.0020$	-	-	ADS + Global (NLTE metals)	
	$37\,206^{+28}_{-24}$	$5.959 \pm 0.004$	$-0.9113 \pm 0.0020$	-	-	ADS + Global	
	$38\,239 \pm 103$	$5.935 \pm 0.017$	$-0.935 \pm 0.093$	-	-	ADS + SPAS	
	$38\,311 \pm 422$	$5.860 \pm 0.054$	$-0.936 \pm 0.098$	-	-	LTE + SPAS	
	$38\,049 \pm 208$	$5.820 \pm 0.056$	$-0.816 \pm 0.037$	-	-	TLUSTY/SYNSPEC + SPAS	
	$37\,375 \pm 110$	$5.957 \pm 0.018$	$-0.818 \pm 0.009$	-	-	ADS + FITPROF	
	$37\,815 \pm 93$	$5.872 \pm 0.018$	$-0.748 \pm 0.020$	-	-	LTE + FITPROF	
	$39\,162 \pm 114$	$5.818 \pm 0.018$	$-0.728 \pm 0.011$	-	-	TLUSTY/SYNSPEC + FITPROF	
	$38\,400 \pm 1100$	$5.77 \pm 0.14$	$-0.73 \pm 0.10$	-	-	[3]	
GALEX J075807.5-043203	-	-	-	-	-	ADS + Global (NLTE + LTE metals)	
	-	-	-	-	-	ADS + Global (NLTE metals)	
	-	-	-	-	-	ADS + Global	
	-	-	-	-	-	ADS + SPAS	
	-	-	-	-	-	LTE + SPAS	
	$41\,136 \pm 72$	$5.734 \pm 0.026$	$0.698 \pm 0.019$	-	-	TLUSTY/SYNSPEC + SPAS	
-	-	-	-	-	ADS + FITPROF		
$41\,721 \pm 86$	$5.697 \pm 0.032$	$0.847 \pm 0.065$	$1.1043 \pm 0.0058$	$0.012 \pm 0.004$	LTE + FITPROF		
$41\,360^{+530}_{-220}$	$5.85^{+0.26}_{-0.06}$	$0.54^{+0.49}_{-0.04}$	-	-	TLUSTY/SYNSPEC + FITPROF		
						[2]	

Table A.5.: Table A.1 continued.

Object	$T_{\text{eff}}$ [K]	$\log(g[\text{cm s}^{-2}])$	$\log n(\text{He})$	$\theta$ [ $10^{-11}$ rad]	$E(44 - 55)$ [mag]	Comments/Ref.
GALEX J042034.8+012041	-	-	-	-	-	ADS + Global (NLTE + LTE metals)
	-	-	-	-	-	ADS + Global (NLTE metals)
	-	-	-	-	-	ADS + Global
	-	-	-	-	-	ADS + SPAS
	-	-	-	-	-	LTE + SPAS
	$44\,310 \pm 246$	$5.664 \pm 0.032$	$\geq 4.00$	-	-	TLUSTY/SYNSPEC + SPAS
	-	-	-	-	-	ADS + FITPROF
$43\,932 \pm 138$	$5.633 \pm 0.026$	$\geq 4.00$	$1.5488 \pm 0.0084$	$0.034 \pm 0.008$	LTE + FITPROF	
$46\,050^{+910}_{-510}$	$5.97^{+0.16}_{-0.11}$	$0.97^{+0.12}_{-0.22}$	-	-	TLUSTY/SYNSPEC + FITPROF	
						[2]
HZ 1	-	-	-	-	-	ADS + Global (NLTE + LTE metals)
	-	-	-	-	-	ADS + Global (NLTE metals)
	-	-	-	-	-	ADS + Global
	-	-	-	-	-	ADS + SPAS
	-	-	-	-	-	LTE + SPAS
	$40\,990 \pm 189$	$5.752 \pm 0.053$	$2.845 \pm 0.083$	-	-	TLUSTY/SYNSPEC + SPAS
	-	-	-	-	-	ADS + FITPROF
$40\,598 \pm 53$	$5.699 \pm 0.024$	$2.762 \pm 0.119$	$2.0230 \pm 0.0105$	$0.247 \pm 0.005$	LTE + FITPROF	
$40\,660 \pm 600$	$5.60 \pm 0.10$	$2.90 \pm 0.30$	-	-	TLUSTY/SYNSPEC + FITPROF	
$40\,700 \pm 1200$	$5.78 \pm 0.25$	$2.50 \pm 0.37$	-	-	[7]	
						[7]
GALEX J095256.6-371940 <sup>c</sup>	-	-	-	-	-	ADS + Global (NLTE + LTE metals)
	-	-	-	-	-	ADS + Global (NLTE metals)
	-	-	-	-	-	ADS + Global
	-	-	-	-	-	ADS + SPAS
	-	-	-	-	-	LTE + SPAS
	$43\,930 \pm 257$	$5.470 \pm 0.028$	$\geq 4.00$	-	-	TLUSTY/SYNSPEC + SPAS
-	-	-	-	-	ADS + FITPROF	
$43\,634 \pm 144$	$5.562 \pm 0.027$	$\geq 4.00$	$1.0257 \pm 0.0056$	$0.038 \pm 0.007$	LTE + FITPROF	
$44\,450 \pm 250$	$5.50 \pm 0.10$	$\geq 3.00$	-	-	TLUSTY/SYNSPEC + FITPROF	
						[7]
PG 0314+146	-	-	-	-	-	ADS + Global (NLTE + LTE metals)
	-	-	-	-	-	ADS + Global (NLTE metals)
	-	-	-	-	-	ADS + Global
	-	-	-	-	-	ADS + SPAS
	-	-	-	-	-	LTE + SPAS
	$46\,569 \pm 382^g$	$5.675 \pm 0.039^g$	$\geq 4.00^g$	-	-	TLUSTY/SYNSPEC + SPAS
	$47\,094 \pm 510^h$	$5.698 \pm 0.040^h$	$\geq 4.00^h$	-	-	TLUSTY/SYNSPEC + SPAS
	-	-	-	-	-	ADS + FITPROF
	-	-	-	-	-	LTE + FITPROF
$46\,602 \pm 194^g$	$5.693 \pm 0.022^g$	$\geq 4.00^g$	$1.6788 \pm 0.0094$	$0.171 \pm 0.008$	TLUSTY/SYNSPEC + FITPROF	
$46\,447 \pm 190^h$	$5.662 \pm 0.018^h$	$\geq 4.00^h$	$1.6788 \pm 0.0093$	$0.171 \pm 0.008$	TLUSTY/SYNSPEC + FITPROF	
$47\,520^{+1030}_{-820}$	$5.96^{+0.15}_{-0.19}$	$0.90^{+0.17}_{-0.21}$	-	-	TLUSTY/SYNSPEC + FITPROF	
						[2]

Table A.6.: Same as Table A.1, but showing the effective temperatures  $T_{\text{eff}}$ , the surface gravities  $\log(g)$ , the helium abundances  $\log n(\text{He}) := \log n(^4\text{He} + ^3\text{He})$ , the angular diameters  $\theta$ , and the monochromatic color excesses  $E(44 - 55)$  of the program stars, which are analyzed by means of high-resolution data from FEROS, FOCES, HIRES, and HRS. The natures of the individual program stars can be found in Tables 8.4 and 8.5.

Object	$T_{\text{eff}}$ [K]	$\log(g[\text{cm s}^{-2}])$	$\log n(\text{He})$	$\theta$ [ $10^{-11}$ rad]	$E(44 - 55)$ [mag]	Comments/Ref.
PHL 25	$18\,440^{+60}_{-110}$	$4.736^{+0.010}_{-0.016}$	$-2.2164^{+0.0365}_{-0.0328}$	$3.4586^{+0.0187}_{-0.0206}$	$0.046 \pm 0.004$	ADS + Global (NLTE metals)
	$18\,860^{+100}_{-70}$	$4.802^{+0.014}_{-0.009}$	$-2.2639^{+0.0388}_{-0.0397}$	-	-	ADS + Global
	$19\,989 \pm 203$	$4.789 \pm 0.022$	$-2.448 \pm 0.051$	-	-	ADS + SPAS
	$19\,000 \pm 278$	$4.706 \pm 0.033$	$-2.384 \pm 0.044$	-	-	LTE + SPAS
	-	-	-	-	-	TLUSTY/SYNSPEC + SPAS
	$19\,108 \pm 231$	$4.707 \pm 0.029$	$-2.346 \pm 0.048$	-	-	ADS + FITPROF
	$19\,252 \pm 252$	$4.666 \pm 0.032$	$-2.331 \pm 0.054$	-	-	LTE + FITPROF
	-	-	-	-	-	TLUSTY/SYNSPEC + FITPROF
	$19\,500 \pm 100$	$4.77^{+0.01}_{-0.02}$	$-2.42 \pm 0.03$	-	-	[1]
	19 500	5.00	-2.00	-	-	[2]
PHL 382 <sup>a</sup>	$17\,195^{+26}_{-28}$	$4.034^{+0.004}_{-0.006}$	$-2.2669^{+0.0195}_{-0.0183}$	$5.2469^{+0.0273}_{-0.0274}$	$0.026 \pm 0.004$	ADS + Global (NLTE metals)
	$17\,030^{+50}_{-40}$	$3.972^{+0.007}_{-0.004}$	$-2.3920^{+0.0140}_{-0.0138}$	-	-	ADS + Global
	$17\,358 \pm 589$	$3.874 \pm 0.040$	$-2.60^e$	-	-	ADS + SPAS
	$17\,601 \pm 425$	$3.887 \pm 0.046$	$-2.60^e$	-	-	LTE + SPAS
	-	-	-	-	-	TLUSTY/SYNSPEC + SPAS
	$17\,238 \pm 100$	$3.970 \pm 0.013$	$-2.60^e$	-	-	ADS + FITPROF
	$17\,293 \pm 139$	$3.925 \pm 0.017$	$-2.60^e$	-	-	LTE + FITPROF
	-	-	-	-	-	TLUSTY/SYNSPEC + FITPROF
	$17\,600 \pm 100$	$3.92 \pm 0.01$	$-2.54 \pm 0.02$	-	-	[1]
	18 200	4.10	-2.20	-	-	[2]

**Notes:** For the results of this work,  $1\sigma$  statistical single parameter errors are given for  $T_{\text{eff}}$ ,  $\log(g)$ ,  $\log n(\text{He})$ , and  $E(44 - 55)$ . If SPAS is used, the uncertainties on  $T_{\text{eff}}$ ,  $\log(g)$ , and  $\log n(\text{He})$  result from bootstrapping, whereas in all other cases the corresponding errors are derived from  $\chi^2$ -statistics (see Sect. 7.1.2). The latter also applies to all listed  $E(44 - 55)$  values (see Sect. 7.2.3). The listed uncertainties on  $\theta$  result from Eq. (7.17), whereby the total uncertainties on  $T_{\text{eff}}$  derived from spectroscopy (combining the individual listed  $1\sigma$  statistical errors and the global systematic ones from Sect. 9.2.7) are considered. Hence,  $\Delta T_{\text{eff,model}} = \Delta T_{\text{eff,spectr.}} = \sqrt{[\Delta T_{\text{eff,spectr.,stat.}}]^2 + [(0.550/100) \cdot T_{\text{eff}}]^2 + [(0.869/100) \cdot T_{\text{eff}}]^2}$  is used in Eq. (7.17) in order to calculate the individual values of  $\Delta\theta$ .

(a) Rotating star.

(b) Pulsating star.

(c) The star is most likely a pre-ELM. For further information, see Sect. 12.2.

(d) RV-variable star.

(e)  $\log n(\text{He})$  not measurable due to stratification effects. Therefore, it is fixed.

**References:** (1) Schneider et al. (2018); (2) Heber & Langhans (1986); (3) Geier et al. (2013a); (4) Németh et al. (2012); (5) Geier et al. (2013b); (6) Edelmann et al. (1999).

Table A.7.: Table A.6 continued.

Object	$T_{\text{eff}}$ [K]	$\log(g[\text{cm s}^{-2}])$	$\log n(\text{He})$	$\theta$ [ $10^{-11}$ rad]	$E(44 - 55)$ [mag]	Comments/Ref.
BD+48° 2721	$21\,040^{+80}_{-50}$	$4.879^{+0.009}_{-0.006}$	$-2.0614^{+0.0208}_{-0.0234}$	$5.9074^{+0.0324}_{-0.0312}$	$0.013 \pm 0.004$	ADS + Global (NLTE metals)
	$21\,110 \pm 60$	$4.876^{+0.007}_{-0.010}$	$-2.0723^{+0.0190}_{-0.0458}$	-	-	ADS + Global
	$20\,456 \pm 1057$	$4.903 \pm 0.043$	$-2.314 \pm 0.126$	-	-	ADS + SPAS
	$20\,390 \pm 1072$	$4.930 \pm 0.088$	$-2.208 \pm 0.092$	-	-	LTE + SPAS
	-	-	-	-	-	TLUSTY/SYNSPEC + SPAS
	$21\,000 \pm 184$	$4.932 \pm 0.022$	$-2.110 \pm 0.022$	-	-	ADS + FITPROF
	$21\,086 \pm 103$	$4.940 \pm 0.019$	$-2.333 \pm 0.021$	-	-	LTE + FITPROF
	-	-	-	-	-	TLUSTY/SYNSPEC + FITPROF
	$20\,700^{+100}_{-200}$	$4.81 \pm 0.02$	$-2.51^{+0.08}_{-0.10}$	-	-	[1]
	$24\,800 \pm 1100$	$5.38 \pm 0.14$	$-2.23 \pm 0.10$	-	-	[3]
PG 0342+026 <sup>b</sup>	$24\,277^{+13}_{-11}$	$5.3669^{+0.0011}_{-0.0042}$	$-2.653^{+0.005}_{-0.003}$	$5.1677^{+0.0267}_{-0.0266}$	$0.100 \pm 0.005$	ADS + Global (NLTE metals)
	$23\,640^{+50}_{-40}$	$5.355 \pm 0.005$	$-2.667^{+0.005}_{-0.004}$	-	-	ADS + Global
	$23\,311 \pm 773$	$5.343 \pm 0.053$	$-2.609 \pm 0.025$	-	-	ADS + SPAS
	$23\,858 \pm 248$	$5.412 \pm 0.041$	$-2.69 \pm 0.02$	-	-	LTE + SPAS
	-	-	-	-	-	TLUSTY/SYNSPEC + SPAS
	$23\,959 \pm 89$	$5.481 \pm 0.012$	$-2.700 \pm 0.014$	-	-	ADS + FITPROF
	$25\,018 \pm 126$	$5.434 \pm 0.014$	$-2.719 \pm 0.016$	-	-	LTE + FITPROF
	-	-	-	-	-	TLUSTY/SYNSPEC + FITPROF
$26\,000 \pm 1100$	$5.59 \pm 0.14$	$-2.69 \pm 0.10$	-	-	[3]	
HD 4539 <sup>b</sup>	$23\,420^{+60}_{-40}$	$5.253 \pm 0.006$	$-2.2937^{+0.0048}_{-0.0049}$	$6.3358^{+0.0336}_{-0.0331}$	$\leq 0.0010$	ADS + Global (NLTE metals)
	$23\,250 \pm 60$	$5.266^{+0.007}_{-0.006}$	$-2.2651 \pm 0.0049$	-	-	ADS + Global
	$23\,356 \pm 211$	$5.294 \pm 0.019$	$-2.273 \pm 0.013$	-	-	ADS + SPAS
	$23\,125 \pm 258$	$5.259 \pm 0.022$	$-2.235 \pm 0.043$	-	-	LTE + SPAS
	-	-	-	-	-	TLUSTY/SYNSPEC + SPAS
	$23\,656 \pm 123$	$5.292 \pm 0.015$	$-2.327 \pm 0.023$	-	-	ADS + FITPROF
	$23\,296 \pm 156$	$5.173 \pm 0.017$	$-2.339 \pm 0.026$	-	-	LTE + FITPROF
	-	-	-	-	-	TLUSTY/SYNSPEC + FITPROF
$23\,200 \pm 100$	$5.20 \pm 0.01$	$-2.27 \pm 0.01$	-	-	[1]	
$24\,650^{+590}_{-200}$	$5.38^{+0.03}_{-0.05}$	$-2.42^{+0.20}_{-0.07}$	-	-	[4]	
CD-35° 15910 <sup>b</sup>	$26\,770 \pm 50$	$5.410^{+0.009}_{-0.007}$	$-2.954^{+0.008}_{-0.009}$	$4.1134 \pm 0.0215$	$\leq 0.0018$	ADS + Global (NLTE metals)
	$26\,630^{+50}_{-70}$	$5.369 \pm 0.009$	$-2.948^{+0.009}_{-0.008}$	-	-	ADS + Global
	$27\,556 \pm 167$	$5.378 \pm 0.014$	$-2.953 \pm 0.020$	-	-	ADS + SPAS
	$27\,206 \pm 84$	$5.287 \pm 0.013$	$-2.938 \pm 0.021$	-	-	LTE + SPAS
	-	-	-	-	-	TLUSTY/SYNSPEC + SPAS
	$26\,693 \pm 96$	$5.403 \pm 0.016$	$-3.023 \pm 0.041$	-	-	ADS + FITPROF
	$27\,554 \pm 139$	$5.316 \pm 0.018$	$-2.907 \pm 0.047$	-	-	LTE + FITPROF
	-	-	-	-	-	TLUSTY/SYNSPEC + FITPROF
$27\,200 \pm 100$	$5.39 \pm 0.01$	$-2.94 \pm 0.01$	-	-	[1]	
$27\,000 \pm 1100$	$5.32 \pm 0.14$	$-2.90 \pm 0.10$	-	-	[3]	

Table A.8.: Table A.6 continued.

Object	$T_{\text{eff}}$ [K]	$\log(g[\text{cm s}^{-2}])$	$\log n(\text{He})$	$\theta$ [ $10^{-11}$ rad]	$E(44 - 55)$ [mag]	Comments/Ref.
EC 03263-6403	$28\,360 \pm 120$	$5.437^{+0.040}_{-0.038}$	$-2.7645^{+0.0225}_{-0.0265}$	$1.3493 \pm 0.0076$	$0.058 \pm 0.004$	ADS + Global (NLTE metals)
	$28\,150^{+140}_{-170}$	$5.449^{+0.042}_{-0.033}$	$-2.7148^{+0.0217}_{-0.0207}$	-	-	ADS + Global
	$28\,206 \pm 336$	$5.353 \pm 0.031$	$-2.648 \pm 0.045$	-	-	ADS + SPAS
	$29\,059 \pm 304$	$5.391 \pm 0.037$	$-2.676 \pm 0.040$	-	-	LTE + SPAS
	-	-	-	-	-	TLUSTY/SYNSPEC + SPAS
	$28\,298 \pm 369$	$5.426 \pm 0.056$	$-2.574 \pm 0.068$	-	-	ADS + FITPROF
	$28\,363 \pm 492$	$5.297 \pm 0.061$	$-2.529 \pm 0.068$	-	-	LTE + FITPROF
	-	-	-	-	-	TLUSTY/SYNSPEC + FITPROF
	$29\,000 \pm 200$	$5.21 \pm 0.02$	$-2.84 \pm 0.03$	-	-	[1]
	$29\,300 \pm 1100$	$5.48 \pm 0.14$	$-2.51 \pm 0.10$	-	-	[3]
EC 03591-3232	$28\,800 \pm 40$	$5.766^{+0.006}_{-0.005}$	$-1.9401 \pm 0.0160$	$3.5604 \pm 0.0185$	$0.025 \pm 0.004$	ADS + Global (NLTE metals)
	$29\,370^{+50}_{-40}$	$5.803^{+0.006}_{-0.005}$	$-1.9548^{+0.0180}_{-0.0146}$	-	-	ADS + Global
	$29\,445 \pm 108$	$5.670 \pm 0.015$	$-1.995 \pm 0.027$	-	-	ADS + SPAS
	$29\,842 \pm 167$	$5.782 \pm 0.019$	$-2.031 \pm 0.039$	-	-	LTE + SPAS
	-	-	-	-	-	TLUSTY/SYNSPEC + SPAS
	$29\,210 \pm 107$	$5.709 \pm 0.016$	$-1.967 \pm 0.024$	-	-	ADS + FITPROF
	$29\,630 \pm 110$	$5.632 \pm 0.016$	$-1.956 \pm 0.024$	-	-	LTE + FITPROF
	-	-	-	-	-	TLUSTY/SYNSPEC + FITPROF
	$28\,700 \pm 100$	$5.61 \pm 0.01$	$-2.09 \pm 0.02$	-	-	[1]
	$28\,000 \pm 1100$	$5.55 \pm 0.14$	$-2.03 \pm 0.10$	-	-	[3]
EC 12234-2607	$28\,490 \pm 80$	$5.668^{+0.027}_{-0.022}$	$-1.2559^{+0.0530}_{-0.0714}$	$1.1652 \pm 0.0063$	$0.075 \pm 0.005$	ADS + Global (NLTE metals)
	$28\,370^{+130}_{-80}$	$5.686^{+0.020}_{-0.011}$	$-1.2384^{+0.0699}_{-0.0830}$	-	-	ADS + Global
	$29\,889 \pm 179$	$5.677 \pm 0.022$	$-1.386 \pm 0.015$	-	-	ADS + SPAS
	$29\,508 \pm 220$	$5.568 \pm 0.025$	$-1.452 \pm 0.022$	-	-	LTE + SPAS
	-	-	-	-	-	TLUSTY/SYNSPEC + SPAS
	$28\,206 \pm 290$	$5.594 \pm 0.041$	$-1.310 \pm 0.026$	-	-	ADS + FITPROF
	$28\,462 \pm 334$	$5.521 \pm 0.044$	$-1.319 \pm 0.028$	-	-	LTE + FITPROF
	-	-	-	-	-	TLUSTY/SYNSPEC + FITPROF
	$28\,900 \pm 100$	$5.62 \pm 0.02$	$-1.53^{+0.03}_{-0.02}$	-	-	[1]
	$28\,000 \pm 1100$	$5.58 \pm 0.14$	$-1.58 \pm 0.10$	-	-	[3]
EC 14338-1445	$27\,620^{+60}_{-70}$	$5.518^{+0.011}_{-0.013}$	$-3.0183^{+0.0244}_{-0.0215}$	$1.4155 \pm 0.0075$	$0.1167 \pm 0.0030$	ADS + Global (NLTE metals)
	$27\,760^{+120}_{-70}$	$5.553^{+0.023}_{-0.012}$	$-2.9441^{+0.0309}_{-0.0275}$	-	-	ADS + Global
	$28\,643 \pm 114$	$5.563 \pm 0.022$	$-2.862 \pm 0.026$	-	-	ADS + SPAS
	$27\,653 \pm 153$	$5.412 \pm 0.020$	$-2.941 \pm 0.029$	-	-	LTE + SPAS
	-	-	-	-	-	TLUSTY/SYNSPEC + SPAS
	$28\,023 \pm 197$	$5.523 \pm 0.032$	$-2.882 \pm 0.049$	-	-	ADS + FITPROF
	$27\,986 \pm 274$	$5.417 \pm 0.035$	$-2.807 \pm 0.052$	-	-	LTE + FITPROF
	-	-	-	-	-	TLUSTY/SYNSPEC + FITPROF
	$27\,900 \pm 100$	$5.46^{+0.01}_{-0.02}$	$-3.01 \pm 0.03$	-	-	[1]
	$27\,700 \pm 1100$	$5.54 \pm 0.14$	$-2.82 \pm 0.10$	-	-	[3]

Table A.9.: Table A.6 continued.

Object	$T_{\text{eff}}$ [K]	$\log(g[\text{cm s}^{-2}])$	$\log n(\text{He})$	$\theta$ [ $10^{-11}$ rad]	$E(44 - 55)$ [mag]	Comments/Ref.
Feige 38	$29\,557 \pm 29$	$5.660 \pm 0.005$	$-2.5899^{+0.0102}_{-0.0115}$	$1.5653 \pm 0.0081$	$0.057 \pm 0.004$	ADS + Global (NLTE metals)
	$29\,890^{+30}_{-40}$	$5.707^{+0.005}_{-0.007}$	$-2.5238^{+0.0066}_{-0.0103}$	-	-	ADS + Global
	$29\,898 \pm 661$	$5.709 \pm 0.020$	$-2.587 \pm 0.048$	-	-	ADS + SPAS
	$29\,663 \pm 226$	$5.693 \pm 0.027$	$-2.681 \pm 0.039$	-	-	LTE + SPAS
	-	-	-	-	-	TLUSTY/SYNSPEC + SPAS
	$29\,917 \pm 188$	$5.791 \pm 0.027$	$-2.474 \pm 0.031$	-	-	ADS + FITPROF
	$29\,940 \pm 212$	$5.696 \pm 0.030$	$-2.499 \pm 0.035$	-	-	LTE + FITPROF
	-	-	-	-	-	TLUSTY/SYNSPEC + FITPROF
	$28\,200 \pm 100$	$5.61 \pm 0.01$	$-2.70 \pm 0.03$	-	-	[1]
	$30\,600 \pm 500$	$5.83 \pm 0.05$	$-2.37 \pm 0.10$	-	-	[3]
PG 1710+490	$29\,180^{+50}_{-40}$	$5.818^{+0.008}_{-0.009}$	$-2.5326^{+0.0242}_{-0.0346}$	$1.6285 \pm 0.0085$	$0.024 \pm 0.005$	ADS + Global (NLTE metals)
	$29\,400 \pm 70$	$5.756^{+0.010}_{-0.014}$	$-2.4535^{+0.0324}_{-0.0377}$	-	-	ADS + Global
	$29\,637 \pm 218$	$5.847 \pm 0.053$	$-2.406 \pm 0.079$	-	-	ADS + SPAS
	$29\,724 \pm 158$	$5.782 \pm 0.047$	$-2.556 \pm 0.068$	-	-	LTE + SPAS
	-	-	-	-	-	TLUSTY/SYNSPEC + SPAS
	$29\,563 \pm 129$	$5.860 \pm 0.023$	$-2.482 \pm 0.047$	-	-	ADS + FITPROF
	$29\,832 \pm 140$	$5.786 \pm 0.025$	$-2.400 \pm 0.043$	-	-	LTE + FITPROF
	-	-	-	-	-	TLUSTY/SYNSPEC + FITPROF
	$29\,200 \pm 100$	$5.72 \pm 0.02$	$-2.66^{+0.02}_{-0.01}$	-	-	[1]
	$30\,600 \pm 500$	$5.66 \pm 0.05$	$-2.43 \pm 0.10$	-	-	[3]
SB 290 <sup>a</sup>	$26\,480^{+40}_{-60}$	$5.407^{+0.007}_{-0.008}$	$-2.4394^{+0.0160}_{-0.0199}$	$5.5847^{+0.0291}_{-0.0295}$	$0.045^{+0.008}_{-0.009}$	ADS + Global (NLTE metals)
	$26\,630^{+40}_{-50}$	$5.3994^{+0.0025}_{-0.0066}$	$-2.4380^{+0.0071}_{-0.0012}$	-	-	ADS + Global
	$26\,009 \pm 114$	$5.320 \pm 0.016$	$-2.551 \pm 0.018$	-	-	ADS + SPAS
	$25\,568 \pm 215$	$5.247 \pm 0.027$	$-2.610 \pm 0.014$	-	-	LTE + SPAS
	-	-	-	-	-	TLUSTY/SYNSPEC + SPAS
	$26\,501 \pm 98$	$5.364 \pm 0.014$	$-2.483 \pm 0.023$	-	-	ADS + FITPROF
	$25\,887 \pm 127$	$5.235 \pm 0.016$	$-2.478 \pm 0.023$	-	-	LTE + FITPROF
	-	-	-	-	-	TLUSTY/SYNSPEC + FITPROF
	$26\,600 \pm 100$	$5.42 \pm 0.01$	$-2.69 \pm 0.03$	-	-	[1]
	$26\,300 \pm 100$	$5.31 \pm 0.01$	$-2.52 \pm 0.08$	-	-	[5]
Feige 36 <sup>c,d</sup>	$28\,640^{+40}_{-70}$	$5.949^{+0.008}_{-0.010}$	$-2.1391^{+0.0178}_{-0.0181}$	$1.7378^{+0.0091}_{-0.0092}$	$0.022^{+0.006}_{-0.007}$	ADS + Global (NLTE metals)
	$28\,650 \pm 60$	$5.953^{+0.009}_{-0.010}$	$-2.1482^{+0.0301}_{-0.0310}$	-	-	ADS + Global
	$29\,255 \pm 79$	$5.968 \pm 0.015$	$-2.107 \pm 0.009$	-	-	ADS + SPAS
	$29\,069 \pm 111$	$5.891 \pm 0.015$	$-2.126 \pm 0.011$	-	-	LTE + SPAS
	-	-	-	-	-	TLUSTY/SYNSPEC + SPAS
	$28\,673 \pm 157$	$5.944 \pm 0.024$	$-2.129 \pm 0.019$	-	-	ADS + FITPROF
	$28\,925 \pm 204$	$5.949 \pm 0.027$	$-2.227 \pm 0.024$	-	-	LTE + FITPROF
	-	-	-	-	-	TLUSTY/SYNSPEC + FITPROF
	$29\,400 \pm 100$	$5.97 \pm 0.01$	$-2.18^{+0.03}_{-0.05}$	-	-	[1]
	$29\,800 \pm 100$	$5.97 \pm 0.02$	$-2.17 \pm 0.02$	-	-	[6]

Table A.10.: Same as Table A.1, but showing the effective temperatures  $T_{\text{eff}}$ , the surface gravities  $\log(g)$ , the helium abundances  $\log n(\text{He}) := \log n(^4\text{He} + ^3\text{He})$ , the angular diameters  $\theta$ , and the monochromatic color excesses  $E(44-55)$  of the program stars, which are analyzed by means of medium-resolution data from UVES. The natures of the individual program stars can be found in Table 8.6.

Object	$T_{\text{eff}}$ [K]	$\log(g[\text{cm s}^{-2}])$	$\log n(\text{He})$	$\theta$ [ $10^{-11}$ rad]	$E(44-55)$ [mag]	Comments/Ref.
HE 0929-0424 <sup>a</sup>	$28\,470^{+110}_{-100}$	$5.833^{+0.018}_{-0.017}$	$-2.0235^{+0.0419}_{-0.0551}$	$0.3758 \pm 0.0021$	$0.066 \pm 0.008$	ADS + Global (NLTE metals)
	$28\,640 \pm 120$	$5.7604^{+0.0221}_{-0.0001}$	$-2.0251^{+0.0545}_{-0.0680}$	-	-	ADS + Global
	$29\,195 \pm 87$	$5.770 \pm 0.011$	$-2.041 \pm 0.017$	-	-	ADS + SPAS
	$29\,705 \pm 126$	$5.698 \pm 0.015$	$-2.082 \pm 0.028$	-	-	LTE + SPAS
	-	-	-	-	-	TLUSTY/SYNSPEC + SPAS
	$28\,744 \pm 153$	$5.759 \pm 0.025$	$-2.020 \pm 0.038$	-	-	ADS + FITPROF
	$30\,050 \pm 157$	$5.691 \pm 0.026$	$-2.030 \pm 0.041$	-	-	LTE + FITPROF
	-	-	-	-	-	TLUSTY/SYNSPEC + FITPROF
	$29\,300 \pm 100$	$5.65 \pm 0.01$	$-1.95 \pm 0.03$	-	-	[1]
	$29\,602 \pm 529$	$5.69 \pm 0.07$	$-2.01 \pm 0.07$	-	-	[2]
HE 1047-0436 <sup>a</sup>	$29\,850^{+80}_{-70}$	$5.747^{+0.011}_{-0.012}$	$-2.3337^{+0.0490}_{-0.0485}$	$0.6095 \pm 0.0033$	$0.048 \pm 0.006$	ADS + Global (NLTE metals)
	$29\,890^{+100}_{-110}$	$5.798^{+0.011}_{-0.015}$	$-2.3414^{+0.0511}_{-0.0645}$	-	-	ADS + Global
	$30\,026 \pm 154$	$5.726 \pm 0.017$	$-2.344 \pm 0.022$	-	-	ADS + SPAS
	$30\,285 \pm 128$	$5.637 \pm 0.023$	$-2.485 \pm 0.021$	-	-	LTE + SPAS
	-	-	-	-	-	TLUSTY/SYNSPEC + SPAS
	$30\,228 \pm 100$	$5.721 \pm 0.017$	$-2.318 \pm 0.040$	-	-	ADS + FITPROF
	$30\,476 \pm 97$	$5.648 \pm 0.018$	$-2.321 \pm 0.040$	-	-	LTE + FITPROF
	-	-	-	-	-	TLUSTY/SYNSPEC + FITPROF
	$29\,800 \pm 100$	$5.65 \pm 0.01$	$-2.44 \pm 0.03$	-	-	[1]
	$30\,280 \pm 529$	$5.71 \pm 0.07$	$-2.35 \pm 0.07$	-	-	[2]
HD 149382	$34\,644^{+27}_{-16}$	$5.8375^{+0.0028}_{-0.0025}$	$-1.4368^{+0.0025}_{-0.0020}$	$9.6383^{+0.0498}_{-0.0497}$ , $8.7096^{+0.0450}_{-0.0449}$	$0.079 \pm 0.008$ <sup>b</sup> , $0.036 \pm 0.005$ <sup>c</sup>	ADS + Global (NLTE metals)
	$34\,574^{+31}_{-19}$	$5.8516^{+0.0043}_{-0.0025}$	$-1.461^{+0.004}_{-0.003}$	-	-	ADS + Global
	$34\,953 \pm 42$	$5.890 \pm 0.005$	$-1.465 \pm 0.006$	-	-	ADS + SPAS
	$34\,409 \pm 52$	$5.793 \pm 0.007$	$-1.431 \pm 0.039$	-	-	LTE + SPAS
	$35\,036 \pm 37$	$5.797 \pm 0.005$	$-1.386 \pm 0.005$	-	-	TLUSTY/SYNSPEC + SPAS
	$34\,231 \pm 55$	$5.880 \pm 0.007$	$-1.437 \pm 0.007$	-	-	ADS + FITPROF
	$34\,577 \pm 43$	$5.784 \pm 0.008$	$-1.401 \pm 0.008$	-	-	LTE + FITPROF
	$35\,564 \pm 42$	$5.786 \pm 0.007$	$-1.382 \pm 0.007$	-	-	TLUSTY/SYNSPEC + FITPROF
	$35\,500 \pm 500$	$5.80 \pm 0.05$	$-1.44 \pm 0.01$	-	-	[3]

**Notes:** For the results of this work,  $1\sigma$  statistical single parameter errors are given for  $T_{\text{eff}}$ ,  $\log(g)$ ,  $\log n(\text{He})$ , and  $E(44-55)$ . If SPAS is used, the uncertainties on  $T_{\text{eff}}$ ,  $\log(g)$ , and  $\log n(\text{He})$  result from bootstrapping, whereas in all other cases the corresponding errors are derived from  $\chi^2$ -statistics (see Sect. 7.1.2). The latter also applies to all listed  $E(44-55)$  values (see Sect. 7.2.3). The listed uncertainties on  $\theta$  result from Eq. (7.17), whereby the total uncertainties on  $T_{\text{eff}}$  derived from spectroscopy (combining the individual listed  $1\sigma$  statistical errors and the global systematic ones from Sect. 9.2.7) are considered. Hence,  $\Delta T_{\text{eff,model}} = \Delta T_{\text{eff,spectr.}} = \sqrt{[\Delta T_{\text{eff,spectr.,stat.}}]^2 + [(0.550/100) \cdot T_{\text{eff}}]^2 + [(0.869/100) \cdot T_{\text{eff}}]^2}$  is used in Eq. (7.17) in order to calculate the individual values of  $\Delta\theta$ .

(a) RV-variable star.

(b) Derived from the single SED fit.

(c) Derived from the binary SED fit.

**References:** (1) Schneider et al. (2018); (2) Lisker et al. (2005); (3) Geier et al. (2009).

Table A.11.: Same as Table A.1, but showing the effective temperatures  $T_{\text{eff}}$ , the surface gravities  $\log(g)$ , the helium abundances  $\log n(\text{He}) := \log n(^4\text{He} + ^3\text{He})$ , the angular diameters  $\theta$ , and the monochromatic color excesses  $E(44 - 55)$  of the program stars, which are analyzed by means of low-resolution data from CAFOS. The natures of the individual program stars can be found in Tables 8.7 and 8.8.

Object	$T_{\text{eff}}$ [K]	$\log(g[\text{cm s}^{-2}])$	$\log n(\text{He})$	$\theta$ [ $10^{-11}$ rad]	$E(44 - 55)$ [mag]	Comments/Ref.
HIP 67513	$10\,432^{+13}_{-7}$	$3.801^{+0.006}_{-0.004}$	$-1.396^{+0.034}_{-0.019}$	$6.5584^{+0.0340}_{-0.0338}$	$0.026 \pm 0.005$	ADS + Global
	$10\,920 \pm 379$	$3.945 \pm 0.184$	$-1.174 \pm 0.243$	-	-	ADS + SPAS
	$10\,829 \pm 591$	$3.831 \pm 0.311$	$-1.199 \pm 0.322$	-	-	LTE + SPAS
	-	-	-	-	-	TLUSTY/SYNSPEC + SPAS
	$10\,708 \pm 63$	$3.816 \pm 0.038$	$-1.329 \pm 0.075$	-	-	ADS + FITPROF
	$10\,490 \pm 75$	$3.789 \pm 0.027$	$-1.344 \pm 0.075$	-	-	LTE + FITPROF
	-	-	-	-	-	TLUSTY/SYNSPEC + FITPROF
17 500	5.00	$\leq -2.00$	-	-	[1]	
BD+49° 2226	$11\,770^{+40}_{-50}$	$4.578^{+0.020}_{-0.013}$	$-1.57^{+0.06}_{-0.08}$	$12.2236^{+0.0662}_{-0.0681}$	$0.057 \pm 0.005$	ADS + Global
	$12\,048 \pm 191$	$4.624 \pm 0.061$	$-1.629 \pm 0.363$	-	-	ADS + SPAS
	-	-	-	-	-	LTE + SPAS
	-	-	-	-	-	TLUSTY/SYNSPEC + SPAS
	$11\,321 \pm 52$	$4.571 \pm 0.025$	$-1.473 \pm 0.073$	-	-	ADS + FITPROF
	-	-	-	-	-	LTE + FITPROF
	-	-	-	-	-	TLUSTY/SYNSPEC + FITPROF
19 700	5.36	$\leq -2.00$	-	-	[1]	
FBS 1850+443	$24\,260^{+10}_{-70}$	$4.154^{+0.012}_{-0.008}$	$-1.099 \pm 0.013$	$2.7002^{+0.0139}_{-0.0145}$	$0.061 \pm 0.005$	ADS + Global
	$26\,094 \pm 539$	$4.144 \pm 0.091$	$-1.053 \pm 0.206$	-	-	ADS + SPAS
	-	-	-	-	-	LTE + SPAS
	-	-	-	-	-	TLUSTY/SYNSPEC + SPAS
	$24\,058 \pm 443$	$4.180 \pm 0.054$	$-1.108 \pm 0.029$	-	-	ADS + FITPROF
	-	-	-	-	-	LTE + FITPROF
-	-	-	-	-	TLUSTY/SYNSPEC + FITPROF	

**Notes:** For the results of this work,  $1\sigma$  statistical single parameter errors are given for  $T_{\text{eff}}$ ,  $\log(g)$ ,  $\log n(\text{He})$ , and  $E(44 - 55)$ . If SPAS is used, the uncertainties on  $T_{\text{eff}}$ ,  $\log(g)$ , and  $\log n(\text{He})$  result from bootstrapping, whereas in all other cases the corresponding errors are derived from  $\chi^2$ -statistics (see Sect. 7.1.2). The latter also applies to all listed  $E(44 - 55)$  values (see Sect. 7.2.3). The listed uncertainties on  $\theta$  result from Eq. (7.17), whereby the total uncertainties on  $T_{\text{eff}}$  derived from spectroscopy (combining the individual listed  $1\sigma$  statistical errors and the global systematic ones from Sect. 9.2.7) are considered. Hence,  $\Delta T_{\text{eff,model}} = \Delta T_{\text{eff,spectr.}} = \sqrt{[\Delta T_{\text{eff,spectr.,stat.}}]^2 + [(0.550/100) \cdot T_{\text{eff}}]^2 + [(0.869/100) \cdot T_{\text{eff}}]^2}$  is used in Eq. (7.17) in order to calculate the individual values of  $\Delta\theta$ .

- (a) Pulsating star.
- (b) The star could be/is most likely a pre-ELM (see Ch. 13 for details).
- (c) RV-variable star.
- (d)  $\log n(\text{He})$  not measurable. Therefore, it is fixed.

**References:** (1) Bixler et al. (1991); (2) Schneider et al. (2018); (3) Németh et al. (2012); (4) Østensen et al. (2010c); (5) Van Grootel et al. (2008); (6) Østensen (in prep.); (7) Geier et al. (2008); (8) Schindewolf et al. (2018).

Table A.12.: Table A.11 continued.

Object	$T_{\text{eff}}$ [K]	$\log(g[\text{cm s}^{-2}])$	$\log n(\text{He})$	$\theta$ [ $10^{-11}$ rad]	$E(44 - 55)$ [mag]	Comments/Ref.
FBS 2158+373	$13\,830 \pm 40$	$4.320 \pm 0.007$	$-1.040^{+0.018}_{-0.017}$	$4.4720 \pm 0.0239$	$0.107 \pm 0.005$	ADS + Global
	$14\,229 \pm 325$	$4.485 \pm 0.085$	$-1.219 \pm 0.349$	-	-	ADS + SPAS
	$13\,656 \pm 1378$	$4.198 \pm 0.403$	$-1.020 \pm 0.288$	-	-	LTE + SPAS
	-	-	-	-	-	TLUSTY/SYNSPEC + SPAS
	$13\,175 \pm 92$	$4.321 \pm 0.031$	$-1.086 \pm 0.040$	-	-	ADS + FITPROF
	$13\,631 \pm 63$	$4.251 \pm 0.028$	$-0.949 \pm 0.099$	-	-	LTE + FITPROF
-	-	-	-	-	-	TLUSTY/SYNSPEC + FITPROF
FBS 2204+364	$12\,348^{+20}_{-65}$	$3.951^{+0.013}_{-0.026}$	$-0.877^{+0.031}_{-0.023}$	$6.0534^{+0.0316}_{-0.0350}$	$0.109 \pm 0.009$	ADS + Global
	$13\,760 \pm 564$	$4.371 \pm 0.256$	$-1.278 \pm 0.126$	-	-	ADS + SPAS
	$13\,414 \pm 456$	$4.352 \pm 0.227$	$-0.997 \pm 0.127$	-	-	LTE + SPAS
	-	-	-	-	-	TLUSTY/SYNSPEC + SPAS
	$12\,648 \pm 77$	$3.893 \pm 0.028$	$-0.797 \pm 0.069$	-	-	ADS + FITPROF
	$12\,264 \pm 75$	$3.851 \pm 0.030$	$-0.934 \pm 0.102$	-	-	LTE + FITPROF
-	-	-	-	-	-	TLUSTY/SYNSPEC + FITPROF
HD 4539 <sup>a</sup>	$22\,980^{+50}_{-100}$	$5.219^{+0.008}_{-0.004}$	$-2.182^{+0.012}_{-0.011}$	$6.4432^{+0.0339}_{-0.0360}$	$\leq 0.0007$	ADS + Global
	$23\,878 \pm 1614$	$5.342 \pm 0.096$	$-2.277 \pm 0.181$	-	-	ADS + SPAS
	$23\,436 \pm 1836$	$5.277 \pm 0.139$	$-2.273 \pm 0.205$	-	-	LTE + SPAS
	-	-	-	-	-	TLUSTY/SYNSPEC + SPAS
	$23\,105 \pm 152$	$5.218 \pm 0.017$	$-2.172 \pm 0.027$	-	-	ADS + FITPROF
	$23\,067 \pm 201$	$5.118 \pm 0.021$	$-2.130 \pm 0.028$	-	-	LTE + FITPROF
	-	-	-	-	-	TLUSTY/SYNSPEC + FITPROF
	$23\,200 \pm 100$	$5.20 \pm 0.01$	$-2.27 \pm 0.01$	-	-	[2]
$24\,650^{+590}_{-200}$	$5.38^{+0.03}_{-0.05}$	$-2.42^{+0.20}_{-0.07}$	-	-	[3]	
BD+42 <sup>o</sup> 3250 <sup>b</sup>	$27\,920^{+60}_{-90}$	$5.098^{+0.011}_{-0.012}$	$-1.516^{+0.013}_{-0.005}$	$4.9671^{+0.0261}_{-0.0268}$	$0.056 \pm 0.004$	ADS + Global
	$27\,854 \pm 749$	$5.165 \pm 0.092$	$-1.612 \pm 0.240$	-	-	ADS + SPAS
	$29\,059 \pm 941$	$5.262 \pm 0.153$	$-1.591 \pm 0.187$	-	-	LTE + SPAS
	-	-	-	-	-	TLUSTY/SYNSPEC + SPAS
	$27\,846 \pm 160$	$5.156 \pm 0.018$	$-1.533 \pm 0.022$	-	-	ADS + FITPROF
	$28\,209 \pm 210$	$5.065 \pm 0.021$	$-1.460 \pm 0.020$	-	-	LTE + FITPROF
-	-	-	-	-	TLUSTY/SYNSPEC + FITPROF	
$28\,700 \pm 100$	$5.08 \pm 0.02$	$-1.60 \pm 0.10$	-	-	[4]	
Balloon 90100001 <sup>a</sup>	$28\,220^{+70}_{-110}$	$5.476^{+0.008}_{-0.009}$	$-2.601^{+0.033}_{-0.036}$	$2.5183^{+0.0134}_{-0.0139}$	$0.067 \pm 0.005$	ADS + Global
	$28\,713 \pm 404$	$5.521 \pm 0.070$	$-2.421 \pm 0.128$	-	-	ADS + SPAS
	$28\,953 \pm 570$	$5.477 \pm 0.064$	$-2.646 \pm 0.153$	-	-	LTE + SPAS
	-	-	-	-	-	TLUSTY/SYNSPEC + SPAS
	$28\,068 \pm 121$	$5.451 \pm 0.019$	$-2.541 \pm 0.040$	-	-	ADS + FITPROF
	$28\,702 \pm 170$	$5.365 \pm 0.022$	$-2.526 \pm 0.030$	-	-	LTE + FITPROF
	-	-	-	-	-	TLUSTY/SYNSPEC + FITPROF
$28\,000 \pm 1200$	$5.383 \pm 0.004$	$\sim -2.60$	-	-	[5]	

Table A.13.: Table A.11 continued.

Object	$T_{\text{eff}}$ [K]	$\log(g[\text{cm s}^{-2}])$	$\log n(\text{He})$	$\theta$ [ $10^{-11}$ rad]	$E(44 - 55)$ [mag]	Comments/Ref.
FBS 0102+362	$31\,720^{+100}_{-140}$	$5.735^{+0.009}_{-0.015}$	$-1.575^{+0.011}_{-0.010}$	$1.8365^{+0.0099}_{-0.0103}$	$0.024 \pm 0.005$	ADS + Global
	$32\,528 \pm 988$	$5.823 \pm 0.088$	$-1.640 \pm 0.234$	-	-	ADS + SPAS
	$32\,622 \pm 893$	$5.788 \pm 0.080$	$-1.631 \pm 0.230$	-	-	LTE + SPAS
	$33\,753 \pm 1256$	$5.828 \pm 0.129$	$-1.549 \pm 0.188$	-	-	TLUSTY/SYNSPEC + SPAS
	$31\,843 \pm 125$	$5.735 \pm 0.017$	$-1.575 \pm 0.022$	-	-	ADS + FITPROF
	$31\,836 \pm 101$	$5.694 \pm 0.016$	$-1.542 \pm 0.023$	-	-	LTE + FITPROF
	$32\,385 \pm 158$	$5.736 \pm 0.026$	$-1.434 \pm 0.051$	-	-	TLUSTY/SYNSPEC + FITPROF
Feige 14	$28\,890^{+23}_{-120}$	$5.6748^{+0.0153}_{-0.0021}$	$-2.735^{+0.036}_{-0.033}$	$1.7290^{+0.0090}_{-0.0096}$	$0.035 \pm 0.004$	ADS + Global
	$29\,597 \pm 1441$	$5.751 \pm 0.120$	$-2.612 \pm 0.092$	-	-	ADS + SPAS
	$30\,599 \pm 1292$	$5.653 \pm 0.119$	$-2.670 \pm 0.082$	-	-	LTE + SPAS
	-	-	-	-	-	TLUSTY/SYNSPEC + SPAS
	$28\,772 \pm 105$	$5.666 \pm 0.018$	$-2.677 \pm 0.078$	-	-	ADS + FITPROF
	$28\,961 \pm 120$	$5.576 \pm 0.018$	$-2.610 \pm 0.043$	-	-	LTE + FITPROF
GALEX J210332.4+303538	$33\,530^{+90}_{-230}$	$5.958^{+0.012}_{-0.033}$	$-1.738^{+0.017}_{-0.016}$	$1.4669^{+0.0078}_{-0.0091}$	$0.074 \pm 0.005$	ADS + Global
	$33\,225 \pm 890$	$6.093 \pm 0.123$	$-1.753 \pm 0.153$	-	-	ADS + SPAS
	$33\,318 \pm 704$	$5.951 \pm 0.123$	$-1.758 \pm 0.132$	-	-	LTE + SPAS
	$33\,819 \pm 894$	$6.036 \pm 0.132$	$-1.796 \pm 0.141$	-	-	TLUSTY/SYNSPEC + SPAS
	$33\,679 \pm 169$	$5.957 \pm 0.025$	$-1.731 \pm 0.017$	-	-	ADS + FITPROF
	$33\,948 \pm 119$	$5.880 \pm 0.023$	$-1.692 \pm 0.021$	-	-	LTE + FITPROF
	$34\,449 \pm 131$	$5.882 \pm 0.025$	$-1.724 \pm 0.037$	-	-	TLUSTY/SYNSPEC + FITPROF
	$33\,845$	$5.98$	$-1.80$	-	-	[6]
	FBS 2347+385 <sup>c</sup>	$22\,780^{+80}_{-50}$	$5.375^{+0.005}_{-0.009}$	$-3.256^{+0.055}_{-0.046}$	$3.8415^{+0.0209}_{-0.0202}$	$0.103 \pm 0.005$
$23\,361 \pm 985$		$5.377 \pm 0.065$	$-3.349 \pm 0.214$	-	-	ADS + SPAS
$21\,757 \pm 531$		$5.525 \pm 0.089$	$-3.371 \pm 0.290$	-	-	LTE + SPAS
-		-	-	-	-	TLUSTY/SYNSPEC + SPAS
$22\,544 \pm 104$		$5.383 \pm 0.013$	$-3.189 \pm 0.055$	-	-	ADS + FITPROF
$23\,000 \pm 117$		$5.263 \pm 0.014$	$-3.257 \pm 0.118$	-	-	LTE + FITPROF
$23\,770^{+330}_{-350}$		$5.38^{+0.05}_{-0.06}$	$-3.44^{+0.25}_{-0.30}$	-	-	TLUSTY/SYNSPEC + FITPROF [3]
PG 0101+039 <sup>ac</sup>	$26\,510^{+60}_{-80}$	$5.478 \pm 0.011$	$-2.608^{+0.021}_{-0.026}$	$2.5357^{+0.0134}_{-0.0136}$	$0.016 \pm 0.004$	ADS + Global
	$26\,535 \pm 825$	$5.494 \pm 0.078$	$-2.542 \pm 0.118$	-	-	ADS + SPAS
	$27\,303 \pm 432$	$5.684 \pm 0.118$	$-2.581 \pm 0.098$	-	-	LTE + SPAS
	-	-	-	-	-	TLUSTY/SYNSPEC + SPAS
	$26\,401 \pm 131$	$5.493 \pm 0.018$	$-2.645 \pm 0.056$	-	-	ADS + FITPROF
	$26\,660 \pm 182$	$5.412 \pm 0.022$	$-2.563 \pm 0.056$	-	-	LTE + FITPROF
	$27\,500 \pm 500$	$5.53 \pm 0.07$	$-2.66 \pm 0.10$	-	-	TLUSTY/SYNSPEC + FITPROF [7]

Table A.14.: Table A.11 continued.

Object	$T_{\text{eff}}$ [K]	$\log(g[\text{cm s}^{-2}])$	$\log n(\text{He})$	$\theta$ [ $10^{-11}$ rad]	$E(44 - 55)$ [mag]	Comments/Ref.
PG 1635+414 <sup>b</sup>	$35\,940^{+140}_{-70}$	$5.494^{+0.008}_{-0.004}$	$< -3.80$	$0.8381^{+0.0047}_{-0.0044}$	$0.054 \pm 0.006$	ADS + Global
	$34\,857 \pm 338$	$5.543 \pm 0.036$	$< -3.80$	-	-	ADS + SPAS
	$34\,332 \pm 416$	$5.388 \pm 0.042$	$< -3.80$	-	-	LTE + SPAS
	$35\,283 \pm 898$	$5.415 \pm 0.052$	$< -3.80$	-	-	TLUSTY/SYNSPEC + SPAS
	$35\,620 \pm 152$	$5.483 \pm 0.016$	$< -3.80$	-	-	ADS + FITPROF
	$33\,327 \pm 124$	$5.399 \pm 0.019$	$< -3.80$	-	-	LTE + FITPROF
	$34\,758 \pm 208$	$5.443 \pm 0.023$	$< -3.80$	-	-	TLUSTY/SYNSPEC + FITPROF
	$26\,850^{+420}_{-310}$	$5.42^{+0.06}_{-0.05}$	$-2.75^{+0.16}_{-0.24}$	-	-	[3]
LS IV +10 <sup>o</sup> 9	-	-	-	-	-	ADS + Global
	-	-	-	-	-	ADS + SPAS
	-	-	-	-	-	LTE + SPAS
	$43\,606 \pm 1063$	$5.492 \pm 0.231$	$2.00^{\text{d}}$	-	-	TLUSTY/SYNSPEC + SPAS
	-	-	-	-	-	ADS + FITPROF
	-	-	-	-	-	LTE + FITPROF
	$44\,017 \pm 340$	$5.605 \pm 0.063$	$2.00^{\text{d}}$	$1.8072 \pm 0.0117$	$0.043 \pm 0.005$	TLUSTY/SYNSPEC + FITPROF
	$43\,850 \pm 200$	$5.43 \pm 0.10$	$2.73 \pm 0.25$	-	-	[8]

**Table A.15.:** Same as Table A.1, but showing the effective temperatures  $T_{\text{eff}}$ , the surface gravities  $\log(g)$ , the helium abundances  $\log n(\text{He}) := \log n(^4\text{He} + ^3\text{He})$ , the angular diameters  $\theta$ , and the monochromatic color excesses  $E(44 - 55)$  of the program stars, which are analyzed by means of low-resolution data from IDS. The natures of the individual program stars can be found in Tables 8.9 and 8.10.

Object	$T_{\text{eff}}$ [K]	$\log(g[\text{cm s}^{-2}])$	$\log n(\text{He})$	$\theta$ [ $10^{-11}$ rad]	$E(44 - 55)$ [mag]	Comments/Ref.
PG 2219+094 <sup>a</sup>	$19\,930^{+50}_{-230}$	$3.789^{+0.016}_{-0.022}$	$-1.082 \pm 0.009$	$3.7515^{+0.0199}_{-0.0290}$	$0.080 \pm 0.005$	ADS + Global
	$22\,648 \pm 1919$	$3.985 \pm 0.244$	$-0.993 \pm 0.139$	-	-	ADS + SPAS
	-	-	-	-	-	LTE + SPAS
	-	-	-	-	-	TLUSTY/SYNSPEC + SPAS
	$19\,635 \pm 243$	$3.708 \pm 0.033$	$-1.074 \pm 0.024$	-	-	ADS + FITPROF
	-	-	-	-	-	LTE + FITPROF
SB 395	$16\,590^{+50}_{-70}$	$4.399^{+0.007}_{-0.010}$	$-3.25^{+0.10}_{-0.11}$	$3.0917^{+0.0166}_{-0.0172}$	$0.026 \pm 0.004$	ADS + Global
	$17\,247 \pm 435$	$4.374 \pm 0.099$	$-2.957 \pm 0.349$	-	-	ADS + SPAS
	$16\,094 \pm 689$	$4.259 \pm 0.170$	$-2.708 \pm 0.295$	-	-	LTE + SPAS
	-	-	-	-	-	TLUSTY/SYNSPEC + SPAS
	$16\,493 \pm 166$	$4.396 \pm 0.027$	$-2.877 \pm 0.008$	-	-	ADS + FITPROF
	$16\,470 \pm 198$	$4.280 \pm 0.032$	$-2.561 \pm 0.098$	-	-	LTE + FITPROF
KUV 03591+0457 <sup>a</sup>	$14\,490^{+50}_{-110}$	$4.304^{+0.015}_{-0.038}$	$-1.195^{+0.014}_{-0.022}$	$5.0304^{+0.0273}_{-0.0322}$	$0.248 \pm 0.005$	ADS + Global
	$15\,754 \pm 624$	$4.528 \pm 0.302$	$-1.372 \pm 0.292$	-	-	ADS + SPAS
	$15\,068 \pm 747$	$4.665 \pm 0.260$	$-1.271 \pm 0.134$	-	-	LTE + SPAS
	-	-	-	-	-	TLUSTY/SYNSPEC + SPAS
	$14\,752 \pm 142$	$4.249 \pm 0.031$	$-1.168 \pm 0.039$	-	-	ADS + FITPROF
	$14\,296 \pm 167$	$4.287 \pm 0.033$	$-1.108 \pm 0.036$	-	-	LTE + FITPROF
-	-	-	-	-	TLUSTY/SYNSPEC + FITPROF	

**Notes:** For the results of this work,  $1\sigma$  statistical single parameter errors are given for  $T_{\text{eff}}$ ,  $\log(g)$ ,  $\log n(\text{He})$ , and  $E(44 - 55)$ . If SPAS is used, the uncertainties on  $T_{\text{eff}}$ ,  $\log(g)$ , and  $\log n(\text{He})$  result from bootstrapping, whereas in all other cases the corresponding errors are derived from  $\chi^2$ -statistics (see Sect. 7.1.2). The latter also applies to all listed  $E(44 - 55)$  values (see Sect. 7.2.3). The listed uncertainties on  $\theta$  result from Eq. (7.17), whereby the total uncertainties on  $T_{\text{eff}}$  derived from spectroscopy (combining the individual listed  $1\sigma$  statistical errors and the global systematic ones from Sect. 9.2.7) are considered. Hence,  $\Delta T_{\text{eff,model}} = \Delta T_{\text{eff,spectr.}} = \sqrt{[\Delta T_{\text{eff,spectr.,stat.}}]^2 + [(0.550/100) \cdot T_{\text{eff}}]^2 + [(0.869/100) \cdot T_{\text{eff}}]^2}$  is used in Eq. (7.17) in order to calculate the individual values of  $\Delta\theta$ .

- (a) Rotating star.
- (b) The star could be a pre-ELM (see Ch. 13 for details).
- (c) RV-variable star.
- (d) Pulsating star.
- (e) Derived from the single SED fit.
- (f) Derived from the binary SED fit.

**References:** (1) Németh et al. (2012); (2) Saffer et al. (1994); (3) Morales-Rueda et al. (2003b); (4) Østensen et al. (2010c); (5) Østensen et al. (2010b); (6) Geier et al. (2013a).

Table A.16.: Table A.15 continued.

Object	$T_{\text{eff}}$ [K]	$\log(g[\text{cm s}^{-2}])$	$\log n(\text{He})$	$\theta$ [ $10^{-11}$ rad]	$E(44 - 55)$ [mag]	Comments/Ref.
HE 0247-0418 <sup>b</sup>	$28\,210^{+120}_{-70}$	$5.636^{+0.017}_{-0.013}$	$-2.446^{+0.032}_{-0.028}$	$1.5574^{+0.0087}_{-0.0083}$	$0.024 \pm 0.005$	ADS + Global
	$28\,609 \pm 630$	$5.681 \pm 0.076$	$-2.331 \pm 0.101$	-	-	ADS + SPAS
	$28\,690 \pm 261$	$5.770 \pm 0.076$	$-2.491 \pm 0.103$	-	-	LTE + SPAS
	-	-	-	-	-	TLUSTY/SYNSPEC + SPAS
	$28\,492 \pm 137$	$5.697 \pm 0.023$	$-2.442 \pm 0.051$	-	-	ADS + FITPROF
	$28\,592 \pm 169$	$5.602 \pm 0.024$	$-2.427 \pm 0.033$	-	-	LTE + FITPROF
	-	-	-	-	-	TLUSTY/SYNSPEC + FITPROF
	$28\,560^{+930}_{-370}$	$5.67^{+0.11}_{-0.09}$	$-2.56^{+0.25}_{-0.35}$	-	-	[1]
GALEX J203913.4+201309 <sup>a</sup>	$29\,570^{+90}_{-120}$	$5.552^{+0.013}_{-0.014}$	$-3.84^{+0.12}_{-0.13}$	$1.5164^{+0.0082}_{-0.0084}$	$0.030 \pm 0.005$	ADS + Global
	$30\,321 \pm 219$	$5.521 \pm 0.029$	$-3.914 \pm 0.445$	-	-	ADS + SPAS
	$30\,370 \pm 659$	$5.464 \pm 0.043$	$-3.6470 \pm 0.2722$	-	-	LTE + SPAS
	$31\,281 \pm 233$	$5.496 \pm 0.031$	$-3.803 \pm 0.388$	-	-	TLUSTY/SYNSPEC + SPAS
	$29\,455 \pm 169$	$5.55 \pm 0.02$	$-3.762 \pm 0.182$	-	-	ADS + FITPROF
	$30\,248 \pm 125$	$5.458 \pm 0.020$	$-3.770 \pm 0.169$	-	-	LTE + FITPROF
	$30\,538 \pm 247$	$5.476 \pm 0.037$	$-3.673 \pm 0.172$	-	-	TLUSTY/SYNSPEC + FITPROF
	$30\,600 \pm 270$	$5.52^{+0.08}_{-0.06}$	$\leq -3.18$	-	-	[1]
	GALEX J202332.7+013618	$29\,020^{+40}_{-90}$	$5.627^{+0.011}_{-0.009}$	$-2.456^{+0.025}_{-0.023}$	$1.7211^{+0.0090}_{-0.0093}$	$0.073 \pm 0.006$
$29\,659 \pm 1146$		$5.706 \pm 0.107$	$-2.404 \pm 0.274$	-	-	ADS + SPAS
$29\,990 \pm 722$		$5.651 \pm 0.095$	$-2.524 \pm 0.121$	-	-	LTE + SPAS
-		-	-	-	-	TLUSTY/SYNSPEC + SPAS
$29\,131 \pm 147$		$5.707 \pm 0.023$	$-2.495 \pm 0.056$	-	-	ADS + FITPROF
$29\,359 \pm 152$		$5.616 \pm 0.023$	$-2.481 \pm 0.070$	-	-	LTE + FITPROF
$29\,450^{+460}_{-170}$		$5.60^{+0.06}_{-0.04}$	$-2.44^{+0.07}_{-0.20}$	-	-	TLUSTY/SYNSPEC + FITPROF [1]
GALEX J172445.5+113224	$31\,110^{+110}_{-70}$	$5.7926^{+0.0063}_{-0.0022}$	$-2.226^{+0.020}_{-0.019}$	$1.9143^{+0.0105}_{-0.0101}$	$0.097 \pm 0.007$	ADS + Global
	$30\,883 \pm 675$	$5.823 \pm 0.109$	$-2.170 \pm 0.193$	-	-	ADS + SPAS
	$31\,126 \pm 282$	$5.820 \pm 0.085$	$-2.281 \pm 0.152$	-	-	LTE + SPAS
	$33\,809 \pm 623$	$5.841 \pm 0.191$	$-2.098 \pm 0.143$	-	-	TLUSTY/SYNSPEC + SPAS
	$31\,126 \pm 132$	$5.814 \pm 0.022$	$-2.204 \pm 0.015$	-	-	ADS + FITPROF
	$31\,348 \pm 115$	$5.747 \pm 0.021$	$-2.157 \pm 0.035$	-	-	LTE + FITPROF
	$32\,141 \pm 94$	$5.762 \pm 0.021$	$-2.196 \pm 0.040$	-	-	TLUSTY/SYNSPEC + FITPROF
	PG 2313-021 <sup>c</sup>	$30\,370^{+40}_{-70}$	$5.870^{+0.008}_{-0.012}$	$-3.35^{+0.06}_{-0.08}$	$1.5234^{+0.0079}_{-0.0081}$	$0.0519 \pm 0.0026$
$30\,401 \pm 1244$		$5.879 \pm 0.056$	$-3.399 \pm 0.434$	-	-	ADS + SPAS
$31\,349 \pm 167$		$5.790 \pm 0.058$	$-3.338 \pm 0.228$	-	-	LTE + SPAS
$31\,464 \pm 473$		$5.825 \pm 0.041$	$-3.356 \pm 0.339$	-	-	TLUSTY/SYNSPEC + SPAS
$30\,053 \pm 135$		$5.876 \pm 0.020$	$-3.269 \pm 0.052$	-	-	ADS + FITPROF
$30\,937 \pm 116$		$5.807 \pm 0.021$	$-3.24 \pm 0.06$	-	-	LTE + FITPROF
$31\,536 \pm 100$		$5.817 \pm 0.018$	$-3.281 \pm 0.082$	-	-	TLUSTY/SYNSPEC + FITPROF
$34\,500 \pm 1000$		$6.01 \pm 0.15$	$\leq -3.00$	-	-	[2]

Table A.17.: Table A.15 continued.

Object	$T_{\text{eff}}$ [K]	$\log(g[\text{cm s}^{-2}])$	$\log n(\text{He})$	$\theta$ [ $10^{-11}$ rad]	$E(44 - 55)$ [mag]	Comments/Ref.
KUV 16256+4034 <sup>c</sup>	23 910 <sup>+70</sup> <sub>-40</sub>	5.4700 <sup>+0.0019</sup> <sub>-0.0015</sub>	-3.092 <sup>+0.041</sup> <sub>-0.040</sub>	2.2034 <sup>+0.0118</sup> <sub>-0.0115</sub>	≤ 0.004	ADS + Global
	24 691 ± 1349	5.537 ± 0.066	-3.022 ± 0.219	-	-	ADS + SPAS
	23 890 ± 955	5.459 ± 0.091	-3.002 ± 0.124	-	-	LTE + SPAS
	-	-	-	-	-	TLUSTY/SYNSPEC + SPAS
	24 366 ± 147	5.461 ± 0.017	-3.103 ± 0.039	-	-	ADS + FITPROF
	23 633 ± 166	5.342 ± 0.019	-3.064 ± 0.021	-	-	LTE + FITPROF
	-	-	-	-	-	TLUSTY/SYNSPEC + FITPROF
	23 560 <sup>+410</sup> <sub>-250</sub>	5.44 <sup>+0.03</sup> <sub>-0.07</sub>	-3.08 <sup>+0.20</sup> <sub>-0.29</sub>	-	-	[1]
PG 0133+114 <sup>c</sup>	27 490 <sup>+19</sup> <sub>-60</sub>	5.639 <sup>+0.006</sup> <sub>-0.009</sub>	-2.264 <sup>+0.018</sup> <sub>-0.015</sub>	2.3078 <sup>+0.0119</sup> <sub>-0.0122</sub>	0.052 ± 0.005	ADS + Global
	28 848 ± 910	5.743 ± 0.133	-2.140 ± 0.195	-	-	ADS + SPAS
	28 326 ± 388	5.761 ± 0.093	-2.270 ± 0.167	-	-	LTE + SPAS
	-	-	-	-	-	TLUSTY/SYNSPEC + SPAS
	27 315 ± 100	5.704 ± 0.014	-2.35 ± 0.04	-	-	ADS + FITPROF
	27 806 ± 126	5.630 ± 0.016	-2.292 ± 0.034	-	-	LTE + FITPROF
	-	-	-	-	-	TLUSTY/SYNSPEC + FITPROF
29 600 ± 900	5.66 ± 0.10	-2.30 ± 0.10	-	-	[3]	
GALEX J032139.8+472718 <sup>c</sup>	28 500 <sup>+50</sup> <sub>-100</sub>	5.431 <sup>+0.007</sup> <sub>-0.006</sub>	-2.607 <sup>+0.024</sup> <sub>-0.022</sub>	3.8726 <sup>+0.0203</sup> <sub>-0.0211</sub> <sup>e</sup> , 3.7154 <sup>+0.0194</sup> <sub>-0.0202</sub> <sup>f</sup>	0.210 ± 0.015 <sup>e</sup> , 0.184 ± 0.018 <sup>f</sup>	ADS + Global
	29 390 ± 1146	5.449 ± 0.146	-2.470 ± 0.192	-	-	ADS + SPAS
	30 083 ± 1020	5.448 ± 0.091	-2.634 ± 0.111	-	-	LTE + SPAS
	-	-	-	-	-	TLUSTY/SYNSPEC + SPAS
	28 670 ± 146	5.443 ± 0.021	-2.624 ± 0.035	-	-	ADS + FITPROF
	28 752 ± 170	5.362 ± 0.021	-2.577 ± 0.032	-	-	LTE + FITPROF
	-	-	-	-	-	TLUSTY/SYNSPEC + FITPROF
27 990 <sup>+460</sup> <sub>-400</sub>	5.34 ± 0.07	-2.52 <sup>+0.17</sup> <sub>-0.22</sub>	-	-	[1]	
2M1938+4603 <sup>cd</sup>	28 080 <sup>+40</sup> <sub>-80</sub>	5.433 <sup>+0.008</sup> <sub>-0.007</sub>	-2.203 <sup>+0.020</sup> <sub>-0.021</sub>	2.3878 <sup>+0.0124</sup> <sub>-0.0128</sub>	0.035 ± 0.011	ADS + Global
	29 170 ± 1403	5.482 ± 0.164	-2.139 ± 0.139	-	-	ADS + SPAS
	29 367 ± 532	5.546 ± 0.088	-2.193 ± 0.181	-	-	LTE + SPAS
	-	-	-	-	-	TLUSTY/SYNSPEC + SPAS
	28 389 ± 138	5.481 ± 0.023	-2.256 ± 0.047	-	-	ADS + FITPROF
	28 544 ± 172	5.383 ± 0.025	-2.156 ± 0.027	-	-	LTE + FITPROF
	-	-	-	-	-	TLUSTY/SYNSPEC + FITPROF
29 600 ± 100	5.42 ± 0.01	-2.40 ± 0.10	-	-	[4]	
FB 29	36 350 <sup>+50</sup> <sub>-150</sub>	5.855 <sup>+0.011</sup> <sub>-0.009</sub>	-1.634 <sup>+0.013</sup> <sub>-0.012</sub>	1.8214 <sup>+0.0095</sup> <sub>-0.0101</sub>	0.207 ± 0.006	ADS + Global
	37 102 ± 943	5.751 ± 0.139	-1.603 ± 0.142	-	-	ADS + SPAS
	36 322 ± 541	5.858 ± 0.089	-1.625 ± 0.131	-	-	LTE + SPAS
	-	-	-	-	-	TLUSTY/SYNSPEC + SPAS
	38 130 ± 712	5.839 ± 0.102	-1.532 ± 0.104	-	-	ADS + FITPROF
	36 182 ± 133	5.888 ± 0.022	-1.641 ± 0.025	-	-	LTE + FITPROF
	36 013 ± 114	5.778 ± 0.019	-1.546 ± 0.019	-	-	TLUSTY/SYNSPEC + FITPROF
37 665 ± 142	5.810 ± 0.022	-1.609 ± 0.019	-	-		

Table A.18.: Table A.15 continued.

Object	$T_{\text{eff}}$ [K]	$\log(g[\text{cm s}^{-2}])$	$\log n(\text{He})$	$\theta$ [ $10^{-11}$ rad]	$E(44 - 55)$ [mag]	Comments/Ref.
EC 01541-1409 <sup>d</sup>	$37\,570^{+60}_{-130}$	$5.750^{+0.010}_{-0.017}$	$-1.329 \pm 0.011$	$1.7906^{+0.0094}_{-0.0098}$	$0.089^{+0.018}_{-0.021}$	ADS + Global
	$37\,685 \pm 540$	$5.763 \pm 0.076$	$-1.284 \pm 0.072$	-	-	ADS + SPAS
	$36\,847 \pm 393$	$5.805 \pm 0.096$	$-1.257 \pm 0.070$	-	-	LTE + SPAS
	$38\,256 \pm 790$	$5.809 \pm 0.140$	$-1.172 \pm 0.082$	-	-	TLUSTY/SYNSPEC + SPAS
	$37\,027 \pm 151$	$5.788 \pm 0.027$	$-1.355 \pm 0.016$	-	-	ADS + FITPROF
	$36\,382 \pm 135$	$5.708 \pm 0.026$	$-1.279 \pm 0.017$	-	-	LTE + FITPROF
	$37\,373 \pm 172$	$5.691 \pm 0.029$	$-1.279 \pm 0.025$	-	-	TLUSTY/SYNSPEC + FITPROF
	$37\,100 \pm 300$	$5.71 \pm 0.10$	$-1.21 \pm 0.10$	-	-	[5]
FBS 0654+366	$24\,300^{+90}_{-60}$	$4.747 \pm 0.009$	$-0.673^{+0.009}_{-0.005}$	$2.9370^{+0.0161}_{-0.0156}$	$0.053 \pm 0.006$	ADS + Global
	$24\,834 \pm 605$	$4.803 \pm 0.090$	$-0.64 \pm 0.08$	-	-	ADS + SPAS
	$23\,642 \pm 870$	$4.810 \pm 0.109$	$-0.521 \pm 0.124$	-	-	LTE + SPAS
	-	-	-	-	-	TLUSTY/SYNSPEC + SPAS
	$24\,642 \pm 174$	$4.732 \pm 0.025$	$-0.666 \pm 0.013$	-	-	ADS + FITPROF
	$24\,716 \pm 194$	$4.705 \pm 0.027$	$-0.649 \pm 0.083$	-	-	LTE + FITPROF
-	-	-	-	-	TLUSTY/SYNSPEC + FITPROF	
[CW83] 0512-08	$37\,711.81^{+0.23}_{-6.00}$	$6.0355^{+0.0097}_{-0.0015}$	$-0.95596^{+0.00005}_{-0.00016}$	$2.8288 \pm 0.0146$	$0.041 \pm 0.004$	ADS + Global
	$38\,232 \pm 521$	$5.870 \pm 0.072$	$-0.900 \pm 0.064$	-	-	ADS + SPAS
	$37\,951 \pm 362$	$5.889 \pm 0.070$	$-0.975 \pm 0.094$	-	-	LTE + SPAS
	$38\,312 \pm 696$	$5.920 \pm 0.115$	$-0.854 \pm 0.090$	-	-	TLUSTY/SYNSPEC + SPAS
	$38\,035 \pm 164$	$5.926 \pm 0.032$	$-0.825 \pm 0.021$	-	-	ADS + FITPROF
	$38\,639 \pm 171$	$5.899 \pm 0.031$	$-0.915 \pm 0.036$	-	-	LTE + FITPROF
	$38\,988 \pm 178$	$5.827 \pm 0.030$	$-0.731 \pm 0.020$	-	-	TLUSTY/SYNSPEC + FITPROF
	$38\,400 \pm 1100$	$5.77 \pm 0.14$	$-0.73 \pm 0.10$	-	-	[6]
GALEX J175548.5+501210	-	-	-	-	-	ADS + Global
	-	-	-	-	-	ADS + SPAS
	-	-	-	-	-	LTE + SPAS
	$41\,144 \pm 511$	$5.866 \pm 0.172$	$1.90 \pm 0.14$	-	-	TLUSTY/SYNSPEC + SPAS
	-	-	-	-	-	ADS + FITPROF
	-	-	-	-	-	LTE + FITPROF
40 697 ± 158	$5.834 \pm 0.078$	$2.019 \pm 0.127$	$1.2494 \pm 0.0069$	$\leq 0.0083$	TLUSTY/SYNSPEC + FITPROF	
	$40\,370^{+940}_{-210}$	$5.96^{+0.05}_{-0.15}$	$1.30^{+0.27}_{-0.10}$	-	[1]	
PG 0314+146	-	-	-	-	-	ADS + Global
	-	-	-	-	-	ADS + SPAS
	-	-	-	-	-	LTE + SPAS
	$46\,637 \pm 1273$	$5.665 \pm 0.180$	$\geq 4.00$	-	-	TLUSTY/SYNSPEC + SPAS
	-	-	-	-	-	ADS + FITPROF
	-	-	-	-	-	LTE + FITPROF
$46\,639 \pm 318$	$5.699 \pm 0.042$	$\geq 4.00$	$1.6749 \pm 0.0104$	$0.171 \pm 0.008$	TLUSTY/SYNSPEC + FITPROF	
$47\,520^{+1030}_{-820}$	$5.96^{+0.15}_{-0.19}$	$0.90^{+0.17}_{-0.21}$	-	-	[1]	
FBS 0224+330	-	-	-	-	-	ADS + Global
	-	-	-	-	-	ADS + SPAS
	-	-	-	-	-	LTE + SPAS
	$42\,611 \pm 658$	$5.892 \pm 0.169$	$1.333 \pm 0.185$	-	-	TLUSTY/SYNSPEC + SPAS
	-	-	-	-	-	ADS + FITPROF
-	-	-	-	-	LTE + FITPROF	
$42\,898 \pm 237$	$5.913 \pm 0.059$	$1.418 \pm 0.100$	$1.0892 \pm 0.0064$	$0.063 \pm 0.006$	TLUSTY/SYNSPEC + FITPROF	

Table A.19.: Effective temperatures  $T_{\text{eff}}$ , surface gravities  $\log(g)$ , helium abundances  $\log n(\text{He}) := \log n(^4\text{He} + ^3\text{He})$ , angular diameters  $\theta$ , and monochromatic color excesses  $E(44 - 55)$  of the program stars from literature, for which no spectra are analyzed in this work.  $\theta$  and  $E(44 - 55)$  are derived from SED fitting to photometric data (see Sect. 7.2), whereby the corresponding atmospheric parameters from literature (references are given) are used as input. The listed  $\theta$  values together with the corresponding spectroscopic parameters from literature are used to derive the fundamental stellar parameters (radius, luminosity, mass) according to Sect. 7.3. To this end, the global systematic errors on  $T_{\text{eff}}$  and  $\log(g)$  (not included here) according to the results of Sect. 9.2.7 as well as the parallaxes of Tables 8.18 and 8.19 are taken into account. The natures of the individual program stars can be found in Table 8.11.

Object	$T_{\text{eff}}$ [K]	$\log(g[\text{cm s}^{-2}])$	$\log n(\text{He})$	$\theta$ [ $10^{-11}$ rad]	$E(44 - 55)$ [mag]
BD+28° 4211	$82\,000 \pm 5000^{\text{b}}$	$6.20^{+0.30}_{-0.10}^{\text{b}}$	$-1.00^{\text{b}}$	$2.5533 \pm 0.0790$	$0.013 \pm 0.005$
	$81\,342 \pm 1219^{\text{c}}$	$6.519 \pm 0.048^{\text{c}}$	$-1.120 \pm 0.049^{\text{c}}$	$2.5574 \pm 0.0233$	$0.013 \pm 0.005$
AGK+81° 266 <sup>a</sup>	$60\,859 \pm 1182^{\text{d}}$	$6.093 \pm 0.063^{\text{d}}$	$-2.986 \pm 0.200^{\text{d}}$	$1.4191 \pm 0.0156$	$0.017 \pm 0.004$
LS II +18° 9 <sup>a</sup>	$57\,767 \pm 1067^{\text{d}}$	$5.996 \pm 0.058^{\text{d}}$	$-1.851 \pm 0.071^{\text{d}}$	$1.4993 \pm 0.0159$	$0.017 \pm 0.005$
Feige 67 <sup>a</sup>	$61\,050 \pm 520^{\text{d}}$	$5.95 \pm 0.03^{\text{d}}$	$-1.59 \pm 0.04^{\text{d}}$	$1.5330 \pm 0.0103$	$0.031 \pm 0.004$
Feige 34 <sup>a</sup>	$62\,550 \pm 600^{\text{d}}$	$5.99 \pm 0.03^{\text{d}}$	$-1.79 \pm 0.04^{\text{d}}$	$2.0070 \pm 0.0142$	$0.018^{+0.008}_{-0.007}$

**Notes:** Information about the listed uncertainties on  $T_{\text{eff}}$ ,  $\log(g)$ , and  $\log n(\text{He})$  can be found in the given references. For  $E(44 - 55)$ ,  $1\sigma$  single parameter errors derived from  $\chi^2$ -statistics are given (see Sect. 7.2.3). The listed uncertainties on  $\theta$  result from Eq. (7.17), whereby the total uncertainties on  $T_{\text{eff}}$  (combining the individual listed errors from literature and the global systematic ones from Sect. 9.2.7) are considered. Hence,  $\Delta T_{\text{eff,model}} = \Delta T_{\text{eff,spectr.}} = \sqrt{[\Delta T_{\text{eff,lit.}}]^2 + [(0.550/100) \cdot T_{\text{eff}}]^2 + [(0.869/100) \cdot T_{\text{eff}}]^2}$  is used in Eq. (7.17) in order to calculate the individual values of  $\Delta\theta$ .

<sup>(a)</sup> Rotating star.

<sup>(b)</sup> Adopted from Latour et al. (2013).

<sup>(c)</sup> Adopted from Latour et al. (2015).

<sup>(d)</sup> Adopted from Latour et al. (2018).

Table A.20.: Same as Table A.1, but showing the effective temperatures  $T_{\text{eff}}$ , the surface gravities  $\log(g)$ , the helium abundances  $\log n(\text{He}) := \log n(^4\text{He} + ^3\text{He})$ , the angular diameters  $\theta$ , and the monochromatic color excesses  $E(44 - 55)$  of the program stars, for which spectra from multiple spectrographs are analyzed. No literature values are listed but weighted averages are calculated for  $T_{\text{eff}}$ ,  $\log(g)$ , and  $\log n(\text{He})$ .  $\theta$  and  $E(44 - 55)$  are derived from SED fitting to photometric data (see Sect. 7.2), whereby the corresponding calculated weighted averages for  $T_{\text{eff}}$ ,  $\log(g)$ , and  $\log n(\text{He})$  are used as input. The listed  $\theta$  values together with the corresponding spectroscopic parameters are used to derive the fundamental stellar parameters (radius, luminosity, mass) according to Sect. 7.3. To this end, the global systematic errors on  $T_{\text{eff}}$  and  $\log(g)$  (not included here) according to the results of Sect. 9.2.7 as well as the parallaxes of Tables 8.18 and 8.19 are taken into account. The natures of the individual program stars can be found in Tables 8.1-8.3.

Object	Instr.	$T_{\text{eff}}$ [K]	$\log(g[\text{cm s}^{-2}])$	$\log n(\text{He})$	$\theta$ [ $10^{-11}$ rad]	$E(44 - 55)$ [mag]	Comments
HD 4539 <sup>a</sup>	XSHOOTER	$23\,971 \pm 14$	$5.2971^{+0.0015}_{-0.0013}$	$-2.2406^{+0.0023}_{-0.0026}$	-	-	ADS + Global (NLTE + LTE metals)
	CAFOS	$22\,980^{+50}_{-100}$	$5.219^{+0.008}_{-0.004}$	$-2.182^{+0.012}_{-0.011}$	-	-	ADS + Global
	FEROS	$23\,420^{+60}_{-40}$	$5.253 \pm 0.006$	$-2.2937^{+0.0048}_{-0.0049}$	-	-	ADS + Global (NLTE metals)
Weighted Average		$23\,925 \pm 14$	$5.2921 \pm 0.0015$	$-2.2498 \pm 0.0023$	$6.2330 \pm 0.0322$	$\leq 0.0044$	ADS + Global
HD 4539 <sup>a</sup>	XSHOOTER	$24\,327 \pm 124$	$5.318 \pm 0.199$	$-2.315 \pm 0.040$	-	-	ADS + SPAS
	CAFOS	$23\,878 \pm 1614$	$5.342 \pm 0.096$	$-2.277 \pm 0.181$	-	-	ADS + SPAS
	FEROS	$23\,356 \pm 211$	$5.294 \pm 0.019$	$-2.273 \pm 0.013$	-	-	ADS + SPAS
Weighted Average		$24\,077 \pm 107$	$5.296 \pm 0.019$	$-2.277 \pm 0.013$	-	-	ADS + SPAS
HD 4539 <sup>a</sup>	XSHOOTER	$23\,694 \pm 386$	$5.332 \pm 0.232$	$-2.283 \pm 0.121$	-	-	LTE + SPAS
	CAFOS	$23\,436 \pm 1836$	$5.277 \pm 0.139$	$-2.273 \pm 0.205$	-	-	LTE + SPAS
	FEROS	$23\,125 \pm 258$	$5.259 \pm 0.022$	$-2.235 \pm 0.043$	-	-	LTE + SPAS
Weighted Average		$23\,303 \pm 214$	$5.260 \pm 0.022$	$-2.242 \pm 0.040$	-	-	LTE + SPAS

**Notes:** In order to calculate the listed weighted averages for the atmospheric parameters, the reciprocals of the individual maximum variances, that is  $\frac{1}{(\max[\text{uncertainty}])^2}$ , are used as weights. For the results of this work,  $1\sigma$  statistical single parameter errors are given for  $T_{\text{eff}}$ ,  $\log(g)$ ,  $\log n(\text{He})$ , and  $E(44 - 55)$ . If SPAS is used, the uncertainties on  $T_{\text{eff}}$ ,  $\log(g)$ , and  $\log n(\text{He})$  result from bootstrapping, whereas in all other cases the corresponding errors are derived from  $\chi^2$ -statistics (see Sect. 7.1.2). The latter also applies to all listed  $E(44 - 55)$  values (see Sect. 7.2.3). The listed uncertainties on  $\theta$  result from Eq. (7.17), whereby the total uncertainties on the weighted averages for  $T_{\text{eff}}$  (combining the individual listed propagated  $1\sigma$  statistical errors and the global systematic ones from Sect. 9.2.7) are considered. Hence,  $\Delta T_{\text{eff,model}} = \Delta T_{\text{eff,spectr.}} = \sqrt{[\Delta T_{\text{eff,spectr.,prop.,stat.}}]^2 + [(0.550/100) \cdot T_{\text{eff}}]^2 + [(0.869/100) \cdot T_{\text{eff}}]^2}$  is used in Eq. (7.17) in order to calculate the individual values of  $\Delta\theta$ .

- (a) Pulsating star.
- (b) He I 6678 Å included in spectral analysis fit.
- (c) He I 6678 Å not included in spectral analysis fit.
- (d) Derived from the single SED fit.
- (e) Derived from the binary SED fit.

Table A.21.: Table A.20 continued.

Object	Instr.	$T_{\text{eff}}$ [K]	$\log(g[\text{cm s}^{-2}])$	$\log n(\text{He})$	$\theta$ [ $10^{-11}$ rad]	$E(44 - 55)$ [mag]	Comments
HD 4539 <sup>a</sup>	XSHOOTER	24 031 ± 39	5.283 ± 0.005	-2.264 ± 0.011	-	-	ADS + FITPROF
	CAFOS	23 105 ± 152	5.218 ± 0.017	-2.172 ± 0.027	-	-	ADS + FITPROF
	FEROS	23 656 ± 123	5.292 ± 0.015	-2.327 ± 0.023	-	-	ADS + FITPROF
Weighted Average		23 946 ± 37	5.279 ± 0.005	-2.263 ± 0.010	-	-	ADS + FITPROF
HD 4539 <sup>a</sup>	XSHOOTER	23 700 ± 55	5.175 ± 0.006	-2.275 ± 0.015	-	-	LTE + FITPROF
	CAFOS	23 067 ± 201	5.118 ± 0.021	-2.130 ± 0.028	-	-	LTE + FITPROF
	FEROS	23 296 ± 156	5.173 ± 0.017	-2.339 ± 0.026	-	-	LTE + FITPROF
Weighted Average		23 619 ± 51	5.171 ± 0.006	-2.2625 ± 0.0118	-	-	LTE + FITPROF
Feige 38	XSHOOTER	29 214 <sup>+25</sup> <sub>-15</sub>	5.7377 <sup>+0.0026</sup> <sub>-0.0029</sub>	-2.5658 <sup>+0.0298</sup> <sub>+0.0328</sub>	-	-	ADS + Global (NLTE + LTE metals)
	FEROS	29 557 ± 29	5.660 ± 0.005	-2.5899 <sup>+0.0102</sup> <sub>-0.0115</sub>	-	-	ADS + Global (NLTE metals)
Weighted Average		29 360 ± 19	5.7182 ± 0.0026	-2.587 ± 0.011	1.5736 ± 0.0082	0.055 ± 0.004	ADS + Global
Feige 38	XSHOOTER	30 271 ± 115	5.766 ± 0.014	-2.526 ± 0.051	-	-	ADS + SPAS
	FEROS	29 898 ± 661	5.709 ± 0.020	-2.587 ± 0.048	-	-	ADS + SPAS
Weighted Average		30 260 ± 114	5.747 ± 0.012	-2.558 ± 0.035	-	-	ADS + SPAS
Feige 38	XSHOOTER	29 614 ± 269	5.643 ± 0.024	-2.591 ± 0.083	-	-	LTE + SPAS
	FEROS	29 663 ± 226	5.693 ± 0.027	-2.681 ± 0.039	-	-	LTE + SPAS
Weighted Average		29 643 ± 174	5.665 ± 0.018	-2.665 ± 0.036	-	-	LTE + SPAS
Feige 38	XSHOOTER	29 599 ± 47	5.734 ± 0.007	-2.533 ± 0.029	-	-	ADS + FITPROF
	FEROS	29 917 ± 188	5.791 ± 0.027	-2.474 ± 0.031	-	-	ADS + FITPROF
Weighted Average		29 618 ± 46	5.738 ± 0.007	-2.505 ± 0.022	-	-	ADS + FITPROF
Feige 38	XSHOOTER	29 938 ± 48	5.667 ± 0.007	-2.488 ± 0.027	-	-	LTE + FITPROF
	FEROS	29 940 ± 212	5.696 ± 0.030	-2.499 ± 0.035	-	-	LTE + FITPROF
Weighted Average		29 938 ± 47	5.668 ± 0.007	-2.4921 ± 0.0214	-	-	LTE + FITPROF
EC 03591-3232	XSHOOTER	28 757 <sup>+15</sup> <sub>-24</sub>	5.8027 <sup>+0.0020</sup> <sub>-0.0017</sub>	-1.8712 <sup>+0.0075</sup> <sub>-0.0081</sub>	-	-	ADS + Global (NLTE + LTE metals)
	FEROS	28 800 ± 40	5.766 <sup>+0.006</sup> <sub>-0.005</sub>	-1.9401 ± 0.0160	-	-	ADS + Global (NLTE metals)
Weighted Average		28 768 ± 21	5.7990 ± 0.0019	-1.885 ± 0.008	3.5645 ± 0.0184	0.024 ± 0.004	ADS + Global
EC 03591-3232	XSHOOTER	29 741 ± 303	5.725 ± 0.025	-1.938 ± 0.066	-	-	ADS + SPAS
	FEROS	29 445 ± 108	5.670 ± 0.015	-1.995 ± 0.027	-	-	ADS + SPAS
Weighted Average		29 478 ± 102	5.685 ± 0.013	-1.987 ± 0.025	-	-	ADS + SPAS
EC 03591-3232	XSHOOTER	30 001 ± 408	5.808 ± 0.098	-1.915 ± 0.070	-	-	LTE + SPAS
	FEROS	29 842 ± 167	5.782 ± 0.019	-2.031 ± 0.039	-	-	LTE + SPAS
Weighted Average		29 865 ± 155	5.783 ± 0.019	-2.004 ± 0.035	-	-	LTE + SPAS

Table A.22.: Table A.20 continued.

Object	Instr.	$T_{\text{eff}}$ [K]	$\log(g[\text{cm s}^{-2}])$	$\log n(\text{He})$	$\theta$ [ $10^{-11}$ rad]	$E(44 - 55)$ [mag]	Comments
EC 03591-3232	XSHOOTER	28 959 ± 33	5.749 ± 0.005	-1.851 ± 0.017	-	-	ADS + FITPROF
	FEROS	29 210 ± 107	5.709 ± 0.016	-1.967 ± 0.024	-	-	ADS + FITPROF
Weighted Average		28 981 ± 32	5.745 ± 0.005	-1.890 ± 0.014	-	-	ADS + FITPROF
EC 03591-3232	XSHOOTER	29 734 ± 33	5.678 ± 0.006	-1.836 ± 0.018	-	-	LTE + FITPROF
	FEROS	29 630 ± 110	5.632 ± 0.016	-1.956 ± 0.024	-	-	LTE + FITPROF
Weighted Average		29 725 ± 32	5.672 ± 0.006	-1.8792 ± 0.0144	-	-	LTE + FITPROF
[CW83] 0512-08	XSHOOTER	37 411 <sup>+21</sup> <sub>-24</sub>	5.963 ± 0.004	-0.9051 <sup>+0.0019</sup> <sub>-0.0018</sub>	-	-	ADS + Global (NLTE + LTE metals)
	IDS	37 711.81 <sup>+0.23</sup> <sub>-6.00</sub>	6.0355 <sup>+0.0097</sup> <sub>-0.0015</sub>	-0.95596 <sup>+0.00005</sup> <sub>-0.00016</sub>	-	-	ADS + Global
Weighted Average		37 694 ± 6	5.974 ± 0.004	-0.95560 ± 0.00016	2.8288 ± 0.0146	0.041 ± 0.004	ADS + Global
[CW83] 0512-08	XSHOOTER	38 239 ± 103	5.935 ± 0.017	-0.935 ± 0.093	-	-	ADS + SPAS
	IDS	38 232 ± 521	5.870 ± 0.072	-0.900 ± 0.064	-	-	ADS + SPAS
Weighted Average		38 239 ± 102	5.932 ± 0.017	-0.911 ± 0.053	-	-	ADS + SPAS
[CW83] 0512-08	XSHOOTER	38 311 ± 422	5.860 ± 0.054	-0.936 ± 0.098	-	-	LTE + SPAS
	IDS	37 951 ± 362	5.889 ± 0.070	-0.975 ± 0.094	-	-	LTE + SPAS
Weighted Average		38 104 ± 275	5.871 ± 0.043	-0.956 ± 0.068	-	-	LTE + SPAS
[CW83] 0512-08	XSHOOTER	38 049 ± 208	5.820 ± 0.056	-0.816 ± 0.037	-	-	TLUSTY/SYNSPEC + SPAS
	IDS	38 312 ± 696	5.920 ± 0.115	-0.854 ± 0.090	-	-	TLUSTY/SYNSPEC + SPAS
Weighted Average		38 071 ± 200	5.839 ± 0.051	-0.821 ± 0.035	-	-	TLUSTY/SYNSPEC + SPAS
[CW83] 0512-08	XSHOOTER	37 375 ± 110	5.957 ± 0.018	-0.818 ± 0.009	-	-	ADS + FITPROF
	IDS	38 035 ± 164	5.926 ± 0.032	-0.825 ± 0.021	-	-	ADS + FITPROF
Weighted Average		37 580 ± 92	5.950 ± 0.016	-0.820 ± 0.009	-	-	ADS + FITPROF
[CW83] 0512-08	XSHOOTER	37 815 ± 93	5.872 ± 0.018	-0.748 ± 0.020	-	-	LTE + FITPROF
	IDS	38 639 ± 171	5.899 ± 0.031	-0.915 ± 0.036	-	-	LTE + FITPROF
Weighted Average		38 003 ± 82	5.879 ± 0.016	-0.7874 ± 0.0175	-	-	LTE + FITPROF
[CW83] 0512-08	XSHOOTER	39 162 ± 114	5.818 ± 0.018	-0.728 ± 0.011	-	-	TLUSTY/SYNSPEC + FITPROF
	IDS	38 988 ± 178	5.827 ± 0.030	-0.731 ± 0.020	-	-	TLUSTY/SYNSPEC + FITPROF
Weighted Average		39 111 ± 96	5.820 ± 0.016	-0.729 ± 0.010	-	-	TLUSTY/SYNSPEC + FITPROF

Table A.23.: Table A.20 continued.

Object	Instr.	$T_{\text{eff}}$ [K]	$\log(g[\text{cm s}^{-2}])$	$\log n(\text{He})$	$\theta$ [ $10^{-11}$ rad]	$E(44 - 55)$ [mag]	Comments
PG 0314+146	XSHOOTER	$46\,569 \pm 382^{\text{b}}$	$5.675 \pm 0.039^{\text{b}}$	$\geq 4.00^{\text{b}}$	-	-	TLUSTY/SYNSPEC + SPAS
	XSHOOTER	$47\,094 \pm 510^{\text{c}}$	$5.698 \pm 0.040^{\text{c}}$	$\geq 4.00^{\text{c}}$	-	-	TLUSTY/SYNSPEC + SPAS
	IDS	$46\,637 \pm 1273$	$5.665 \pm 0.180$	$\geq 4.00$	-	-	TLUSTY/SYNSPEC + SPAS
Weighted Average		$46\,751 \pm 298$	$5.686 \pm 0.028$	$\geq 4.00$	-	-	TLUSTY/SYNSPEC + SPAS
PG 0314+146	XSHOOTER	$46\,602 \pm 194^{\text{b}}$	$5.693 \pm 0.022^{\text{b}}$	$\geq 4.00^{\text{b}}$	-	-	TLUSTY/SYNSPEC + FITPROF
	XSHOOTER	$46\,447 \pm 190^{\text{c}}$	$5.662 \pm 0.018^{\text{c}}$	$\geq 4.00^{\text{c}}$	-	-	TLUSTY/SYNSPEC + FITPROF
	IDS	$46\,639 \pm 318$	$5.699 \pm 0.042$	$\geq 4.00$	-	-	TLUSTY/SYNSPEC + FITPROF
Weighted Average		$46\,541 \pm 125$	$5.677 \pm 0.014$	$\geq 4.00$	$1.6788 \pm 0.0090$	$0.171 \pm 0.008$	TLUSTY/SYNSPEC + FITPROF
HD 149382	XSHOOTER	$35\,000^{+14}_{-11}$	$5.9217 \pm 0.0020$	$-1.4401^{+0.0019}_{-0.0022}$	-	-	ADS + Global (NLTE + LTE metals)
	UVES	$34\,644^{+27}_{-16}$	$5.8375^{+0.0028}_{-0.0025}$	$-1.4368^{+0.0025}_{-0.0020}$	-	-	ADS + Global (NLTE metals)
Weighted Average		$34\,925 \pm 13$	$5.8933 \pm 0.0017$	$-1.4387 \pm 0.0017$	$9.5940 \pm 0.0494^{\text{d}}$ , $8.6696 \pm 0.0447^{\text{e}}$	$0.081 \pm 0.008^{\text{d}}$ , $0.038 \pm 0.005^{\text{e}}$	ADS + Global
HD 149382	XSHOOTER	$35\,338 \pm 404$	$5.938 \pm 0.056$	$-1.515 \pm 0.110$	-	-	ADS + SPAS
	UVES	$34\,953 \pm 42$	$5.890 \pm 0.005$	$-1.465 \pm 0.006$	-	-	ADS + SPAS
Weighted Average		$34\,957 \pm 42$	$5.890 \pm 0.005$	$-1.465 \pm 0.006$	-	-	ADS + SPAS
HD 149382	XSHOOTER	$34\,822 \pm 187$	$5.865 \pm 0.043$	$-1.409 \pm 0.066$	-	-	LTE + SPAS
	UVES	$34\,409 \pm 52$	$5.793 \pm 0.007$	$-1.431 \pm 0.039$	-	-	LTE + SPAS
Weighted Average		$34\,439 \pm 51$	$5.795 \pm 0.007$	$-1.425 \pm 0.034$	-	-	LTE + SPAS
HD 149382	XSHOOTER	$35\,237 \pm 499$	$5.871 \pm 0.059$	$-1.388 \pm 0.103$	-	-	TLUSTY/SYNSPEC + SPAS
	UVES	$35\,036 \pm 37$	$5.797 \pm 0.005$	$-1.386 \pm 0.005$	-	-	TLUSTY/SYNSPEC + SPAS
Weighted Average		$35\,037 \pm 37$	$5.798 \pm 0.005$	$-1.386 \pm 0.005$	-	-	TLUSTY/SYNSPEC + SPAS
HD 149382	XSHOOTER	$35\,171 \pm 42$	$5.884 \pm 0.006$	$-1.451 \pm 0.007$	-	-	ADS + FITPROF
	UVES	$34\,231 \pm 55$	$5.880 \pm 0.007$	$-1.437 \pm 0.007$	-	-	ADS + FITPROF
Weighted Average		$34\,825 \pm 34$	$5.882 \pm 0.005$	$-1.444 \pm 0.005$	-	-	ADS + FITPROF
HD 149382	XSHOOTER	$34\,673 \pm 30$	$5.843 \pm 0.006$	$-1.403 \pm 0.008$	-	-	LTE + FITPROF
	UVES	$34\,577 \pm 43$	$5.784 \pm 0.008$	$-1.401 \pm 0.008$	-	-	LTE + FITPROF
Weighted Average		$34\,642 \pm 25$	$5.822 \pm 0.005$	$-1.4020 \pm 0.0057$	-	-	LTE + FITPROF
HD 149382	XSHOOTER	$35\,454 \pm 30$	$5.831 \pm 0.006$	$-1.378 \pm 0.007$	-	-	TLUSTY/SYNSPEC + FITPROF
	UVES	$35\,564 \pm 42$	$5.786 \pm 0.007$	$-1.382 \pm 0.007$	-	-	TLUSTY/SYNSPEC + FITPROF
Weighted Average		$35\,491 \pm 25$	$5.812 \pm 0.005$	$-1.380 \pm 0.005$	-	-	TLUSTY/SYNSPEC + FITPROF

## B. Comparison of the Abundance Results for PHL 25 and PHL 382 to Hämmerich (2020)

Hämmerich (2020) also performed a detailed metal abundance analysis of the two (post-)BHB stars PHL 25 and PHL 382 (see Figures 8.30 and 8.32 as well as Tables 18-23 in their work), whereby the improvements of the hybrid LTE/NLTE model atmosphere approach as well as of the global analysis strategy described in Sects. 6.8 and 7.1.2 (for instance, level dissolution or the local normalization procedure) were implemented. The author also made use of the same observed spectra as the present work. For both stars, a comparison of the results of this work to those of Hämmerich (2020) therefore seems reasonable.

Overall, the abundance pattern of PHL 25 found in this work is rather similar to the one determined by Hämmerich (2020). Yet, Hämmerich (2020) found carbon to be significantly more enhanced (by  $\sim +0.43$  dex). Although the uncertainties of the carbon abundance derived in the present work are quite large (see the respective entry in Table 11.2), they do not cover the measurement of Hämmerich (2020). Moreover, the silicon abundance of PHL 25 determined by Hämmerich (2020) is higher (by  $\sim +0.16$  dex) than the one measured in this work. Last but not least, the sulfur abundance measured by Hämmerich (2020) is  $\sim +0.56$  dex higher than the upper limit of  $-7.20$  derived in this work. In this case, however, the uncertainties of Hämmerich (2020) are large and, after all, cover a value of  $-7.00$ . For PHL 382, the carbon, magnesium, aluminum, silicon, and iron abundances derived in both studies match. Nonetheless, Hämmerich (2020) measured less nitrogen (by  $\sim -0.18$  dex), less oxygen (by  $\sim -0.44$  dex), less neon (by  $\sim -0.13$  dex), and less argon (by  $\sim -0.12$  dex) but slightly more sulfur (by  $\sim +0.10$  dex).

When comparing the results of PHL 25 and PHL 382 derived in this work to the ones determined by Hämmerich (2020), it becomes rather difficult to find an explanation for the fact that certain elements are discrepant, whereas others are not. A possible explanation could be the fact that Hämmerich (2020) has derived different atmospheric parameters for both stars compared to the present work. While this is only conditionally true for the helium abundance, the effective temperature and the surface gravity are more affected (see the results presented in Sect. 10.1). Particularly, this applies to PHL 25: compare  $T_{\text{eff}} = 17\,585 \pm 200$  K and  $\log(g) = 4.57 \pm 0.05$  derived by Hämmerich (2020) to  $T_{\text{eff}} = 18\,440_{-110}^{+60}$  K and  $\log(g) = 4.736_{-0.016}^{+0.010}$  determined in this work. In the case of PHL 382, the deviations are less pronounced:  $T_{\text{eff}} = 17\,903 \pm 190$  K and  $\log(g) = 4.08 \pm 0.05$  (Hämmerich, 2020) vs.  $T_{\text{eff}} = 17\,195_{-28}^{+26}$  K and  $\log(g) = 4.034_{-0.006}^{+0.004}$  (this work). A second explanation for the measured abundance deviations may be given by the fact that Hämmerich (2020) has also fitted the microturbulence  $\xi$  as well as the macroturbulence  $\zeta$ , both of which are set to zero within the framework of this thesis. It has to be mentioned, however, that Hämmerich (2020) did not determine any unusual values for  $\xi$  and  $\zeta$  for both objects (see Table 17 in their work), which is why this hypothesis seems rather unlikely. Last, the analyzed

## B. Comparison of the Abundance Results for PHL 25 and PHL 382 to Hämmerich (2020)

wavelength regime as well as the number of investigated spectral lines may differ in both studies. This, however, seems also rather unlikely because the present work makes use of the same observed spectra as Hämmerich (2020).

## Bibliography

- Abolfathi, B., Aguado, D. S., Aguilar, G. et al. 2018, ApJS, 235, 42
- Ahmad, A. & Jeffery, C. S. 2005, A&A, 437, L51
- Ahmad, A., Jeffery, C. S. & Fullerton, A. W. 2004, A&A, 418, 275
- Alam, S., Albareti, F. D., Allende Prieto, C. et al. 2015, ApJS, 219, 12
- Arenou, F., Luri, X., Babusiaux, C. et al. 2018, A&A, 616, A17
- . 2017, A&A, 599, A50
- Asplund, M., Grevesse, N., Sauval, A. J. et al. 2009, ARA&A, 47, 481
- Astraatmadja, T. L. & Bailer-Jones, C. A. L. 2016a, ApJ, 832, 137
- . 2016b, ApJ, 833, 119
- Astropy Collaboration, Price-Whelan, A. M., Sipőcz, B. M. et al. 2018, AJ, 156, 123
- Astropy Collaboration, Robitaille, T. P., Tollerud, E. J. et al. 2013, A&A, 558, A33
- Atutov, S. N. 1986, Physics Letters A, 119, 121
- Auer, L. H. & Mihalas, D. 1969, ApJ, 158, 641
- . 1973, ApJS, 25, 433
- Aznar Cuadrado, R. & Jeffery, C. S. 2002, A&A, 385, 131
- Babel, J. 1996, A&A, 309, 867
- Bailer-Jones, C. A. L. 2015, PASP, 127, 994
- Bailer-Jones, C. A. L. 2017, Practical Bayesian Inference
- Bailer-Jones, C. A. L., Rybizki, J., Fouesneau, M. et al. 2018, AJ, 156, 58
- Ballester, P., Vernet, J., Modigliani, A. et al. 2020, Very Large Telescope - X-Shooter Pipeline User Manual, European Southern Observatory [LINK]
- Barnard, A. J., Cooper, J. & Smith, E. W. 1974, J. Quant. Spec. Radiat. Transf., 14, 1025
- Battich, T., Miller Bertolami, M. M., Córscico, A. H. et al. 2018, A&A, 614, A136
- Beauchamp, A., Wesemael, F. & Bergeron, P. 1997, ApJS, 108, 559

- Becker, S. R. 1998, in *Astronomical Society of the Pacific Conference Series*, Vol. 131, *Properties of Hot Luminous Stars*, ed. I. Howarth, 137
- Becker, S. R. & Butler, K. 1988, *A&A*, 201, 232
- Behr, B. B. 2003, *ApJS*, 149, 101
- Bergeron, P., Saffer, R. A. & Liebert, J. 1992, *ApJ*, 394, 228
- Bevington, P. R. & Robinson, D. K. 1992, *Data reduction and error analysis for the physical sciences*
- Bianchi, L., Shiao, B. & Thilker, D. 2017, *ApJS*, 230, 24
- Bixler, J. V., Bowyer, S. & Laget, M. 1991, *A&A*, 250, 370
- Blanchette, J. P., Chayer, P., Wesemael, F. et al. 2008, *ApJ*, 678, 1329
- Blanco-Cuaresma, S. 2019, *MNRAS*, 486, 2075
- Bohlender, D. 2005, in *EAS Publications Series*, Vol. 17, *EAS Publications Series*, ed. G. Alecian, O. Richard, & S. Vauclair, 83–88
- Bohlender, D. A., Rice, J. B. & Hechler, P. 2010, *A&A*, 520, A44
- Bonifacio, P., Castelli, F. & Hack, M. 1995, *A&AS*, 110, 441
- Brown, T. M., Sweigart, A. V., Lanz, T. et al. 2001, *ApJ*, 562, 368
- Brown, W. R., Anderson, J., Gnedin, O. Y. et al. 2015, *ApJ*, 804, 49
- Brown, W. R., Kilic, M., Allende Prieto, C. et al. 2013, *ApJ*, 769, 66
- Butkevich, A. G., Klioner, S. A., Lindegren, L. et al. 2017, *A&A*, 603, A45
- Butler, K. & Giddings, J. R. 1985, in *Newsletter on Analysis of Astronomical Spectra*, No. 9, (Daresbury Laboratory, Daresbury, England)
- Cadelano, M., Pallanca, C., Ferraro, F. R. et al. 2015, *ApJ*, 812, 63
- Cantiello, M., Langer, N., Brott, I. et al. 2009, *A&A*, 499, 279
- Carnochan, D. J. & Wilson, R. 1983, *MNRAS*, 202, 317
- Carrasco, J. M., Evans, D. W., Montegriffo, P. et al. 2016, *A&A*, 595, A7
- Casali, M., Adamson, A., Alves de Oliveira, C. et al. 2007, *A&A*, 467, 777
- Cassisi, S., Schlattl, H., Salaris, M. et al. 2003, *ApJL*, 582, L43
- Castellani, M. & Castellani, V. 1993, *ApJ*, 407, 649
- Castellani, M., Castellani, V. & Prada Moroni, P. G. 2006, *A&A*, 457, 569
- Castelli, F. & Hubrig, S. 2007, *A&A*, 475, 1041

## Bibliography

---

- Chambers, K. C. et al. 2017, *VizieR Online Data Catalog*, II/349
- Charpinet, S., Brassard, P., Fontaine, G. et al. 2019, *A&A*, 632, A90
- Charpinet, S., Fontaine, G., Brassard, P. et al. 1997, *ApJL*, 483, L123
- . 1996, *ApJL*, 471, L103
- . 2011, *Nature*, 480, 496
- Chayer, P., Fontaine, M., Fontaine, G. et al. 2006, *Baltic Astronomy*, 15, 131
- Chen, X., Han, Z., Deca, J. et al. 2013, *MNRAS*, 434, 186
- Cioni, M. R. L., Clementini, G., Girardi, L. et al. 2011, *A&A*, 527, A116
- Clausen, D. & Wade, R. A. 2011, *ApJL*, 733, L42
- Clough, S. A., Shephard, M. W., Mlawer, E. J. et al. 2005, *J. Quant. Spec. Radiat. Transf.*, 91, 233
- Code, A. D. & Welch, G. A. 1979, *ApJ*, 228, 95
- Collins, George W., I. 1989, *The fundamentals of stellar astrophysics II*.
- Copperwheat, C. M., Morales-Rueda, L., Marsh, T. R. et al. 2011, *MNRAS*, 415, 1381
- Cowley, C. R. & Hubrig, S. 2005, *A&A*, 432, L21
- Cowley, C. R., Hubrig, S. & González, J. F. 2009, *MNRAS*, 396, 485
- Cox, A. N. 2000, *Allen's astrophysical quantities*
- Cross, N. J. G., Collins, R. S., Mann, R. G. et al. 2012, *A&A*, 548, A119
- Şener, H. T. & Jeffery, C. S. 2014, *MNRAS*, 440, 2676
- Cutri, R. M., Skrutskie, M. F., van Dyk, S. et al. 2003, *VizieR Online Data Catalog*, II/246
- Cutri, R. M. et al. 2014, *VizieR Online Data Catalog*, II/328
- D'Cruz, N. L., Dorman, B., Rood, R. T. et al. 1996, *ApJ*, 466, 359
- de Bruijne, J., Kohley, R. & Prusti, T. 2010, in *Society of Photo-Optical Instrumentation Engineers (SPIE) Conference Series*, Vol. 7731, *Space Telescopes and Instrumentation 2010: Optical, Infrared, and Millimeter Wave*, ed. J. Oschmann, Jacobus M., M. C. Clampin, & H. A. MacEwen, 77311C
- de Jong, J. T. A., Verdoes Kleijn, G. A., Erben, T. et al. 2017, *A&A*, 604, A134
- Dekker, H., D'Odorico, S., Kaufer, A. et al. 2000, in *Proceedings of the SPIE*, Vol. 4008, *Optical and IR Telescope Instrumentation and Detectors*, ed. M. Iye & A. F. Moorwood, 534–545
- Demircan, O. & Kahraman, G. 1991, *Ap&SS*, 181, 313

- DENIS Consortium. 2005, VizieR Online Data Catalog, II/263
- Dimitrijevic, M. S. & Sahal-Brechot, S. 1984, *J. Quant. Spec. Radiat. Transf.*, 31, 301
- . 1990, *A&AS*, 82, 519
- Dorman, B., Rood, R. T. & O'Connell, R. W. 1993, *ApJ*, 419, 596
- Dorsch, M. 2017, The chemical composition of the He-enriched sdO-star HD 127493, Friedrich-Alexander-Universität Erlangen-Nürnberg [LINK]
- Dorsch, M., Latour, M. & Heber, U. 2019, *A&A*, 630, A130
- Dorsch, M., Latour, M., Heber, U. et al. 2020, *A&A*, 643, A22
- Downes, R. A. 1986, *ApJS*, 61, 569
- Drechsel, H. et al. 2020, Praktikumsanleitung des Astronomischen Praktikums, Friedrich-Alexander-Universität Erlangen-Nürnberg [LINK]
- Drilling, J. S., Jeffery, C. S., Heber, U. et al. 2013, *A&A*, 551, A31
- Dworetzky, M. M. 2004, in *The A-Star Puzzle*, ed. J. Zverko, J. Ziznovsky, S. J. Adelman, & W. W. Weiss, Vol. 224, 727–733
- Edelmann, H., Heber, U., Altmann, M. et al. 2005, *A&A*, 442, 1023
- Edelmann, H., Heber, U., Hagen, H. J. et al. 2003, *A&A*, 400, 939
- Edelmann, H., Heber, U., Lisker, T. et al. 2004, *Ap&SS*, 291, 315
- Edelmann, H., Heber, U. & Napiwotzki, R. 2001, *Astronomische Nachrichten*, 322, 401
- Edelmann, H., Heber, U., Napiwotzki, R. et al. 1997, in *Astronomische Gesellschaft Abstract Series*, Vol. 13, *Astronomische Gesellschaft Abstract Series*, 206
- Edelmann, H., Heber, U., Napiwotzki, R. et al. 1999, in *Astronomical Society of the Pacific Conference Series*, Vol. 169, *11th European Workshop on White Dwarfs*, ed. S. E. Solheim & E. G. Meistas, 546
- El-Badry, K., Rix, H.-W. & Heintz, T. M. 2021, *MNRAS*
- ESA. 1997, in *ESA Special Publication*, Vol. 1200, *ESA Special Publication*
- ESO. 2019, *Very Large Telescope - User Manual for molecfit*, European Southern Observatory [LINK]
- Evans, D. W., Riello, M., De Angeli, F. et al. 2017, *A&A*, 600, A51
- . 2018, *A&A*, 616, A4
- Farthmann, M., Dreizler, S., Heber, U. et al. 1994, *A&A*, 291, 919
- Feautrier, P. 1964, *Comptes Rendus Academie des Sciences (serie non specifiée)*, 258, 3189

## Bibliography

---

- . 1967, *Annales d'Astrophysique*, 30, 125
- . 1968, *Annales d'Astrophysique*, 31, 257
- Finch, C. T. & Zacharias, N. 2016, *VizieR Online Data Catalog*, I/333
- Fink, M., Hillebrandt, W. & Röpkke, F. K. 2007, *A&A*, 476, 1133
- Fink, M., Röpkke, F. K., Hillebrandt, W. et al. 2010, *A&A*, 514, A53
- Fitzpatrick, E. L., Massa, D., Gordon, K. D. et al. 2019, *ApJ*, 886, 108
- Fontaine, G., Brassard, P., Charpinet, S. et al. 2012, *A&A*, 539, A12
- Fontaine, G. & Chayer, P. 1997, in *The Third Conference on Faint Blue Stars*, ed. A. G. D. Philip, J. Liebert, R. Saffer, & D. S. Hayes, 169
- Fred, M., Tomkins, F. S., Brody, J. K. et al. 1951, *Physical Review*, 82, 406
- Gaia Collaboration, Brown, A. G. A., Vallenari, A. et al. 2018, *A&A*, 616, A1
- . 2020, arXiv e-prints, arXiv:2012.01533
- . 2016a, *A&A*, 595, A2
- Gaia Collaboration, Prusti, T., de Bruijne, J. H. J. et al. 2016b, *A&A*, 595, A1
- Geier, S. 2013, *A&A*, 549, A110
- . 2020, *A&A*, 635, A193
- Geier, S., Classen, L. & Heber, U. 2011a, *ApJL*, 733, L13
- Geier, S., Edelmann, H., Heber, U. et al. 2009, *ApJL*, 702, L96
- Geier, S., Fürst, F., Ziegerer, E. et al. 2015, *Science*, 347, 1126
- Geier, S. & Heber, U. 2012, *A&A*, 543, A149
- Geier, S., Heber, U., Edelmann, H. et al. 2012, in *Astronomical Society of the Pacific Conference Series*, Vol. 452, *Fifth Meeting on Hot Subdwarf Stars and Related Objects*, ed. D. Kilkeny, C. S. Jeffery, & C. Koen, 57
- Geier, S., Heber, U., Edelmann, H. et al. 2013a, *A&A*, 557, A122
- Geier, S., Heber, U., Heuser, C. et al. 2013b, *A&A*, 551, L4
- Geier, S., Heber, U., Podsiadlowski, P. et al. 2010, *A&A*, 519, A25
- Geier, S., Marsh, T. R., Dunlap, B. H. et al. 2013c, in *Astronomical Society of the Pacific Conference Series*, Vol. 469, *18th European White Dwarf Workshop.*, ed. J. Krzesiński, G. Stachowski, P. Moskalik, & K. Bajan, 373
- Geier, S., Marsh, T. R., Wang, B. et al. 2013d, *A&A*, 554, A54
- Geier, S., Maxted, P. F. L., Napiwotzki, R. et al. 2011b, *A&A*, 526, A39

- 
- Geier, S., Nesslinger, S., Heber, U. et al. 2007, *A&A*, 464, 299
- . 2008, *A&A*, 477, L13
- Giddings, J. R. 1980, PhD thesis, University College London, UK
- Goldoni, P., Royer, F., François, P. et al. 2006, in *Society of Photo-Optical Instrumentation Engineers (SPIE) Conference Series*, Vol. 6269, Society of Photo-Optical Instrumentation Engineers (SPIE) Conference Series, 62692K
- Graczyk, D., Pietrzyński, G., Gieren, W. et al. 2019, *ApJ*, 872, 85
- Gray, D. F. 2005, *The Observation and Analysis of Stellar Photospheres*
- Green, E. M., Fontaine, G., Reed, M. D. et al. 2003, *ApJL*, 583, L31
- Green, E. M., Guvenen, B., O'Malley, C. J. et al. 2011, *ApJ*, 734, 59
- Green, R. F., Schmidt, M. & Liebert, J. 1986, *ApJS*, 61, 305
- Greenstein, G. S. 1967, *Nature*, 213, 871
- Greenstein, J. L. 1956, in *Third Berkeley Symposium on Mathematical Statistics and Probability*, 11–29
- Groth, H. G., Kudritzki, R. P. & Heber, U. 1985, *A&A*, 152, 107
- Haas, S. E. 1997, PhD thesis, Friedrich Alexander University of Erlangen-Nuremberg, Germany
- Hagen, H. J., Groote, D., Engels, D. et al. 1995, *A&AS*, 111, 195
- Hambly, N. C., Collins, R. S., Cross, N. J. G. et al. 2008, *MNRAS*, 384, 637
- Hämmerich, S. 2020, *Quantitative spectral analyses of blue horizontal branch stars*, Friedrich-Alexander-Universität Erlangen-Nürnberg [LINK]
- Han, Z., Podsiadlowski, P., Maxted, P. F. L. et al. 2003, *MNRAS*, 341, 669
- . 2002, *MNRAS*, 336, 449
- Hartoog, M. R. 1979, *ApJ*, 231, 161
- Hartoog, M. R. & Cowley, A. P. 1979, *ApJ*, 228, 229
- Harwit, M. 1988, *Astrophysical Concepts*
- Hauck, B. & Mermilliod, M. 1998, *A&AS*, 129, 431
- Heber, U. 1986, *A&A*, 155, 33
- . 1987, *Mitteilungen der Astronomischen Gesellschaft Hamburg*, 70, 79
- Heber, U. 1991, in *Evolution of Stars: the Photospheric Abundance Connection*, ed. G. Michaud & A. V. Tutukov, Vol. 145, 363
- . 2009, *ARA&A*, 47, 211

## Bibliography

---

- . 2016, *PASP*, 128, 082001
- Heber, U. & Edelman, H. 2004, *Ap&SS*, 291, 341
- Heber, U., Edelman, H., Lisker, T. et al. 2003a, *A&A*, 411, L477
- Heber, U., Hunger, K., Jonas, G. et al. 1984, *A&A*, 130, 119
- Heber, U., Irrgang, A. & Schaffenroth, J. 2018, *Open Astronomy*, 27, 35
- Heber, U. & Langhans, G. 1986, in *ESA Special Publication*, Vol. 263, *New Insights in Astrophysics. Eight Years of UV Astronomy with IUE*, ed. E. J. Rolfe & R. Wilson
- Heber, U., Maxted, P. F. L., Marsh, T. R. et al. 2003b, in *Astronomical Society of the Pacific Conference Series*, Vol. 288, *Stellar Atmosphere Modeling*, ed. I. Hubeny, D. Mihalas, & K. Werner, 251
- Heber, U., Reid, I. N. & Werner, K. 2000, *A&A*, 363, 198
- Henden, A. A., Templeton, M., Terrell, D. et al. 2016, *VizieR Online Data Catalog*, 2336
- Hewett, P. C., Warren, S. J., Leggett, S. K. et al. 2006, *MNRAS*, 367, 454
- Hilditch, R. W. 2001, *An Introduction to Close Binary Stars*
- Hill, G. J., Drory, N., Good, J. M. et al. 2018, in *Society of Photo-Optical Instrumentation Engineers (SPIE) Conference Series*, Vol. 10700, *Ground-based and Airborne Telescopes VII*, 107000P
- Hillebrandt, W., Kromer, M., Röpke, F. K. et al. 2013, *Frontiers of Physics*, 8, 116
- Hirsch, H. A. 2009, PhD thesis, Friedrich Alexander University of Erlangen-Nuremberg, Germany
- Hirsch, H. A., Heber, U., O'Toole, S. J. et al. 2005, *A&A*, 444, L61
- Hodgkin, S. T., Irwin, M. J., Hewett, P. C. et al. 2009, *MNRAS*, 394, 675
- Høg, E., Fabricius, C., Makarov, V. V. et al. 2000, *A&A*, 355, L27
- Holdsworth, D. L., Østensen, R. H., Smalley, B. et al. 2017, *MNRAS*, 466, 5020
- Houck, J. C. & Denicola, L. A. 2000, in *Astronomical Society of the Pacific Conference Series*, Vol. 216, *Astronomical Data Analysis Software and Systems IX*, ed. N. Manset, C. Veillet, & D. Crabtree, 591 [ADS]
- Hu, H., Dupret, M.-A., Aerts, C. et al. 2008, *A&A*, 490, 243
- Hu, H., Tout, C. A., Glebbeek, E. et al. 2011, *MNRAS*, 418, 195
- Hubeny, I. 1988, *Computer Physics Communications*, 52, 103
- Hubeny, I., Hummer, D. G. & Lanz, T. 1994, *A&A*, 282, 151
- Hubeny, I. & Lanz, T. 1995, *ApJ*, 439, 875

- 
- Hubeny, I. & Lanz, T. 2003, in *Astronomical Society of the Pacific Conference Series*, Vol. 288, *Stellar Atmosphere Modeling*, ed. I. Hubeny, D. Mihalas, & K. Werner, 51
- . 2017a, ArXiv e-prints [ADS]
- . 2017b, ArXiv e-prints [ADS]
- . 2017c, ArXiv e-prints [ADS]
- Hubeny, I. & Mihalas, D. 2014, *Theory of Stellar Atmospheres*
- Hughes, D. S. & Eckart, C. 1930, *Physical Review*, 36, 694
- Humason, M. L. & Zwicky, F. 1947, *ApJ*, 105, 85
- Hummer, D. G. & Mihalas, D. 1988, *ApJ*, 331, 794
- Hunger, K. & Groote, D. 1999, *A&A*, 351, 554
- Hunger, K., Groote, D. & Heber, U. 1996, in *Astronomical Society of the Pacific Conference Series*, Vol. 96, *Hydrogen Deficient Stars*, ed. C. S. Jeffery & U. Heber, 179
- Hunter, J. D. 2007, *Computing in Science and Engineering*, 9, 90 [ADS]
- Husser, T. O., Wende-von Berg, S., Dreizler, S. et al. 2013, *A&A*, 553, A6
- Iben, I., J. & Tutukov, A. V. 1984, *ApJS*, 54, 335
- Irrgang, A. 2014, PhD thesis, Friedrich Alexander University of Erlangen-Nuremberg, Germany
- Irrgang, A., Kreuzer, S., Heber, U. et al. 2018, *A&A*, 615, L5
- Irrgang, A., Przybilla, N., Heber, U. et al. 2014, *A&A*, 565, A63
- Irwin, M. J., Lewis, J., Hodgkin, S. et al. 2004, in *Society of Photo-Optical Instrumentation Engineers (SPIE) Conference Series*, Vol. 5493, *Proceedings of the SPIE*, ed. P. J. Quinn & A. Bridger, 411–422
- Istrate, A. G., Marchant, P., Tauris, T. M. et al. 2016, *A&A*, 595, A35
- Jacobs, V. A., Østensen, R. H., van Winckel, H. et al. 2011, in *American Institute of Physics Conference Series*, Vol. 1331, *American Institute of Physics Conference Series*, ed. S. Schuh, H. Drechsel, & U. Heber, 304–309
- Jao, W.-C., Henry, T. J., Beaulieu, T. D. et al. 2008, *AJ*, 136, 840
- Jeffery, C. S. 2011, *Information Bulletin on Variable Stars*, 5964, 1
- Jeffery, C. S., Baran, A. S., Behara, N. T. et al. 2017, *MNRAS*, 465, 3101
- Jeffery, C. S. & Miszalski, B. 2019, *MNRAS*, 489, 1481
- Jeffery, C. S., Pereira, C., Naslim, N. et al. 2012, in *Astronomical Society of the Pacific Conference Series*, Vol. 452, *Fifth Meeting on Hot Subdwarf Stars and Related Objects*, ed. D. Kilkeny, C. S. Jeffery, & C. Koen, 41

## Bibliography

---

- Jeffery, C. S. & Saio, H. 2006, *MNRAS*, 372, L48
- Jeffery, S., Naslim, N., Behara, N. et al. 2015, *Astronomy and Geophysics*, 56, 2.32
- Jones, E., Oliphant, T. & Peterson, P. 2001
- Justham, S., Podsiadlowski, P. & Han, Z. 2011, *MNRAS*, 410, 984
- Kaler, J. B. 1994, *Sterne und ihre Spektren. Astronomische Signale aus Licht.*
- Karl, C. 2004, PhD thesis, Friedrich-Alexander-Universität Erlangen-Nürnberg [LINK]
- Karl, C., Heber, U., Jeffery, S. et al. 2006, *Baltic Astronomy*, 15, 151
- Karttunen, H., Kröger, P., Oja, H. et al. 2007, *Fundamental Astronomy*
- Kaufer, A., Stahl, O., Tubbesing, S. et al. 1999, *The Messenger*, 95, 8
- Kausch, W., Noll, S., Smette, A. et al. 2015, *A&A*, 576, A78
- Kawka, A., Pigulski, A., O'Toole, S. et al. 2012, in *Astronomical Society of the Pacific Conference Series*, Vol. 452, *Fifth Meeting on Hot Subdwarf Stars and Related Objects*, ed. D. Kilkenny, C. S. Jeffery, & C. Koen, 121
- Kawka, A., Vennes, S., O'Toole, S. et al. 2015, *MNRAS*, 450, 3514
- Kellermann, H., Grupp, F., Brucalassi, A. et al. 2015, in *Society of Photo-Optical Instrumentation Engineers (SPIE) Conference Series*, Vol. 9605, *Techniques and Instrumentation for Detection of Exoplanets VII*, 96051R
- Khalack, V., LeBlanc, F. & Behr, B. B. 2010, *MNRAS*, 407, 1767
- Khalack, V., Yameogo, B., LeBlanc, F. et al. 2014, *MNRAS*, 445, 4086
- Khalack, V. R., Leblanc, F., Behr, B. B. et al. 2008, *A&A*, 477, 641
- Khalack, V. R., Leblanc, F., Bohlender, D. et al. 2007, *A&A*, 466, 667
- Kilkenny, D., O'Donoghue, D., Crause, L. et al. 2009, *MNRAS*, 396, 548
- Kilkenny, D., O'Donoghue, D., Koen, C. et al. 1997, *MNRAS*, 287, 867
- Kilkenny, D., O'Donoghue, D., Worters, H. L. et al. 2015, *MNRAS*, 453, 1879
- Kilkenny, D., Worters, H. L., O'Donoghue, D. et al. 2017, *VizieR Online Data Catalog*, J/MNRAS/459/4343
- Klepp, S. & Rauch, T. 2011, *A&A*, 531, L7
- Kohley, R., Garé, P., Vétel, C. et al. 2012, in *Society of Photo-Optical Instrumentation Engineers (SPIE) Conference Series*, Vol. 8442, *Space Telescopes and Instrumentation 2012: Optical, Infrared, and Millimeter Wave*, ed. M. C. Clampin, G. G. Fazio, H. A. MacEwen, & J. Oschmann, Jacobus M., 84421P
- Kupfer, T., Bauer, E. B., Burdge, K. B. et al. 2020a, *ApJL*, 898, L25

- Kupfer, T., Bauer, E. B., Marsh, T. R. et al. 2020b, *ApJ*, 891, 45
- Kurucz, R. 1993, *ATLAS9 Stellar Atmosphere Programs and 2 km/s grid*. Kurucz CD-ROM No. 13. Cambridge, 13
- Kurucz, R. L. 1979, *ApJS*, 40, 1
- Kurucz, R. L. 1996, in *Astronomical Society of the Pacific Conference Series*, Vol. 108, M.A.S.S., *Model Atmospheres and Spectrum Synthesis*, ed. S. J. Adelman, F. Kupka, & W. W. Weiss, 160
- Lamontagne, R., Demers, S., Wesemael, F. et al. 2000, *AJ*, 119, 241
- Lanz, T., Brown, T. M., Sweigart, A. V. et al. 2004, *ApJ*, 602, 342
- Latour, M., Chayer, P., Green, E. M. et al. 2018, *A&A*, 609, A89
- Latour, M., Dorsch, M. & Heber, U. 2019a, *A&A*, 629, A148
- Latour, M., Fontaine, G., Chayer, P. et al. 2013, *ApJ*, 773, 84
- Latour, M., Fontaine, G., Green, E. M. et al. 2015, *A&A*, 579, A39
- Latour, M., Green, E. M. & Fontaine, G. 2019b, *A&A*, 623, L12
- Latour, M., Heber, U., Irrgang, A. et al. 2016, *A&A*, 585, A115
- Lawrence, A., Warren, S. J., Almaini, O. et al. 2007, *MNRAS*, 379, 1599
- . 2013, *VizieR Online Data Catalog*, II/319
- LeBlanc, F., Hui-Bon-Hoa, A. & Khalack, V. R. 2010, *MNRAS*, 409, 1606
- LeBlanc, F. & Michaud, G. 1993, *ApJ*, 408, 251
- Lemke, M. 1997, *A&AS*, 122, 285
- Leone, F. & Lanzafame, A. C. 1997, *A&A*, 320, 893
- Leung, H. W. & Bovy, J. 2019, *arXiv e-prints*, arXiv:1902.08634
- Lindegren, L. & Bastian, U. 2010, in *EAS Publications Series*, Vol. 45, *EAS Publications Series*, 109–114
- Lindegren, L., Hernández, J., Bombrun, A. et al. 2018, *A&A*, 616, A2
- Lindegren, L., Lammers, U., Bastian, U. et al. 2016, *A&A*, 595, A4
- Lindegren, L., Lammers, U., Hobbs, D. et al. 2012, *A&A*, 538, A78
- Lisker, T., Heber, U., Napiwotzki, R. et al. 2005, *A&A*, 430, 223
- . 2004, *Ap&SS*, 291, 351
- Livne, E. & Glasner, A. S. 1990, *ApJ*, 361, 244

## Bibliography

---

- Lucas, P. W., Hoare, M. G., Longmore, A. et al. 2008, MNRAS, 391, 136
- Luri, X., Brown, A. G. A., Sarro, L. M. et al. 2018, A&A, 616, A9
- Luyten, W. J. 1953, AJ, 58, 75
- Maíz Apellániz, J. & Weiler, M. 2018, A&A, 619, A180
- Maoz, D., Mannucci, F. & Nelemans, G. 2014, ARA&A, 52, 107
- Markarian, B. E., Lipovetsky, V. A., Stepanian, J. A. et al. 1989, Soobshcheniya Spetsial'noj Astrofizicheskoy Observatorii, 62, 5
- Marsh, T. R., Dhillon, V. S. & Duck, S. R. 1995, MNRAS, 275, 828
- Martin, P., Jeffery, C. S., Naslim, N. et al. 2017, MNRAS, 467, 68
- Maxted, P. F. L., Bloemen, S., Heber, U. et al. 2014, MNRAS, 437, 1681
- Maxted, P. F. L., Heber, U., Marsh, T. R. et al. 2001, MNRAS, 326, 1391
- Maxted, P. F. L., Marsh, T. R. & North, R. C. 2000, MNRAS, 317, L41
- Maza, N. L., Nieva, M.-F. & Przybilla, N. 2014a, A&A, 572, A112
- Maza, N. L., Nieva, M. F., Przybilla, N. et al. 2014b, in Revista Mexicana de Astronomia y Astrofisica Conference Series, Vol. 44, Revista Mexicana de Astronomia y Astrofisica Conference Series, 159–159
- McMahon, R. G., Banerji, M., Gonzalez, E. et al. 2013, The Messenger, 154, 35
- Meisenheimer, K. 1998, User Guide to the CAFOS2.2 [LINK]
- Mermilliod, J. C. 2006, VizieR Online Data Catalog, II/168
- Michalik, D., Lindegren, L. & Hobbs, D. 2015, A&A, 574, A115
- Michaud, G., Alecian, G. & Richer, J. 2015, Atomic Diffusion in Stars
- Michaud, G., Montmerle, T., Cox, A. N. et al. 1979, ApJ, 234, 206
- Michaud, G., Richer, J. & Richard, O. 2008, ApJ, 675, 1223
- . 2011, A&A, 529, A60
- Mickaelian, A. M., Nesci, R., Rossi, C. et al. 2007, A&A, 464, 1177
- Mieske, S., Dumas, C., Kaufer, A. et al. 2019, Very Large Telescope - X-shooter User Manual, European Southern Observatory [LINK]
- Mieske, S., Kaufer, A., Sbordone, L. et al. 2020, Very Large Telescope - Paranal Science Operations - UV-Visual Echelle Spectrograph User manual, European Southern Observatory
- Miller Bertolami, M. M., Althaus, L. G., Unglaub, K. et al. 2008, A&A, 491, 253

- Modigliani, A., Goldoni, P., Royer, F. et al. 2010, in Society of Photo-Optical Instrumentation Engineers (SPIE) Conference Series, Vol. 7737, Observatory Operations: Strategies, Processes, and Systems III, 773728
- Moehler, S., Richtler, T., de Boer, K. S. et al. 1990, *A&AS*, 86, 53
- Möller, L. 2021, Elemental abundances of sdB-Stars as benchmark for diffusion models, Friedrich-Alexander-Universität Erlangen-Nürnberg [LINK]
- Moore, C. E. 1959, A multiplet table of astrophysical interest. Part 1
- Morales-Rueda, L., Marsh, T. R., North, R. C. et al. 2003a, in NATO Advanced Study Institute (ASI) Series B, Vol. 105, White Dwarfs, 57
- Morales-Rueda, L., Maxted, P. F. L., Marsh, T. R. et al. 2003b, *MNRAS*, 338, 752
- Moran, C., Maxted, P., Marsh, T. R. et al. 1999, *MNRAS*, 304, 535
- Morel, M. & Magnenat, P. 1978, *A&AS*, 34, 477
- Morel, T. & Butler, K. 2008, *A&A*, 487, 307
- Morel, T., Butler, K., Aerts, C. et al. 2006, *A&A*, 457, 651
- Münch, G. 1958, *ApJ*, 127, 642
- Napiwotzki, R. 1999, *A&A*, 350, 101
- Napiwotzki, R. 2008, in Astronomical Society of the Pacific Conference Series, Vol. 392, Hot Subdwarf Stars and Related Objects, ed. U. Heber, C. S. Jeffery, & R. Napiwotzki, 139
- Napiwotzki, R., Christlieb, N., Drechsel, H. et al. 2001a, *Astronomische Nachrichten*, 322, 411
- Napiwotzki, R., Edelmann, H., Heber, U. et al. 2001b, *A&A*, 378, L17
- Napiwotzki, R., Karl, C. A., Lisker, T. et al. 2004a, *Ap&SS*, 291, 321
- Napiwotzki, R., Yungelson, L., Nelemans, G. et al. 2004b, in Astronomical Society of the Pacific Conference Series, Vol. 318, Spectroscopically and Spatially Resolving the Components of the Close Binary Stars, ed. R. W. Hilditch, H. Hensberge, & K. Pavlovski, 402–410
- Naslim, N., Geier, S., Jeffery, C. S. et al. 2012, *MNRAS*, 423, 3031
- Naslim, N., Jeffery, C. S., Ahmad, A. et al. 2010, *MNRAS*, 409, 582
- Naslim, N., Jeffery, C. S., Behara, N. T. et al. 2011, *MNRAS*, 412, 363
- Naslim, N., Jeffery, C. S., Hibbert, A. et al. 2013, *MNRAS*, 434, 1920
- Naslim, N., Jeffery, C. S. & Woolf, V. M. 2020, *MNRAS*, 491, 874
- Nelder, J. A. & Mead, R. 1965, *The Computer Journal*, 7, 308 [LINK]
- Nelson, L. A., Dubeau, E. & MacCannell, K. A. 2004, *ApJ*, 616, 1124

## Bibliography

---

- Németh, P. 2017, *Open Astronomy*, 26, 280
- Németh, P., Kawka, A. & Vennes, S. 2012, *MNRAS*, 427, 2180
- Niemczura, E., Vennes, S., Róžański, T. et al. 2018, *Contributions of the Astronomical Observatory Skalnaté Pleso*, 48, 287
- Nieva, M. F. & Przybilla, N. 2006, *ApJ*, 639, L39
- . 2007, *A&A*, 467, 295
- . 2008, *A&A*, 481, 199
- . 2012, *A&A*, 539, A143
- Norris, J. E., Ryan, S. G. & Beers, T. C. 1999, *ApJS*, 123, 639
- Oliphant, T. 2006, *Guide to NumPy*
- Oreiro, R., Ulla, A., Pérez Hernández, F. et al. 2004, *A&A*, 418, 243
- Østensen, R., Heber, U. & Maxted, P. 2005, in *Astronomical Society of the Pacific Conference Series*, Vol. 334, 14th European Workshop on White Dwarfs, ed. D. Koester & S. Moehler, 435
- Østensen, R. H. 2012, in *Astronomical Society of the Pacific Conference Series*, Vol. 452, Fifth Meeting on Hot Subdwarf Stars and Related Objects, ed. D. Kilkenney, C. S. Jeffery, & C. Koen, 233
- Østensen, R. H., Green, E. M., Bloemen, S. et al. 2010a, *MNRAS*, 408, L51
- Østensen, R. H., Jeffery, C. S., Saio, H. et al. 2020, *MNRAS*, 499, 3738
- Østensen, R. H., Oreiro, R., Solheim, J. E. et al. 2010b, *A&A*, 513, A6
- Østensen, R. H., Silvotti, R., Charpinet, S. et al. 2010c, *MNRAS*, 409, 1470
- O'Toole, S. J. & Heber, U. 2006, *A&A*, 452, 579
- Paczynski, B. 1976, in *IAU Symposium*, Vol. 73, Structure and Evolution of Close Binary Systems, ed. P. Eggleton, S. Mitton, & J. Whelan, 75
- Paunzen, E. 2015, *A&A*, 580, A23
- Pedregosa, F., Varoquaux, G., Gramfort, A. et al. 2011, *Journal of Machine Learning Research*, 12, 2825 [LINK]
- Pelisoli, I., Neunteufel, P., Geier, S. et al. 2021, *Nature Astronomy*, 5, 1052
- Pereira, C. 2011, PhD thesis, Queens University Belfast, Ireland
- Perryman, M. 2009, *Astronomical Applications of Astrometry: Ten Years of Exploitation of the Hipparcos Satellite Data*
- Perryman, M. A. C., de Boer, K. S., Gilmore, G. et al. 2001, *A&A*, 369, 339

- 
- Perryman, M. A. C., Hassan, H., Batut, T. et al. 1989, The Hipparcos mission. Pre-launch status. Volume I: The Hipparcos satellite.
- Pfeiffer, M. J., Frank, C., Baumüller, D. et al. 1998, *A&AS*, 130, 381
- Podsiadlowski, P. 2008, in *Astronomical Society of the Pacific Conference Series*, Vol. 401, RS Ophiuchi (2006) and the Recurrent Nova Phenomenon, ed. A. Evans, M. F. Bode, T. J. O'Brien, & M. J. Darnley, 63
- Politano, M., Taam, R. E., van der Sluys, M. et al. 2008, *ApJL*, 687, L99
- Postnov, K. A. & Yungelson, L. R. 2014, *Living Reviews in Relativity*, 17, 3
- Powell, M. J. D. 1964, *The Computer Journal*, 7, 155 [LINK]
- Press, W. H., Flannery, B. P. & Teukolsky, S. A. 1986, *Numerical recipes. The art of scientific computing*
- Przybilla, N. 2005, *A&A*, 443, 293
- Przybilla, N. & Butler, K. 2001, *A&A*, 379, 955
- . 2004, *ApJ*, 609, 1181
- Przybilla, N., Butler, K., Becker, S. R. et al. 2001, *A&A*, 369, 1009
- . 2006a, *A&A*, 445, 1099
- . 2000, *A&A*, 359, 1085
- Przybilla, N., Nieva, M.-F. & Butler, K. 2011, in *Journal of Physics Conference Series*, Vol. 328, *Journal of Physics Conference Series*, 012015
- Przybilla, N., Nieva, M. F. & Edelmann, H. 2006b, *Baltic Astronomy*, 15, 107
- Quievry, D., Charbonneau, P., Michaud, G. et al. 2009, *A&A*, 500, 1163
- Raddi, R., Hollands, M. A., Koester, D. et al. 2019, *MNRAS*, 489, 1489
- Ramspeck, M., Heber, U. & Moehler, S. 2001, *A&A*, 378, 907
- Randall, S. K., Bagnulo, S., Ziegerer, E. et al. 2015, *A&A*, 576, A65
- Randall, S. K., Calamida, A., Fontaine, G. et al. 2011, *ApJL*, 737, L27
- Randall, S. K., Matthews, J. M., Fontaine, G. et al. 2005, *ApJ*, 633, 460
- Ratzloff, J. K., Kupfer, T., Barlow, B. N. et al. 2020, *ApJ*, 902, 92
- Rauch, T., Rudkowski, A., Kampka, D. et al. 2014, *A&A*, 566, A3
- Rauch, T., Werner, K. & Kruk, J. W. 2010, *Ap&SS*, 329, 133
- Recio-Blanco, A., de Laverny, P., Allende Prieto, C. et al. 2016, *A&A*, 585, A93
- Reed, M. D., Baran, A. S., Telting, J. H. et al. 2018, *Open Astronomy*, 27, 157

## Bibliography

---

- Riello, M., De Angeli, F., Evans, D. W. et al. 2018, *A&A*, 616, A3
- Riess, A. G., Casertano, S., Yuan, W. et al. 2018, *ApJ*, 861, 126
- Rivera-Sandoval, L. E., van den Berg, M., Heinke, C. O. et al. 2015, *MNRAS*, 453, 2707
- Rothman, L. S., Gordon, I. E., Barbe, A. et al. 2009, *J. Quant. Spec. Radiat. Transf.*, 110, 533
- Rufener, F. 1988, *Catalogue of stars measured in the Geneva Observatory photometric system : 4 : 1988*
- Ruiz-Lapuente, P. 2014, *NewAR*, 62, 15
- Rybicki, G. B. & Hummer, D. G. 1991, *A&A*, 245, 171
- Sadakane, K. & Nishimura, M. 2017, *Publications of the Astronomical Society of Japan*, 69, 48
- . 2019, *Publications of the Astronomical Society of Japan*, 71, 45
- Saffer, R. A., Bergeron, P., Koester, D. et al. 1994, *ApJ*, 432, 351
- Saffer, R. A., Livio, M. & Yungelson, L. R. 1998, *ApJ*, 502, 394
- Sahoo, S. K., Baran, A. S., Heber, U. et al. 2020, *MNRAS*, 495, 2844
- Salgado, J., González, J., Gutiérrez, R. et al. 2017a, in *Astronomical Society of the Pacific Conference Series*, Vol. 512, *Astronomical Data Analysis Software and Systems XXV*, ed. N. P. F. Lorente, K. Shorridge, & R. Wayth, 293
- Salgado, J., González-Núñez, J., Gutiérrez-Sánchez, R. et al. 2017b, *Astronomy and Computing*, 21, 22
- Sargent, A. W. L. W. & Jugaku, J. 1961, *ApJ*, 134, 777
- Sargent, W. L. W. & Searle, L. 1968, *ApJ*, 152, 443
- Schaffenroth, V., Barlow, B. N., Geier, S. et al. 2019, *A&A*, 630, A80
- Schaffenroth, V., Classen, L., Nagel, K. et al. 2014, *A&A*, 570, A70
- Schaller, G., Schaerer, D., Meynet, G. et al. 1992, *A&AS*, 96, 269
- Schindewolf, M. 2018, PhD thesis, Friedrich-Alexander-Universität Erlangen-Nürnberg [[LINK](#)]
- Schindewolf, M., Németh, P., Heber, U. et al. 2018, *A&A*, 620, A36
- Schlafly, E. F. & Finkbeiner, D. P. 2011, *ApJ*, 737, 103
- Schlafly, E. F., Meisner, A. M. & Green, G. M. 2019, *ApJS*, 240, 30
- Schlegel, D. J., Finkbeiner, D. P. & Davis, M. 1998, *ApJ*, 500, 525
- Schmid-Burgk, J. 1975, *A&A*, 40, 249

- 
- Schneider, D. 2017, Spectroscopic Analysis of the  $^3\text{He}$  Anomaly in B-Type Stars, Friedrich-Alexander-Universität Erlangen-Nürnberg [LINK]
- Schneider, D., Irrgang, A., Heber, U. et al. 2017, *Open Astronomy*, 26, 139
- . 2018, *A&A*, 618, A86
- Schoening, T. & Butler, K. 1989, *A&AS*, 78, 51
- Schönrich, R., McMillan, P. & Eyer, L. 2019, *MNRAS*, 487, 3568
- Schrijvers, C., Telting, J. H., Aerts, C. et al. 1997, *A&AS*, 121, 343
- Schwab, J. 2018, *MNRAS*, 476, 5303
- Secrest, N. J., Dudik, R. P., Dorland, B. N. et al. 2015, *ApJS*, 221, 12
- Serenelli, A. M., Althaus, L. G., Rohrmann, R. D. et al. 2002, *MNRAS*, 337, 1091
- Shamey, L. J. 1969, PhD thesis, University of Colorado, Boulder
- Shanks, T., Metcalfe, N., Chehade, B. et al. 2015, *MNRAS*, 451, 4238
- Silvotti, R., Uzundag, M., Baran, A. S. et al. 2019, *MNRAS*, 489, 4791
- Sim, S. A., Röpke, F. K., Hillebrandt, W. et al. 2010, *ApJL*, 714, L52
- Slettebak, A. & Brundage, R. K. 1971, *AJ*, 76, 338
- Smette, A., Sana, H., Noll, S. et al. 2015, *A&A*, 576, A77
- Soszyński, I., Stępień, K., Pilecki, B. et al. 2015, *Acta Astronomica*, 65, 39
- Stark, M. A. & Wade, R. A. 2003, *AJ*, 126, 1455
- Stassun, K. G. & Torres, G. 2018, *ApJ*, 862, 61
- Stepanian, J. A. 2005, *Revista Mexicana de Astronomía y Astrofísica*, 41, 155
- Sterzik, M., Schuez, O., Conn, B. et al. 2006, *La Silla Observatory - FEROS-II User Manual*, European Southern Observatory [LINK]
- Stobie, R. S., Kilkeny, D., O'Donoghue, D. et al. 1997, *MNRAS*, 287, 848
- Stroeer, A., Heber, U., Lisker, T. et al. 2007, *A&A*, 462, 269
- Sweigart, A. V. 1987, *ApJS*, 65, 95
- . 1997a, *ApJL*, 474, L23
- Sweigart, A. V. 1997b, in *The Third Conference on Faint Blue Stars*, ed. A. G. D. Philip, J. Liebert, R. Saffer, & D. S. Hayes, 3
- Taylor, M. B. 2005, in *Astronomical Society of the Pacific Conference Series, Vol. 347, Astronomical Data Analysis Software and Systems XIV*, ed. P. Shopbell, M. Britton, & R. Ebert, 29

## Bibliography

---

- Thompson, G. I., Nandy, K., Jamar, C. et al. 1978, Catalogue of stellar ultraviolet fluxes : a compilation of absolute stellar fluxes measured by the Sky Survey Telescope (S2/68) aboard the ESRO satellite TD-1 /
- Tremblay, P. E. & Bergeron, P. 2009, *ApJ*, 696, 1755
- Tull, R. G. 1998, in *Proceedings of the SPIE*, Vol. 3355, *Optical Astronomical Instrumentation*, ed. S. D'Odorico, 387–398
- UKIDSS Consortium. 2012, *VizieR Online Data Catalog*, II/316
- Unglaub, K. 2008, *A&A*, 486, 923
- Unglaub, K. & Bues, I. 2001, *A&A*, 374, 570
- van Altena, W. F., Lee, J. T. & Hoffleit, E. D. 1995, *The general catalogue of trigonometric [stellar] parallaxes*
- Van Der Walt, S., Colbert, S. C. & Varoquaux, G. 2011, *ArXiv e-prints [ADS]*
- Van Grootel, V., Charpinet, S., Fontaine, G. et al. 2014, in *Astronomical Society of the Pacific Conference Series*, Vol. 481, *6th Meeting on Hot Subdwarf Stars and Related Objects*, ed. V. van Grootel, E. Green, G. Fontaine, & S. Charpinet, 115
- Van Grootel, V., Charpinet, S., Fontaine, G. et al. 2008, *A&A*, 488, 685
- van Kerkwijk, M. H., Bassa, C. G., Jacoby, B. A. et al. 2005, in *Astronomical Society of the Pacific Conference Series*, Vol. 328, *Binary Radio Pulsars*, ed. F. A. Rasio & I. H. Stairs, 357
- van Leeuwen, F. 2007, *A&A*, 474, 653
- van Leeuwen, F., Evans, D. W., De Angeli, F. et al. 2017, *A&A*, 599, A32
- Vauclair, G. & Liebert, J. 1987, in *Astrophysics and Space Science Library*, Vol. 129, *Exploring the Universe with the IUE Satellite*, ed. Y. Kondo & W. Wamsteker, 355–376
- Vauclair, S. 1975, *A&A*, 45, 233
- Vauclair, S., Michaud, G. & Charland, Y. 1974, *A&A*, 31, 381
- Vennes, S., Kawka, A. & Németh, P. 2011, *MNRAS*, 410, 2095
- Vennes, S., Kawka, A., O'Toole, S. J. et al. 2012, *ApJL*, 759, L25
- Vernet, J., Dekker, H., D'Odorico, S. et al. 2011, *A&A*, 536, A105
- Vidal, C. R., Cooper, J. & Smith, E. W. 1970, *J. Quant. Spec. Radiat. Transf.*, 10, 1011
- . 1971, *J. Quant. Spec. Radiat. Transf.*, 11, 263
- . 1973, *ApJS*, 25, 37
- Virtanen, P., Gommers, R., Oliphant, T. E. et al. 2020, *Nature Methods*, 17, 261

- 
- Vogt, S. S., Allen, S. L., Bigelow, B. C. et al. 1994, in Proceedings of the SPIE, Vol. 2198, Instrumentation in Astronomy VIII, ed. D. L. Crawford & E. R. Craine, 362
- Vos, J., Østensen, R. & Van Winckel, H. 2014, in Astronomical Society of the Pacific Conference Series, Vol. 481, 6th Meeting on Hot Subdwarf Stars and Related Objects, ed. V. van Grootel, E. Green, G. Fontaine, & S. Charpinet, 265
- Vos, J., Østensen, R. H., Degroote, P. et al. 2012, A&A, 548, A6
- Vos, J., Østensen, R. H., Németh, P. et al. 2013, A&A, 559, A54
- Vos, J., Østensen, R. H., Vučković, M. et al. 2017, A&A, 605, A109
- Vrancken, M., Butler, K. & Becker, S. R. 1996, A&A, 311, 661
- Wall, R. E., Kilic, M., Bergeron, P. et al. 2019, MNRAS, 489, 5046
- Wamsteker, W., Skillen, I., Ponz, J. D. et al. 2000, Ap&SS, 273, 155
- Wang, B. & Han, Z.-W. 2010, Research in Astronomy and Astrophysics, 10, 681
- Webbink, R. F. 1984, ApJ, 277, 355
- Werner, K. 1986, A&A, 161, 177
- . 1989, A&A, 226, 265
- Wes McKinney. 2010, in Proceedings of the 9th Python in Science Conference, ed. Stéfan van der Walt & Jarrod Millman, 56 – 61
- Wisotzki, L., Koehler, T., Groote, D. et al. 1996, A&AS, 115, 227
- Wolf, C., Onken, C. A., Luvaul, L. C. et al. 2018, PASA, 35, e010
- Woudt, P. A., Kilkenny, D., Zietsman, E. et al. 2006, MNRAS, 371, 1497
- Xiong, H., Chen, X., Podsiadlowski, P. et al. 2017, A&A, 599, A54
- Xu, S., Zhang, B., Reid, M. J. et al. 2019, ApJ, 875, 114
- Yi, S. K. & Yoon, S.-J. 2004, Ap&SS, 291, 205
- Zangwill, W. I. 1967, The Computer Journal, 10, 293 [LINK]
- Zhang, X. & Jeffery, C. S. 2012, MNRAS, 419, 452
- Zinn, J. C., Pinsonneault, M. H., Huber, D. et al. 2019, ApJ, 878, 136

## Acknowledgements

The author of this work was supported by the Deutsche Forschungsgemeinschaft (DFG) under grants HE 1356/70-1 and IR 190/1-1. The author is very grateful to the DFG for financing several business trips, including international meetings at conferences (for instance, the *8th/9th Meeting on Hot Subdwarfs and Related Objects* in Cracow 2017/Hendaye 2019) and workshops (for instance, the *Second Gaia Data Workshop* in Heidelberg 2018). Furthermore, the DFG financed the author's first observing run at the William Herschel Telescope (WHT) on La Palma in 2017. The author is also very grateful to the European Southern Observatory (ESO) for financing the observing run at the La Silla Observatory in Chile in 2019. This work is based on observations collected at the Cerro Paranal Observatory of ESO in Chile under the following program IDs: 096.D-0055(A), 098.C-0754(A), 093.D-0415(A), 60.A-9022(C), 189.B-0925(C), 076.B-0055(A), 69.C-0171(A), and 167.D-0407(A). Moreover, it is based on observations collected at the La Silla Observatory of ESO in Chile under the following program IDs: 073.D-0495(A), 074.B-0455(A), 076.D-0355(A), 077.D-0515(A), 078.D-0098(A), and 086.D-0714(A). Based on observations made at the Centro Astronómico Hispano Alemán (CAHA) at Calar Alto, operated jointly by the Max-Planck-Institut für Astronomie (MPIA) and the Instituto de Astrofísica de Andalucía (IAA), which belongs to the Consejo Superior de Investigaciones Científicas (CSIC). Based on observations conducted at the Observatorio del Roque de los Muchachos operated by the Isaac Newton Group of Telescopes (ING) on La Palma as well as on observations made at the McDonald Observatory in Austin operated by the University of Texas. Some of the data presented in this work were obtained at the W. M. Keck Observatory, which is operated as a scientific partnership among the California Institute of Technology, the University of California, and the National Aeronautics and Space Administration. The Observatory was made possible by the generous financial support of the W. M. Keck Foundation. The author wishes to recognize and acknowledge the very significant cultural role and reverence that the summit of Mauna Kea has always had within the indigenous Hawaiian community. We are most fortunate to have the opportunity to conduct observations from this mountain. The MMT spectra mentioned in this work were obtained at the Multiple Mirror Telescope Observatory (MMTO), a joint facility of the University of Arizona and the Smithsonian Institution. The author wants to thank Prof. Dr. Ulrich Heber, Prof. Dr. Dr. Stephan Geier, Dr. Marilyn Latour, and Dr. Heinz Edelman for sharing their observational data. This work has made use of data from the European Space Agency (ESA) mission *Gaia* (<https://www.cosmos.esa.int/gaia>), processed by the *Gaia* Data Processing and Analysis Consortium (DPAC, <https://www.cosmos.esa.int/web/gaia/dpac/consortium>). Funding for the DPAC has been provided by national institutions, in particular the institutions participating in the *Gaia* Multilateral Agreement. This publication makes use of data products from the Two Micron All Sky Survey (2MASS), which is a joint project of the University of

Massachusetts and the Infrared Processing and Analysis Center/California Institute of Technology, funded by the National Aeronautics and Space Administration and the National Science Foundation. This publication makes use of data products from the Wide-field Infrared Survey Explorer (WISE), which is a joint project of the University of California, Los Angeles, and the Jet Propulsion Laboratory/California Institute of Technology. WISE is funded by the National Aeronautics and Space Administration. This research makes use of data collected within the third observation period of The Sloan Digital Sky Survey (SDSS-III). Funding for SDSS-III has been provided by the Alfred P. Sloan Foundation, the Participating Institutions, the National Science Foundation, and the U.S. Department of Energy Office of Science. The SDSS-III web site is <http://www.sdss3.org/>. SDSS-III is managed by the Astrophysical Research Consortium for the Participating Institutions of the SDSS-III Collaboration including the University of Arizona, the Brazilian Participation Group, Brookhaven National Laboratory, University of Cambridge, Carnegie Mellon University, University of Florida, the French Participation Group, the German Participation Group, Harvard University, the Instituto de Astrofísica de Canarias, the Michigan State/Notre Dame/JINA Participation Group, Johns Hopkins University, Lawrence Berkeley National Laboratory, Max Planck Institute for Astrophysics, Max Planck Institute for Extraterrestrial Physics, New Mexico State University, New York University, Ohio State University, Pennsylvania State University, University of Portsmouth, Princeton University, the Spanish Participation Group, University of Tokyo, University of Utah, Vanderbilt University, University of Virginia, University of Washington, and Yale University. This research makes use of data collected within SkyMapper's Southern Sky Survey. The national facility capability for SkyMapper has been funded through ARC LIEF grant LE130100104 from the Australian Research Council (ARC), awarded to the University of Sydney, the Australian National University (ANU), Swinburne University of Technology, the University of Queensland, the University of Western Australia, the University of Melbourne, Curtin University of Technology, Monash University, and the Australian Astronomical Observatory. SkyMapper is owned and operated by The Australian National University's Research School of Astronomy and Astrophysics. The survey data were processed and provided by the SkyMapper Team at ANU. The SkyMapper node of the All-Sky Virtual Observatory (ASVO) is hosted at the National Computational Infrastructure (NCI). Development and support of the SkyMapper node of the ASVO has been funded in part by Astronomy Australia Limited (AAL) and the Australian Government through the Commonwealth's Education Investment Fund (EIF) and National Collaborative Research Infrastructure Strategy (NCRIS), particularly the National eResearch Collaboration Tools and Resources (NeCTAR) and the Australian National Data Service (ANDS) Projects. This research makes use of data obtained with the Pan-STARRS1 Surveys (PS1), which have been made possible through contributions of the Institute for Astronomy, the University of Hawaii, the Pan-STARRS Project Office, the Max-Planck Society and its participating institutes, the Max Planck Institute for Astronomy, Heidelberg, and the Max Planck Institute for Extraterrestrial Physics, Garching, The Johns Hopkins University, Durham University, the University of Edinburgh, Queen's University Belfast, the Harvard-Smithsonian Center for Astrophysics, the Las Cumbres Observatory Global Telescope Network Incorporated, the National Central University of Taiwan, the Space Telescope Science Institute, the National Aeronautics and Space Administration under Grant No. NNX08AR22G issued

through the Planetary Science Division of the NASA Science Mission Directorate, the National Science Foundation under Grant No. AST-1238877, the University of Maryland, and Eötvös Loránd University (ELTE). Based on observations made with the NASA Galaxy Evolution Explorer (GALEX). GALEX is operated for NASA by the California Institute of Technology under NASA contract NAS5-98034. Based on observations made with the Deep Near Infrared Survey (DENIS) of the Southern Sky. The DENIS project has been partly funded by the SCIENCE and the HCM plans of the European Commission under grants CT920791 and CT940627. It is supported by INSU, MEN and CNRS in France, by the State of Baden-Württemberg in Germany, by DGICT in Spain, by CNR in Italy, by FFwFBWF in Austria, by FAPESP in Brazil, by OTKA grants F-4239 and F-013990 in Hungary, and by the ESO C&EE grant A-04-046. Jean Claude Renault from IAP was the Project manager. Observations were carried out thanks to the contribution of numerous students and young scientists from all involved institutes, under the supervision of P. Fouqué, survey astronomer resident in Chile. This work has used data releases 6 (Lucas et al., 2008; UKIDSS Consortium, 2012) and 9 (Lawrence et al., 2013) of the UKIRT Infrared Deep Sky Survey (UKIDSS). The UKIDSS project is defined in Lawrence et al. (2007). UKIDSS uses the UKIRT Wide Field Camera (WFCAM; Casali et al. 2007). The photometric system is described in Hewett et al. (2006) and the calibration is described in Hodgkin et al. (2009). The pipeline processing and science archive are described in Irwin et al. (in prep.) and Hambly et al. (2008). This publication has made use of data from the VISTA Kilo-Degree Infrared Galaxy Survey (VIKING), from the VISTA Magellanic Survey (VMC) as well as from the VISTA Hemisphere Survey (VHS) at the ESO Paranal Observatory. This work has used data release 4 of VIKING, data release 4 of VMC, and data release 6 of VHS (<http://horus.roe.ac.uk/vsa/index.html>). Data processing has been contributed by the VISTA Data Flow System at CASU, Cambridge and WFAU, Edinburgh. The VISTA Data Flow System pipeline processing and science archive are described in Irwin et al. (2004), Hambly et al. (2008), and Cross et al. (2012). Some of the data presented in this work were obtained from the Mikulski Archive for Space Telescopes (MAST) at the Space Telescope Science Institute (STScI), including data collected by the Transiting Exoplanet Survey Satellite (TESS) mission. STScI is operated by the Association of Universities for Research in Astronomy, Inc., under NASA contract NAS 5-26555. Support for MAST for non-HST data is provided by the NASA Office of Space Science via grant NNX13AC07G and by other grants and contracts. Funding for the TESS mission is provided by the NASA Explorer Program. This work made use of observations performed by the International Ultraviolet Explorer (IUE). The corresponding data were extracted from the INES (IUE Newly Extracted Spectra) System. This research made use of the Tool for Operations on Catalogues and Tables (TOPCAT), an interactive graphical viewer and editor for tabular data (Taylor, 2005). This work made use of the Interactive Spectral Interpretation System (ISIS; Houck & Denicola 2000), which is based on the S-Lang scripting language. This work used part of the set of ISIS-functions developed and supported by the Massachusetts Institute of Technology (MIT) and the Dr. Remeis-Observatory & Erlangen Centre for Astroparticle Physics (ECAP; <http://www.sternwarte.uni-erlangen.de/isis/>, stellar-isiscripts). Part of the figures in this work were rendered using the slxfig interface of S-Lang that was developed by J. E. Davis. This research made use of the extensive standard library as well as of some

of the additional packages, modules, and libraries incorporated in the interpreted high-level general-purpose programming language python (<https://www.python.org/>), which was developed by the Python Software Foundation in 1991. Inter alia, SciPy (Jones et al., 2001; Virtanen et al., 2020), Matplotlib (Hunter, 2007), NumPy (Oliphant, 2006; Van Der Walt et al., 2011), pandas (Wes McKinney, 2010), scikit-learn (Pedregosa et al., 2011), and Astropy (Astropy Collaboration et al., 2013, 2018) have been used. Moreover, this research has made extensive use of NASA's Astrophysics Data System (ADS) and the SIMBAD and VizieR databases, operated at CDS, Strasbourg, France. Special thanks to Ralf Napiwotzki for the development of the spectral analysis program FITPROF (Napiwotzki, 1999) and its successor FITSB2 (Napiwotzki et al., 2004b) as well as to Heiko Hirsch, the developer of the Spectrum Plotting and Analysis Suite (SPAS; Hirsch 2009). The hybrid approach (ADS) used in this work is based on Kurucz' ATLAS9/ATLAS12 local thermodynamic equilibrium (LTE) model atmospheres (Kurucz 1993; 1996, extended and updated), on non-LTE (NLTE) occupation number density calculations within DETAIL as well as on spectral syntheses with SURFACE (Giddings 1980; Butler & Giddings 1985, extended and updated). Inter alia, the three codes ATLAS12, DETAIL, and SURFACE have been extensively updated by Dr. Andreas Irrgang and Prof. Dr. Norbert Przybilla (Irrgang et al., 2014, 2018). This work also used the latest version of the TLUSTY code for atmospheric modelling as well as that of the SYNSPEC code for NLTE line formation and synthesis (Hubeny & Lanz, 2017a,b,c). Some parts of these acknowledgements were compiled using the (Astronomy) Acknowledgement Generator (<https://astrofrog.github.io/acknowledgment-generator/>).

## The “Real” Acknowledgements

This is where I would like to thank each and everyone without whom the analysis and the writing of this thesis certainly would not have been possible at all. Without the technical and not to forget mental support, I would never have been able to reach such an important milestone in my personal career.

First of all, I would like to thank my (doctoral) supervisors Prof. Dr. Ulrich Heber from the Dr. Remis-Observatory & ECAP (University of Erlangen-Nürnberg) and Prof. Dr. Dr. Stephan Geier from the Institute for Physics and Astronomy (University of Potsdam) for their tremendous support during the last five years of research on this very interesting topic. On the one hand, I would like to explicitly thank you both for the great opportunities you have given me to get involved in the international research environment, that is, to visit conferences and seminars to get in touch with PhD students, postdocs, and professors from all around the globe (Thank you Tiara, Roberto, Peter, Thomas, Ingrid, Conor, Joris, Alexander, and Barbara for the incredible time we had together!) as well as to be able to write proposals for observing time and, not least, to observe with different telescopes around the world myself. To mention only some examples: I enjoyed the conferences on *Hot Subdwarf Stars and Related Objects* in Cracow in July 2017 as well as in Hendaye in June 2019 (it was funny to observe an impressed Zhanwen Han taking pictures of my mass distribution while I was presenting it on stage), including all of the numerous social events and the sightseeing that took place, and I only have good memories of my very first observing run together with Stephan Geier at the William Herschel Telescope on La Palma (also in July 2017), despite the fact that I had quite a hard time getting to the site... The same applies to my second observing run, which took place at the La Silla Observatory in Chile in August 2019. It was incredible to watch the most beautiful night sky that I have ever seen! Moreover, the *Second Gaia Data Workshop* at the “Haus der Astronomie” on Königstuhl in Heidelberg in June 2018 has helped me a lot in order to correctly interpret the astrometric data from *Gaia*. I really enjoyed my time in Heidelberg visiting one of the most beautiful castles I have ever seen and going for a long walk on the “Philosophenweg”. In this context: Sorry, Roberto, for taking the wrong connection (to Berlin) on our outward journey from Frankfurt Central Station! On the other hand, I am grateful for having had the opportunity to work as an independent researcher, not least because of the privilege to publish papers (and conference proceedings) as a (co-)author. I am very proud of my contribution to the publication “*A hot subdwarf-white dwarf super-Chandrasekhar candidate supernova Ia progenitor*” in *Nature Astronomy* (Pelisoli et al., 2021) that lead to press releases at various institutes around the world. I also enjoyed the supervision of several bachelor, master and teacher students at the Dr. Remis-Observatory in Bamberg. In particular, however, I would like to emphasize the friendly but professional relationship with my doctoral supervisor Prof. Dr. Ulrich Heber, who always had an open ear and was able to

help me enormously in understanding the theoretical background of my thesis. Although he sometimes completely disagreed with me and my own ideas due to his long-term professional experience, our discussions were very fruitful and only improved the quality of the present work.

My explicit thanks go to Dr. Andreas Irrgang who provided me most of his ISIS analysis scripts and assisted and advised me on how to use them correctly. Whenever I had questions about the hybrid LTE/NLTE ADS models and the global analysis strategy, I always could address myself to him. Furthermore, I am extremely grateful that Dr. Marilyn Latour, Dr. Markus Schindewolf, and Matti Dorsch helped me to understand the deep mechanisms, the structure, and the usage of TLUSTY/SYNSPEC. This has really saved me hours reading manuals. I am very grateful for having worked at the Dr. Remeis-Observatory. It is not self-evident to work together with people sharing their experience and knowledge in such a warm atmosphere. I tremendously benefited from the long-established people, but also loved to share my own knowledge with the younger generation of astronomers during the  $\sim 15$  lab courses that took place at Remeis during my time there or with all of the curious children and adults during my guided tours at the observatory. Actually, the whole astronomy group made life so much easier. My special thanks here go to Marilyn (Thanks for the fun time we spent together at numerous lunch meetings and walks, in bars/restaurants, and, of course, in front of numerous stands that sold mulled wine!), Dr. Manuel Castro (I hope, you are doing fine on the other side of the world and you are having a Schnitzel while I am writing this!), Dominic Bernreuther, Dr. Simon Kreuzer, Matti (I will never forget our numerous cinema evenings, especially the one in August 2017, where we could watch "Mission Impossible - Fallout" in an otherwise completely empty cinema auditorium!), and Jakob Stierhof. In addition, I would like to thank my (former) Drechsel room (crazy office?) mates Dr. Jonathan Knies (Thanks for spending so much time with me on hiking trips, in bars/restaurants, in the cinema, at movie evenings at your place, on the "Age of Empires" and "Warhammer" battlefields, in the enchanting worlds of Trine, on the deck of the ghost ship "SS Ourang Medan", and at the numerous other (virtual) opportunities I forgot to mention here! You have really become one of my closest friends, with whom I would also remove old finger nails from dirty and moldy dishes! Euh, wait a second...), Dr. Roberto Raddi (Will Napoli ever become champion of the Serie A again? Thanks for all the fun (and memes) you brought to our office!), Markus (Thanks for sharing your Remeis secrets with me and for showing me how to handle the astronomical clock on the second floor!), Dr. Sara Saeedi (Thanks for the "fresh air" in our office and the nice dinner evenings we spent together as a group at your place!), Maximilian Wolz (Thanks for becoming one of my closest friends, for being such a nice person in general, and for spending so much time with me at "Spezi", at your place, in the train on our way to Erlangen/Bamberg, etc.. Also, thanks for your "flying visits" in Bamberg, while working hard for your own traineeship and, of course, thank you for the basketball hoop that you brought to our office! The "ball accidents" were absolutely legendary! Well, at least for all but Sarah...), Steven Hämmerich (Thanks for all the memes you brought into my life and for realizing many of my own ideas! The "Remeis Meme Wall" that you created is absolutely amazing!), Lars Möller (Thanks for all the time we spent together on "Summoner's Rift"!), and, last but not least, Katrin Reisdorf (Thanks for letting me become one of your friends and making it possible to take my first steps in the

endless worlds of “Dungeons and Dragons”! Special thanks also to Felix Schmidt!). I also enjoyed the extremely helpful discussions we had, not only about my own work, but also about your interesting scientific research projects. Certainly, there has also been room for plenty of fun, which made daily working life so much easier for me. I love the fact that the Drechsel office has potentially created a new era at Remeis by inventing the concept of “The book of...”. Furthermore, our “Machs-Doch-Einfach” motto has really helped me a lot to carry on! This work has greatly benefited from the well-organized team of administrators at the Dr. Remeis-Observatory. In particular, Prof. Dr. Jörn Wilms, Dr. Ingo Kreykenbohm, Dr. Thomas Dauser, Dr. Matthias Kühnel, Dr. Simon Kreuzer, Philipp Weber, Jakob Stierhof and others always invest(ed) an enormous time for maintaining and improving the “Remeis Computer Cluster” that has been extensively used for the present work. Thank you all for keeping the `kubuntu KDE/Xfce` desktop environments up-to-date and for taking care of the strong computing resources at Remeis such that we “users” have the possibility to run parallelized jobs via the integrated workload manager `slurm`. I would also like to take this opportunity to deeply thank the entire Förderverein for the support and care of the old but lovely institute. Additionally, I would like to highlight my former fellow students Jens Holzmeier, Lisa Seitz, Philipp Schuster, Maximilian Düll, Mona Pistel, and Florian Wolz. Although working on very different (physical) topics for your own PhD/master or not at all working in science anymore, you have been very helpful by just letting me know that I am not the only one that has difficulties and struggles in everyday life. I really appreciate our motivating regular meetings here and there and the fruitful discussions, especially the ones at home, on hiking trips, in bars, in cinemas, and/or at (outdoor) concerts. This has certainly helped me to keep my own work-life balance, especially during difficult times. Special thanks to Jens for being the best and most reliable lab course partner that you can imagine! And thanks to both of you, Lisa and Jens, for two unforgettable weeks on Iceland in September 2019, right before the start of the COVID-19 pandemic! I have really fallen in love with this island ever since! Not only my former fellow students but also my former school friends in and around Erlangen have always encouraged me to not just quit but continue my research project, although it was not easy with me from time to time. Thank you so so much Andreas Voinea, Dominik Penk, Florian Zmija, Maximilian Pritsching, Christoph Biernoth, David Weiß, Jonas Wilkes, Sabine Thiele, and Timo Spiekermann, especially for our weekly/monthly Skype sessions during the pandemic! I am extremely grateful for having such long-term friends like you because this is really refreshing in the short-lived times of instant messaging and social networking. I really hope that our paths will not diverge in the future! Thanks to you too, Mikola Schlottke, my childhood friend, that our bond has not broken after such a long time. Last but not least, this entire work would definitely not have been possible at all without the enormous support and love that I always receive from my parents Edgar Josef Schneider and Veronika Marie Schneider, née Bucek. They always provide me a safe environment and a place which I really can call my home, even though I am not living there anymore. Especially during the changing year of 2017 (submission of my master thesis, start of my PhD phase, move to the lovely city of Bamberg) they helped me incredibly. But not only that they essentially supported me financially, they have always been a great support in extremely bad mental breakdowns, not only because of COVID being omnipresent. Thank you dad for making me

what I am today and for always being there for me (#back office)! Thanks for introducing me to the world of computer games and for playing with me and my friends (even today after so many years!). Who can really say this about their father? I am so so grateful for this! Thank you mom for preparing me to stand on my own feet! I am very thankful that both of you always believe in me and that I have your full support and confidence at all the things I (still want to) do in my life. Thank you for accepting my decision to pursue a PhD in astronomy and for going through the last five difficult years with me (sorry it took so long...)! Therefore, this work is definitely dedicated to both of you!

I would like to thank each and every person and moment on my journey that helped me directly or indirectly to reach this crucial point in my life. Honestly, I would be lying if I said my life has always been great. Sometimes "Life Is Strange", right? Of course, there have been valleys and mountains that made me what I am today. Namely, personally grown, grateful for my family and friends, and, last but not least, incredibly happy that I reached this milestone. I am looking forward to a bright future and to new challenges to come!

P.S.: Thank you very much, Nili, for all the #GerMondays (and other streams) we have spent together. These events really lifted my mood during the extremely difficult times of the COVID-19 pandemic and during my own demotivation phases. Thank you for always cheering me up with your gameplay and your (non-)professional casting! You are a true humorous "Age of Empires" legend ("A castle age conquistador walks into a bar. Sadly, there is no counter...")!

Holy guacamole, that was (it)!

*"I wish, I could stay in this moment forever. I guess, I actually can now, but then it wouldn't be a moment."*

**Maxine Caulfield in Life Is Strange**

*"Wherever I end up after this... in whatever reality... all those moments between us were real, and they'll always be ours."*

**Chloe Elizabeth Price in Life Is Strange**

*"When a door closes, a window opens... Or something like that."*

**Maxine Caulfield in Life Is Strange**